

Sheffield Hallam University

Novel aluminium alloys for thermal spray applications to steel substrates.

SETH, Sampan.

Available from the Sheffield Hallam University Research Archive (SHURA) at:

<http://shura.shu.ac.uk/20345/>

A Sheffield Hallam University thesis

This thesis is protected by copyright which belongs to the author.

The content must not be changed in any way or sold commercially in any format or medium without the formal permission of the author.

When referring to this work, full bibliographic details including the author, title, awarding institution and date of the thesis must be given.

Please visit <http://shura.shu.ac.uk/20345/> and <http://shura.shu.ac.uk/information.html> for further details about copyright and re-use permissions.

Learning and Information Services
Adsetts Centre, City Campus
Sheffield S1 1WD

28079

102 056 933 6



Sheffield Hallam University
Learning and Information Services
Adsetts Centre, City Campus
Sheffield S1 1WD

REFERENCE

ProQuest Number: 10700991

All rights reserved

INFORMATION TO ALL USERS

The quality of this reproduction is dependent upon the quality of the copy submitted.

In the unlikely event that the author did not send a complete manuscript and there are missing pages, these will be noted. Also, if material had to be removed, a note will indicate the deletion.



ProQuest 10700991

Published by ProQuest LLC (2017). Copyright of the Dissertation is held by the Author.

All rights reserved.

This work is protected against unauthorized copying under Title 17, United States Code
Microform Edition © ProQuest LLC.

ProQuest LLC.
789 East Eisenhower Parkway
P.O. Box 1346
Ann Arbor, MI 48106 – 1346

**Novel aluminium alloys for thermal
spray applications to steel
substrates**

Sampan Seth

Thesis submitted for the award of Doctor of
Philosophy

Materials and Engineering Research Institute,
Sheffield Hallam University

March 2015

I would like to dedicate this work to my wife
(Mrs. Tanvi Seth), mother (Mrs. Shilpi Seth),
father (Dr. Deepak Seth) and grandfather
((Late) Dr. P.N. Seth)

Table of Contents

Acknowledgement	v
Declaration	vi
Nomenclature	vii
Abstract	xxxii
CHAPTER 1:Introduction	1
1.1 Motivation	1
1.1 Aim of the project	3
1.2 Objectives.....	4
CHAPTER 2:Literature Review	5
2.1 Introduction, background and use of coatings	5
2.2 Thermal spraying: A brief history and current status	7
2.3 Important thermal spraying processes.....	13
2.4 Formation and Microstructure of thermal spray coating.....	16
2.5 Thermally sprayed aluminium (Al) coatings.....	18
2.6 Sacrificial anodes.....	21
2.6.1 A brief introduction to Galvanic corrosion.....	21
2.6.2 Factors affecting Galvanic corrosion.....	22
2.6.3 Requirements of sacrificial anode.....	24
2.6.4 A brief history of cathodic protection.....	26
2.6.5 The basics of cathodic protection.....	27
2.7 A brief introduction to application and limitation of Al as sacrificial anode material.....	29
2.8 Alloying of Al : Enhancement of sacrificial properties.....	31

2.8.1 Background on alloying Al for improving the electrochemical properties.....	32
2.8.2 Mechanism of activation of Al alloys: Lattice expansion.....	39
2.8.3: Thermodynamics of activation of Al alloys: Surface enrichment.....	45
2.8.4 Experimental validation of Surface enrichment theory for Al alloys.....	58
2.8.5 The effect of Zn addition on electrochemical properties of Al alloys.....	79
2.8.6 The effects of ternary addition on Al-Zn alloys.....	84
2.8.6.1 The effects of Si and Cu on the electrochemical performance of Al-Zn- (In,Sn,Hg,Ga) alloys.....	85
2.8.6.2 Understanding the mechanism of activation of Al-Zn alloys by depassivators.....	90
2.8.6.3 Understanding the activation of Al-Zn and In.....	96
2.9 The addition of Ti to produce wear resistant Al alloys.....	110
2.9.1 Background on wear of materials.....	110
2.9.2 Aluminium-Titanium (Ti) alloy system.....	114
2.9.3 Aluminium-Titanium-Carbon alloy system.....	124

CHAPTER 3: Experimental Methodology 136

3.1 Introduction.....	136
3.2 Sample Preparation.....	137
3.2.1 Materials used.....	137
3.2.2 Substrate preparation - Grit blasting.....	137
3.2.3 Coating preparation - Arc Spraying.....	138
3.3 Sample preparation of arc sprayed coatings for metallographic analysis.....	141
3.3.1 Background.....	141
3.3.2 Sample preparation for microstructural investigations – Alloys.....	142
3.3.3 Sample preparation for microstructural investigations – Coatings.....	143
3.4 Electron Microscopy.....	145
3.4.1 A brief introduction to operating principles of SEM.....	145

3.4.2 Back scattered electron imaging, Secondary electron imaging and EDS analysis.....	147
3.5 X-Ray Diffraction (XRD).....	150
3.5.1 A brief introduction to operating principles of XRD.....	150
3.5.2 X-ray Diffractometer and Bragg-Brentano geometry arrangement.....	151
3.6 Determination of corrosion resistance of Al-Zn-In and Al-Ti-C coatings.....	153
3.6.1 Neutral Salt Spray Corrosion Tests.....	154
3.6.2 Open-circuit potential (OCP) measurements.....	157
3.6.3 Galvanic corrosion test- Zero resistance Ammetry (ZRA).....	158
3.6.4 Electrochemical Impedance Spectroscopy (EIS).....	160
3.7 Assessment of mechanical properties of coatings.....	165
3.7.1 Micro-hardness measurement.....	166
3.8 Wear Resistance performance of Al-Ti-C coating.....	168
CHAPTER 4: Results and Discussion-Part 1	173
4.1 Neutral salt spray corrosion testing.....	174
4.1.1 Sacrificial corrosion protection analysis of Al-Zn-In coating in comparison with Zn-Al and pure Al coating.....	174
4.1.1.1 Microstructural analysis of Al and Al-Zn-In coating before and after neutral salt spray corrosion test.....	193
4.2 Open circuit potential vs. time.....	225
4.3 Galvanic corrosion test.....	235
4.4 Electrochemical Impedance Spectroscopy (EIS) analysis.....	255
CHAPTER 4: Results and Discussion-Part 2	278
4.5 Evaluation of coefficient of wear for Al-Ti-C coatings.....	279
4.5.1 Microstructure of Al-Ti-C and pure Al feedstock.....	279
4.5.2 Microstructure of Al-Ti-C alloy and pure Al coatings.....	283

4.5.3 Micro-hardness of Al-Ti-C alloy and pure Al feedstock and coatings.....	287
4.5.4 Coefficient of wear for Al-Ti-C and pure Al feedstock material and coatings.....	290
4.6 The effect of exposure temperature on the microstructure and wear resistance performance of Al-Ti-C coating.....	296
4.6.1 Microstructure of Al-Ti-C coating subjected to 150 ^o C for 1 hour and 3 hours followed by rapid quenching.....	298
4.6.2 Microstructure of Al-Ti-C coating subjected to 350 ^o C for 1 hour and 3 hours followed by rapid quenching.....	305
4.6.3 Microstructure of Al-Ti-C coating subjected to 550 ^o C for 1 hour and 3 hours followed by rapid quenching.....	313
4.6.4 Micro-hardness of Al-Ti-C coating subjected to 150 ^o C, 350 ^o C, 550 ^o C for 1 hour and 3 hours followed by rapid quenching.....	320
4.6.5 Coefficient of wear for Al-Ti-C coating subjected to 150 ^o C, 350 ^o C, 550 ^o C for 1 hour and 3 hours followed by rapid quenching.....	325
4.6.6 Microstructure of Al-Ti-C coating subjected to 150 ^o C for 1 hour and 3 hours followed by exposure to normal room temperature (25 ^o C) for 5 hours.....	337
4.6.7 Microstructure of Al-Ti-C coating subjected to 350 ^o C for 1 hour and 3 hours followed by exposure to normal room temperature (25 ^o C) for 5 hours.....	345
4.6.8 Microstructure of Al-Ti-C coating subjected to 550 ^o C for 1 hour and 3 hours followed by exposure to normal room temperature (25 ^o C) for 5 hours.....	352
4.6.9 Micro-hardness of Al-Ti-C coating subjected to 150 ^o C, 350 ^o C, 550 ^o C for 1 hour and 3 hours followed by normal room temperature cooling for 5 hours.....	359
4.6.10 Coefficient of wear for Al-Ti-C coating subjected to 150 ^o C, 350 ^o C, 550 ^o C for 1 hour and 3 hours followed by room temperature cooling for 5 hours.....	364
CHAPTER 5: Conclusion.....	378
CHAPTER 6 Recommendation of future work.....	387
References.....	389
Appendix.....	412

Acknowledgement

I would like to express my profound gratitude towards Dr O.D. Lewis and Dr A.H. Jones for their input as supervisor on the project. I would also like to thank my colleagues and all the technical staff especially Bob Burton and Stuart Creasey from the Materials and Engineering Research Institute (MERI) who have assisted me in the project. A special thanks to all my friends, who have made this endeavour enjoyable.

I would like to thank London and Scandinavian Metallurgical Company (Now AMG-AI) at Rotherham for providing the funding for the project. I would also like to thank Metallisation Ltd at Dudley and Celcoat Ltd at Sheffield to allow me to use their facility and technical advice for producing samples for this project.

Last but not the least, I would like to thank my wife Tanvi and my parents who have supported me throughout my academic career. A special thanks to Dr Greg Gibbons at Warwick Manufacturing group (WMG), University of Warwick, to provide me an opportunity to work as a research assistant at WMG.

Declaration

I hereby declare that this thesis is entirely my own work unless otherwise acknowledged and has not been submitted for the award of a degree at any other Institution. The thesis is set out as per the guidelines issued by Sheffield Hallam University

Part of this thesis has appeared in:

- S.Seth, A.H. Jones, O.D. Lewis, *Wear resistance performance of thermally sprayed Al-Ti alloy measured by three body micro-scale abrasive wear test*, *Wear*, 302(1-2),972-980.
- S.Seth, O.D. Lewis, A.H. Jones, D. Stephenson, M. Boden, S. Thistlethwaite, *A study of corrosion and wear resistance performance of thermally sprayed Al-Zn-In and Al-Ti-C coatings*, In 53rd Corrosion Science Symposium, National Physical Laboratory, Teddington, 6-7 September 2012 (unpublished).
- O.D. Lewis, S. Seth, A.H. Jones, N. Farmilo, D. Stephenson, M. Boden, S. Thistlethwaite, *The development and optimization of aluminium alloys for thermal spray coating application to steel substrates*, In 5th RIPT (Les Recontres Internationales sur la Projection Thermique), Limoges, France, 7-9 December 2011 (Unpublished)
- S.Seth, O.D. Lewis, A.H. Jones, D. Stephenson, M. Boden, S. Thistlethwaite, *A study of novel aluminium alloys for thermally sprayed metallic coatings*, In 52nd Corrosion Science Symposium, September 2011.

Nomenclature

I_{corr}	Corrosion current
I_{anode}	Anodic current
I_{cathode}	Cathodic current
A_{anode}	Area of the anode
A_{cathode}	Area of the cathode
S_1, S_2	Different species of metallic atoms in Al alloy system
$\Delta\sigma$	Surface tension
Γ_{S1}, Γ_{S2}	Gibbs excess concentration per unit area in moles
$\Delta\mu_{S1}, \Delta\mu_{S2}$	Change in chemical potentials of species
X_{S1}, X_{S2}	Mole fraction of the atoms of the species at the surface
N_{S1}, N_{S2}	Mole fraction of the atoms of the species at the bulk
γ_s, γ_b	Activity coefficient of species at surface and bulk
μ_{S1}^0, μ_{S2}^0	Chemical potentials when $a_{S1}=a_{S2}=1$
ΔG^0	Gibbs excess surface energy
A_{S1}, A_{S2}	Surface area of one mole of metal for S_1 and S_2
ΔH	Partial Enthalpies
$H_{\text{Al-Al}}, H_{\text{Al-B}}$	Enthalpies of formation of similar and cross-interaction of Al and B atoms
R	Gas constant
Ω	Atomic interaction parameters
L_m	Latent heat of melting
T_m	Melting temperature
D	Diffusivity
h	Depth
t	Time of sputtering
$N_{V(s)}$	Concentration of vacancies formed on the surface
D_V	Diffusivity due to formation of vacancies
γ_{lp}	Interfacial surface energy of liquid-particle interaction
γ_{sp}	Interfacial surface energy of solid-particle interaction
γ_{ls}	Interfacial surface energy of liquid-solid interaction
ω	Frequency
$V(\omega), I(\omega)$	AC potential and current
θ	Phase difference between applied AC potential and AC current response.
$Z(\omega)$	Impedance
i	Complex number $\sqrt{-1}$
b	Diameter of the wear crater
R	Radius of the rotating ball
Z_p	Impedance of the semi-infinite cylindrical pore
R_p	Resistance per unit depth of the pore
Φ	Phase angle of the defined impedance function Z_p

List of Figures

Figure 2.1	Diagrammatic representation of initial concept of thermal spraying based on pulverising of fluids by high velocity gas ejecting from a nozzle [8,10].	7
Figure 2.2	The famous postcard with Latin inscription " <i>Mucius Scaevola redivivus</i> " (meaning Mucius Scaevola returns) showing Dr Schoop and co-worker with thermal spraying gun or pistol [11].	8
Figure 2.3	Graph showing predictive growth in the thermal spray market in USA [13].	10
Figure 2.4	Graph showing contributions of different countries in European Union in generating € 2.066 billion annual turnover from thermal spraying applications [16].	11
Figure 2.5	Graphs showing contribution of thermal spraying in (a) various industrial sectors (b) application of thermal spraying based on various feedstock materials and (c) application based on different thermal spraying processes [17].	12
Figure 2.6	Schematic diagram of wire arc spraying gun [37].	16
Figure 2.7	Schematic of coating deposition by thermal spraying process [38].	17
Figure 2.8	Schematic of corrosion and wear protection mechanism offered by aluminium alloy coatings to steel structures.	20
Figure 2.9	Galvanic series of metals and alloys in sea water at 25 ⁰ C [55].	22
Figure 2.10	Schematic of formation of a corrosion cell in a metallic structure when exposed to corrosive environment [55].	28
Figure 2.11	The effect of various elements on the electrochemical properties of Al shown by <i>Reding and Newport</i> [82].	33
Figure 2.12	Graphs showing the effect of alloying of (a) de-passivators (b) modifiers on the OCP of Al (vs. SCE) [82,83].	34
Figure 2.13	Al-Sn phase diagram [70].	37

Figure 2.14	Graph showing the effect of Sn concentration (wt%) on the closed circuit potential (CCP) of Al-Sn alloy, coupled with mild steel in 0.1M NaCl solution for 48 hours[85].	38
Figure 2.15	Graph showing the effect of alloying concentration of depassivators and modifiers on the ratio of volume expansion of Al alloys lattice to that of pure Al lattice [88].	43
Figure 2.16	Graph showing the effect of Mg concentration at 1.11mol%, 2.22mol%, 3.32mol% and 4.43mol% (1.00wt%, 2.23wt%, 3.00wt% and 4.00wt%) on solubility of Sn in FCC Al lattice [88].	44
Figure 2.17	Anodic polarisation curves for (1) Al-1wt%Sn, (2) and (2') Al-1wt%In, Al-1wt%In (prepared by vacuum melting), (3) Al-1wt%Zn, (4) Al-5wt%Zn, (5) high purity Al in 0.5M Na ₂ SO ₄ [90].	60
Figure 2.18	Anodic polarisation curves for Al-1wt%Sn alloy subjected to various heat treatment as shown, in 0.5M Na ₂ SO ₄ (high purity Al for comparison) [90].	60
Figure 2.19	The XPS spectra with various sputter times for : (a) Al , (b) Sn, (c) O and (d) Cl, where 1 and 2 represents pure Al and Al-Sn alloys exposed in 3.5%w/v NaCl solution for 1 hour [98].	63
Figure 2.20	Diagrammatic representation of preferential dissolution mechanism (1-6 represents different stages of dissolution), where ○ represents Al ³⁺ ions and ● are Sn ²⁺ and Sn ⁴⁺ ions [51,52].	67
Figure 2.21	GD-OES profile of Al-Pb ₁ alloy subjected to (a) polishing, (b) polishing and heat treatment, (c) polished, heat treated and immersed in 10%w/v NaOH solution for 10 seconds [103].	71
Figure 2.22	TEM analysis of (a) cross-section of heat treated Al-Pb ₁ alloy and (b) cross-section analysis of metal-oxide interface of heat treated Al-Pb ₁ alloy (marked A) with corresponding EDX spectra (point analysis) [103].	72

Figure 2.23	Graphs showing the effect of variation in Pb concentration on: (a) potential vs. time curve for binary Al-Pb alloy in synthetic sea water (ASTM D1141, which was acidified),(b) anodic polarisation behaviour in 5%w/v NaCl solution and (c) the effect of cyclic sample preparation on Al-Pb ₃ alloy in 5%w/v NaCl solution [103].	74
Figure 2.24	Graphs showing (a) Potential vs. time curve for Al alloyed with Bi, In and Sn in acidified artificial sea water (ASTM D1141) and anodic polarisation curves for (b) polished and heat treatment section of Al alloyed with Pb, In,Sn, Bi, (c) polished and heat treated Al-Bi alloy and (d) polished and heat treated Al-In alloys. All the polarisation experiments were conducted in 5%w/v NaCl solution [103].	76
Figure 2.25	Graphs showing (a) potential vs. time for heat treated Al alloyed with Zn and Mg in acidified artificial sea water (ASTM D1141) and (b) heat treated potentiodynamic polarisation of Al alloyed with Zn and Mg in comparison with Pb in 5%w/v NaCl solution [103].	78
Figure 2.26	Al-Zn phase diagram [70].	80
Figure 2.27	Potentiodynamic polarisation curve obtained for Al ₃₂ Zn ₄₉ in 0.1M NaCl solution [107].	81
Figure 2.28	XRD analysis of Al alloyed with (a), (b) 1wt% and 5wt%Zn in comparison with pure Al and Zn (c), (d) 20wt% to 80wt% Zn [106].	82
Figure 2.29	Polarisation curve for Al alloyed with (a) 1wt%, 3wt% and 5wt%Zn (chill and equiaxed macrostructure) and (b) 20wt%, 40wt%, 60wt% and 80wt%Zn in 0.5M NaCl [106].	83
Figure 2.30	Potential vs. time graph comparing the performance of binary Al-Zn and Al-In alloys with ternary Al-Zn-In with different Zn and In concentration in artificial sea water [108].	85
Figure 2.31	Graph showing the effect of In in combination with Fe and Si on the (a) OCP and (b) galvanic efficiency of Al anodes (the experiment was performed in sea water, not specified to ASTM D1141 by the authors, at 1 mA/cm ²) [110].	88
Figure 2.32	Diagrammatic representation of proposed activation mechanism of Al sacrificial anode (a) in presence of In rich phase acting as an anode with Al ₂ O ₃ leading to (b)	90

exposure of Al matrix and (c) subsequent detachment of In rich phase after exposure of Al matrix, suggested by *Hejian and Shizhong* [110].

Figure 2.33	Potential vs. time curve for Al in 0.001M $\text{Hg}(\text{C}_2\text{O}_2\text{H}_3)_2$ solution at pH= 4.2 [112].	92
Figure 2.34	Diagrammatic representation of activation of Al by Hg^{2+} ions showing (a) re-formation of Al_2O_3 oxide layer and (b) surface wetting of Al by Hg when contact angle $\beta < \alpha$ [112].	93
Figure 2.35	(a) Potentiodynamic polarisation and (b) potential vs. time graphs of Al exposed to 0.5M NaCl solution in addition with 0.005 M of Zn^{2+} , Ga^{3+} , In^{3+} and Hg^{2+} ions [114].	94
Figure 2.36	Potentiodynamic polarisation curves for (a) Al alloyed with Zn, In and Hg in binary and ternary form [114] and (b) ternary Al-Zn-In and Al-Zn-Hg alloy [115]. Both exposed to 0.5M NaCl solution.	96
Figure 2.37	Graphs showing the effect of Cl^- , ClO_4^- and SO_4^{2-} anions on the rate of diffusion calculated for different scan rates of polarisation in (a) aqueous and (b) non aqueous media (Dimethylformamide with 0.03wt% water was used as a non-aqueous media by the authors) [119].	98
Figure 2.38	Potentiostatic curve for Zn and Zn-5wt%In in 0.5M NaCl solution, pH maintained at 3 (the authors have corrected for cathodic current, shown in black) [125].	101
Figure 2.39	Potential vs. time graph for Al exposed to 0.5M NaCl solution with addition of Zn^{2+} and In^{3+} sulphate salt of concentration 0.01M ZnSO_4 , 0.005M $\text{In}_2(\text{SO}_4)_3$ or 0.005M ZnSO_4 , 0.0025M $\text{In}_2(\text{SO}_4)_3$ [126].	101
Figure 2.40	SIMS depth profile of Al exposed after exposure to 2M NaCl with 0.0005M In^{3+} and 0.08M Zn^{2+} ions [127].	103
Figure 2.41	Experimental Nyquist plots of Al in 4M KOH solution at (a) -1.95 V, (b) -1.88 V, (c) -1.74 V, (d) -1.70 V, (e) -1.68 V, (f) -1.64 V, (g) -1.60 V, (h) -1.50, (i) -1.46 V, (j) -1.38 V, (k)-1.35 V vs. Hg/HgO [135,136].	105
Figure 2.42	Nyquist plot for Al exposed to 1M H_2SO_4 under potential control condition in order to draw mechanistic information on formation of passive layer [137].	107

Figure 2.43	Nyquist plot for Al-5wt%Zn alloys in 3.5%NaCl solution with In^{3+} addition at concentrations (a) no addition (b) 0.001M (c) 0.002M (d) 0.003M (e) 0.004M (f) 0.005M and (g) 0.006M [138].	108
Figure 2.44	Nyquist plot for Al-0.005wt%In alloy in 3.5% NaCl solution with Zn^{2+} addition at concentrations (a) no addition (b) 0.01M (c) 0.02M (d) 0.03M and (e) 0.04M [138].	108
Figure 2.45	Engraving found on the walls at Saqqara, Egypt showing the use of some kind of lubrication in order to move a heavy metallic statue [141].	110
Figure 2.46	Diagrammatic representation of various forms of wear mechanisms [143].	111
Figure 2.47	Crystal structure of Al_3Ti intermetallic showing (a) L1_2 , (b) DO_{22} and (c) DO_{23} type structure, where \bigcirc represents Al atoms and \bullet Ti atoms [154].	118
Figure 2.48	Optical micrographs showing directionally solidified (a) Al-3.5wt%Ti alloy with coarse plate like Al_3Ti intermetallic growth at cooling rate of $400^\circ/\text{cm}$ and (b) Al-1.15wt%Ti showing fine petal shape growth of Al_3Ti intermetallic at cooling rate of $205^\circ\text{C}/\text{cm}$. Magnification X 40 [153].	118
Figure 2.49	Variation in the micro-hardness of the intermetallics with respect to exposure temperature [158].	121
Figure 2.50	Stress vs. strain graph showing decrease in yield stress value of Al_3Ti intermetallic when alloyed with Cr and Mn. The test was performed using indentation method (shown with black legends) and under compression (hollow legends) [158].	121
Figure 2.51	Graph showing increase in plasticity characteristic when Al_3Ti intermetallic is alloyed with Cr and Mn with respect to temperature [158].	122
Figure 2.52	Tetragonal crystal structure of Al_2Ti intermetallic, where \bigcirc represents Al atoms and \bullet represents Ti atoms [161].	122
Figure 2.53	Backscattered electron micrographs showing distribution of blocky Al_3Ti and spherical equiaxed TiC phases in (a) Al-3.5wt%Ti-0.15wt%C, (b) Al-5wt%-0.3wt%C and (c) Al-10wt%Ti-1wt%C alloys [177].	127

Figure 2.54	Optical micrograph of Al-3wt%Ti-0.75wt%C alloy [178].	128
Figure 2.55	XRD pattern of rapidly solidified Al-Ti-C alloy with varying Ti and C composition [177].	129
Figure 2.56	Optical micrograph of Al-6wt%Ti-0.02wt%C, showing the presence of large block like Al ₃ Ti particles [179].	129
Figure 2.57	XRD pattern of Al-3wt%Ti-0.75wt%C alloy [179].	129
Figure 2.58	Diagrammatic representation of particles interaction with nucleating solid in terms of interfacial energies and contact angles [187].	132
Figure 3.1	The Metallisation Arc140/S250-CL spray system [147].	139
Figure 3.2	Photographs of (a) transverse section and (b) Bakelite mounted Al-Ti-C alloy.	143
Figure 3.3	Photographs of (a) prepared sample and (b) epoxy mounted coating for metallographic examination.	144
Figure 3.4	Schematic of the structure of the Scanning electron microscope [209].	146
Figure 3.5	Schematic of electron interaction zone under the surface of the specimen [209].	147
Figure 3.6	Schematic of the operating principle of a X-ray tube [209].	150
Figure 3.7	Schematic diagram showing arrangement of X-ray diffractometer [209].	151
Figure 3.8	Photograph of sprayed mild steel coupon with artificially induced defect (dimensioning not to the scale).	155
Figure 3.9	Photographs of arc sprayed Al mild steel coupon and (b) Al feedstock in form of rod used for set 2 ASTM B117 salt spray test.	157
Figure 3.10	Diagrammatic representation of galvanic corrosion test (ZRA) setup.	159
Figure 3.11	Diagrammatic representation of principles of EIS [242].	161
Figure 3.12	Nyquist plot shown from ASTM G3, showing Real vs. Imaginary component of Z starting from highest frequency (left) to lower frequency (right) [240].	162

Figure 3.13	Blode plot shown from ASTM G3 representing (a) modulus of impedance vs. frequency and (b) phase angle vs. frequency [240].	162
Figure 3.14	Simple Randle's equivalent circuit representing simple corrosion process from impedance data [241,244].	164
Figure 3.15	Diagrammatic representation of Vickers Indenter [249].	166
Figure 3.16	Schematic of a micro-scale abrasive wear tester [259].	170
Figure 3.17	Secondary electron micrograph showing SiO ₂ powder morphology.	171
Figure 4.1	Photographs of Al-Zn-In coating with artificially induced defect exposed to 5%w/v NaCl in ASTM B117 salt spray test, taken (a) before the experiment, after (b) 24 hours, (c) 48 hours, (d) 168 hours, (e) 500 hours and (f) 1008 hours.	175,176
Figure 4.2	Photographs of pure Al coating with artificially induced defect exposed to 5%w/v NaCl in ASTM B117 salt spray test, taken (a) before the experiment, after (b) 24 hours, (c) 48 hours, (d) 168 hours, (e) 500 hours and (f) 1008 hours.	177,178
Figure 4.3	Photographs of Zn-Al coating with artificially induced defect exposed to 5%w/v NaCl in ASTM B117 salt spray test, taken (a) before the experiment, after (b) 24 hours, (c) 48 hours, (d) 168 hours, (e) 500 hours and (f) 1008 hours.	179,180
Figure 4.4	Bragg-Brentano XRD trace of as sprayed Al coating. The scan was conducted from 2θ ⁰ ranging from 10 ⁰ to 80 ⁰ .	181
Figure 4.5	Bragg-Brentano XRD trace of as sprayed Al-Zn-In coating. The scan was conducted from 2θ ⁰ ranging from 10 ⁰ to 80 ⁰ .	182
Figure 4.6	Bragg-Brentano XRD trace of Al coating after 24 hours of exposure in 5%w/v NaCl. The scan was conducted from 2θ ⁰ ranging from 10 ⁰ to 80 ⁰ .	183
Figure 4.7	Bragg-Brentano XRD trace of Al-Zn-In coating after 24 hours of exposure in 5%w/v NaCl. The scan was conducted from 2θ ⁰ ranging from 10 ⁰ to 80 ⁰ .	184

Figure 4.8	Bragg-Brentano XRD trace of Al coating after 48 hours of exposure in 5%w/v NaCl. The scan was conducted from $2\theta^0$ ranging from 10^0 to 80^0 .	185
Figure 4.9	Bragg-Brentano XRD trace of Al-Zn-In coating after 48 hours of exposure in 5%w/v NaCl. The scan was conducted from $2\theta^0$ ranging from 10^0 to 80^0 .	186
Figure 4.10	XRD trace of corrosion product of Al coating after (a) 500 hours and (b) 1000 hours in salt spray neutral test.	191
Figure 4.11	XRD trace of corrosion product of Al-Zn-In coating after (a) 500 hours and (b) 1000 hours in salt spray neutral test.	192
Figure 4.12	High contrast backscattered electron micrograph of a cross-section of as sprayed Al coating. The enclosed area was used for EDX analysis.	193
Figure 4.13	EDX spectrum of as sprayed Al coating from the enclosed region shown in Figure 4.12 .	194
Figure 4.14	Secondary electron micrograph of as sprayed Al coating surface.	195
Figure 4.15	EDX map of the entire area of Al coating shown in Figure 4.14 at X 1000 magnification.	195
Figure 4.16	High contrast backscattered electron micrograph of a cross-section of as sprayed 300 μm thick as sprayed Al-Zn-In coating. The enclosed area was used for EDX analysis.	196
Figure 4.17	EDX spectrum of as sprayed Al-Zn-In coating from the enclosed region shown in Figure 4.16 .	197
Figure 4.18	Backscattered electron micrograph of (a) Al coating after 1000 hours of neutral salt spray test (b) cross-section of the masked area showing exposed mild steel substrate	198
Figure 4.19	(a'), (b') and (c') shows the EDX spectrum of the cross-section of the exposed Al coating shown in (a), (b) and (c).	199
Figure 4.20	Backscattered electron micrograph of (a) Al-Zn-In coating after 1000 hours of neutral salt spray test (b) cross-section of the masked area showing the exposed mild steel substrate	201
Figure 4.21	(a'), (b') and (c') shows the EDX spectrum of the cross-section of the exposed Al-Zn-In coating shown in (a), (b) and (c).	202

Figure 4.22	Pure Al feedstock rods after (a) 48 hours (b) 336 hours (c) 672 hours and (d) 1008 hours of exposure in neutral salt spray test.	204
Figure 4.23	Al-Zn feedstock rods after (a) 48 hours (b) 336 hours (c) 672 hours and (d) 1008 hours of exposure in neutral salt spray test.	205
Figure 4.24	Al-Zn-In feedstock rods after (a) 48 hours (b) 336 hours (c) 672 hours and (d) 1008 hours of exposure in neutral salt spray test.	206
Figure 4.25	Al-Ti-C feedstock rods after (a) 48 hours (b) 336 hours (c) 672 hours and (d) 1008 hours of exposure in neutral salt spray test.	207
Figure 4.26	Pure Al coating after (a) 48 hours (b) 336 hours (c) 672 hours and (d) 1008 hours of exposure in neutral salt spray test.	209
Figure 4.27	Al-Zn coating after (a) 48 hours (b) 336 hours (c) 672 hours and (d) 1008 hours of exposure in neutral salt spray test.	210
Figure 4.28	Al-Zn-In coating after (a) 48 hours (b) 336 hours (c) 672 hours and (d) 1008 hours of exposure in neutral salt spray test.	211
Figure 4.29	Al-Ti-C coating after (a) 48 hours (b) 336 hours (c) 672 hours and (d) 1008 hours of exposure in neutral salt spray test.	212
Figure 4.30	Change in weight per unit area vs. time of exposure for (a) Pure Al, (b) Al-Zn, (c) Al-Zn-In and (d) Al-Ti-C feedstock alloys.	218
Figure 4.31	Change in weight per unit area vs. time of exposure for (a) Pure Al, (b) Al-Zn, (c) Al-Zn-In and (d) Al-Ti-C coatings.	222
Figure 4.32	Open circuit potential vs. time plot for Al coating subjected to 3.5%w/v, 1.0%w/v, 0.1%w/v and 0.01%w/v NaCl solution.	226
Figure 4.33	Open circuit potential vs. time plot for Al-Zn coating subjected to 3.5%w/v, 1.0%w/v, 0.1%w/v and 0.01%w/v NaCl solution.	226

Figure 4.34	Open circuit potential vs. time plot for Al-Zn-In coating subjected to 3.5%w/v, 1.0%w/v, 0.1%w/v and 0.01%w/v NaCl solution.	227
Figure 4.35	Open circuit potential vs. time plot for Al-Ti-C coating subjected to 3.5%w/v, 1.0%w/v, 0.1%w/v and 0.01%w/v NaCl solution.	227
Figure 4.36	Open circuit potential plot for Al coating during 24 hours of immersion in 3.5%w/v, 1.0%w/v, 0.1%w/v, 0.01%w/v NaCl solution.	228
Figure 4.37	Open circuit potential plot for Al-Zn coating during 24 hours of immersion in 3.5%w/v, 1.0%w/v, 0.1%w/v, 0.01%w/v NaCl solution.	228
Figure 4.38	Open circuit potential plot for Al-Zn-In coating during 24 hours of immersion in 3.5%w/v, 1.0%w/v, 0.1%w/v, 0.01%w/v NaCl solution.	229
Figure 4.39	Open circuit potential plot for Al-Ti-C coating during 24 hours of immersion in 3.5%w/v, 1.0%w/v, 0.1%w/v, 0.01%w/v NaCl solution.	229
Figure 4.40	Current vs. time plot for Al coating subjected to 3.5%w/v NaCl solution. The anode to cathode area ratios used was 1:1, 1:1/2 and 1:1/4 respectively.	236
Figure 4.41	Current vs. time plot for Al-Zn coating subjected to 3.5%w/v NaCl solution. The anode to cathode area ratios used was 1:1, 1:1/2 and 1:1/4 respectively.	237
Figure 4.42	Current vs. time plot for Al-Zn-In coating subjected to 3.5%w/v NaCl solution. The anode to cathode area ratios used was 1:1, 1:1/2 and 1:1/4 respectively.	237
Figure 4.43	Current vs. time plot for Al-Ti-C coating subjected to 3.5%w/v NaCl solution. The anode to cathode area ratios used was 1:1, 1:1/2 and 1:1/4 respectively.	238
Figure 4.44	Current vs. time plot for Al-Zn-In coating subjected to 1.0%w/v NaCl solution. The anode to cathode area ratios used was 1:1/2 and 1:1/4 respectively.	238
Figure 4.45	Current vs. time plot for Al-Zn-In coating subjected to 0.1%w/v NaCl solution. The anode to cathode area ratios used was 1:1/2 and 1:1/4 respectively.	239

Figure 4.46	Current vs. time plot for Al-Zn-In coating subjected to 0.01%w/v NaCl solution. The anode to cathode area ratios used was 1:1/2 and 1:1/4 respectively.	239
Figure 4.47	CCP vs. time plot for Al coating subjected to 3.5%w/v NaCl solution. The anode to cathode area ratios used was 1:1,1:1/2 and 1:1/4 respectively.	240
Figure 4.48	CCP vs. time plot for Al-Zn coating subjected to 3.5%w/v NaCl solution. The anode to cathode area ratios used was 1:1,1:1/2 and 1:1/4 respectively.	241
Figure 4.49	CCP vs. time plot for Al-Zn-In coating subjected to 3.5%w/v NaCl solution. The anode to cathode area ratios used was 1:1,1:1/2 and 1:1/4 respectively.	242
Figure 4.50	CCP vs. time plot for Al-Ti-C coating subjected to 3.5%w/v NaCl solution. The anode to cathode area ratios used was 1:1,1:1/2 and 1:1/4 respectively.	242
Figure 4.51	CCP vs. time plot for Al-Zn-In coating subjected to 1.0%w/v NaCl solution. The anode to cathode area ratios used was 1:1/2 and 1:1/4 respectively.	241
Figure 4.52	CCP vs. time plot for Al-Zn-In coating subjected to 0.1%w/v NaCl solution. The anode to cathode area ratios used was 1:1/2 and 1:1/4 respectively.	243
Figure 4.53	CCP vs. time plot for Al-Zn-In coating subjected to 0.01%w/v NaCl solution. The anode to cathode area ratios used was 1:1/2 and 1:1/4 respectively.	243
Figure 4.54	Logarithmic plots showing relationship between galvanic corrosion current and cathode to anode area ratio for (a) Al, (b) Al-Zn, (c) Al-Zn-In and (d) Al-Ti-C coatings exposed to 3.5% w/v NaCl solution for 168 hours.	244
Figure 4.55	Logarithmic plots showing relationship between galvanic corrosion current and cathode to anode area ratio for Al-Zn-In coating exposed to (a) 1.0% w/v, (b) 0.1% w/v, and (c) 0.01% w/v NaCl solution for 168 hours	245
Figure 4.56	Log plots showing the variation in galvanic corrosion current vs chloride concentration for Al-Zn-In coating coupled with mild steel with cathode to anode area ratio of 1:1, 2:1 and 4:1 respectively.	246

Figure 4.57	Nyquist plots for Al coating exposed to (a) 3.5%w/v , (b) 1.0%w/v, (c) 0.1%w/v and (d) 0.01%w/v NaCl solution for 1, 24, 48 and 168 hours.	256
Figure 4.58	Nyquist plots for Al-Zn coating exposed to (a) 3.5%w/v , (b) 1.0%w/v, (c) 0.1%w/v and (d) 0.01%w/v NaCl solution for 1, 24, 48 and 168 hours.	257
Figure 4.59	Nyquist plots for Al-Zn-In coating exposed to (a) 3.5%w/v , (b) 1.0%w/v, (c) 0.1%w/v and (d) 0.01%w/v NaCl solution for 1, 24, 48 and 168 hours.	258
Figure 4.60	Nyquist plots for Al-Ti-C coating exposed to (a) 3.5%w/v , (b) 1.0%w/v, (c) 0.1%w/v and (d) 0.01%w/v NaCl solution for 1, 24, 48 and 168 hours.	259
Figure 4.61	Diagrammatic representation of (a) $R(Q(R(QR)))$ or $R(C(R(QR)))$, (b) $R(QR)(QR)$, (c) $R(Q(R(LR)))$, (d) $R(Q(R(RW)))$, the equivalent circuit models used during the interpretation of impedance data shown in Table 4.10 and Table 4.13 .	265
Figure 4.62	Backscattered electron micrograph of transverse section of (a) Al and (b) Al-Ti-C feedstock material.	279
Figure 4.63	EDX analysis of the enclosed area shown in figure 1(b) showing different phases observed in the Al-Ti-C feedstock alloy (a) large blocky phase (A) with large aspect ratio and (b) smaller equiaxed particle (B).	281
Figure 4.64	XRD trace of Al-Ti-C feedstock alloy confirming the presence of Al_3Ti and TiC phase. The unmarked peak at $2\theta^0 \approx 58^0$ is the Cu K_{β} .	282
Figure 4.65	Backscattered electron micrograph showing the cross-section of (a) pure Al and (b) Al-Ti-C coating.	283
Figure 4.66	Backscattered electron micrograph of Al-Ti-C coating showing (a) speckled region and (b) dark and light grey regions.	284
Figure 4.67	XRD trace of as sprayed Al-Ti-C coating showing formation of different phases (see appendix for more details). The unmarked peaks at $2\theta^0 \approx 40^0, 58^0, 69^0$ are Cu K_{β} .	287
Figure 4.68	Frequency distribution histogram of micro-hardness ($HV_{0.98}$) for pure Al and Al-Ti-C feedstock alloy material.	288

Figure 4.69	Frequency distribution histogram of variation in micro-hardness of pure Al and Al-Ti-C coating.	289
Figure 4.70	Graphs showing wear crater volume vs. Sliding distance x load for (a) pure Al and (b) Al-Ti-C feedstock material.	290
Figure 4.71	Graphs showing wear crater volume vs. sliding distance x Load for (a) Pure Al and (b) Al-Ti-C coatings.	291
Figure 4.72	Backscattered micrographs showing the directionality of the wear tracks for (a) Al and (b) Al-Ti-C feedstock.	293
Figure 4.73	Backscattered micrographs showing directionality of the wear tracks for (a) Al and (b) Al-Ti-C coating.	293
Figure 4.74	Comparison of coefficient of wear and hardness of pure Al and Al-Ti-C alloy feedstock material and coatings with 13% Cr steel coating and mild steel substrate.	295
Figure 4.75	Backscattered electron micrograph of Al-Ti-C coating exposed to 150 ⁰ C for (a) 1 hour and (b) 3 hours, followed by rapid quenching.	298
Figure 4.76	A higher magnification, @ x 5000, Backscattered electron micrographs of Al-Ti-C coating exposed to 150 ⁰ C for 1 hour showing (a) small and large speckled spots (b) light and dark grey regions and (c) higher atomic number contrast light grey region. The coating was rapidly quenched post exposure.	299
Figure 4.77	A higher magnification (a) and (b) @ x 5000 and (c) @ x 10,000, backscattered electron micrograph of Al-Ti-C coating exposed to 150 ⁰ C for 3 hours showing (a) distinctive growth of large speckled spots, (b) high atomic number contrast region and (c) spherical equiaxed phase. The coatings were rapidly quenched post exposure.	300
Figure 4.78	XRD trace of Al-Ti-C coating post 150 ⁰ C exposure for (a) 1 hour and (b) 3 hours followed by rapid quenching. The unmarked peaks at $2\theta^0 \approx 40^0, 58^0$ and 69^0 are $\text{CuK}\beta$.	304
Figure 4.79	Backscattered electron micrograph of Al-Ti-C coating exposed to 350 ⁰ C for (a) 1 hour and (b) 3 hours, followed by rapid quenching. (The linear features are caused due to polishing).	305

Figure 4.80	A higher magnification, (a) @ x 5000, (b) and (c) @ x 10,000, backscattered electron micrograph of Al-Ti-C coating exposed to 350 ⁰ C for 1 hour showing (a) small and large speckled spots (b) a higher aspect ratio phase and (c) spherical equiaxed phase. The coating was rapidly quenched post exposure.	306
Figure 4.81	A higher magnification, (a), (b) @ x 5000 and (c) @ x 10,000, backscattered electron micrograph of Al-Ti-C coating exposed to 350 ⁰ C for 3 hours showing (a) small and large speckled spots, (b) dark and light grey regions and (c) spherical equiaxed phase. The coating was rapidly quenched post exposure.	307
Figure 4.82	XRD trace of Al-Ti-C coating post 350 ⁰ C exposure for (a) 1 hour and (b) 3 hours followed by rapid quenching. The unmarked peaks at $2\theta^0 \approx 40^0$, 58^0 are $\text{CuK}\beta$.	311
Figure 4.83	Backscattered electron micrograph of Al-Ti-C coating exposed to 550 ⁰ C for (a) 1 hour and (b) 3 hours, followed by rapid quenching.	313
Figure 4.84	A higher magnification @ x 10,000, Backscattered electron micrograph of Al-Ti-C coating exposed to 550 ⁰ C for 1 hour showing (a) formation of brittle phase, with high atomic number contrast, (b) phase with rectangular geometry within the speckled region and (c) spherical equiaxed phase. The coating was rapidly quenched post exposure.	314
Figure 4.85	A higher magnification @ x 10,000, Backscattered electron micrograph of Al-Ti-C coating exposed to 550 ⁰ C for 3 hour showing (a) formation of speckled region,(b) and (c) formation of brittle phase with high atomic number contrast with uniform distribution of speckled region.	315
Figure 4.86	XRD trace of Al-Ti-C coating post 550 ⁰ C exposure for (a) 1 hour and (b) 3 hours followed by rapid quenching. The unmarked peaks at $2\theta^0 \approx 40^0$, 58^0 are $\text{CuK}\beta$.	319
Figure 4.87	Frequency distribution histogram of micro-hardness ($\text{HV}_{0.98}$) for Al-Ti-C coating exposed to 150 ⁰ C for 1 hour (violet shade) and 3 hours (Dark red shade).	321
Figure 4.88	Frequency distribution histogram of micro-hardness ($\text{HV}_{0.98}$) for Al-Ti-C coating exposed to 350 ⁰ C for 1 hour (violet shade) and 3 hours (Dark red shade).	321

Figure 4.89	Frequency distribution histogram of micro-hardness ($HV_{0.98}$) for Al-Ti-C coating exposed to 550 ⁰ C for 1 hour (violet shade) and 3 hours (Dark red shade).	322
Figure 4.90	Comparison of micro-hardness values obtained for as sprayed Al-Ti-C coating and Al-Ti-C coating exposed to 150 ⁰ C, 350 ⁰ C and 550 ⁰ C for 1 hour and 3 hours followed by rapid quenching.	324
Figure 4.91	Graphs showing wear crater volume vs. sliding distance x load for Al-Ti-C coating subjected to 150 ⁰ C for (a) 1 hour and (b) 3 hours followed by rapid quenching.	326
Figure 4.92	Graphs showing wear crater volume vs. sliding distance x load for Al-Ti-C coating exposed to 350 ⁰ C for (a) 1 hour and (b) 3 hours followed by rapid quenching.	327
Figure 4.93	Graphs showing wear crater volume vs. sliding distance x load for Al-Ti-C coating exposed to 550 ⁰ C for (a) 1 hour and (b) 3 hours followed by rapid quenching.	328
Figure 4.94	Backscattered electron micrograph showing directionality of the wear tracks and precipitation of various phases in Al-Ti-C coating @150 ⁰ C for 1 hour. (a),(b) and (c) are backscattered electron micrographs at different magnifications.	329
Figure 4.95	Backscattered electron micrograph showing directionality of the wear tracks and precipitation of various phases in Al-Ti-C coating @ 150 ⁰ C for 3 hour. (a),(b) and (c) are backscattered electron micrographs at different magnifications.	330
Figure 4.96	Backscattered electron micrograph showing directionality of the wear tracks and precipitation of various phases in Al-Ti-C coating @ 350 ⁰ C for 1 hour. (a), (b) and (c) are backscattered electron micrographs at different magnifications.	332
Figure 4.97	Backscattered electron micrograph showing directionality of the wear tracks and precipitation of various phases in Al-Ti-C coating @ 350 ⁰ C for 3 hour. (a), (b) and (c) are backscattered electron micrographs at different magnifications.	333

Figure 4.98	Backscattered electron micrograph showing directionality of the wear tracks and precipitation of various phases in Al-Ti-C coating @ 550 ⁰ C for 1 hour. (a), (b) and (c) are backscattered electron micrographs at different magnifications.	335
Figure 4.99	Backscattered electron micrograph showing directionality of the wear tracks and precipitation of various phases in Al-Ti-C coating @ 550 ⁰ C for 3 hour. (a), (b) and (c) are backscattered electron micrographs at different magnifications.	336
Figure 4.100	Comparison of wear coefficient values obtained for as sprayed Al-Ti-C coating and Al-Ti-C coating exposed to 150 ⁰ C, 350 ⁰ C and 550 ⁰ C for 1 hour and 3 hours followed by rapid quenching.	337
Figure 4.101	Backscattered electron micrograph of Al-Ti-C coating exposed to 150 ⁰ C for (a) 1 hour and (b) 3 hours, followed by normal room temperature exposure (25 ⁰ C) for 5 hours.	338
Figure 4.102	A higher magnification, @ (a) x 2000, (b) x 5000 and (c) x 10,000, (d) x 30,000 backscattered electron micrograph of Al-Ti-C coating exposed to 150 ⁰ C for 1 hour showing (a) speckled region, (b) high contrast region, (c) triangular shaped brittle phase and (d) a brittle spherical equiaxed phase. The coatings were exposed to room temperature for 5 hours after 150 ⁰ C exposure.	339
Figure 4.103	A higher magnification, @ (a) x 2000, (b) x 5000 ,(c) and (d) x 20,000,backscattered electron micrograph of Al-Ti-C coating exposed to 1500C for 3 hours showing (a) speckled region with observable growth in size (formation of a crater observed in (a), could be a result of coating removal during mechanical polishing), (b) high contrast region, (c) and (d) brittle spherical equiaxed phase. Notice the difference in the size of phases shown in (c) and (d). The coatings were exposed to room temperature for 5 hours after 1500C exposure.	340
Figure 4.104	XRD trace of Al-Ti-C coating post 150 ⁰ C exposure for (a) 1 hour and (b) 3 hours followed by normal room temperature exposure for 5 hours.	344
Figure 4.105	Backscattered electron micrograph of Al-Ti-C coating exposed to 350 ⁰ C for (a) 1 hour and (b) 3 hours, followed by normal room temperature exposure (25 ⁰ C) for 5 hours.	346

Figure 4.106	A higher magnification, @ (a) x 2000, (b) x 5000 and (c) 20,000, backscattered electron micrograph of Al-Ti-C coating exposed to 350 ⁰ C for 1 hour showing (a) speckled region with observable growth in size, (b) high contrast region and (c) brittle spherical equiaxed phase. The coatings were then exposed to normal room temperature for 5 hours.	347
Figure 4.107	A higher magnification, @ (a) x 2000, (b) x 4000 and (c) 12,000 and (d) 30,000 backscattered electron micrograph of Al-Ti-C coating exposed to 350 ⁰ C for 3 hours showing (a) speckled region with observable growth in size, (b) high contrast region and (c) brittle spherical equiaxed phase. The coatings were then exposed to normal room temperature for 5 hours.	348
Figure 4.108	XRD trace of Al-Ti-C coating post 350 ⁰ C exposure for (a) 1 hour and (b) 3 hours followed by normal room temperature exposure for 5 hours.	349
Figure 4.109	Backscattered electron micrograph of Al-Ti-C coating exposed to 550 ⁰ C for (a) 1 hour and (b) 3 hours, followed by normal room temperature exposure (25 ⁰ C) for 5 hours.	353
Figure 4.110	A higher magnification, @ (a) and (b) x 20,000 backscattered electron micrograph of Al-Ti-C coating exposed to 550 ⁰ C for 1 hour showing (a) speckled region with feather shaped regions and (b) showing brittle spherical equiaxed phase along with large speckled spots. The coatings were then exposed to normal room temperature for 5 hours.	354
Figure 4.111	A higher magnification, @ (a) x 3000, (b) and (c) x 30,000 backscattered electron micrograph of Al-Ti-C coating exposed to 550 ⁰ C for 1 hour showing (a) speckled region (b) Speckled region with observable growth and feather shaped region and (c) brittle phase along with speckled spots. The coatings were then exposed to normal room temperature for 5 hours.	355
Figure 4.112	XRD trace of Al-Ti-C coating post 550 ⁰ C exposure for (a) 1 hour and (b) 3 hours followed by normal room temperature exposure for 5 hours.	358

Figure 4.113	Frequency distribution histogram of micro-hardness (HV _{0.98}) for Al-Ti-C coating exposed to 150 ⁰ C for 1 hour (violet shade) and 3 hours (Dark red shade). The coatings were room temperature cooled (5 hours) after exposure.	361
Figure 4.114	Frequency distribution histogram of micro-hardness (HV _{0.98}) for Al-Ti-C coating exposed to 350 ⁰ C for 1 hour (violet shade) and 3 hours (Dark red shade). The coatings were room temperature cooled (5 hours) after exposure.	362
Figure 4.115	Frequency distribution histogram of micro-hardness (HV _{0.98}) for Al-Ti-C coating exposed to 550 ⁰ C for 1 hour (violet shade) and 3 hours (Dark red shade). The coatings were room temperature cooled (5 hours) after exposure.	362
Figure 4.116	Comparison of micro-hardness values obtained for as sprayed Al-Ti-C coating and Al-Ti-C coating exposed to 150 ⁰ C, 350 ⁰ C and 550 ⁰ C for 1 hour and 3 hours followed by room temperature cooling for 5 hours.	363
Figure 4.117	Graphs showing wear crater volume vs. sliding distance x load for Al-Ti-C coating subjected to 150 ⁰ C for (a) 1 hour and (b) 3 hours followed by room temperature cooling for 5 hours.	365
Figure 4.118	Graphs showing wear crater volume vs. sliding distance x load for Al-Ti-C coating subjected to 350 ⁰ C for (a) 1 hour and (b) 3 hours followed by room temperature cooling for 5 hours.	366
Figure 4.119	Graphs showing wear crater volume vs. sliding distance x load for Al-Ti-C coating subjected to 550 ⁰ C for (a) 1 hour and (b) 3 hours followed by room temperature cooling for 5 hours.	367
Figure 4.120	Backscattered electron micrograph showing directionality of the wear tracks and precipitation of various phases in Al-Ti-C coating @150 ⁰ C for 1 hour followed by room temperature cooling for 5 hours (a), (b) and (c) are backscattered electron micrographs at different magnifications.	368
Figure 4.121	Backscattered electron micrograph showing directionality of the wear tracks and precipitation of various phases in Al-Ti-C coating @150 ⁰ C for 3 hour followed by room temperature cooling for 5 hours (a), (b) and (c) are backscattered electron micrographs at different	371

magnifications.

- Figure 4.122** Backscattered electron micrograph showing directionality of the wear tracks and precipitation of various phases in Al-Ti-C coating @350⁰C for 1 hour followed by room temperature cooling for 5 hours (a), (b) and (c) are backscattered electron micrographs at different magnifications. 373
- Figure 4.123** Backscattered electron micrograph showing directionality of the wear tracks and precipitation of various phases in Al-Ti-C coating @350⁰C for 3 hours followed by room temperature cooling for 5 hours (a), (b) and (c) are backscattered electron micrographs at different magnifications. 375
- Figure 4.124** Backscattered electron micrograph showing directionality of the wear tracks and precipitation of various phases in Al-Ti-C coating @550⁰C for 1 hour followed by room temperature cooling for 5 hours (a), (b) and (c) are backscattered electron micrographs at different magnifications. 376
- Figure 4.125** Backscattered electron micrograph showing directionality of the wear tracks and precipitation of various phases in Al-Ti-C coating @550⁰C for 3 hours followed by room temperature cooling for 5 hours (a), (b) and (c) are backscattered electron micrographs at different magnifications. 377
- Figure 4.126** Comparison of wear coefficient values obtained for as sprayed Al-Ti-C coating and Al-Ti-C coating exposed to 150⁰C, 350⁰C and 550⁰C for 1 hour and 3 hours followed by room temperature cooling for 5 hours. 378

List of Tables

Table 2.1	Important properties of unalloyed aluminium [66].	29
Table 2.2	Elements (depassivators and modifiers) and their melting temperatures which significantly lower the OCP of Al [82,83].	35
Table 2.3	The thermodynamic potential of various elements (at pH 8) that have been alloyed with Al to form sacrificial anodes and working potential of Al alloys measured (at 6.2 A/m ²) in ASTM D 1141-52 (left) [83,84].	36
Table 2.4	Composition of Al alloys tested by <i>Kier et.al.</i> , coupled with mild steel in 0.1M NaCl solution exposed for 48 hours[85]. The experiments were conducted in duplicates and triplicates	37
Table 2.5	The effect of ternary alloying addition on the corrosion current of alloys when coupled with mild steel in 0.1M NaCl solution for 48 hours [89].	41
Table 2.6	Data on effect of alloying per unit wt% on Al lattice [88].	42
Table 2.7	The effect of alloying element on the Al latttice [88].	42
Table 2.8	Table showing the lattice parameters of Al, Sn, In and Zn with the 2 dimensional area of a low index face for each element [92].	51
Table 2.9	Table showing the values of enrichment factor for Al alloyed with Zn ,Sn and In at 0.1wt% and 1.0wt% alloying concentration [90].	57
Table 2.10	SIMS analysis of Al-1wt%Sn alloy (SHT0) before and after 24 hours of exposure in 0.5M Na ₂ SO ₄ solution [90].	61
Table 2.11	AES concentration depth profile of Al-1wt%Sn alloy post anodic polarisation in 0.5M Na ₂ SO ₄ solution (after 24 hours of exposure) [90].	61
Table 2.12	The composition (in wt%) of binary Al alloys with Fe and Si as major impurities which were used for experimental investigation by Gundersen <i>et al.</i> [53].	69
Table 2.13	Effect of alloying 99.99% and 99.85%Al with various concentrations of Zn and In on galvanic efficiency (tests conducted in sea water) [108].	87
Table 2.14	Effect of impurities (Fe, Si and Cu) on the galvanic efficiency of Al anodes [108].	87

Table 2.15	Effect of Cd addition on galvanic efficiency of Al anodes [109].	87
Table 2.16	Quantitative electroprobe analysis of Al-6wt%Zn0.05wt%In0.01wt%Si and segregated phases after potentiostatic polarisation at -1000 mV vs. SCE for 25 minutes in 0.5M NaCl solution [110].	89
Table 2.17	Properties of Al ₃ Ti intermetallic compound [158].	120
Table 3.1	The composition of the alloys which were used for thermal spraying [195-200]. * Available from manufacturers data sheet.	140
Table 3.2	Arc spraying parameters [204].	140
Table 4.1	Semi-quantitative analysis showing the ratio of Al(OH) ₃ to Al phase present in Al and Al-Zn-In coating when as sprayed and after 24 and 48 hours in neutral salt spray test condition.	187
Table 4.2	Semi-quantitative analysis showing the ratio of Al(OH) ₃ to Al phase present in Al and Al-Zn-In coating after 500 and 1000 hours in neutral salt spray test condition.	189
Table 4.3	Average composition analysis of as sprayed Al coating using EDX semi-quantitative data.	194
Table 4.4	Average composition analysis of as sprayed Al-Zn-In coating using EDX semi-quantitative data.	197
Table 4.5	Weight measurements after specific exposure period of the alloy feedstock samples exposed to neutral salt spray corrosion test.	208
Table 4.6	Weight measurements after specific exposure period of the coated samples exposed to neutral salt spray corrosion test.	213
Table 4.7	Change in weight per unit area of the feedstock alloys at specified intervals. The measurements are the average value from three different samples.	216
Table 4.8	Change in weight per unit area of the coatings at specified intervals. The measurements are the average value from three different samples.	217

Table 4.9	The measured, actual and R_a values of Al, Al-Zn, Al-Zn-In and Al-Ti-C coating.	236
Table 4.10	Electrochemical parameters obtained by fitting Impedance data obtained for Al exposed to 3.5%w/v, 1.0%w/v, 0.1%w/v and 0.01%w/v NaCl solution for 1, 24, 48 and 168 hours.	260
Table 4.11	Electrochemical parameters obtained by fitting Impedance data obtained for Al-Zn exposed to 3.5%w/v, 1.0%w/v, 0.1%w/v and 0.01%w/v NaCl solution for 1, 24, 48 and 168 hours.	261
Table 4.12	Electrochemical parameters obtained by fitting Impedance data obtained for Al-Zn-In exposed to 3.5%w/v, 1.0%w/v, 0.1%w/v and 0.01%w/v NaCl solution for 1, 24, 48 and 168 hours.	262
Table 4.13	Electrochemical parameters obtained by fitting Impedance data obtained for Al-Ti-C exposed to 3.5%w/v, 1.0%w/v, 0.1%w/v and 0.01%w/v NaCl solution for 1, 24, 48 and 168 hours.	263
Table 4.14	Symbols and operational impedance functions of the elements used in equivalent circuit models shown in Table 4.10 to Table 4.13 .	264
Table 4.15	Behaviour of CPE according to n values.	267
Table 4.16	Average composition analysis of different phases observed in Al-Ti-C feedstock alloy.	280
Table 4.17	Average composition analysis of different phases observed in Al-Ti-C coating.	284
Table 4.18	Vickers micro-hardness of the pure Al and Al-Ti-C feedstock.	287
Table 4.19	Vickers micro-hardness of the pure Al, Al-Ti-C and 13%Cr steel coatings.	288
Table 4.20	Coefficient of wear for Al and Al-Ti-C feedstock alloys.	292
Table 4.21	Coefficient of wear for Al and Al-Ti-C coatings.	292
Table 4.22	Average composition analysis of different phases observed in Al-Ti-C coating @ 150 ⁰ C for 1 hour followed by rapid	301

quenching.

Table 4.23	Average composition analysis of different phases observed in Al-Ti-C coating @ 150 ⁰ C for 3 hours followed by rapid quenching.	302
Table 4.24	Average composition analysis of different phases observed in Al-Ti-C coating @ 350 ⁰ C for 1 hour followed by rapid quenching.	308
Table 4.25	Average composition analysis of different phases observed in Al-Ti-C coating @ 350 ⁰ C for 3 hours followed by rapid quenching.	308
Table 4.26	Average composition analysis of different phases observed in Al-Ti-C coating @ 550 ⁰ C for 1 hour followed by rapid quenching.	316
Table 4.27	Average composition analysis of different phases observed in Al-Ti-C coating @ 550 ⁰ C for 3 hours followed by rapid quenching.	316
Table 4.28	Vickers micro-hardness of Al-Ti-C coating subjected to 150 ⁰ C, 350 ⁰ C and 550 ⁰ C for 1 hour and 3 hours followed by rapid quenching.	320
Table 4.29	Coefficient of wear for Al-Ti-C coating exposed to 150 ⁰ C, 350 ⁰ C and 550 ⁰ C for 1 hour and 3 hours followed by rapid quenching.	325
Table 4.30	Average composition analysis of different phases observed in Al-Ti-C coating @ 150 ⁰ C for 1 hour followed by normal room temperature exposure for 5 hours.	340
Table 4.31	Average composition analysis of different phases observed in Al-Ti-C coating @ 150 ⁰ C for 3 hours followed by normal room temperature exposure for 5 hours.	341
Table 4.32	Average composition analysis of different phases observed in Al-Ti-C coating @ 350 ⁰ C for 1 hour followed by normal room temperature exposure for 5 hours.	348
Table 4.33	Average composition analysis of different phases observed in Al-Ti-C coating @ 350 ⁰ C for 3 hours followed by normal room temperature exposure for 5 hours.	348
Table 4.34	Average composition analysis of different phases observed in Al-Ti-C coating @ 550 ⁰ C for 1 hour followed by normal room temperature exposure for 5 hours.	355

Table 4.35	Average composition analysis of different phases observed in Al-Ti-C coating @ 550 ⁰ C for 3 hours followed by normal room temperature exposure for 5 hours.	355
Table 4.36	Vickers micro-hardness of Al-Ti-C coating subjected to 150 ⁰ C, 350 ⁰ C and 550 ⁰ C for 1 hour and 3 hours followed by room temperature cooling for 5 hours.	359
Table 4.37	Coefficient of wear for Al-Ti-C coating exposed to 150 ⁰ C, 350 ⁰ C and 550 ⁰ C for 1 hour and 3 hours followed by room temperature cooling for 5 hours.	365

Abstract

Extensive research on alloying aluminium (Al) with zinc (Zn), indium (In) and titanium (Ti) to improve corrosion and wear resistance has been conducted since 1950's to meet the increased demand of Al in construction, automotive, aerospace and food industries in the form of coatings deposited using thermal spraying, hot dipping and cladding. This research has investigated the performance of arc sprayed Al-5wt%Zn-(0.02-0.05wt%)In and Al-3wt%Ti-0.15wt%C coatings to protect steel structures from corrosion and wear.

The accelerated and electrochemical tests conducted on Al-5wt% Zn-(0.02-0.05wt%) In showed that its superior corrosion performance was attributed to the synergetic interaction of Zn and In. Cyclic formation and rupturing of passive Al oxide layer was found to be the underlying mechanism of activation produced by combination of both Zn and In. The presence of In in the corrosion product or on the surface of the coating In was not detected, hence validation of surface enrichment theory was improbable.

The micro-scale abrasive wear test showed that the wear coefficient of an arc sprayed Al-3wt%Ti-0.15wt% C coating was found to be very close to that of an arc sprayed 13wt%Cr steel coating with a much higher hardness. This was attributed to the formation of Al_3Ti and $(Ti,Al)C$ particles due to rapid cooling that takes place in arc spraying . This resulted in precipitation strengthening, explaining the increase in the hardness of the sprayed Al-3wt%Ti-0.15wt%C coating compared to its feedstock alloy. To establish a mechanism by which the identified phases in the microstructure of arc sprayed Al-3wt%Ti-0.15wt%C alloy coating showed improved hardness and wear resistance than the bulk alloy, growth of identified phases in the coating was promoted by two different heat treatment cycles. The coated samples were held at three chosen temperatures of 150⁰C, 350⁰C and 550⁰C separately for 1 hour and 3 hours, followed by two different cooling regimens; the first involved rapid quenching of samples and the other was room temperature exposure for 5 hours.

After both heat treatment cycles

- Precipitations of Ti rich high contrast and near spherical brittle phases were observed in the microstructure of Al-3wt%Ti coatings.
- A reduction in the spread of micro-hardness value with increase in exposure temperature from 150⁰C to 550⁰C was also observed.

An overall increase in the wear coefficient value of rapidly quenched coatings in comparison to as-sprayed Al-3wt%Ti-0.15wt%C coating was seen. A similar increase in the wear coefficient value was also observed after room temperature cooled coatings. However, an exceptional 15 % reduction in wear coefficient value was seen in the room temperature cooled coating after 3 hours of exposure at 550⁰C. The role of precipitated phases and possible mechanism of their effect on micro-hardness and wear resistance of Al-3wt%Ti-0.15wt%C alloy coating has also been discussed.

Chapter 1: Introduction

1.1 Motivation

Corrosion and wear of materials are universal problems, which cause the majority of catastrophic failures of metallic structures and have implications in terms of both safety and economic losses. Generally, corrosion can be defined as the degradation of materials by chemical or electrochemical reaction with the environment causing the material to lose mechanical strength and ductility whereas wear is related to the loss of material by the action of friction on two interacting materials having same or different hardness which are constantly subjected to rubbing action. To understand the methods to mitigate the effects from various forms of both corrosion and wear, it is imperative to understand the underlying principle for both phenomena, which encompasses elements of physics, chemistry and metallurgy.

Numerous surface protection methods such as use of metallic and non-metallic coatings which not only provide adequate corrosion resistance, but also impart high wear resistance and provide lubrication between the interacting materials have been deployed by various industries in order to protect metallic structures from ubiquitous phenomena of corrosion and wear. The application of metallic coatings is the most widely used technique in the industrial sector to protect metallic structures during their service life.

The current project focuses on the application of Al based metallic coatings to the steel substrate by thermal spraying.

The thermal spray coating process originated in early 1900's, where it was initially used for depositing zinc. The process was originally constrained by the availability of a satisfactory heat source, typically an oxyacetylene flame, until the development of other techniques such as arc and plasma spraying. The thermal spraying process is very adaptable, being capable of depositing a wide variety of materials, including ceramics in addition to metals. Furthermore, a range of precursors can be used, including powder, rods and wires. The main advantage of thermal spraying in comparison to other deposition processes such as electro-deposition, physical and chemical vapour deposition, is that thermal spraying can be used to deposit coatings on large metallic structures at high deposition rates.

The thermally sprayed aluminium alloy coatings have been mostly used to protect underlying steel structures exposed to aggressive environments (such as marine or industrial) from corrosion. In order to increase the use of aluminium alloy coatings in industrial environments, addition of various alloying elements have been studied to improve the corrosion and wear resistance of the coatings. The current project has focused on spraying aluminium alloyed with zinc (Zn) indium (In), titanium (Ti) and carbon (C) to produce coatings which are used for corrosion and wear protection of metallic substrates. During the project, Al-Zn-In and Al-Ti-C alloys were sprayed on mild steel substrates using arc spraying technique. The coatings were subjected to various experimental tests which included accelerated and electrochemical corrosion tests for Al-Zn-In and Al-Ti-C coatings and wear

test for Al-Ti-C coating in conjunction with analytical characterisation techniques to understand coatings corrosion and wear performance. The project has not only immensely contributed to the existing literature on Al-Zn-In alloys which are used as sacrificial anodes but has also created an in-depth understanding of the mechanism of corrosion resistance provided by Al-Zn-In alloy in form of arc sprayed coatings. The current project has also established a quantitative evidence of the use of Al alloyed with Ti and C as a wear resistant coating on to mild steel structures which can perform equally as other commercially available widely used wear resistant coatings, in addition to wear resistance can also provide optimum corrosion protection.

1.1 Aim of the project

The aim of the research was to understand the corrosion and wear resistance properties of Al-Zn-In and Al-Ti-C alloy coatings which have been sprayed on to metallic substrates. The research has developed a profound understanding of the microstructure and composition of Al-Zn-In and Al-Ti-C alloy coatings, related this to the performance of the coatings in different environments by conducting various experimental investigations and in turn used the knowledge obtained from various experiments to understand the underlying mechanism of corrosion and wear protection offered by these coatings, when sprayed using industrial spraying parameters.

1.2 Objectives

The objectives of the study have been:

- To identify the role of Zn, In, Ti and C as alloying elements on the corrosion and wear resistance of aluminium.
- Characterisation of the coatings using analytical techniques such as scanning electron microscopy (SEM) with energy dispersive X-ray analysis (EDS) and X-ray diffraction (XRD) to analyse the microstructure of arc sprayed Al-Zn-In and Al-Ti-C alloy coatings.
- Using accelerated and electrochemical corrosion tests on Al-Zn-In and Al-Ti-C alloy coatings to analyse coating lifetime and sacrificial behaviour.
- By conducting micro-scale abrasive wear test, the wear resistance capabilities of Al-Ti-C was identified. Further heat treatment tests were conducted to pin down the role of different phases present in the Al-Ti-C alloy coatings which played a significant role in enhanced wear resistance performance of the coatings.

Chapter 2: Literature Review

2.1 Introduction, background and use of coatings

The use of coatings either to protect surfaces from deterioration or for decoration is an ancient technique. The first evidence of coatings being used for protection against corrosion dates to 4000 B.C, where Egyptians used varnishes, while Chinese artists used coatings for the purpose of decoration [1-3]. Even today, the main tasks of a coating system are the protection of the substrate from degradation and to provide a decorative finish to the surface [2,3].

The application of coatings requires an understanding of the use of specific materials used for coating, design or geometry of substrate and application process. The process for application of coating is usually dependent on energy consumption, raw material and cost of labour during the coating process [4]. The use of coatings is an effective and economical method of corrosion control, increasing the service life of a component and reducing the long term maintenance cost [4]. The cost of coatings is typically 5% to 21% of total cost which does not include the cost of preparing the surface [5].

When selecting a coating, it is also important to analyse the combination of substrate and coating. The coating-substrate combination should work efficiently without impairing the properties of the substrate, e.g. mechanical and thermal properties [6].

Selection of coatings is further complicated by the variety of mechanisms by which coatings protect substrates from corrosion [6]. Coatings can physically separate the metal from the environment or another metal, they can act as a source of corrosion inhibition, provide cathodic protection or can protect the metallic structure by a combination of all these mechanisms [6]. This combined protection can also be provided by using multilayer coating. Coatings can be broadly classified as organic, inorganic or metallic [5-7].

- **Metallic coatings** act as a barrier between the substrate material and environment, providing the mechanical properties of the substrate but with the ability to perform in the necessary working environment. The metallic coatings generally provide good corrosion resistance to the substrate even if the coating is damaged. The various processes for applying metallic coating include electroplating, hot dipping, thermal spraying, cladding and diffusion coating.
- **Inorganic coatings**, such as enamel coatings, are mainly used as water resistant coatings used for plumbing applications, while conversion coatings are formed by reacting the surface of the substrate metal in a controlled environment. These coatings provide corrosion resistance in a moderate environment but are usually less effective in aggressive environment.
- **Organic coatings** are typically paints, varnishes and lacquers. The essential features of a paint system include a vehicle that provides the

fluidity to the system, a pigment controlling the corrosion reaction and additives which promote drying of the coating.

2.2 Thermal spraying: A brief history and current status

During the early 1900's, Dr Max Ulrich Schoop , of the Swiss Republic, proposed that, when gas is projected from a nozzle at high velocity it causes the fluids to pulverise, similarly, a stream of molten metallic or non-metallic material can be projected towards a surface to produce coating, see **Figure 2.1** [8].

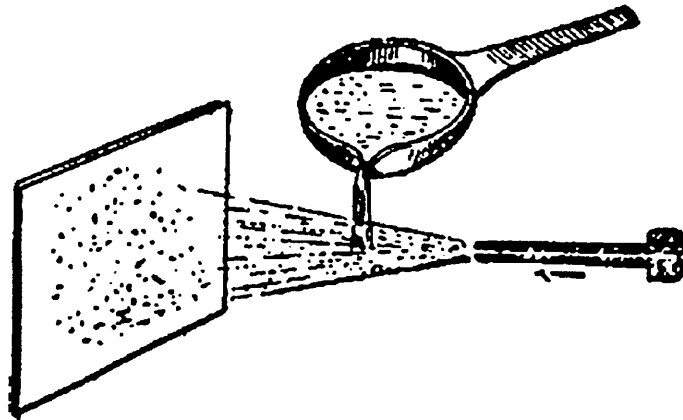


Figure 2.1: Diagrammatic representation of initial concept of thermal spraying based on pulverising of fluids by high velocity gas ejecting from a nozzle [8,10].

During the early stages of development, Dr Schoop and co-workers focused on pouring molten metal, such as zinc and lead, into a jet of gas at high pressure to deposit coatings [8]. The equipment designed for molten metal spraying was termed as Mellozing gun, which was rather challenging equipment in terms of obtaining a hot gas stream [8]. This lead Dr Schoop and co-workers to introduce a new Schori metallising process, which used

combustion of a fuel gas in presence of oxygen in order to heat the molten powder material along with a jet of high velocity hot gas [8].

Later in 1915, Dr Schoop submitted a patent to the United States Patent office [9], which was an initial design of spraying equipment that used electric arc to melt the metal wires and compressed air to project the molten metal on to the surface to be coated, laid the foundations of modern thermal spraying process [10]. During the period of First World War, the commercial use of thermal spraying started in Germany and was followed by France [8]. In the year 1922, the establishment of Metallisation Ltd in Dudley, formed the roots of commercial application of thermal spraying in United Kingdom [8,11]. **Figure 2.2** shows a famous image of Dr Schoop holding a sample in front of a thermal spraying gun which inspired the formation of Metallisation Ltd [11].

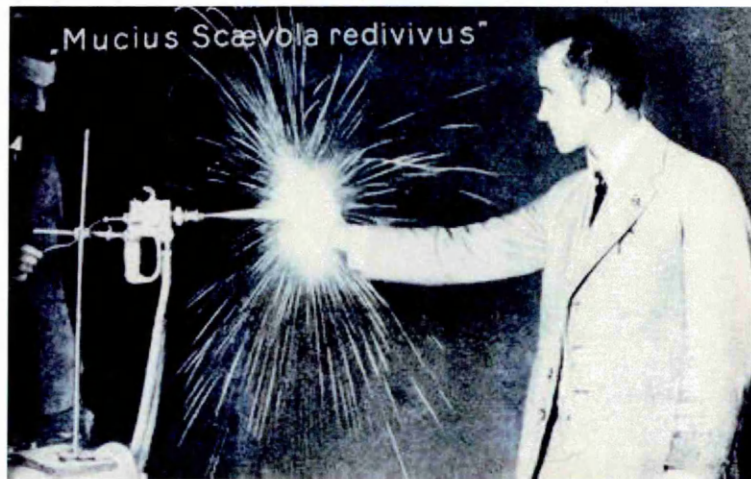


Figure 2.2: The famous postcard with Latin inscription "*Mucius Scaevola redivivus*" (meaning Mucius Scaevola returns) showing Dr Schoop and co-worker with thermal spraying gun or pistol [11].

With over a hundred years, since the initial development of thermal spraying, improvements in the process and better understanding of materials, has led to a wide variety of materials, including metals and ceramics, to be sprayed on to a prepared substrate [8,11,12]. Now, thermal spraying is a widely used technique in different engineering fields such as construction, oil, gas and petrochemical, where corrosion and wear resistant coatings are required [12]. The main advantages of using thermal spraying include [3,4,8,11,12]:

- Coating can be done *in-situ* meaning that large structural works can be coated.
- A wide range of coating thicknesses can be achieved by thermal spraying.
- Materials with a higher melting point can be sprayed on the surface, due to a high heat output of the energy sources used in thermal spraying.
- Thermal spraying is a lifetime economic process, which produces coating with long service life and less maintenance cost.
- Materials in form of powders, rods and wires can be sprayed using thermal spraying techniques.

During early 2013, a quarterly report submitted by SPRAYTIME [13] suggested that by 2020, the thermal spraying equipment and consumables market in the United States of America will value approximately \$275 million as compared to \$130 million in 2013, see **Figure 2.3**.

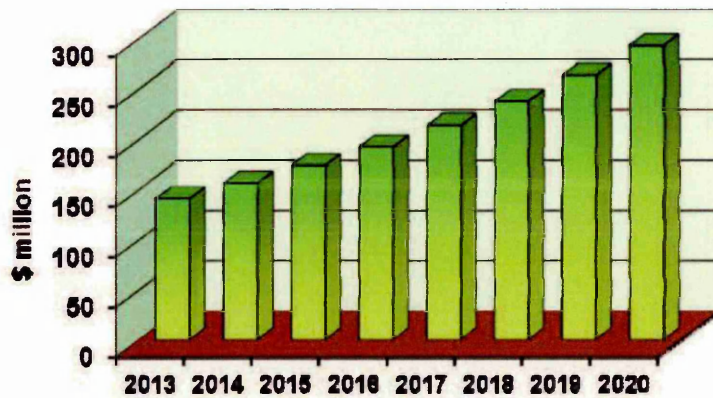


Figure 2.3: Graph showing predictive growth in the thermal spray market in USA [13].

A similar statistical report published by the United States Energy Information Administration (EIA) [14] and Exxon Mobil Corporation [15] also predicted that with almost 40% of global energy consumption will contribute towards power generation, thermal spraying will be widely adopted in the industry sectors such as coal petroleum, natural gas, biofuel, wind and solar power stations to protect the structures from corrosion and wear. In 2011, the annual turnover of thermal spray industry in Europe union was approximately € 2.066 billion, see **Figure 2.4**, with maximum thermal spray applications in automotive sector (21%), Mechanical engineering sector (19%), Aerospace (17%), Paper printing (15%) [16]. The highest market contribution of 30.2% was reported by Germany followed by United Kingdom, France and Italy at 19.2%, 18.5% and 11% respectively [16].

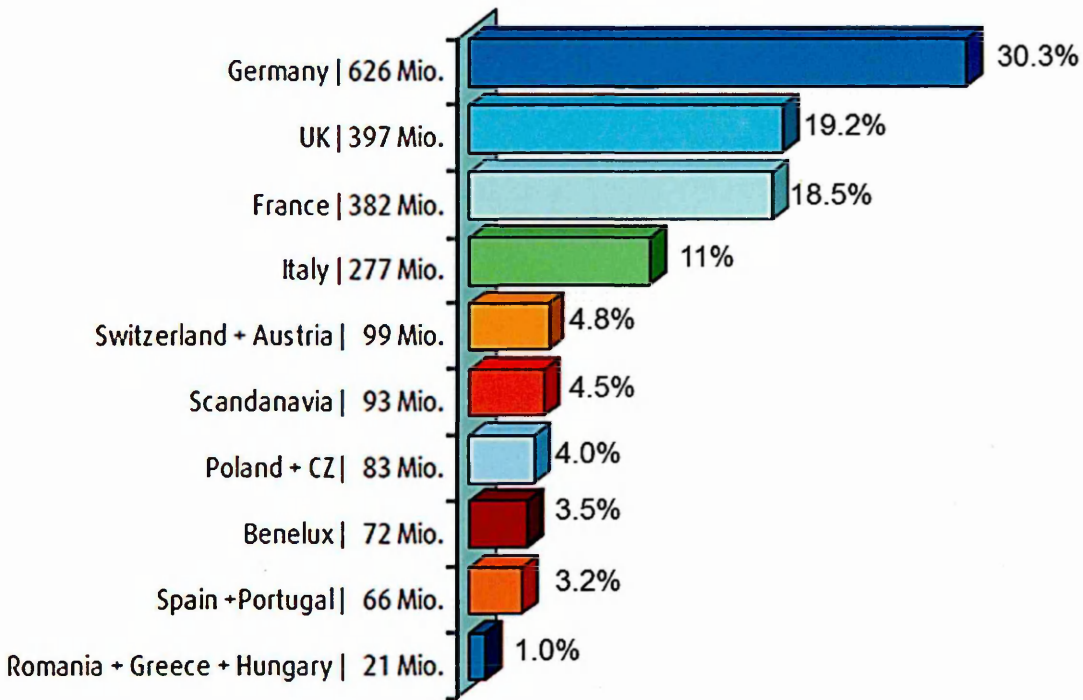


Figure 2.4: Graph showing contributions of different countries in European Union in generating € 2.066 billion annual turnover from thermal spraying applications [16].

A comprehensive report presented by 'Fukomoto' [17] stated that China's gross output from thermal spray industry increased from U.S \$0.14 billion to U.S \$ 0.24 during the period of 2002 to 2005. **Figure 2.5** (a), (b) and (c) shows the use to thermal spraying applications, feedstock materials and various spraying process which have contributed in growing the thermal spray market in China [17].

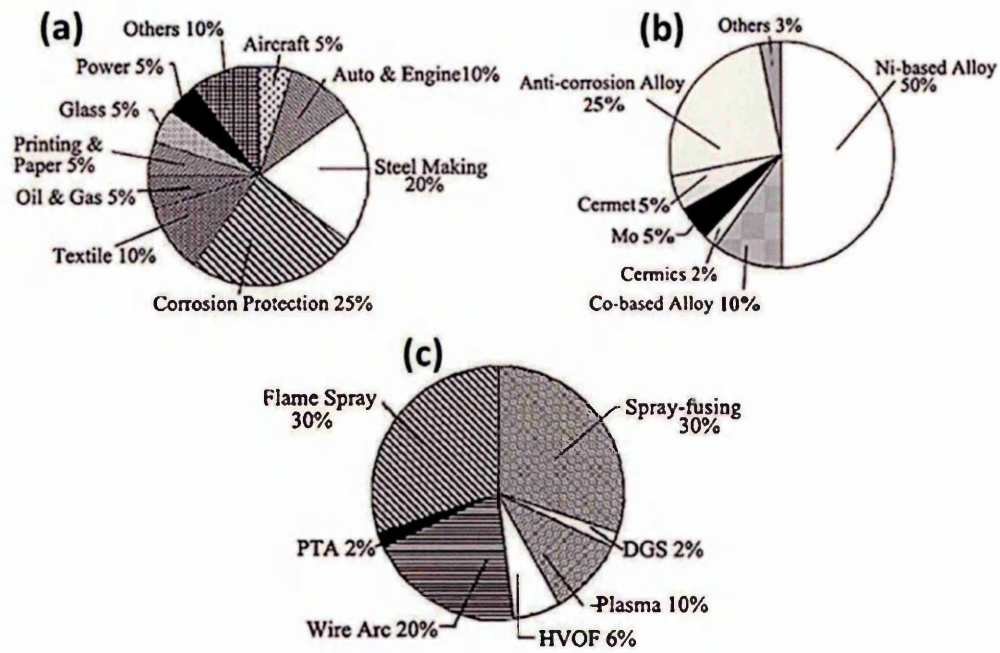


Figure 2.5: Graphs showing contribution of thermal spraying in (a) various industrial sectors (b) application of thermal spraying based on various feedstock materials and (c) application based on different thermal spraying processes [17].

Since 1970's considerable investment has also been done in exploring the use of thermal spraying in electronic industries to produce thick film electrical conductors, bioactive materials and solid oxide fuel cells [18]

2.3 Important thermal spraying processes

Various application techniques for thermal spraying exists, the most commonly used industrial spraying techniques include:

- **Flame Spraying [19-21]:** Flame spraying, also known as combustion flame spraying. According to the choice of material, flame spraying can be categorised as powder flame spraying and wire flame spraying. In the wire flame spraying gun the material in form of wire, typically 3-5 mm in diameter, is fed into the spraying gun. Ceramic or metal rods or wires can be used in spraying, with an average feed rate of 80 to 650 g/min. The flame generated by the combustion of fuel gas and oxygen, melts the end of the wire or rod, the melted wires or rod are atomised by a compressed gas and propelled towards the substrate.

The principles of powder flame spraying are similar except that the material fed in the gun is into the form of powder. The average powder particle size used in a flame spraying is in the range of 5-100 μm and is usually kept spherical in shape to maintain ease in handling and reducing the spraying spots. In flame spraying, the oxygen to fuel ratio is in range of 1:1 to 1.1:1 which produces a carburising to oxidising flame, the flame temperatures lies in the range of 3000-3350 K with a velocity of 80-100 m/s. Other process parameters, such as flow rate and pressure depend upon the flame torch type

A spraying distance from 120 to 250 mm is typically maintained, usually with a 90° spraying angle, but this may vary due to geometry

of the substrate. Typically, thick coatings ranging from 100-2500 μm and with porosity of 10-20 % can be produced by flame spraying.

- **High Velocity Oxy-fuel (HVOF) spraying** [19-21]: In high velocity oxy-fuel spraying (HVOF), the fuel (gases such as acetylene, kerosene, propane or hydrogen) is burnt with oxygen under high pressure to produce a high velocity exhaust jet. The powdered material to be sprayed is injected into the exhaust jet by carrier gas, which is burned in the combustion chamber. The flow rate of the gas is usually in the range of 40-60 NI/min (6-8 l/min). The powder size in the range of 5-45 μm is typically used, with a feed rate of 20-80 g/min. Carbides, for the purpose of producing wear resistant coatings, are the most commonly sprayed powders using HVOF. The carbide coatings sprayed using HVOF can have a very high bond strength (approximately 90 MPa), with less than 1% porosity with thickness ranging from 100-300 μm .
- **Arc Spraying** [22-36]: In an arc spraying process, two wires, which act as consumable electrodes are used as shown in **Figure 2.6**. The tips of the electrically conductive wires come into contact producing an arc, the heat generated by arc melts the wire and the molten metal atomised by compressed gas is then propelled towards the substrate. Typically, a conductive metal wire of diameter ranging from 2-5 mm is used. Cored wires, which are used to give particular alloy or composites, are also used in the arc spraying. The molten metal

particles formed can attain a velocity up to 150 m/sec. The characteristic property of an arc includes temperature, which during the process may reach 6000 K, the arc voltage, in the range of 20-40 V and arc current of 280 A, depending upon the material to be sprayed. These parameters can be altered during spraying to tailor the properties of the coatings, such as varying the oxide content in the coatings. The bond strength of the coating deposited by arc spraying varies in the range 10-30 MPa (typically for Al and Zn, can be higher for other alloys). Coating thickness can be controlled during the process. Arc spraying has also been used to produce moulds for plastic product applications and also for self-lubricating coatings.

During the current project, arc spraying was used to produce Al-Zn-In and Al-Ti-C coatings on to mild steel coupons in order to study the corrosion and wear resistance properties of the mentioned coatings.

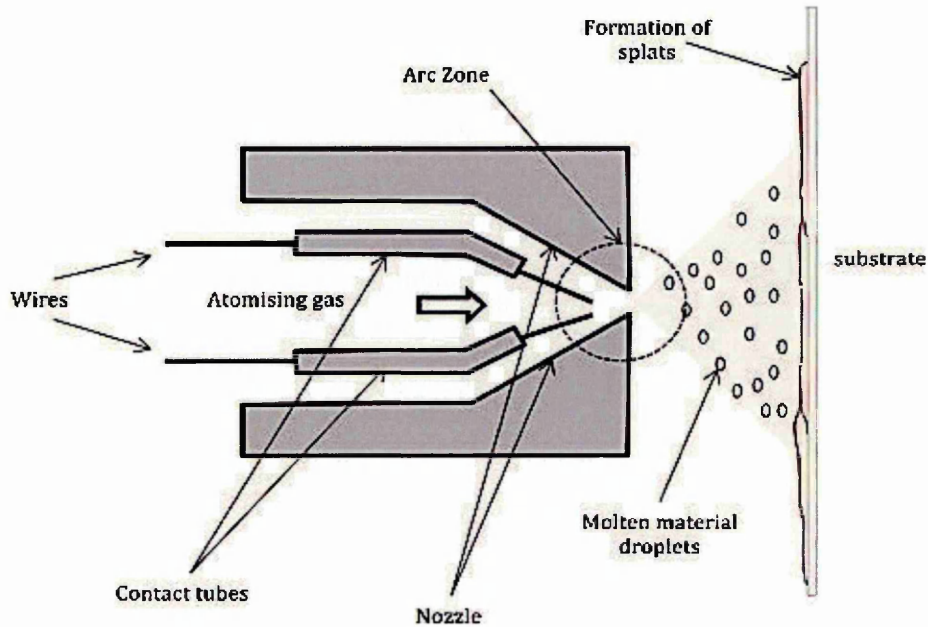


Figure 2.6: Schematic diagram of wire arc spraying gun [37].

2.4 Formation and Microstructure of thermal spray coating

The schematic of coating deposited using a thermal spraying process, where the metal or ceramic to be sprayed is melted and then projected towards a prepared substrate is shown in **Figure 2.7** [38]. The molten metal particles solidify rapidly to form a lenticular shape [38,39]. The formation of the sprayed layer is dependent on the spraying parameters such as, feed rate of powder or wires, working distance and linear speed of deposition [40]. Hence these spraying parameters play a significant role in formation of porosity and micro-cracks and the presence of oxides in the sprayed coating [40]. The formation of oxides in thermally sprayed metallic coating is attributed to oxidation of molten particles in-flight and oxidation of molten particles after impact on the substrate [41-45].

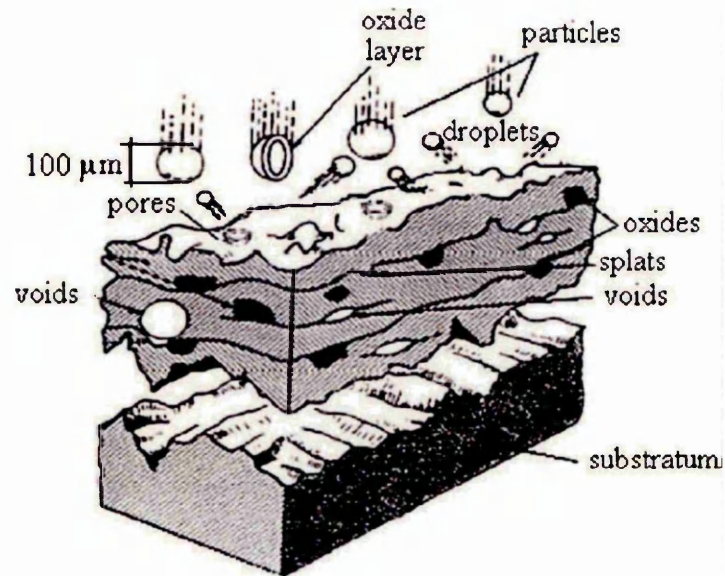


Figure 2.7: Schematic of coating deposition by thermal spraying process [38].

The coating adheres to the substrate by mechanical keying i.e. mechanically bonding to the substrate, hence for this reason the substrate has to have a sufficient degree of roughness [38-41].

The preparation of the surface of the substrate prior to deposition plays a major role in producing an optimum coating by achieving good bond strength between coating and substrate. The substrate is degreased, using organic solvents such as methanol or acetone to remove surface contamination, as traces of any contamination, such as oil or dirt on the surface is detrimental to the adhesion of the coating.

Occasionally, the substrate can be preheated to prevent any condensation on the surface [38,42]. The next step in surface preparation involves increasing surface roughness, which can be achieved by abrasive blasting. The blasting medium must be clean and the sharp edges of the grit particles

must be maintained. The blasting of the substrate leaves the surface more susceptible to oxidation; hence coating should be done as soon as the surface is blasted [21,38].

2.5 Thermally sprayed aluminium (Al) coatings

Aluminium (Al), unalloyed, provides a high degree of corrosion resistance due to formation of a thin tenacious oxide layer when exposed to the atmosphere. This natural protective mechanism of aluminium against corrosion is beneficial in many industrial applications. However aluminium is alloyed with elements such as Sn, Bi, In, Hg and Zn, which are used to increase the corrosion resistance of aluminium, while other elements such as Cr, Ti, Zr, Li and Ni increase the mechanical properties of aluminium [46].

Due to the inherent properties and effect of various alloying elements on the corrosion and wear resistance of aluminium, it has been used extensively as corrosion and wear resistant thermally sprayed coating to protect structural steel exposed to high temperature and marine environment [47].

Thermally sprayed aluminium coatings typically contain 1 to 3% of oxide and have a density of about 2.3-2.4 g/cm³, and when alloyed with elements such as Ti, Zr, Ni, it can also be used for high temperature (823 K-1173 K) application [47]. As an active metal, the rate of corrosion of aluminium under immersion conditions depends on the dissolved oxygen content of water, the concentration of chloride and percentage of other heavy metal present, hence aluminium combined with zinc is used for extended lifetime during

service of the coating by providing it good galvanic protection ability [47-50]. The protective mechanism of the thermally sprayed aluminium alloy coating [46-50] is illustrated in **Figure 2.8**, which shows:

- During thermal spraying, increasing the level of oxide in the coating (varied by changing the spray parameters) or using Al alloyed with elements such as Ti, Ni, C to produce coatings which significantly reduces the number of active corrosion sites and increases the wear resistance, acts as a physical barrier between the substrate and environment.
- The corrosion products formed act to block porosity in the coating, thus further improving the barrier properties of the coating.
- Aluminium, when alloyed with zinc and other elements such as In, Sn, Hg, are sprayed to steel structures, the alloys sprayed increase the galvanic protection ability, which results in, enhanced protection ability of the coating, in which the coating when damaged, corrodes preferentially and in doing so protects the substrate [14,30].

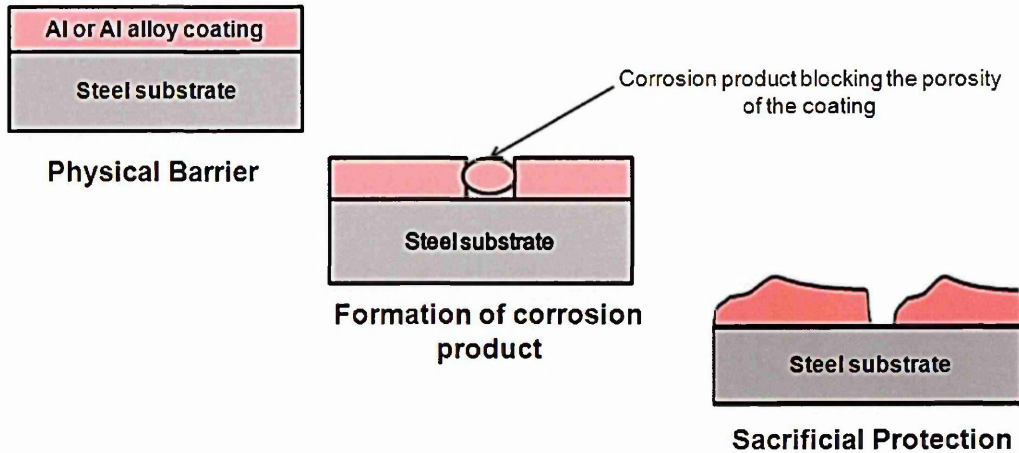


Figure 2.8: Schematic of corrosion and wear protection mechanism offered by aluminium alloy coatings to steel structures.

The focus of this project was to investigate the two Al based coating system; the Al-Zn-In coating was primarily investigated for corrosion resistance and Al-Ti-C coating primarily for wear resistance, however corrosion resistance of Al-Ti-C coating was also evaluated. The next few sections of this chapter contains a comprehensive literature which lucidly explains the nature of both ternary alloy systems in terms of alloying effects and mechanism of corrosion and wear for the alloys.

2.6 Sacrificial anodes

2.6.1 A brief introduction to Galvanic corrosion

The effect of coupling dissimilar metals in an aqueous electrolytic solution resulting in an electrochemical potential difference between the metals was observed by Luigi Galvani in 1791 [51].

Figure 2.9 shows the galvanic series of various metals and alloys exposed to sea water at 25⁰C. It can be seen that the free corrosion potential or open circuit potential (OCP) varies from a negative values (active) to a positive potential (noble) values measured with respect to saturated calomel electrode (SCE).

Whenever two dissimilar metals are coupled together in presence of an electrolyte, consider zinc coupled with steel, the metal which has more negative open circuit potential, in this case Zinc, acts as an anode and corrodes preferentially. The other metal which has a more positive open circuit potential, steel with respect to zinc, acts as a cathode. In doing so, zinc sacrificially protects the steel. This coupling action forms the basis of cathodic protection system by using sacrificial anodes [52-54].

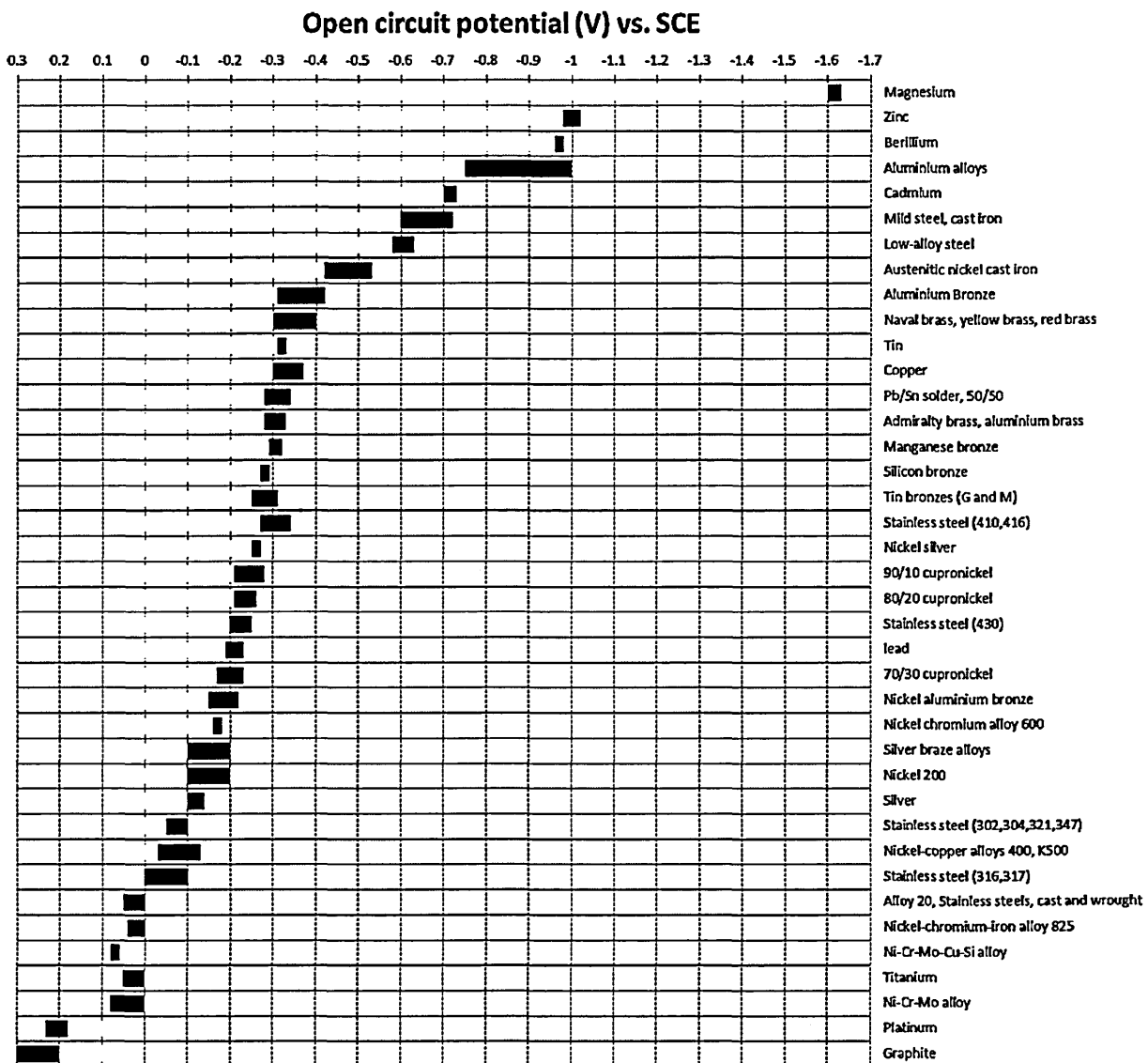


Figure 2.9: Galvanic series of metals and alloys in sea water at 25⁰C [55].

2.6.2 Factors affecting galvanic corrosion

It is important to note that the galvanic coupling of metals and alloys which can be potentially used as sacrificial anodes in cathodic protection system must be chosen with careful consideration [60-61].

Some key factors that significantly affect the performance of metals and alloys used as sacrificial anodes and are discussed in following points:

1. The values of open circuit potential (OCP) shown in the galvanic series, see **Figure 2.9** are used as guidelines for considering the optimum galvanic couple. The variation of composition of electrolyte, motion of the electrolyte and the exposure temperature considerably affect the values of OCP of the metals and hence the performance of metals chosen as sacrificial anodes [52,53].

For example, as mentioned in the earlier paragraph, zinc and steel form a galvanic couple with zinc (the anode) being more electronegative than steel (the cathode) and corroding preferentially, protecting the steel. However, when the zinc-steel couple is exposed to an electrolyte containing nitrates, carbonates and bicarbonates above 60⁰C, the anodic nature of zinc reduces [53,56,57]. It was also demonstrated in the previous research that addition of chlorides to a specific ratio regained the anodic nature of zinc [58].

2. In the formation of a galvanic couple, the ratio of the area of the anode and cathode must be chosen correctly. Mathematically, in a galvanic corrosion process [59]

$$I_{\text{corr}} = I_{\text{anode}} = -I_{\text{cathode}} \quad \text{Equation 1}$$

If the areas of anode and cathode in galvanic cell are same then **Equation 1** can be rewritten in terms of corrosion current densities as [2]

$$\frac{I_{\text{anode}}}{A_{\text{anode}}} = \frac{-I_{\text{cathode}}}{A_{\text{cathode}}} \quad \text{Equation 2}$$

From **Equation 2**, it can be stated that a larger anodic area with respect to cathodic area will prove to be detrimental as the anode will have a larger current density for a smaller anode, which will accelerate corrosion at anode [2,7]. For this reason, anodes are preferred to have a larger area as compared to cathodes.

2.6.3 Requirements of sacrificial anode

The outlines of the sacrificial anode have been discussed in the previous section. From **Figure 2.9**, it can be seen from their position in galvanic series that aluminium, zinc and magnesium are the suitable commercially available candidates for forming potential sacrificial anodes for steel structures [52]. The performance of materials used as sacrificial anodes are usually measured in terms of current discharged continuously by a unit mass of anode during the process and is expressed as $Ahkg^{-1}$ and is termed as anode capacity [52,60]. In reality, the anode capacity which can be calculated from Faraday's law or the theoretical value of anode capacity is less than the actual capacity of the anode material when used in cathodic protection systems and is expressed mathematically as anode efficiency, given as [60].

$$(\%) \text{ Anode efficiency} = \frac{\text{Anode capacity}}{\text{Theoretical capacity}} \times 100 \quad \text{Equation 3}$$

The consumption rate of anode is also an important parameter which is a measure of anode material which will be consumed if it operates at a certain anode capacity and is expressed in $\text{kgA}^{-1}\text{Year}^{-1}$ [60].

In order to choose anodic materials to cater the requirements of cathodic protection the two most important factors that must be taken into consideration [52,60,61]:

1. The primary requirement of a material to be effective for cathodic protection is that the open circuit potential of the anodic material should be more electronegative than the structure to be protected in a given corrosive environment.

2. The anodic material should have a high anode capacity, i.e the material should corrode uniformly and provide a higher current per unit mass consumed without passivation from the corrosive environment of exposure.

Cathodic protection using sacrificial anodes has successfully been used in protecting pipelines both subsea, underground and concrete structures and other wide areas on industries where components are exposed to corrosive environment. In order to achieve the desired protection, most of the metals which are commonly used as sacrificial anodes are alloyed [60].

A sacrificial cathodic protection system is a preferred choice for structures exposed to a marine environment [62]. Structures exposed to marine environment encounter degradation caused due to sea water, which has high levels of dissolved oxygen and high chloride content [63]. The highly corrosive nature of the sea water adds to another requirement of understanding the interaction of the anodic material with the sea water in

terms of both corrosion and its operational capability for optimum service life [63].

Various commercially available alloys of aluminium, zinc and magnesium have been successfully used in sacrificial cathodic protection systems, but only aluminium alloys will be discussed further as this project focuses on thermally sprayed novel aluminium alloys for protecting steel structures.

2.6.4 A brief history of cathodic protection

The written evidences on corrosion have been reported since the time of Plato in early 400 B.C. Ever since then, other ancient philosophers tried to explain corrosion as naturally occurring phenomena and worked on methods to protect the metals from the detrimental effects of corrosion by applying coatings of red or white lead and tar .

In 1936, some sealed copper cylinders with iron cores were excavated near Baghdad which were believed to have been used as a battery source for jewellery decoration by electrolysis. These findings supported the fact that people of that era knew about the effects of dissimilar metal contact even before galvanic coupling effect was recognised [61]. Many more such historical evidences have been logged (such as India's iron pillar) that affirm the fact that methods of protecting metallic structures from corrosion have been studied for centuries [59].

It was in the year 1824 that Sir Humphry Davy, who accepted a commission from the British admiralty for protection of copper clad vessels from corrosion, due to the marine environment. He reported the use of zinc or iron

coupled with copper will reduce the effect of corrosion. However his endeavour was partially successful as coupling of copper with zinc or iron did cathodically protect copper, but made the copper susceptible to marine fouling.

It was then in 1950's that it was realised that the use of fouling resistant paints would make cathodic protection of sea freighting vessels feasible. For over a century now cathodic protection has been a major corrosion mitigation method being used onto metallic structures buried in soil and exposed to a marine environment [61,64].

2.6.5 The basics of cathodic protection

The metallic structures buried in soil or exposed to marine environment under unprotected conditions will favour formation of a localised corrosion cell as shown in **Figure 2.10**. This formation of anodes and cathodes (formation of local anodes and cathodes on same metallic structure depends on exposure of the metallic surface to operations such as machining, forming etc.) on the metallic structure causes a potential difference to exist between the localised areas. Due to this potential difference a circuit is formed in which the ionic current from the anode with corrosive environment as a conductive medium flows to local cathodic region and the conductivity of the metallic structures allows the flow of electrons to the anode. This completes the corrosion cell and causes metal loss at anodic sites [55].

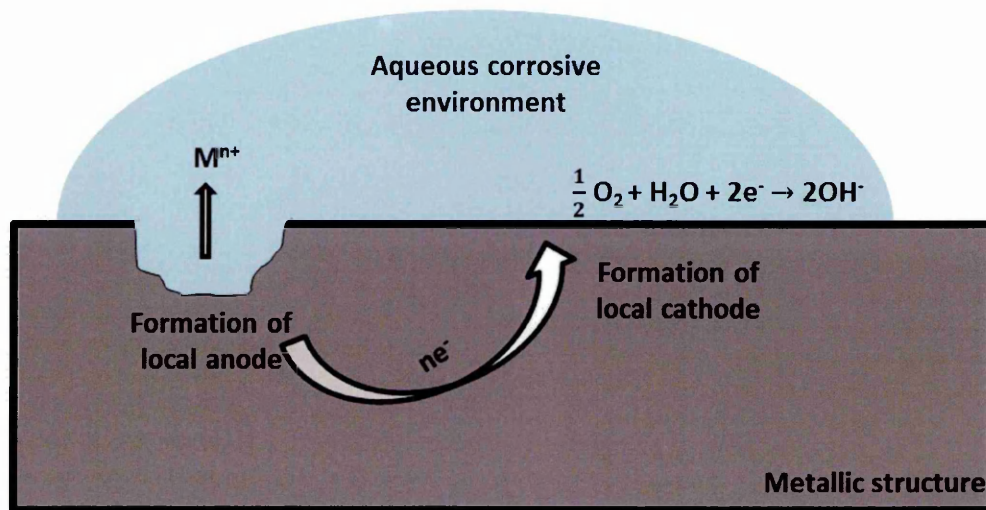


Figure 2.10: Schematic of formation of a corrosion cell in a metallic structure when exposed to corrosive environment [55].

In order to avoid the formation of localised corrosion cell either the metallic structure is connected to an external power supply and anode which makes the structure cathode by continuous supply of current (known as impressed current protection) or by attaching a less noble metal which acts as an anode with respect to the metallic structure and corrodes preferentially and protects the structure from the adverse effects of corrosion (sacrificial anodes). These two methods form the basis of cathodic protection system [51,55]. The impressed current cathodic protection method will not be discussed further as the major emphasis of the project will be on sacrificial anodes.

2.7 A brief introduction to application and limitation of Al as sacrificial anode material

Aluminium (Al) is mostly abundant in earth's crust in form of silicates, oxides (Al_2O_3), bauxite ore ($\text{Al}_2\text{O}_3 \cdot n\text{H}_2\text{O}$) and in form of complex $\text{Al}(\text{H}_2\text{O})_6^{3+}$ ion in water [62]. When extracted from its ores, due to its inherent mechanical, electrical and thermal properties, see **Table 2.1**, aluminium is most suited for wide range of engineering applications [65].

Table 2.1: Important properties of unalloyed aluminium [66].

Properties of unalloyed Al (atomic no. 13)	
Density (gcm^{-3})	2.70
Melting Point ($^{\circ}\text{C}$)	660.32
Boiling point ($^{\circ}\text{C}$)	2520
Thermal conductivity ($\text{Wm}^{-1}\text{K}^{-1}$), temperature range $^{\circ}\text{C}$	
0-100	238
200	238
400	238
Coefficient of expansion 10^{-6}K^{-1} , temperature range $^{\circ}\text{C}$	
0-100	23.5
100	23.9
200	24.3
300	25.3
400	26.49
Electrical resistivity $\mu\Omega^{-1}$, temperature range $^{\circ}\text{C}$	
20	2.67
100	3.55
200	4.78
300	5.99
400	7.30
Temperature coefficient of resistivity 0-100 $^{\circ}\text{C}$, 10^{-3}K	4.5

Considering the properties of unalloyed aluminium listed in **Table 2.1** and the electronegative potential with respect to steel as shown in galvanic series in **Figure 2.9**, Al is used as a sacrificial anode to steel structures used in marine and oil and gas industry [67,68].

One of the major limitations of using pure Al as a sacrificial anode is that when Al is exposed to air or a marine environment, the rapid formation of an adherent passive oxide layer (Al_2O_3) takes place which prevents the uniform corrosion and lowers the anode capacity of Al [69,70]. Thus Al is alloyed with various other metals to mitigate the formation of this passive oxide layer and maintain a constant electronegative potential when coupled as a galvanic anode [68]. Al alloys have been a preferred choice as sacrificial anodes in marine environment in comparison to magnesium (Mg) and zinc (Zn) due to following reasons:

1. The average life of Mg sacrificial anodes is in the range of 6 to 12 months as it is highly reactive and is generally used in a electrolyte medium which has a higher resistivity (such as river water) [71].

2. Zn is also a favourable anodic material with high anode capacity, but a major limitations is that when Zn is exposed to temperature above 60°C it loses its anodic nature (discussed under section 2.6.2) therefore limits its usage [57,71].

3. Al and its alloys in comparison with Zn and Mg has a higher anode capacity (anode capacities in decreasing order: Al (2700 Ah/kg) >Mg (1230 Ah/kg)>Zn (780 Ah/kg)) [71,72]. The other properties such as lower cost, longer service life and light weight of aluminium broadens the use of Al not only as sacrificial anode in light weight structures but also structures exposed to marine environment [72].

2.8 Alloying of Al: Enhancement of sacrificial properties

The main purpose of alloying the metals used as sacrificial anodes is to improve the performance of the anodes by driving the operating potential to a more electronegative region, avoid passivation and make the surface of the anode corrode uniformly [60].

Considering aluminium (Al), which is well known for its application as sacrificial anodes to protect metallic structures exposed to marine environment (especially sea water) , when it comes in contact with a high chloride content of the sea water, forms a passive oxide layer at OCP \approx -0.80 V vs.SCE [73]. The formation of this oxide layer hinders the use of unalloyed Al as sacrificial anode for steel structures as it significantly reduces its anode capacity [74].

In order to maintain the electronegativity of Al anode by reducing the formation of tenacious passive oxide layer, elements such as zinc (Zn), magnesium (Mg), cadmium (Cd), barium (Ba) known as modifiers and indium (In), mercury (Hg), tin (Sn), gallium (Ga), titanium (Ti), thallium (Tl) known as depassivators are used [75].

2.8.1 Background on alloying Al for improving the electrochemical properties

The understanding of the electrochemical properties of both binary and ternary Al alloys formed by combination of modifiers and depassivators had started almost fifty years ago [75-81]. *Reding and Newport* published a paper in 1966 which discussed the effects of various alloying elements at various alloying concentrations (modifiers and depassivators) on the electrochemical properties of Al sacrificial anodes [82].

The significance of alloying composition (%mass) on the OCP of Al was evaluated in sea water, as shown in **Figure 2.11** [82]. As it can be seen from **Figure 2.11**, the elements shaded with light grey reportedly had no effect on the OCP of Al, while Mn and Cu (shaded light green) produced a positive shift in the OCP of Al [82]. The elements shaded with light red (Mg, Ba, Zn and Cd), also termed as modifiers lowered the OCP of Al alloy by 0.1 V to 0.3 V (vs.SCE) in comparison with pure Al [76,82].

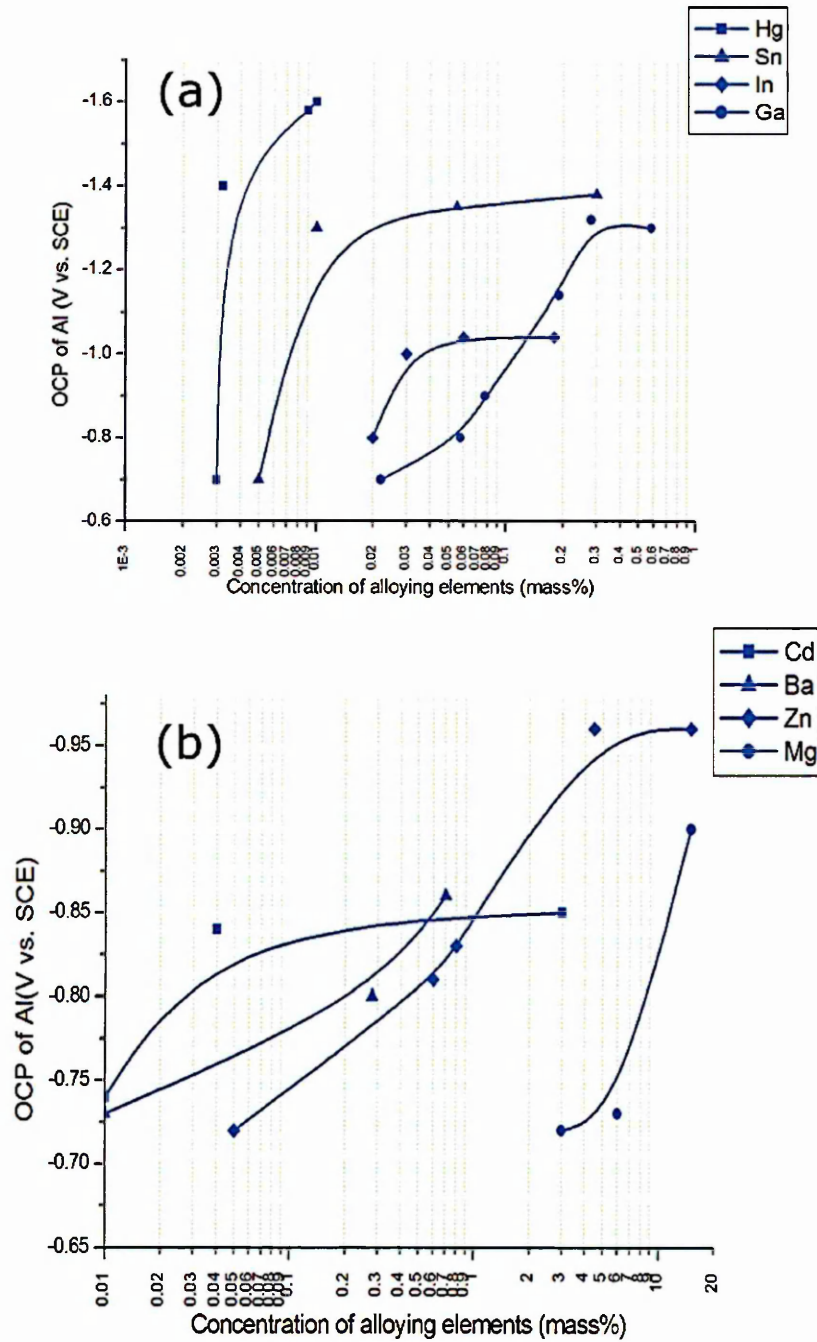


Figure 2.12: Graphs showing the effect of alloying of (a) depassivators (b) modifiers on the OCP of Al (vs. SCE) [82,83].

The authors reported that the addition of modifiers such as Zn and Mg up to 10wt%, similarly Ba and Cd up to 0.6wt% and 3wt% respectively, were effective in reducing (shifting in more electronegative direction) the OCP (vs. SCE) Al, as shown in **Figure 2.12(b)** [82]. Comparing **Figure 2.12 (a)** and (b), the addition of depassivators to a much lower concentration such as Hg up to 0.01wt%, Sn up to 0.3wt%, In up to 0.2wt% (however the graph indicated that addition of In further from $\approx 0.05\text{wt}\%$ to 0.2wt% did not significantly affect the OCP of Al) and Ga up to 0.6wt% produced a greater electronegative shift in the OCP of Al (vs.SCE) than larger additions of modifiers [82].

During this study, it was reported that alloying elements including depassivators and moderators, which produce the highest electronegative shift in the OCP of Al showed similar properties [82]:

- It was observed that the elements which produced the maximum electronegative shift in the OCP of Al have lower melting points than Al (exception being Ba), see **Table 2.2**.

Table 2.2: Elements (depassivators and modifiers) and their melting temperatures which significantly lower the OCP of Al [82,83].

Elements		Melting temperature ($^{\circ}\text{C}$)
Hg	Lowering OCP by 0.3 V to 0.9 V	-39
Ga		29.6
In		156
Sn		232
Bi		271
Cd	Lowering OCP by 0.1 V to 0.3 V	321
Zn		420
Mg		650
Ba		727

- The elements producing maximum negative shift of the Al OCP, the solubility of these elements such as In, Ga, Sn, Hg, Cd, Ba, exception being Zn and Mg in Al and vice-versa was found low.
- The authors also reported that depassivators do not form intermetallic compounds with Al.

In addition to the deductions by *Reding* and *Newport* on the alloying elements which make Al more electronegative, *Reboul et al.* [84] added that there existed no co-relation between the working potentials of the Al alloys and individual theoretical potentials of the alloying elements. It can be seen from **Table 2.3**, considering Hg which is cathodic to Al, when alloyed with Al produces maximum electronegative shift in the working potential (proposing that depassivating elements are cathodic to Al) [84].

Table 2.3: The thermodynamic potential of various elements (at pH 8) that have been alloyed with Al to form sacrificial anodes and working potential of Al alloys measured (at 6.2 A/m²) in ASTM D 1141-52 (left) [83,84].

Al binary and ternary alloys	Working potential (V vs. SCE)	Individual elements	Thermodynamic potential (V vs. SCE)
Al	-0.73	Hg	+0.15
Al-Li		Fe } Sn }	-0.85
Al-Mg			
Al-In	-0.85	In	-0.95
Al-Zn	-0.95	Zn	-1.2
Al-Zn-Hg	-1.05	Al	-2.3
Al-Zn-In } Al-Zn-Sn }	-1.1	Mg	-2.8
		Li	-3.3
Al-Sn	-1.35		
Al-Hg	-1.6		

Table 2.4: Composition of Al alloys tested by *Kier et al.*, coupled with mild steel in 0.1M NaCl solution exposed for 48 hours[85]. The experiments were conducted in duplicates and triplicates.

Alloying elements with Fe and Si as major impurities			Corrosion current (A)
(wt%)element	(wt%)Fe	(wt%) Si	
0.12 Sn	0.004	0.003	4.55×10^{-3} , 5.12×10^{-3} , 5.69×10^{-3}
0.10 Ge	0.004	0.003	4.05×10^{-5} , 4.05×10^{-5}
0.20 Si	0.004	-	5.20×10^{-5} , 2.54×10^{-5}
0.10 Ti	0.004	0.003	1.45×10^{-4} , 6.36×10^{-5}
0.17 Zr	0.008	0.003	2.31×10^{-5} , 3.47×10^{-5}
99.997 Al	0.001	0.001	1.16×10^{-4} , 1.22×10^{-4}

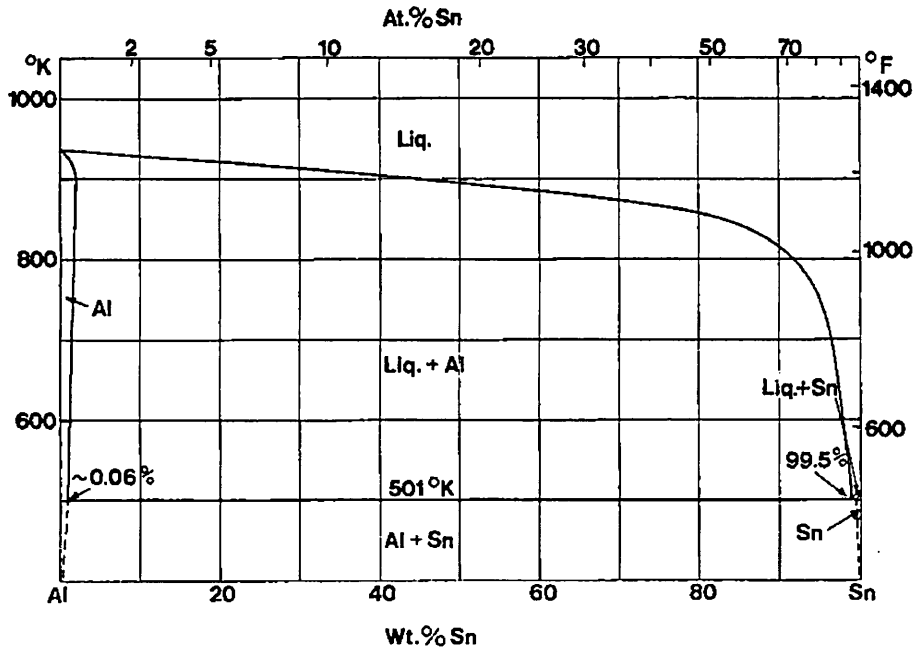


Figure 2.13: Al-Sn phase diagram [70].

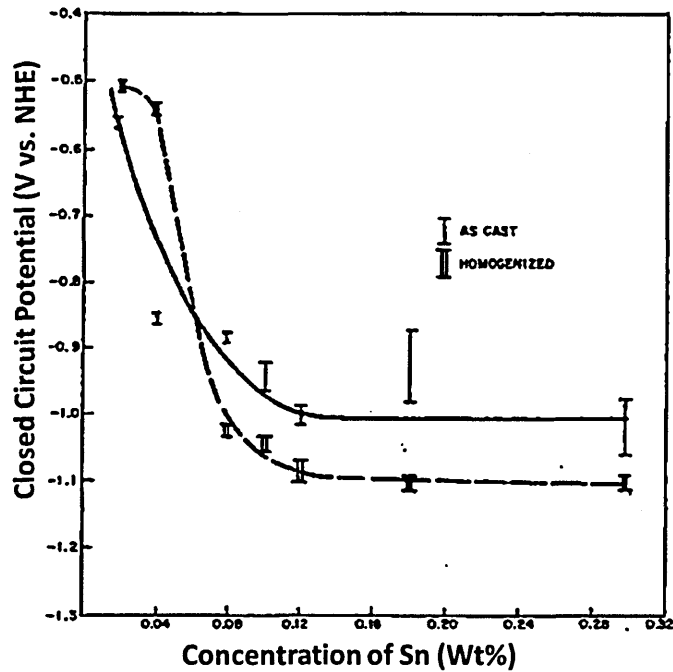


Figure 2.14: Graph showing the effect of Sn concentration (wt%) on the closed circuit potential (CCP) of Al-Sn alloy, coupled with mild steel in 0.1M NaCl solution for 48 hours[85].

The work conducted by *Kier et al.* [85] on Al alloys with composition as shown in **Table 2.4** was also in accordance with findings by *Reding* and *Newport*, that elements (depassivators, see **Figure 2.11**) that make Al more electronegative have low melting points.

The authors observed that out of all the alloying elements mentioned in **Table 2.4**, only Al-Sn alloy (with 0.12wt%Sn) showed increase in galvanic current significantly when coupled with mild steel in 0.1M NaCl solution [85]. The investigations were conducted on Al-Sn binary alloys containing 0.02wt% to 0.3wt%Sn, but ≈ 0.1 wt%Sn was found to be effective in lowering the closed circuit potential (CCP) (see **Figure 2.14**) of Al-Sn alloy by -1.0 V (vs.NHE) in galvanic coupling experiment with mild steel in 0.1M NaCl [85].

As seen from **Figure 2.14**, It is important to note that in order to produce consistency in results, the Al-Sn alloy was homogenised at ≈ 900 K for 16 hours, as at this temperature Sn has been reported to have maximum solid solubility (0.10wt%) in Al which decreases to ≈ 0.05 wt% to 0.07wt% at eutectic temperature of 500 K, see **Figure 2.13** [60,84-86].

2.8.2 Mechanism of activation of Al alloys: Lattice expansion

Song *et al.* [87] employed a probabilistic computer simulation model to understand the phenomena of passivation and activation of metallic alloys, and analysed binary Al alloys formed by modifiers and depassivators to study activation of Al alloys.

The authors considered addition of Zn (< 5wt%) in Al lattice exposed in alkaline environment. The authors proposed that activation of Al is caused by diffusion of Zn atom on Al lattice surface causing the breakdown of Al_2O_3 passive layer (Al-O-Al bond). This produces end points of Al-O-Al chain of the form $Al(OH)OAl(OH)_2$, which increases the probability of dissolution of Al atoms neighbouring Zn atom surface [87].

However, not producing any quantitative results but the model generated by the authors showed that the activation of Al is not just dependent on the kinetics of dissolution caused by modifiers and depassivators but also on the rate of diffusivity of activator elements in the Al alloys [87].

A similar study to understand the effects of depassivators and modifiers on the lattice of the Al when alloyed with depassivators and modifiers was

performed by *Sharma et al.* [88] by using ab-initio and thermodynamic modelling methods.

The authors conducted a study on Al-Sn alloy system by adding de-passivators and modifiers such as Ga, In, Bi and Mg (in addition, the authors also used Zr as an alloying element, which has been previously reported to show no effect on sacrificial performance of Al alloy anodes) at varying molar concentrations of 0.93%, 1.85%, 3.13% and 6.25% respectively.

It is important to note that the work conducted by *Sharma et al.* is in accordance with the lattice expander theory which was used by *Kier et al.* [89] in explaining that how ternary alloying of Al-Sn system in form of Al-Sn-X alloys (where X can be Bi, Mg, Zr, Ag, Co, Fe, As, Ni, Zn, Cu & Mn) can either enhance or reduce the sacrificial anode properties of Al-Sn alloys. As shown in **Table 2.5**, the addition of 0.16wt%Bi (note that the authors choose all the alloying concentrations in the range of 0.012wt% to 1.0wt% as per the solubility of each element in Al) in Al-0.2wt% Sn alloy significantly increased the corrosion current when coupled with mild steel in 0.1M NaCl solution [88].

Following their previous work [84], the authors proposed that presence of Sn in Al as a solid solution not only de-passivates the oxide film formed on Al alloy by reducing the oxide film resistivity by creating cation vacancy by replacing Al^{3+} ions by Sn^{4+} ions but also expands the Face Centred Cubic lattice of Al [88].

The authors showed (see **Table 2.6**) in addition with Sn, elements such as Bi, Mg, Zr and Ag show a similar expansion in the lattice of Al and in doing

so support further addition of Sn, while elements such as Zn, Cu, Mn and Si (which is commonly found impurity in Al alloys) contracts the Al lattice [88].

The authors suggest that this mechanism of lattice expansion underpins the evidence that how ternary addition to Al-0.2wt%Sn alloy increases or decreases the corrosion current, as shown in **Table 2.5**.

Further explanation by *Sharma et al.*[88], as shown in **Table 2.6** and **Figure 2.15** by ab-initio calculations to obtain the effective atomic radii of each of the alloying element in FCC Al lattice proves to be the major contributing factor in Al lattice expansion. **Table 2.6** shows that in FCC Al lattice Bi and In produce the largest change in the alloy volume(see **Figure 2.15**) due to increases in the effective atomic radii of each element in Al lattice followed by Zr and Mg (approximately similar effective atomic radii for Mg and Zr) and least being Ga [88].

Table 2.5: The effect of ternary alloying addition on the corrosion current of alloys when coupled with mild steel in 0.1M NaCl solution for 48 hours [89].

Addition of elements to Al-0.2wt%Sn alloy	Corrosion current (A)
No addition to Al-0.2wt%Sn	4.92×10^{-3} , 5.38×10^{-3}
+ 0.16wt%Bi	7.00×10^{-3} , 9.14×10^{-3}
+1.10wt%Mg	4.57×10^{-3} , 5.84×10^{-3}
+0.094wt%Zr	4.57×10^{-3} , 4.69×10^{-3}
+0.013 wt%Ag	5.61×10^{-3} , 6.02×10^{-3}
+ 0.021wt%Co	3.65×10^{-3} , 5.21×10^{-3}
+0.076wt%Fe	4.63×10^{-3} , 4.86×10^{-3}
+ 0.012wt%As	3.99×10^{-3} , 3.99×10^{-3}
+0.096wt%Ni	1.79×10^{-3} , 2.14×10^{-3}
+1.05wt%Zn	2.03×10^{-3}
+0.10wt%Cu	1.74×10^{-3}
+ 0.84wt%Mn	1.45×10^{-3}

Table 2.6: Data on effect of alloying per unit wt% on Al lattice [88].

Alloying elements		Effect of alloying element on the Al Lattice (+ expansion, - contraction) in Å/wt% addition
Sn		+0.0045
Bi	} Lattice expanders	-0.0052
Mg		
Zr		
Ag	} No effect	0.00002
Co		
Fe		
As		
Ni		
Zn	} Lattice contractors	-0.0003
Cu		-0.0022
Mn		-0.0033
Si		-0.0017

Table 2.7: The effect of alloying element on the Al lattice [88].

Elements	Crystal structure	Experimental value of atomic radii in crystal structure (Å)	Effective atomic radii of alloying element in FCC Al lattice by ab initio calculations (Å)
Al	Face Centred Cubic (FCC)	1.43	1.43
Ga	Orthorhombic	1.35	1.49
Mg	Hexagonal	1.60	1.60
Zr	Hexagonal	1.60	1.60
In	Tetragonal	1.67	1.70
Bi	Rhombohedral	1.50(covalent radius)	1.78

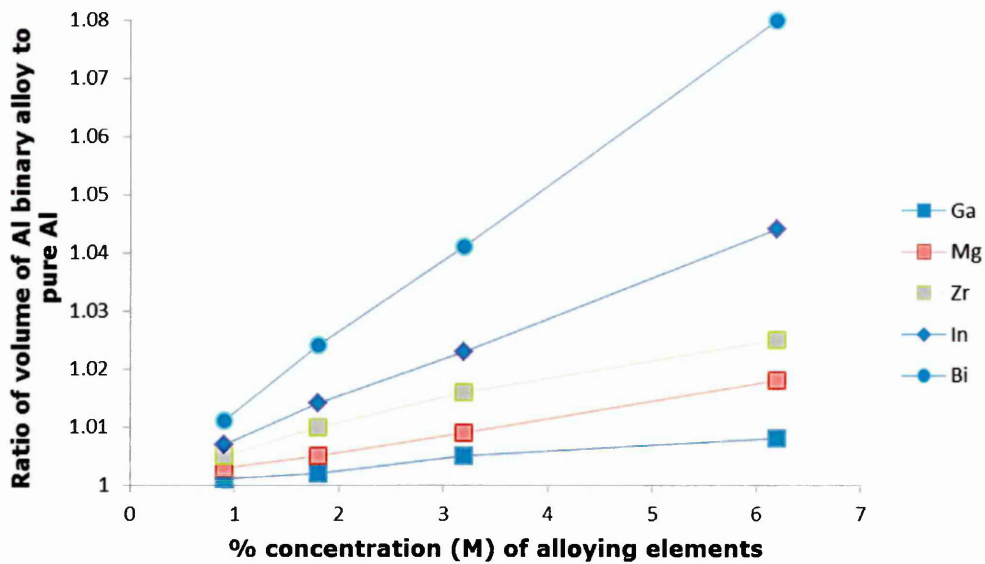


Figure 2.15: Graph showing the effect of alloying concentration of depassivators and modifiers on the ratio of volume expansion of Al alloys lattice to that of pure Al lattice [88].

Sharma *et al.* [88] investigated the ternary alloying of Mg in Al-0.034mol% Sn (Al-0.15wt%Sn) by varying the concentration of alloying as 1.11mol%, 2.22 mol%, 3.32mol% and 4.43mol% Sn (\approx 1.00wt%Sn, 2.23wt%Sn, 3.00wt%Sn and 4.00wt%Sn) respectively.

As seen from **Figure 2.16**, the authors demonstrated that increasing Mg addition proves detrimental to the solubility of Sn in Al due to formation of Mg_2Sn intermetallic compound [88]. However, authors performed experimental investigation on heat treated Al-Sn-Mg anodes by heating the anodes (to \approx 900 K for 20 hours followed by rapid quenching in water) and found that the sacrificial performance of Al-Sn-Mg anodes was not affected, proposing that heat treatment restricts the formation of Mg_2Sn intermetallic compound [88].

According to the authors, even though the thermodynamic calculations shows that higher concentration of Mg enables forming Mg_2Sn intermetallic compound, restricting Sn solubility in Al lattice. But experiments showed no effect in the sacrificial performance of Al-Sn-Mg ternary alloy after performing heat treatment which restricts the formation of intermetallic Mg_2Sn and thereby maintain the effect of Sn in Al lattice [88].

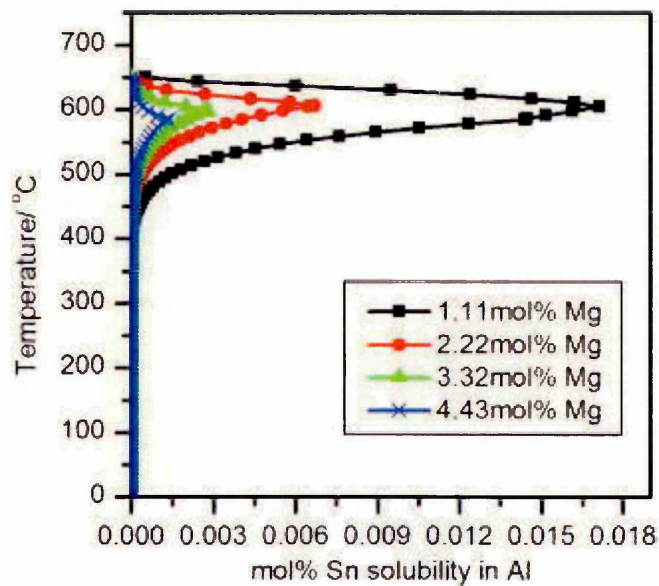


Figure 2.16: Graph showing the effect of Mg concentration at 1.11mol%, 2.22mol%, 3.32mol% and 4.43mol% (1.00wt%, 2.23wt%, 3.00wt% and 4.00wt%) on solubility of Sn in FCC Al lattice [88].

2.8.3: Thermodynamics of activation of Al alloys: Surface enrichment

Andreev et al. [90] also studied the effects of alloying Al with Zn, In and Sn (in form of binary Al-B alloys, where B can be Zn, In or Sn) on sacrificial performance of the Al anodes by using thermodynamic calculations and experimental methods. Considering the thermodynamics of the Al alloy systems, the authors emphasised on the fact that firstly, the activation of alloys is possibly due to increase in the conductivity of the oxide film owing to complex oxide formation (of the form $\text{Al}_2\text{O}_3(\text{B}_a\text{O}_y)$) by the alloying elements. This in turn induces the uniform dissolution of the alloy and secondly by segregation of alloying elements at the interface of oxide layer and alloy surface [90].

The work conducted by *Andreev et al.* primarily focused on understanding the phenomena of surface segregation (or enrichment) of In, Sn and Zn on the oxide and surface of Al alloys [90].

The authors while explaining the thermodynamics of binary Al alloys with Zn, Sn and In, have used equations, which have previously been used by *Hondros* [91] to study the surface enrichment phenomena of other metallic binary alloy systems (in this study, *Hondros* have considered 31 binary alloy systems, majorly consisting of elements such as Fe, Cu, Ge, Au, Ni as solvents alloyed with both high and low concentrations of elements such as Ag, Ti, Pb, La, As, S, In, Te). The surface enrichment data was gathered either from already published surface tension isotherms or from previously conducted surface spectroscopy experiments on alloy systems.

It is important to note that all the thermodynamic analysis of binary Al-B alloys performed by *Andreev et al.* was done at normal room temperature (≈ 298 K) assuming that equilibrium exists between the bulk and the surface of Al alloys [40]. However, it has been reported in previous researches that, during alloying process, the elements with lower melting points or lower values of surface tension enrich the surface of the alloys [91].

During the thermodynamic analysis, *Andreev et al.* considered, adsorption of two different species of atoms from the bulk to the surface [90]. According to the Gibb's adsorption equation for binary alloying systems [90], showing the equilibrium between the bulk(b) and surface(s), considering the low index face of the surface layer, usually (111), (100) and (110) for Face Centred Cubic (FCC) Al [92]:

$$\Delta\sigma = -\sum_{i=1}^2 \Gamma_{Si} \Delta\mu_{Si} \quad \text{Equation 4}$$

The atoms of species S_1 and S_2 , during surface adsorption causes the change in the chemical potentials as shown in **Equation 4**, mathematically $\Delta\mu_{S1}$ and $\Delta\mu_{S2}$ can be represented as [90]:

$$\Delta\mu_{S1} = \Delta\mu_{S1}(s) - \Delta\mu_{S1}(b) \quad \text{Equation 5}$$

$$\Delta\mu_{S2} = \Delta\mu_{S2}(s) - \Delta\mu_{S2}(b) \quad \text{Equation 6}$$

If the species S_1 is considered to be adsorbed by the surface causing surface enrichment, then **Equation 4** in terms of individual effects of species S_1 and S_2 can be written as [90]

$$\Delta\sigma = \Delta\sigma_{S1} + \Delta\sigma_{S2} \quad \text{Equation 7}$$

In a metallic crystal, due spontaneous transfer of atoms from the bulk to the surface as a self-adsorption process, this causes formation of vacancies and makes the crystal thermodynamically unstable [93]. Now if the species S_1 is adsorbed by the surface and atoms of species S_2 transferred from the surface to the bulk, then from **Equation 7** it can be stated as [90]:

$$\Delta\sigma = -\Gamma_{S_1}\Delta\mu_{S_1} + \Gamma_{S_2}\Delta\mu_{S_2} \text{ Equation 8}$$

Where negative and positive signs indicate the decrease and increase in the $\Delta\sigma_{S_1}$ and $\Delta\sigma_{S_2}$ due to adsorption and desorption of species S_1 and S_2 [90]. However considering this binary alloy system, in order to attain thermodynamic stability, the decrease in the $\Delta\sigma_{S_1}$ due to adsorption of atoms of species S_1 should be equal to desorption of atoms of species S_2 , which mathematically can be represented as [90]:

$$-\Delta\sigma_{S_1} = \Delta\sigma_{S_2} \text{ Equation 9}$$

Now from **Equations 7, 8 and 9** it can be stated that [90]:

$$\Delta\sigma_{S_1} + \Delta\sigma_{S_2} = -\Gamma_{S_1}\Delta\mu_{S_1} + \Gamma_{S_2}\Delta\mu_{S_2} = 0 \text{ Equation 10}$$

Substituting the values of $\Delta\mu_{S_1}$, $\Delta\mu_{S_2}$ from **Equations 5 and 6** in **Equation 10** to be re-written as [90]

$$\Gamma_{S1} \Delta\mu_{S1} = \Gamma_{S2} \Delta\mu_{S2}$$

Or

$$\Gamma_{S1} (\mu_{S1}(s) - \mu_{S1}(b)) = \Gamma_{S2} (\mu_{S2}(s) - \mu_{S1}(b)) \quad \text{Equation 11}$$

The change in the chemical potentials for S_1 and S_2 (for bulk material) using **Equation 11** can be written as (case of non-ideal solutions) [90]:

$$\mu_{S1}(b) = \mu_{S1}^0(b) + RT \ln a_{S1(b)} \quad \text{Equation 12}$$

And

$$\mu_{S2}(b) = \mu_{S2}^0(b) + RT \ln a_{S2(b)} \quad \text{Equation 13}$$

Where $a_{i(b)}$ (i can be S_1 and S_2 or other species i in the bulk) is defined as the product of activity coefficient and the mole fraction of the atoms of the species, where $N_{S1} + N_{S2} = 1$, R and T are the gas constant and temperature in Kelvin [90]:

$$a_{i(b)} = \gamma_{i(b)} N_{i(b)} \quad \text{Equation 14}$$

As shown in **Equations 12 and 13**, similarly the change in chemical potentials at the surface for S_1 and S_2 can be written as [90]:

$$\mu_{S1}(s) = \mu_{S1}^0(s) + RT \ln a_{S1(s)} \quad \text{Equation 15}$$

And

$$\mu_{S2}(s) = \mu_{S2}^0(s) + RT \ln a_{S2(s)} \quad \text{Equation 16}$$

Similarly where $a_{i(s)}$, is defined as the product of activity coefficient of species S_1 and S_2 at the surface and mole fraction of the atoms of the species at the surface, in this case $x_{S1} + x_{S2} = 1$ and like **Equation 14** , it can be written as [90]:

$$a_{i(s)} = \gamma_{i(s)} x_{i(s)} \quad \text{Equation 17}$$

Now substituting **Equations 12, 13, 14 and 16** in **Equation 11** [40]:

$$\begin{aligned} \Gamma_{S1} (\mu_{S1}^0 (s) + RT \ln a_{S1 (s)} - (\mu_{S1}^0 (b) + RT \ln a_{S1 (b)}) = \\ \Gamma_{S2} (\mu_{S2}^0 (s) + RT \ln a_{S2 (s)} - (\mu_{S2}^0 (b) + RT \ln a_{S2 (b)}) \end{aligned} \quad \text{Equation 18}$$

Rearranging **Equation 18**,

$$\begin{aligned} \Gamma_{S1} (\mu_{S1}^0 (s) - \mu_{S1}^0 (b)) + \Gamma_{S1} RT (\ln a_{S1 (s)} - \ln a_{S1 (b)}) = \\ \Gamma_{S2} (\mu_{S2}^0 (s) - \mu_{S2}^0 (b)) + \Gamma_{S2} RT (\ln a_{S2 (s)} - \ln a_{S2 (b)}) \end{aligned}$$

Or

$$\begin{aligned} \Gamma_{S1} (\mu_{S1}^0 (s) - \mu_{S1}^0 (b)) + \Gamma_{S1} RT \ln \left(\frac{a_{S1 (s)}}{a_{S1 (b)}} \right) = \\ \Gamma_{S2} (\mu_{S2}^0 (s) - \mu_{S2}^0 (b)) + \Gamma_{S2} RT \ln \left(\frac{a_{S2 (s)}}{a_{S2 (b)}} \right) \end{aligned} \quad \text{Equation 19}$$

Considering the case of self-adsorption (as in this case for species S_1 and S_2), the Gibb's excess concentration is related to the surface area of one mole of metal as [90,94]:

$$\Gamma_{S_1}^{-1} = A_{S_1} \text{ Equation 20 (a)}$$

And

$$\Gamma_{S_2}^{-1} = A_{S_2} \text{ Equation 20 (b)}$$

Now from **Equation 19**, the terms $(\mu_{S_1}^0(s) - \mu_{S_1}^0(b))$ and $(\mu_{S_2}^0(s) - \mu_{S_2}^0(b))$ are equal to the $\Delta G_{S_1}^0$ and $\Delta G_{S_2}^0$ [90,92]. Further, if Gibb's excess free surface energy terms are divided by the respective molar surface area of one mole of species S_1 and S_2 , this gives the specific Gibb's excess free surface energy as [90]:

$$\sigma_{S_1}^0 = \Delta G_{S_1}^0 / A_{S_1} \text{ Equation 21 (a)}$$

$$\sigma_{S_2}^0 = \Delta G_{S_2}^0 / A_{S_2} \text{ Equation 21 (b)}$$

Substituting the values of $\Gamma_{S_1}^{-1}$, $\Gamma_{S_2}^{-1}$ from **Equations 20 a, b**, $\sigma_{S_1}^0$, $\sigma_{S_2}^0$ from **Equation 21 a, b** and $a_{i(b)}$, $a_{i(s)}$ from **Equation 14 and 17** into **Equation 19** [90,94]:

$$\sigma_{S_1}^0 + \frac{RT}{A_{S_1}} \ln \left(\frac{\gamma_{S_1(s)} X_{S_1}}{\gamma_{S_1(b)} N_{S_1}} \right) = \sigma_{S_2}^0 + \frac{RT}{A_{S_2}} \ln \left(\frac{\gamma_{S_2(s)} X_{S_2}}{\gamma_{S_2(b)} N_{S_2}} \right) \text{ Equation 22}$$

Multiplying the left and right hand side of the Equation 22 by the respective molar surface areas of species S_1 and S_2 to give [90]:

$$\sigma_{S_1}^0 A_{S_1} + RT \ln \left(\frac{\gamma_{S_1(s)} X_{S_1}}{\gamma_{S_1(b)} N_{S_1}} \right) = \sigma_{S_2}^0 A_{S_2} + RT \ln \left(\frac{\gamma_{S_2(s)} X_{S_2}}{\gamma_{S_2(b)} N_{S_2}} \right) \text{ Equation 22a}$$

Or

$$\sigma_{S_1}^0 A_{S_1} + RT \ln \left(\frac{y_{S_1(s)}}{y_{S_1(b)}} \right) + RT \ln \left(\frac{X_{S_1}}{N_{S_1}} \right) =$$

$$\sigma_{S_2}^0 A_{S_2} + RT \ln \left(\frac{y_{S_2(s)}}{y_{S_2(b)}} \right) + RT \ln \left(\frac{X_{S_2}}{N_{S_2}} \right) \quad \text{Equation 22b}$$

Or

$$\Delta G_{S_1}^0 + RT \ln \left(\frac{y_{S_1(s)}}{y_{S_1(b)}} \right) + RT \ln \left(\frac{X_{S_1}}{N_{S_1}} \right) = \Delta G_{S_2}^0 + RT \ln \left(\frac{y_{S_2(s)}}{y_{S_2(b)}} \right) + RT \ln \left(\frac{X_{S_2}}{N_{S_2}} \right)$$

Equation 22 (c)

The left and right hand side of **Equation 22c**, represents the energy characteristics of two different species of atoms S_1 and S_2 implying that the left and right hand side of **Equation 22c** represents the partial specific free energy of formation of alloy with species S_1 and S_2 [90,95]. Considering that the thermodynamic analysis was being conducted on binary Al-B alloys (where B can be Sn, In, Zn), in order to calculate molar surface areas of low index faces of species S_1 and S_2 , which can be either of Sn, In, both of which have a Body centred tetragonal (BCT) structure or Zn, which is hexagonal closed packed (HCP) structure (see **Table 2.8**) [90,92].

Table 2.8: Table showing the lattice parameters of Al, Sn, In and Zn with the two dimensional area of a low index face for each element [92].

Elements	Crystal structure	Low index faces	Lattice Parameters (Å)	Area (in two dimensions, Å ²)
Al	FCC	(111)	a = 4.049	$\frac{\sqrt{3}}{4} a^2 = 7.098$
		(100)		$\frac{1}{2} a^2 = 8.197$
		(110)		$\frac{1}{\sqrt{2}} a^2 = 11.592$
Sn	BCT	(001)	a = 3.187,	a ² = 10.157
		(110)	c/a = 1.83	$\frac{1}{\sqrt{2}} ac = 13.142$
		(100)		ac = 18.586
In	BCT	(001)	a = 3.352,	a ² = 11.235
		(110)	c/a = 1.52	$\frac{1}{\sqrt{2}} ac = 12.076$
		(100)		ac = 17.079
Zn	HCP	(0001)	a = 2.684 , c/a = 1.86	$\frac{\sqrt{3}}{2} a^2 = 6.238$

As **Equation 22 c** represents the partial specific free energies of formation of alloy with species S_1 and S_2 in this case Al alloyed with In, Sn and Zn, the molar surface area of low index faces of alloying elements in FCC Al lattice will be considered \approx to molar surface of low index face Al (implying, A_{In} , A_{Sn} , $A_{Zn} \approx A_{Al}$) [40]. Hence left hand side of the **Equation 22 c** represents [90]:

$$\Delta G_{S_1}^0 + RT \ln \left(\frac{\gamma_{S_1(s)}}{\gamma_{S_1(b)}} \right) + RT \ln \left(\frac{X_{S_1}}{N_{S_1}} \right) = \sigma_{Al-B} A_{S_1} \quad \text{Equation 22(d)}$$

Similarly right hand side of **Equation 22 c** [40]:

$$\Delta G_{S_2}^0 + RT \ln \left(\frac{\gamma_{S_2(s)}}{\gamma_{S_2(b)}} \right) + RT \ln \left(\frac{X_{S_2}}{N_{S_2}} \right) = \sigma_{Al-B} A_{S_2} \quad \text{Equation 22 (e)}$$

During the alloy formation, not only Gibbs free energy of surface formation plays a major role ($\Delta G_{S_1}^0$, $\Delta G_{S_2}^0$) but also the interaction energy of the alloying elements, in terms of partial enthalpies of formation of alloys in the bulk ($\Delta H_{(b)}$) and surface ($\Delta H_{(s)}$) which can be represented as [90, 95]:

$$\Delta H_{(b)} = RT \ln \gamma_{i(b)} \quad \text{Equation 23(a)}$$

$$\Delta H_{(s)} = RT \ln \gamma_{i(s)} \quad \text{Equation 23 (b)}$$

Now it is important to note that interaction of the elements in binary Al-B alloy is due to interaction between the similar atoms of Al matrix along with similar

atoms of alloying elements B and cross-interaction of Al and B atoms which can be mathematically represented as [90,96]:

$$H_{Al-B} = n_{Al-Al}H_{Al-Al} + n_{Al-B}H_{Al-B} + n_{B-B}H_{B-B} \quad \text{Equation 24}$$

But considering the fact that the alloying elements B (Zn,Sn,In) are in FCC Al lattice, so the enthalpy of breaking of each bond in the bulk Al-B lattice with effective coordination number $Z_0=12$ and 6 bond pairs ($Z_0/2$) will be $\Delta H_{(b)}/6$ [90,93,96]. Now, for adsorption of the atoms from the bulk Al-B alloy to the surface of alloy with a particular face index, which has a coordination number Z_b , the excess enthalpy of formation of bond at the surface can be written as [90]:

$$\Delta H_{(s)} = (Z_b - 12) \frac{-\Delta H_b}{6} \quad \text{Equation 25}$$

If at the surface, the bond formation happens on (111) face, which has a coordination number $Z_b = 9$, then **Equation 25** changes to [90]:

$$\Delta H_{(s)} = \frac{1}{2} \Delta H_{(b)} \quad \text{Equation 26}$$

For Al-B alloy surface with low index value (111), **Equations 22 c** changes to [90]:

$$\Delta G_{Al}^0 + RT \ln \left(\frac{Y_{Al(s)}}{Y_{Al(b)}} \right) + RT \ln \left(\frac{x_{Al}}{N_{Al}} \right) = \Delta G_B^0 + RT \ln \left(\frac{Y_{B(s)}}{Y_{B(b)}} \right) + RT \ln \left(\frac{x_B}{N_B} \right)$$

Equation 27

Substituting the values of $Y_{Al(b)}$, $Y_{B(b)}$, $Y_{Al(s)}$, $Y_{B(s)}$ from **Equations 23 a and b** into **Equation 27** [90]:

$$\Delta G_{Al}^0 + (\Delta H_{Al(s)} - \Delta H_{Al(b)}) + RT \ln \left(\frac{x_{Al}}{N_{Al}} \right) = \Delta G_B^0 + (\Delta H_{B(s)} - \Delta H_{B(b)}) + RT \ln \left(\frac{x_B}{N_B} \right)$$

Equation 28

For (111) orientation, substituting the values of $\Delta H_{Al(s)}$, $\Delta H_{B(s)}$, in terms of $\Delta H_{Al(b)}$ and $\Delta H_{B(b)}$ in **Equation 28** [90]:

$$\Delta G_{Al}^0 + \left(\frac{-\Delta H_{Al(b)}}{2} \right) + RT \ln \left(\frac{x_{Al}}{N_{Al}} \right) = \Delta G_B^0 + \left(\frac{-\Delta H_{B(b)}}{2} \right) + RT \ln \left(\frac{x_B}{N_B} \right) \quad \text{Equation 29}$$

Solving further, the **Equation 29** leads to:

$$\frac{x_B}{N_B} = \frac{x_{Al}}{N_{Al}} e^{\left(\frac{\Delta G_{Al} - \Delta G_B}{RT} \right)} e^{\left(\frac{\Delta H_B - \Delta G_{Al}}{2RT} \right)} \quad \text{Equation 30}$$

Equation 30 represents the enrichment factor of Al-B alloying system which is defined as ratio of molar concentration of alloying elements (In, Sn, Zn) on the surface to the bulk $\left(\frac{x_B}{N_B} \right)$, in terms of molar Al concentration on the surface to the bulk, excess Gibbs free energy for Al (ΔG_{Al}) and B (ΔG_B) and enthalpy of formation of Al (ΔH_{Al}) and B (ΔH_B) bonds on (111) orientation of the surface of the alloy [90,91].

Considering the binary Al-B solid solution close to be an ideal solution (or regular solution), the values of ΔH_{Al} and ΔH_B in terms of molar concentrations can be written as [90,96]:

$$\Delta H_{Al} = (1 - N_{Al})^2 \Omega \quad \text{Equation 31 (a)}$$

$$\Delta H_B = (1 - N_B)^2 \Omega \quad \text{Equation 31 (b)}$$

Where Ω is a function of coordination number and partial enthalpies of the alloying elements in the binary Al-B solution [90,96]. From **Equation 30**, the term $(\Delta H_B - \Delta H_{Al})$ can be rewritten as [90,96]:

$$(\Delta H_B - \Delta H_{Al}) = (1 - N_B)^2 \Omega - (1 - N_{Al})^2 \Omega = (1 - 2N_B) \Omega \quad \text{Equation 32}$$

Now substituting the value of $(\Delta H_B - \Delta H_{Al})$ from **Equation 32** into **Equation 30**:

$$\frac{x_B}{N_B} = \frac{x_{Al}}{N_{Al}} e^{\left(\frac{\Delta G_{Al} - \Delta G_B}{RT}\right)} e^{\left(\frac{(1 - 2N_B)\Omega}{2RT}\right)} \quad \text{Equation 33}$$

For binary Al-B alloys, the solubility of Sn ($\approx 0.10\text{wt\%}$ at 900 K), In ($\approx 0.07\text{wt\%}$ In at 800 K) except for Zn (from $\approx 2.5\text{wt\%}$ to 70.0wt\% at the temperature range of 350 K to 716 K) in Al is low, which leads to the value of atomic interaction parameter, $\Omega > 0$ (or positive deviation from Raoult law) [70,90,96].

In order to calculate the surface enrichment factor for Al-B alloys, the solid solution was considered to be ideal, implying $\Omega = 0$ ($\Delta H_{Al} = \Delta H_B = 0$), which converts **Equation 33** to [90]:

$$\frac{x_B}{N_B} = \frac{1-x_B}{1-N_B} e^{\left(\frac{\Delta G_{Al} - \Delta G_B}{RT}\right)} \quad \text{Equation 34}$$

Since the alloying elements such as Sn, In have a body centred tetragonal and Zn with hexagonal close packed structure are in Al lattice. The value of molar surface area of lower index of each of the alloying element was considered similar to the face centred cubic low index Al face. Hence substituting the values of ΔG_{Al} and ΔG_B from **Equations 21a and b** into **Equation 34** to obtain [90]:

$$\frac{x_B}{N_B} = \frac{1-x_B}{1-N_B} e^{\left(\frac{\sigma_{Al}^0 - \sigma_B^0}{RT} A_{Al}\right)} \quad \text{Equation 35}$$

Table 2.9 shows the calculated values of the enrichment factor for binary Al-B alloys (the enrichment factor was calculated for FCC (111) face) using **Equation 35**. It is important to note that the enrichment factor shown in **Table 2.9** were calculated for 0.1wt% and 1.0wt%B (In,Sn,Zn) addition with ΔG_{Al} and ΔG_B calculated at 0 K and 298 using the relation [90,97]:

$$\Delta G^0_{(Al-B)}(T) = \Delta H_{(Al-B)} - T\Delta S_{(Al-B)} \quad \text{Equation 36}$$

Where $\Delta S_{(Al,Sn,In,Zn)}$ and $\Delta H_{(Al,Sn,In,Zn)}$ are the entropy and enthalpy of binary Al-B alloy at (111) face of the alloy. When the temperature is considered to be close to the melting point of each element, the value of $\Delta S_{(Al-B)} \approx L_m/RT_m$ [97]. For (111) face of binary Al-B alloy, the relation between the temperature and Gibb's free surface energy as shown by **Equation 36** can be rewritten as [90,97]:

$$\Delta G^0_{(Al-B)}(T) = \frac{\Delta H_{(Al-B)(b)}}{2} - L_m \frac{T}{T_m} \text{ Equation 37}$$

Now to infer the value of $\Delta G^0_{(Al-B)}$ at $T= 298 \text{ K}$, $\Delta G^0_{(Al-B)}$ at $T= 0 \text{ K}$ was calculated by substituting $T = 0 \text{ K}$ into **Equation 37** [90,97]:

$$\Delta G^0_{(Al-B)}(T= 298 \text{ K}) = \Delta G^0_{(Al-B)}(T= 0 \text{ K}) - L_m \frac{298}{T_m} \text{ Equation 38}$$

Table 2.9: Table showing the values of enrichment factor for Al alloyed with Zn ,Sn and In at 0.1wt% and 1.0wt% alloying concentration [90].

	Al	Zn	Sn	In
Tm, in 0C	660	420	232	156
Lm, in J/mol	10470	7200	7080	3270
$\Delta G^0_{(Al-B)}(T= 0 \text{ K})$, in J/mol	51233	37146	37339	32998
$\Delta G^0_{(Al-B)}(T= 298 \text{ K})$ in J/mol	47890	34049	33162	30729
$\frac{x_B}{N_B}$, at 1.0wt%B	-	126.3	203.2	298.6
$\frac{x_B}{N_B}$, at 0.1wt%B	-	239.7	350.0	819.9

The values of the enrichment factor $(\frac{x_B}{N_B})$ for binary Al-B (In, Sn, Zn) alloys at 0.1wt% and 1.0wt% concentration, which were calculated using **Equation 35** and thermodynamic data for each of the element at 0 K, showed an increase in the $(\frac{x_B}{N_B})$ values as the melting point of alloying element decreased, $(\frac{x_B}{N_B})_{Al-In} > (\frac{x_B}{N_B})_{Al-Sn} > (\frac{x_B}{N_B})_{Al-Zn}$ (see **Table 2.9**), hence concurring the initial findings by

Reding and Newport that low melting point elements, depassivators, activate the Al alloys [90,92].

2.8.4 Experimental validation of Surface enrichment theory for Al alloys

The thermodynamic approach to understand the phenomena of activation of various binary Al alloys by surface enrichment of elements such as In and Sn [90-97] was also underpinned by experimental investigations [90,98-103].

Andreev produced binary Al alloys with Zn (1wt% and 5wt%), Sn (0.1wt% and 1.0wt%) and In (1wt%In) by flux melting (the flux contains 50wt%NaCl, 20wt%KCl and 30wt%LiCl) of high purity Al with Zn, In and Sn. In addition, Al-1wt%In alloy was also prepared by vacuum melting to compare the effect on electrochemical performance of the alloys prepared by both processes [90].

Some of alloy samples were rapidly quenched by water immersion (S_{HT0}) and others were subjected to annealing [90]:

- At 600⁰C for 8 hours and then rapidly quenched using water (S_{HT1}).
- At 600⁰C followed by furnace cooling (S_{HT2}).
- At 600⁰C for 8 hours followed by another annealing at 400⁰C for 16 hours and then rapidly quenched by water immersion (S_{HT3}).

To validate the thermodynamic theory of surface enrichment by low melting points elements such as Sn and In, polished cross section of the alloys were subjected to 0.5M Na₂SO₄ electrolytic solution (reagent grade with <0.0005wt%Cl⁻ ions) [90].

The authors used Secondary Ion Mass Spectroscopy (SIMS) to measure the change in surface concentration of Sn in the binary Al alloy after 24 hours of exposure in 0.5M Na₂SO₄. Followed by the depth concentration profile, Auger Electron Spectroscopy (AES) was also used to analyse the surface concentration profile for Al-Sn alloys which were subjected to heat treatment processes as discussed earlier. The oxide film formation on the surface of the binary Al-Sn alloy after 24 hours of exposure in 0.5M Na₂SO₄ was also examined using Electron Spectroscopy for Chemical analysis (ESCA) [90].

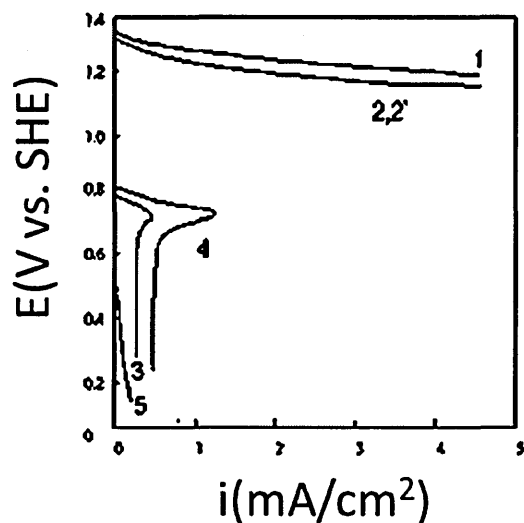


Figure 2.17: Anodic polarisation curves for (1) Al-1wt%Sn, (2) and (2') Al-1wt%In, Al-1wt%In (prepared by vacuum melting), (3) Al-1wt%Zn, (4) Al-5wt%Zn, (5) high purity Al in 0.5M Na₂SO₄ [90].

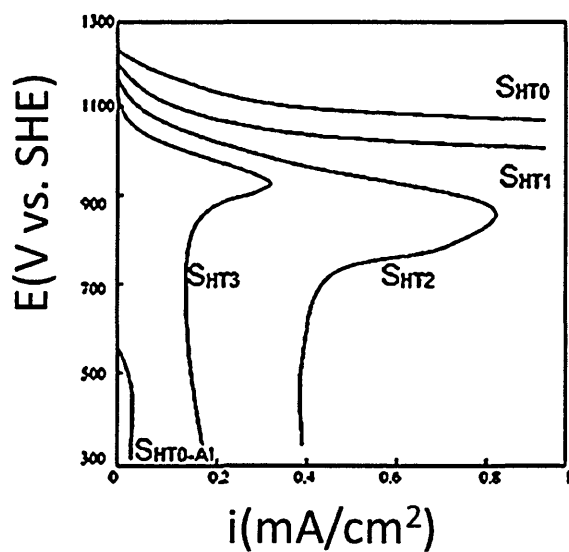


Figure 2.18: Anodic polarisation curves for Al-1wt%Sn alloy subjected to various heat treatment as shown, in 0.5M Na₂SO₄ (high purity Al for comparison) [90].

Table 2.10: SIMS analysis of Al-1wt%Sn alloy (S_{HT0}) before and after 24 hours of exposure in 0.5M Na_2SO_4 solution [90].

State of exposition	Counts/s of spectral lines		Intensity ratio of Sn^+ to Al^{2+}
	Al ²⁺	Sn ⁺	
Before exposure	179500	3000	0.017
After 24 hours of exposure	4280	9860	2.304

Table 2.11: AES concentration depth profile of Al-1wt%Sn alloy post anodic polarisation in 0.5M Na_2SO_4 solution (after 24 hours of exposure) [90].

Depth (nm)	Al (at%)		Sn (at%)		O (at%)	
	S_{HT0}	S_{HT3}	S_{HT0}	S_{HT3}	S_{HT0}	S_{HT3}
0.6	68.9	71.8	1.3	0.5	29.3	27.7
2.4	75.5	79.5	1.8	0.5	21.2	20.0
5.1	80.8	83.9	0.74	0.3	17.5	15.9
7.5	81.8	85.0	0.98	0.4	16.1	14.6
22.5	88.8	84.8	0.9	0.4	9.3	14.9
37.5	92.9	88.3	0.43	0.2	6.3	11.5
67.5	95.2	91.1	0.42	0.2	3.9	8.7
157.5	96.1	94.6	0.51	0.4	2.8	5.0
277.5	97.1	96.1	0.31	0.3	2.2	3.6

The anodic polarisation curves, see **Figure 2.17**, showed that Sn and In (1wt% addition) had an enhanced activating effect than 1wt% and 5wt%Zn when alloyed with Al in binary form (all the alloying followed S_{HT0}). However it was shown that alloying process, which was flux and vacuum melting did not had significant effect on activation of Al alloy by 1wt%In (see curve 2 and 2' from **Figure 2.17**) [90].

Figure 2.18 shows that S_{HT0} process profoundly increased the activation caused by 1wt%Sn in Al than the other heat treatment processes and the order of activation was $S_{HT0} > S_{HT1} > S_{HT2} > S_{HT3}$ [90]. This decreasing order of activation caused by 1wt%Sn was attributed to the fact, that at ≈ 900 K, a maximum of 0.10wt%Sn is retained in the solid solution of Al matrix which decreases to 0.05wt%-0.07wt% as the temperature lowers to ≈ 500 K (see **Figure 2.13**) [90,70].

The chemical analysis at nominal surface depth of 300-400 nm of Al-1wt%Sn alloy after 24 hours of exposure in 0.5 M Na_2SO_4 revealed the formation of Al and Sn oxides or hydroxides at the surface, which diminished in intensity with increasing depth (> 400 nm).[90]. The authors reported presence of Stannous (Sn^{2+}) and Stannic (Sn^{4+}) oxides on the corroded surface of the Al-1wt%Sn alloy in 0.5M Na_2SO_4 for 24 hours [90]. This result was in agreement with previous research conducted by *Venugopal et al.*[98], who examined the oxide layer formed on the surface of Al-3wt%Sn alloy exposed to 3.5%w/w NaCl solution for 1 hour, using X-Ray Photoelectron Spectroscopy (XPS) technique, see **Figure 2.19** (a),(b), (c) and (d).

However, the results obtained by *Andreev et al.*[90] and *Venugopal et al.*[98] by exposing alloyed Al with 1wt% and 3wt%Sn were in different electrolytic media containing SO_4^{2-} and Cl^{-1} ions, both reflected the same fact that Sn^{2+} and Sn^{4+} ions co-existed on the corroded surface of Al alloy. These experimental results were an additional support to the proposed theory that activator elements tends to form complex oxide layer with high ionic

conductivity during the oxidation of the alloy , therefore avoiding the passivation of Al [84,85, 87-89].

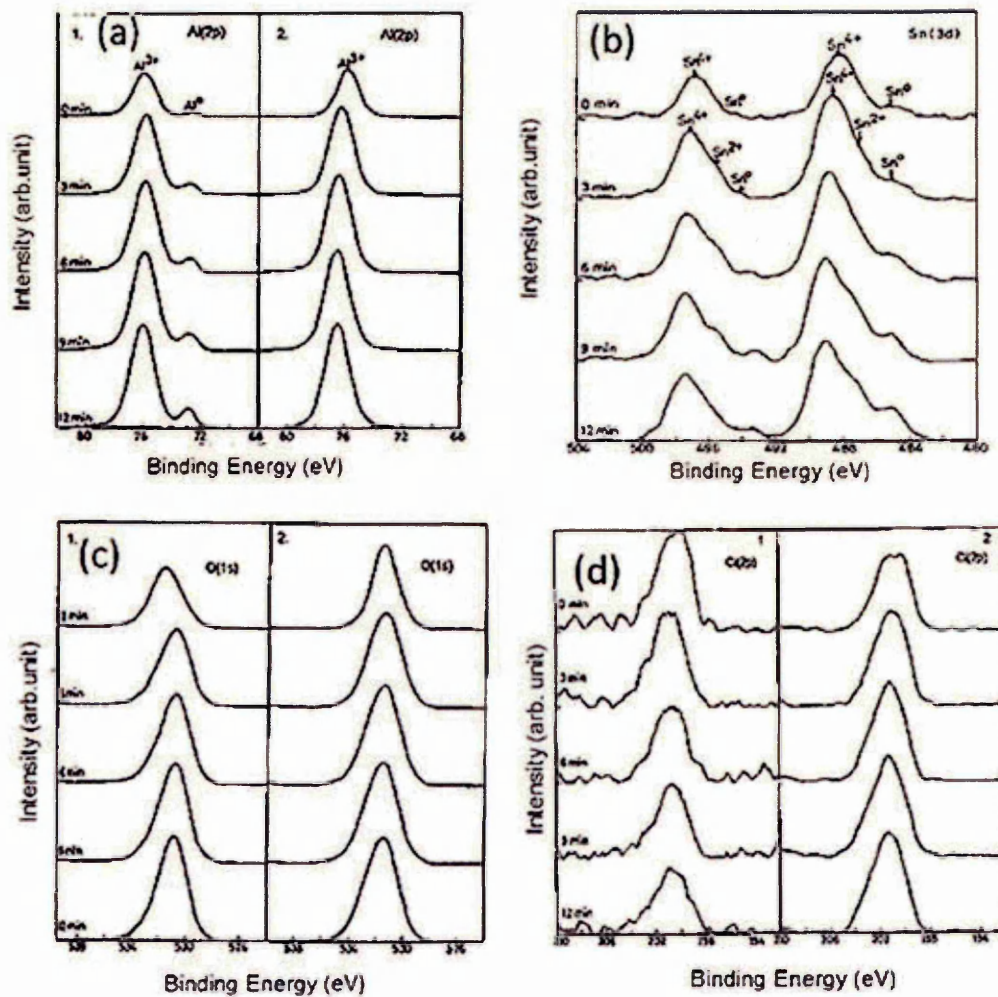


Figure 2.19: The XPS spectra with various sputter times for : (a) Al , (b) Sn, (c) O and (d) Cl, where 1 and 2 represents pure Al and Al-Sn alloys exposed in 3.5%w/v NaCl solution for 1 hour [98].

It is important to note that, under the condition of pH 1-12, the equilibrium for oxide formation of Sn can either be [99]:



Equation 39 (a)

Or



Equation 39 (b)

With a difference of -0.002 V (vs. NHE) in the equilibrium potentials under the given pH range, co-existence of Sn^{2+} and Sn^{4+} ions is favourable [99]. During the formation of complex oxide layer, Al^{3+} can be replaced by either Sn^{2+} or Sn^{4+} , it was proposed that however Sn^{2+} ions are thermodynamically more stable than Sn^{4+} , but the atomic radii of Sn^{4+} ($\approx 0.71 \text{ \AA}$) is close to Al^{3+} ($\approx 0.51 \text{ \AA}$) than Sn^{2+} ($\approx 0.93 \text{ \AA}$), substitution of stannic (Sn^{4+}) ions is preferable [99].

It was also proposed that if the Sn concentration was higher than 1wt% and higher potential was required to form oxide then Stannous (Sn^{2+}) ions could replace Al^{3+} ions to form spinel structure SnAl_2O_4 oxide, while under vice versa condition formation of Al_2O_3 will be favoured [99]. A similar study on Al, alloyed with 0.09wt%, 0.2wt% and 0.4wt% of Sn was conducted by *Kliškić et al.*[100] showed that under cathodic polarisation condition, Sn favours formation of hydride (gaseous state)



Equation 40

According to the authors, the formation of SnH_4 was thermodynamically favoured due to development of local hyperactive regions in the alloy, when subjected to cathodic polarisation condition in 2M NaCl solution. This effect was found to be more pronounced in the alloy with lower Sn concentration leading to high yield of H_2 [100].

The SIMS analysis on Al-1wt%Sn (S_{HT0}) alloy after 24 hours of exposure in 0.5M Na_2SO_4 solution by *Andreev et al.* [40], see **Table 2.10**, showed a significant increase in the relative concentration of Sn ions, 0.017 to 2.304, before and after exposure. Comparing with thermodynamically calculated values of enrichment factor from table 9 which was $\left(\frac{x_{\text{Sn}}}{N_{\text{Sn}}}\right) = 203.2$ to SIMS calculated value of $\left(\frac{x_{\text{Sn}}}{N_{\text{Sn}}}\right) = \left(\frac{2.304}{0.017}\right) = 136$ from **Table 2.10**, for 1wt%Sn addition, it was clear that, the former value represented the uppermost limit of enrichment factor which could be achieved during the activation of Al by 1wt%Sn [90].

In conjunction with the SIMS analysis, the AES analysis of Al-1wt%Sn alloy (for both S_{HT0} and S_{HT3}), see **Table 2.11**, also showed an increase in the Sn concentration (from 0.31at% to 1.3at%) nearing the surface (at 0.6 nm) than towards the bulk (at a depth of ≈ 278 nm) for S_{HT0} heat treated alloys [90]. An increase in the at%O (from 2.2at% to 29.3at%) and decrease in the at%Al (from 97.1at% to 68.9at%) was also observed for S_{HT0} heat treated alloy from near the surface moving towards the bulk (0.6nm to 277.5nm), a similar effect was found in S_{HT3} heat treated alloy but with lower scale [90].

The SIMS and AES analysis of Al-1wt%Sn, for both S_{HT0} and S_{HT3} heat treated samples, revealed that the dissolution of the alloy wasn't independent of the scale in which the atoms of the lattice (Al) and the alloying species (Sn) were distributed on the surface. Instead were showing evidence of preferential dissolution of Al from Al-Sn binary alloy [90,101,102].

These results showed similarity with the work conducted by *Pickering and Wagner* [101], who explored the preferential dissolution mechanism of binary Au-Cu alloy. According to *Pickering and Wagner* [101], the mechanism underpinning preferential dissolution for binary alloys could include:

- Ionisation and subsequent re-deposition of a more noble element in the binary alloy, or
- Ionisation of only the active element in the alloy which enters the electrolytic solution leaving behind the noble metal to aggregate via surface diffusion, or
- Ionisation of only the active element in the alloying which enters the electrolytic solution and both active and noble metal ions are adsorbed to the bulk by volume diffusion.

The results presented by *Andreev et al.*[90], see **Table 2.10 and Table 2.11**, relied on a similar explanation of preferential dissolution mechanism suggested by *Pickering and Wagner* [101]. They suggested that during the exposure, the Al^{3+} ions leaves the alloy surface to form oxide layer while Sn^{2+} and Sn^{4+} ions aggregate on the surface (see the values of enrichment factor calculated experimentally ,136, after the exposure of Al-1wt%Sn alloy in

0.5M Na₂SO₄ solution), see **Figure 2.20**. The diagrammatic representation of this preferential dissolution mechanism represents that the Al³⁺ ions migrate the surface of the alloy, as shown in **Figure 2.20(1)**. The removal of the top layer Al atoms causes the exposure of the closely packed lower layer atoms to participate in the dissolution, leaving the Sn²⁺ and Sn⁴⁺ ions on the surface, see figure 12(2-6) [51,52].

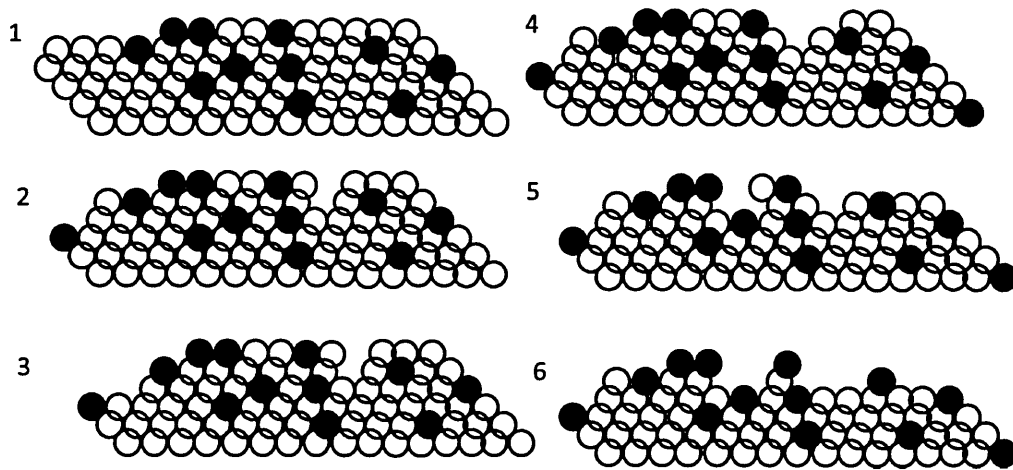


Figure 2.20: Diagrammatic representation of preferential dissolution mechanism (1-6 represents different stages of dissolution), where ○ represents Al³⁺ ions and ● are Sn²⁺ and Sn⁴⁺ ions [51,52].

A mathematical explanation to the diagrammatic representation of preferential dissolution mechanism of Al-1wt%Sn alloy given by Andreev *et al.* [90] was based on Pickering and Wagner's [91] calculation of the diffusion depth for Au-Cu binary alloy.

Considering the SIMS results, see **Table 2.10**, with sputter time of 1.25 minutes, a depth profile of 1.33 nm/sec was analysed, which yielded in diffusivity (D) $\approx h^2/2t$, where t was of the order 10^{-13} cm²/sec. This was a same order of magnitude for AES analysis, which was conducted at 0.52 nm/sec to the maximum depth \approx 280 nm, see **Table 2.11** [90,101]. The value of diffusivity calculated was strongly dependent on the concentration of vacancies formed on the surface due to migration of Al³⁺ ions, as shown in **Figure 2.20**, mathematically written as [101,102]:

$$D = D_v N_{v(s)} \text{ Equation 41}$$

The experimental evidence showed that for FCC metals, the value of N_v was \approx of the order 10^{-2} [90,101,102]. The value of D from **Equation 41** was found to be 5.3×10^{-14} cm²/sec, at near room temperature 298 K, which was comparable with the SIMS and AES data [90,101,102].

The thermodynamic calculations in conjunction with the experimental work showed that activation of Al by Sn, In (depassivators) and Zn (modifier) in presence of an electrolytic solution proceeded by formation of complex oxide layer with high ionic conductivity. In addition, also showed that phenomena of surface enrichment by depassivators (experimental work focused on Sn addition) with higher diffusion rates ($\approx 10^{-13}$ cm²/sec) from the bulk to surface aided the alloy to maintain an active surface throughout the electrochemical interaction with solution containing Cl⁻¹ and SO₄⁻² ions [90-102].

A significant experimental study was also conducted by *Gundersen et al.* [103,104] on the electrochemical effects of alloying Al with In,Sn,Bi, Pb, Mg, Zn along with a separate study on the effects of trace elements on Al-0.42wt%Fe, 0.21wt%Mn, 0.07wt% alloy (AA3102 alloy). **Table 2.12** shows the composition of the alloys which were examined by the authors [103].

Table 2.12: The composition (in wt%) of binary Al alloys with Fe and Si as major impurities which were used for experimental investigation by *Gundersen et al.*[53].

Al alloys	Bi	In	Sn	Mg	Zn	Pb	Fe	Si
All the additions are in wt%								
Al-Bi	0.2	-	-	-	-	-	0.05	0.03
Al-In	-	0.1	-	-	-	-	0.006	0.003
Al-Sn	-	-	0.01	-	-	-	0.004	0.004
Al-Mg	-	-	-	0.005	-	-	-	0.01
Al-Zn	-	-	-	-	0.06	-	-	0.01
Al-Pb ₁	-	-	-	-	0.002	0.002	-	0.004
Al-Pb ₂	-	-	-	-	-	0.003	-	0.004
Al-Pb ₃	-	-	-	-	-	0.006	-	0.004

The alloys containing Mg, Zn and Pb were produced by casting (99.98% purity Al was used) which was subsequently scalped. Pb containing alloy was excluded from scalping, while alloys containing In, Sn and Bi were produced by direct chill (DC) casting (using 99.998% and 99.88% pure Al) which were then scalped and exposed to 738 K for 16 hours for homogenisation followed by exposure at 903 K for another 16 hours as a heat treatment of solid solution [103].

Prior to examination using electrochemical and analytical surface characterisation techniques, the authors subjected the samples to a cyclic heat treatment and mechanical polishing stages. The samples were subjected to heat treatment at 873 K for an hour in a furnace with air circulating facility, followed by rapid quenching (using deionised water at near room temperature). Then alloy samples were subjected to various stages of mechanical grinding using SiC paper and polishing to 1 μm surface finish, followed by the same heat treatment and immersion in 10%w/v NaOH solution for 10 seconds and in concentrated HNO_3 for a minute for desmutting, finally followed by the same heat treatment [103].

Gundersen et al. [103], choose this cyclic sample preparation method in order to investigate whether or not the activation of Al by these alloying elements was just due to surface enrichment phenomena or inter diffusion of ions from the bulk of the alloy, as studied by various authors [87,88,90-95, 97-99]. All the electrochemical experiments by *Gundersen et al.* [103] were conducted in artificial sea water, with a maintained pH value in the range of 2.8-3.0 with an addition of anhydrous acetic acid at 298 K.

In order to understand the effect of alloying elements as shown in **Table 2.12**, upon exposure and after electrochemical measurements, Glow Discharge Optical Emission Spectroscopy (GD-OES) was used to investigate the composition of surface and Transmission Electron Microscopy (TEM) was used to analyse the microstructure of the alloys [103].

The polished cross section of the alloy showed formation of oxide on the surface, as seen from GD-OES profile in **Figure 2.21 (a)**. With a uniform distribution of Pb which has a maximum solubility of 0.012wt% in Al at $\approx 938\text{K}$ [105] (the authors have reported that using GD-OES, $\text{Pb} < 20 \text{ ppm}$ could not be detected) [103]. The effect of heat treatment was evident from **Figure 2.21 (b)** which showed increase in the Pb concentration on the surface of the alloy, a broad peak of $\approx 0.9\text{wt\%Pb}$ was observed, which after 10 seconds of exposure in 10%w/v NaOH was narrowed, as shown in **Figure 2.21 (c)**, indicating reduction in Pb surface enrichment [103].

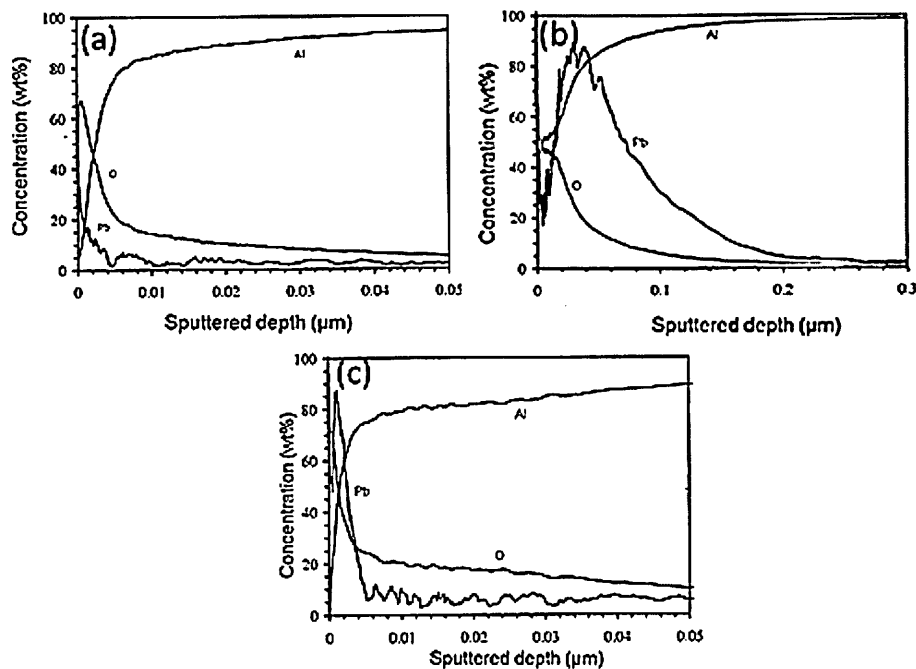


Figure 2.21: GD-OES profile of Al-Pb₁ alloy subjected to (a) polishing, (b) polishing and heat treatment, (c) polished, heat treated and immersed in 10%w/v NaOH solution for 10 seconds [103].

On further investigation using TEM (coupled with EDX facility), the authors underpinned the results from GD-OES profile by analysing the cross-section of the heat treated Al-Pb₁ alloy as shown in **Figure 2.22** (a) and (b) [103].

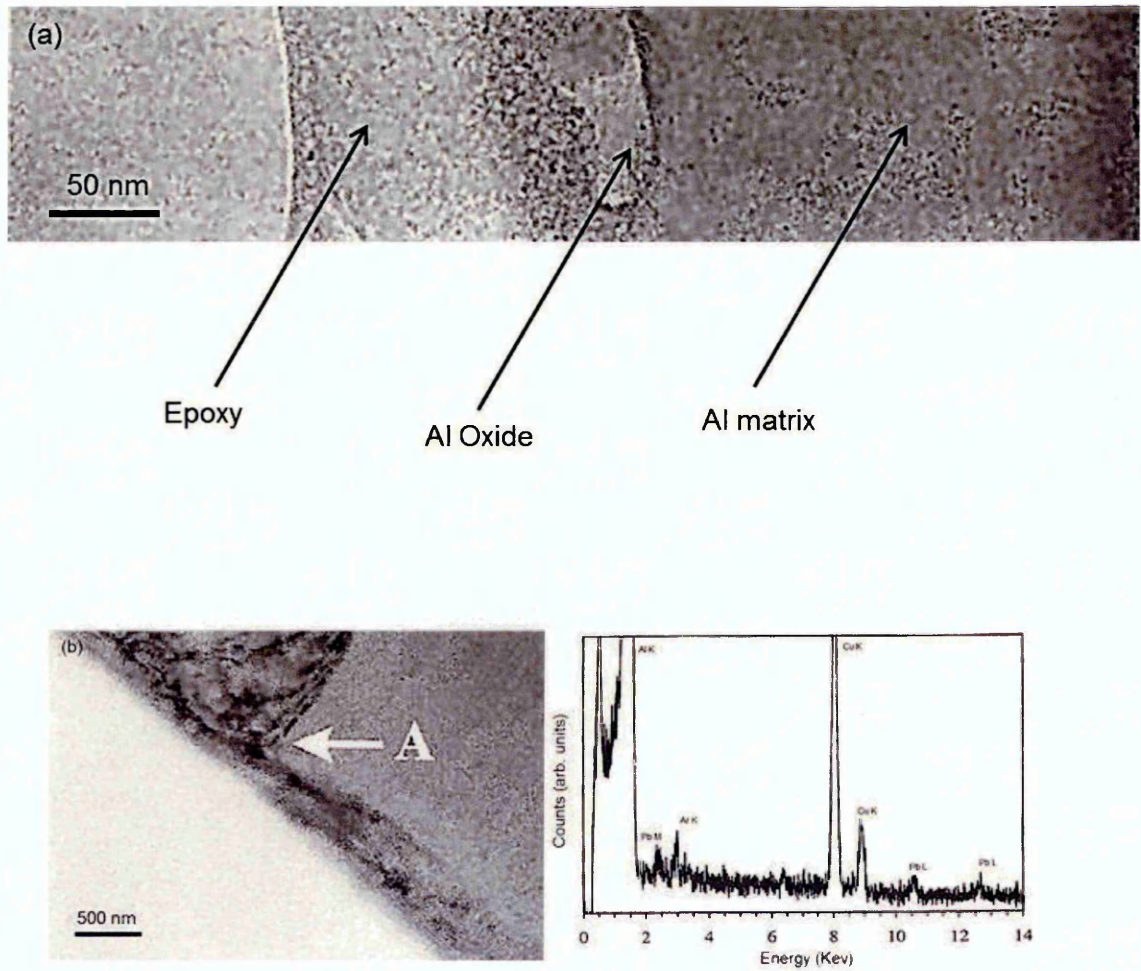


Figure 2.22: TEM analysis of (a) cross-section of heat treated Al-Pb₁ alloy and (b) cross-section analysis of metal- oxide interface of heat treated Al-Pb₁ alloy (marked A) with corresponding EDX spectra (point analysis) [103].

A formation of Al oxide layer was observed as shown in **Figure 2.22(a)**, having a closer look at the metal oxide interface as shown in **Figure 2.22(b)**, marked by A, revealed Pb at the interface. However, the authors did not report any lead inclusions in the area of the analysed sample owing to the fact that Pb has a low solubility in Al [103,105].

The presence of Pb was reported at the interface of metal and oxide as shown in the EDX spectra in **Figure 2.22 (b)**. The Cu peaks were due to the Cu grid in which the samples were analysed [103]. The combination of TEM and GD-OES results presented by the authors affirmed that heat treatment of Al-Pb₁ alloy did cause Pb segregation but treatment with alkaline NaOH solution (10%w/v NaOH solution for 10 seconds) proved detrimental. As it caused removal of segregated Pb from the surface of the alloy (the authors did not show the TEM cross-section after NaOH exposure, but relied on GD-OES result as shown in **Figure 2.21 (c)**).

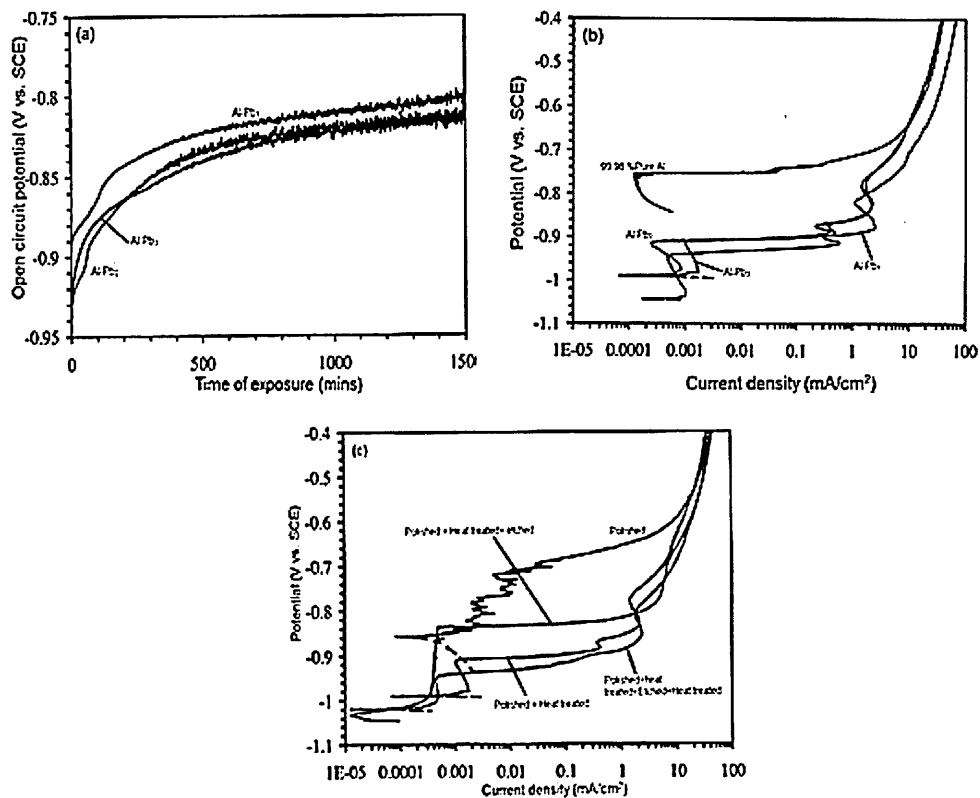


Figure 2.23 Graphs showing the effect of variation in Pb concentration on: (a) potential vs. time curve for binary Al-Pb alloy in synthetic sea water (ASTM D1141, which was acidified), (b) anodic polarisation behaviour in 5%w/v NaCl solution and (c) the effect of cyclic sample preparation on Al-Pb₃ alloy in 5%w/v NaCl solution [103].

The potential vs. time curve, see **Figure 2.23 (a)**, for polished and heat treated sections of Al-Pb alloys exposed to artificial sea water showed that with an increase in Pb concentration from 0.002wt% in Al-Pb₁ to 0.006wt% in Al-Pb₃ alloy, over time did not show a significant shift in the potential.

The graph showed that Al-Pb₁ alloy started with ≈ -0.89 V(vs.SCE) during initial period of immersion and just over 24 hours of immersion time the potential recorded was ≈ -0.80 V (vs.SCE), whereas Al-Pb₁ and Al-Pb₂ started with a potential between - 0.92 to -0.93 V (vs.SCE) and over same exposure period stabilised at ≈ -0.82 V (vs.SCE) [103].

It is important to note that the graphs showed wavy patterns after ≈ 3 hours of immersion, which were similar in nature to the potential vs time graph for AA3102 alloys reported by *Gundersen et al.* [104]. However the authors did not suggest that these wavy patterns were a result of impurities such as Fe and Si, see **Table 2.12**. The polarisation curve as shown in **Figure 2.23(b)** clearly showed the activation effect of Pb on high purity Al. The graph indicated a more pronounced effect of Pb in Al-Pb₁ alloy, which showed a significant negative shift in the potential of Al-Pb₁ alloy than Al-Pb₂ and Al-Pb₃ alloys [103].

In an attempt to understand the effect of cyclic sample preparation on Pb activation, Al-Pb₃ alloy which was subjected to combination of three procedures such as simple mechanical polishing, heat treatment and etching was subjected to potentiodynamic polarisation experiment in 5%w/v NaCl solution, as shown in **Figure 2.23 (c)**. The polished Al-Pb₃ alloy section showed a region of passivity (wavy pattern) from ≈ -0.86 to -0.70 V (vs. SCE), whereas a significant increase in the anodic activity of Al-Pb₃ alloy was seen post heat treatment, however when the alloy was subjected to 10% w/v NaOH for etching, a decrease in the anodic activity, with a clear passive region from -0.99 to -0.84 V (vs. SCE) was observed [103].

The increase in current density for both polished and polished + heat treated + etched alloy indicated formation of pits [103]. A further heat treatment of polished + heat treated + etched alloy showed restoration of anodic activity of Al-Pb₃ alloy.

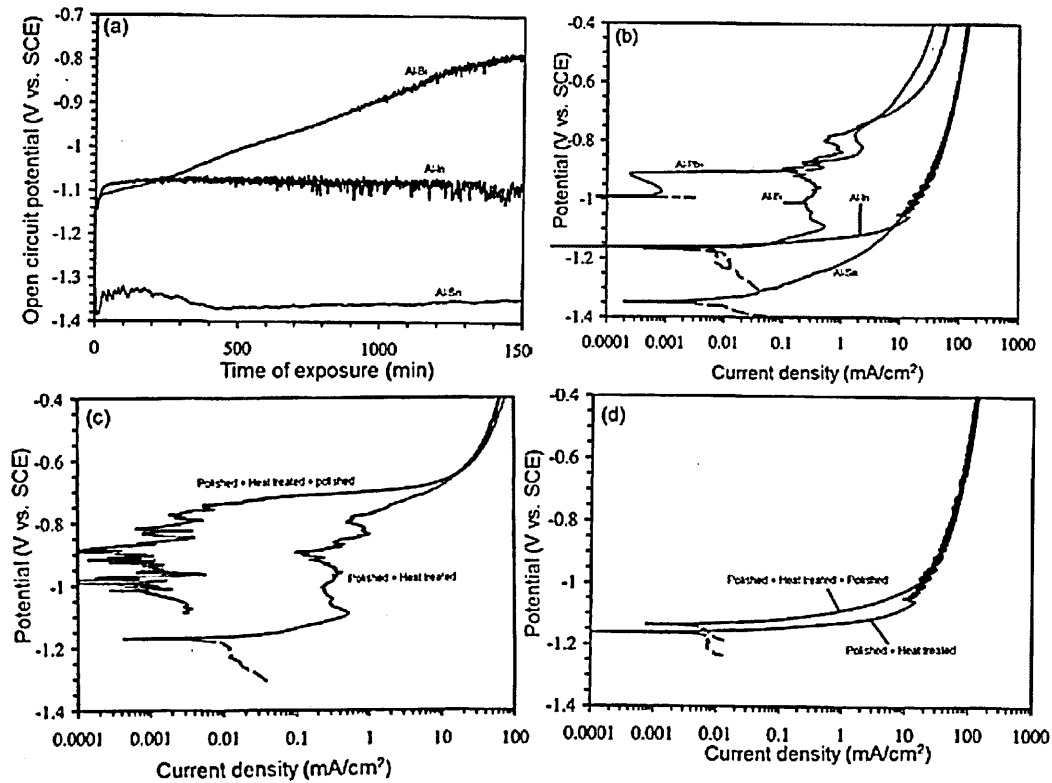


Figure 2.24: Graphs showing (a) Potential vs. time curve for Al alloyed with Bi, In and Sn in acidified artificial sea water (ASTM D1141) and anodic polarisation curves for (b) polished and heat treatment section of Al alloyed with Pb, In, Sn, Bi, (c) polished and heat treated Al-Bi alloy and (d) polished and heat treated Al-In alloys. All the polarisation experiments were conducted in 5%w/v NaCl solution [103].

Comparing the potential vs. time behaviour of polished and heat treated Al alloyed with Pb, Sn, In and Bi over a period of 24 hours, the order in which the elements shifted the Potential more negative was Sn (-1.36 V vs.SCE) < In (-1.08 V vs.SCE) < Bi (-0.8 V vs.SCE). Except Sn, In and Bi showed a similar wavy pattern after few hours of immersion [103].

The anodic polarisation behaviour of polished and heat treated Al-Bi, Al-Sn, Al-In and Al-Pb₂ also showed Sn, In and Bi had a significant effect in lowering the potential than Pb when alloyed with Al, see **Figure 2.24(b)**. Few sharp anodic peaks were observed for Al-Bi alloy (at \approx -1.1 V, -0.90 and -0.8 V vs. SCE), Al-Sn alloy showed a smoother curve with Al-In showing some wavy patterns as the potential shifted from -1.05 V vs. SCE towards positive direction [103].

Figure 2.24 (c) and (d) shows the comparison of anodic behaviour of the Al-Bi and Al-In alloys subjected to mechanical polishing. It was clear from the graphs that Al-In alloy showed almost no change in the anodic behaviour however polishing caused a significant reduction in the anodic activity for Al-Bi alloy [103].

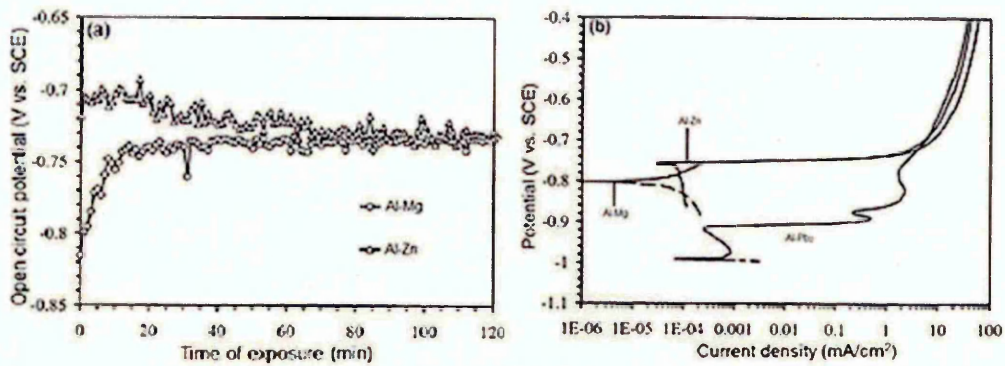


Figure 2.25: Graphs showing (a) potential vs. time for heat treated Al alloyed with Zn and Mg in acidified artificial sea water (ASTM D1141) and (b) heat treated potentiodynamic polarisation of Al alloyed with Zn and Mg in comparison with Pb in 5%w/v NaCl solution [103].

The effect of Zn and Mg on Al activation in comparison with Sn, In, Pb and Bi was found to be lower in acidified artificial sea water (ASTM D1141) condition, as seen in **Figure 2.25** (a). The OCP of Al-Zn and Al-Mg started at ≈ -0.72 V and -0.82 V vs. SCE but almost after 2 hours of immersion the OCP stabilised at ≈ -0.74 V vs. SCE for both the alloys, which was significantly lower than what was observed for Sn, In, Bi and Pb [103].

The polarisation curve (**Figure 2.25** (b)) showed increase in the current density of Al-Mg and Al-Zn alloy between potentials -0.78 V to -0.74 V vs. SCE indicating pitting of the alloy. However Al-Pb₂ alloy showed superior activation at potential more negative than pitting potential reported for Al-Zn and Al-Mg alloy [103]. The work conducted by *Gundersen et al.* [103,104] clearly showed that activation of Al by Sn and In was found far more superior and unaffected by the cyclic sample preparation method as Al alloyed with Bi

and Pb. Even though Pb and Bi provided the electrochemical properties to the alloy needed for being a sacrificial anode but were significantly subdued when the surface removal operations were performed on the alloy. The research also showed that addition of Zn and Mg did not show significant change in the electrochemical behaviour of Al when alloys were subjected to the heat treatment [103].

2.8.5 The effect of Zn addition on electrochemical properties of Al alloys

Zn has been primarily used as an alloying addition to Al along with other elements such as Sn, In, Hg, Ga and has been widely investigated experimentally by many researchers on how it affects the electrochemistry of Al on its own and in combination with other alloying addition.

Salinas et al. [106] studied the effect of various concentrations of Zn addition, 1, 3, 5, 20, 40, 60 and 80wt%, on the electrochemical performance of Al sacrificial anodes. The alloys were prepared by casting under specified cooling rates to obtain equiaxed, chill and columnar macro-structure. As seen from the Al-Zn phase diagram, see **Figure 2.26**, two distinct phases were present in the alloy, with Zn concentration less than 5wt% α phase, for Zn higher than 5wt% β phase, however α' was seen in the transition of Zn from lower to higher concentration [106].

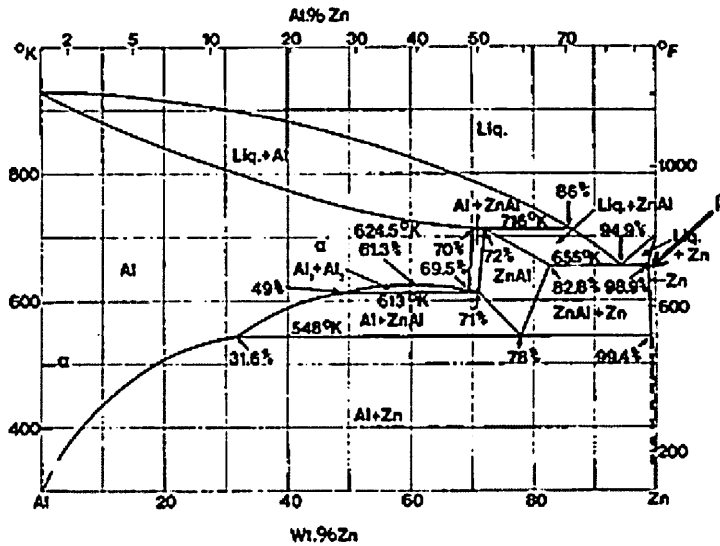


Figure 2.26: Al-Zn phase diagram [70].

It is important to note that α , β phases studied by the *Salinas et al.* [106] were a result of equilibrium casting condition, however Zn forms precipitates with Al when subjected to non-equilibrium condition. For instance, *Birblis and Buchheit* [107] conducted an experimental investigation on the localised electrochemical properties of intermetallic compounds formed by Zn, Mg, Ti, Mn, Cu, Fe, Cr, Zr with Al (all the elements either in form of precipitates, constituent particles and dispersoids), showed that the open circuit potentials of $Al_{32}Zn_{49}$ (stoichiometric ratio) were -1009 mV, -1004 mV and -1063 mV vs. SCE in 0.01M, 0.1M and 0.6M NaCl solution respectively. The active behaviour of $Al_{32}Zn_{49}$ was also confirmed by the polarisation curve which was obtained by exposing the intermetallic to 0.1M NaCl solution, see **Figure 2.27**.

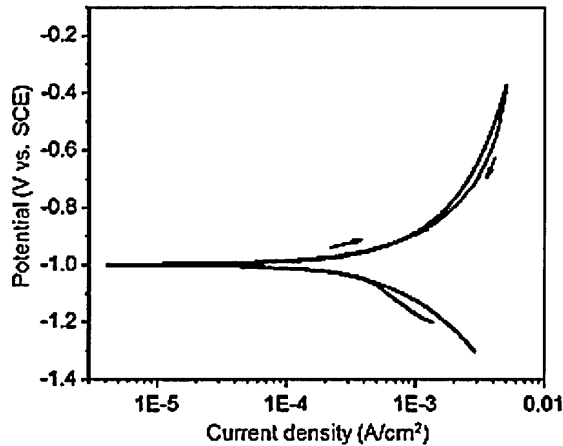


Figure 2.27: Potentiodynamic polarisation curve obtained for $\text{Al}_{32}\text{Zn}_{49}$ in 0.1M NaCl solution [107].

Salinas et al. [106] observed that under galvanostatic test condition for 30 days at 1 mA/cm^2 in 0.5M NaCl solution, the operating potential of the alloy shifted from -720 mV for unalloyed Al to -955 mV (vs. SCE) for Al alloyed with 5wt%Zn. This change in the operating potential was observed for all the three macro-structures. The authors stressed that at lower Zn content, the loss in the operating potential was due local galvanic action within the alloy due to presence of Fe and Cu as impurities, which eventually reduced by increasing the Zn content [106].

The authors also reported that the columnar structure did show evidence of variation in performance for Al-1wt%Zn alloy than other two structures. This was due to the fact that the corrosion morphology observed for Al-1wt%Zn was concentric band like, which caused non uniform dissolution of the alloy leading to fluctuation in operating potential, which wasn't the case for Al alloyed with 5wt% alloy [106].

X-Ray Diffraction (XRD) analysis was also conducted on Al alloyed with both lower ($< 5\text{wt}\%$) and higher ($> 5\text{wt}\%$) Zn concentration to understand the effects of phases present in the alloy, see **Figure 2.28** (a), (b), (c) and (d) [106].

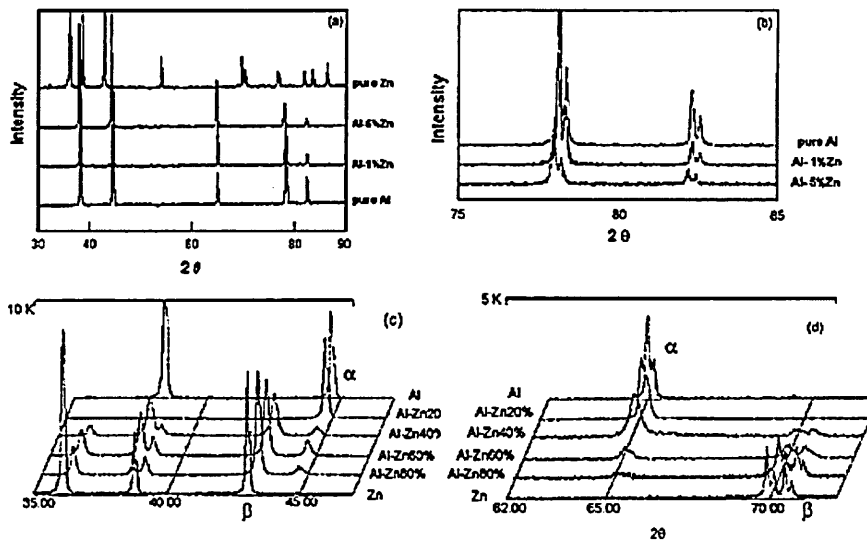


Figure 2.28: XRD analysis of Al alloyed with (a), (b) 1wt% and 5wt%Zn in comparison with pure Al and Zn (c), (d) 20wt% to 80wt%Zn [106].

The diffraction pattern shown in **Figure 2.28** (a) revealed that in Al alloyed 1wt%Zn, Al rich α was the dominant phase. The higher $2\theta^0$ angle diffraction observed for 5wt%Zn addition, showed slight shift in the peaks indicating Zn in the solid solution of Al matrix. This was confirmed by the change in lattice parameters, see **Figure 2.28(b)**, at $2\theta \approx 78^0$ and 82^0 , lattice parameters for Al, Al-1wt%Zn and Al-5wt%Zn were 4.053 Å, 4.056 Å and 4.062 Å [106].

A clear increase in the Zn rich β phase was observed for Al alloyed with > 5wt%Zn, see **Figure 2.28** (c) and (d), with no recorded peak shift [106]. The authors, by applying semi-quantitative analysis reported 3.08%, 24.83%, 54.62% and 67.43% β phase when Zn concentrations of (wt%) 20, 40, 60, 80 respectively [106].

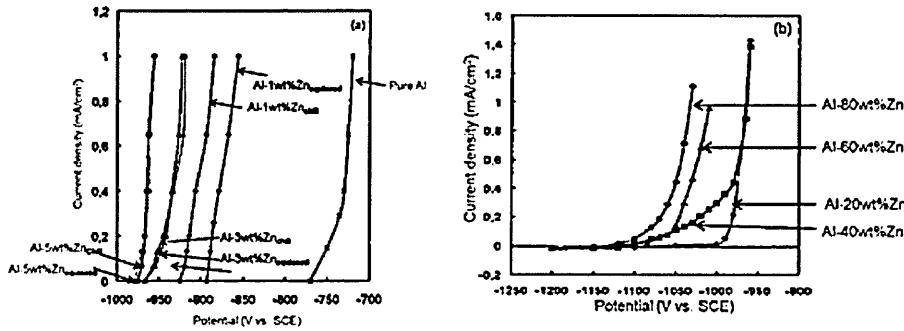


Figure 2.29: Galvanostatic Polarisation curve for Al alloyed with (a) 1wt%, 3wt% and 5wt%Zn (chill and equiaxed macrostructure) and (b) 20wt %, 40wt %, 60wt% and 80wt%Zn in 0.5M NaCl [106].

In conjunction with the XRD analysis, the galvanostatic polarisation curve clearly showed that the operating potential of the Al alloyed with Zn < 3wt%, was dependent on the macrostructure (which was either chill, equiaxed or columnar), see **Figure 2.29** (a). This becomes independent as the concentration of Zn increases from 3wt% [106]. However in the range 5wt% \leq Zn concentration \leq 40wt%, the operating potential at 5wt%Zn showed no changes with the microstructure, see **Figure 2.29** (a). But as the concentration of Zn increases to 40wt%, the build-up of localised corrosion areas takes place at β rich phase areas keeping the operating potential similar to that of Al-5wt%Zn alloy [106].

A further negative shift in the operating potential was observed for Al alloyed with Zn concentration > 40wt% due to increase in the β rich phase areas. The authors clearly showed that with zinc content \geq 5wt%, the operating potential and anode performance significantly increased with increase in β phase [106].

2.8.6 The effects of ternary addition on Al-Zn alloys

The combination of Zn (modifier) with depassivators such as In, Sn, Hg and Ga to form ternary Al sacrificial anode of the form Al-Zn-(In, Sn, Hg, Ga) has been an area of focus to many researchers in the field of Al activation and has been extensively studied using experimental techniques.

In the early 1960's, *Sakano et al.* [108,109] investigated the performance Al alloyed with \approx 1wt% to 30wt%Zn, \approx 0.001wt% to 0.1wt%In and \approx upto 0.50wt%Cd. Comparing the potential vs. time characteristics by exposing the alloys to artificial sea water (not specified by the authors as ASTM D1141), see **Figure 2.30**, indicated that binary addition of Zn upto 3wt% and In upto 0.12wt% maintained the potential of the alloy at -0.95 V and -1.05 V (vs. SCE) over the same period of exposure. However the ternary combination of Al with \approx 0.02wt%In and \approx 3wt%Zn shifted the potential to a constant value of -1.1 V (vs. SCE) after 100 hours of exposure in sea water [108]. The alloy containing 0.018wt%In and 2.8wt%Zn had a similar effect, but fluctuations in the potential values were observed [108].

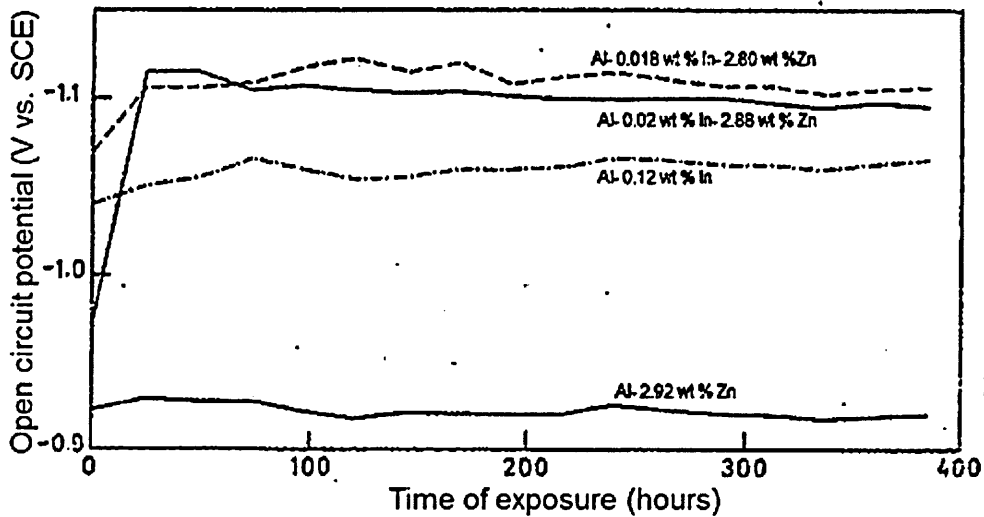


Figure 2.30: Potential vs. time graph comparing the performance of binary Al-Zn and Al-In alloys with ternary Al-Zn-In with different Zn and In concentration in artificial sea water [108].

2.8.6.1 The effects of Si and Cu on the electrochemical performance of Al-Zn-(In,Sn,Hg,Ga) alloys

Sakano *et al.* [108] also investigated the effect of commonly found impurities such as Fe, Si and Cu on the performance of the sacrificial anodes. The authors showed that even trace amount of Cu ($\approx 0.019\text{wt}\%$) significantly lowered the galvanic efficiency of the alloy by formation of corrosion pits and causing a strong adhesion of corrosion product to the surface of the alloy [108].

The presence of Si in the concentration ranging from $0.041\text{wt}\%$ to $0.212\text{wt}\%$ increased the galvanic efficiency of the alloy, however the authors observed non uniform corrosion pattern on the alloys causing fluctuation in the potentials, no significant effect of Fe was reported by the authors [108].

Sakano et al. [108,109] also reported that the quaternary addition of Cd (upto 0.05wt%) to Al alloyed with 2.5wt%Zn and 0.02wt%In showed uniform corrosion patterns leading to an increase in the galvanic efficiency of the alloy. **Table 2.13**, **Table 2.14** and **Table 2.15** shows the effect of alloying Al with Zn and In on galvanic efficiency of the anodes, the effect of impurities such as Fe, Cu and Si and addition of Cd on the galvanic efficiency of Al anodes.

A similar study was conducted by *Hejian and Shizhong* [110] in order to understand the effect of impurities on electrochemical behaviour of Al alloyed with Zn and In. After examining various Al alloys with different concentrations of Zn and In along with impurities such as Si and Fe, the authors highlighted that Al alloys containing a ratio of In to Fe and Si of $\approx 1:8$ produced galvanic efficiency up to 85% with ≈ -1110 mV vs. SCE working potential, see **Figure 23** [110].

Table 2.13: Effect of alloying 99.99% and 99.85% Al with various concentrations of Zn and In on galvanic efficiency (tests conducted in sea water) [108].

Composition of the alloy			Time of exposure	Galvanic efficiency (%)
Al(wt%)	Zn(wt%)	In (wt%)		
97.14	2.82	0.004	400	81
96.99	3.00	0.010	400	84.4
99.99	2.80	0.019	400	70
97.18	2.85	0.046	400	40.2
99.48	0.5	0.02	190	86
94.98	5.0	0.02	190	85
89.98	10.0	0.02	190	87
84.98	15.0	0.02	190	90
69.98	30.0	0.02	190	< 75

Table 2.14: Effect of impurities (Fe, Si and Cu) on the galvanic efficiency of Al anodes [108].

Composition of the alloy						Time of exposure	Galvanic efficiency (%)
Al (wt%)	Zn (wt%)	In (wt%)	Fe (wt%)	Si (wt%)	Cu (wt%)		
97.17	2.77	0.018	0.042	-	-	410	84
96.99	2.89	0.022	0.092	-	-	410	84
96.92	2.87	0.022	0.185	-	-	410	86
97.08	2.86	0.018	-	0.041	-	410	92
97.00	2.88	0.020	-	0.094	-	410	92
96.87	2.89	0.020	-	0.212	-	410	92
97.07	2.89	0.020	-	-	0.019	400	<78
97.24	2.69	0.021	-	-	0.048	400	<72
96.96	2.84	0.021	-	-	0.117	400	<81

Table 2.15: Effect of Cd addition on galvanic efficiency of Al anodes [109].

Composition of the alloy				OCP after 500 hours of exposure in sea water (V vs. SCE)	Galvanic efficiency (%)
Al(wt%)	Zn(wt%)	In (wt%)	Cd(wt%)		
97.47	2.5	0.02	0.005	-1.12	85
97.47	2.5	0.02	0.01	-1.125	85
97.43	2.5	0.02	0.05	-1.12	84
97.38	2.5	0.02	0.1	-1.115	84
99.47	0.5	0.02	0.01	-1.115	83
79.97	20	0.02	0.01	-1.11	80
97.48	2.5	0.005	0.01	-1.11	84
99.85	2.5	0.09	0.01	-1.115	80

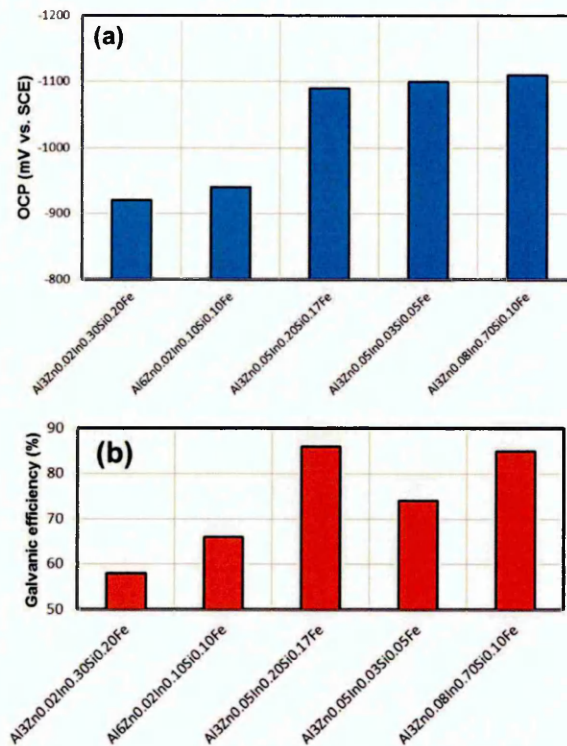


Figure 2.31: Graph showing the effect of In in combination with Fe and Si on the (a) OCP and (b) galvanic efficiency of Al anodes (the experiment was performed in sea water, not specified to ASTM D1141 by the authors, at 1 mA/cm²) [110].

In order to study the elemental distribution of Zn and In along with other impurities, *Hejian and Shizhong* [110] also conducted a quantitative electroprobe (electron probe analysis) analysis on Al anodes with different Zn and In concentrations, see **Table 2.16**, before and after potentiostatic polarisation (at -1000 mV vs. SCE for 25 minutes in 0.5M NaCl solution). The results obtained from electroprobe analysis (pre and post polarisation scan) clearly showed evidence of increase in concentration of In, Si and Cu

(present as an impurity) in the segregated phases than in the matrix of the alloy. Uniform Zn distribution was observed in both segregated phases and matrix (no trace of In was reported by the authors in the alloy matrix). From the results obtained, the authors theorised that In with presence of impurities such as Fe and Si segregate to form local anodes with Al₂O₃ layer which in turn actively dissolves till the Al matrix is exposed to the electrolyte. The exposed Al matrix then forms a galvanic cell with the Al₂O₃ oxide and starts actively dissolving, while the segregated In rich phase separates from the Al matrix and dissolves in the electrolytic solution, see figure 24 [110].

Table 2.16: Quantitative electroprobe analysis of Al-6wt%Zn-0.05wt%In 0.01wt%Si and segregated phases after potentiostatic polarisation at -1000 mV vs. SCE for 25 minutes in 0.5M NaCl solution [110].

	Quantitative analysis of individual elements (in at%)				
	Al	Zn	In	Si	Cu
Al-6wt%Zn-0.05wt%In0.10wt%Si (pre-polarisation)	93.62	6.28	0	0.09	0.007
Segregate phase 1 (post polarisation)	75.34	7.18	16.70	0.75	0.03
Segregate phase 2 (post polarisation)	77.35	5.18	16.91	0.47	0.09

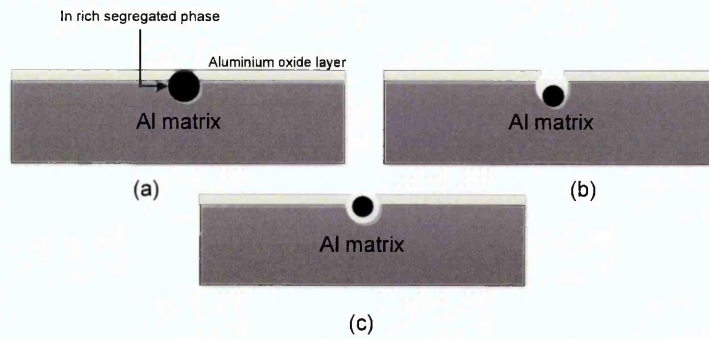


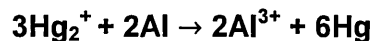
Figure 2.32: Diagrammatic representation of proposed activation mechanism of Al sacrificial anode (a) in presence of In rich phase acting as an anode with Al_2O_3 leading to (b) exposure of Al matrix and (c) subsequent detachment of In rich phase after exposure of Al matrix, suggested by *Hejian and Shizhong* [110].

2.8.6.2 Understanding the mechanism of activation of Al-Zn alloys by depassivators

Similar to the activation of Al-Zn anodes by In, *Reboul and Delatte* [111] also focused on understanding the effective mechanism of activation of Al-Zn anode by Hg ions, using alloy containing 2.0 to 2.5wt%Zn, 0.04wt%Hg and impurities (such as Fe and Si) <0.2wt%.

After exposing the alloy to ASTM D1141-52 sea water for 480 hours, the authors found non uniform corrosion morphology. The quantitative microprobe (electron probe microanalysis) analysis conducted prior to exposure confirmed heterogeneous distribution of Hg rich phase in the alloy but the analysis after exposure indicated no correlation between the Hg rich phase and corrosion morphology [111].

The authors proposed that in presence of electrolytic solution, Hg ions get deposited on the Al₂O₃ oxide layer, with following reaction step:



this causes the removal of oxide layer from the surface of the bare alloy causing formation of localised pits which in turns shifts the potential of the Al-Zn-Hg alloy to a more electronegative region (-710 mV to 1050 mv vs. SCE, reported by the authors). The deposited Hg on the oxide layer takes no part in further activation or dissolves in the electrolytic solution, was not described by the authors [111].

Many researchers conducted electrochemical experiments to further understand this proposed activation mechanism of Al by elements such as Zn, Hg, In and Ga in binary and ternary alloy form [62-72]. Bessone [112] and Al-Shaffer [113] investigated the effect of Hg addition to Al sacrificial anodes in Hg(II) acetate and artificial sea water (ASTM D1141) solution. Bessone [112] identified the activation of Al by Hg²⁺ ions as a process of crack and healing of Al₂O₃ oxide film formed on the surface of the Al alloy. **Figure 2.33** shows three distinct regions of the potential vs. time response of Al subjected to Hg(II) acetate (Hg(C₂O₂H₃)₂) solution at maintained pH of 4.2 [112].

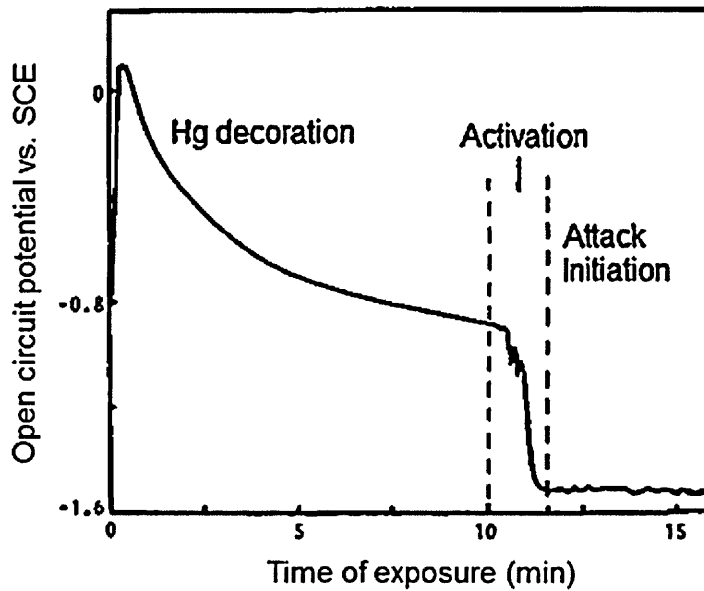


Figure 2.33: Potential vs. time curve for Al in 0.001M $\text{Hg}(\text{C}_2\text{O}_2\text{H}_3)_2$ solution at pH= 4.2 [112].

The authors reported the formation of Hg droplets on Al surface after initial 10 minutes of exposure of Al in 0.001M $\text{Hg}(\text{C}_2\text{O}_2\text{H}_3)_2$. This was attributed to the redox couple between the Al/Al^{3+} ions (-1901 mV vs. SCE) to Hg/Hg^{2+} ions (+560 mV vs. SCE) causing the oxidation of Al to Al^{3+} while reducing Hg^{2+} from the electrolytic solution to cathodic sites on the alloys (sites rich in impurities such as Fe and Cu) [112].

The SEM examination of Al sample exposed to Hg(II) acetate solution for 10 minutes also revealed formation of tail like structure to the Hg droplets which suggested cracking of the Al_2O_3 layer causing Hg^{2+} ions to reduce on localised cathodic sites [112].

With just over 10 minutes of exposure in 0.001M Hg(II) acetate solution, the authors observed a profound shift in the potential of Al to a more electronegative region (from ≈ -0.8 V vs.SCE to ≈ -1.5 V vs.SCE), as shown

in **Figure 2.33**, which was referred as activation state of the alloy [112]. The authors suggested that the cause of activation was due to the wetting of Hg droplets formed on the Al surface with oxide free Al surface, which is shown in **Figure 2.34** [62].

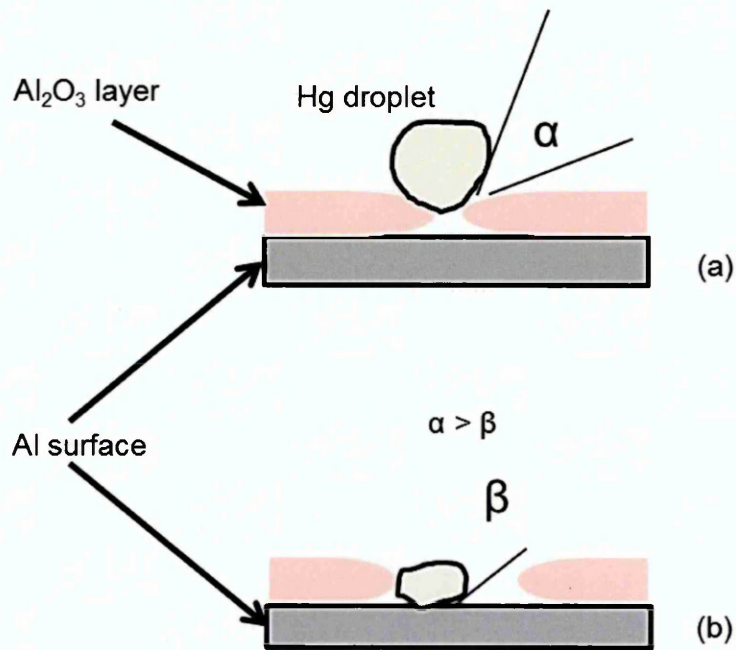


Figure 2.34: Diagrammatic representation of activation of Al by Hg²⁺ ions showing (a) re-formation of Al₂O₃ oxide layer and (b) surface wetting of Al by Hg when contact angle $\beta < \alpha$ [112].

The authors reported that wetting of Al by Hg²⁺ ions causes formation of Al amalgam which shifts the potential of Al to more electronegative region as shown in **Figure 2.33** (activation region) [112]. Al-Saffar *et al.*[113] investigated the effect of Hg implantation on Al-Hg alloy, and found similar effects as described by Bessone [112].

However, Al-Saffer *et al* [113] reported that the Hg implanted Al alloy showed uniform dissolution when exposed to artificial sea water (ASTM D1141) and no evidence of preferential dissolution along the grain boundary was observed as in cast Al-Zn-Hg alloys reported by Reboul *et al.* [111,113].

Carroll and Breslin [114] conducted a comparative study on activation of Al by Hg, In, Zn and Ga in form of ions ($5 \times 10^{-3}M$ of In^{3+} , Hg^{2+} , Zn^{2+} and Ga^{3+} were used during experiments) in the electrolytic solution with ternary Al-Zn-In (3.0wt%Zn and 0.02wt%In) and Al-Zn-Hg (0.4wt%Zn and 0.04wt%Hg) and binary Al-Ga (the authors varied the Ga concentration of alloys as 0.026wt%, 0.1wt% and 2.6wt%) alloys.

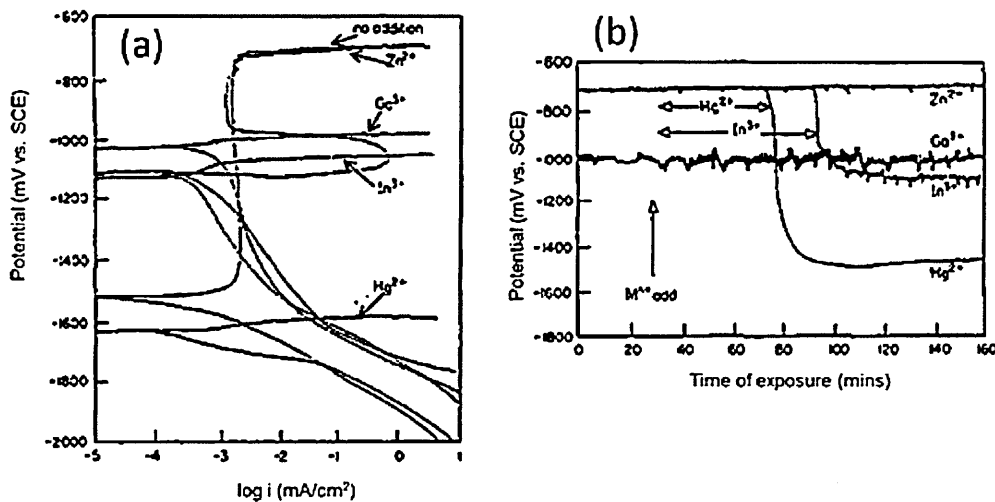


Figure 2.35: (a) Potentiodynamic polarisation and (b) potential vs. time graphs of Al exposed to 0.5M NaCl solution in addition with 0.005M of Zn^{2+} , Ga^{3+} , In^{3+} and Hg^{2+} ions [114].

The potentiodynamic polarisation curve as shown in **Figure 2.35** (a) clearly showed the reduction in passivation caused by Hg^{2+} , In^{3+} and Ga^{3+} ions with Zn^{2+} showing the least effect. The potential vs. time curve, see **Figure 2.35** (b) also showed the same effect however, the addition of 0.005M In^{3+} and Hg^{2+} shifted the potential to ≈ -1.1 V (vs. SCE) and ≈ -1.5 V (vs. SCE) respectively. However the authors emphasised on the time taken to shift the potential more negative upon addition of In^{3+} and Hg^{2+} ions to 0.5M Cl^- solution, referred as induction period [114].

The authors also reported that for In^{3+} ions to produce a similar activation effect with decreasing Cl^- concentration (at 0.01M Cl^-), the induction period increased to few hours rather than few minutes as shown in **Figure 2.35** (b), which was not observed for Hg^{2+} ions [114]. The authors also reported the effect of Hg, In, Zn and Ga in cast Al binary and ternary alloys as shown in **Figure 2.36** (a), with almost similar effects of Hg and In as seen from **Figure 2.35** (a) [114]. Carroll and Breslin's [114] results were in agreement with Breslin *et al.* [65] who investigated the effect of ternary alloying of Al and Zn with In and Hg, as shown in **Figure 2.36**(b).

Both the authors observed that the activation caused by Hg^{2+} and In^{3+} ions is similar in nature but only in the chloride environment. The effect of activation of In^{3+} decreases considerably when exposed to solution containing SO_4^{2-} , NO_3^- and ClO_4^{2-} ions [114,115]. The previous research conducted had showed that Hg had pronounced effects on activation of Al, but one of the major concerns over the use of Hg in Al sacrificial anode has been due to its toxicity. Due to which the major focus of the research had shifted to the use of other activator elements such as In [116,117].

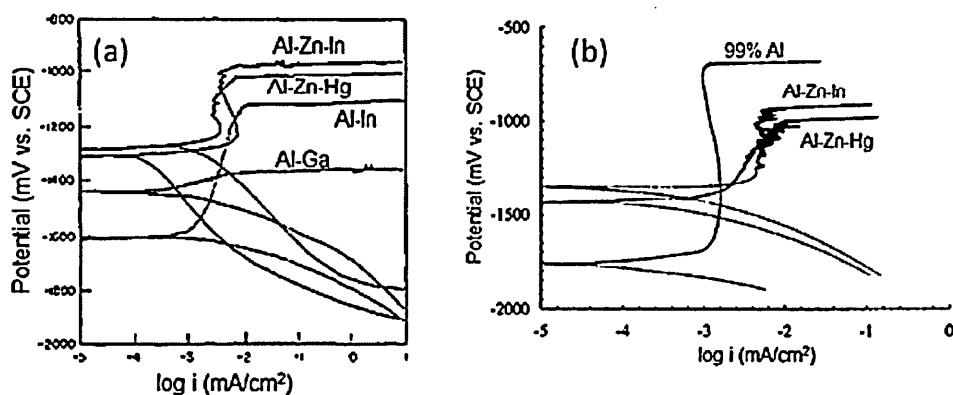
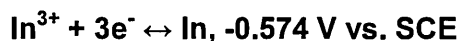


Figure 2.36: Potentiodynamic polarisation curves for (a) Al alloyed with Zn, In and Hg in binary and ternary form [114] and (b) ternary Al-Zn-In and Al-Zn-Hg alloy [115]. Both exposed to 0.5M NaCl solution.

2.8.6.3 Understanding the activation of Al by Zn and In:

(a) D.C Electrochemical methods

From early 1970's, In has been widely used as a replacement of Hg in the Al sacrificial anodes and electrochemical properties of In were investigated by many researchers [118-121]. Piercy and Hampson [118] were among the early researchers who investigated the electrochemical mechanism of formation of complex In ions when exposed to aqueous environments containing halide and perchlorate ions. The authors reported, that In favoured formation of chloro-complex ion, InCl_2^+ , when exposed to aqueous solution containing Cl^- ions [68]. This suggested that the oxidation state of In with standard redox potentials [118,119]:



Formation of In^{3+} was favoured during the reaction owing to fact that In^{3+} cation forms a more stable complex with Cl^{-} ion than In^{+} cation, which was vice-versa for In exposed to perchlorate (ClO_4^{-}) ion [118].

The authors also suggested that this equilibrium reaction of In^{+} to In^{3+} was the rate determining step during the anodic dissolution of In when exposed to Cl^{-} and ClO_4^{-} environment [118].

Muñoz and Bessone [119,120] conducted further work on investigating the effects of Cl^{-} , SO_4^{2-} , F^{-} and ClO_4^{-} ions in aqueous and non-aqueous solutions on $\text{In}^{+}/\text{In}^{3+}$ equilibrium. The authors concluded that under the aqueous conditions, the presence of hydroxide ion (OH^{-}) creates active sites on In surface which then causes adsorption of present anion, especially Cl^{-} ions, forming of complex InCl_2^{-} species at a potential $\approx -1.2 \text{ V vs. SCE}$, which allows further diffusion of Cl^{-} ion to the surface of indium and mitigates formation of any surface passive oxide layer [119,120].

Similar mechanism was proposed for In in the non-aqueous media, however the complex InCl_2^{-} was suggested to be less stable than aqueous media for similar concentrations of anions [119,120]. The authors attributed the difference in the stability of the complex chloride ion film on the surface due to the different diffusivity rates observed for aqueous and non- aqueous Cl^{-} , ClO_4^{-} and SO_4^{2-} anions. However in both cases the chloride ion complex was

found to be less stable than ClO_4^- and SO_4^{2-} ion complex, see **Figure 2.37** (a) and (b), explaining the enhanced activity of In in chloride media [119,120].

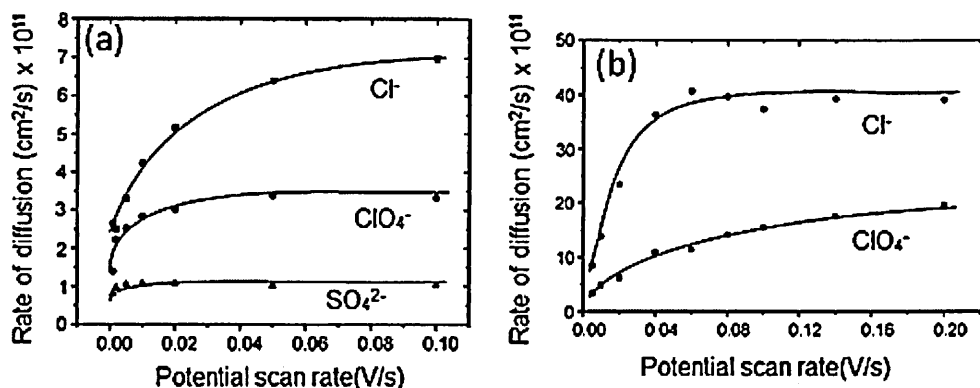


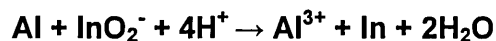
Figure 2.37 Graphs showing the effect of Cl^- , ClO_4^- and SO_4^{2-} anions on the rate of diffusion calculated for different scan rates of polarisation in (a) aqueous and (b) non aqueous media (Dimethylformamide with 0.03wt% water was used as a non-aqueous media by the authors) [119].

This phenomenon of In forming complex ions in presence of chloride media was used by authors to explain the mechanism of activation of Al induced by In [114,115,119,120].

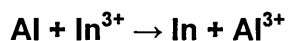
This explanation was also supported by Breslin and Carroll [121] who investigated the mechanism of Al activation by In in presence of aqueous solution containing Cl^- , Br^- and I^- ions. In addition to the formation of halide complex's on the surface of Al in presence of In was reported previously [69,70]. *Breslin and Carroll* [121] also suggested that these halide complex's contribute in formation of $\alpha\text{-Al}(\text{OH})_3$ or a stable $\gamma\text{-Al}_2\text{O}_3 \cdot 3\text{H}_2\text{O}$ species, however prolonged exposure to chloride environment favours formation of

stable $\gamma\text{-Al}_2\text{O}_3\cdot 3\text{H}_2\text{O}$ which causes fluctuations in potential vs time transients as observed in **Figure 2.35** (b). Aqueous solution contain Cl^- and Br^- showed similar mechanism, however presence of I^- to form complex iodide salts followed a rather complex mechanism. With initial formation of I_3^- species, which disintegrated further to form hypiodous acid (HIO), due to instability of HIO, further disintegration to I_2 and IO_3^- causes the pH of the solution to shift to acidic region causing further attack on Al surface [121]. The liberated I_2 then combines with Al to form AlI_3 complex, but due to the acidic pH level AlI_3 disintegrates allowing the fresh surface to Al to form $\alpha\text{-Al}(\text{OH})_3$ or $\gamma\text{-Al}_2\text{O}_3\cdot 3\text{H}_2\text{O}$ [121].

The formation of In complex with chlorides (or halide ions in general) was shown to depend on the adsorption of Cl^- on the surface of the alloys with in turn affected the $\text{In}^{3+}/\text{In}^+$ equilibrium during the active dissolution of Al in aqueous chloride media [122-124]. It was also shown that with $\approx 0.005\text{M}$ concentration of In^{3+} ion in the solution, In complex such as $(\text{In}(\text{H}_2\text{O})_5\text{OH})^{2+}$ and $(\text{In}(\text{H}_2\text{O})_4(\text{OH})_2)^+$ co-existed in the initial hydrolysis stage of In before contributing to form hydroxide and hydrated oxide of Al as reported Breslin and Carroll [121,122-124]. As it was reported before that the formation of initial In complex ions takes place at potential $\approx -1.2\text{ V}$ vs. SCE, it was also found that, as the potential was lowered to about -1.5 V vs. SCE, the formation of initial In complex occurred via galvanic coupling of Al and InO_2^- ion, which can be represented as [122-124]:



However, the complex In ion formation took place via Al and In^{3+} displacement reaction as follows [72-74]:



Apart from the research conducted on understanding the mechanism of activation of Al induced by In in the aqueous electrolytic solution, many researchers also focused on mechanism of activation of binary and ternary Al, alloyed with Zn and In [125-130].

Muñoz *et al.*[125] investigated the effect of In addition to Zn in order to understand the synergetic electrochemical interaction of Zn and In by analysing commercially pure Zn (99.999wt%Zn) and Zn alloyed with 5wt%In in aqueous solution containing Cl^- and ClO_4^- ions. The authors demonstrated that in aqueous condition, the activation of Zn with 5wt%In was also dependent on chloride adsorption to form chloro complex as suggested previously [119,120,122-124] and occurred at ≈ -1.1 V vs. SCE, see **Figure 2.38** [125].

The authors also suggested that, in aqueous Cl^- solution for both Zn and Zn-5wt%In, the intermediate ZnCl_n^{2-n} complex was formed which participated in active dissolution of the alloy. Whereas in presence of aqueous ClO_4^- , ZnOH intermediate was reported to be formed and with addition of 5wt%In, this ZnOH intermediate was further oxidised to ZnOH^+ before active dissolution of Zn [125]. *Breslin and Friery* [126] studied the effect of Zn and In combination on activation of Al by exposing commercially pure Al (99.99wt%) to 0.5M NaCl solution added with sulphate salts of Zn^{2+} and In^{3+} of In^{3+} to Zn^{2+} ratio of 1:2, see **Figure 2.39**.

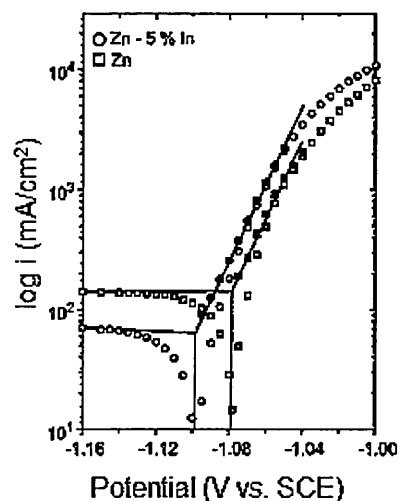


Figure 2.38: Potentiostatic curve for Zn and Zn-5wt%In in 0.5M NaCl solution, pH maintained at 3 (the authors have corrected for cathodic current, shown in black) [125].

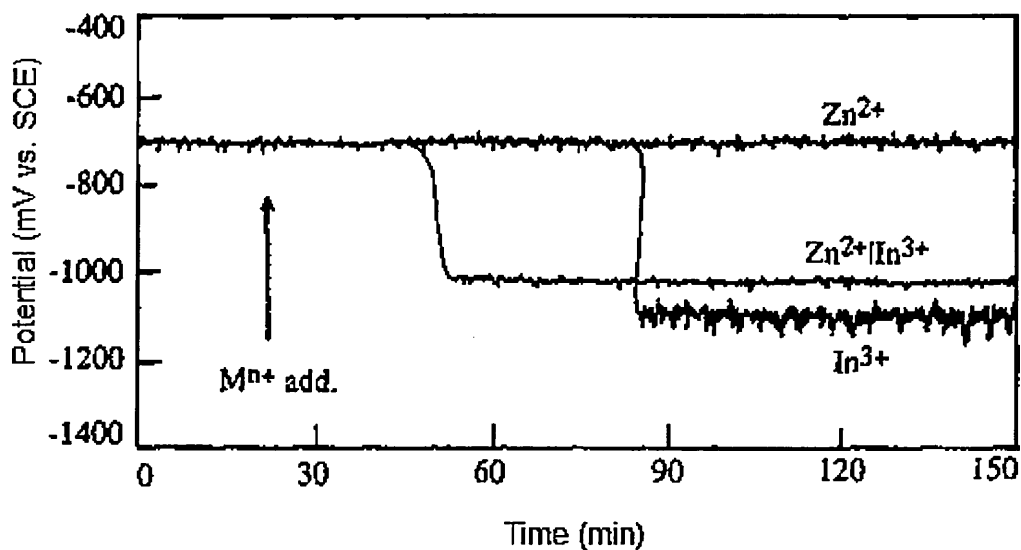


Figure 2.39: Potential vs. time graph for Al exposed to 0.5M NaCl solution with addition of Zn^{2+} and In^{3+} sulphate salt of concentration 0.01M $ZnSO_4$, 0.005M $In_2(SO_4)_3$ or 0.005M $ZnSO_4$, 0.0025M $In_2(SO_4)_3$ [126].

Addition of Zn^{2+} and In^{3+} sulphate salts were made after ≈ 25 mins of Al exposure in 0.5M NaCl solution as shown in **Figure 2.39** [126]. The potential vs. time transient clearly showed that addition of Zn^{2+} alone did not alter the potential of Al in Cl^- ion environment, however Zn^{2+} with In^{3+} lowered the potential of Al to ≈ -1.02 V vs. SCE with a much lesser induction time as compared to In^{3+} addition (however In^{3+} addition caused the potential to shift to ≈ -1.1 V vs. SCE).

These results were in accordance with the research conducted by other authors [114,115,121-124] that activation of Al caused by In^{3+} ions was found more effective in halide solution with order of activation as $Cl^- > Br^- > I^-$ but also the potential fluctuations, see **Figure 2.39 and 2.35** (b) were indicative of the formation and rupture of oxide induced by In [126]. Burri *et al.* [127] and Equey *et al.* [128] analyse Al exposed to 2M NaCl solution with addition of 0.0005M In^{3+} and 0.08 M Zn^{2+} ions and showed that even at this lower concentration of In^{3+} ion, Al reported a potential as reported by Breslin and Friery [126], of ≈ -1.02 V vs. SCE. Using SIMS, see **Figure 2.40**, the authors also reported a much deeper profile of In^{3+} ions in the Al than Zn^{2+} ions indicating enhanced activation effect of In in halide environment which was investigated by researchers [118-120,127,128].

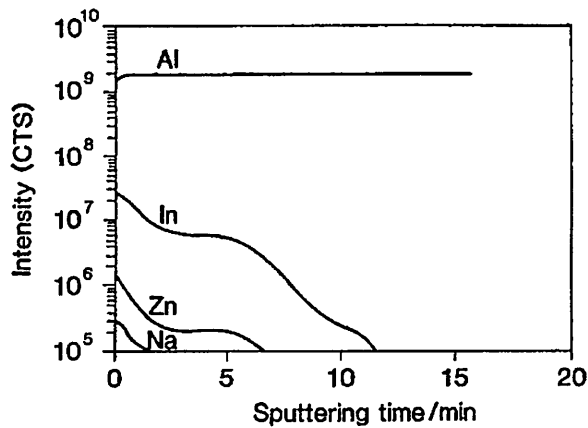


Figure 2.40: SIMS depth profile of Al exposed after exposure to 2M NaCl with 0.0005M In³⁺ and 0.08M Zn²⁺ ions [127].

According to various researches conducted on Al alloyed with ≈5wt%Zn and ≈0.02wt%In in electrolytic media containing 0.5M Cl⁻ ions [129-131] showed that the synergetic mechanism of Zn and In which produced activation of Al included:

- Formation of initial chloride complex induced by In which in turn increases the chloride adsorption.
- The presence of Zn rich regions in the alloys promote the formation of these In chloro complexes and in doing so increases the rate of chloride adsorption which shifts the potential of the alloys to ≈ -1.2 V vs. SCE.
- These In chloro complexes (InCl₂⁻) further transform to produce Al oxides, either α-Al(OH)₃ or a stable γ-Al₂O₃·3H₂O, which produces fluctuations in the potentials upon long term exposure.
- Due to presence of Zn rich regions favouring chloride adsorption induced by In to form InCl₂⁻ species, continuous adsorption of Cl⁻ ions from the electrolytic media maintains an active Al surface.

(b) A.C Electrochemical methods

Many researchers undertook studies to obtain mechanistic information on Al activation by Zn and In using Electrochemical Impedance Spectroscopy (EIS) technique [132-134]. Prior to understanding the mechanism of activation of Al, many researchers focused on understanding the mechanism of dissolution and passive film formation on Al in various electrolytic solutions by conducting EIS [135-137]. Macdonald [135,136] studied the impedance spectra (Nyquist plots) obtained for Al exposed to 4M KOH solution in steps of 30 to 80mV in the range of -1.96 V to -1.35 V vs Hg/HgO , see **Figure 2.41**, and proposed mechanism of dissolution of Al under alkaline conditions.

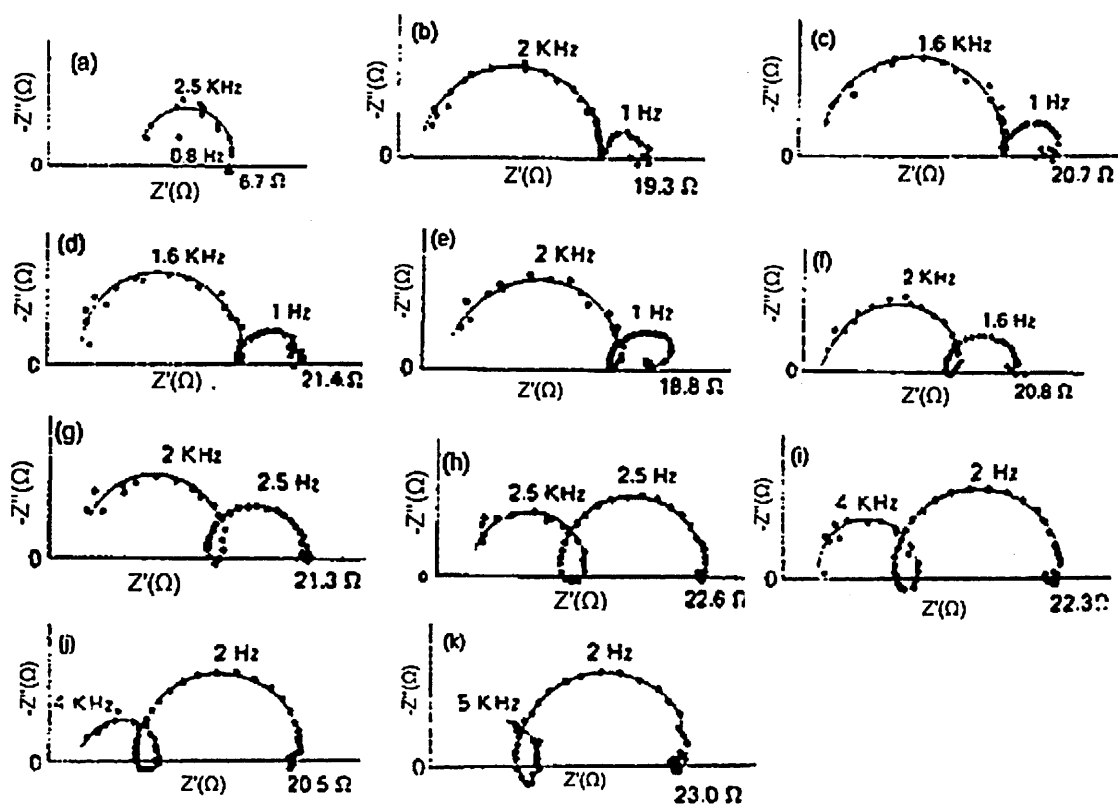
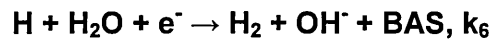
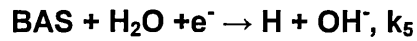
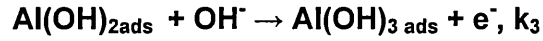
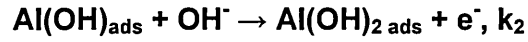


Figure 2.41: Experimental Nyquist plots of Al in 4M KOH solution at (a) -1.95 V, (b) -1.88 V, (c) -1.74 V, (d) -1.70 V, (e) -1.68 V, (f) -1.64 V, (g) -1.60 V, (h) -1.50, (i) -1.46 V, (j) -1.38 V, (k) -1.35 V vs. Hg/HgO [135,136].

The author emphasised that under strong alkaline conditions (4M KOH), formation of capacitive loops towards lower frequencies as the potential was shifted towards electropositive direction were observed, see **Figure 2.41** (a)-(k). This suggested anodic dissolution of Al at the electrolyte surface interface, which was explained further by using one of the reaction mechanism suggested by author and represented in following reaction steps [135,136]:



Where BAS is bare aluminium surface, ads are adsorbed species and k_1 to k_6 are rate of each reaction. The above mentioned reaction steps suggest that under the influence of strong alkaline solution, the Al atoms are initially removed from the surface of the metal forming intermediate $\text{Al}(\text{OH})_{\text{ads}}$ species which further reacts with OH^- ions to form stable $\text{Al}(\text{OH})_3$.

However due to large concentration of OH^- ions, stable $\text{Al}(\text{OH})_3$ forms aluminate ($\text{Al}(\text{OH})_4^-$) ions exposing the bare aluminium surface and in doing so, maintains constant dissolution of Al [135,136]. *Wit and Lenderink* [137] studied the formation of passive oxide layer on Al surface exposed to solution containing SO_4^{2-} and Cl^- ions. The Nyquist plot for Al exposed to 1M solution of H_2SO_4 , see **Figure 2.42**, showed formation of two capacitive loops at a higher frequency (1kHz) and lower frequency (1mHz) with formation of an inductive loop at intermediate frequency [137].

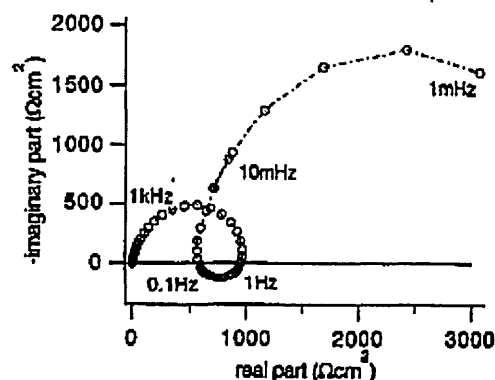


Figure 2.42: Nyquist plot for Al exposed to 1M H₂SO₄ under potential control condition in order to draw mechanistic information on formation of passive layer [137].

The authors suggested that the first capacitive loop (at higher frequency) was evidence of oxidation of Al at the metal solution interface, the intermediate inductive loop showed formation of passive oxide layer [137].

However the capacitive loop observed in the lower frequency region was attributed to formation of defects in the solution oxide interface layer which caused further dissolution of Al to fill the vacancies. But as the vacancies were filled by Al(OH)₃ ions as indicated previously by *Macdonald* [132,133] no further dissolution of Al was observed [137]. *Venugopal and Raja* [138] and *Gudić et al.*[139] studied the effect of In and Zn using EIS on activation of Al in chloride media. *Venugopal and Raja* [138] analysed the binary Al-5wt%Zn and Al-0.05wt%In alloys using EIS within frequency range of 100kHz to 1mHz, by exposing the alloys to 3.5wt% NaCl solution with various concentration of Zn²⁺ and In³⁺ ions, as shown in **Figure 2.43** (a)-(g) and **Figure 2.46** (a)-(d) and proposed the mechanism of activation of the Al by Zn and In.

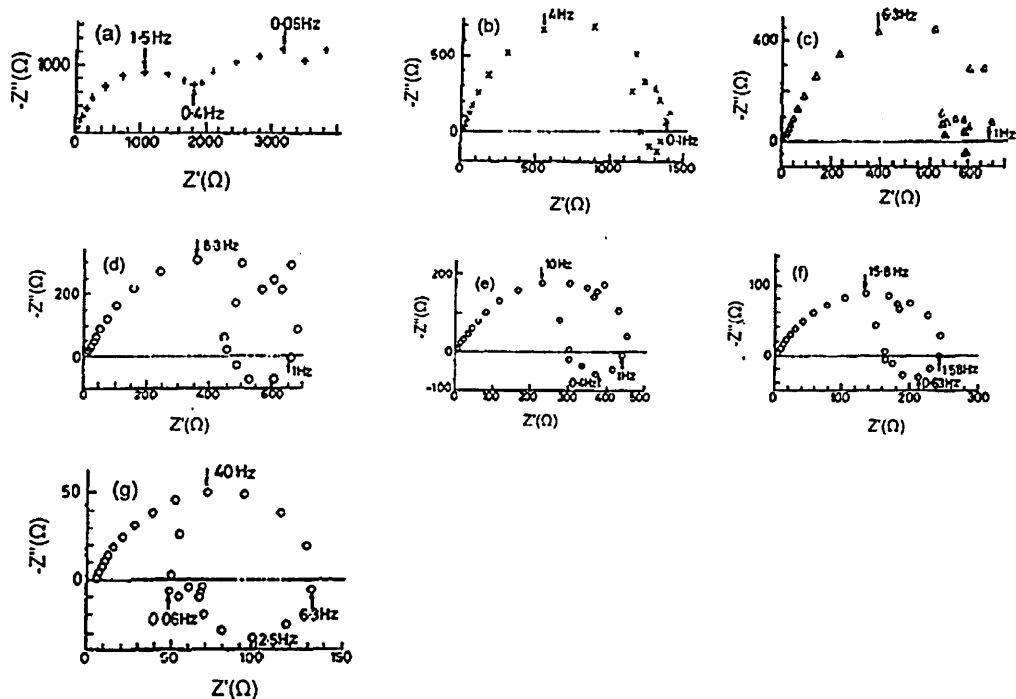


Figure 2.43: Nyquist plot for Al-5wt%Zn alloys in 3.5%NaCl solution with In^{3+} addition at concentrations (a) no addition (b) 0.001M (c) 0.002M (d) 0.003M (e) 0.004M (f) 0.005M and (g) 0.006M [138].

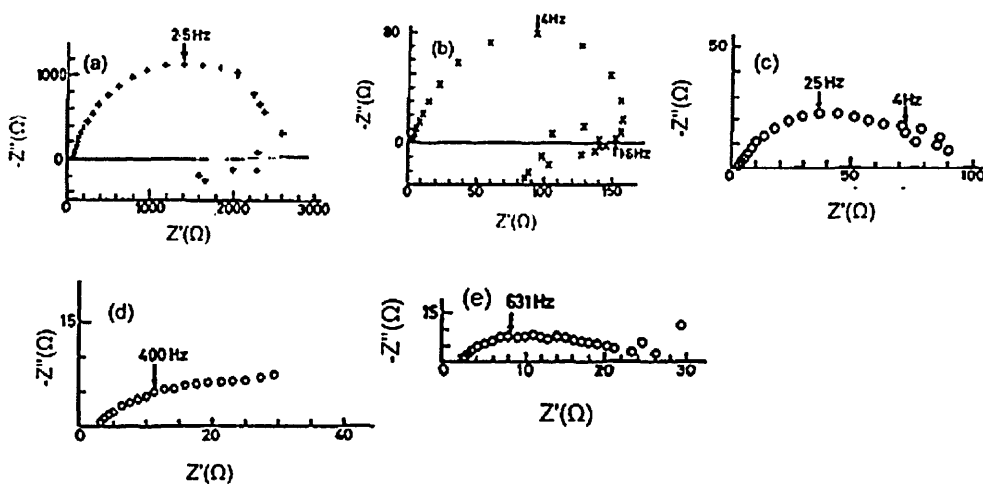


Figure 2.44: Nyquist plot for Al-0.005wt%In alloy in 3.5%NaCl solution with Zn^{2+} addition at concentrations (a) no addition (b) 0.01M (c) 0.02M (d) 0.03M and (e) 0.04M [138].

The authors stressed on significant difference found in the Nyquist plots for Al-5wt%Zn and Al-0.05wt%In alloys in 3.5% NaCl solution without addition of In^{3+} and Zn^{2+} ions, see **Figure 2.43 (a)** and **Figure 2.36 (a)** [138]. For Al-5wt%Zn system, prior to In addition, two capacitive loops were observed, see **Figure 2.43 (a)**, the capacitive loop at higher frequency was oxidation of Al, while the second suggested initial formation of $\text{Zn}(\text{OH})_2$ on the surface of the alloy [138].

For Al-5wt%Zn alloy, the authors observed formation of inductive loops with the increased addition of In^{3+} ions in the chloride solution, see **Figure 2.43 (b)-(g)** [138]. The authors attributed the formation of these inductive loops due to presence of intermediate In^+ and In^{2+} species which on further exposure enhances the Cl^- adsorption onto the surface of the alloy promoting dissolution as stated previously by many researchers [120-124].

However, for Al-0.05wt%In alloy, the inductive behaviour was subdued by addition of Zn^{2+} ions in chloride ion solution, see **Figure 2.44 (b)-(e)** [138]. The observed depression in the inductive nature was reported to be caused by adsorption of Zn^{2+} ions on Al_2O_3 to form spinel ZnAl_2O_4 structure reported previously [87-89], which in turn increases the Zn^{2+} ion mobility causing dissolution of Al only on Zn^{2+} ion adsorbed sites [138]. A similar Nyquist plot with inductive loop was obtained by Gudić *et al.* [139] and Breslin and Rudd [140] by exposing Al alloyed with 0.1wt%In to 2M NaCl solution which supported the evidence of formation of intermediate In^{3+} chloro-complexes which increased the Cl^- adsorption on the surface of the alloy making the Al alloy active in the chloride media.

2.9 The addition of Ti to produce wear resistant Al alloys

This section will focus on the understanding of microstructural and mechanical properties of Al alloyed with Ti, which has been thermally sprayed (arc sprayed) onto steel structure to provide adequate wear resistance under abrasive condition.

2.9.1 Background on wear of materials

The existing literature reveals that the understanding of the ubiquitous phenomena of wear of materials dates back to approximately 2400 B.C. Where people of ancient Egyptian civilization used some form of lubrication to prevent the wearing of surfaces in relative motion as shown in **Figure 2.45** [141].

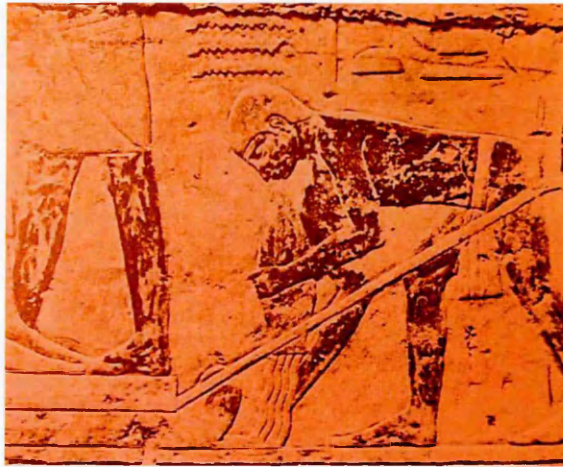


Figure 2.45: Engraving found on the walls at Saqqara, Egypt showing the use of some kind of lubrication in order to move a heavy metallic statue [141].

Over the years, knowledge of wear as phenomena of loss of material from the surfaces in relative motion enabled the researchers to build various models to understand the interaction of surfaces and devise methods to mitigate the detrimental effects of wear [142]. **Figure 2.46** shows the diagrammatic representation of various forms of wear mechanisms which attribute to loss of materials either acting individually or in combination depending on the environment to which materials are exposed.

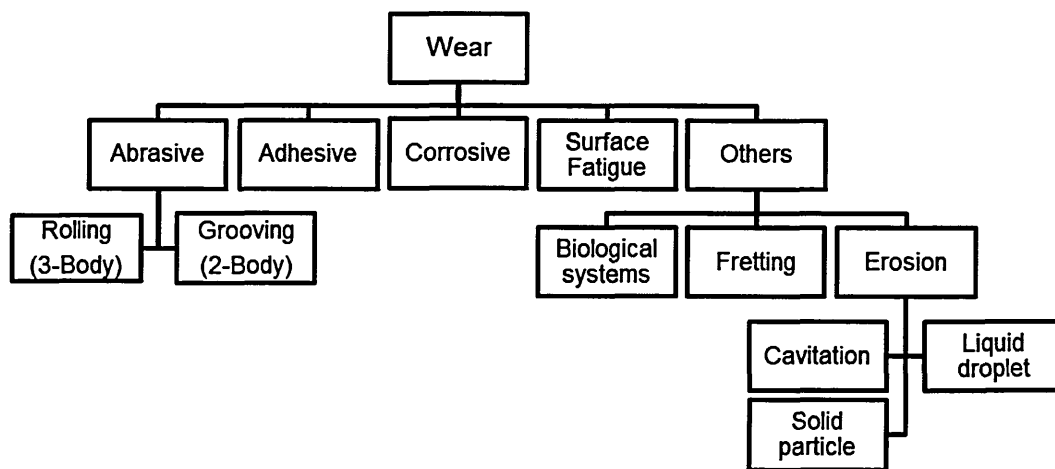


Figure 2.46: Diagrammatic representation of various forms of wear mechanisms [143].

The four main forms of wear mechanisms can be described as [144]:

1. **Abrasive wear:** This is caused by the interaction (sliding) of two surfaces (2 body interactions) with different hardness values causing the removal of softer material by ploughing action caused by hard material. A similar possibility arises when the interaction of two surfaces takes place in presence of a third body (mainly grit particles, slurry etc.), commonly referred as 3-body interaction, causing abrasion of softer material or in some cases both

materials by ploughing action caused by the third body. Abrasion by 3 body mechanism causes maximum loss of material in an industrial environment (e.g. automotive industries).

2. **Adhesive wear:** often referred as galling wear is primarily caused when the adhesive force at the interacting points (due to presence of surface asperities) between the two surfaces causes removal of material from either surface forming wear debris. The formation of wear debris between the surfaces causes further removal of material by abrasive action, hence wear of materials purely under adhesive mechanism is only possible under controlled environment.
3. **Corrosive wear:** the combination of sliding condition and corrosive industrial environment such as high temperature, humidity or vapours, chlorides and CO₂ causes formation of loosely adherent chemical product on metallic surfaces, also referred as tribofilm. The formation of these tribofilm either improves or deteriorates the wear resistance of the metallic systems.
4. **Surface fatigue wear:** whenever the surfaces of material are exposed to continuous sliding or rolling action, a sudden removal of large material from the surfaces can take place causing localised loss of materials on the interacting surfaces. The loss of material due to fatigue on the interacting surfaces is more pronounced than abrasive, adhesive and corrosive wear causing drastic reduction in operating life of such a system.

Since the industrial revolution, various machines and structures have been designed to perform complex operations under challenging working environments. This causes loss of material from the surfaces caused by mechanisms such as abrasion, corrosion and fatigue and in turn reduces the nominal working life of structures and machine components.

Due to increasing complexities in the design of modern machines, apart from lubrication, various common industrial methods such as surface hardening, application of soft and hard coatings (both metallic and non-metallic) have also been developed to protect the parent material from detrimental effects of wear [145].

Aluminium, mostly in alloyed form has been an attractive material for thermal spraying (electric arc spraying) on to steel structures used in diverse industrial applications for protection against wear and corrosion [146]. Aluminium-titanium-carbon alloy coatings have been commercially used as wear resistance coatings on offshore bridge decks, loading and unloading ramps for containers carried by forklift trucks [147]. In order to understand the performance of arc sprayed Al-Ti-C coatings, tribological properties of the Al-Ti and Al-Ti-C alloy systems in relation with microstructure and phase formation in the alloys has been investigated by researchers.

2.9.2 Aluminium-Titanium (Ti) alloy system

Aluminium (Al) alloyed with titanium (Ti) (which constitute approximately 0.63% of the earth's crust) has been widely used engineering alloy finding their application in various industries such as, aerospace, naval, automobile and even medical applications [148]. To fully exploit the industrial applications of Al-Ti alloys, properties such as micro-structure and formation of different phases due to variation in composition of either of its constituents, or even the addition of a third alloying element such as carbon has been investigated by many researchers.

2.9.2.1 Properties of Al-Ti alloys

The focus of the literature for Al alloyed with group 4 transition metals such as Ti, Hf, Zr has been on the study of formation of intermetallic compounds at various transformation stages of alloying which imparts the alloys properties such as thermal stability and creep resistance [148,149]. As many as twelve forms of intermetallic Al-Ti compounds of varying composition have been reported during the alloying stages. However properties of few of these intermetallic compounds such as AlTi, Al₃Ti, Al₂Ti and AlTi₃ have been of considerable interest to the researchers [148].

Batalu *et al* [148] critically reviewed variants of Ti-Al phase diagram studied previously by researchers and attributed the formation of intermetallic phases (by varying at% Al) due to following transformations during alloying process:

- **Peritectic transformations**

L 49.4 at% Al + (β_{Ti}) 44.80 at% Al \leftrightarrow (α_{Ti}) 47.30 at% Al at 1763 K

L 55.10 at% Al + (α_{Ti}) 51.40 at% Al \leftrightarrow (AlTi) 55.0 at% Al at 1735.8 K

L 55.10 at% Al + (AlTi) 55.0 at% Al \leftrightarrow ($\text{Al}_{11}\text{Ti}_5$) 63.70 at% Al at 1688 K

L 77.46 at% Al + ($\text{Al}_{11}\text{Ti}_5$) 72.2 at% Al \leftrightarrow (Al_3Ti) 74.39 at% Al at 1688 K

L 99.90 at% Al + (Al_3Ti) 75.0 at% Al \leftrightarrow (Al) 99.30 at% Al at 938 K

- **Eutectoid transformations**

(α_{Ti}) 39.60 at% Al \leftrightarrow (AlTi_3) 38.20 at% Al + (AlTi) 46.70 at% Al at 1391.5 K

($\text{Al}_{11}\text{Ti}_5$) 69.76 at% Al \leftrightarrow (Al_2Ti) 66.70 at% Al + (Al_3Ti) 74.60 at% Al at 1263 K

- **Peritectoid transformation**

(AlTi) 63.81 at% Al + ($\text{Al}_{11}\text{Ti}_5$) 68.31 at% Al \leftrightarrow (Al_2Ti) 66.50 at% Al at 1448 K

- **Order-disorder transformation**

(α_{Ti}) 30.90 at% Al \leftrightarrow (AlTi_3) 30.90 at% Al at 1437 K

- **Polymorphic transformation**

(α_{Ti}) \leftrightarrow (β_{Ti}) at 1155 K

(a) Tri-aluminide (Al_3Ti) intermetallic compounds formation by Ti

The formation of tri-aluminide, when Al is alloyed with group 4 transition metal Ti, has attracted many researchers to study the properties of these compounds for nearly 40 years. The primary importance being, that addition of Ti promotes formation of Al_3Ti which acts as a nucleation point for the alloys during the solidification process, fostering the growth of equiaxed macrostructure rather than conventional columnar macrostructure [149,150]. This property of macrostructure enhancement by tri-aluminide formation caused by Ti addition has been exploited to form Al alloys with capabilities of operating under high temperature and high creep conditions [150-152]. The next few sections of this chapter will focus on microstructure and mechanical properties of Al_3Ti intermetallic compound.

(b) Formation and microstructural properties of Al_3Ti intermetallic compound.

The tri-aluminide intermetallic compound Al_3Ti under equilibrium exhibits either body centred tetragonal ($a = 5.45 \text{ \AA}$, $c = 8.60 \text{ \AA}$) or face centred tetragonal ($a = 3.849 \text{ \AA}$, $c = 8.60 \text{ \AA}$) DO_{22} or DO_{23} type crystal structure which are precipitated initially as cubic $L1_2$ type structure, see **Figure 2.47** [149,153,154].

Due to lower symmetry of tetragonal DO_{22} or DO_{23} type crystal structure, the Al_3Ti intermetallic is brittle at room temperature, hence $L1_2$ crystal structure of Al_3Ti , which shows ductility under compression, is preferred during the alloy formation [155,156].

Due to lower diffusivity of Ti in Al, the formation of coarse plate-like Al_3Ti intermetallic with high aspect ratio readily occurs during the normal casting process. However at lower Ti addition of up to 1.2wt%, petal-shaped Al_3Ti intermetallic compound is formed [149,156]. The formation of either coarse plate-like structure or petal-shaped structure of Al_3Ti intermetallic is governed by concentration of Ti and cooling rate of the alloy. It has been observed that with Ti addition up to 3.5wt% and cooling rate of $400^{\circ}C/cm$, coarse plate-like Al_3Ti intermetallic is formed, as shown in **Figure 2.48(a)**, with Ti concentration up to 1.15wt% and cooling rate of $205^{\circ}C/cm$, fine petal-shaped Al_3Ti is formed, as shown in **Figure 2.48 (b)** [153-155].

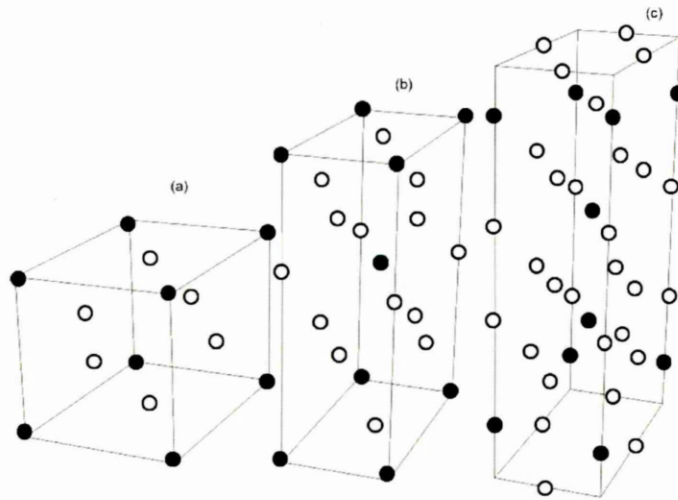


Figure 2.47: Crystal structure of Al_3Ti intermetallic showing (a) $L1_2$, (b) DO_{22} and (c) DO_{23} type structure, where \bigcirc represents Al atoms and \bullet Ti atoms [154].

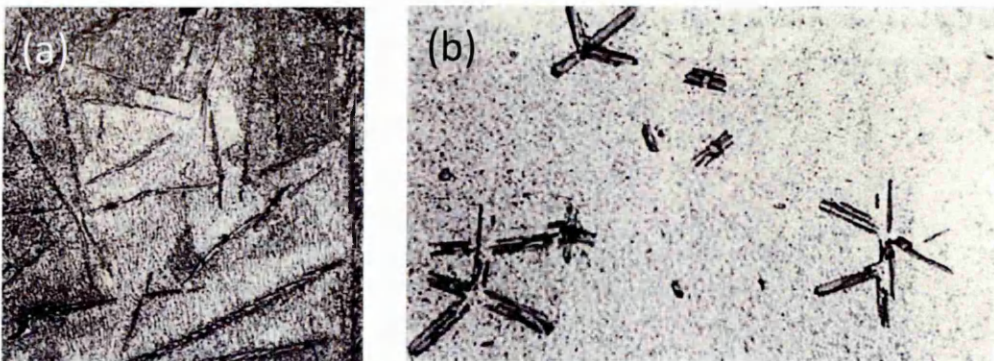


Figure 2.48: Optical micrographs showing directionally solidified (a) Al-3.5wt%Ti alloy with coarse plate like Al_3Ti intermetallic growth at cooling rate of $400^\circ\text{C}/\text{cm}$ and (b) Al-1.15wt%Ti showing fine petal shape growth of Al_3Ti intermetallic at cooling rate of $205^\circ\text{C}/\text{cm}$. Magnification X 40 [153].

Even with a low solubility limit of Ti in Al. which is $\approx 1.06\text{wt}\%$ at 938 K, the formation of stable Al_3Ti intermetallic is also achieved by controlled rapid solidification of the alloys, depending upon the concentration of Ti and cooling rates, the following microstructural features of Al_3Ti intermetallic compound (post etching) is observed [153,157]:

- In alloys containing 1.15wt%Ti to 2wt%Ti, formed at cooling rates in the range of $200^{\circ}\text{C}/\text{cm}$ to $550^{\circ}\text{C}/\text{cm}$, dendritic microstructure with single plane growth of Al_3Ti intermetallic.
- Fine petal shaped Al_3Ti intermetallic growth in alloys containing 1.15wt%Ti formed at cooling rate in the range of $200^{\circ}\text{C}/\text{cm}$ to $280^{\circ}\text{C}/\text{cm}$.
- Dendritic Al_3Ti intermetallic growth in random direction for alloys containing 3.5wt%Ti to 5wt%Ti, formed at cooling rates in the range of $200^{\circ}\text{C}/\text{cm}$ to $255^{\circ}\text{C}/\text{cm}$.

(c) Mechanical properties of Al_3Ti tri-aluminide intermetallic compound.

Al_3Ti intermetallic possesses exceptional characteristics such as low density $\approx 3.3 \text{ g}/\text{cm}^3$, higher melting temperature $\approx 1673 \text{ K}$, see **Table 2.17** for other mechanical properties, which as exploited in the grain refinement of commercial Al alloys used for high temperature applications [158,159].

As stated in the earlier section, upon formation, the tri-aluminide Al_3Ti , exhibits non-symmetrical tetragonal DO_{22} type structure, this reduces ductility and makes the alloy brittle at low temperatures.

In order to achieve ductility, symmetrical L1₂ type structure of Al₃Ti intermetallic is preferred and is effectively obtained by addition of elements such as Cr and Mn to the alloy [158].

Table 2.17: Properties of Al₃Ti intermetallic compound [158].

Mechanical properties of Al ₃ Ti intermetallic	
Young's Modulus (GPa)	156
Fracture stress (MPa)	162 (under bending) 354 (under compression)
Yield stress (MPa)	980
Plasticity characteristic (δ_H)	0.68
Strain hardening parameter N (GPa)	2.4
(obtained by indentation method)	
Liquidus temperature (°C)	1420
Solidus temperature (°C)	1395

The investigation conducted by previous researchers, comparing the mechanical properties of DO₂₂ type Al₃Ti with Al₃Ti alloyed with Cr and Mn to form L1₂ type Al₆₁Cr₁₂Ti₂₇ and Al₆₆Mn₁₁Ti₂₃ intermetallic compound revealed that [157-160] :

- The change in the crystalline structure of Al₃Ti intermetallic from tetragonal DO₂₂ type to cubic L1₂ type Al₆₁Cr₁₂Ti₂₇ and Al₆₆Mn₁₁Ti₂₃ intermetallic compound showed decrease in the micro-hardness with increase in the exposure temperature from 25⁰C to 900⁰C, as shown in **Figure 2.49**.
- The yield stress decreases when DO₂₂ type Al₃Ti intermetallic is alloyed with Cr and Mn to form cubic L1₂ Al₆₁Cr₁₂Ti₂₇ and Al₆₆Mn₁₁Ti₂₃ intermetallic, as shown in the stress vs. strain curve in **Figure 2.50**.

- The plasticity characteristic value (δ_H) of the intermetallic compounds increases in the order $Al_3Ti < Al_{61}Cr_{12}Ti_{27} < Al_{66}Mn_{11}Ti_{23}$ with respect to exposure temperature, see **Figure 2.51**.

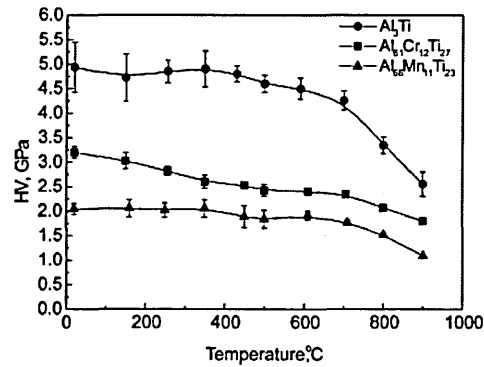


Figure 2.49: Variation in the micro-hardness of the intermetallics with respect to exposure temperature [158].

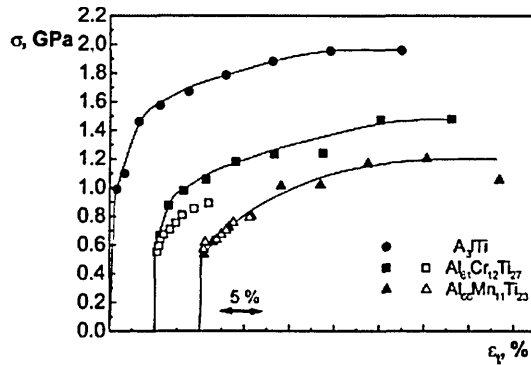


Figure 2.50: Stress vs. strain graph showing decrease in yield stress value of Al_3Ti intermetallic when alloyed with Cr and Mn. The test was performed using indentation method (shown with black legends) and under compression (hollow legends) [158].

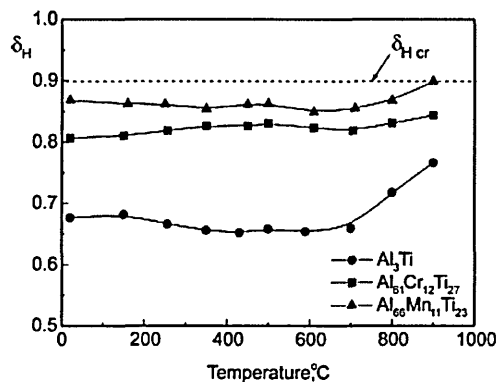


Figure 2.51: Graph showing increase in plasticity characteristic when Al_3Ti intermetallic is alloyed with Cr and Mn with respect to temperature [158].

(c) Microstructure and mechanical properties of Al_2Ti intermetallic compound

Apart from the formation of tetragonal DO_{22} or DO_{23} type Al_3Ti intermetallic tri-aluminide, formation of another titanium aluminide Al_2Ti has also been reported in the literature [160-163]. The Al_2Ti intermetallic also exhibits a tetragonal structure with lattice parameters $a = 3.976 \text{ \AA}$ and $c = 24.36 \text{ \AA}$, see **Figure 2.52** [161].

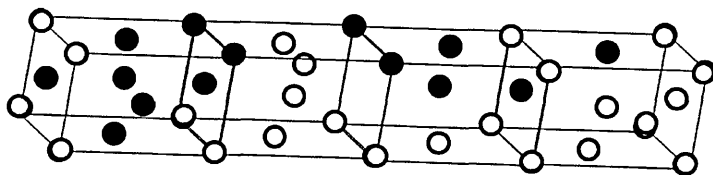


Figure 2.52: Tetragonal crystal structure of Al_2Ti intermetallic, where \bigcirc represents Al atoms and \bullet represents Ti atoms [161].

Researchers reported the precipitation of Al_2Ti intermetallic as thin platelets in ternary Al-Ti-Cu alloy with two different forms of crystal structure [162,163]. The first Al_2Ti intermetallic showed orthorhombic structure similar to Ga_2Zr and was referred as $\text{Al}_2\text{Ti}^{\text{i}}$ type, while the second was tetragonal $\text{Al}_2\text{Ti}^{\text{ii}}$ type, similar to Ga_2Hf crystal structure [162,163].

Further investigation showed that $\text{Al}_2\text{Ti}^{\text{ii}}$ type structure was stable up to 1473 K, with temperature > 1473 K, the probability of either $\text{Al}_2\text{Ti}^{\text{ii}}$ type structure changing to $\text{Al}_2\text{Ti}^{\text{i}}$ type or decomposition of $\text{Al}_2\text{Ti}^{\text{ii}}$ to AlTi and Al_2Ti_5 existed [162,163]. The evidence that Al_2Ti exists as a reentrant phase (exhibiting same crystal structure at highest and lowest temperatures, 289 K and 1473 K, with different crystal structure in mid temperature ranges) or only as a polymorphic intermetallic compound, remained conflicting [162,163].

In comparison with tri-aluminide Al_3Ti intermetallic, Al_2Ti possesses properties which make the intermetallic attractive for alloying with Al for high temperature application [162-164]:

- The low density cast Al_2Ti intermetallic ($\approx 3.53 \text{ g/cm}^3$ to 3.54 g/cm^3) has a compressive yield strength value of $\approx 700 \text{ MPa}$ at 298 K ($\approx 75\%$ larger than yield strength of cast Al_3Ti intermetallic) which decreases linearly with increase in temperature to $\approx 400 \text{ MPa}$ at 1073 K.
- Under as cast condition, Al_2Ti intermetallic is reported to have 0.3% strain to failure ratio at 298 K which increases to $\approx 4\%$ at 1123 K.

- Al_2Ti and Al_3Ti intermetallic compounds prepared by powder processing were exposed in air for 100 hours at 1073 K in order to compare oxidation resistance. Al_2Ti was reported to show 20 % less weight gain than Al_3Ti providing evidence of higher oxidation resistance at elevated temperature condition.

Some literature also exists on potential industrial applications of Ti rich AlTi (or γ AlTi, in most Ti-Al phase diagrams) intermetallic compound which also shows high oxidation and high creep resistance [165,166]. The AlTi intermetallic has been under series of experimental evaluations to find its application in aircraft industry (such as in gas turbine shafts, blades, vanes) as a replacement of ferrous alloys, however major disadvantages such as requirement of variation in mechanical properties, inherent brittle nature making the intermetallic susceptible to external damages and cost of manufacturing hinders its application [165,166].

2.9.3 Aluminium-Titanium-Carbon alloy system

The formation of titanium aluminide intermetallic compounds in binary Al-Ti alloy system has fostered its use in various high temperature engineering applications due to attractive properties such as high temperature and oxidation resistance [167-170]. Even though Ti acts as a grain refiner to cast Al alloys, addition of elements such as boron and carbon during casting also aids in the grain refining process, which produces Al alloys with improved ductility [171].

2.9.3.1 A brief introduction to ternary grain refiner

The use of ternary addition of B to Al-Ti alloys as a grain refiner dates back to 1950's, where formation of TiB_2 , which acts as a nucleation point during solidification of the alloy, was achieved by addition of KBF_4 and K_2TiF_6 during melting of Al [172]. This *in situ* addition of KBF_4 and K_2TiF_6 caused salt segregation and uneven distribution of TiB_2 particles in the alloys, minimising the effects of grain refinement [172].

The introduction of grain refiners such as TiB_2 and Al_3Ti in form of rods before the casting stage of the alloys started in 1970's, which not only resulted in even distribution of grain refiners in the alloys producing fine grained macro-structure but also proved to be efficient and economical process for aluminium grain refining industries [171]. Since then this method has been widely adopted for direct Chill (DC) cast aluminium alloys, with various alloying compositions of Ti and B [172,173].

Like Ti and B, the combination of Ti and C as a grain refiner started in the mid 1990's and was found to have advantages such as lesser particle agglomeration than Ti-B addition, resistance to poisoning against Zr containing alloy and showed enhanced surface finish, when alloyed with Al alloys containing Mg [172,173].

2.9.3.2 Understanding of various phases in Al-Ti-C alloys.

In Al-Ti-C system, the role of grain refiners is achieved by Al_3Ti and TiC particles [174], hence it becomes imperative to understand the formation and microstructural characteristics of these phases during ternary alloying. The focus of many researchers have been on the understanding the microstructural properties of carbides formed in the ternary Al-Ti-C alloys system [35], which mainly includes forms such as [176]:

- $\text{AlTi}_3\text{C}_{1-x}$, which has a cubic crystal structure,
- $\text{AlTi}_2\text{C}_{1-x}$ and $\text{AlTi}_3\text{C}_{2-x}$, having hexagonal crystal structure.

Where x is the stoichiometric ratio of C in the alloy. Out of all the above mentioned intermediate carbides, which are formed during the alloying, with varying stoichiometric ratios of Al,Ti and C, the formation and stability of TiC_{1-x} (titanium carbide) has been widely investigated by the researchers due to its application as grain refiner [176].

Zang *et al.* [177] and Birol [178] primarily focused on the microstructural characterisation of Al-Ti-C alloys by altering the stoichiometric ratios of Ti and C present in the alloy. Zang *et al.* [177] investigated microstructure of rapidly solidified (rate of solidification of the melt $\approx 10^4$ K/s to 10^8 K/s) Al-3.5wt%Ti-0.15wt%C, Al-5wt%-0.3wt%C and Al-10wt%Ti-1wt%C alloys, as shown in **Figure 2.53** (a), (b) and (c), while Birol [178] investigated the microstructure of Al-3wt%Ti-0.75wt%C alloy (prepared by dispersing TiC particles in the Al melt), see **Figure 2.54**.

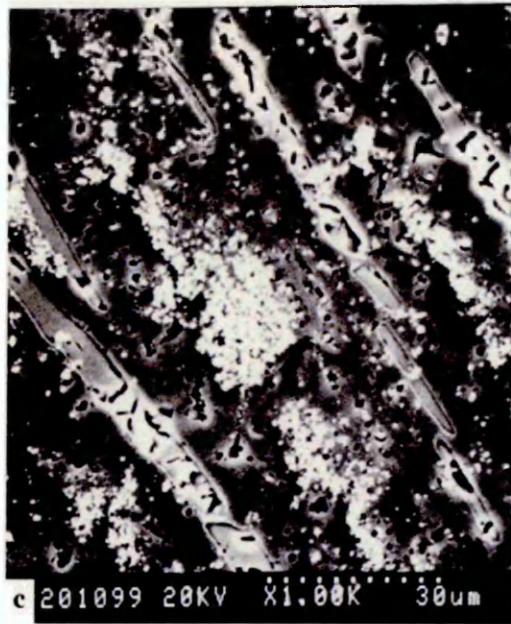


Figure 2.53: Backscattered electron micrographs showing distribution of blocky Al₃Ti and spherical equiaxed TiC phases in (a) Al-3.5wt%Ti-0.15wt%C, (b) Al-5wt%-0.3wt%C and (c) Al-10wt%Ti-1wt% C alloys [177].

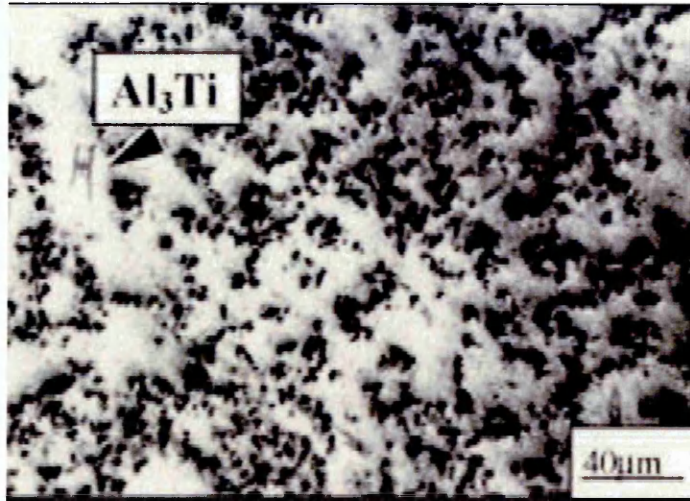


Figure 2.54: Optical micrograph of Al-3wt%Ti-0.75wt%C alloy [178].

The dominant phases which were observed in the alloys included:

- Large blocky or slab-like structure ($\approx 50 \mu\text{m}$ to $100 \mu\text{m}$ in size), shown in **Figure 2.53** (a), (b) and (c), which was confirmed as Al_3Ti phase by the X-ray diffraction (XRD) analysis as shown in **Figure 2.55**. The formation of such blocky aluminium tri-aluminide was also reported by Mayes *et al.* [179] while analysing the microstructure of commercially available Al-6wt%Ti-0.02wt%C alloy with V as an impurity, see **Figure 2.56**.
- Small nearly spherical or equiaxed particles recognised as TiC particles by XRD analysis see **Figure 2.57**. The TiC were found evenly distributed in the Al matrix, however a significant increase in the formation and distribution of TiC phase was observed with increasing concentration of Ti and C in the alloy, see **Figure 2.53** (a), (b), (c) and **Figure 2.54**.

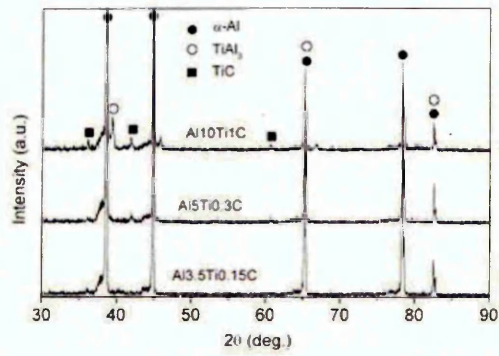


Figure 2.55: XRD pattern of rapidly solidified Al-Ti-C alloy with varying Ti and C composition [177].

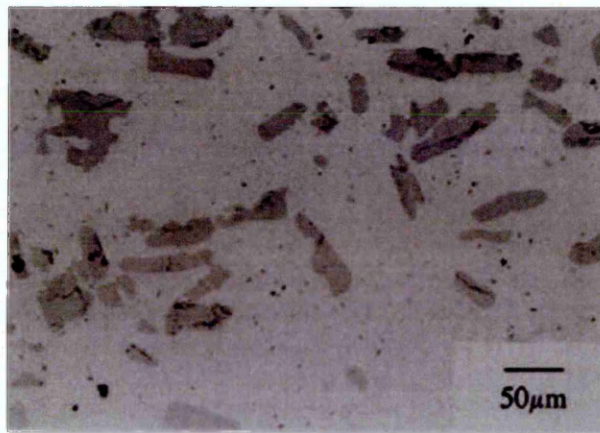


Figure 2.56: Optical micrograph of Al-6wt%Ti-0.02wt%C, showing the presence of large block like Al_3Ti particles [179].

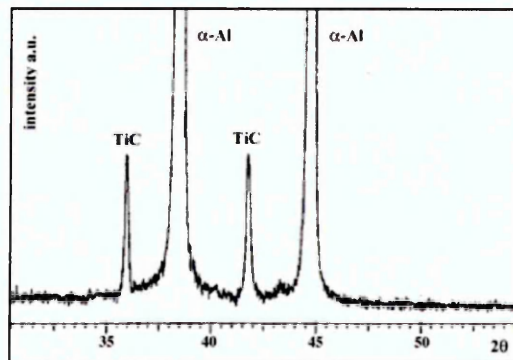


Figure 2.57: XRD pattern of Al-3wt%Ti-0.75wt%C alloy [179].

2.9.3.3 The effect of Al₃Ti and TiC phases on the grain refinement mechanism in Al-Ti-C alloys

The microstructural investigation conducted by researchers showed the presence of blocky Al₃Ti and equiaxed TiC particles in the Al-Ti-C alloys [176-180], however the presence of these phases on the mechanism of grain refinement in Al alloys has been debatable [178,179].

The primary condition of grain refining includes formation of large number of active potential nucleation sites, in the case of Al-Ti-C alloys, tri-aluminide Al₃Ti and TiC which form those sites, have been subjected to various experimental investigations to understand their role in nucleation of Al matrix to produce refine microstructure [180,181].

Most of the researchers focused their study on commercially available Al-3wt%Ti-0.15wt%C alloys(prepared by either direct chill casting method or rapid solidification method) [176-183] with an intention to reveal the effect of formation processes on the microstructure of the grain refining particles formed in the Al matrix of the alloys.

The investigations showed that the Al₃Ti phase which was present in both slow cooled direct chill casting method or fast cooled rapid solidification method was not essentially required for formation of nucleation site [179-181]. It was also shown that Al-5wt%Ti-1.2wt%C alloy , prepared by adding K₂TiF₆ and graphite as Ti and C source in molten Al, had almost restrictive growth of blocky Al₃Ti phase [182,183], but was effective in grain refining, owing to the presence of TiC particles.

Since the use to C, as ternary addition to Al-Ti system, which had an advantage of alloying with Al (that alloys which contained Zr, V and Cr) over B to form evenly populated TiC particles unlike agglomerated TiB₂ particles, the stability of TiC particle at elevated temperatures during alloying has been extensively investigated [183-186].

Initially, during the transition from using Ti-B to Ti-C in obtaining equiaxed grain structure to produce Al alloys with high strength and enhanced machinability, a unifying theory which underlined the requirement of TiB₂, Al₃Ti and TiC particles to act as sites of nucleation during the solidification of alloys was proposed [187,188].

The theory was based on the interfacial surface energies of liquid - particle (γ_{lp}), solid - particle (γ_{sp}) and liquid - solid (γ_{ls}) interactions during alloying and stated that any of the particles (inoculants) which possesses a tendency of wetting the solidifying melt (in this case Al) acts as grain refiners [188,189]. This is achieved when the crystal structure of the grain refining particle matches with the nucleating solid or have a close atomic arrangement as nucleating solid to obtain minimum contact angle, as shown in **Figure 2.58** [188,189].

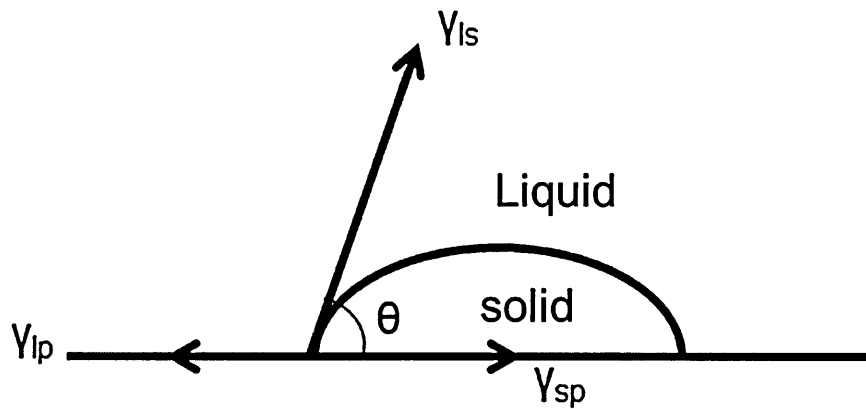


Figure 2.58: Diagrammatic representation of particles interaction with nucleating solid in terms of interfacial energies and contact angles [187].

For both C and B containing Al-Ti system, the TiB_2 , Al_3Ti and TiC particles have satisfied the above mentioned theory of nucleating sites in the alloy. Higher melting temperature than Al, solidification at even low cooling rates and even distribution of Al_3Ti and TiC particles except TiB_2 also aids in the effective nucleation of the alloys.

The researchers have shown that TiB_2 , Al_3Ti and TiC particles acts as nucleation sites during solidification of alloys, however the following theories have been proposed to understand the grain refinement caused by the presence of these particles [188-194]:

(a)The carbide/boride theory:

This was one of the initial theories which suggested that addition of C to Al-Ti system was not mandatory to form TiC particles, even trace amounts of C (to hundreds of ppm) was sufficient to promote formation of TiC particles (nucleation sites), which was essential in the grain refining for Al and external

addition of TiC particles would decrease the effects of grain refining in binary Al-Ti alloys.

However, many researchers who were working on understanding the ternary Al-Ti-C phase diagram showed by thermodynamic modelling and experimental data that the Ti:C ratio was non-stoichiometric and the particle existed in form of TiC_x (where $x \approx 0.48$ to 0.98) and significantly affected the stability of the carbide.

The octahedral TiC_x was reported to show stability within the temperature range of 1028 K to 1450 K, but beyond the mentioned temperature range, formation of stable Al_4C_3 degraded the grain refining efficiency of TiC particles. It was also noted that formation of Al_4C_3 was possible if the TiC particles were held in the Al melt at 1450 K for almost a 100 h exposure time, which is not a regular practice in the Al grain refining industry. The maximum operating temperatures during grain refining of Al are mostly under 1028 K which inhibits the growth of stable Al_4C_3 , hence the effects of fading are practically removed.

(b)The peritectic theory:

The peritectic theory or the phase diagram theory suggested that, the formation of titanium tri-aluminide (Al_3Ti) during alloying of Al, nucleates Al via the peritectic reaction as mentioned in section 2.9.2.1, to produce fine microstructure of the alloy. However, the concentration of Ti in molten Al should be ≈ 0.15 wt % to have peritectic reaction, but during ternary alloying

the Ti concentration remains as low as 0.01 wt %, which poses major problems while adopting this theory to explain formation of Al_3Ti to act as a nucleant.

(c) The peritectic hulk theory:

According to the peritectic hulk theory, which was an extension of peritectic theory, for Al-Ti-B alloy system, the formation of TiB_2 resulted in the slower dissolution of Al_3Ti particles as the borides form a shell around Al_3Ti particles. The theory also suggested that when dissolution occurs within the boride shell, the Ti concentration reaches the peritectic requirement for grain refining by the tri-aluminide as stated in peritectic theory.

This theory could not explain the presence of borides within the Al_3Ti particles, which were reported by other researchers. Some researchers even showed that exposing the alloy system to repeat heating and cooling cycles did not affect the grain refinement properties of aluminides, which according to this theory was not possible.

(d) The hyper-nucleation theory:

This theory suggested segregation of Ti to TiB_2 particles, which results in solidification of Al from this Ti rich TiB_2 particle (hyper-nucleation) [187]. The theory suggested the hyper-nucleation effect of Ti with Al as a result of

similar atomic sizes of both elements, however there has been no experimental validation of this theory on grain refining of Al alloys.

(e) The duplex nucleation theory:

This theory suggested that addition of TiB_2 particles with different Ti concentration ($\approx 5\text{wt}\%$ and $6\text{wt}\%\text{Ti}$) to the Al melts does not produce grain refinement because TiB_2 does not form nucleating sites, but is precipitated at the grain boundaries of Al. With Ti addition, just over peritectic composition, the TiB_2 particles precipitate at the centre of Al grains with Al_3Ti layers above the boride particles, however the reason of formation of such type of tri-aluminide layer was not explained by this theory.

(f) The solute theory:

This theory stated that there exists a critical value of number of nucleating particles per unit volume ($\leq 10^2/\text{mm}^3$) such as Al_3Ti , TiC , TiB_2 above which, any further addition of these particles does not contribute in grain refining of Al alloys. This was due to the fact that the particles do not increase the number of grains per unit volume of solidifying Al. The researchers had shown that at peritectic composition, Ti exhibited the highest critical value which explained why Ti had the highest grain refining capability than Zr and Cr.

Chapter 3: Experimental Methodology

3.1 Introduction

This chapter provides detailed information on the materials used, coating process and characterisation of the coatings in terms of corrosion and wear resistance.

The aim of this study was to investigate the corrosion and wear resistance of thermally sprayed Al-Zn-In and Al-Ti-C coatings sprayed on to mild steel substrates. All the coatings were prepared by arc spraying, the relevant information on the process parameters will be discussed in the following section in this chapter.

The chapter 2, has provided a lucid review on the electrochemical properties of Al-Zn-In alloy along with mechanical and microstructural properties of Al-Ti-C alloy to understand the tribology of Al-Ti-C alloy, which has been used as a benchmark to conduct experimental investigation for this project, as this project has focused primarily on investigating sacrificial protection performance of arc sprayed Al-Zn-In coating and wear resistance performance of Al-Ti-C coating.

This chapter covers the experiments undertaken, relevant parameters and a brief review of the theory behind each.

3.2 Sample Preparation

3.2.1 Materials used

Table 3.1 shows the nominal composition [195-200] of the commercially available pure Al, Al-Zn, Al-Zn-In, Zn-Al, Al-Ti-C and 13% chrome steel alloys which were used during the study. The Al, Al-Zn, Zn-Al and 13%Cr steel coatings, which were chosen as relevant commercially available alternatives, were used as a benchmark to evaluate the corrosion and wear resistance performance of Al-Zn-In and Al-Ti-C coatings. The alloys were obtained from London and Scandinavian Metallurgical (now AMG Al) Ltd and were deposited on commercially available 150 mm X 100 mm X 0.8 mm mild steel coupons. According to the manufacturers specification, these have a nominal composition of 0.60wt%Mn, 0.15wt%C, 0.03wt%P, 0.035wt%S and \approx 99wt%Fe) and surface roughness $R_a \approx 0.50 \mu\text{m}$ - $1.14 \mu\text{m}$ (ground finish) [201].

3.2.2 Substrate preparation - Grit blasting

The mild steel coupons were solvent degreased (commercially available) to remove surface contamination, and then abrasive blasted using chilled iron grit to increase roughness and remove surface oxides. The blasting of the surface was done to an SA3 finish according to ISO 8501-1[202].

3.2.3 Coating preparation - Arc Spraying

The coatings were applied at Metallisation Ltd or Celcoat Ltd (two different facilities at different locations were chosen based on availability of the arc spray gun) using a Metallisation Arc140/S250-Closed Loop (CL) system. The Arc140/S250-CL consists of a Metallisation Arc140 spray gun coupled with an electric wire drive system, see **Figure 3.1**, and can operate at a maximum of 250 A [203].

The system uses wire diameter ranging from 1.6 mm to 2.5 mm, and at 250 A, the maximum deposition rate (kg/hr) and area coverage (m²/kg) per 100 μm for Al/Al alloys is 6 and 2.88, Zn-Al alloy is 22 and 1.00 and for steels is 11.3 and 1.02 respectively [203].

The procedure outlined in section 3.2.2 was followed prior arc spraying The mild steel coupons were then attached vertically on a magnetic disc and the spray gun was mounted on an automated vertical traversing unit, so as to keep the spray gun perpendicular to the coupon and maintain a constant traversing speed. Each vertical pass of the spray gun deposited ≈ 50 μm thickness of coating. A nominal coating thickness of 300 μm was therefore produced during spraying using six passes. The coating thickness was measured after every pass using a micrometer. **Table 3.2** shows the spraying parameters, which were used during spraying and which were chosen following discussion with staff from Metallisation Ltd prior to coating preparation [204].



Figure 3.1: The Metallisation Arc140/S250-CL spray system [147]

Table 3.1: The composition of the alloys which were used for thermal spraying [195-200]. * Available from manufacturers data sheet.

Materials	Composition* (%wt)													
	Al	Zn	In	Ti	C	Cr	Fe	Si	Cu	Mn	Sn	Mg	Pb	Cd
Pure Al	99.5	0.07	-	0.05	-	-	0.40	0.25	0.05	0.05	-	0.05	-	-
Al-Zn	94.5	4.5-5.1	-	-	-	-	0.7	0.3	0.05	-	0.2	-	-	-
Zn-Al	14-16	84-86	-	-	-	-	0.05	0.12	0.01	-	0.001	-	0.005	0.005
13%Cr steel	-	-	-	-	-	13	87	-	-	-	-	-	-	-
Al-Zn-In	≈ 95	4.5-5.5	0.02-0.05	-	-	-	0.1	0.1	-	0.1	0.1	-	-	-
Al-Ti-C	≈ 97	-	-	3	0.15	-	-	-	-	-	-	-	-	-

Table 3.2: Arc spraying parameters [204].

Arc spraying parameters	Arc spraying parameters						
	Pure Al coating	Al-Zn coating	Zn-Al coating	13%Cr steel coating	Al-Zn-In coating	Al-Ti-C coating	
Spray current (A)	200	200	200	200	200	200	200
Spray voltage (V)	30	30	30	30	30	30	30
Spray Distance (mm)	150	150	150	150	150	150	150
Air pressure (MPa)	0.5	0.5	0.5	0.5	0.5	0.5	0.5
Wire Diameter (mm)	2.0	2.0	2.0	1.6	2.0	2.0	2.0
Number of Passes (≈ 50 μm/pass)	6	6	6	6	6	6	6

3.3 Sample preparation of arc sprayed coatings for metallographic analysis

3.3.1 Background

Metallographic investigation is one of the most important experimental investigations used to characterise thermally sprayed coatings. The complex lamellar microstructure or "splat" morphology of thermally sprayed coatings is primarily responsible for imparting properties such as corrosion resistance, wear resistance and hardness, to the coatings [205-207].

Even a single layer metallic coated system may contain hard and soft phases, oxides, porosities, which create intense challenges in sectioning, mounting, grinding and polishing of the coatings [205-207]. The next section will describe in details the sample preparation techniques which were adopted to study the microstructure of the coatings.

In order to compare the microstructure of the Al-Ti-C coatings with the parent feedstock material, pure Al and Al-Ti-C alloys were also examined. The details of alloys microstructure preparation are also mentioned under next separate subsection of this chapter.

3.3.2 Sample preparation for microstructural investigations – Alloys

Transverse sections, see **Figure 3.2 (a)**, of the pure Al and Al-Ti-C alloys which were in form of rods with diameter 9.79 ± 0.07 mm were taken for microstructural evaluation. A series of steps were followed during preparation of the sections, which were as follows:

1. The transverse sections of the alloys were mounted in conductive Bakelite to produce mounted specimens approximately ≈ 30 mm diameter see **Figure 3.2 (b)**.
2. After mounting, the samples were subjected to manual grinding using SiC abrasive paper, starting with grade 120 (180 grit) and finishing with 1200 (800 grit). A minimum grinding time of 60 seconds was used. Samples were rinsed with deionised water after each grinding stage.
3. The samples were then polished, using a $6 \mu\text{m}$ and then $1 \mu\text{m}$ diamond suspension liquid to give the samples a mirror-like surface finish.
4. Ultrasonic cleaning in methyl alcohol solution, of the sectioned samples was carried out after polishing to remove embedded silicon and polishing suspension from the surface.
5. The samples were dried and were kept in vacuum desiccators to avoid atmospheric contact.

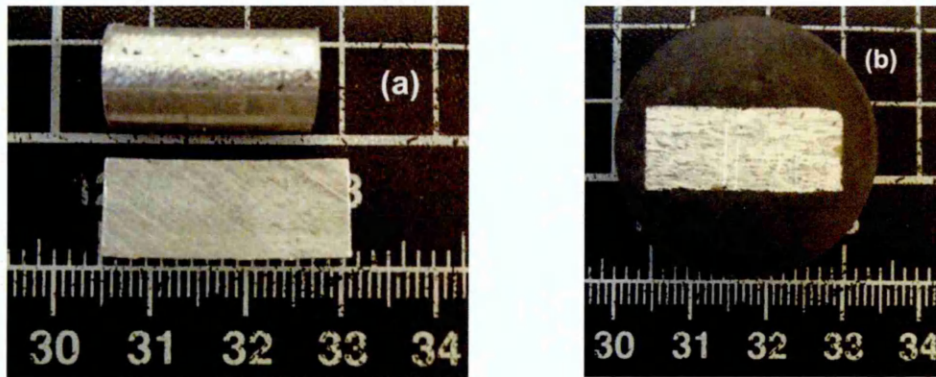


Figure 3.2: Photographs of (a) transverse section and (b) Bakelite mounted Al-Ti-C alloy.

3.3.3 Sample preparation for microstructural investigations – Coatings

The cross-section of the coatings for metallographic examination was prepared in accordance with the technical notes published by Buehler Ltd. on preparation of thermally sprayed coatings [208]. The procedure followed included following sequential steps:

1. The cross-section of the coating was done using an ISOMET 4000 precision saw using a diamond 15HC blade. The rotational speed of 4500 rpm to 5000 rpm with sample feed rate of 3.5 mm/min to 4.5 mm/min was used.
2. The cross-section was then cleaned using soap solution followed by deionised water rinsing and finally drying using an electric hand dryer.
3. The cleaned cross-section was then cold mounted using epoxy resin (100 parts,wt% of Buehler Epothin resin no. 20-8140 mixed with 39 wt% parts of Buehler Epothin hardener), see **Figure 3.3** (a) and (b). Bakelite hot mounting was not used for coatings as the pressure

required for curing could cause false assessment of the microstructure.

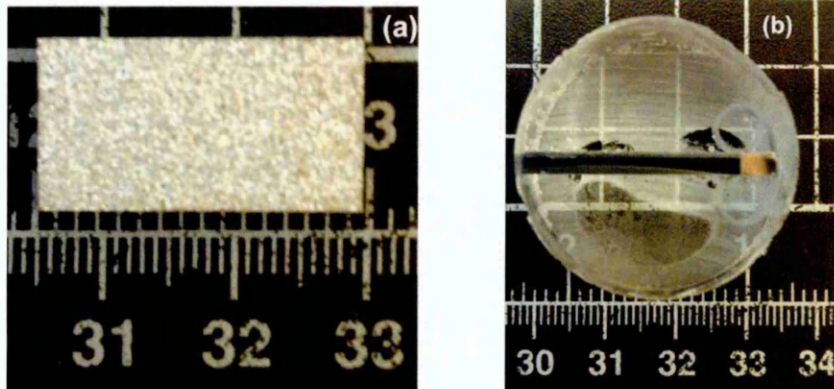


Figure 3.3: Photographs of (a) prepared sample and (b) epoxy mounted coating for metallographic examination.

4. After mounting, the samples were subjected to manual grinding using SiC abrasive paper. Starting with 180 grit, a minimum 60 seconds grinding time was used, followed by 240 grit to 800 grit with minimum grinding time of 30-50 seconds during each stage. The rotational speed of the grinding base was kept constant at 300 rpm throughout the grinding stages.
5. The coated samples were then polished, using a 6 μm and 1 μm diamond suspension liquid to give the samples a mirror-like surface finish. Once again, a minimum grinding time of 30-50 seconds was used.
6. The prepared samples were dried and were kept in vacuum desiccators to avoid atmospheric contact.

3.4 Electron Microscopy

In order to analyse the microstructure of the coatings and feedstock alloys, an FEI Nova Nano 200 Scanning Electron Microscope (SEM) equipped with Energy Dispersive X-Ray Spectroscopy (EDS) was used. An accelerating voltage of 20 kV and working distance between 5.0 mm and 5.5 mm was chosen for acquisition of images in both secondary electron and backscattered electron mode (atomic number contrast).

3.4.1 A brief introduction to operating principles of SEM

SEM is a widely used technique, which scans the surface with higher resolution and depth of the field with enhanced magnification [209-213]. An SEM equipped with EDS also allows chemical analysis of the material [209]. **Figure 3.4** shows the arrangement of the scanning electron microscope, which consists of an electron gun, electromagnetic lenses and apertures [209].

The electron gun used to generate electrons is either thermionic or field emission type guns. Field emission guns are used to produce high beam brightness for producing high quality images [210]. The accelerating voltage used for generation of electrons is usually of the order 1-40 kV [209,210]. The electromagnetic lenses including condenser and objective lenses helps in formation of electron probe reduce the cross over diameter of the electron beam and focus the electron beam to a nanometre scale [209,210].

The scanning of the electron probe over the surface is operated by a deflection system, as the deflection system moves the electron probe of the

surface and displaces it to next scan point on the surface [210]. The emitted electrons from the surface are then collected by the detector which amplifies the signal to reconstruct the image of the surface by one to one correlation between the scan points and picture points on the screen which can be either cathode ray tube or liquid crystal display [210].

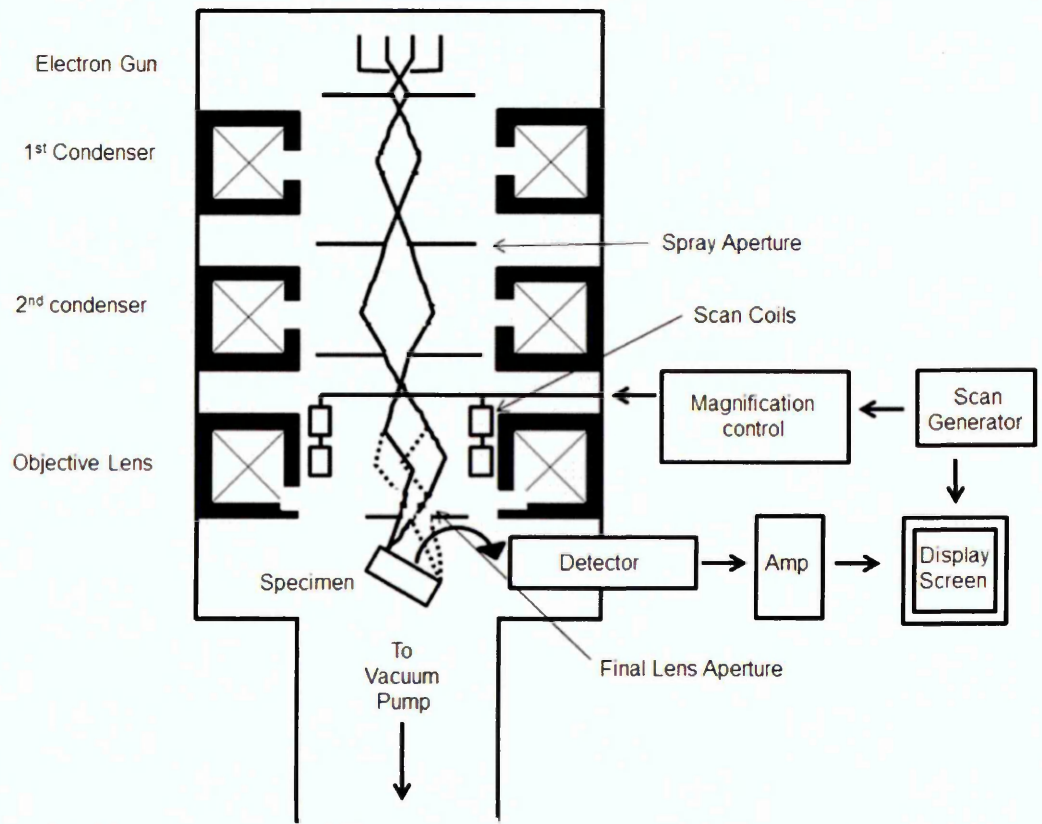


Figure 3.4: Schematic of the structure of the Scanning electron microscope [209].

3.4.2 Back scattered electron imaging, Secondary electron imaging and EDS analysis.

The electron signal that is detected can be either secondary electron (SE) or backscattered electrons (BSE), depending on the electron beams striking the surface either scatters elastically or inelastically [211-213]. When the electrons are scattered by the atoms in the specimen, the elastic scattering produces backscattered electrons, whereas when electrons are released from the surface of the specimen, the inelastic scattering produces secondary electrons [211,212].

The secondary and backscattered electrons which are collected by detector are basically from different location in the specimen as shown in **Figure 3.5**, which is usually described as a pear shaped and shows increase in size with the energy of incident electrons [212,213]. The main importance of using secondary electron (SE) as a signal is to generate a topographic scan, while backscattered electrons provide compositional contrast [213].

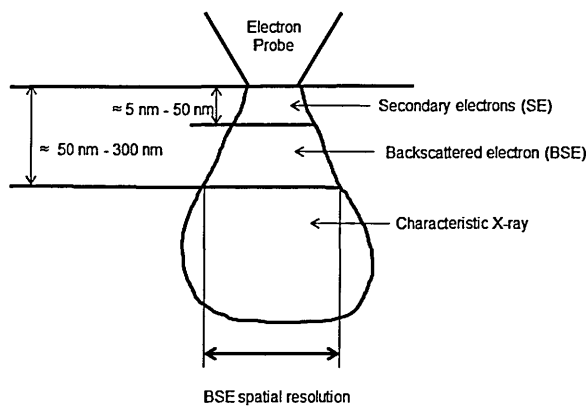


Figure 3.5: Schematic of electron interaction zone under the surface of the specimen [209].

The energy dispersive x-ray spectrometer (EDS) coupled with SEM allows elemental analysis along with microstructure examination. The EDS system uses the same beam energy as SEM for elemental analysis, making it suitable for analysing small area of the samples [210-213]. The spectrum obtained from EDS is characteristic intensity of the x-ray over the energy range of the x-ray [210-213].

As backscattered electron imaging (BSE) for compositional contrast along with energy dispersive x-ray (EDS) elemental analysis has been used to examine Al-Zn-In and Al-Ti-C coatings, the following limitations of the techniques must be considered [209,211,213]:

- The ratio of elastically scattered BSE electrons from the specimen to number of incident electrons (or backscattered coefficient, η) increases with increase in atomic number of the elements present in the specimen. Hence the relative difference in the compositional contrast of elements such as Al, Zn, Ti was more evident than C and O ($\eta_{In} (\sim 0.42) > \eta_{Zn} (\sim 0.33) > \eta_{Ti} (\sim 0.27) > \eta_{Al} (\sim 0.17) > \eta_O \approx \eta_C (\sim 0.07)$ at 20 KV accelerating voltage).
- Commercially available EDS analysis system (INCA, supplied by Oxford Instruments) installed on FEI Nova Nano 200 SEM was used. The default x-ray spectra of elements were used to collect the data (which was averaged over three to five regions with similar microstructural features). Due to this, the EDS data presented in results and discussion is treated as 'semi-quantitative' results (limited accuracy and precision).

- Even though the backscattered coefficient of In was higher than Zn, Ti and Al, detection of In in the Al-Zn-In coating was not possible as concentration of In in Al-Zn-In coating (0.02wt%-0.05wt% or 200ppm-500ppm) was below the detection limit of the EDS technique (1000ppm-3000 ppm).
- For light elements such as C and O, the valence electrons take part in both production of characteristic x-rays and bonding, hence quantification of light elements using EDS technique is not appropriate. Stoichiometric ratios of other elements with C and O is commonly used during analysis (XRD data along with EDS quantification is used the analysis of Al-Zn-In and Al-Ti-C coatings).

3.5 X-Ray Diffraction (XRD)

To analyse the crystalline phases present in the coatings and feedstock alloys, X-ray diffraction was employed. The XRD was also used to study the coatings exposed to salt spray corrosion test (discussed in next section) and in the analysis of corrosion products.

A Philips X'Pert Pro X-ray diffraction instrument with Cu anode capable of operating at 2.2 kW was used during the analysis [214]. The Cu anode was operated at 40 kV and 40 mA to produce CuK_α radiation (1.54184 Å) with Ni as β filter material. A ($1/4^\circ$) divergence slit, 20 mm soller slit and ($1/2^\circ$) anti-scatter slit was used in the Bragg-Brentano geometry arrangement, θ - 2θ range from 10° to 110° with 0.0167° step size to obtain diffraction spectrum for analysis, with PW3071 flat sample stage.

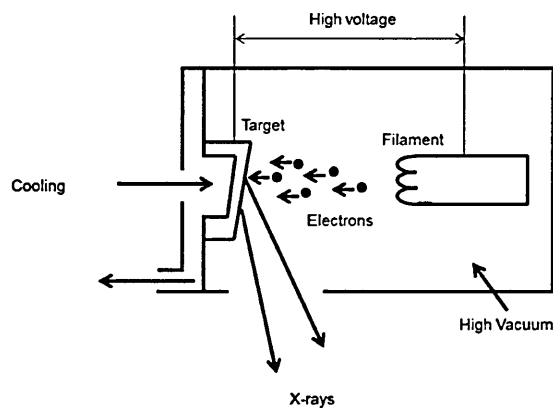


Figure 3.6: Schematic of the operating principle of an X-ray tube [209].

3.5.1 A brief introduction to operating principles of XRD.

X-ray diffraction is a technique that can be used to identify the materials from their crystal structures. The X-rays (which have short wavelength and are high energy electromagnetic radiation) are produced by the X-ray tube which consists of two electrodes and an electron source under vacuum conditions, see **Figure 3.6**. Maintaining a high voltage across the electrodes, the electrons are drawn towards the target, the X-rays are produced, which consists of a minimum wavelength continuous X-ray and a maximum intensity characteristic X-ray, when the electrons impact the target surface [209,215].

3.5.2 X-ray Diffractometer and Bragg-Brentano geometry arrangement.

The X-ray diffraction instrument (Diffractometer) measures the intensity of the diffracted X-rays as a function of diffraction angle. The arrangement of X-ray source, specimen and detector are shown in **Figure 3.7**.

The X-ray radiation passes through soller slit and divergence slit to strike the specimen. The X-rays which are diffracted by the specimen pass through a monochromator filter that reduces the background radiation from the specimen except the characteristic $K\alpha$ radiation. In order to obtain X-ray data from the material, various geometrical arrangements are being used by diffractometers and the commonly used arrangement is called as Bragg-Brentano arrangement in which the incident beam is fixed while the sample stage and detector can rotate in a plane perpendicular to the plane of figure [209,215]. To maintain θ - 2θ angular correlation between detector and specimen, the angular speed of detector is maintained at twice that of the sample stage.

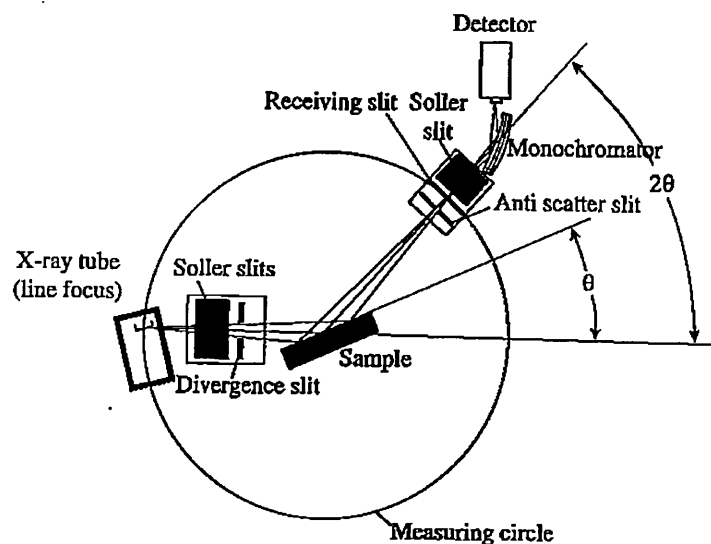


Figure 3.7: Schematic diagram showing arrangement of X-ray diffractometer [209].

The x-ray diffraction trace obtained using Bragg-Brentano geometry was analysed using X'Pert Highscore plus v3.0 software. The following procedure was followed during XRD data analysis [209,214,215]:

- The peak positions were determined by choosing the minimum significance value between 2 and 5 (large values were avoided to record small peaks) followed by curve fitting to the data obtained (Gaussian fitting was used). The identified peaks were then checked for K_{β} peaks, which were excluded from further data analysis.
- For further improvement in the phase identification, the $K_{\alpha 1}$ - $K_{\alpha 2}$ split was compensated by removing the $K_{\alpha 2}$ signals from the peak list.
- 'Stick' patterns or 'reference' patterns published by International Centre for Diffraction Data (ICDD) were used to identify the crystalline phases.
- The ratio of the maximum intensity peaks of the identified phases, for example maximum intensity peaks of pure Al and $\text{Al}(\text{OH})_3$, were used as 'direct comparison' for semi-quantitative analysis (for high accuracy and precision quantitative data, the comparison of peak intensities of identified phases should have been done with those phases in pure form).

3.6 Determination of corrosion resistance of Al-Zn-In and Al-Ti-C coatings

One of the primary aspects of the project was to evaluate the corrosion resistance of Al-Zn-In and Al-Ti-C alloy coating in a chloride media or environment and benchmarking the performance of these coatings against commonly used commercially available pure Al, Al-Zn and Zn-Al coating systems.

In order to evaluate the corrosion resistance of the coatings, the coatings were subjected to long term exposure tests [207,216] and a series of direct current (DC) and alternating current (AC) electrochemical tests [217,218] at various chloride concentrations. All the experiments were conducted to reproduce real life exposure scenario of the Al-Zn-In and Al-Ti-C coatings during their service life. The relevant details of the experiments conducted will be given in the following sections of the chapter.

3.6.1 Neutral Salt Spray Corrosion Tests

The neutral salt spray fog test was conducted according to ASTM B117 [219] standard. The fog chamber of the salt spray cabinet was maintained at $\approx 35^{\circ}$ C throughout the test and 5 % w/v NaCl solution (prepared using deionised water) was used to produce the salt fog. Two sets of ASTM B117 salt spray test were conducted to evaluate the corrosion resistance performance of Al-Zn-In alloy coating (primarily) and Al-Ti-C alloy coating. The details of the two sets of experiments are as follows:

3.6.1.1 Set 1: Neutral Salt Spray Corrosion Tests for Al, Zn-Al and Al-Zn-In coating with artificially induced defect and corrosion product analysis

The Al, Zn-Al and Al-Zn-In sprayed mild steel coupons were prepared by masking a 50 mm X 3 mm area with masking tape prior to coating, to induce an artificial defect as shown in **Figure 3.8** for the purpose of assessing the sacrificial corrosion resistance of the coatings.

The coatings were subjected to 5% w/v NaCl for 1000 hours in a salt spray cabinet and examined at approximately 250 hours intervals. The samples with induced defects were tested in triplicate. Additional unmasked samples were tested for corrosion product analysis, this type of tests has been carried out previously by researchers in order to study the phases present in the corrosion product [220-222].

The corrosion product was mechanically scraped off using soft bristle brush [223] after 500 and 1000 hours exposure in the salt spray cabinet. Analysis of the corrosion product was performed using the Philips X'pert Pro XRD instrument.

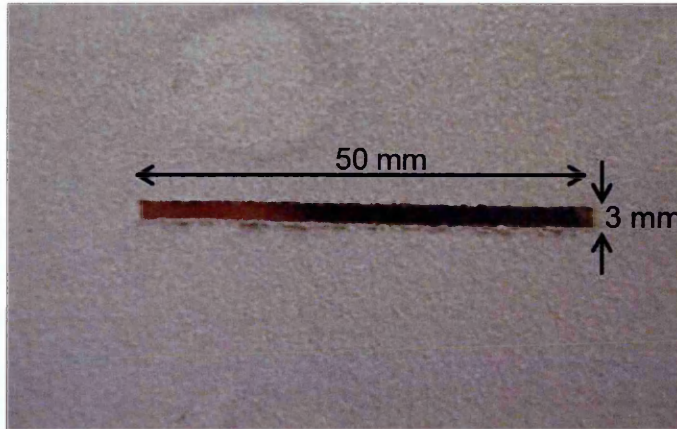


Figure 3.8: Photograph of sprayed mild steel coupon with artificially induced defect (dimensioning not to the scale).

3.6.1.1 Set 2: Neutral Salt Spray Corrosion Tests for Al, Al-Zn, Al-Zn-In, Al-Ti-C alloy coatings and alloy feedstock for oxidative weight change analysis.

The pure Al, Al-Zn, Al-Zn-In and Al-Ti-C alloy material and coatings, see **Figure 3.9** (a) and (b) were subjected to 5 % w/v NaCl for 1000 hours in ASTM B117 neutral salt spray test to obtain information on the weight change upon exposure.

Both alloys and coatings were initially weighed and then the first change in weight was recorded after 48 hours of exposure followed by weight measurements after every 168 hours till the exposure time reached 1008 hours. A Precisa series 360 precision weighing balance (with least count of 0.0001 g) with draft shield was used to weigh the samples.

The corrosion product was mechanically scraped off using soft bristle brush [223] and then samples were finally weighed. Oxidative weight change per unit area for both alloys and coatings was plotted against exposure time. To account for coating roughness in the dimensional measurement, Alicona Infinite focus microscope was used to measure the actual dimension (including surface roughness) of the sprayed coupons to compute the area of exposure. In order to produce comprehensive weight change results with minimum scattering in the data [224], the experiments were done in triplicates.

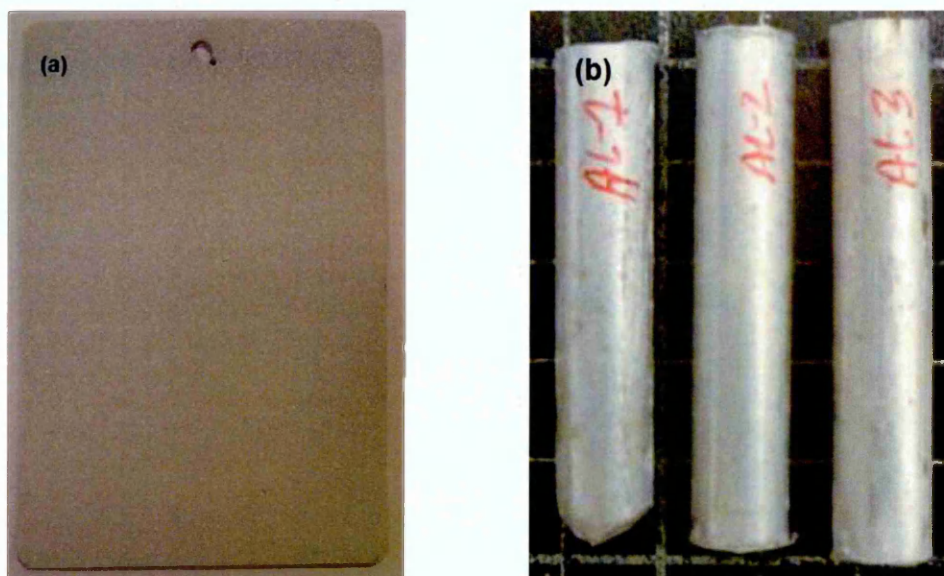


Figure 3.9: Photographs of arc sprayed Al mild steel coupon and (b) Al feedstock in form of rod used for set 2 ASTM B117 salt spray test.

3.6.2 Open-circuit potential (OCP) measurements

The open circuit potential measurements of Al-Zn-In and Al-Ti-C alloy coatings were made in a sodium chloride electrolyte at concentrations of 3.5%w/v, 1.0%w/v, 0.1%w/v and 0.01%w/v respectively. An Ag/AgCl/4M KCl reference electrode with porous liquid junction was used, the area of the working electrodes (coatings) used was $16 \pm 0.1 \text{ cm}^2$.

To minimise the resistance offered by the solution during the test (or the IR drop), the reference electrode was placed within 10 mm of the working electrode. The experiments, performed in duplicate, were run for 168 hours for each of the coating systems. For the purpose of comparison, pure Al and Al-Zn coatings were also exposed to the similar test conditions. It is important to note that the OCP measurement was performed by closely

following ASTM G69 [225] standard, however H_2O_2 was not used while preparing the electrolytic solution.

3.6.3 Galvanic corrosion test- Zero resistance Ammetry (ZRA)

The galvanic corrosion tests were conducted using EG and G multichannel potentiostat, on Al-Zn-In and Al-Ti-C alloy coatings in accordance with ASTM G71 [226] standard, see **Figure 3.10**. The main aim of the experiment was to investigate the protective power of the Al-Zn-In (primarily) and Al-Ti-C alloy coatings when sprayed on to mild steel with different anode to cathode area ratio. Pure Al and Al-Zn coatings were used for benchmarking.

The experiment was conducted in 3.5 % w/v, 1.0 % w/v, 0.1 w/v and 0.01 % w/v NaCl solutions. During the experiment , the geometric area of anode, coatings, (A_a) was kept constant at $16 \pm 0.1 \text{ cm}^2$, while the geometric area of cathode, mild steel coupons, (A_c) chosen were $16 \pm 0.1 \text{ cm}^2$, $32 \pm 0.1 \text{ cm}^2$ and $64 \pm 0.1 \text{ cm}^2$ to have A_c to A_a ratio of 1:1, 2:1 and 4:1 respectively. All the samples were exposed for 168 hours and covered with parafilm to reduce the evaporation losses during experiment [227,228].

Prior to the commencement of experiment, the coated samples were masked using a paraffin wax and colophony (rosin) mix (1:1 wt% ratio) to cover the edges and extra area from electrical connection. The mild steel coupons were masked in the same manner and then were pickled for 30 seconds using mixture of 4M HCl and deionised water (1:1 by vol%) to remove any surface contamination. A distance of 6 cm to 8 cm was maintained between

the anode and cathode while a Ag/AgCl/4M KCl reference electrode with porous liquid junction was placed between the electrodes. A minimum of two experiments were conducted for each set of test condition.

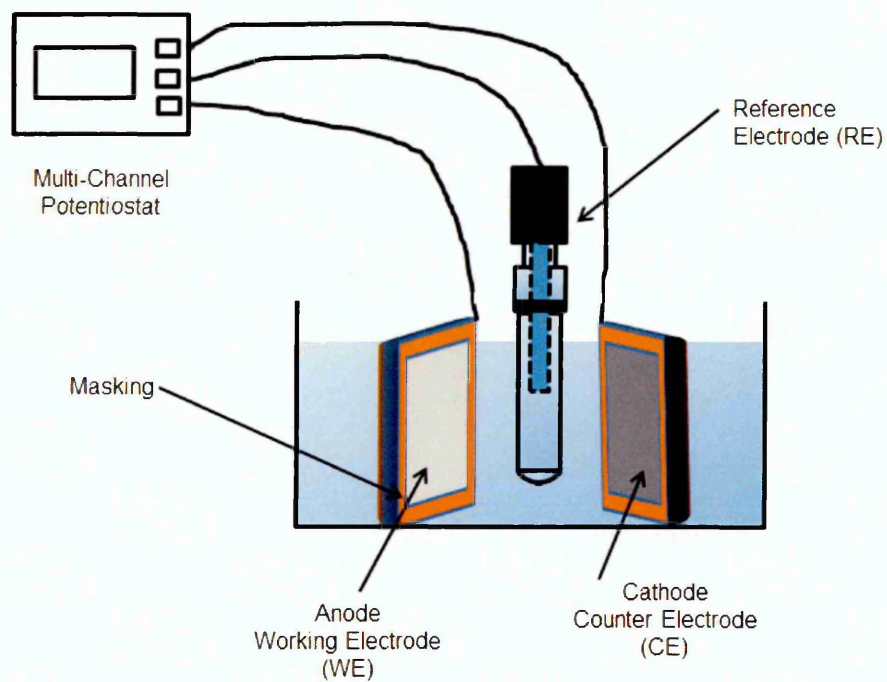


Figure 3.10: Diagrammatic representation of galvanic corrosion test (ZRA) setup.

3.6.4 Electrochemical Impedance Spectroscopy (EIS)

Electrochemical Impedance Spectroscopy (EIS) is a widely used AC electrochemical technique with applications in the field of batteries, semiconductors, fuel cells and has been extensively used to study corrosion and inhibitors [229,230]. The EIS technique has been extensively reviewed by researchers for its advantages and disadvantages in comparison with DC electrochemical techniques of corrosion monitoring [229,230] and has been used to investigate corrosion mechanisms in organic coatings and on steel substrates [231-234], galvanised steels [235,236], uncoated bare metals and sacrificial anodes [237,238]. A vast amount of literature exists on EIS, hence basic underlying principle and only a few selected references encompassing the scope of the technique relevant to the project have been discussed and which were used in data analysis and interpretation.

When an AC perturbation or potential is applied using a potentiostat across a linear system (which obeys Ohm's law), it produces a resultant AC current response with some phase difference (lag or lead). The ratio of the AC potential to AC current is the transfer function $Z(\omega)$ or Z known as impedance (which is derived using Fourier transformation similar to DC Ohm's law) [237,239].

Due to the presence of this phase difference (θ) between applied AC voltage and current, the impedance is often represented as combination of both real and imaginary component of the impedance. The diagrammatic representation of the principle of EIS is shown in **Figure 3.11** and governing equations include [240,241].

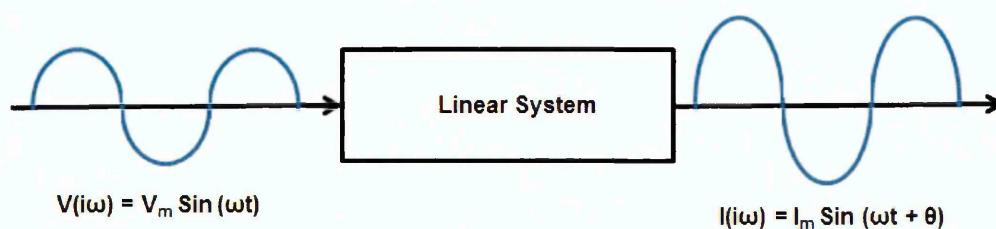


Figure 3.11: Diagrammatic representation of principles of EIS [242].

$$V(i\omega) = V_m \sin(\omega t) \quad \text{Equation 3.1}$$

$$I(i\omega) = I_m \sin(\omega t + \theta) \quad \text{Equation 3.2}$$

$$Z(i\omega) = V(i\omega) / I(i\omega) \quad \text{Equation 3.3}$$

$$Z(i\omega) \text{ or } Z = Z' + i Z'' \quad \text{Equation 3.4}$$

The results obtained from EIS are commonly represented in form of *Nyquist* plots, see **Figure 3.12**, which are representation of real and imaginary components of the impedance Z plotted in Argand or complex plane, or, *Bode* plots, which are modulus of impedance vs. frequency or phase angle vs. frequency graphs, as shown in **Figure 3.13** (a), (b) [237,239-241].

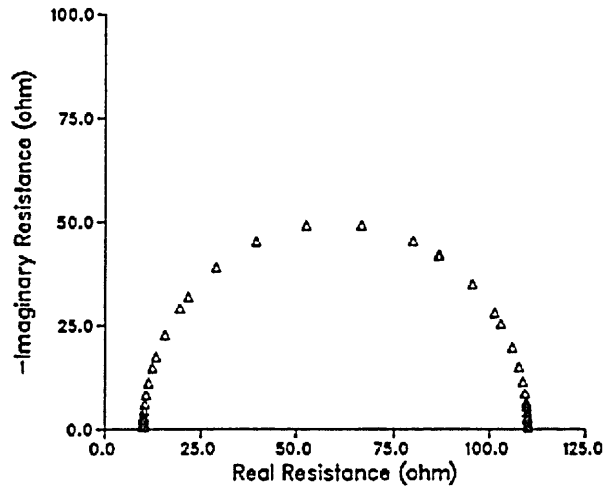


Figure 3.12: Nyquist plot shown from ASTM G3, showing Real vs. Imaginary component of Z starting from highest frequency (left) to lower frequency (right) [240].

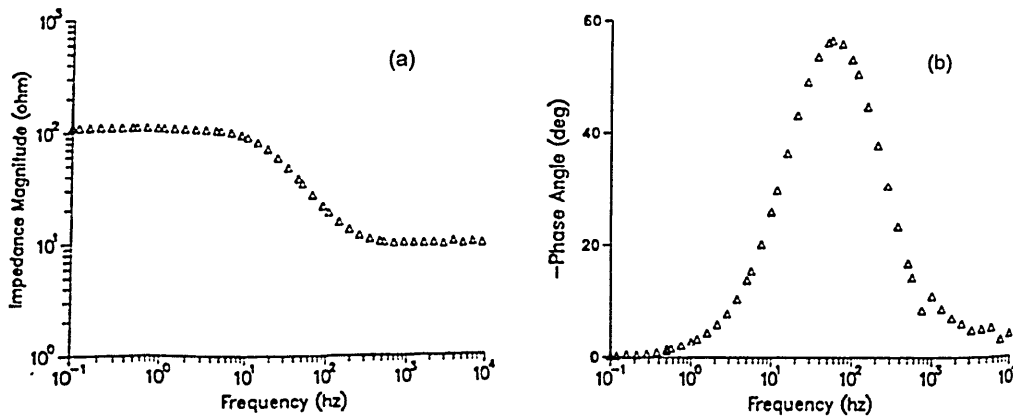


Figure 2.13: Blode plot shown from ASTM G3 representing (a) modulus of impedance vs. frequency and (b) phase angle vs. frequency [240].

Apart from the graphical representation of impedance data in form of Nyquist and Bode plots, the data is subjected to Kramer-Kronig (K-K) transformation [243] for data relaxation and then modelled using *equivalent circuits*. **Equation 3.4**, which graphically presents Nyquist plot, during modelling of EIS data is split into components such as resistance (R, Z' , real part), which usually is resistance offered by electrolytes and in case of coated system, the charge transfer resistance [239,244]. The Nyquist plot shown in **Figure 3.12** shows the resistance offered by electrolytic solution (R_s) and the combination of R_s and charge transfer resistance (R_{ct}).

The imaginary part of **Equation 3.4**, Z'' can be modelled as either a capacitor (C), which represents accumulation of charge at the coating electrolyte interface (in the case of coated system), known as double layer capacitance (C_{dl}), however during modelling a *constant phase element* (CPE) may be used to represent a non ideal capacitor, or, an Inductor (L), which represents formation of passive layer on the system [239,244]. Another important component during modelling of EIS data also includes the effects of diffusion on the electrochemical behaviour of the corroding system, represented by *Warburg impedance* (W) [244]. In order to select and fit the EIS data, which on its own is a complex process, electrochemical software packages which are mostly commercially available are used.

The simplest equivalent circuit model which can be used to represent corrosion is *Randle's* circuit, as shown in **Figure 2.14**, which presents a simple corrosion reaction in the presence of electrolyte offering resistance R_s , a double layer capacitance created at surface-electrolyte interface (C_{dl}) and polarisation resistance R_p when measured at free corrosion potential

[241,244]. However a more complex equivalent circuit models are required to represent corrosion processes [244].

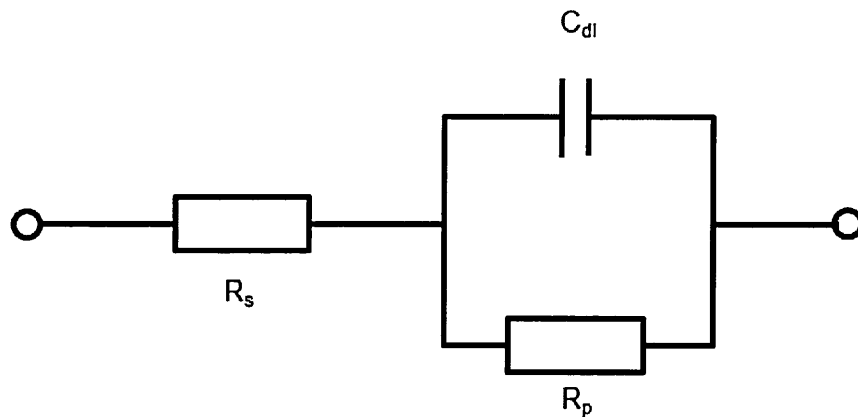


Figure 3.14: Simple Randle's equivalent circuit representing simple corrosion process from impedance data [241,244].

The EIS was performed on Al-Zn-In and Al-Ti-C alloy coatings using both a Basic Electrochemical System (BES) and Parstat potentiostats supplied by Princeton Applied Research and controlled using PowerSuit electrochemical software. It is important to note that although BES, a lock-in-amplifier and Parstat, a frequency response analyser both required considerable amount of data acquisition time at lower frequencies, but as an FRA Parstat was able to collect low frequency data faster than BES the lock-in amplifier. The similar tests were also conducted on pure Al and Al-Zn coatings for benchmarking the performance of Al-Zn-In and Al-Ti-C coatings. The working electrode (coatings) were prepared by mounting open ended acrylic tube cylinders using silicone adhesive sealant followed by application of paraffin wax and colophony mixture (1:1). The EIS was a three-electrode cell with \approx

865.16 mm² area of working electrodes, Pt wire mesh as auxiliary working electrode and Ag/AgCl/4M KCl reference electrode. The tests were conducted by exposing the coatings to 3.5%w/v, 1.0%w/v, 0.1%w/v and 0.01%w/v NaCl solution for maximum of 200 hours. The tests were performed by applying a potential perturbation of 10 mV (rms value) with frequency ranging from 100kHz to 1mHz at 10 points per decade after 1, 24, 48, 72, 168 and 200 hours. ZsimpWin software package was used in order to model the data with an appropriate equivalent circuit [245,246]. All the tests were conducted in duplicates or triplicates.

3.7 Assessment of mechanical properties of coatings

In order to assess the mechanical properties of the arc sprayed Al-Ti-C alloy coating, standard tests such as hardness measurement were conducted. Once again, for the purpose of comparison, similar tests were also conducted on pure Al coatings. Owing to the fact that thermally sprayed coatings have a heterogeneous microstructure, the properties of the coatings are profoundly dependent on the lamellar or splat microstructure of the coatings [247,248], therefore the selection of test parameters was critical in order to gather correct information. The details of the tests are given under section 3.7.1.

3.7.1 Micro-hardness measurement

Vickers micro-hardness measurements using a Mitutoyo MVK-H1 hardness testing machine in accordance with BS EN ISO 4516 [249] were performed on a polished cross-section of the coatings. The Vickers micro-hardness indenter is a diamond shaped pyramidal structure, see **Figure 3.15**, with an angle of $136^{\circ} \pm 0.5^{\circ}$ between two faces of the pyramid and has a square base [249]. The ratio of the diagonals d_1 and d_2 to depth of penetration is $\approx 7:1$ [249].

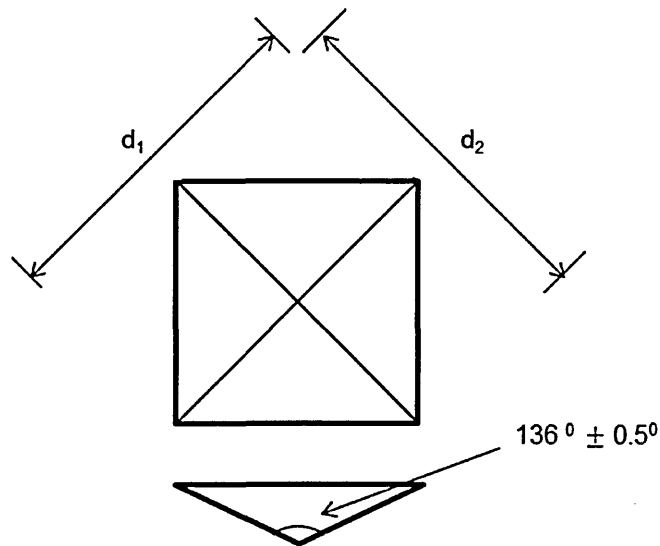


Figure 3.15: Diagrammatic representation of Vickers Indenter [249].

A load of 0.98 N (100 g) was applied for 10 s to obtain a single measurement of the hardness. Thirty indentations on the polished cross-sections of Al-Ti-C and Al-Zn-In coatings along with pure Al coating were carried out in order to determine the range of hardness values caused by the complex microstructure of the coatings.

The micro-hardness of Al–Ti–C and pure Al feedstock alloys was also carried out in order to determine the influence of the spraying process on the hardness of the coating. A frequency distribution histogram was plotted to represent the spread of hardness values in the coatings [250]. Macro-hardness measurements using a 9.8 N (1 kg) load were also carried out on the polished surface of the coatings. The depths of the indentations were always 25% less than the thickness of the coating.

In making micro-hardness measurements care was taken to avoid obvious porosity within the coating. As such the micro-hardness measurements will be higher than a higher load macroscopic measurement that will be influenced by the porosity of the coatings.

3.8 Wear Resistance performance of Al-Ti-C coating

In order to understand the wear behaviour and performance of arc sprayed Al-Ti-C coating, the coating's microstructure was characterised in conjunction with wear tests. A large range of wear tests can be applied but guidance as to the most appropriate test can be found, for example, in ASTM G190 [254] which lists tests which to some extent replicate the actual conditions of exposure during the service life of a coating designed for the purpose of wear resistance [255-257].

In the present study, to evaluate the wear resistance performance of the Al-Ti-C coating, a three body micro-scale abrasive wear test was used [258]. The three body micro-scale abrasive wear test, also referred as the ball-crater wear test was initially used as a method to induce a wear crater in thick films, coatings and other forms of surface treatments for composition depth profiling using Auger electron spectroscopy [259,260].

Based on the principle that, when a rotating spherical ball (metallic or non-metallic) is made to contact the surface of a sample to be examined, under influence of an external force, in presence of abrasive media, produces a wear crater or scar which is used as a measure of wear induced on the sample [259,260]. Over the years researchers have worked towards identifying the effects of variation of test parameters such as hardness of the ball, role of abrasive media, altering the applied load on the micro-scale abrasive wear test to determine the mechanism of wear under specific exposure conditions of material [261-270].

The micro-scale abrasive wear test has been used to analyse soft materials [271], various polymeric materials [272] and coated systems [273,275]. After having reviewed the literature from the previous work on different types of materials, the test parameters were chosen during the present study.

A Commercially available Phoenix Tribology Ltd. model PLINT TE-66 micro-scale abrasive wear tester was used and is shown schematically in **Figure 3.16**. The sample to be tested was vertically mounted on a lever that rotates about the pivot and is pressed against the rotating ball under the application of the applied load. A constant feed of abrasive slurry of specific concentration is maintained between rotating ball and the sample.

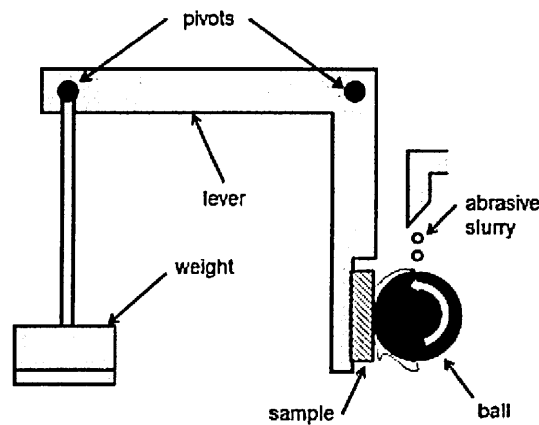


Figure 3.16: Schematic of a micro-scale abrasive wear tester [259].

A constant load of 0.2 N was applied and the abrasive slurry had a concentration of 20vol% (0.66 g/cm^3) of crystalline silicon dioxide in deionised water (nominal particle size $D_{50}=2.5 \text{ }\mu\text{m}$ Silicon (IV) oxide, crystalline quartz, Alfa Aesar).

During the experiment the slurry was constantly stirred using a magnetic stirrer to avoid settling of the silicon dioxide. In a steel ball on a flat aluminium sample configuration the Hertzian contact pressure at 0.2 N is in theory 0.04 GPa. However, in the wear test the two materials are separated by a layer of liquid containing the abrasive slurry and thus it is unlikely that this contact pressure is ever experienced. **Figure 3.17** shows the morphology of the silica particles. A particle shape with rounded edges was observed with the average particle of the silicon dioxide in the range of 2.0 μm –3.0 μm but with some larger agglomerates. **Table 3.3** shows the test parameters used in the experiment.

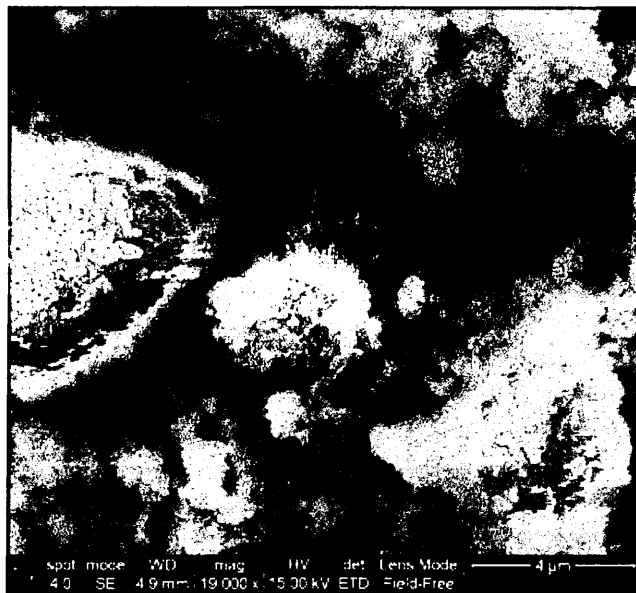


Figure 3.17: Secondary electron micrograph showing SiO_2 powder morphology.

Table 3.3: Micro-scale abrasive wear test parameters.

Test parameters	
Diameter of the steel ball	25.4 mm
Ball material	Tool steel, HV \approx 800
Ball sliding speed	0.13 m/s
Sliding distance	50 m, 100 m, 150 m

All test samples were ground and polished to a final stage of 1 μm diamond suspension. The wear test was repeated three times at each sliding distance to ensure the reproducibility of the results. The diameter of the circular wear craters was measured using an optical microscope and the volume loss was calculated assuming the spherical cap geometry of the wear crater given by

$$V = \pi b^4 / 64 R \quad \text{Equation 3.5}$$

where b is the diameter of the wear crater and R is the radius of the rotating ball, the above equation is used when $b \ll R$. The graph of the volume of the wear crater vs. sliding distance multiplied by the load was plotted to calculate the coefficient of wear ($\text{mm}^3 \text{N}^{-1} \text{m}^{-1}$) from the gradient of the graph. During the micro-scale abrasion test the wear crater did not penetrate to the substrate. For comparison purpose, the Al-Ti-C alloy along with pure Al alloy and their respective coatings, 13%Cr steel coating was also subjected to the wear test under similar conditions.

Based on the preliminary SEM and XRD analysis conducted on Al-Ti-C coating, further effects of various phases present in the Al-Ti-C alloy coatings, micro-scale abrasive wear test was performed on the heat treated Al-Ti-C coating samples. The coated samples were exposed to 150⁰C, 350⁰C and 550⁰C for 1 and 3 hours respectively.

Two different cooling strategies were adopted during the test, the first set of coatings were rapidly quenched (RQ) by immersing the samples into deionised water when removed from the furnace, while the other set of samples were slow air cooled (AC) by leaving the samples for ≈ 5 hours at the ambient room temperature.

Hardness measurements, as described in section 3.7.1 were taken on both RQ and AC coated samples and micro-scale abrasive wear tests were repeated with the same parameters mentioned in **Table 3.3**. Once again, the wear test was repeated three times at each sliding distance to ensure the reproducibility of the results.

Chapter 4: Results and Discussion-Part 1

The project focused on two Al alloy coatings, which were:

- Al-Zn-In alloy coating, primarily tested for corrosion resistance
- Al-Ti-C alloy coating, primarily tested for wear resistance performance, in addition, corrosion evaluation of the coating was also conducted.

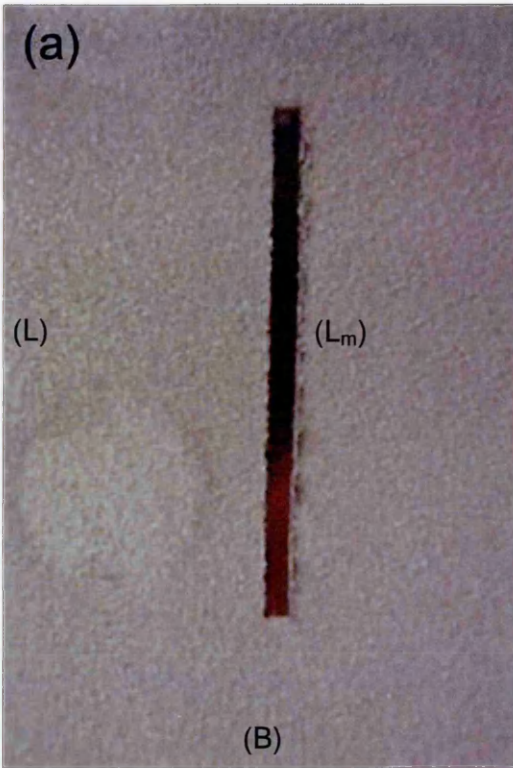
This chapter will be sub-divided into two major sections, one of which will focus on corrosion evaluation using both accelerated and electrochemical techniques (part 1) while the other sub-section will focus on the mechanical properties of coatings along with micro-scale abrasion test (part 2). All the corrosion and wear tests were conducted in conjunction with microstructural characterisation of the coatings, hence the results obtained from the analytical characterisation of the coatings have been incorporated within the results and discussion of the corrosion and wear tests.

4.1 Neutral salt spray corrosion testing

Primarily focusing on corrosion resistance performance of Al-Zn-In coating, neutral salt spray corrosion test was performed according to ASTM B117 standard. The detailed procedure of the experiment was given under section 3.6 of chapter 3. As mentioned in section 3.6.1, two sets of ASTM B117 neutral salt spray tests were conducted. The results of the two sets have been discussed separately in the following sections.

4.1.1 Sacrificial corrosion protection analysis of Al-Zn-In coating in comparison with Zn-Al and pure Al coating.

Triplicate samples of Al-Zn-In, Zn-Al and pure Al coatings with artificially induced defects were used to perform neutral salt spray corrosion tests. The intention was to analyse the sacrificial corrosion protection ability and study the corrosion products obtained after 500 hours and 1000 hours of exposure of Al-Zn-In coating and compare the results obtained with pure Al and Zn-Al coating. **Figure 4.1 (a-f)**, **Figure 4.2 (a-f)** and **Figure 4.3 (a-f)** shows the photographs of the arc sprayed Al-Zn-In, pure Al and Zn-Al coatings exposed to 5% w/v NaCl during the salt spray corrosion test.



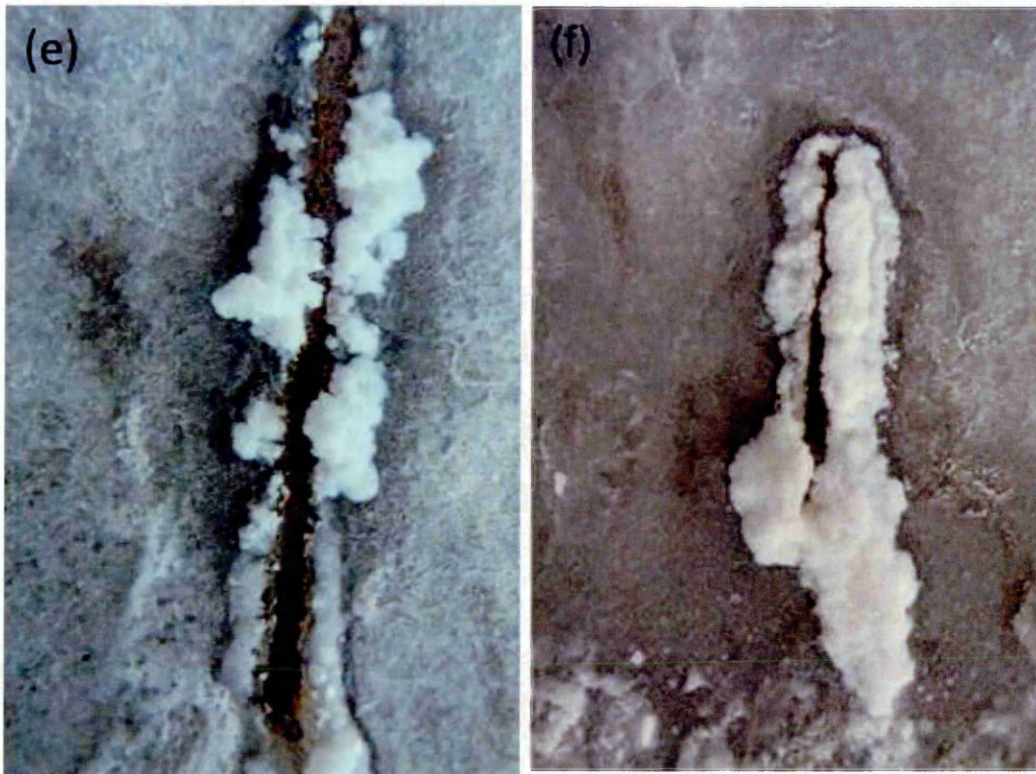
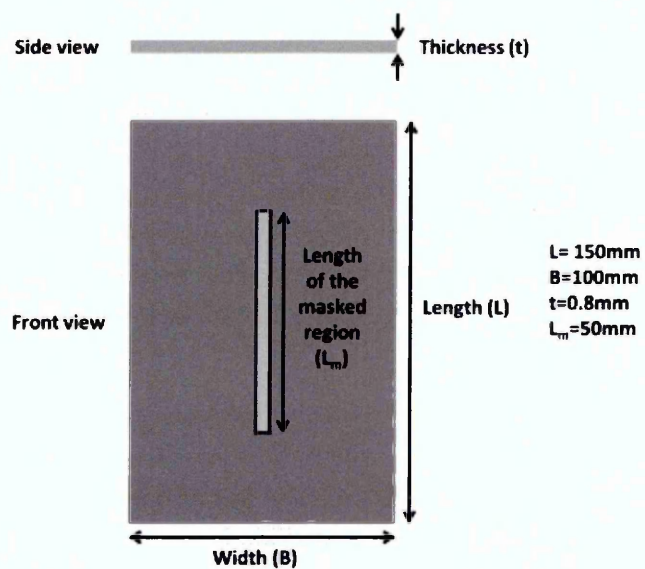
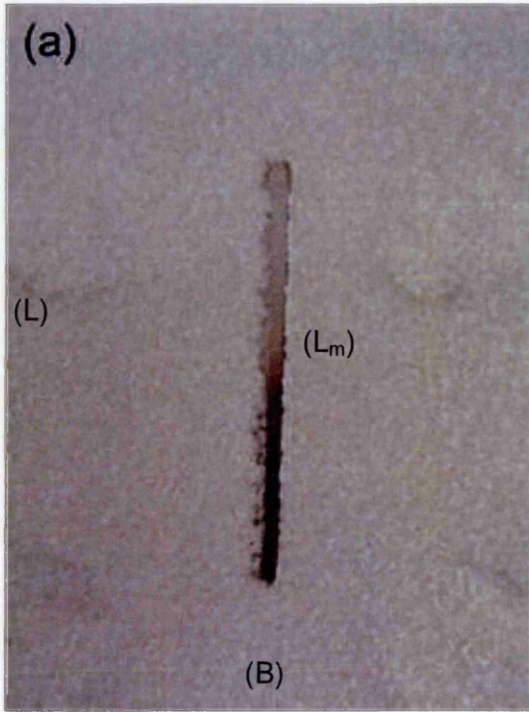


Figure 4.1: Photographs of Al-Zn-In coating with artificially induced defect exposed to 5 % w/v NaCl in ASTM B117 salt spray test, taken (a) before the experiment, after (b) 24 hours, (c) 48 hours, (d) 168 hours, (e) 500 hours and (f) 1008 hours. The dimensions are shown below (scale not to exact size).





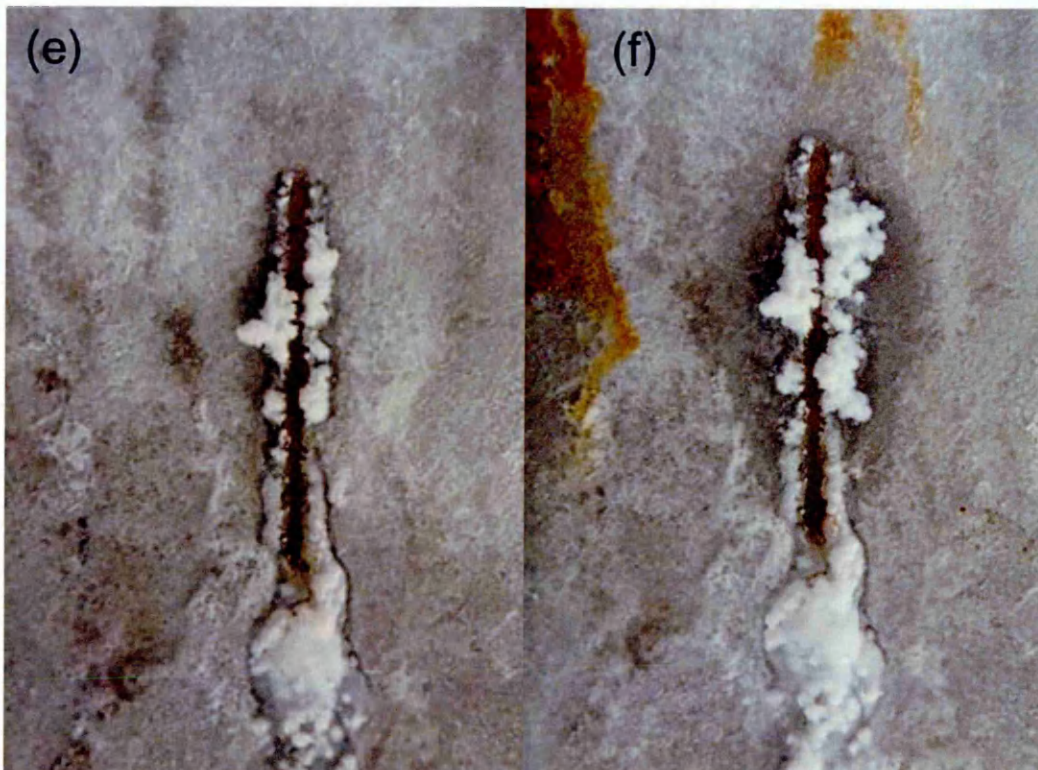
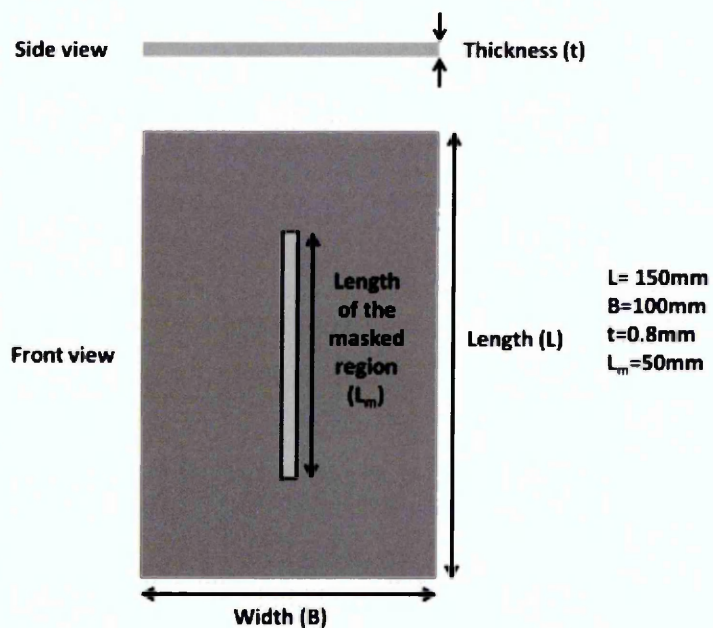


Figure 4.2: Photographs of pure Al coating with artificially induced defect exposed to 5 % w/v NaCl in ASTM B117 salt spray test, taken (a) before the experiment, after (b) 24 hours, (c) 48 hours, (d) 168 hours, (e) 500 hours and (f) 1008 hours. The dimensions are shown below (scale not to exact size).



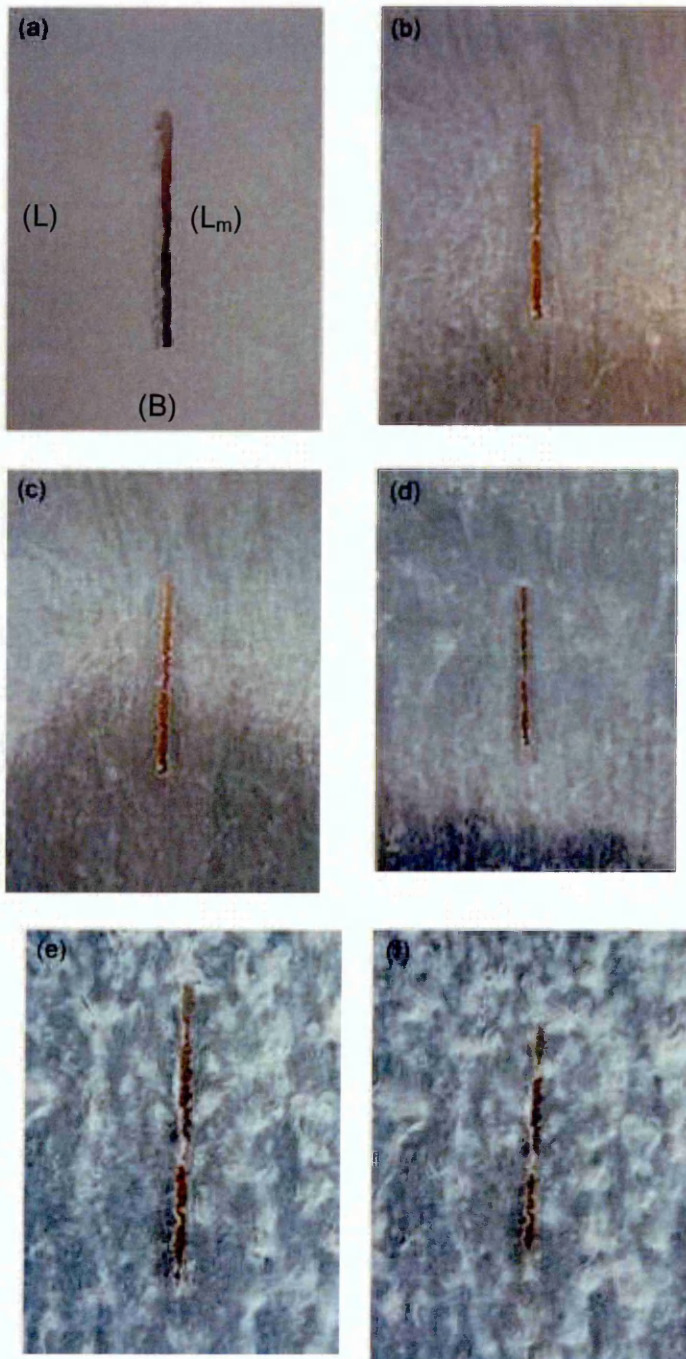
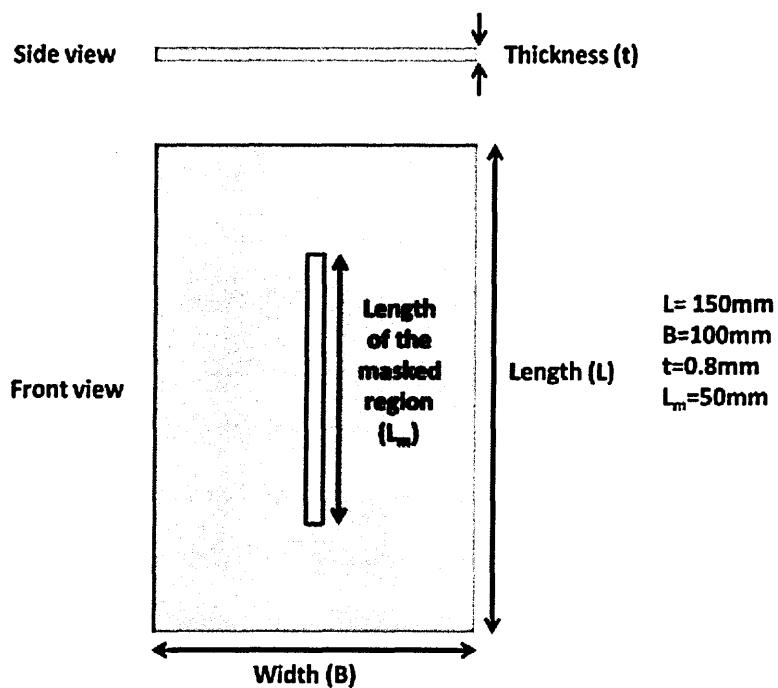


Figure 4.3: Photographs of Zn-Al coating with artificially induced defect exposed to 5 % w/v NaCl in ASTM B117 salt spray test, taken (a) before the experiment, after (b) 24 hours, (c) 48 hours, (d) 168 hours, (e) 500 hours and (f) 1008 hours. The dimensions are shown on the following page (scale not to exact size).



When visual inspection of the coatings with artificial defects, which were tested in triplicates, was carried out after 24 hours of exposure, *surface staining* of Al and Al-Zn-In coatings was apparent. The surface staining of the samples could have been due the initiation of oxide layer formation, which was also reported previously by Rodriguez *et al.*[146]. The XRD analysis of the as sprayed Al and Al-Zn-In confirmed the presence of hydrated Al oxide, in form of monoclinic Bayerite phase ($\text{Al}(\text{OH})_3$).

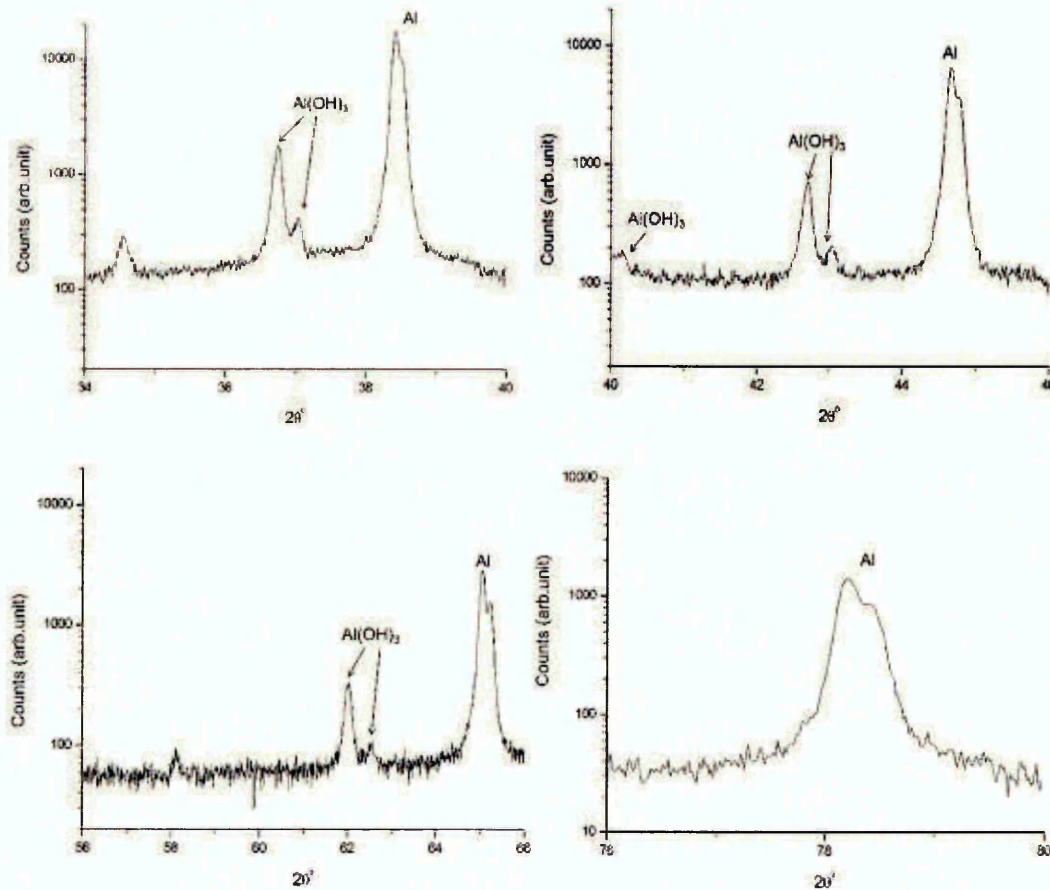


Figure 4.4: Bragg-Brentano XRD trace of as sprayed Al coating. The scan was conducted from $2\theta^{\circ}$ ranging from 10° to 80° .

Figure 4.4 and **Figure 4.5** shows the Bragg-Brentano XRD trace of as sprayed Al and Al-Zn-In coating. The dominant peaks of cubic Al phase in Al coating at 38.20° , 44.80° , 65.10° and 78.20° were identified using crystallographic data from X'Pert High Score XRD data analysis software. Similar peak positions of cubic Al in Al-Zn-In coatings were also identified. It is important to note that at $\approx 34.20^{\circ}$ a visible peak in both Al and Al-Zn-In

XRD traces can be seen from **Figure 4.4** and **Figure 4.5**, which was identified as Cu K_{β} and was not considered during the data analysis.

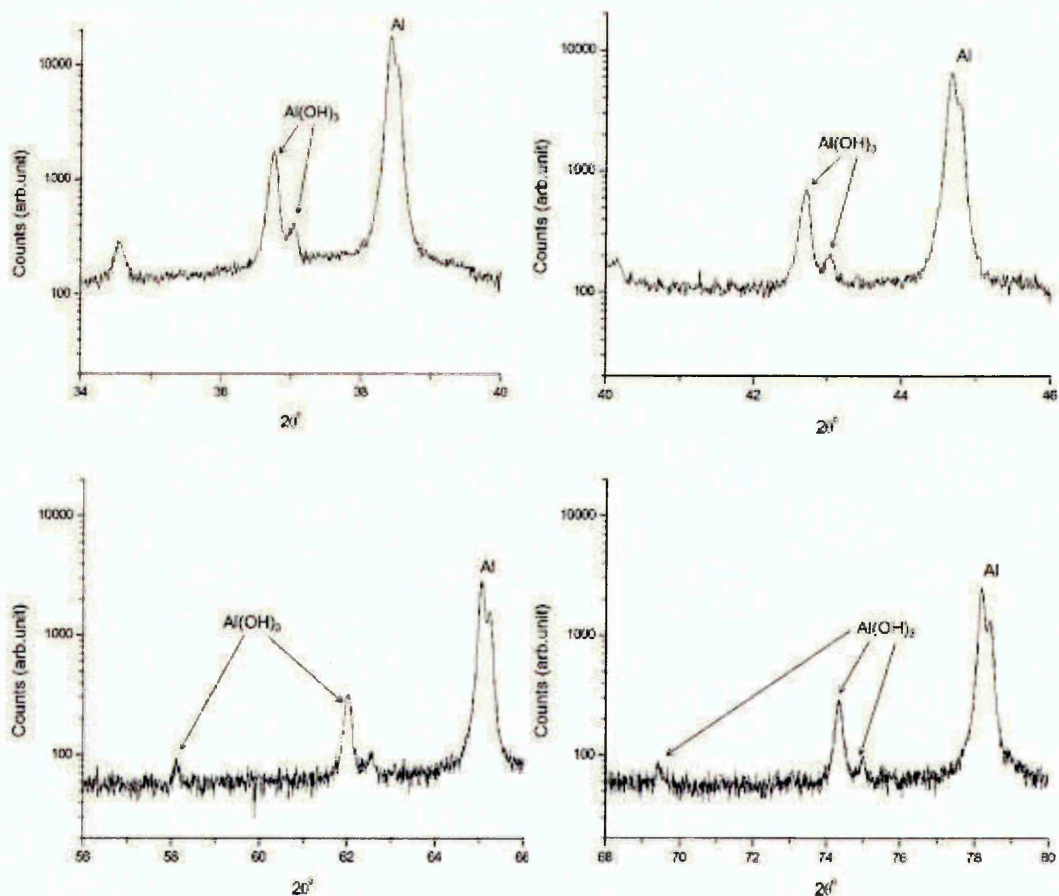


Figure 4.5: Bragg-Brentano XRD trace of as sprayed Al-Zn-In coating. The scan was conducted from $2\theta^{\circ}$ ranging from 10° to 80° .

Sharp peaks of $Al(OH)_3$ at 36.80° , 42.70° and 62.10° were seen in both Al and Al-Zn-In coating, with additional sharp peak at 74.20° in Al-Zn-In. Small observable peaks of $Al(OH)_3$ were also evident at 35.10° , 43.10° , 58.20° and 62.30° in Al coating. Al-Zn-In also showed small peaks of $Al(OH)_3$ similar to Al but additional small peaks at 69.20° and 75.10° were also seen. Majority of the $Al(OH)_3$ peaks were within the 0.05° to 0.1° expected $2\theta^{\circ}$ range,

however slight shift in the peaks were observed due to some change in the unit cell parameters of monoclinic $\text{Al}(\text{OH})_3$ phase.

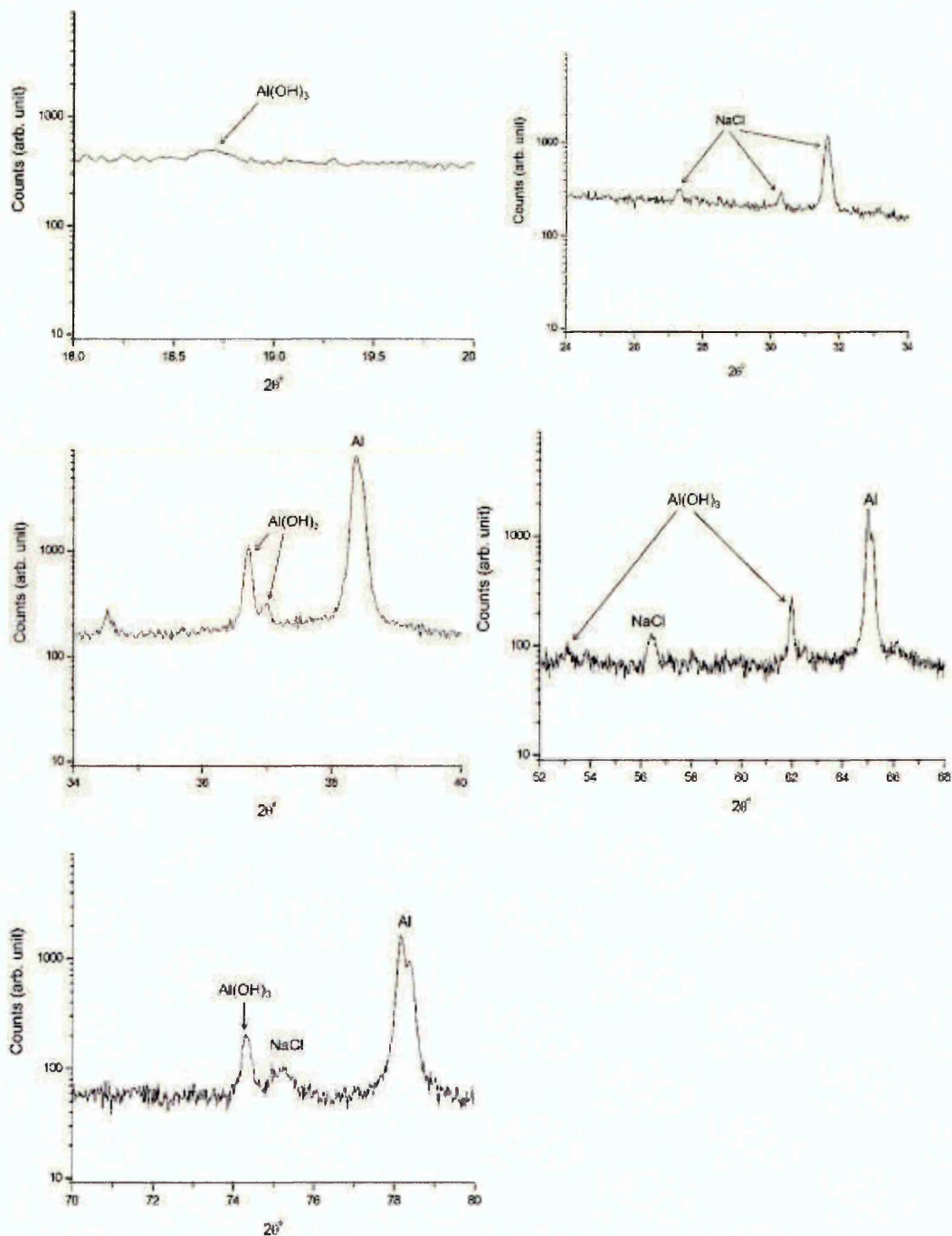


Figure 4.6: Bragg-Brentano XRD trace of Al coating after 24 hours of exposure in 5 % w/v NaCl. The scan was conducted from $2\theta^\circ$ ranging from 10° to 80° .

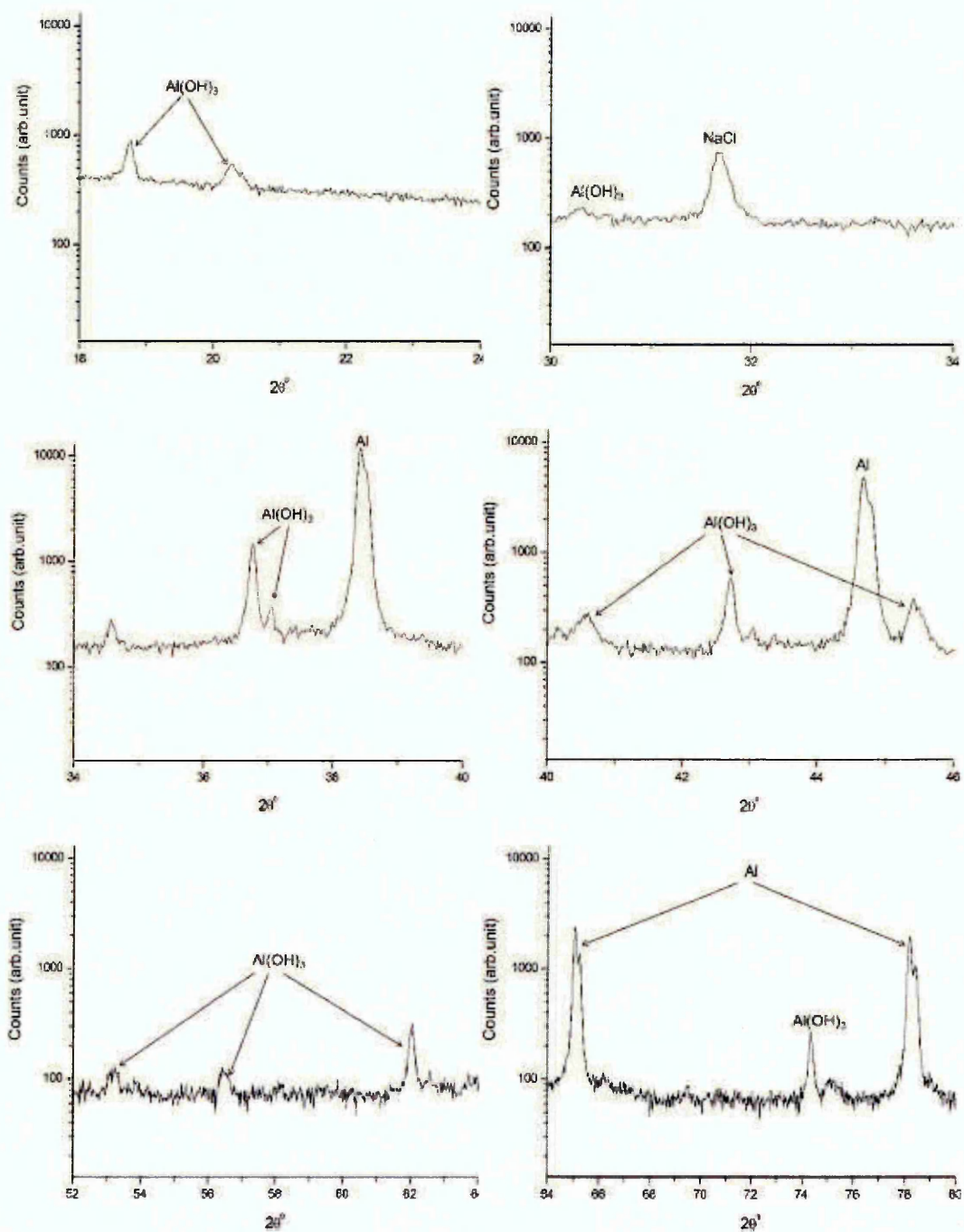


Figure 4.7: Bragg-Brentano XRD trace of Al-Zn-In coating after 24 hours of exposure in 5 % w/v NaCl. The scan was conducted from $2\theta^\circ$ ranging from 10° to 80° .

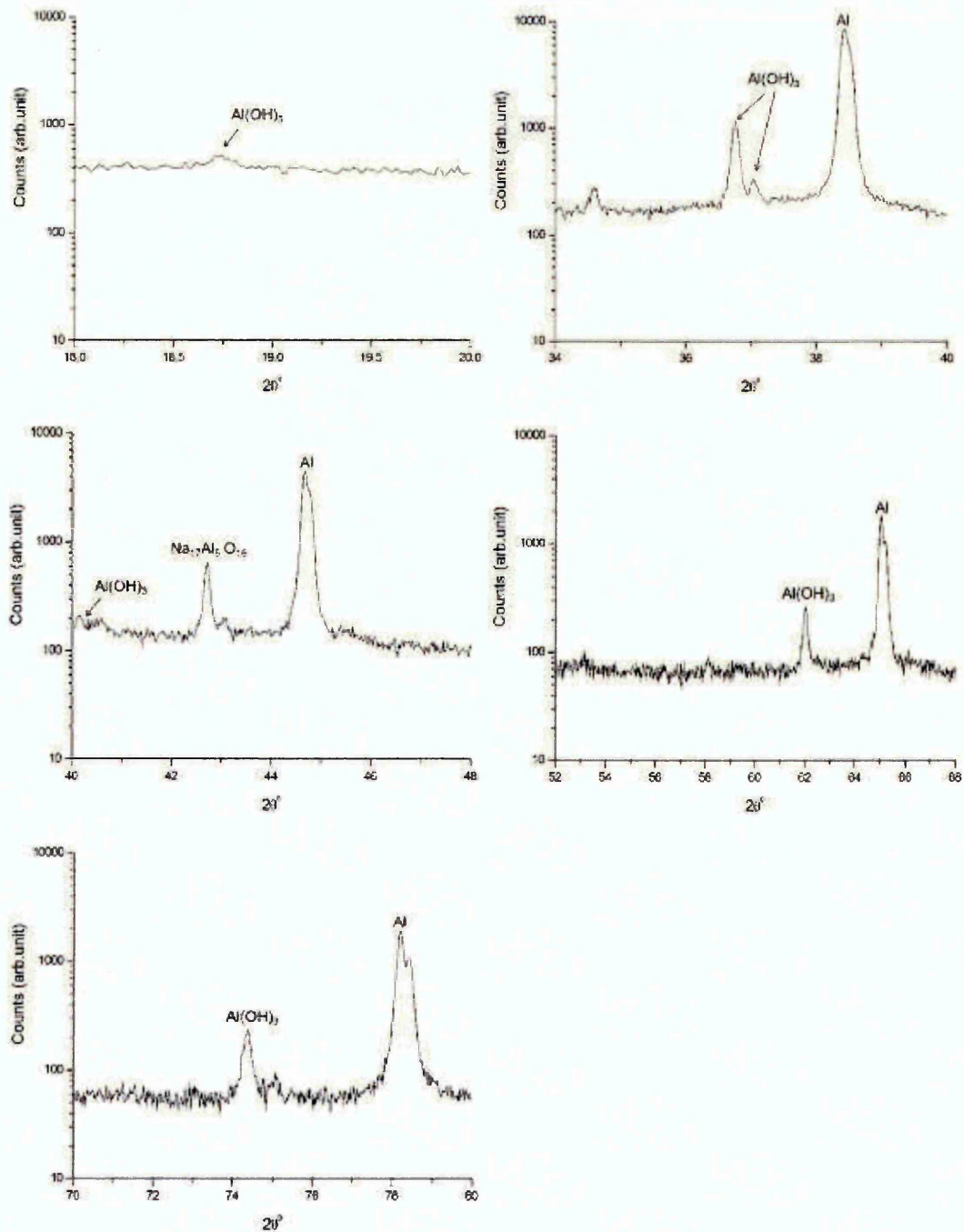


Figure 4.8: Bragg-Brentano XRD trace of Al coating after 48 hours of exposure in 5 % w/v NaCl. The scan was conducted from $2\theta^{\circ}$ ranging from 10° to 80° .

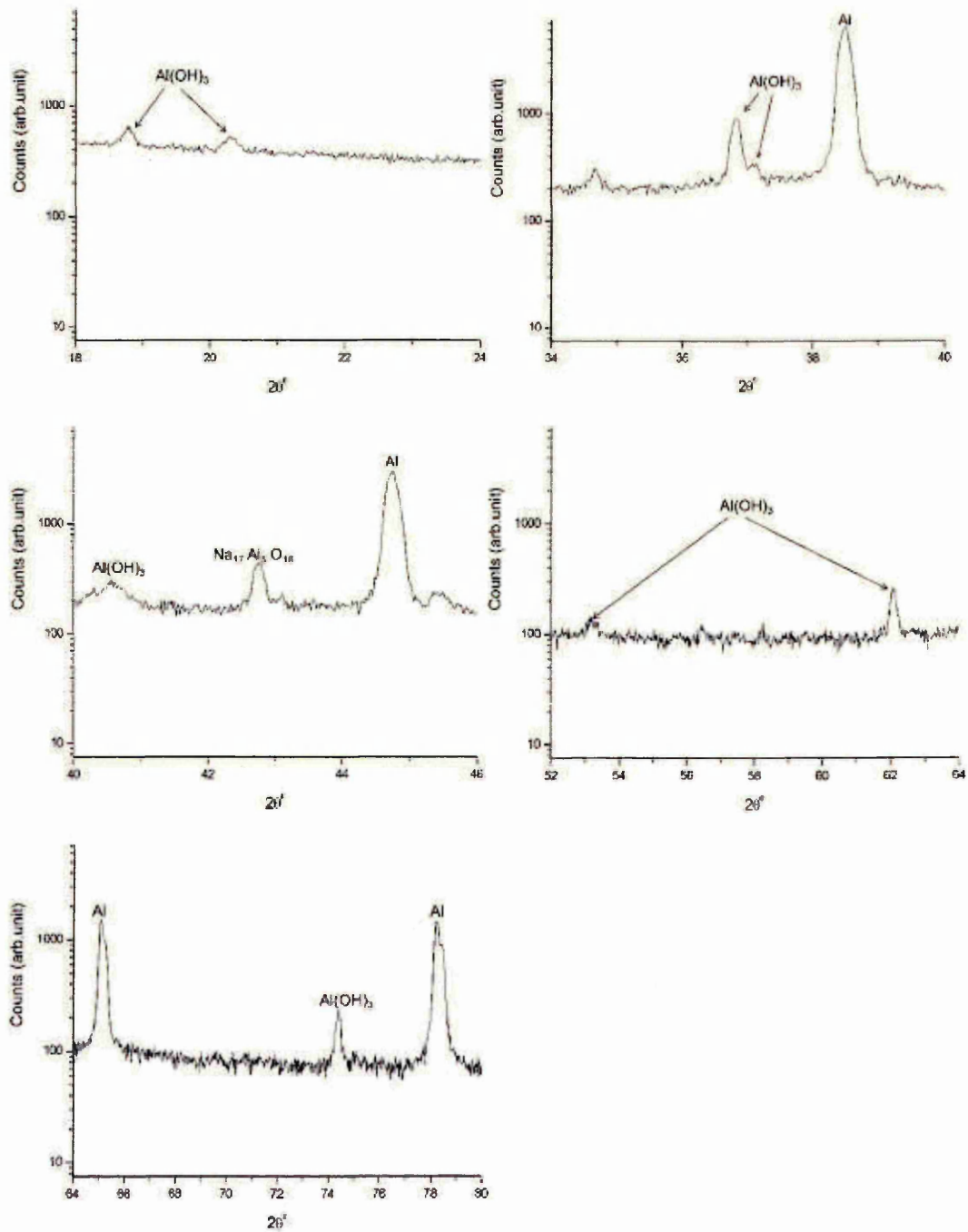


Figure 4.9: Bragg-Brentano XRD trace of Al-Zn-In coating after 48 hours of exposure in 5 % w/v NaCl. The scan was conducted from $2\theta^{\circ}$ ranging from 10° to 80° .

Figure 4.6 and **Figure 4.7** shows the XRD traces of Al and Al-Zn-In coating after 24 hours of exposure in the salt spray cabinet. A smaller but broader peak of Al(OH)_3 at $\approx 18.50^\circ$ was observed for Al coating in addition to the peaks recorded for Al under as sprayed condition.

Similarly for Al-Zn-In coating, two distinct peaks of Al(OH)_3 at lower 2θ values of 18.7° and 20.1° , in addition, peaks at 40.5° , 45.5° , 53.2° , 56.5° were also observed. Due to deposition of NaCl on the surface of the exposed coatings, additional peaks of halite were also recorded in the XRD trace of both Al and Al-Zn-In coating. With increase in the exposure time of the Al and Al-Zn-In coating in the salt spray cabinet to 48 hours, a sharp peak of complex sodium aluminium oxide ($\text{Na}_{17}\text{Al}_5\text{O}_{16}$) at $\approx 42.3^\circ$ was observed, see **Figure 4.8** and **Figure 4.9**. Broad peaks of Al(OH)_3 at $\approx 40.2^\circ$ was also reported for both Al and Al-Zn-In after 48 hours of exposure.

A semi-quantitative analysis was conducted using XRD traces to compares the ratio of monoclinic Bayerite Al(OH)_3 to cubic Al phase, as shown in **Table 4.1**.

Table 4.1: Semi-quantitative analysis showing the ratio of Al(OH)_3 to Al phase present in Al and Al-Zn-In coating when as sprayed and after 24 and 48 hours in neutral salt spray test condition.

	$\text{Al(OH)}_3/\text{Al}$, Al coating	$\text{Al(OH)}_3/\text{Al}$, Al-Zn-In coating
As sprayed	0.18	0.04
After 24 hours	0.08	0.07
After 48 hours	0.06	0.17

It can be seen from **Table 4.1** that with increasing exposure time in the salt spray cabinet, Al coating showed reduction in formation of Al(OH)_3 while Al-Zn-In showed increased formation of Al(OH)_3 elucidating that Al-Zn-In coating was more actively corroding than Al coating, producing more Al(OH)_3 phase on the surface of the coating than Al coating. It is important to note that slight shift in the peak positions of Al(OH)_3 for Al and Al-Zn-In coating, while calculating the phase ratio may have been caused due to misalignment of the samples during the experiment.

After 500 hours of exposure, the Al coating showed the formation of white corrosion products around the area of artificial defects, see **Figure 4.2** (e). A similar observation was made for Al-Zn-In coating, with a greater degree of corrosion product formation along the artificial defect area, see **Figure 4.1** (e), confirming the deductions based from semi-quantitative phase ratio data from **Table 4.1**. The XRD trace of Al and Al-Zn-In coating showed formation of Bayerite phase of hydrated aluminium oxide (Al(OH)_3) after 500 hours of exposure, but after 1000 hours of exposure the hydrated aluminium oxide primarily was anorthic Nordstrandite phase.

Table 4.2 shows the semi-quantitative phase ratio of Al(OH)_3 to Al for Al-Zn-In and Al coating, which once again follows a similar trend observed from **Table 4.1** indicating that Al-Zn-In exhibited 10% increase in the Al(OH)_3 to Al ratio from 500 hours to 1000 hours of exposure, while for same exposure period, Al coating showed 40% decrease in the ratio. This suggested that even after 500 hours and 1000 hours of exposure period Al-Zn-In coating was more actively corroding than Al coating.

Table 4.2: Semi-quantitative analysis showing the ratio of Al(OH)₃ to Al phase present in Al and Al-Zn-In coating after 500 and 1000 hours in neutral salt spray test condition.

	Al(OH) ₃ /Al, Al coating	Al(OH) ₃ /Al, Al-Zn-In coating
After 500 hours	0.14	0.09
After 48 hours	0.10	0.10

For the Zn-Al coating, the formation of white corrosion product was uniform, i.e. the corrosion product was formed all over the coating surface. The degree of corrosion observed on the exposed mild steel substrate in the artificial defect region was found to be greater in the Zn-Al coating in comparison to Al and Al-Zn-In coatings. This suggested that Al and Al-Zn-In coatings showed evidence of superior sacrificial corrosion protection ability, with qualitative assessment suggesting that Al-Zn-In coating performed better in this respect than the Al coating.

Figure 4.3 (e) showed that after 500 hours, the Zn-Al coating displayed a change in colouration to dark blue appearance. The Al and Al-Zn-In coating displayed the same coloration after 500 hours of exposure in the corrosion test, see **Figure 4.1 (e)** and **Figure 4.2 (e)**. After 1000 hours of exposure, appearance of the red-brown corrosion product along the corners of Al coating was observed, see **Figure 4.2 (f)**. The formation of red-brown corrosion product is indicative of corrosion of the mild steel substrate. Loss of coating thickness over time has been reported when Al is deposited using arc spray technique [146]. Al-Zn-In coating showed good corrosion resistance, with formation of corrosion product near the defect area and no evidence of corrosion of mild steel suggested the coating was satisfactorily

protecting the mild steel substrate. An increase in the formation of white corrosion product on the Zn-Al coating surface was observed after 1000 hours of exposure, see **Figure 4.3** (f). The neutral salt spray corrosion test conducted indicated little evidence of sacrificial corrosion protection of mild steel substrate by Zn-Al coating.

Figure 4.10 (a), (b) and **Figure 4.11** (a), (b) shows the X-Ray diffraction traces of the corrosion product formed on Al and Al-Zn-In coating after 500 and 1000 hours of exposure. The major peaks of Dawsonite ($\text{NaAl}(\text{CO}_3)(\text{OH})_2$) at $\approx 15.50^\circ 2\theta$ was identified for Al and Al-Zn-In corrosion product formed after 500 and 1000 hours of exposure (see **appendix**). The other phase identified was Bayerite for both Al and Al-Zn-In coating. These phases were present in the corrosion product analysed after 500 and 1000 hour of exposure. Formation of Bayerite in the corrosion product was due to the fact that the surface of Al and Al-Zn-In were subjected to a humid environment, favouring the formation of adherent aluminium hydrated oxides. The X-ray diffraction analysis indicated that although Al and Al-Zn-In coating have different alloy composition as mentioned in **Table 3.1**, similar phases were identified in the corrosion product after 500 and 1000 hours exposure in salt spray corrosion test.

Zinc aluminium carbonate hydroxide hydrate
 $(\text{Zn}_{0.61}\text{Al}_{0.39}(\text{OH})_2(\text{CO}_3)_{0.195} \cdot x\text{H}_2\text{O})$ was identified as the major phase present in the corrosion product of Zn-Al coating. The other phases present were Zinc carbonate hydroxide hydrate $(\text{Zn}_4(\text{CO}_3)(\text{OH})_6 \cdot \text{H}_2\text{O})$ and zinc oxide (ZnO), corresponding with the findings of other researchers [146]. No significant changes in the corrosion product of Zn-Al coating were reported

after 500 and 1000 hours of exposure. However, the researchers have reported that $(Zn_{0.61}Al_{0.39}(OH)_2(CO_3)_{0.195} \cdot xH_2O)$ phase present in the corrosion product shows increases with increasing aluminium content in such coatings [146].

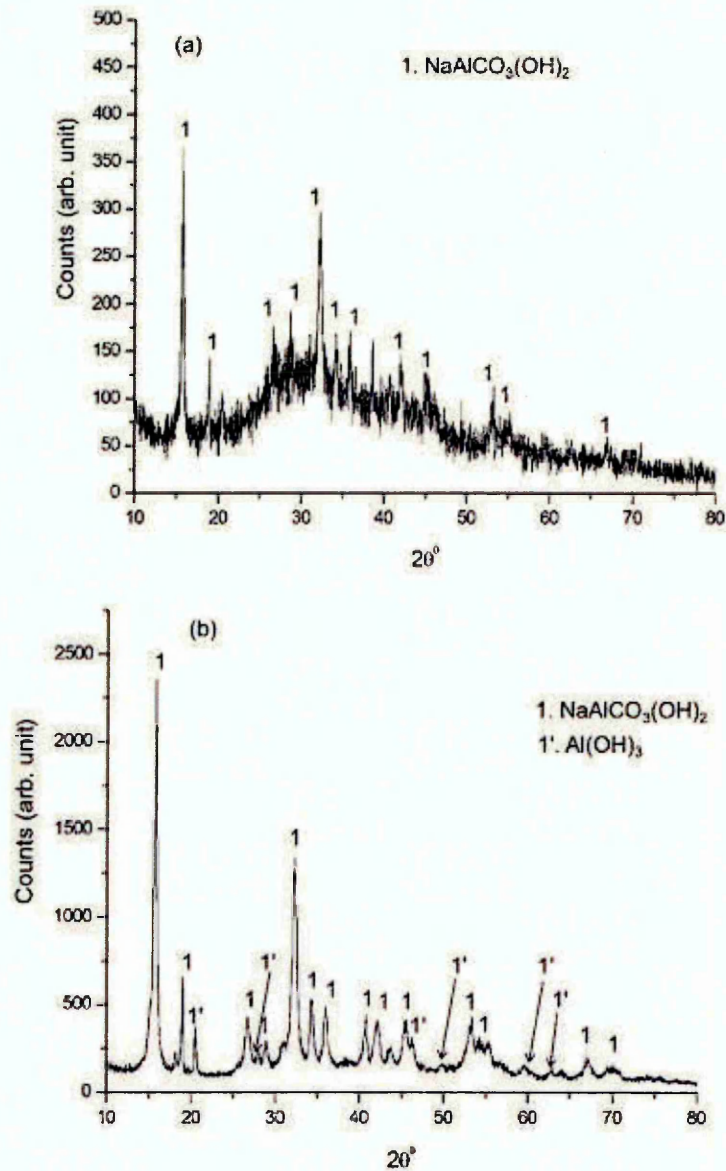


Figure 4.10: XRD trace of corrosion product of Al coating after (a) 500 hours and (b) 1000 hours in salt spray neutral test.

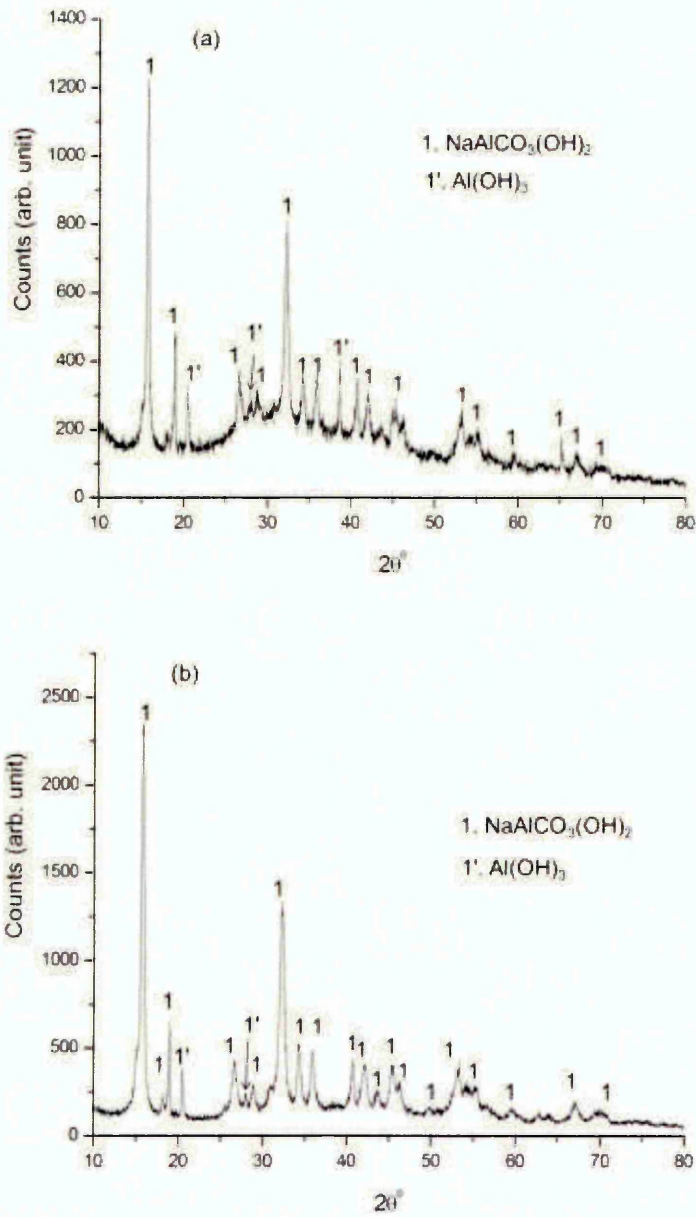


Figure 4.11: XRD trace of corrosion product of Al-Zn-In coating after (a) 500 hours and (b) 1000 hours in salt spray neutral test.

4.1.1.1 Microstructural analysis of Al and Al-Zn-In coating before and after neutral salt spray corrosion test

Figure 4.12 and **Figure 4.16** shows a high contrast backscatter electron SEM micrographs of the cross-sectioned 300 μm thick Al, Al-Zn-In coatings before exposure to the neutral salt spray testing.

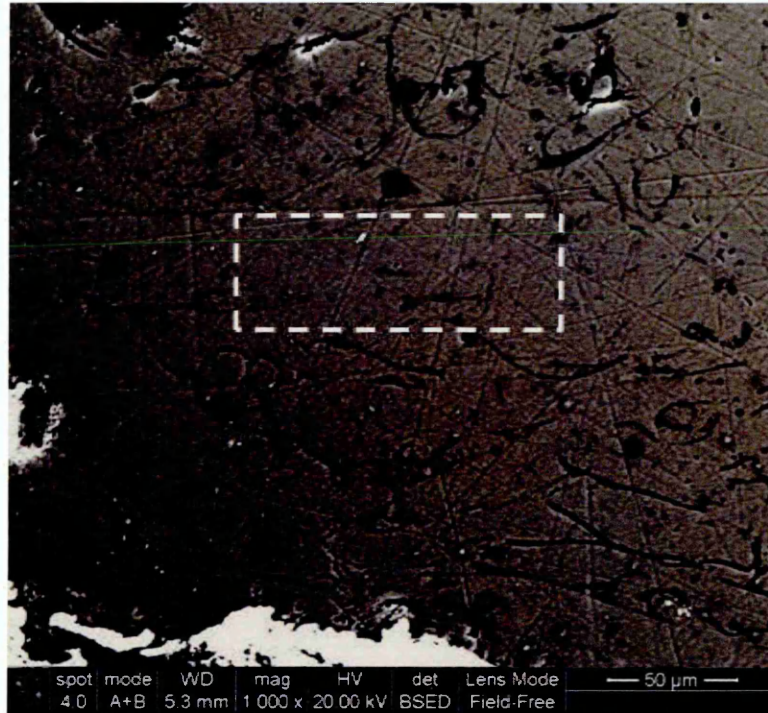


Figure 4.12: High contrast backscattered electron micrograph of a cross-section of as sprayed 300 μm thick Al coating. The enclosed area was used for EDX analysis.

The arc sprayed Al coating showed presence of porosity distributed along the cross section of the coating (dark patches, the dark patch on the top left corner of the micrograph is portion of epoxy mount) apparent in **Figure 4.12**.

The average of the semi-quantitative EDX analysis data from three different areas of the cross-section of the coating showed in **Table 4.3** revealed that the majority of the as-sprayed coating was predominantly Al with trace amount of oxygen.

Table 4.3: Average composition analysis of as sprayed Al coating using EDX semi-quantitative data.

	Average composition	
	Al (at %)	O (at %)
As sprayed Al coating	81 ± 9	8 ± 3

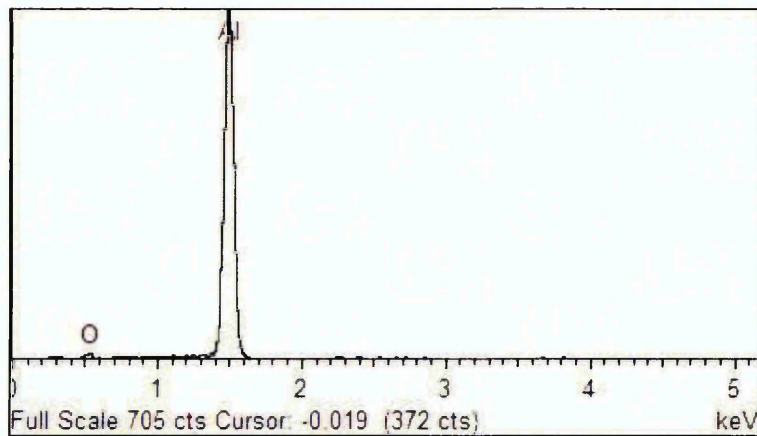


Figure 4.13: EDX spectrum of as sprayed Al coating from the enclosed region shown in **Figure 4.12**.

The EDX spectrum of the enclosed region shown in **Figure 4.12**, showed a large Al peak with a relatively small but visible O peak. This complemented with the fact that Al was present in much higher concentration with formation of oxide. However, the XRD trace of as sprayed Al coating shown in **Figure 4.4** suggested the formation of hydrated Al oxide in form of Bayerite.

This can be attributed to the fact that the penetration depth of X-rays during XRD analysis of Al coating was calculated to be $\approx 23 \mu\text{m}$ to $25 \mu\text{m}$ and the EDX elemental map generated from the as sprayed surface of the Al coating shown in **Figure 4.14** revealed areas on the surface of the coating rich in oxygen, see **Figure 4.15**.

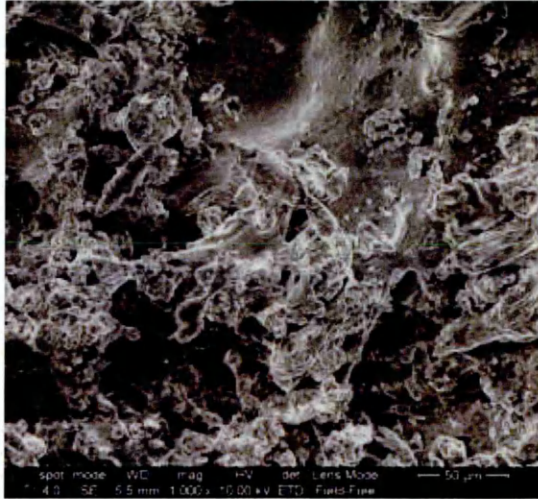


Figure 4.14: Secondary electron micrograph of as sprayed Al coating surface.

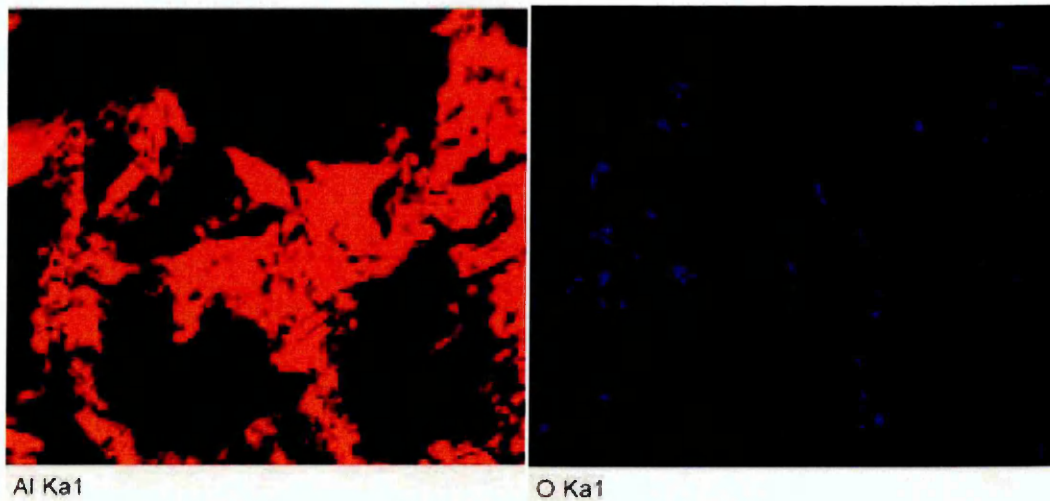


Figure 4.15: EDX map of the entire area of Al coating shown in **Figure 4.14** at X 1000 magnification.

The analysis from the EDX composition data showed concentration of oxygen as $22 \pm 0.3\text{at}\%$, which is significantly higher than what was reported in **Table 4.3**. The higher concentration of oxygen is indicative of formation of oxide on the surface of the as sprayed Al coating, which was detected by the XRD analysis. Note that the dark regions in the EDX map shown in **Figure 4.15**, it is evident that these dark regions correspond to the surface topography of the coating shown in **Figure 4.14**.

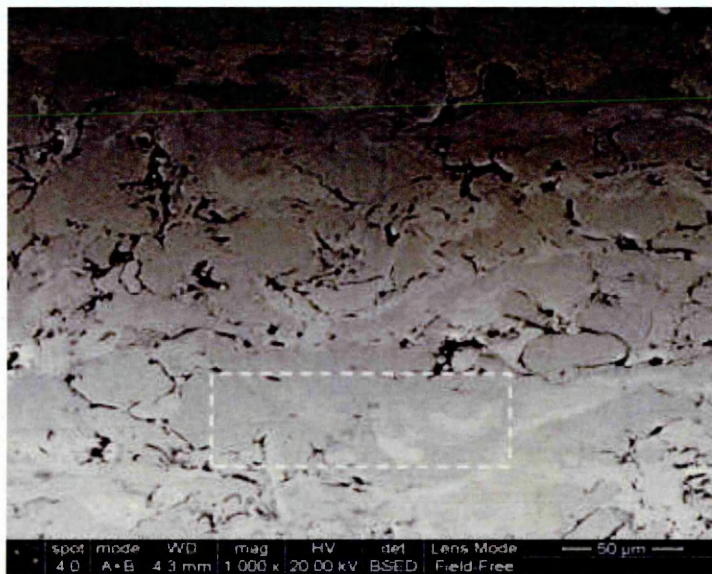


Figure 4.16: High contrast backscattered electron micrograph of a cross-section of as sprayed 300 μm thick as sprayed Al-Zn-In coating. The enclosed area was used for EDX analysis.

The microstructure of the as sprayed 300 μm thick Al-Zn-In coating is shown in **Figure 4.16**. Two distinct phases, that appears to be dark and light grey in colour, were clearly evident from the backscattered micrograph shown in **Figure 4.16**. The average composition of the two distinct phases is given in **Table 4.4**.

Table 4.4: Average composition analysis of as sprayed Al-Zn-In coating using EDX semi-quantitative data.

Average composition			
As sprayed Al-Zn-In coating	Al (at %)	Zn (at %)	O (at %)
Light grey region	91 ± 4.	1 ± 0	8 ± 5
Dark grey region	93 ± 2	-	7 ± 2

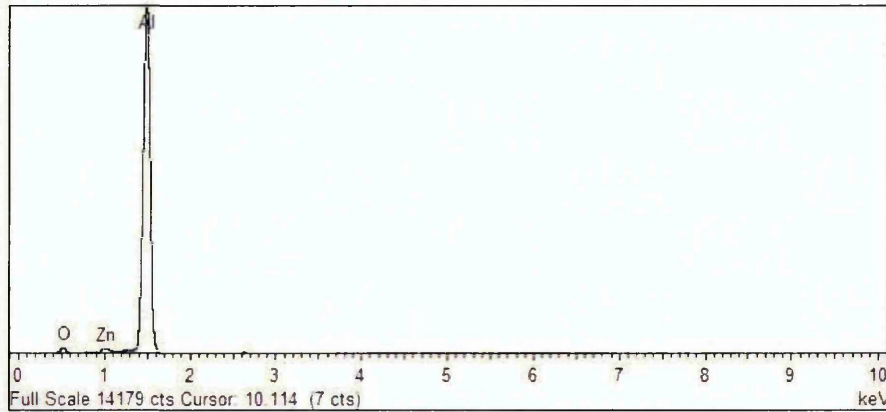


Figure 4.17: EDX spectrum of as sprayed Al-Zn-In coating from the enclosed region shown in **Figure 4.16**.

The EDX spectrum of the enclosed area shown in **Figure 4.16**, which covers both dark and light grey regions, affirms presence of higher concentration of Al in those phases than Zn and O. The presence of indium was not traced using EDX as the concentration of indium in the coating, as shown in **Table 3.1**, was below the detection limit of the technique.

Figure 4.18 (a) and (b) shows the backscattered electron micrographs of the Al coating and underlying masked mild steel substrate after 1000 hours in neutral salt spray test.

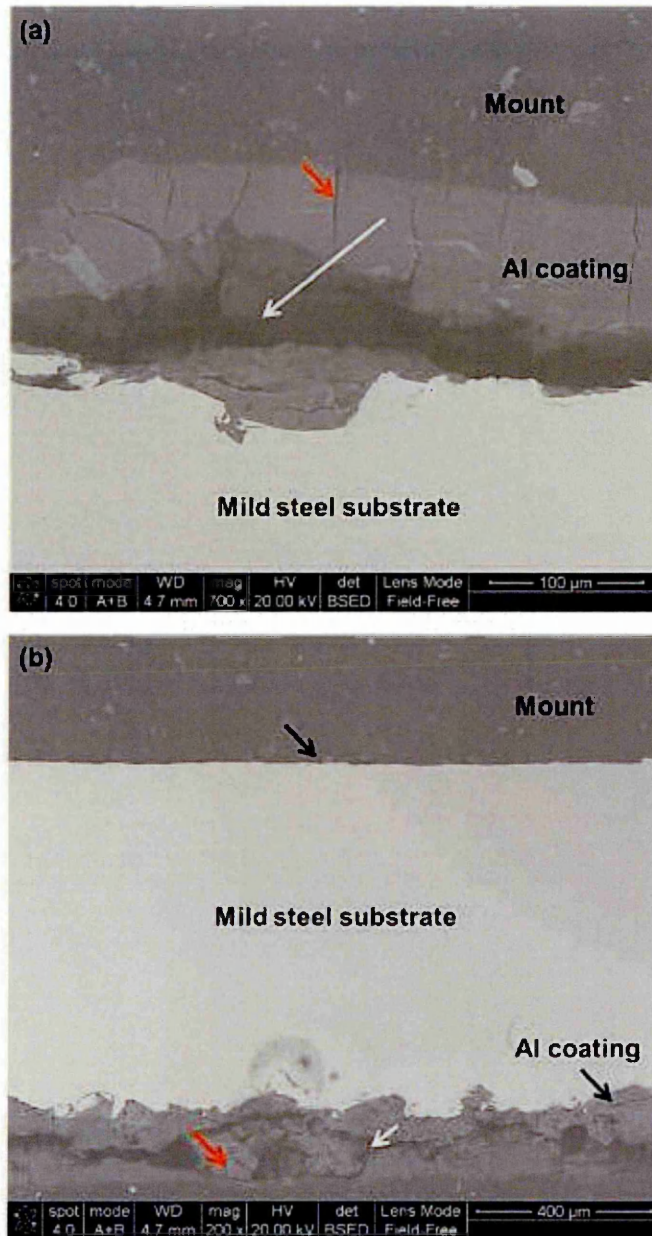


Figure 4.18: Backscattered electron micrograph of (a) Al coating after 1000 hours of neutral salt spray test (b) cross-section of the masked area showing exposed mild steel substrate. The thickness of the coating was 50 μm.

It is evident from **Figure 4.18** (a) that Al coating showed discontinuities, marked by red arrow after the salt spray test, delamination of the coating was also observed which is shown by the white arrow in both **Figure 4.18** (a) and (b).

Figure 4.19 (a'), (b') and (c') shows the EDX spectrum obtained from different regions of the cross-section of the exposed Al coatings shown in **Figure 4.18** (a).

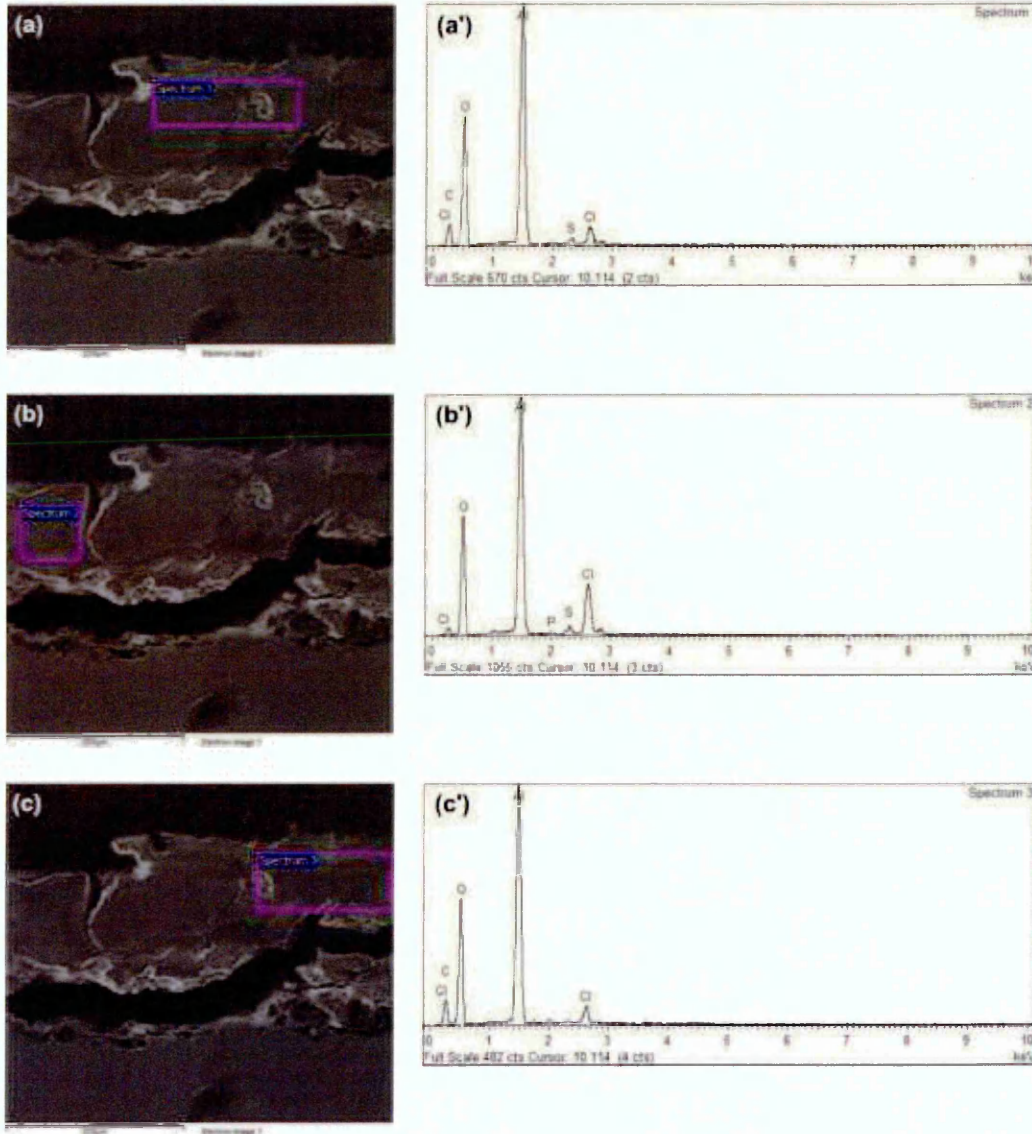


Figure 4.19: (a'), (b') and (c') shows the EDX spectrum of the cross-section of the exposed Al coating shown in (a), (b) and (c).

The EDX analysis at different areas of the cross-section of the Al coating, as shown in **Figure 4.19** (a'), (b') and (c') indicated the presence of oxygen in higher concentrations than in the as-sprayed coating, shown in **Figure 4.13**, suggesting aluminium oxides after exposure. This was confirmed by the X-ray diffraction analysis of Al coating corrosion product formed after 500 and 1000 hours, shown in **Figure 4.10** (a) and (b), which indicated the presence of bayerite and dawsonite as the dominant phases. The cross-section of the masked area of the underlying mild steel substrate, see **Figure 4.18** (b) marked by black arrow showed no significant signs of corrosion confirming the fact that Al coating was mostly consumed, see lower part of **Figure 4.18** (b).

The cross-section of Al-Zn-In, as shown in **Figure 4.20** (a) revealed the presence of different phases, one marked with red arrow is the light grey appearing phase and the phase marked with white arrow appears dark grey, possibly indicating oxidised and metallic regions of the coating. Unlike the Al coating after 1000 hours of exposure in the neutral salt spray test, no convincing evidence of coating discontinuity or delamination was observed, see **Figure 4.20** (a). **Figure 4.20** (b) showed no conclusive evidence of underlying mild steel substrate corrosion, however the formation of two distinct phases can be clearly seen from **Figure 4.20(b)**.

The EDX analysis of different regions of the cross-section of Al-Zn-In coating, shown in **Figure 4.21** (a'), (b') and (c') confirmed that the light grey regions were rich in oxygen, indicating formation of oxides, while the dark grey regions still showed the presence of un-oxidised Al, suggesting the

presence of metallic aluminium in the Al-Zn-In coating in comparison to Al coating, as shown in **Figure 4. 19** (a'), (b') and (c').

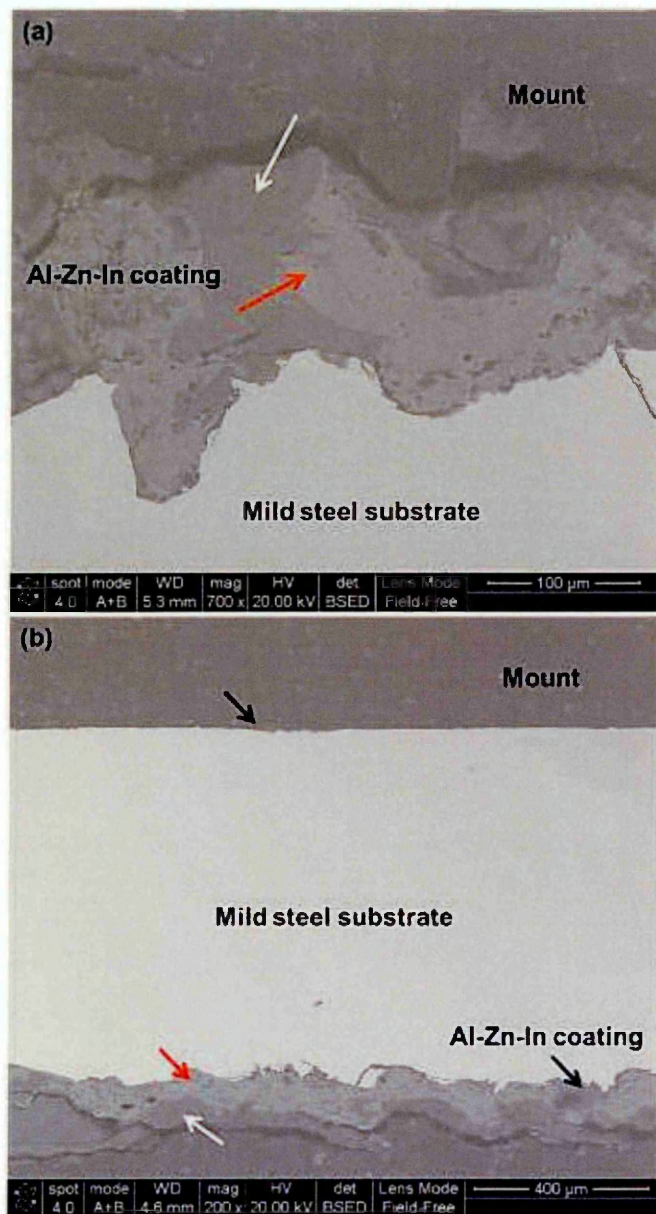


Figure 4.20: Backscattered electron micrograph of (a) Al-Zn-In coating after 1000 hours of neutral salt spray test (b) cross-section of the masked area showing the exposed mild steel substrate. The thickness of the coating was 50 μm.

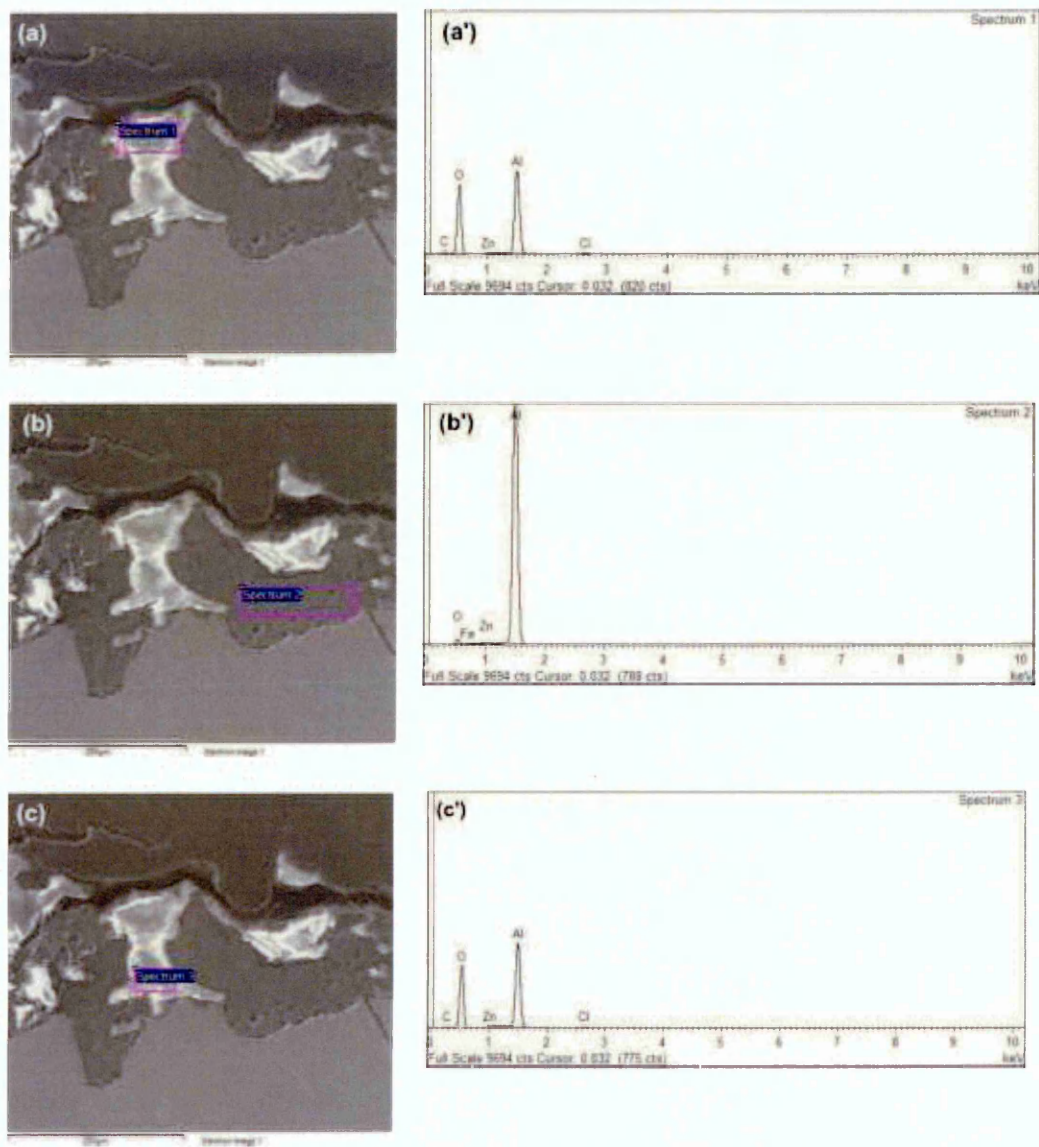


Figure 4.21: (a'), (b') and (c') shows the EDX spectrum of the cross-section of the exposed Al-Zn-In coating shown in (a), (b) and (c).

The Zn-Al coating showed formation of cracks, suggestive of a cohesive failure of the coating. The EDX analysis of the Zn-Al coating showed variation in oxide content throughout different regions of the coating suggesting uniform corrosion throughout the cross-section of the coating, which was also reported by other researchers [146].

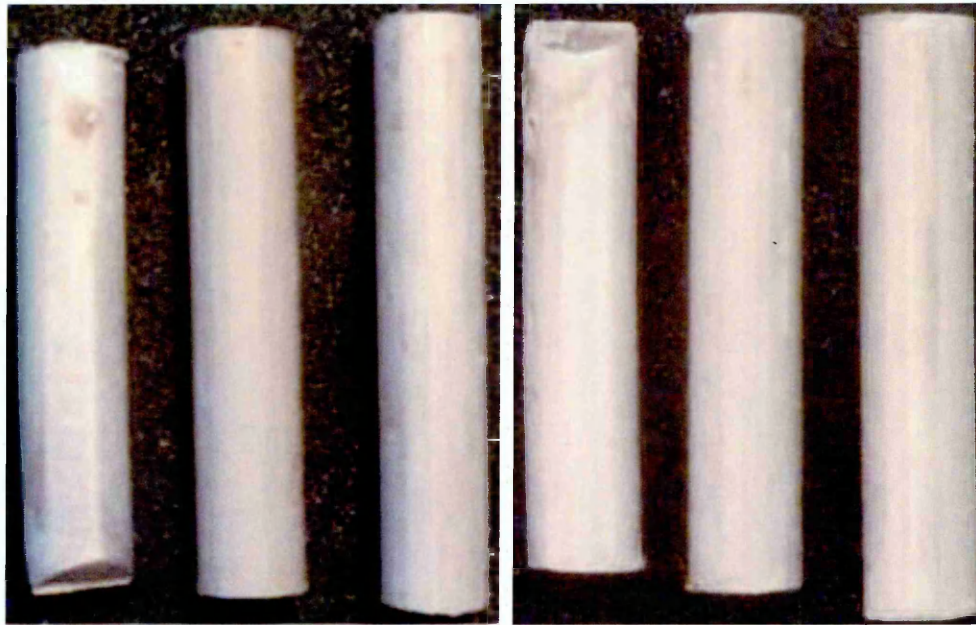
4.1.2 Oxidative weight change measurement of Al-Zn-In and Al-Ti-C coatings

The neutral salt spray corrosion test to ASTM B117 was conducted on Al-Zn-In and Al-Ti-C alloy coatings in order to understand the weight change per unit area of the coatings in comparison to their feedstock alloys. Pure Al and Al-Zn in form of feedstock and coatings were used for comparison purposes. **Figure 4.22** (a-d), **Figure 4.23** (a-d), **Figure 4.24** (a-d) and **Figure 4.25** (a-d) shows the photographs of pure Al, Al-Zn, Al-Zn-In and Al-Ti feedstock alloys exposed to neutral salt spray test. **Table 4.5** shows the measured weights of the feedstock alloys during specified durations of the tests. **Figure 4.26** (a-d), **Figure 4.27** (a-d), **Figure 4.28** (a-d) and **Figure 4.29** (a-d) shows the photographs of pure Al, Al-Zn, Al-Zn-In and Al-Ti coatings exposed to neutral salt spray test. **Table 4.6** shows the measured weights of the coatings during specified durations of the tests.



(a)

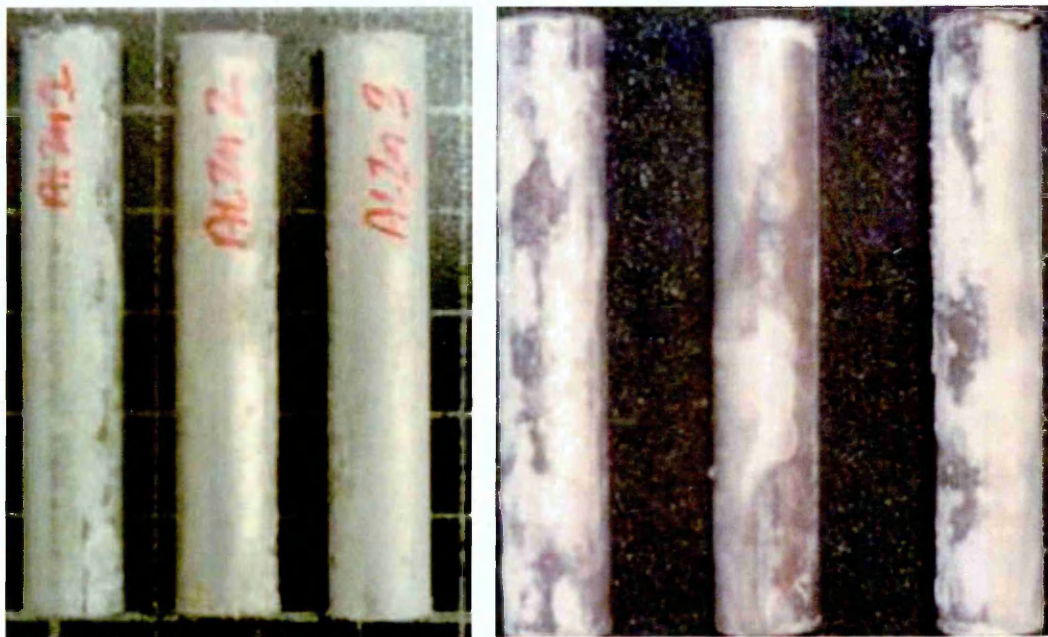
(b)



(c)

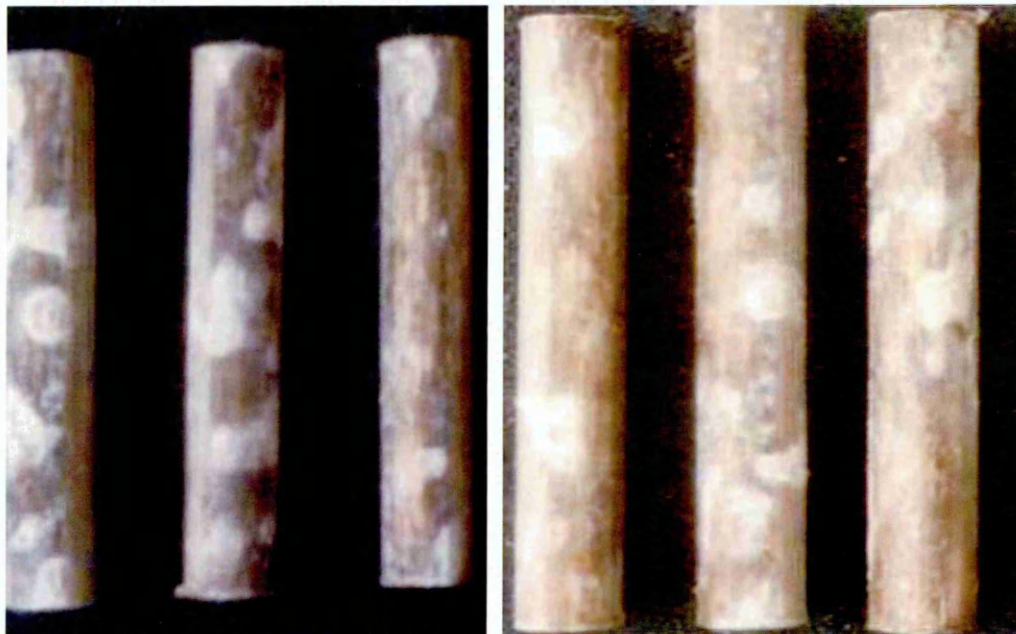
(d)

Figure 4.22: Pure Al feedstock rods after (a) 48 hours (b) 336 hours (c) 672 hours and (d) 1008 hours of exposure in neutral salt spray test.



(a)

(b)



(c)

(d)

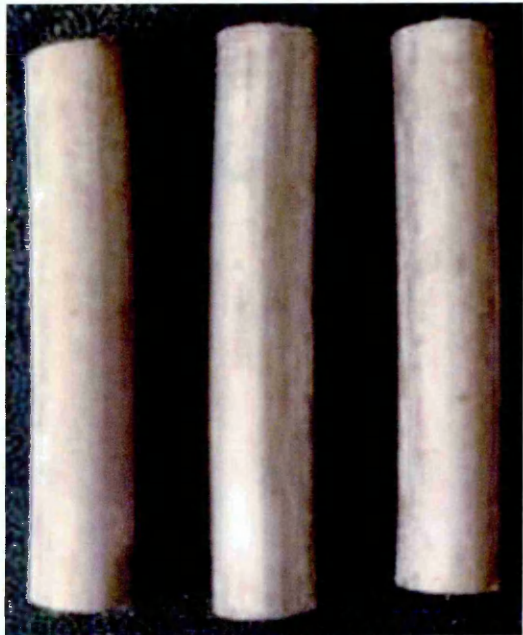
Figure 4.23: Al-Zn feedstock rods after (a) 48 hours (b) 336 hours (c) 672 hours and (d) 1008 hours of exposure in neutral salt spray test.



(a)



(b)



(c)



(d)

Figure 4.24: Al-Zn-In feedstock rods after (a) 48 hours (b) 336 hours (c) 672 hours and (d) 1008 hours of exposure in neutral salt spray test.

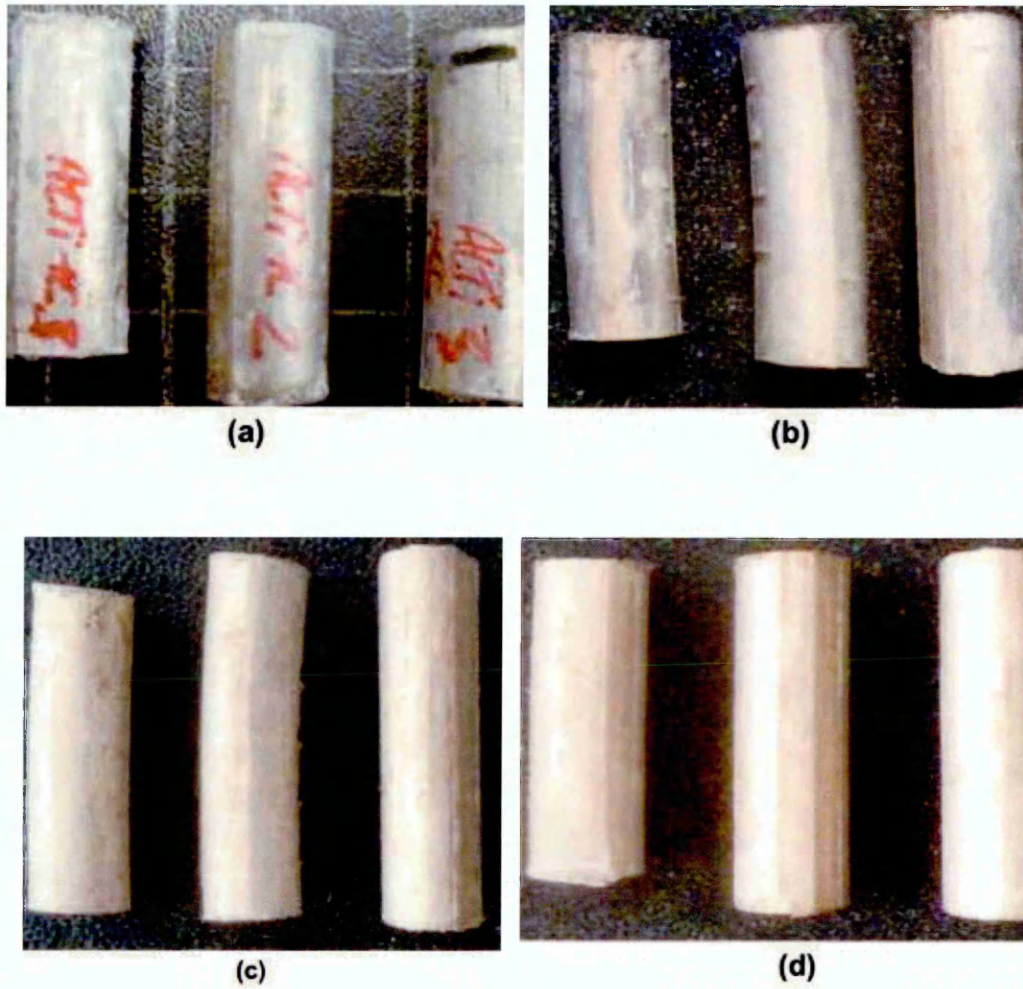


Figure 4.25: Al-Ti-C feedstock rods after (a) 48 hours (b) 336 hours (c) 672 hours and (d) 1008 hours of exposure in neutral salt spray test.

Table 4. 5: Weight measurements after specific exposure period of the alloy feedstock samples exposed to neutral salt spray corrosion test.

Alloys	Weight measurements (g)							
	Initial weight	48 hours	168 hours	336 hours	504 hours	672 hours	840 hours	
Pure Al								
1	9.1934	9.1932	9.1930	9.1932	9.1936	9.1939	9.1937	
2	9.9015	9.9034	9.9037	9.9043	9.9046	9.9053	9.9057	
3	10.3088	10.3078	10.3106	10.3106	10.3112	10.3124	10.3127	
Al-Zn								
1	11.2820	11.2824	11.2820	11.2798	11.2821	11.2831	11.2850	
2	11.0996	11.1008	11.1019	11.1029	11.1036	11.1056	11.1061	
3	11.1932	11.1958	11.1943	11.1929	11.1931	11.1956	11.1968	
Al-Zn-In								
1	10.9487	10.9500	10.9454	10.9459	10.9482	10.9488	10.9490	
2	11.3969	11.3979	11.3981	11.3948	11.3957	11.3963	11.3969	
3	10.9490	10.9499	10.9486	10.9471	10.9461	10.9466	10.9472	
Al-Ti-C								
1	5.3266	5.3279	5.3273	5.3268	5.3273	5.3273	5.3284	
2	5.9202	5.9214	5.9207	5.9204	5.9212	5.9214	5.9219	
3	5.9201	5.9210	5.9223	5.9216	5.9216	5.9221	5.9228	

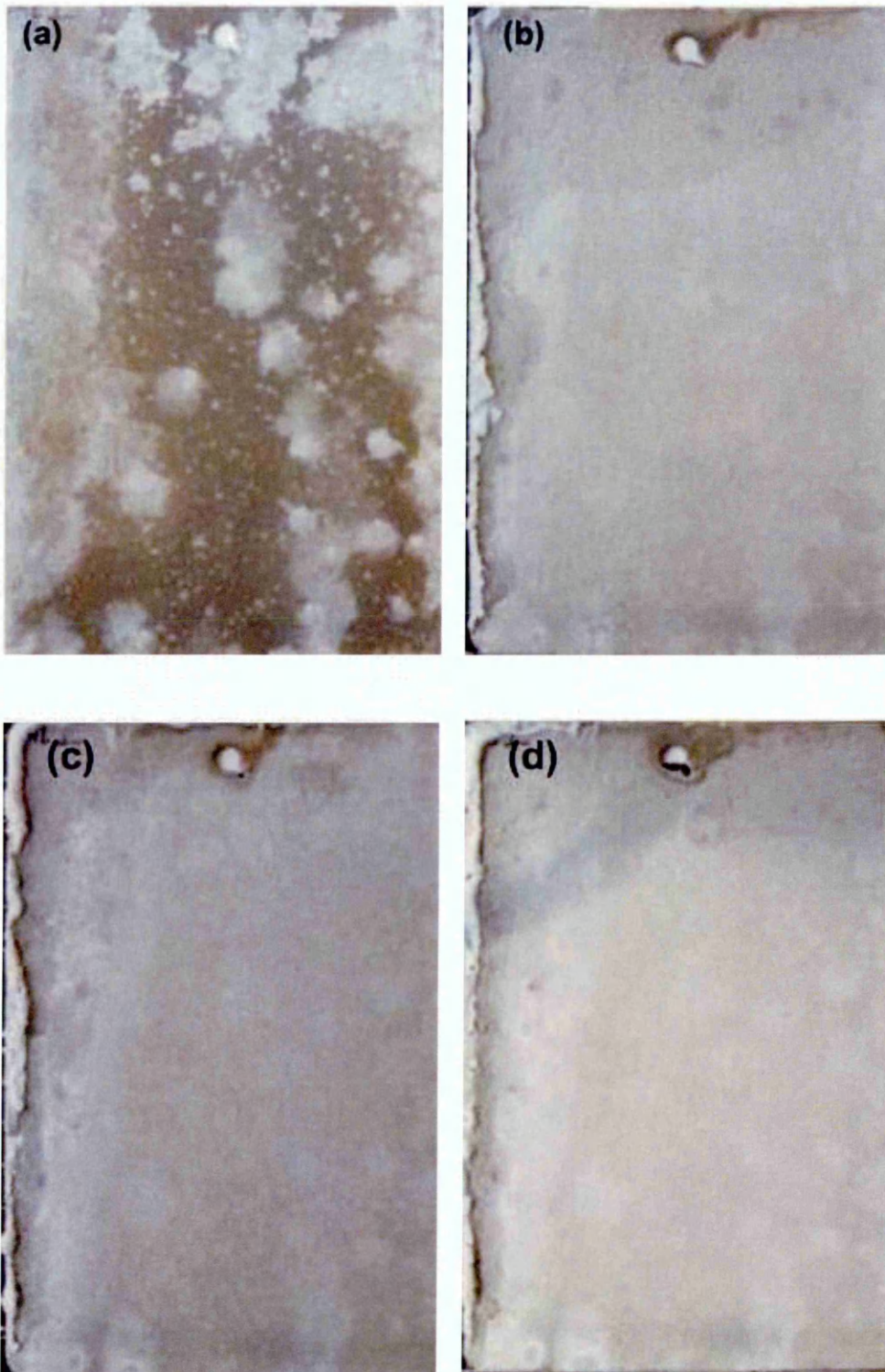


Figure 4.26: Pure Al coating after (a) 48 hours (b) 336 hours (c) 672 hours and (d) 1008 hours of exposure in neutral salt spray test.

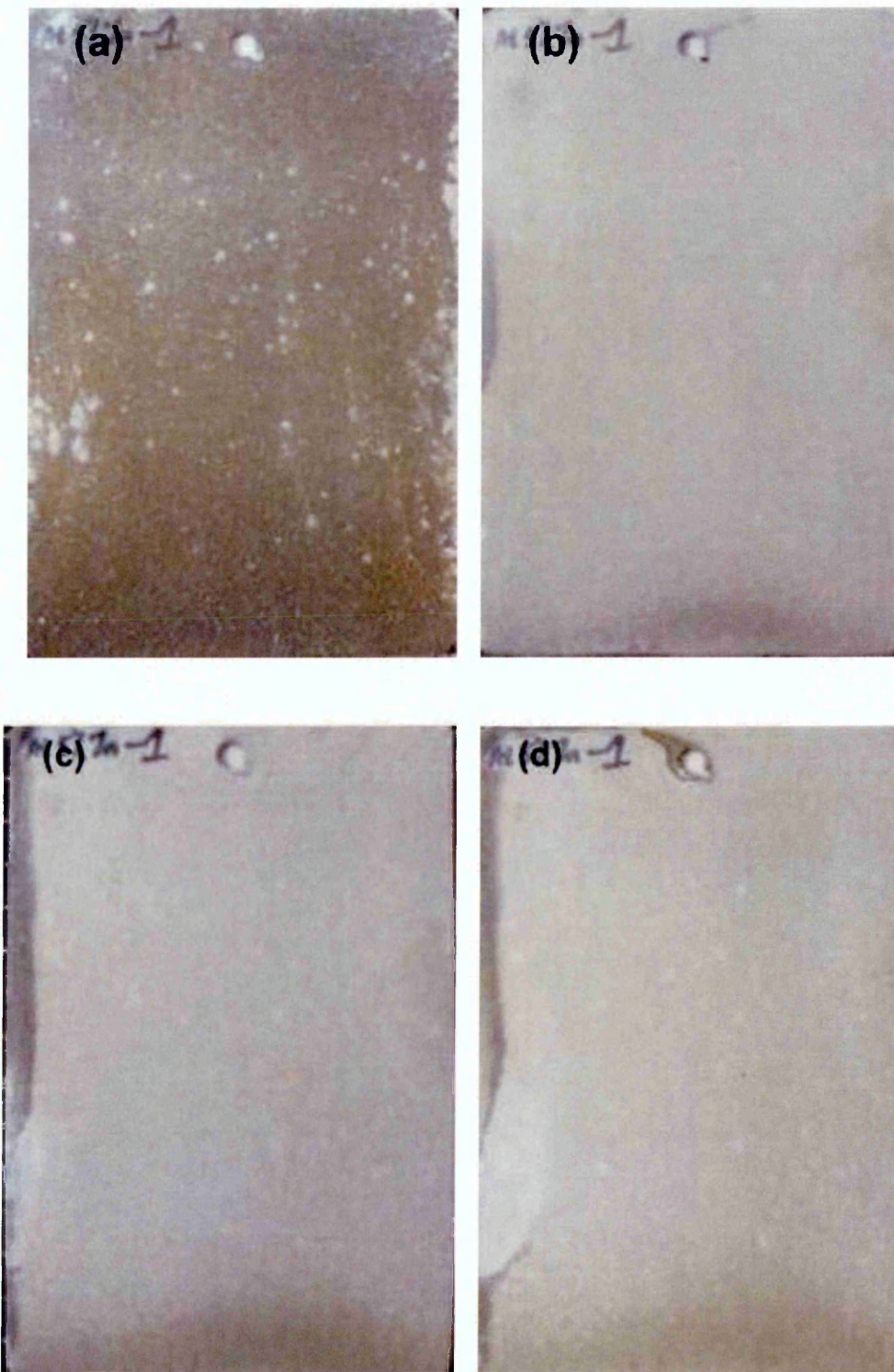


Figure 4.27: Al-Zn coating after (a) 48 hours (b) 336 hours (c) 672 hours and (d) 1008 hours of exposure in neutral salt spray test.

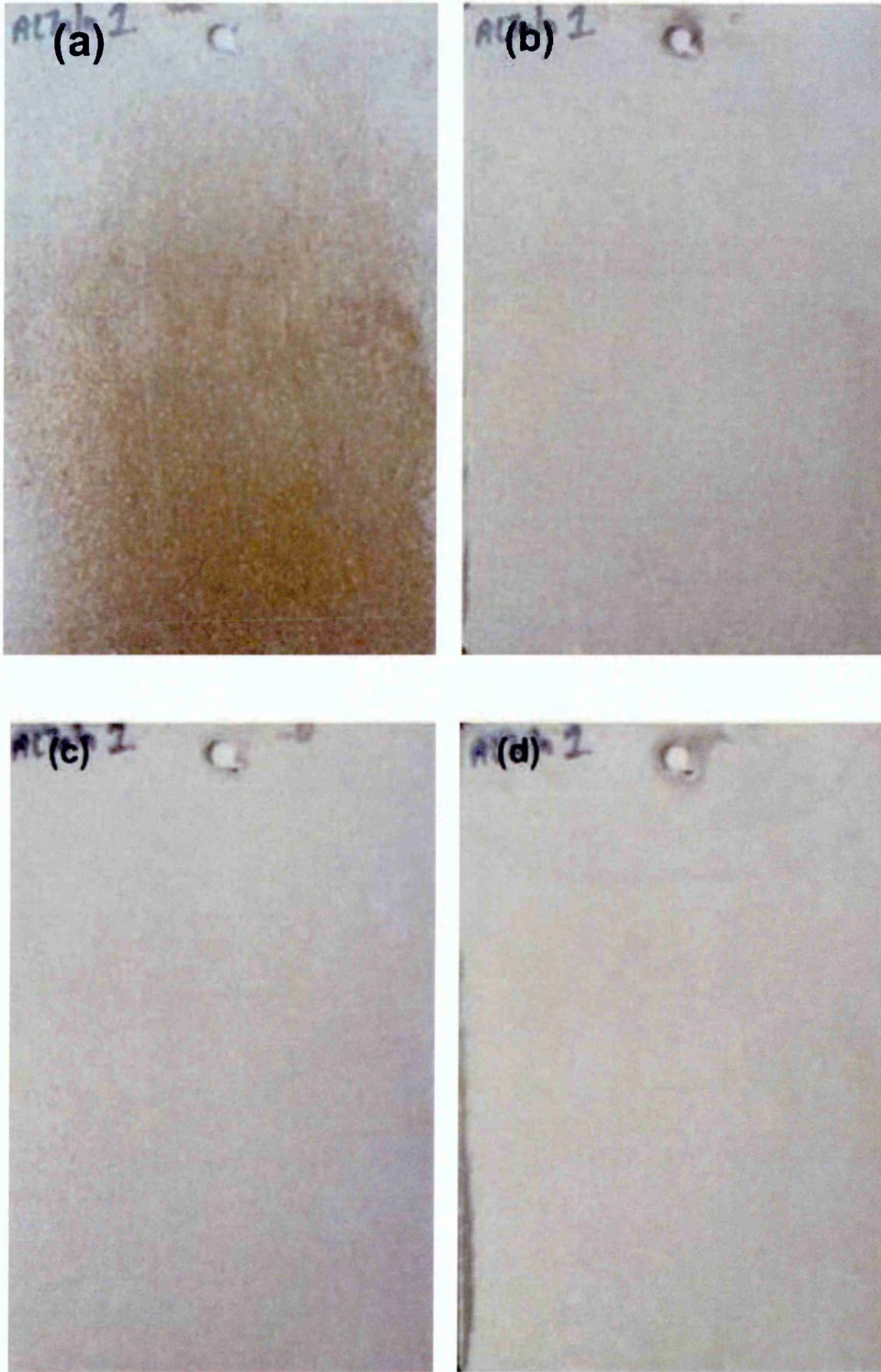


Figure 4.28: Al-Zn-In coating after (a) 48 hours (b) 336 hours (c) 672 hours and (d) 1008 hours of exposure in neutral salt spray test.

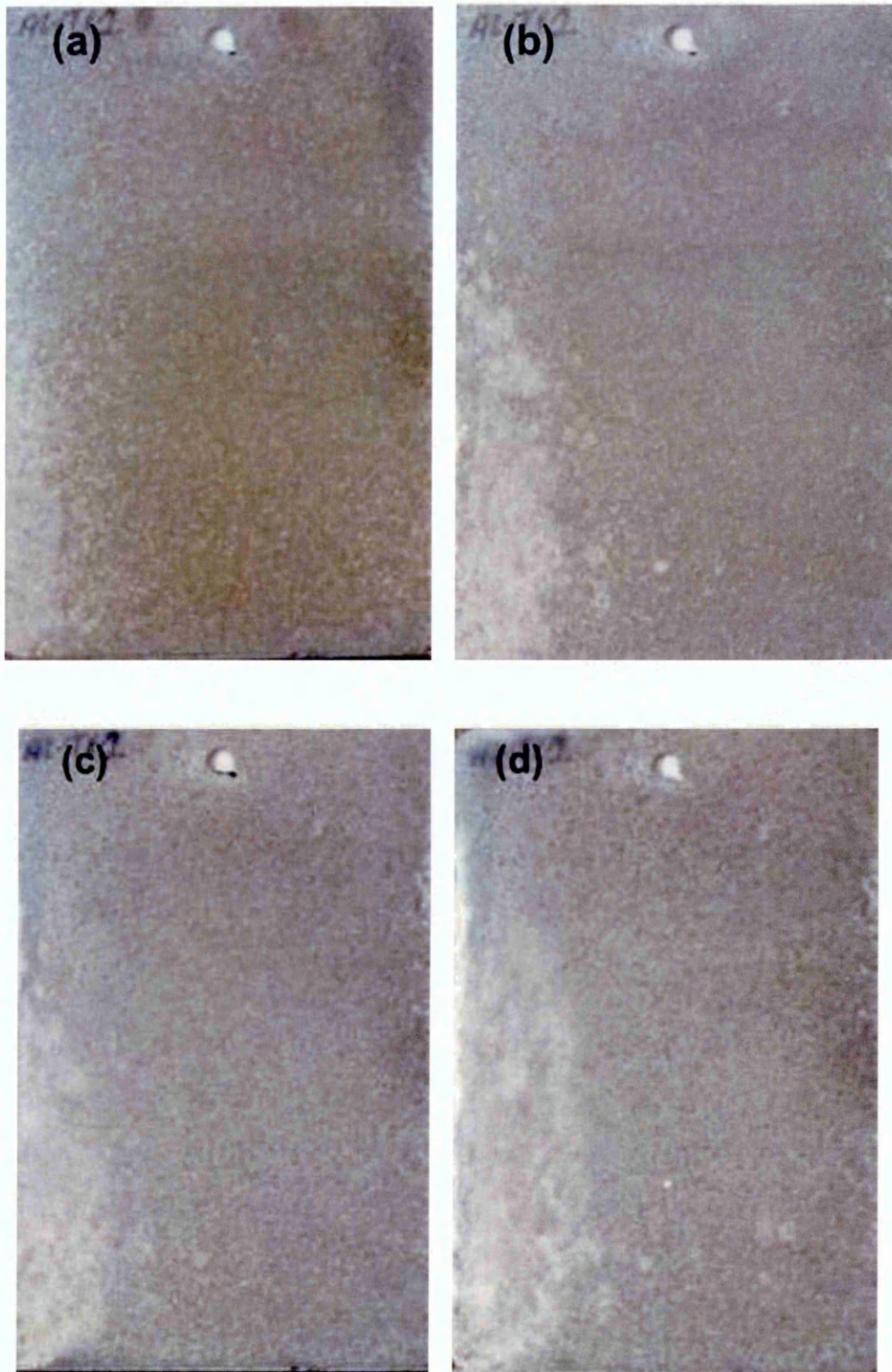


Figure 4.29: Al-Ti-C coating after (a) 48 hours (b) 336 hours (c) 672 hours and (d) 1008 hours of exposure in neutral salt spray test.

Table 4.6: Weight measurements after specific exposure period of the coated samples exposed to neutral salt spray corrosion test.

Coatings	Weight measurements (g)						
	Weight of the mild steel substrate = 95.775 g						
Pure Al	Initial weight	48 hours	168 hours	336 hours	504 hours	672 hours	840 hours
1	114.6330	115.5806	116.1306	116.0194	116.0234	115.9492	115.9106
2	110.2342	111.1990	111.6852	111.6796	111.7456	111.7546	111.7706
3	110.9392	111.8698	112.4256	112.4898	112.6196	112.6410	112.6954
Al-Zn							
1	120.4455	121.4360	122.0735	122.2185	122.3990	122.4660	122.5245
2	110.7784	111.6622	112.1500	112.1674	112.30778	112.3662	112.4284
3	116.9654	117.8048	118.3974	118.4926	118.6538	118.7100	118.7700
Al-Zn-In							
1	113.8302	114.5856	115.0636	115.0776	115.2092	115.2610	115.3200
2	113.5482	114.4220	114.9092	114.9044	115.0400	115.0812	115.1480
3	115.1786	115.8860	116.3194	116.3500	116.4942	116.5514	116.6180
Al-Ti-C							
1	109.7352	110.1574	110.5930	110.5920	110.7604	110.8206	110.8922
2	108.6310	109.1490	109.7388	109.8412	110.0152	110.0712	110.1190
3	108.6278	109.0854	109.6636	109.8092	109.9900	110.0630	110.1228

It is important to note that the photographs of the feedstock alloys and the coatings shown in **Figure 4.22** to **Figure 4.25** (a-d) and **Figure 27** to **Figure 30** (a-d) were just before measuring the weights of the samples after specified exposure period. The samples were manually cleaned, without using any chemical reagents, by using a soft bristle brush until the loose corrosion product was removed from the surface. Any manual cleaning procedure which could have resulted in distorting the surface, such as scrubbing using hard bristle brush or excessive rubbing of surface, of either alloy or coating while removal of corrosion product was avoided. However, overzealous cleaning may result in underestimated rate of corrosion.

After 48 hours of exposure, Al feedstock alloy shown in **Figure 4.22** (a) showed no significant changes, however the Al-Zn alloy, see **Figure 4.23** (a) and Al-Zn-In alloy, see **Figure 4.24** (a) showed formation of adherent corrosion product on the surface. Similar observation was made for Al-Ti-C alloy feedstock after 48 hours, see **Figure 4.25** (a), but was less than the Al-Zn and Al-Zn-In alloys. With an increase in the exposure time to 336 hours, the Al-Zn and Al-Zn-In feedstock alloys see **Figure 4.23** (b) and **Figure 4.24** (b), confirmed that the alloys were actively corroding in comparison to Al and Al-Ti-C feedstock alloys, see **Figure 4.22** (b) and **Figure 4.25** (b).

Similar observation for Al-Zn and Al-Zn-In feedstock alloys was also made after 672 hours of exposure, see **Figure 4.23** (c) and **Figure 4.24** (c) in comparison to Al and Al-Ti-C feedstock alloy, see **Figure 4.22** (c) and **Figure 4.25** (c). After 1000 hours of exposure, the formation of corrosion product on the surface of the Al-Zn and Al-Zn-In feedstock alloys, see **Figure 4.23** (d)

and **Figure 4.24** (d) was more pronounced than Al and Al-Ti-C feedstock alloys, see **Figure 4.22** (d) and **Figure 4.25** (d).

This illustrated that even after 1000 hours of exposure, the Al-Zn and Al-Zn-In alloys were actively corroding, confirming that Zn and In were key alloying elements responsible for maintaining the surface of Al alloy active [115,220].

Surface staining of Al coatings after 48 hours of exposure in the neutral salt spray test was evident from **Figure 4.26** (a), similar to what was observed during the salt spray test of Al coatings with artificial defect, see **Figure 4.2** (c). Comparing the Al-Zn and Al-Zn-In coatings after 48 hours of exposure revealed that Al-Zn coating showed formation of spots of adherent corrosion product on the surface of the coating, see **Figure 4.27** (a) while Al-Zn-In also showed some dark regions on the surface, but not as pronounced as Al coating.

After 336 hours of exposure, Al coating exhibited formation of adherent corrosion product on the edge of the coating, see **Figure 4.26** (b), while the Al-Zn coating showed initiation of dark area near the edges of the coating. Appearance of a similar dark area formation on the edges of the Al-Zn-In coating surface, see **Figure 4.28** (b) was also reported, which was more pronounced in Al-Zn coating. With increase in the exposure period to 672 and 1008 hours, the appearance of the dark area at the edges of the Al-Zn coating, see **Figure 4.27** (c-d), increased, however for Al-Zn-In coating, no significant change in the dark area along the edge of the coating, see **Figure 4.28** (c-d) was observed. For Al coating after 672 and 1008 hours of

exposure, increase in the formation of corrosion product on the edge of the coating was observed, see **Figure 4.26** (c-d).

For Al-Ti-C coating, with the increase in the exposure period from 48 hours to 1008 hours, increase in the formation of adherent corrosion product was observed, see **Figure 4.29** (a-d). The visual observation clearly showed that the corrosion product formed near the edges of the Al-Ti-C coating, with increase in the exposure period, increased over the surface of the coating. It is important to note that for all the coatings, no sign of substrate corrosion was observed.

The weights of pure Al, Al-Zn-In, Al-Zn and Al-Ti-C in form of feedstock alloys and coatings at various intervals till 840 hours were recorded in **Table 4.5** and **Table 4.6** respectively. In order to analyse and compare the change in weights after exposure of the coated and feedstock alloy samples during neutral salt spray corrosion test, oxidative change in weight per unit area for both alloys and coatings were calculated, which is reported in **Table 4.7** and **Table 4.8** respectively.

Table 4.7: Change in weight per unit area of the feedstock alloys at specified intervals. The measurements are the average value from three different samples.

Time (hours)	Change in weight per unit area (X 10 ⁻⁷ g/mm ²)			
	Al	Al-Zn	Al-Zn-In	Al-Ti-C
48	2.84 ± 0.77	3.60 ± 0.95	2.67 ± 0.17	4.72 ± 0.30
168	4.03 ± 0.86	2.91 ± 0.98	4.09 ± 1.25	4.72 ± 1.30
336	4.40 ± 1.20	4.97 ± 1.30	5.68 ± 0.39	2.64 ± 1.04
504	5.22 ± 1.30	3.59 ± 1.92	3.84 ± 1.03	4.44 ± 0.56
672	7.23 ± 1.60	8.13 ± 2.17	2.59 ± 1.01	5.41 ± 0.91
840	7.70 ± 1.90	11.22 ± 1.60	1.75 ± 0.80	8.61 ± 0.76

Table 4.8: Change in weight per unit area of the coatings at specified intervals. The measurements are the average value from three different samples.

Time (hours)	Change in weight per unit area ($\times 10^{-7}$ g/mm ²)			
	Al	Al-Zn	Al-Zn-In	Al-Ti-C
48	96.75 \pm 1.74	92.35 \pm 7.92	79.52 \pm 8.74	47.57 \pm 4.94
168	150.93 \pm 2.48	150.82 \pm 13.68	127.12 \pm 11.28	102.14 \pm 13.13
336	149.14 \pm 8.49	159.58 \pm 19.85	128.47 \pm 9.84	110.55 \pm 20.03
504	155.95 \pm 14.80	175.99 \pm 21.87	142.41 \pm 9.19	129.58 \pm 21.77
672	154.46 \pm 19.69	182.17 \pm 22.36	181.62 \pm 28.74	134.79 \pm 20.76
840	155.53 \pm 24.45	188.32 \pm 23.27	154.13 \pm 8.37	140.89 \pm 19.72

The plots shown in **Figure 4.30** (a-d) and **Figure 4.31** (a-d) was an attempt to understand the relation of change in weight per unit area of alloys and coatings with respect to time of exposure in the neutral salt spray test.

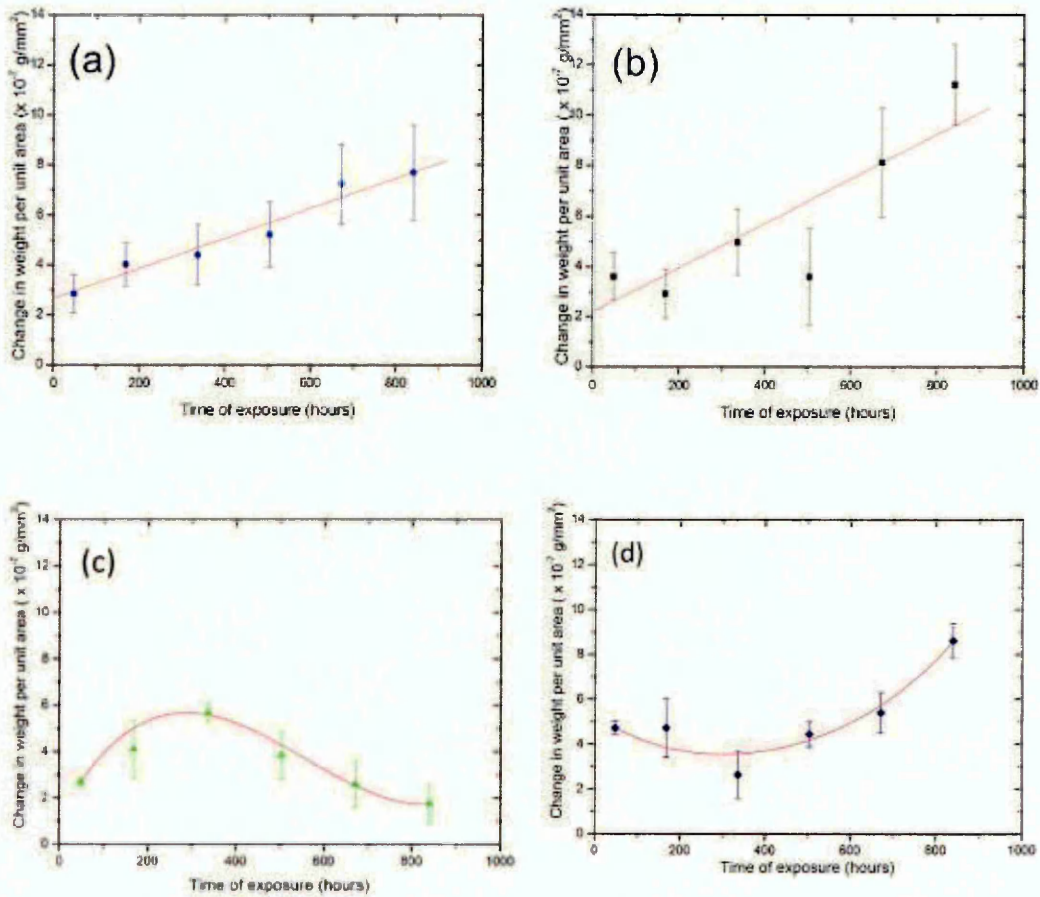


Figure 4.30: Change in weight per unit area vs. time of exposure for (a) Pure Al, (b) Al-Zn, (c) Al-Zn-In and (d) Al-Ti-C feedstock alloys.

A linear increase in the weight change per unit area vs. time of exposure, with an excellent linear regression fit, $R^2 \approx 0.98$, was reported for Al feedstock alloy, see **Figure 4.30** (a). A similar linear relation of change in weight per unit area vs. exposure time with R^2 value ≈ 0.90 was seen for Al-Zn feedstock alloy, see **Figure 4.30** (b). Comparing the behaviour of Al-Zn and Al feedstock's after 48 hours in neutral salt spray test, the Al-Zn feedstock alloy exhibited 27% more increase in the weight per unit area than pure Al feedstock. With over a week of exposure, the Al-Zn feedstock alloy

showed 27 % less increase in the weight per unit area in comparison to pure Al feedstock. These results were supported by the photographs of the pure Al and Al-Zn after 48 hours of exposure, see **Figure 4.22 (a)** and **Figure 4.23 (a)** which as mentioned earlier, clearly indicated that Al-Zn showed initiation of corrosion while pure Al surface was unaffected. The photographs of pure Al and Al-Zn, see **Figure 4.22 (b)** and **Figure 4.23 (b)** taken after 168 hours of exposure revealed a uniform corrosion of Al-Zn alloy feedstock. The 27 % difference in the weight change per unit area between pure Al and Al-Zn feedstock can be attributed to the removal of loose corrosion product from the surface of Al-Zn feedstock alloy, during the cleaning of the alloys prior to weight measurement.

After 2 and 4 weeks of exposure in the neutral salt spray test, the Al-Zn feedstock alloy displayed $\approx 11\%$ increase in the weight per unit area than pure Al feedstock, see **Figure 4.30 (a)** and (b) indicating that Al-Zn alloy was actively corroding even after 4 weeks of exposure. However, at the end of 840 hours of exposure, the difference between the weight increased per unit area of Al-Zn feedstock and pure Al increased to $\approx 31\%$

The Al-Zn-In, showed an unusual behaviour pattern in the change in weight per unit area vs. time of exposure, a polynomial fit with $R^2 \approx 0.9$ was observed, see **Figure 4.30 (c)**. During the first 48 hours, the increase in weight per unit area of Al-Zn-In feedstock was reported to be $\approx 26\%$ and 6% less than what was reported for Al-Zn and pure Al feedstock's respectively. With increase in the exposure time to 1 week, the Al-Zn-In feedstock reported an increase in weight per unit area which was $\approx 28\%$ greater than what was reported for Al-Zn feedstock and marginally same ($\approx 1\%$) as reported for Al

feedstock. Among the weight gain per unit area recorded for Al, Al-Zn and Al-Zn-In feedstock's after 2 weeks of exposure in the neutral salt spray test, Al-Zn-In feedstock showed the highest weight gained per unit area ($\approx 13\%$ > than Al-Zn and 22% > Al feedstock's).

However from the third week to fifth week of exposure, the change in weight per unit area for Al-Zn-In feedstock showed decrease in the value as compared with Al and Al-Zn feedstock. A difference in the weight gained per unit area of Al-Zn-In and Al-Zn coating after 504 hours was reduced to 6%, and was found to be $\approx 26\%$ less than Al feedstock. With exposure time increasing to 672 and 840 hours, the weight change per unit area recorded for Al-Zn-In feedstock was almost 70% less than what was recorded for Al-Zn and pure Al feedstock's. The possible explanation for such behaviour exhibited by Al-Zn-In could be attributed to:

- A large degree of variation in the weight change recorded for Al-Zn-In feedstock. As seen from **Table 4.5**, the variation in the average value of the change in weight showed reduction from the initial weight of the feedstock. This could either be a possible source of experimental error while cleaning the feedstock samples before measuring the weight at each specified intervals or could be that the corrosion product formed on the surface of Al-Zn-In feedstock, with increase in exposure time were not adhering to the surface and were removed during the manual cleaning process. However, the latter is in completed contradiction with Bessone *et al.* [227] who tested Al-Zn, Al-Zn-In and Al-Zn-Sn anodes in sea water and reported that corrosion products formed on

Al-Zn-In were adherent and required long exposure of the alloy in the chemical to clean the surface of the alloy.

As observed from **Figure 4.30** (d), the Al-Ti-C feedstock also showed non-linear (3rd degree polynomial) relation between weight change per unit area vs. time ($R^2 \approx 0.80$). During the first 48 hours of exposure, the increase in the weight per unit area of Al-Ti-C feedstock was found $\approx 40\%$ greater than Al, Al-Zn and Al-Zn-In feedstock's. With 1 week of exposure, no change in the weight per unit area was recorded for Al-Ti-C feedstock. However after completion of 2 weeks of exposure time, $\approx 40\%$ and 53% decrease in the weight change per unit area in comparison with Al, Al-Zn and Al-Zn-In feedstock's was recorded for Al-Ti-C feedstock.

After 672 hours, the increase in weight per unit area for Al-Ti-C was found to significantly higher than Al-Zn-In feedstock ($> 50\%$) but was $\approx 25\%$ lower than pure Al and Al-Zn feedstock's. With completion of 840 hours of exposure time, the increase in weight per unit area for Al-Ti-C feedstock was comparable with the value recorded for pure Al coating but $\approx 30\%$ less than Al-Zn coating. This indicated that after 840 hours of exposure, the corrosion performance of Al-Ti-C was similar to that of pure Al feedstock.

Due to non-linear relation between the weight change per unit area vs. time for Al-Zn-In and Al-Ti-C feedstock alloys, rate of corrosion of the alloys could not be estimated from **Figure 4.30** (c)-(d).

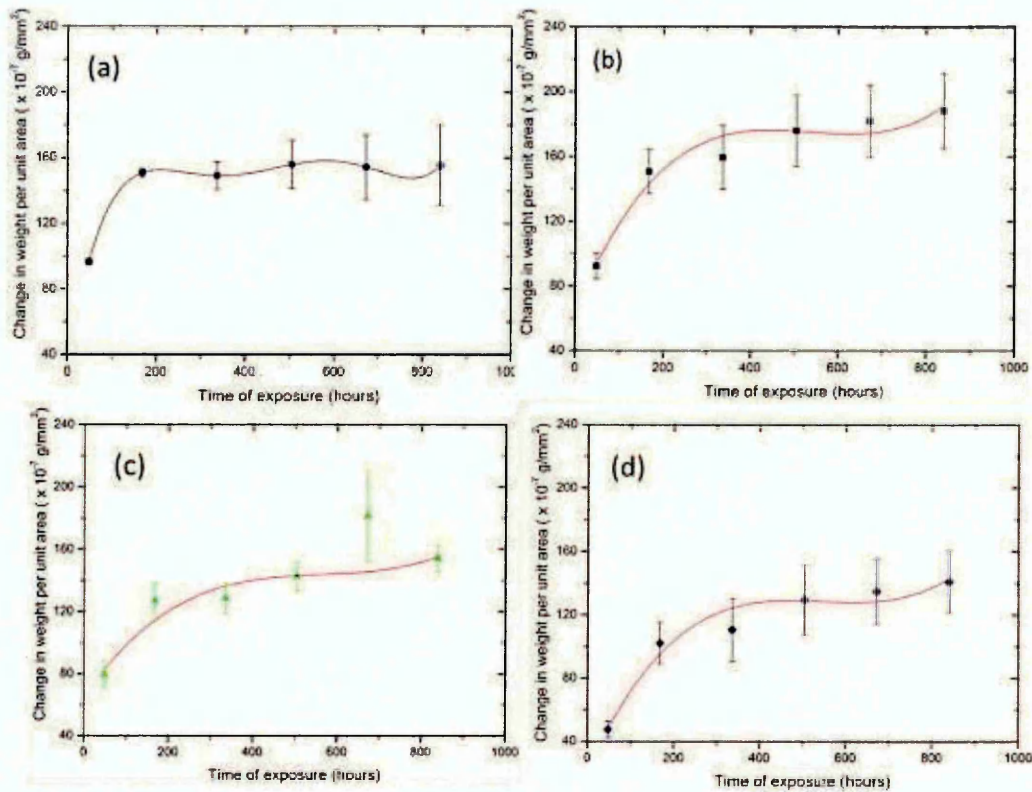


Figure 4.31: Change in weight per unit area vs. time of exposure for (a) Pure Al, (b) Al-Zn, (c) Al-Zn-In and (d) Al-Ti-C coatings.

A non-linear (polynomial function with degree > 3) relation of change in weight per unit area vs. time of exposure for pure Al, Al-Zn, Al-Zn-In and Al-Ti-C coatings was observed, see **Figure 4.31** (a), (b), (c) and (d). A fast increase in the weight change per unit area during initial 168 hours of exposure was seen for all coatings. This fast increase in weight change can be attributed to:

- Due to inherent porosity (non-unique surface of coatings as compared to alloys) the formation of initial corrosion product within the pores could result in 'densification' of coating.

- Higher surface roughness, see **Table 4.9**, causing the oxides entrapment on the surface of the coatings (also changing the surface roughness with respect to time).

During the initial 48 hours of exposure, the weight gain per unit area for Al-Zn coating was found to almost similar to the Al coating, with only a difference of 4% the weight gained per unit area of Al-Zn coating was more than Al coating. After 1 week of exposure period, both Al and Al-Zn coating reported similar increase in the weight per unit area, see **Figure 4.31** (a) and (b).

Now after 2 weeks of immersion time, comparing the graphs of Al and Al-Zn coating, almost a plateau region in weight change per unit area was observed for Al coating, see **Figure 4.31** (a), while a steady increase in the weight change per unit area with increase in exposure time for Al-Zn coating was observed. At the end of 840 hours of exposure, the weight gain per unit area for Al-Zn coating was $\approx 17\%$ > than the value of the weight gain per unit area reported for Al coating. **Figure 4.31** (a) and (b) illustrated that with increase in the exposure period, the Al coating reported a minimal weight gain between each exposure period, however, Al-Zn coating showed $\approx 10\%$ increase in weight per unit area between each exposure period.

From **Figure 4.31** (c), which showed change in weight per unit area vs. time for Al-Zn-In coating, the value of weight gained per unit area was found to be $\approx 17\%$ less than the value reported for Al and Al-Zn coating. With the increase in the exposure time from 48 hours to 1 week, the gain in weight per unit area observed for Al-Zn-In coating was also found to be $\approx 16\%$ less than both Al and Al-Zn coatings. Notice the similarity in the trends of the weight

change per unit area for Al-Zn-In and Al-Zn coatings after 336 hours of exposure, see **Figure 4.31** (b) and (c), unlike Al coating which forms a plateau, see **Figure 4.31** (a), the Al-Zn-In coating like Al-Zn coating showed increase in the weight per unit area between each exposure period till 840 hours. However, after 504 hours, the Al-Zn coating exhibited the value of weight gained per unit area, which was $\approx 19\% >$ than the value reported for Al-Zn-In coating, but after 672 hours this difference was reduced to $< 0.5\%$, this was evident from the data point in the plot shown in **Figure 4.31** (c) at 672 hours. This can be attributed to a greater variation in the weight change within the triplicate Al-Zn-In samples, see table 6 under 672 hours. However, after 840 hours of exposure, the value of the weight gained by Al-Zn-In was reported to be $19\% <$ than the value reported by Al-Zn coating, see **Figure 4.31** (b) and (c), but was similar to the value reported for Al coating

Like the trend in curve obtained for weight change per unit area vs. time for Al-Zn and Al-Zn-In coating, similar trend was obtained for Al-Ti-C coating, see figure 32 (d), except that during the initial 48 hours of exposure, the Al and Al-Zn and Al-Zn-In coatings showed $\approx 40\% >$ increase in the weight per unit area than reported for Al-Ti-C coating. As seen from **Figure 4.31** (d), throughout the various time periods of exposure, the values of the weight gained per unit area for Al, Al-Zn and Al-Zn-In coatings have been a minimum of $25\% >$ than the values observed for Al-Ti-C coating. It is also evident from **Figure 4.31** (d), that Al-Ti-C coating exhibited a minimum of 7% increase in weight per unit area between each of the exposure period unlike Al coating, see **Figure 4.31** (a) and (d).

4.2 Open circuit potential vs. time

Figure 4.32 to **Figure 4.35** represents the open circuit potential (OCP) vs. time plots for Al, Al-Zn, Al-Zn-In and Al-Ti-C coatings respectively. All the measurements were conducted in aerated aqueous media with varying concentrations of 3.5%w/v, 1.0%w/v, 0.1%w/v and 0.01%w/v NaCl solution (OCP was measured for 168 hours, where the potentiostat was set to record potential value in every 100 seconds during all the experiments).

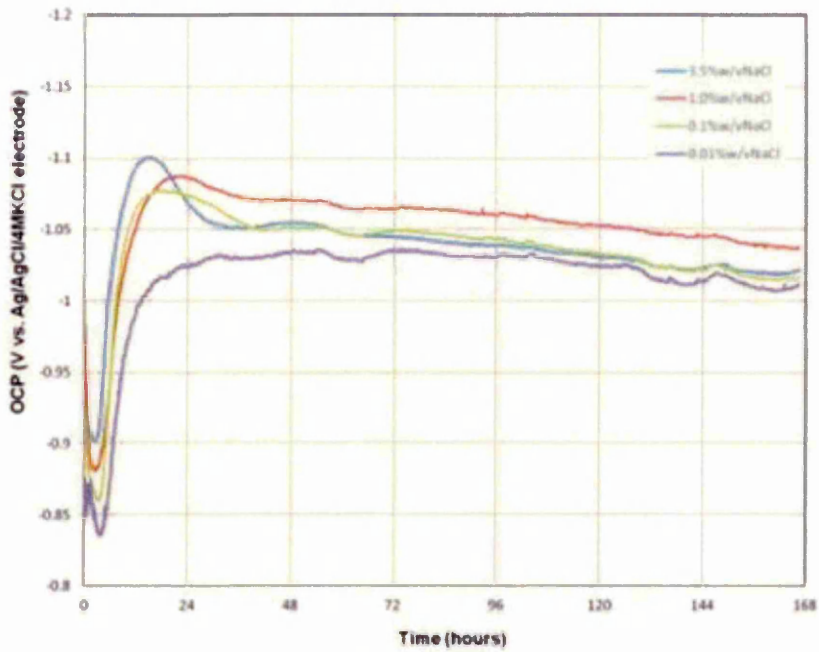


Figure 4.32: Open circuit potential vs. time plot for Al coating subjected to 3.5 % w/v, 1.0% w/v, 0.1%w/v and 0.01%w/v NaCl solution.

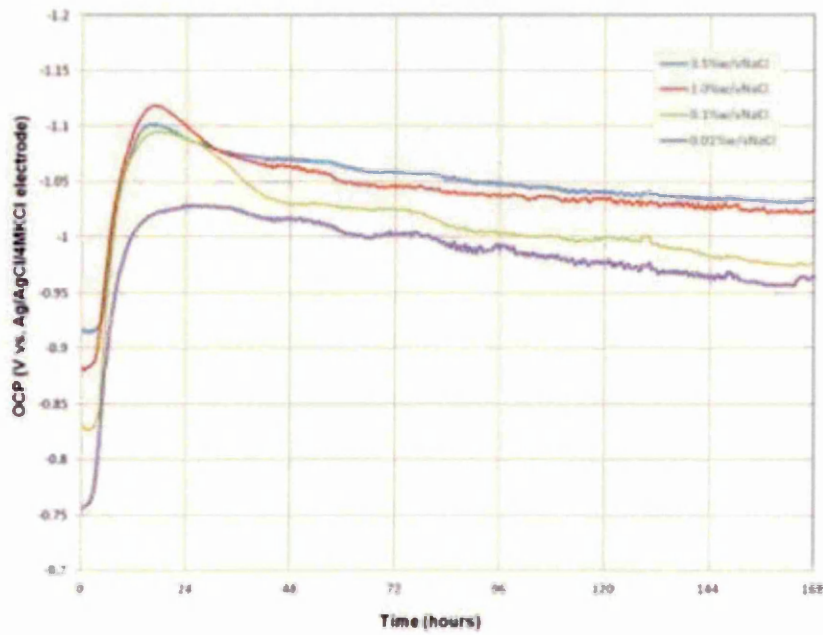


Figure 4.33: Open circuit potential vs. time plot for Al-Zn coating subjected to 3.5 % w/v, 1.0% w/v, 0.1%w/v and 0.01%w/v NaCl solution.

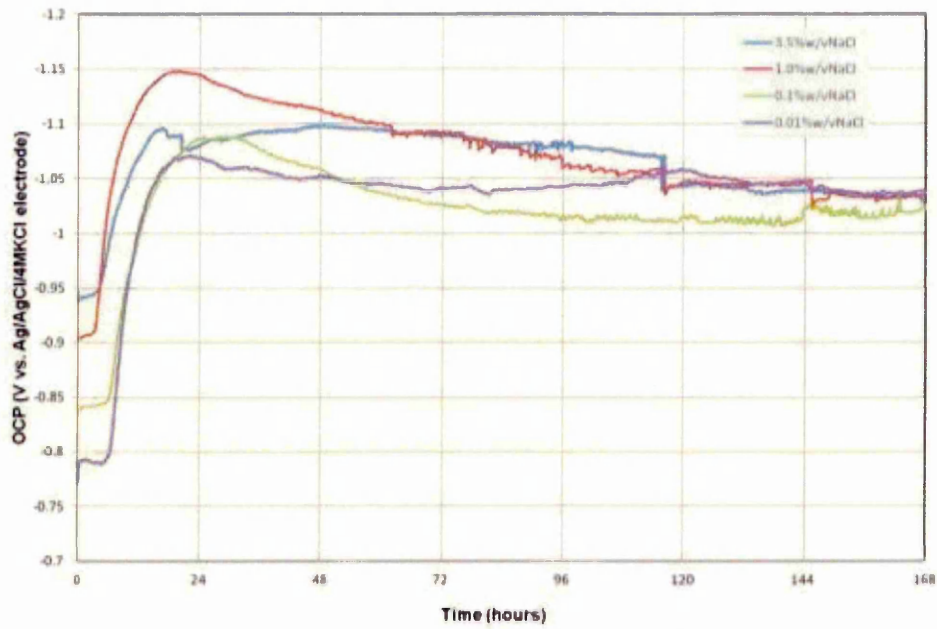


Figure 4.34: Open circuit potential vs. time plot for Al-Zn-In coating subjected to 3.5 % w/v, 1.0% w/v, 0.1%w/v and 0.01%w/v NaCl solution.

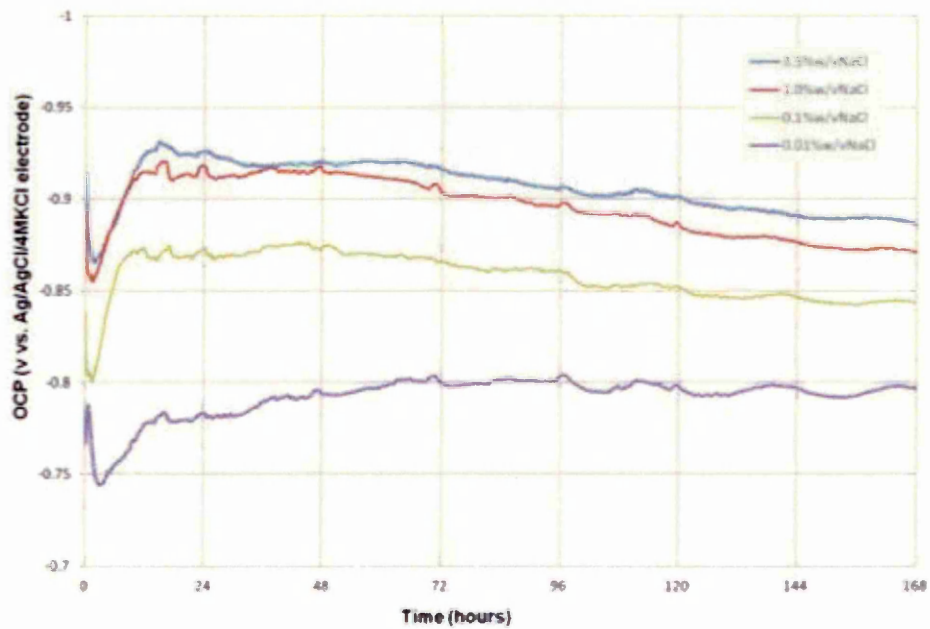


Figure 4.35: Open circuit potential vs. time plot for Al-Ti-C coating subjected to 3.5 % w/v, 1.0% w/v, 0.1%w/v and 0.01%w/v NaCl solution.

The OCP behaviour of Al, Al-Zn, Al-Zn-In and Al-Ti-C coatings in the first 24 hours are shown in **Figure 4.36** to **Figure 4.39** (these plots are the magnified view of the graphs shown in **Figure 4.32** to **Figure 4.35**).

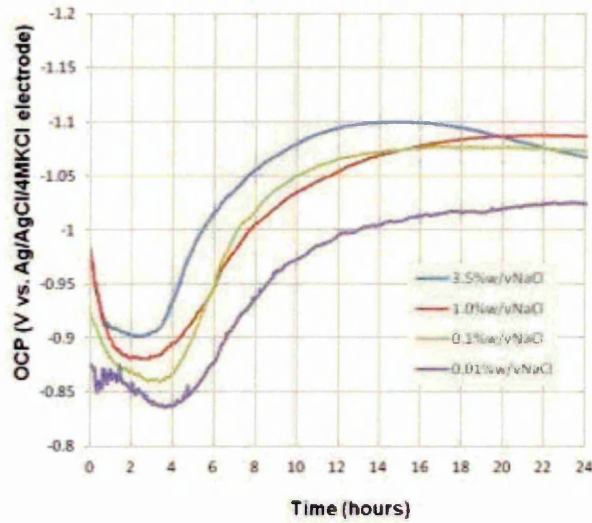


Figure 4.36: Open circuit potential plot for Al coating during 24 hours of immersion in 3.5%w/v, 1.0%w/v, 0.1%w/v, 0.01%w/v NaCl solution.

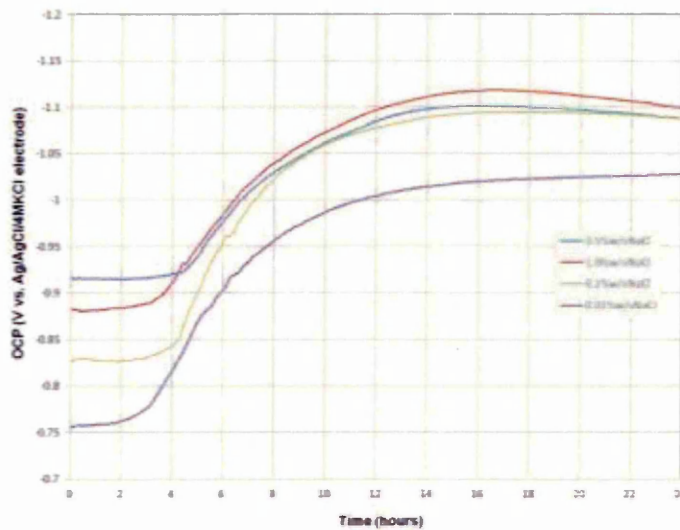


Figure 4.37: Open circuit potential plot for Al-Zn coating during 24 hours of immersion in 3.5%w/v, 1.0%w/v, 0.1%w/v, 0.01%w/v NaCl solution.

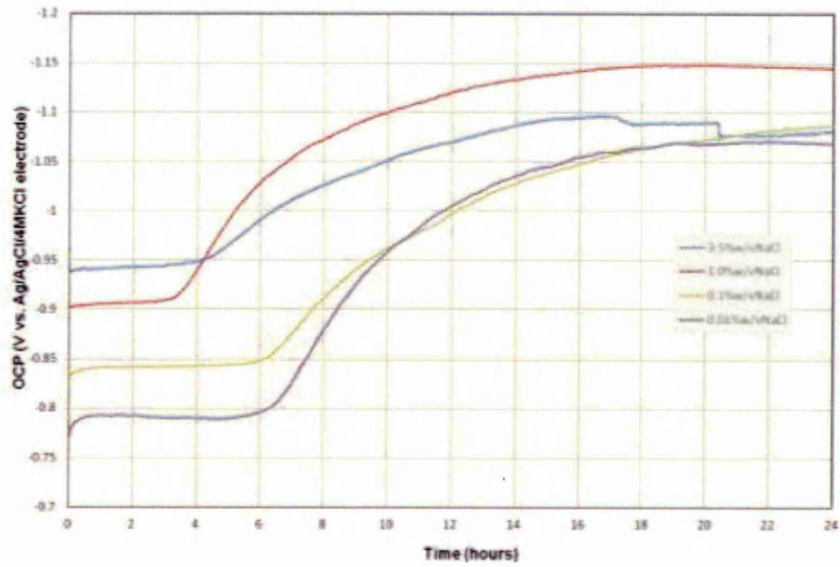


Figure 4.38: Open circuit potential plot for Al-Zn-In coating during 24 hours of immersion in 3.5%w/v, 1.0%w/v, 0.1%w/v, 0.01%w/v NaCl solution.

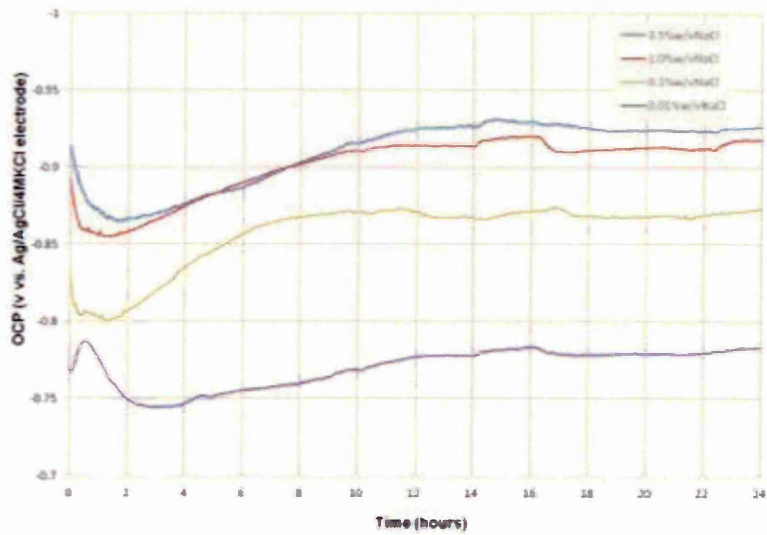


Figure 4.39: Open circuit potential plot for Al-Ti-C coating during 24 hours of immersion in 3.5%w/v, 1.0%w/v, 0.1%w/v, 0.01%w/v NaCl solution.

Al-Zn, Al-Zn-In and Al-Ti-C coating during the first hour of immersion showed similar potential values at 3.5%w/v NaCl (≈ -0.94 V), 1.0% w/v NaCl (≈ -0.9 V), 0.1%w/v NaCl (-0.85 V) and 0.01%w/v NaCl (≈ -0.8 V), see **Figure 4.37**, **Figure 4.38** and **Figure 4.39**. The Al coating reported potential values ≈ -0.04 V lower than the potential values which were recorded for Al-Zn and Al-Zn-In coatings, see **Figure 4.36**.

During the first hour of immersion, Al-Zn, Al-Zn-In and Al-Ti-C coating showed smooth OCP traces, however small abrupt potential fluctuations were observed for Al coating, see **Figure 4.36**. This could be attributed to the increased solution resistance offered by 0.01% w/v NaCl solution, which could have resulted in these abrupt potential oscillations.

The evidence of existence of time required for activation of Al, Al-Zn, Al-Zn-In and Al-Ti-C coatings was evident from the OCP vs. time plots shown in **Figure 4.36** to **Figure 4.39**. This time period has been referred as induction time by *Breslin and Friery* [126] while studying the activation of Al by Zn and In ions, see **Figure 2.39**. Note that the authors used external addition of Zn^{2+} and In^{3+} ions to Al in 3.5%w/v NaCl solution in order to study the synergetic interaction of Zn and In on activation of Al surface.

A similar observation, in terms of induction time, was observed from the OCP vs. time plots within the first 24 hours of exposure for Al, Al-Zn, Al-Zn-In and Al-Ti-C coatings, see **Figure 4.36** to **Figure 4.39**. Comparing Al and Al-Zn coatings, a sharp shift in the OCP towards more electronegative values for all the chloride concentrations (3.5%,1.0%,0.1% and 0.01%) was seen for Al and Al-Zn coatings, see **Figure 4.36** and **Figure 4.37**.

For 3.5 % w/v NaCl, after 4 hours Al coating showed shift in the OCP from -0.87 V to -1.1 V, which then reverted to -1.06 V nearing 24 hours of exposure time. Similar transitions in the OCP values from -0.87 V to -1.08, -0.85 V to -1.06 V and -0.83 V to -1.02 V for 1.0 %, 0.1 % and 0.01 % w/v NaCl was reported for Al coatings, see **Figure 4.36**. Note that just before the sharp shift in the OCP values for Al coating, a drop in the OCP vs time plots (before 4 hours of exposure) was also recorded for all concentrations of NaCl solution.

The Al-Zn coating exposed to 3.5 %, 1.0%, 0.1% w/v NaCl solution showed shift in OCP values from -0.93V, -0.87 V , -0.83 V to \approx - 1.1 V nearing 24 hours of exposure period, see **Figure 4.37**. However for Al-Zn coating exposed to 0.01 % w/v NaCl solution, the shift in the OCP value was recorded from -0.75 V to -1.03 V. However, Al-Zn coating showed no evidence of drop in the OCP values for all concentrations of NaCl solution, which were observed for Al coatings, see **Figure 4.36** and **Figure 4.37**.

The Al-Zn-In coating showed different induction time period for different chloride concentration, see **Figure 4.38**. It can be seen from **Figure 4.38**, that for NaCl concentrations of 3.5 % w/v and 1.0 % w/v, the shift in the potential to more electronegative regions was observed post 4 hours of exposure, however at lower NaCl concentrations of 0.1 % w/v and 0.01% w/v this shift was observed after 6 hours of exposure. It is worthy to be noted that for Al-Zn-In coating exposed to 3.5 % w/v , 0.1 %w/v and 0.01 % w/v NaCl solutions, the shift in the OCP values from -0.94 V, -0.84 V and -0.80 V to \approx -1.06 V was recorded, however for Al-Zn-In coating exposed to 1.0% w/v NaCl solution, the shift in the OCP was \approx 8% more electronegative than the values recorded for 3.5 %, 0.1% and 0.01 % NaCl

For Al-Ti-C coating exposed to 3.5% w/v and 1.0% w/v NaCl solution, the shift in the OCP values from ≈ -0.9 V to -0.92 V was observed, with Al-Ti-C coating exposed to 0.1 % w/v NaCl solution the shift in the OCP from -0.80 V to -0.86 V was recorded. It is important to note that for the above mentioned chloride concentrations (3.5%, 1.0% and 0.1% w/v NaCl), the shift in the OCP towards more electronegative regions was observed after 2 hours of exposure. However, for Al-Ti-C coating exposed to 0.01% w/v NaCl solution, no significant shift in the OCP was observed (from -0.75 V to -0.78 V).

After 24 hours of exposure, Al and Al-Ti-C coating exposed to 3.5% w/v, 1.0%w/v, 0.1% w/v and 0.01% w/v NaCl solutions exhibited a smooth OCP trace with values ranging from -1.0 V to -1.05 V for Al coatings and -0.8 V to -0.9 V for Al-Ti-C coatings till 168 hours, see **Figure 4.32** and **Figure 4.35**. This smooth OCP trace could have been a result of formation of tenacious Al oxide film on the surface of both Al and Al-Ti-C coatings exposed to different NaCl concentrations.

For Al coatings exposed to 3.5%w/v, 1.0%w/v, 0.1% and 0.01%w/v NaCl solution, the formation of this passivating oxide film was evident from the fact that the smooth trace showed gradual shift in OCP value from ≈ -1.08 V at 24 hours to < -1.05 V after completion of 168 hours, see **Figure 4.32** (note that the Al coating exposed to 3.5%w/v NaCl solution recorded the lowest potential value of -1.1 V during the 24 hours of exposure, however for coating exposed to 0.01% w/v NaCl solution, no significant change in the OCP after 24 hours was observed, the value remained in the region of -1.01 V to -1.02 V).

Similar observations have been recorded in the earlier research conducted on Al exposed to halide and sulphate solutions [114,276]. The researchers showed that the penetration power or the ability of the halide ions to detach or penetrate the Al oxide film formed on the surface decreases in the following order $F < Cl < Br < I$ [276].

In the present study, only various concentrations of NaCl were used, it has been shown that even though Cl^- ions were reported to have better penetration effect (following F^- ions in the above mentioned series) on the Al oxide films, this effect was only seen on formation of $\gamma-Al_2O_3$ layer on Al surface [276]. However, in the present study, XRD analysis of the Al coatings post 24 hours and 48 hours of exposure in salt spray cabinet revealed formation of hydrated Al oxide film on the surface of the coating, see **Figure 4.4** and **Figure 4.8**, confirming lesser effectivity of Cl^- ions to cause activation of Al coating resulting in smooth trace with gradual shift in OCP value < -1.05 V, see **Figure 4.32**.

The Al-Ti-C coating exposed to 3.5% w/v and 1.0% w/v NaCl solution showed shift in the OCP values from ≈ -0.93 V at 24 hours to ≈ -0.87 V after 168 hours of exposure, see **Figure 4.35**. For Al-Ti-C coating exposed to 0.1 % w/v and 0.01 % w/v NaCl solution, no significant shift in the OCP values were observed after 24 hours of exposure, see **Figure 4.35**. Although, both Al-Ti-C and Al coating showed smooth potential traces till 168 hours of exposure for all concentrations of NaCl, it is important to note that for Al-Ti-C the OCP recorded for all concentrations of NaCl was < -0.9 V, the lowest of -0.8 V was recorded for Al-Ti-C coating exposed to 0.01% w/v NaCl solution.

The OCP vs. time plot for Al-Ti-C coating was similar to one obtained during previous research [107,276], where addition of various concentrations of Ti were chosen to study their effect on the electrochemical properties of Al alloys (the alloys were tested using standard 0.5M NaCl solution). The earlier research showed that Ti addition > 0.2wt% promoted non-uniform dissolution of the alloy causing to OCP of the Al alloys to shift to a more electropositive region. During the present study, the evidence of non-uniform corrosion was seen for Al-Ti-C coating exposed to salt spray corrosion test, see **Figure 4.29**, where formation of corrosion products on specific regions of the coatings were observed in comparison to Al coating, see **Figure 4.26**. Ti in combination with C has been proven to show grain refinement effect on Al alloys [177,178], however, addition of Ti > 0.2wt% has also been reported to reduce the uniform dissolution of the Al alloys [107,276].

The Al-Zn and Al-Zn-In coatings showed fluctuation in the OCP values after 48 hours of exposure for all concentrations of NaCl solution, see **Figure 4.33** and **Figure 4.34**, however these effects were seen more pronounced for Al-Zn-In coating exposed to 3.5%w/v and 1.0%w/v NaCl solution, see **Figure 4.34**. Similar fluctuation in the OCP values have been observed during earlier research conducted on understanding the mechanism of Zn and In on activation of Al [114,115,121,122,129,130].

It has been shown in the earlier researches that when Al alloys containing Zn as an alloying element are exposed to Cl⁻ media, the dissolution of Zn occurs from the surface at a higher rate than it diffuses in the bulk Al matrix, which drives the OCP of the alloy to more electronegative region [126].

This phenomenon causes the fluctuations in the OCP values, similar to the ones observed in **Figure 4.33** in the OCP values of the Al when alloyed with Zn. However, when Al is alloyed with Zn and In, a higher degree of OCP fluctuations have been reported, when the alloys have been exposed to Cl⁻ media [122,124]. This has been attributed to the fact that thermodynamically diffusion of In in Al matrix is significantly higher than Zn [90,96] during chloride exposure favouring adsorption of Cl⁻ on the Zn rich regions. The adsorbed Cl⁻ species forms In chloro complex's which initiates and breaks the formation of Al oxides during long term exposure period causing the significant fluctuations in the OCP values. Hence these deductions can potentially explain a higher degree of OCP fluctuations seen for Al-Zn-In coating, see **Figure 4.34** than Al-Zn coating. Reduction in the induction period was also reported for Al in contact with Zn and In together than Zn alone, see **Figure 2.39**, however this behaviour was not observed in the present study.

4.3 Galvanic corrosion test

Table 4.9 shows the measured and actual values of the areas including the R_a values for Al, Al-Zn, Al-Zn-In and Al-Ti-C coatings. **Figure 4.40** to **Figure 4.43** shows the corrosion current vs. time plot for Al, Al-Zn, Al-Zn-In and Al-Ti-C coatings with anode to cathode area ratios of 1:1, 1:1/2, 1:1/4 subjected to 3.5%w/v NaCl solution. Note that the current values have been normalised to area of the anode to aid direct comparison for coatings with varying surface roughness values mentioned in **Table 4.9**.

Table 4.9: The measured, actual and R_a values of Al, Al-Zn, Al-Zn-In and Al-Ti-C coating.

Coatings	Measured area (mm ²)	Actual area (mm ²)	R_a (μm)
Al	1600	4480	24 ± 2
Al-Zn	1600	3575	18 ± 1
Al-Zn-In	1600	5208	20 ± 2
Al-Ti-C	1600	6048	48 ± 4

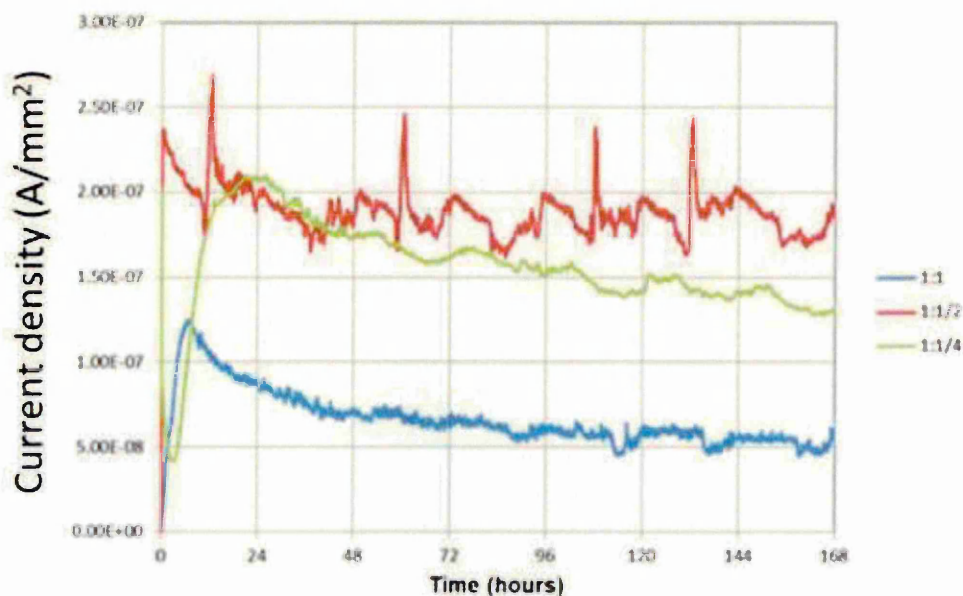


Figure 4.40: Current density vs. time plot for Al coating subjected to 3.5 % w/v NaCl solution. The anode to cathode area ratios used was 1:1, 1:1/2 and 1:1/4 respectively.

Al-Zn-In coatings were also exposed to lower concentrations of NaCl solution of 1.0% w/v, 0.1% w/v and 0.01% w/v with anode to cathode ratios of 1:1/2 and 1:1/4 respectively, see **Figure 4.44** to **Figure 4.46**.

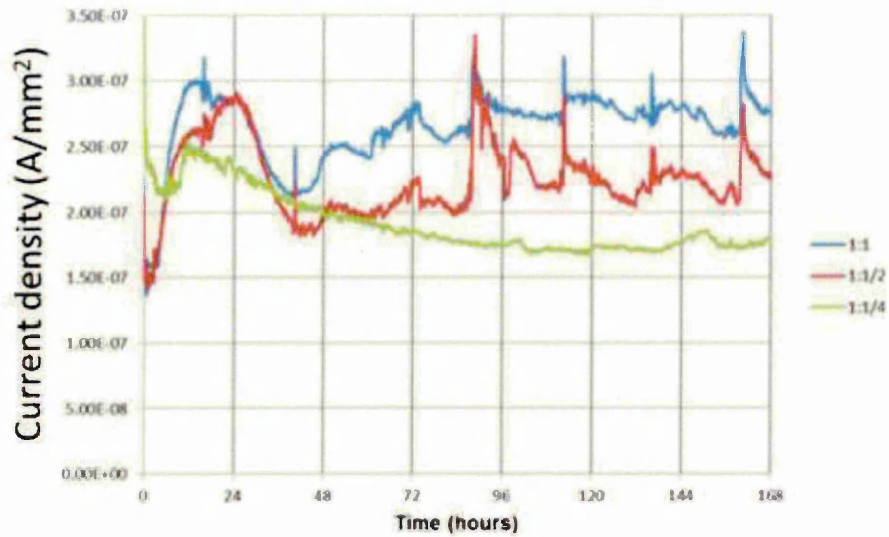


Figure 4.41: Current density vs. time plot for Al-Zn coating subjected to 3.5 % w/v NaCl solution. The anode to cathode area ratios used was 1:1, 1:1/2 and 1:1/4 respectively.

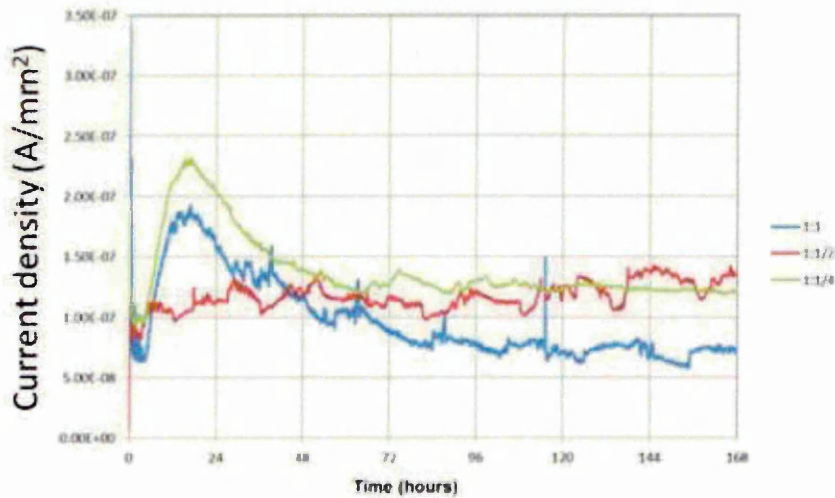


Figure 4.42: Current density vs. time plot for Al-Zn-In coating subjected to 3.5 % w/v NaCl solution. The anode to cathode area ratios used was 1:1, 1:1/2 and 1:1/4 respectively.

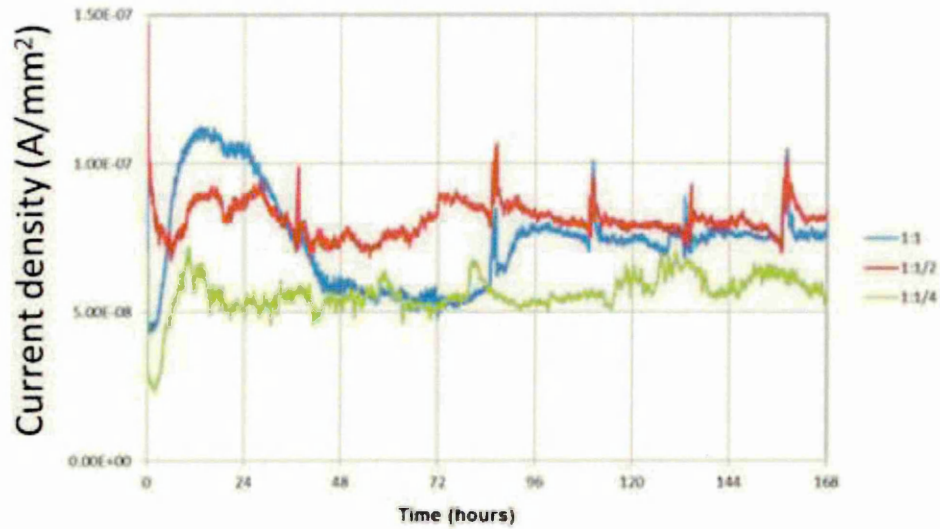


Figure 4.43: Current density vs. time plot for Al-Ti-C coating subjected to 3.5 % w/v NaCl solution. The anode to cathode area ratios used was 1:1, 1:1/2 and 1:1/4 respectively.

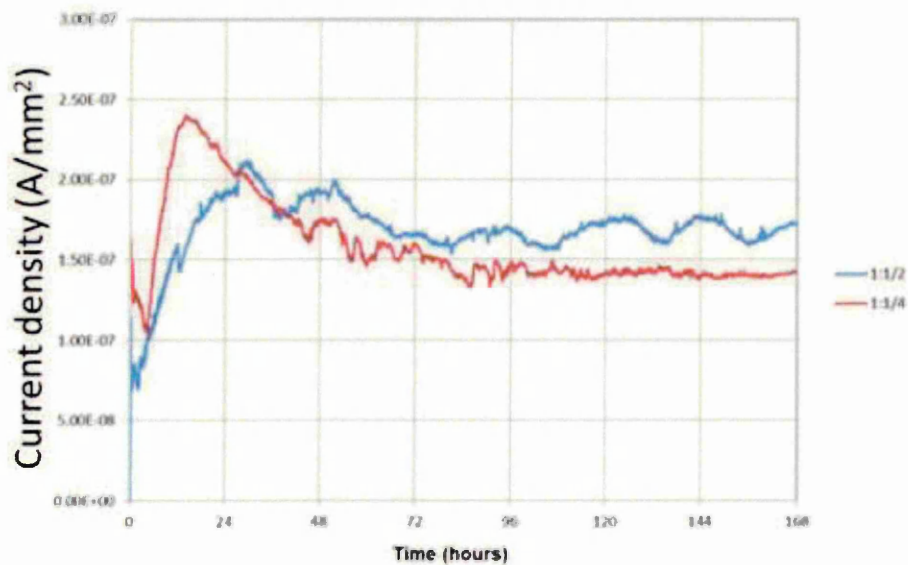


Figure 4.44: Current density vs. time plot for Al-Zn-In coating subjected to 1.0 % w/v NaCl solution. The anode to cathode area ratios used was 1:1/2 and 1:1/4 respectively.

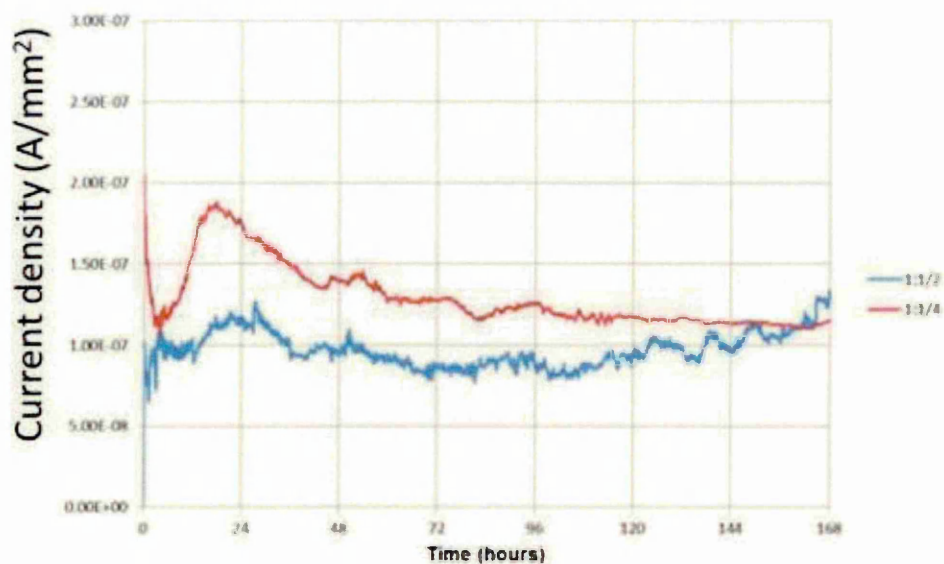


Figure 4.45: Current density vs. time plot for Al-Zn-In coating subjected to 0.1 % w/v NaCl solution. The anode to cathode area ratios used was 1:1/2 and 1:1/4 respectively.

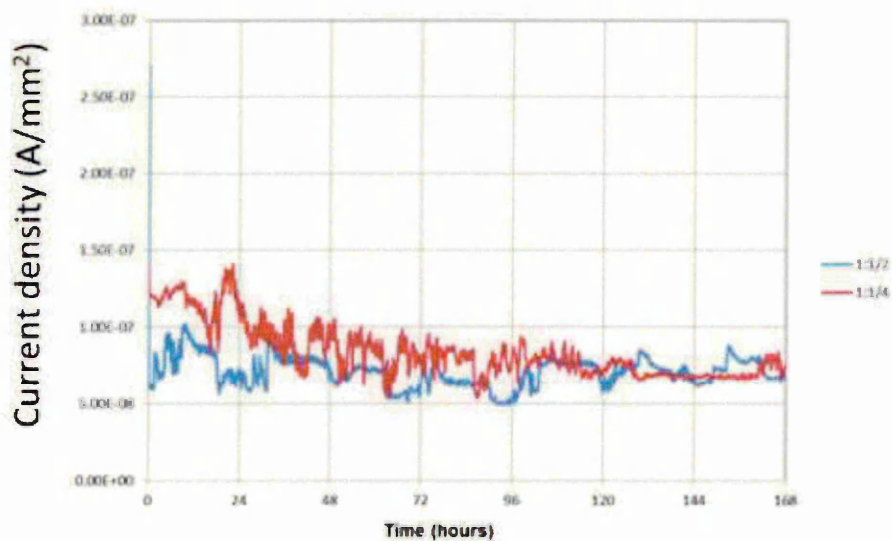


Figure 4.46: Current density vs. time plot for Al-Zn-In coating subjected to 0.01 % w/v NaCl solution. The anode to cathode area ratios used was 1:1/2 and 1:1/4 respectively.

Figure 4.47 to **Figure 4.50** shows the closed circuit potential (CCP) vs. time plots for Al, Al-Zn, Al-Zn-In and Al-Ti-C coatings exposed to 3.5% w/v NaCl solution with anode to cathode area ratio of 1:1, 1:1/2 and 1:1/4. The CCP vs. time plot was also recorded for Al-Zn-In coating exposed to 1.0% w/v, 0.1% w/v and 0.01% w/v NaCl solution with anode to cathode area ratio of 1:1/2 and 1:1/4, see **Figure 4.51** to **Figure 4.53**.

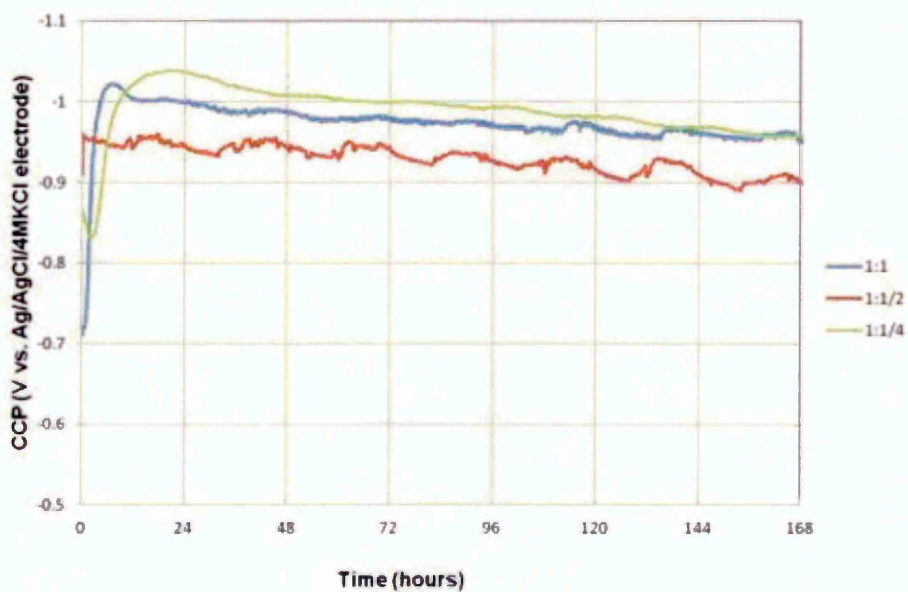


Figure 4.47: CCP vs. time plot for Al coating subjected to 3.5 % w/v NaCl solution. The anode to cathode area ratios used was 1:1, 1:1/2 and 1:1/4 respectively.

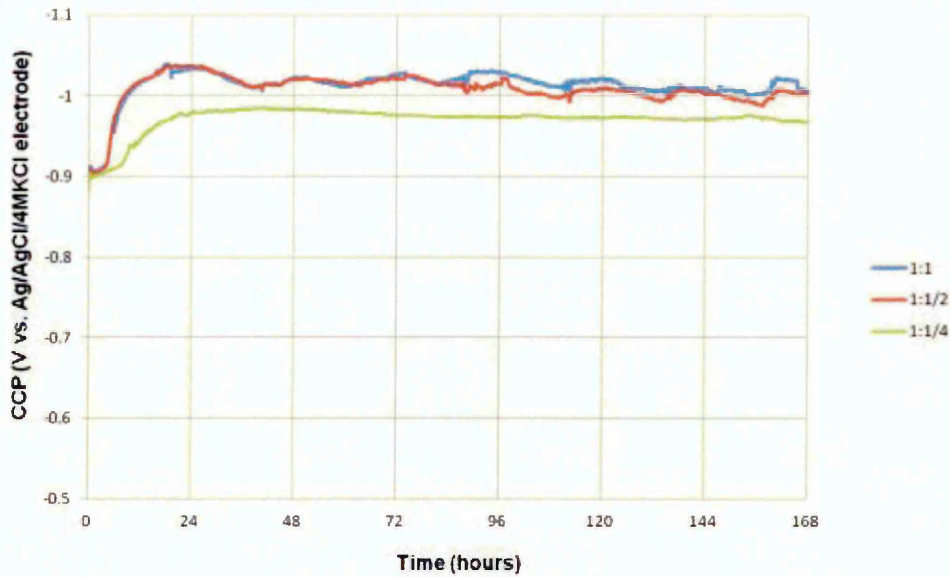


Figure 4.48: CCP vs. time plot for Al-Zn coating subjected to 3.5 % w/v NaCl solution. The anode to cathode area ratios used was 1:1, 1:1/2 and 1:1/4 respectively.

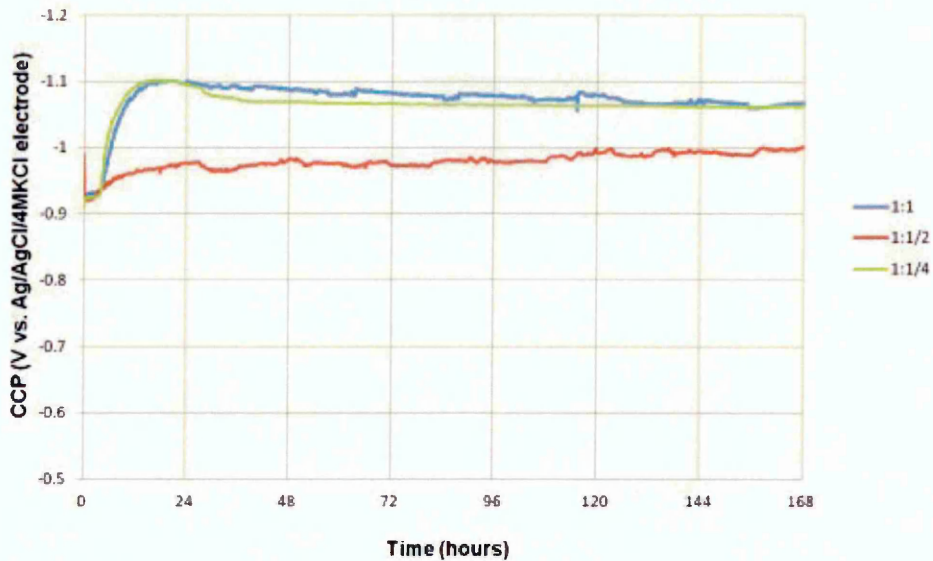


Figure 4.49: CCP vs. time plot for Al-Zn-In coating subjected to 3.5 % w/v NaCl solution. The anode to cathode area ratios used was 1:1, 1:1/2 and 1:1/4 respectively.

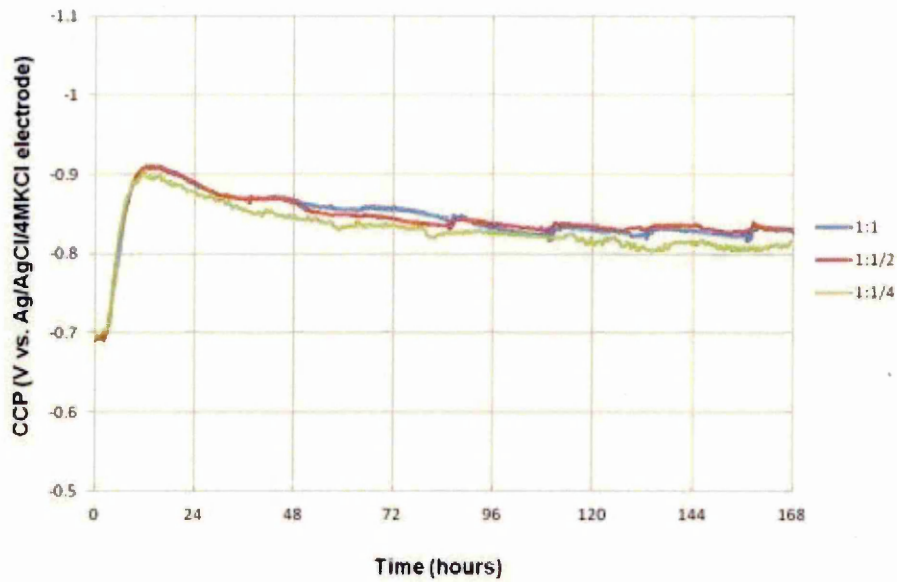


Figure 4.50: CCP vs. time plot for Al-Ti-C coating subjected to 3.5 % w/v NaCl solution. The anode to cathode area ratios used was 1:1, 1:1/2 and 1:1/4 respectively.

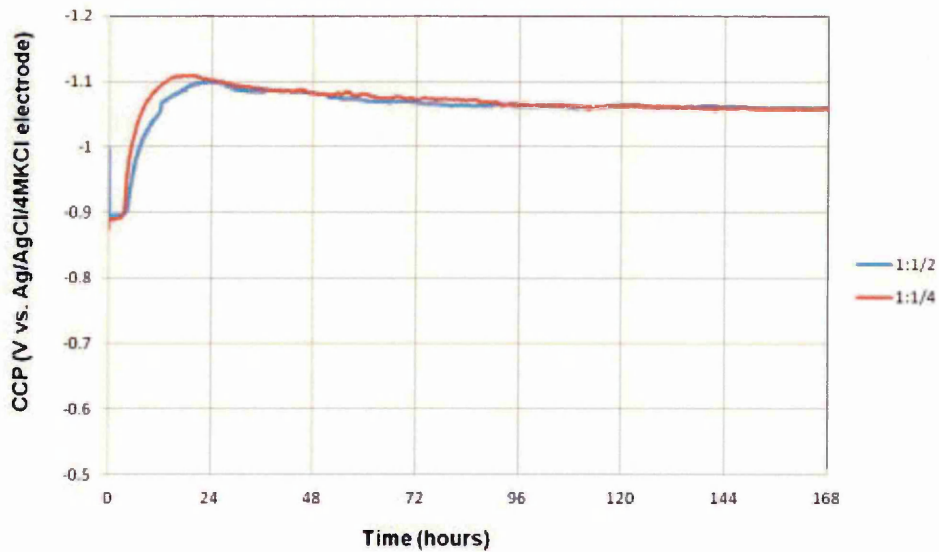


Figure 4.51: CCP vs. time plot for Al-Zn-In coating subjected to 1.0 % w/v NaCl solution. The anode to cathode area ratios used was 1:1/2 and 1:1/4 respectively.

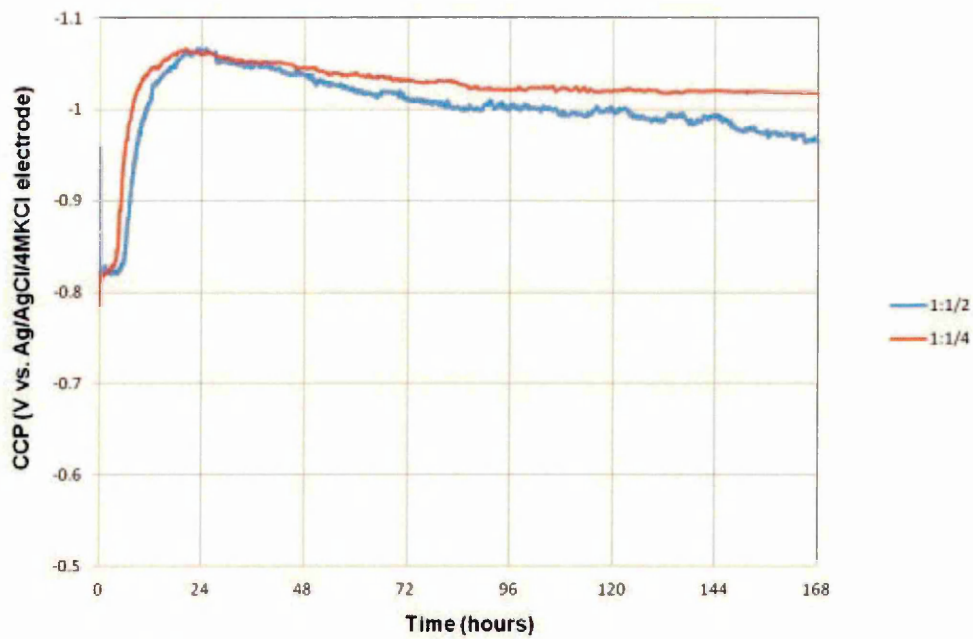


Figure 4.52: CCP vs. time plot for Al-Zn-In coating subjected to 0.1 % w/v NaCl solution. The anode to cathode area ratios used was 1:1/2 and 1:1/4 respectively.

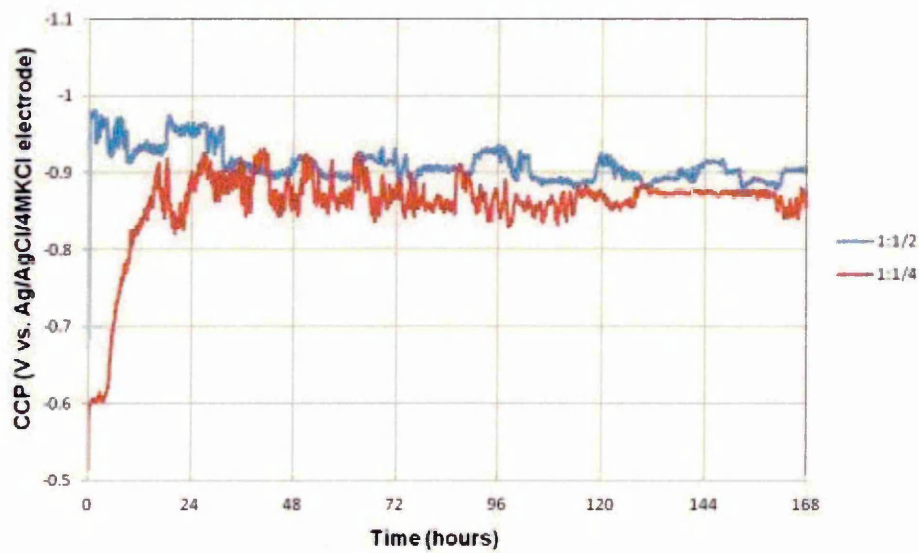


Figure 4.53: CCP vs. time plot for Al-Zn-In coating subjected to 0.01 % w/v NaCl solution. The anode to cathode area ratios used was 1:1/2 and 1:1/4 respectively.

In an attempt to formulate an empirical relation between the galvanic corrosion current density (A/mm^2) and the area ratio of cathode to anode used during the study, the results shown in **Figure 4.40** to **Figure 4.43** were re-plotted on a log scale vs area ratio, see **Figure 4.54**. Note that the graph shown in **Figure 4.54**, shows relation between corrosion current and area ratio for Al, Al-Zn, Al-Zn-In and Al-Ti-C coatings exposed to 3.5% w/v NaCl solution for 168 hours.

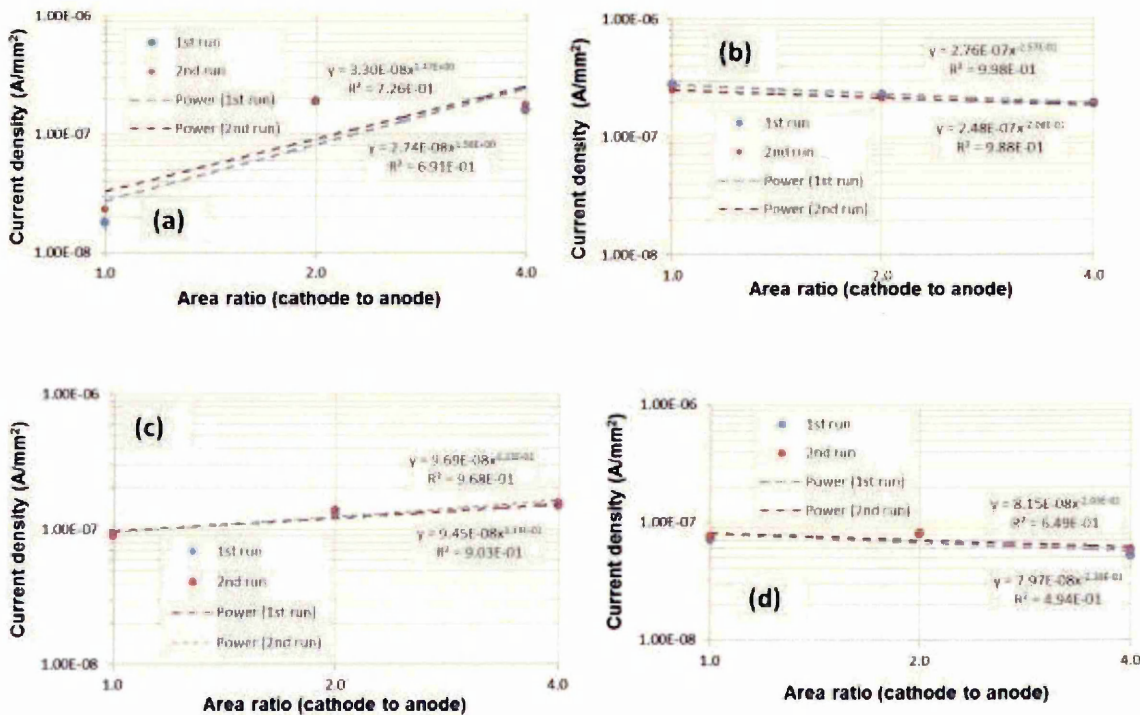


Figure 4.54: Logarithmic plots showing relationship between galvanic corrosion current density and cathode to anode area ratio for (a) Al, (b) Al-Zn, (c) Al-Zn-In and (d) Al-Ti-C coatings exposed to 3.5% w/v NaCl solution for 168 hours. Duplicate experimental data plotted on the graph (shown as 1st and 2nd run).

For Al-Zn-In coatings subjected to 1.0% w/v, 0.1% w/v and 0.01% w/v NaCl solution, similar log plots to establish relation between galvanic current and area ratio are shown in **Figure 4.55**.

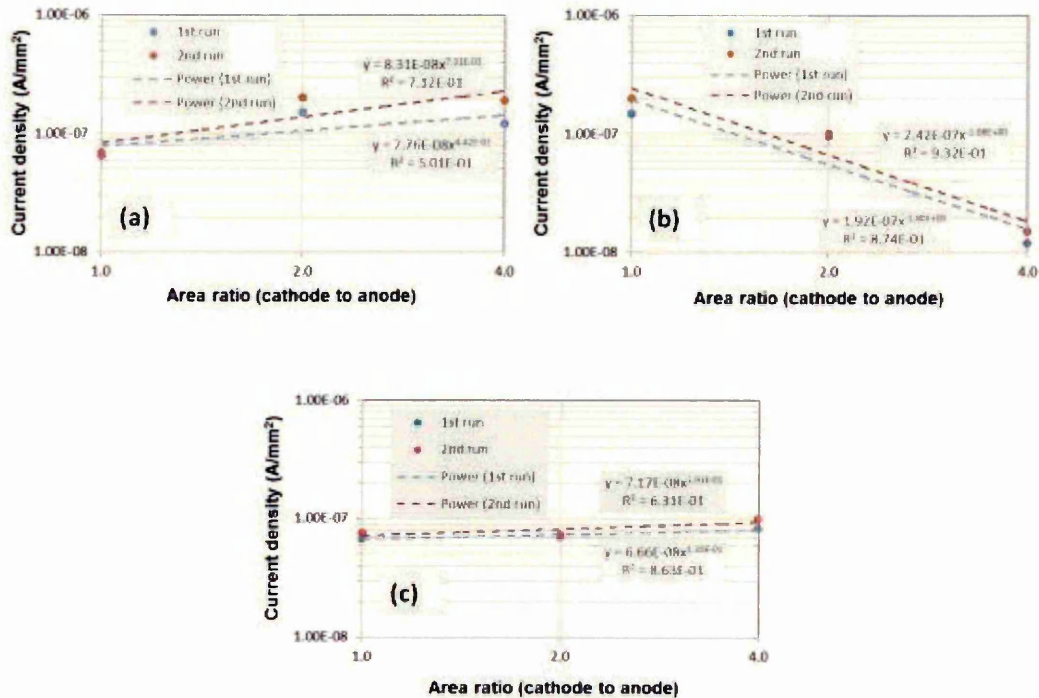


Figure 4.55: Logarithmic plots showing relationship between galvanic corrosion current and cathode to anode area ratio for Al-Zn-In coating exposed to (a) 1.0% w/v, (b) 0.1% w/v, and (c) 0.01% w/v NaCl solution for 168 hours. Duplicate experimental data plotted on the graph (shown as 1st and 2nd run).

The plot in **Figure 4.56** also shows the effect of changing chloride concentration on the galvanic current for Al-Zn-In coatings coupled with mild steel with cathode to anode ratio of 1:1, 2:1 and 4:1 respectively.

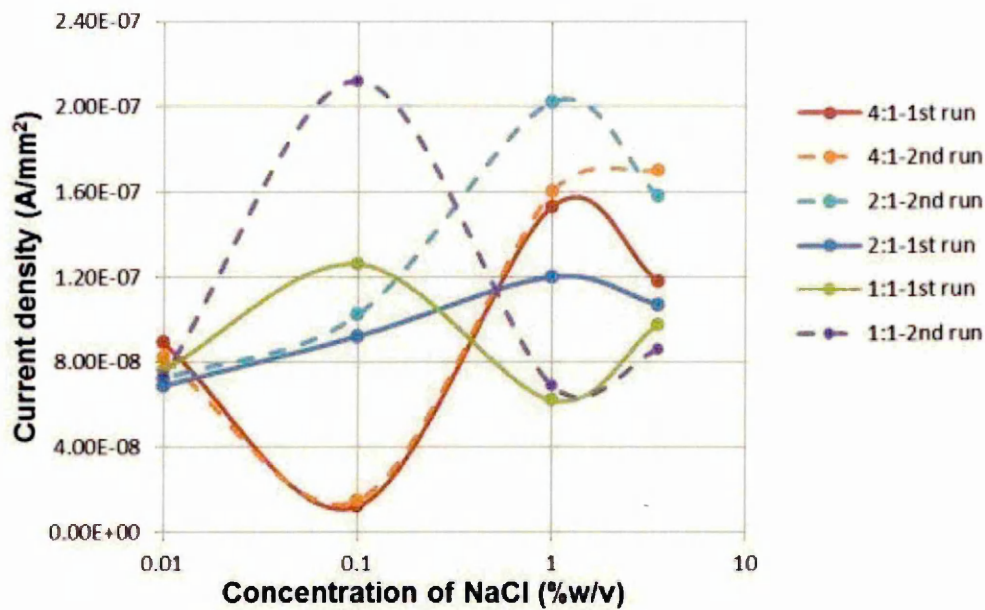


Figure 4.56: Log plots showing the variation in galvanic corrosion current vs chloride concentration for Al-Zn-In coating coupled with mild steel with cathode to anode area ratio of 1:1, 2:1 and 4:1 respectively.

The galvanic corrosion tests conducted for 168 hours in the study were to gain comprehensive understanding of the effectiveness of sacrificial protection offered by Al-Zn-In coatings to the underlying steel structures when exposed to chloride media (3.5% w/v NaCl). The different cathode to anode area ratios were chosen during the study in order to understand the sacrificial behaviour of the Al-Zn-In coating in a condition in which the defect or removal of coatings subjected the underlying substrate exposed to corrosive media. Al, Al-Zn and Al-Ti-C coatings were examined for the sake of comparison and benchmarking the performance of Al-Zn-In coating. The effect of Cl⁻ ion concentration on sacrificial performance of Al-Zn-In coating was also established by varying the NaCl concentration (1.0% w/v, 0.1% w/v and 0.01% w/v) during the galvanic corrosion test.

A sharp rise in the corrosion current was observed for Al-Zn-In coatings exposed to 3.5% w/v NaCl solution with cathode to anode ratio of 1 to 1 and 4 to 1 within the first 24 hours of exposure, see **Figure 4.42**. However no significant change in the corrosion current was seen for Al-Zn-In coating with cathode to anode ratio of 2:1 at 3.5% w/v NaCl solution, see **Figure 4.42**.

A similar rise in the corrosion current values was also observed for Al-Zn coatings exposed to 3.5% w/v NaCl solution, however this time this sharp rise was seen for cathode to anode ratios of 1:1 and 2:1, see **Figure 4.41**. For Al-Zn coating coupled with mild steel with the ratio of 4 to 1 showed decay in the current values within the first 24 hours of exposure, see **Figure 4.41**.

Unlike Al-Zn-In and Al-Zn coating, the Al-Ti-C coating after a sharp rise in the corrosion current values showed formation of a plateau region in the current vs. time plot during first 24 hours of exposure in 3.5% w/v NaCl solution for cathode to anode ratio of 1 to 1, see **Figure 4.43**. After a continuous decay of current values till 48 hours, once again formation of a plateau was seen in current vs. time plot for Al-Ti-C coating coupled with mild steel with area ratio 1:1 in 3.5% w/v NaCl solution see **Figure 4.43**. However, after rise in the current values after the formation of plateau, steady current values were observed for Al-Ti-C coating coupled with mild steel in 3.5% w/v NaCl solution till 168 hours of exposure. Note that no significant change in the current values were seen for Al-Ti-C coatings in 3.5% w/v NaCl solution with cathode to anode area ratio of 2 to 1 and 4 to 1, except for the higher values of corrosion current which were seen for area ratio of 2 to 1, see **Figure 4.43**.

Note the fluctuations observed in the current vs. time plots for Al, Al-Zn, Al-Zn-In and Al-Ti-C coatings exposed to 3.5% w/v NaCl solution for cathode to anode area ratios of 1 to 1, 2 to 1 and 4 to 1, see **Figure 4.40** to **Figure 4.43**. These fluctuations were more profound for Al-Zn coatings, see **Figure 4.41**. The fluctuations similar to the ones observed during the present study have also been reported previously by researchers working on Al anodes alloyed with both Zn and In [114,115,121-130,280].

The fluctuations in the current vs. time plots observed for both Al-Zn-In and Al-Zn coatings suggested the instability of passive Al oxide layer during formation. It has been shown in the previous researches that the synergetic interaction of Zn and In produces the activation of Al alloys in chloride containing media by rupturing the passive Al oxide layer and increasing the Cl⁻ adsorption on the surface [114,115]. This cyclic formation and rupturing of Al oxide layer could have resulted in fluctuations of the corrosion current observed for Al-Zn and Al-Zn-In coating, see **Figure 4.41** and **Figure 4.42**.

The fluctuations in the corrosion current values of Al-Zn coatings were recorded to be higher than Al-Zn-In coatings exposed to 3.5% NaCl solution. This can be explained stating that Zn favours formation of ZnAl₂O₄ spinel with Al oxide which in turn ruptures the Al oxide layer due to increase in stress values in oxide [126]. However, the molar volume of ZnAl₂O₄ has been reported ≈ 51% higher than Al oxide [91,92,126]. This suggested that the volume of the corrosion product formed on the surface of Al-Zn coating would be higher than Al-Zn-In coating resulting in a higher degree of current fluctuations observed in **Figure 4.41**.

The decay in the current values observed for Al-Zn-In coating coupled with mild steel with area ratio of 1 to 1 and 4 to 1 after 24 hours of exposure in 3.5% w/v NaCl solution could be attributed either due to the formation of Al oxide on the surface of the coating or due to deposition of corrosion product on the surface of mild steel. The steady current values observed for Al-Zn-In coating coupled with mild steel with area ratio of 2 to 1 indicated the likelihood of latter to occur more probable. Similar behaviour was also recorded for Al-Zn coating coupled with mild steel with area ratios of 1 to 1 and 2 to 1 and Al-Ti-C coating with area ratio 1 to 1 in 3.5% w/v NaCl solution.

In addition to the corrosion current values, the CCP values recorded for Al-Zn-In coating coupled with mild steel with the area ratio 1 to 1 and 4 to 1 exposed to 3.5% w/v NaCl solution, see **Figure 4.49** were found to be ≈ 1.06 V vs. Ag/AgCl electrode, similar to the OCP values of Al-Zn-In coatings exposed to 3.5% w/v NaCl solution, see **Figure 4.34** (However for Al-Zn-In coating coupled with mild steel with area ratio of 2 to 1 reported CCP value ≈ -1.0 V vs. Ag/AgCl electrode). The Al-Zn coating for area ratios 1:1, 2:1 and 4:1 showed a stable CCP values close to -1.0 V vs. Ag/AgCl electrode. This showed that for Al-Zn-In coating coupled with mild steel, the CCP values were found more electronegative than Al-Zn coating in 3.5% w/v NaCl solution. Compared with Al-Zn and Al-Zn-In coating, a CCP value ≈ -0.83 V vs. Ag/AgCl electrode for Al-Ti-C coating coupled with mild steel with area ratios 1:1, 2:1 and 4:1 in 3.5% w/v NaCl solution was recorded (this value was found to be in a more electropositive region even compared to Al coating under similar condition, see **Figure 4.47**).

The previous researchers showed that OCP of mild steel in chloride media was -0.72 V vs. SCE (-0.68 V vs. Ag/AgCl electrode) which theoretically is between equilibrium potential of Fe/Fe^{2+} and O_2/OH^- [278,279]. This suggested that Al, Al-Zn, Al-Zn-In and Al-Ti-C coatings which exhibited OCP values more electronegative than mild steel in chloride solution, see **Figure 4.32** to **Figure 4.35**, even after coupling with mild steel with varying cathode to anode ratio, the CCP values were found to be more active in the order Al-Zn-In>Al-Zn>Al>Al-Ti-C.

Further investigation of Al-Zn-In coating at lower chloride concentration of 1.0% w/v NaCl solution also showed a sharp rise in the corrosion current value within the first 24 hours of exposure when coupled with mild steel with area ratio of 2 to 1 and 4 to 1 respectively, see **Figure 4.44**. A steady current values of the magnitude $\approx 1.7 \times 10^{-7}$ A/mm² were recorded for cathode to anode area ratio 2 to 1 while $\approx 1.5 \times 10^{-7}$ A.mm² for cathode to anode area ratio of 4 to 1 over a period of 168 hours. With further decrease in the NaCl concentration to 0.1% w/v for both the area ratios, the current values obtained over a period of 168 hours were reported to be $\approx 30\%$ lower than the values observed for Al-Zn-In coating exposed to 1.0% w/v NaCl solution, see **Figure 4.45**. A further reduction of $\approx 64\%$ in the current values were observed for Al-Zn-In coating exposed to 0.01% w/v NaCl solution as compared to 1.0% w/v NaCl solution exposure condition, see **Figure 4.46**. Note the fluctuations observed in the current vs. time plot for Al-Zn-In coating exposed to 0.01% w/v NaCl solution, see **Figure 4.46**, apart from cyclic formation and breakdown of the Al oxide layer, a higher solution resistance could also have caused these fluctuations.

The closed circuit potential values for Al-Zn-In coating coupled with mild steel with area ratios 2 to 1 and 4 to 1 also showed shift in the CCP values towards less electronegative region, see **Figure 4.51** to **Figure 4.53**, with decrease in the NaCl concentration from 1.0% w/v to 0.01% w/v over the period of 168 hours. The CCP values of the order $\approx -1.08\text{V}$ vs. Ag/AgCl electrode at 1.0% w/v NaCl, $\approx -1.0\text{ V}$ vs. Ag/AgCl electrode at 0.1% w/v NaCl and $\approx -0.9\text{ V}$ vs. Ag/AgCl electrode at 0.01% w/v NaCl for Al-Zn-In coatings were recorded (for both the area ratios used in the experiment), see **Figure 4.51** to **Figure 4.53**.

These results strongly suggested the dependency of activation of Al-Zn-In coating with chloride ion concentration. It can be stated that these results were in line with the previous research conducted [121,122,127] on Al-Zn-In anodes which showed that activation of Al by Zn and In in halide solution was strongly dependent on the halide anion in the following order $\text{F} > \text{Cl} > \text{Br} > \text{I}$. Even though in the present study only NaCl solution with varying concentrations was used, the activation of Al-Zn-In coating with increase in chloride concentration was evident from the results.

The logarithmic plots shown in **Figure 4.54** aided in establishing an empirical relationship between the galvanic corrosion current and the area ratio of anode to cathode used during the experiment. Very satisfactory R^2 values of 0.98 and 1 were obtained for Al-Zn and Al-Zn-In coating, see **Figure 4.54** (b) and (c), however for Al and Al-Ti-C coating R^2 values of 0.69 and 0.54 were obtained. From the plots shown in **Figure 4.54** (a) and (b), the following empirical relation for Al-Zn-In and Al-Zn coating were found:

$$I_{\text{Al-Zn-In}} = 9.28 \times 10^{-7} (\text{Area of Cathode/Area of Anode})^{0.30}$$

And

$$I_{\text{Al-Zn}} = 2.67 \times 10^{-7} (\text{Area of Cathode/Area of Anode})^{-0.24}$$

It is important to note that the above relation has been formulated using the measured area of anodes (see **Table 4.9**) used during the experimentation. Increase in the corrosion current values per unit area with increase in the area ratio was observed for Al-Zn-In coatings in 3.5% w/v NaCl solution for 168 hours. This relation was similar to the one observed by *Lin and Shih* [278] who investigated the performance of Al-Zn-In anodes subjected to heat treatment. A negative correlation was seen for Al-Zn coating subjected to 3.5% w/v NaCl solution for 168 hours.

It was apparent from the above results that even though both Al-Zn-In and Al-Zn coating consisted of similar concentration of Zn (4.5wt% to 5.1wt%), the presence of 0.02wt% to 0.05wt% In governed the enhanced performance of Al-Zn-In coating.

As investigated in the previous electrochemical studies of Al-Zn-In alloys in halide solution, it has been showed that rate of Zn dissolution on the surface of the alloy exceeds the rate of Zn diffusion in Al matrix resulting in electro-oxidation of Zn providing active alloy surface [129]. This has shown to produce a ZnAl_2O_4 spinel with a higher molar volume than corresponding Al oxide [126] which results in rupturing of Al oxide layer due to development of internal stresses.

In the present study, this fact has not been established as the corrosion products obtained from electrochemical testing were not analysed, the precipitation of this spinel on the surface of Al-Zn coating could have resulted in decrease in corrosion current with increase in the area ratio as seen from **Figure 4.54 (b)**. The adsorption of Cl^- ions at In rich regions of Al-Zn-In coating producing activation of the alloy could have resulted in increased galvanic corrosion current with increase in the area ratio shown for Al-Zn-In coating, see **Figure 4.54 (c)**.

A similar relation between the galvanic corrosion current and area ratio was also established by *Mansfeld and Kenkel* [281] who investigated coupling Al series 2024 and 7075 with different cathode area ratio (the cathode used were Cu, stainless steel, Ti 6Al 4V). The relation stated by authors [281] was applicable for cathodic reaction governed by reduction of oxygen, which could also be applicable in the present study as both Zn and In has been shown to interact with the Al oxide layer on the anode surface [126,278].

Similar galvanic corrosion current vs area ratio relations were also established for Al-Zn-In coatings exposed to lower NaCl concentrations of 1.0% w/v , 0.1% w/v and 0.01% w/v , see **Figure 4.55 (a), (b), (c)**, however the R^2 value of 0.9 was only observed for Al-Zn-In coating exposed to 0.1% NaCl solution. This indicated that Cl^- ion concentration played a crucial role in the performance of Al-Zn-In coating coupled with mild steel reinstating the fact that higher chloride concentrations ($\geq 3.5\%$ w/v NaCl) was favourable for getting the increased galvanic current with increase in area ratio, see **Figure 4.54 (c)**.

Figure 4.56 showed a very interesting relation between galvanic corrosion current per unit area vs NaCl concentration plotted on a log scale. Theoretically, the graph shown in **Figure 4.56** should have shown a linear increase in the corrosion current per unit area values for Al-Zn-In coating as the NaCl concentration increased from 0.01% w/v to 3.5% w/v, based on previous deductions [121]. However, both negative and positive slopes in the graphs were observed, see **Figure 4.56**. In order to explain this behaviour, relation between galvanic corrosion current per unit area and area ratio of cathode to anode can be used. The following relations were observed for Al-Zn-In coating exposed to various NaCl concentrations:

$$\begin{aligned}
 I_{\text{Al-Zn-In}} &\propto (A_c/A_a)^{0.30} \text{ for } 3.5\% \text{ w/v NaCl} \\
 I_{\text{Al-Zn-In}} &\propto (A_c/A_a)^{0.60} \text{ for } 1.0\% \text{ w/v NaCl} \\
 I_{\text{Al-Zn-In}} &\propto (A_c/A_a)^{-1.84} \text{ for } 0.1\% \text{ w/v NaCl} \\
 I_{\text{Al-Zn-In}} &\propto (A_c/A_a)^{0.11} \text{ for } 0.01\% \text{ w/v NaCl}
 \end{aligned}$$

Where A_c is the area of cathode and A_a is the Area of anode. The above mentioned relations were established using the measured or geometric areas of anode and cathode during the experiment. However, as stated in **Table 4.9**, the actual area of the coating used was significantly higher than the geometric area. Hence for this reason, the $A_a \gg A_c$ for A_c to A_a area ratio of 1:1 and 2:1. Using the above mentioned fact, it can be seen from **Figure 4.56**, that with increase in the NaCl concentration from 0.01% w/v to 0.1% w/v, the galvanic corrosion current values per unit area for Al-Zn-In coating

coupled with mild steel with area ratio of 1:1 and 2:1 showed increased value while for 4:1 decrease in the current value was observed. Similar explanation can also be used in understanding the behaviour of galvanic current of Al-Zn-In coating at higher chloride concentrations used during the study, see **Figure 4.56**. However, another important factor affecting the galvanic corrosion current values in the present study could be deposition of loose corrosion product on the surface of the coatings due to higher surface roughness values (the earlier electrochemical studies were conducted on polished Al-Zn-In alloy surfaces).

4.4 Electrochemical Impedance Spectroscopy (EIS) analysis

Figure 4.57 (a), (b), (c) , (d) to **Figure 4.60** (a), (b), (c),(d) shows the Nyquist plots for Al, Al-Zn, Al-Zn-In and Al-Ti-C coatings exposed to 3.5% w/v , 1.0% w/v, 0.1% w/v and 0.01% w/v NaCl solution for 1, 24, 48 and 168 hours. The corresponding electrochemical parameters were obtained from fitting the impedance data using Zsimpwin 3.10 software and were recorded in **Table 4.10** to **Table 4.13**. The impedance data used for analysis was corrected from the measured value of the working electrode area (which was 8.65 cm² for all the coatings) to the actual value (including the surface roughness as shown in **Table 4.9**).

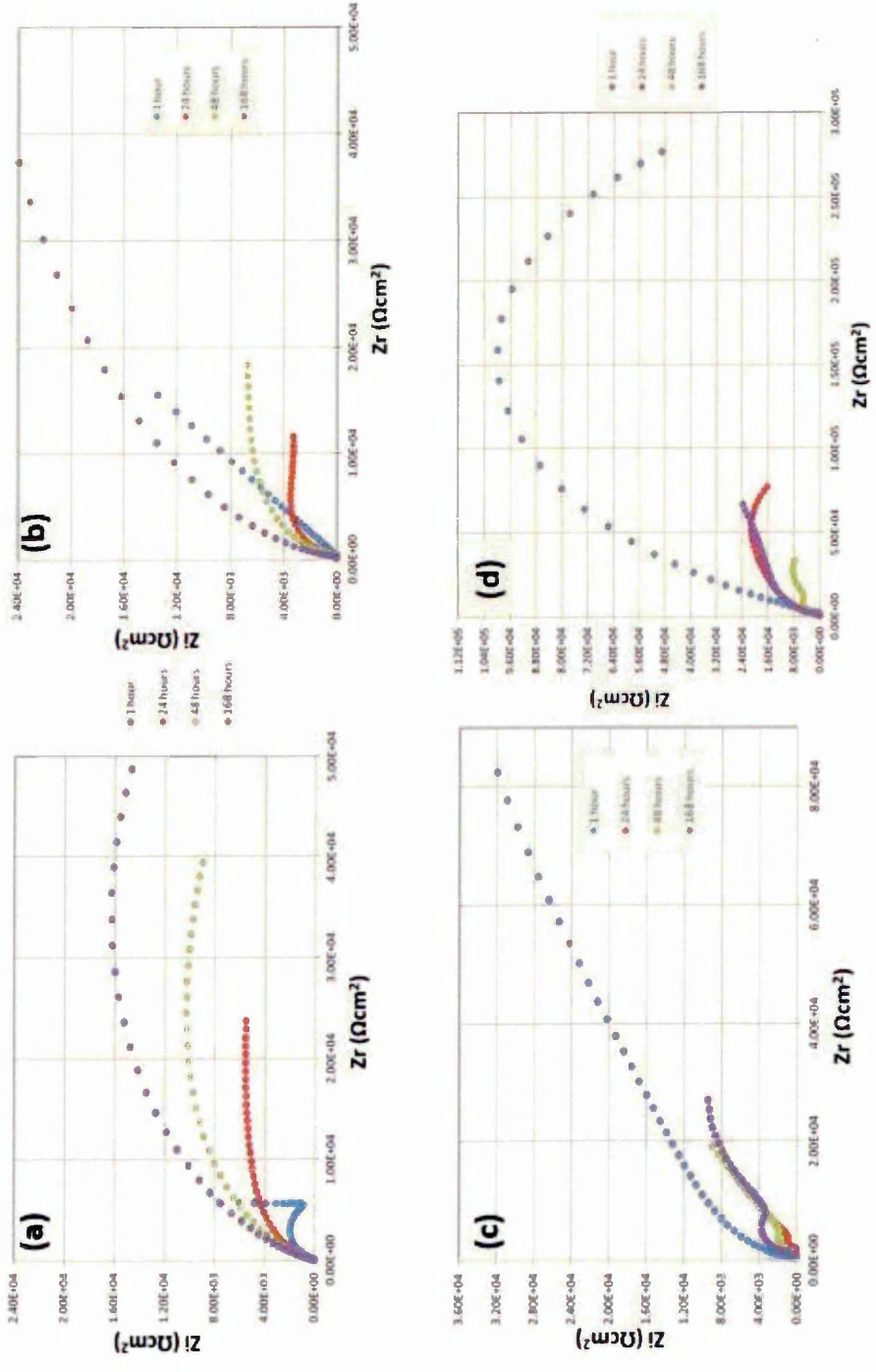


Figure 4.57: Nyquist plots for Al coating exposed to (a) 3.5% w/v , (b) 1.0% w/v, (c) 0.1% w/v and (d) 0.01% w/v NaCl solution for 1, 24, 48 and 168 hours.

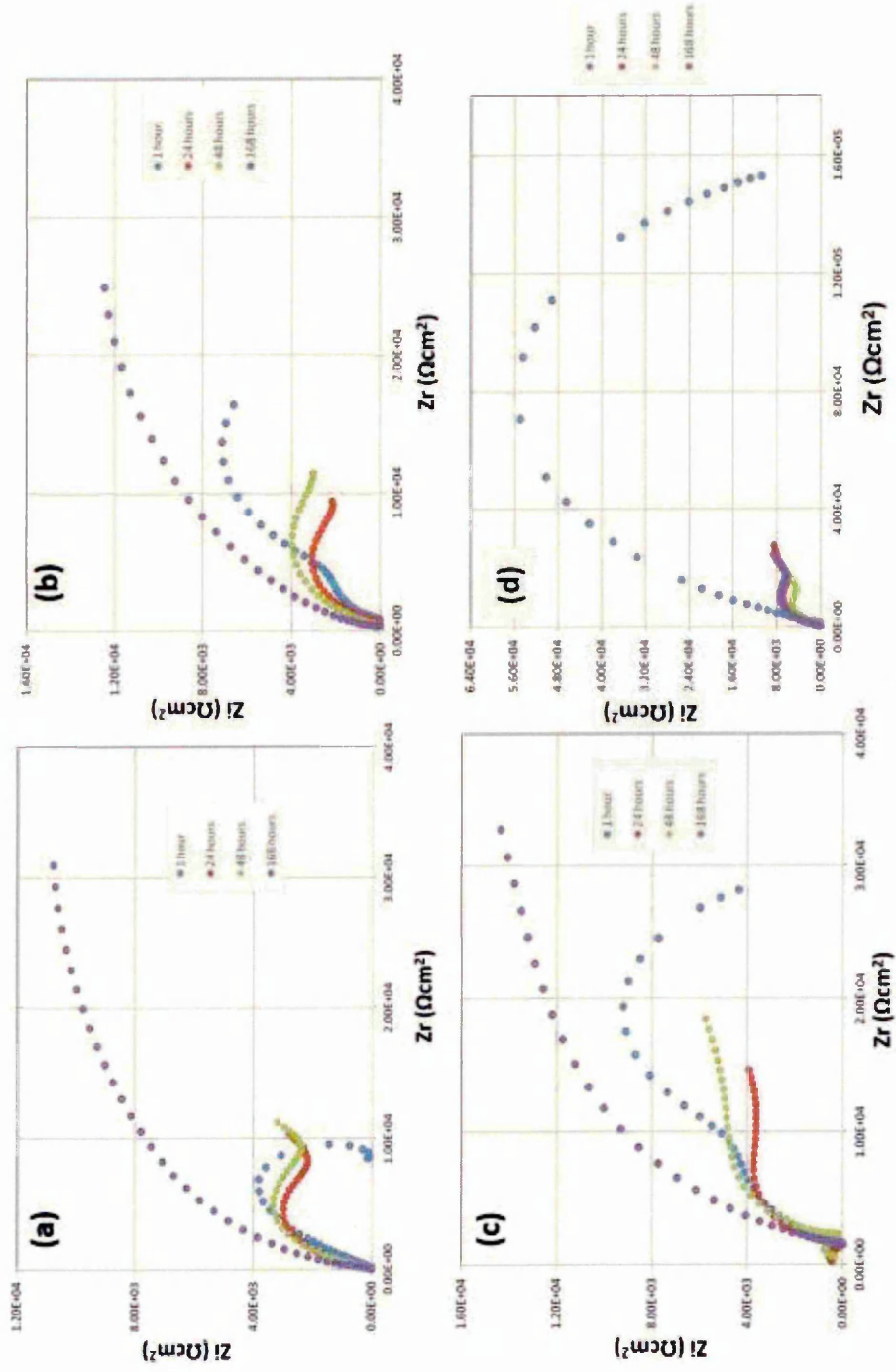


Figure 4.58: Nyquist plots for Al-Zn coating exposed to (a) 3.5% w/v , (b) 1.0% w/v, (c) 0.1% w/v and (d) 0.01% w/v NaCl solution for 1, 24, 48 and 168 hours.

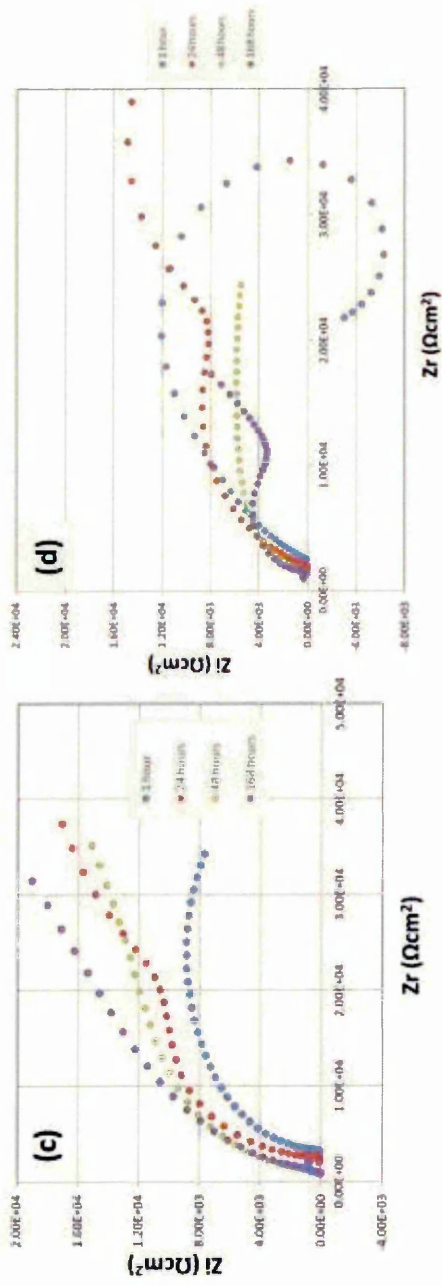
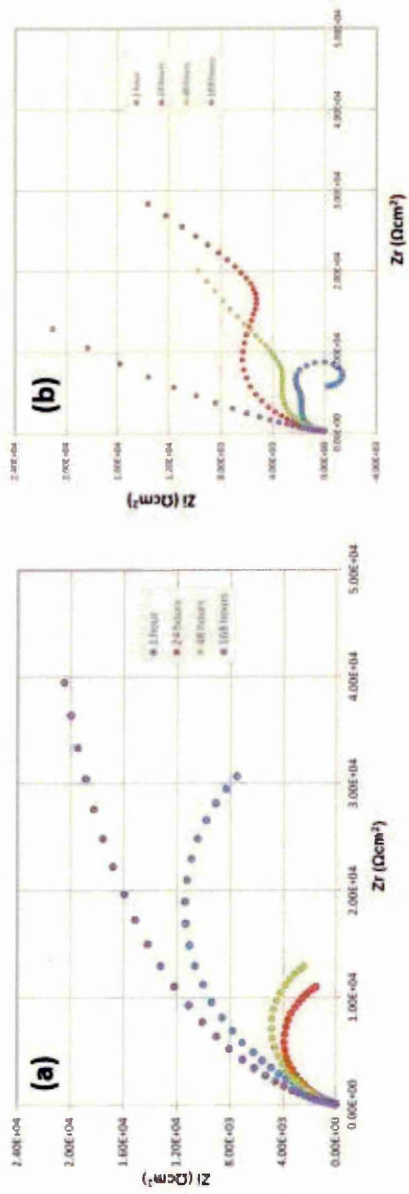


Figure 4.59: Nyquist plots for Al-Zn-In coating exposed to (a) 3.5% w/v , (b) 1.0% w/v, (c) 0.1% w/v and (d) 0.01% w/v NaCl solution for 1, 24, 48 and 168 hours.

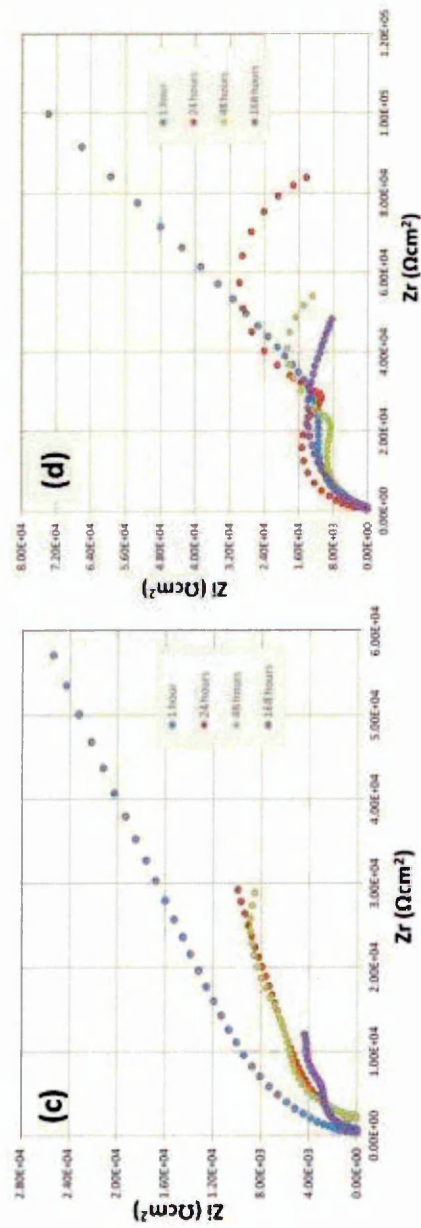
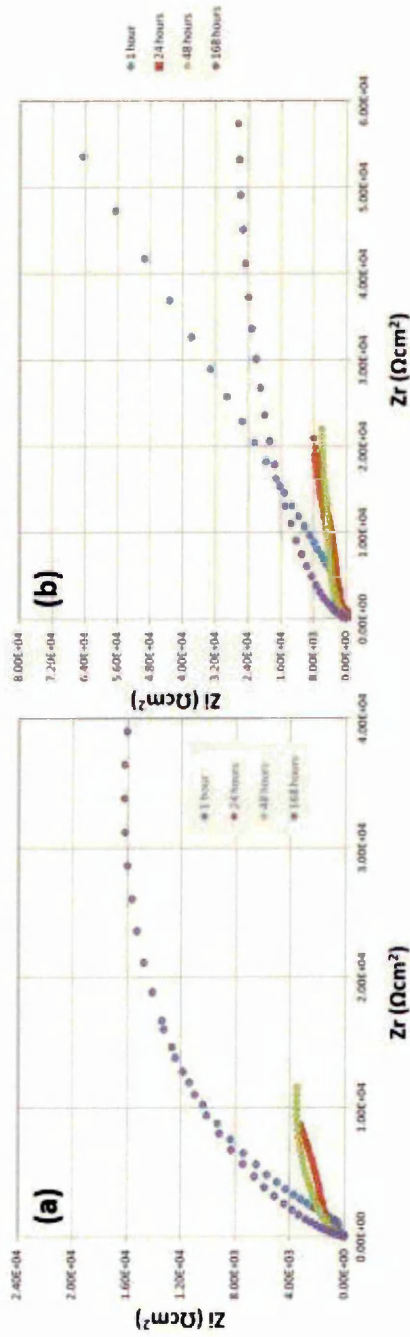


Figure 4.60: Nyquist plots for Al-Ti-C coating exposed to (a) 3.5% w/v , (b) 1.0% w/v and (c) 0.1% w/v and (d) 0.01% w/v NaCl solution for 1, 24, 48 and 168 hours

Table 4.10: Electrochemical parameters obtained by fitting Impedance data obtained for Al exposed to 3.5% w/v, 1.0% w/v, 0.1% w/v and 0.01% w/v NaCl solution for 1, 24, 48 and 168 hours.

%w/v NaCl	Time (h)	OCP (V vs. Ag/AgCl)	Equivalent circuit model	R ₁ (Ω cm ²)	Q ₁ x 10 ⁻⁵ (Ss ⁿ cm ⁻²)	n ₁	R ₂ x 10 ⁴ (Ω cm ²)	C x 10 ⁴ (Fcm ⁻²)	Q ₂ x 10 ⁻⁵ (Ss ⁿ cm ⁻²)	n ₂	R ₃ x 10 ⁴ (Ω cm ²)
3.5	1	-0.92 ± 0.002	R(Q(R(CR)))	52.88	9.24	0.8	0.51	2.06	-	-	4650.0
	24	-1.02 ± 0.004	R(Q(R(QR)))	45.12	8.61	0.8	0.13	-	4.23	0.8	4.60
	48	-1.10 ± 0.004	R(Q(R(QR)))	-	5.28	0.7	0.86	-	4.42	0.9	6.50
	168	-1.15 ± 0.004	R(Q(R(QR)))	-	5.28	0.7	0.86	-	4.29	0.8	6.84
1.0	1	-0.92 ± 0.002	R(Q(R(CR)))	3.09	14.32	0.5	10.0	1.6	-	-	1200.0
	24	-1.02 ± 0.002	R(Q(R(QR)))	91.04	13.87	0.9	4.20	-	48.90	1.0	1.41
	48	-0.98 ± 0.002	R(Q(R(QR)))	441	14.87	0.8	4.70	-	6.25	0.3	1.00
	168	-0.98 ± 0.002	R(Q(R(QR)))	168	3.70	0.4	1.40	-	50.02	0.4	14.05
0.1	1	-0.82 ± 0.004	R(Q(R(QR)))	437.4	4.25	0.3	0.85	-	1.07	1.0	31.89
	24	-1.09 ± 0.004	R(Q(R(QR)))	1035	277.1	1.0	7.34	-	50.0	0.4	7.40
	48	-1.10 ± 0.004	R(Q(R(QR)))	273.1	306.1	0.4	1.35	-	223.0	1.0	5.62
	168	-1.15 ± 0.004	R(Q(R(QR)))	413.7	40.18	0.5	39.00	-	356.0	0.8	3.50
0.01	1	-0.84 ± 0.004	R(Q(R(QR)))	1389	122.27	0.9	0.40	-	2.83	0.7	30.85
	24	-1.05 ± 0.004	R(Q(R(QR)))	786	3.78	0.7	30.00	-	104.60	0.5	6.84
	48	-1.10 ± 0.004	R(Q(R(QR)))	1363	23.82	0.5	3.70	-	5.30	0.9	7.50
	168	-1.01 ± 0.004	R(Q(R(QR)))	1826	1.91	0.8	5.50	-	96.77	0.4	100.00

Table 4.11: Electrochemical parameters obtained by fitting Impedance data obtained for Al-Zn exposed to 3.5% w/v, 1.0% w/v, 0.1% w/v and 0.01% w/v NaCl solution for 1, 24, 48 and 168 hours.

%w/v NaCl	Time (h)	OCV (V vs. Ag/AgCl)	Equivalent circuit model	R ₁ (Ω cm ²)	Q ₁ x 10 ⁻⁵ (Ss ⁿ cm ⁻²)	n ₁	R ₂ x 10 ⁴ (Ω cm ²)	L x 10 ⁵ (Hcm ²)	W (Ss ⁵ cm ⁻²)	Q ₂ x 10 ⁻⁵ (Ss ⁿ cm ⁻²)	n ₂	R ₃ x 10 ⁴ (Ω cm ²)
3.5	1	-0.92 ± 0.003	R(Q(R(LR)))	136.7	20.74	0.5	29.35	1.46	-	-	-	1.38
	24	-1.08 ± 0.002	R(Q(R(RW)))	136.1	7.35	0.8	8.69	-	0.0018	-	-	6.80
	48	-1.07 ± 0.002	R(Q(R(QR)))	23.9	42.89	0.8	10.8	-	0.0014	6.91	0.8	8.78
	168	-0.99 ± 0.003	R(Q(R(QR)))	69.83	6.12	0.4	4.01	-	-	4.01	0.8	10.70
1.0	1	-0.87 ± 0.002	R(Q(R(QR)))	-	3.49	0.8	0.51	-	-	18.71	0.8	1.65
	24	-1.09 ± 0.002	R(Q(R(QR)))	665.1	6.56	0.8	0.81	-	-	157.9	0.5	2.56
	48	-1.05 ± 0.001	R(Q(R(QW)))	-	8.36	0.2	0.12	-	0.03	1.87	0.8	-
	168	-1.01 ± 0.001	R(Q(R(QR)))	316.6	55.17	0.8	0.15	-	-	1.79	0.8	6.23
0.1	1	-0.83 ± 0.001	R(Q(R(QR)))	-	7.43	0.9	2.70	-	-	2.39	0.7	2.88
	24	-1.07 ± 0.001	R(Q(R(QR)))	0.01	9.88	0.2	0.17	-	-	0.9	0.9	22.50
	48	-1.04 ± 0.001	R(Q(R(RW)))	477.5	6.90	0.7	1.90	-	0.0013	55.87	0.8	-
	168	-0.98 ± 0.001	R(Q(R(QR)))	1579	4.25	0.8	1.40	-	-	7.77	0.3	18.20
0.01	1	-0.84 ± 0.001	R(Q(R(QR)))	0.01	15.66	0.8	0.17	-	-	1.07	0.8	15.60
	24	-1.09 ± 0.001	R(Q(R(QR)))	-	1.86	0.8	0.28	-	-	28.86	0.8	2.60
	48	-1.07 ± 0.001	R(Q(R(QR)))	72.6	2.49	0.8	0.41	-	-	40.01	0.6	28.90
	168	-1.08 ± 0.001	R(Q(R(QR)))	106.3	3.07	0.8	0.66	-	-	61.16	0.7	2.39

Table 4.12: Electrochemical parameters obtained by fitting Impedance data obtained for Al-Zn-In exposed to 3.5% w/v, 1.0% w/v, 0.1% w/v and 0.01% w/v NaCl solution for 1, 24, 48 and 168 hours.

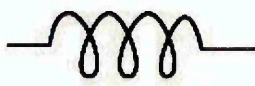
%w/v NaCl	Time (h)	OCp (V vs. Ag/AgCl)	Equivalent circuit model	R ₁ (Ω cm ²)	Q ₁ x 10 ⁻⁵ (Ss ⁿ cm ⁻²)	n ₁	R ₂ x 10 ⁴ (Ω cm ²)	L x 10 ⁵ (Fcm ⁻²)	W x 10 ⁻⁵ (Ss ⁵ cm ⁻²)	Q ₂ x 10 ⁻⁵ (Ss ⁿ cm ⁻²)	n ₂	R ₃ x 10 ⁴ (Ω cm ²)
3.5	1	-0.96 ± 0.020	R(QR)(QR)	-	5.88	0.7	3.71	-	-	15.73	1.0	0.64
	24	-1.17 ± 0.010	R(QR)(QR)	0.01	14.33	1.0	1.19	-	-	102.7	0.6	0.63
	48	-1.17 ± 0.010	R(QR)(QR)	-	22.51	0.8	1.44	-	-	11.75	0.6	0.58
	168	-1.12 ± 0.003	R(QR)(QR)	-	3.79	0.3	1.65	-	-	3.49	0.6	8.06
1.0	1	-0.91 ± 0.003	R(Q(R(LR)))	197	2.68	0.7	2.59	2.59	-	-	-	1.29
	24	-1.12 ± 0.003	R(Q(R(RW)))	0.01	5.24	0.8	1.56	-	66.81	-	-	1.50
	48	-1.11 ± 0.002	R(Q(R(RW)))	310.9	10.0	0.8	7.56	-	51.4	-	-	74.04
	168	-0.96 ± 0.002	R(QR)(QR)	15.67	1.83	0.4	38.9	-	-	3.97	0.6	0.60
0.1	1	-0.88 ± 0.002	R(QR)(QR)	1354	17.82	0.9	4.84	-	-	3.99	0.4	0.40
	24	-1.13 ± 0.002	R(QR)(QR)	1182	4.24	0.2	4.59	-	-	2.22	0.5	0.16
	48	-1.12 ± 0.002	R(Q(R(QR)))	873.6	5.68	0.9	1.31	--	--	19.54	0.6	6.14
	168	-1.25 ± 0.002	R(QR)(QR)	468.3	9.35	0.7	6.60	--	-	29.41	1.0	0.04
0.01	1	-0.85 ± 0.003	R(QR)(QR)	726.3	2.43	0.5	4.20	-	-	4.20	0.8	1.47
	24	-1.21 ± 0.003	R(QR)(QR)	1950	4.82	0.8	24.09	-	-	116.9	0.8	2.57
	48	-1.12 ± 0.003	R(QR)(QR)	1004	6.65	0.3	70.4	-	-	2.82	0.8	4.14
	168	-1.27 ± 0.003	R(QR)(QR)	438.5	13.13	0.9	157.73	-	-	20.46	0.7	7.27

Table 4.13: Electrochemical parameters obtained by fitting Impedance data obtained for Al-Ti-C exposed to 3.5% w/v, 1.0% w/v, 0.1% w/v and 0.01% w/v NaCl solution for 1, 24, 48 and 168 hours.

%w/v NaCl	Time (h)	OCP (V vs. Ag/AgCl)	Equivalent circuit model	R ₁ (Ω cm ²)	Q ₁ x 10 ⁻⁵ (S s ⁿ cm ⁻²)	n ₁	R ₂ x 10 ⁴ (Ω cm ²)	Q ₂ x 10 ⁻⁵ (S s ⁿ cm ⁻²)	n ₂	R ₃ x 10 ⁴ (Ω cm ²)
3.5	1	-0.92 ± 0.003	R(Q(R(RQ)))	136.3	2.70	0.8	0.1	40.26	0.7	4.81
	24	-1.08 ± 0.001	R(Q(R(RQ)))	139.3	4.70	0.8	0.3	24.84	0.3	1.58
	48	-1.07 ± 0.001	R(Q(R(QR)))	73.06	14.17	0.4	0.2	2.13	0.8	1.57
	168	-0.99 ± 0.001	R(Q(R(QR)))	6458.0	8.18	0.4	0.7	3.31	0.8	12.10
1.0	1	-0.87 ± 0.004	R(Q(R(QR)))	336.6	67.3	0.9	68.3	22.38	0.6	26.12
	24	-1.09 ± 0.002	R(Q(R(QR)))	229.3	14.84	0.2	45.5	1.51	0.8	48.40
	48	-1.05 ± 0.001	R(Q(R(QR)))	362.2	3.51	0.9	0.1	1.11	0.2	5.70
	168	-1.01 ± 0.002	R(Q(R(QR)))	245.1	7.48	0.8	88.58	3.57	0.8	90.30
0.1	1	-0.83 ± 0.004	R(Q(R(QR)))	-	10.52	0.5	74.0	88.03	0.8	28.58
	24	-1.07 ± 0.003	R(Q(R(QR)))	-	80.52	1.0	19.67	7.66	0.3	5.02
	48	-1.04 ± 0.001	R(Q(R(QR)))	10.0	25.32	0.6	3.11	6.81	0.8	8.03
	168	-0.98 ± 0.002	R(Q(R(QR)))	646.8	3.98	0.8	2.48	16.09	0.8	4.37
0.01	1	-0.84 ± 0.002	R(Q(R(QR)))	1826	1.41	0.8	5.85	96.77	0.4	100.0
	24	-1.09 ± 0.003	R(Q(R(QR)))	772.6	2.63	0.9	2.84	70.66	0.8	5.84
	48	-1.07 ± 0.002	R(Q(R(QR)))	78.43	5.77	0.8	2.97	27.07	1.0	8.64
	168	-1.08 ± 0.003	R(Q(R(QR)))	-	2.50	0.3	9.54	6.11	0.8	6.93

The Nyquist plots shown in **Figure 4.57** (a)-(d) to **Figure 4.60** (a)-(d) were plotted from the data which was validated using Kramers-Kronig (K-K) transformation (to validate the compliance of experimental impedance data according to the linear system theory for linearity, causality, stability and finiteness) [133-136,243]. The electrochemical parameters shown in **Table 4.10** to **Table 4.13** were also obtained post K-K transformation of the experimental impedance data plotted in the Nyquist plots (Figure 4.57 (a)-(d) to Figure 4.60 (a)-(d)) and were interpreted using the equivalent circuit models explained in **Table 4.14**.

Table 4.14: Symbols and operational impedance functions of the elements used in equivalent circuit models shown in Table 4.10 to Table 4.13.

Circuit Element symbol	Circuit element meaning	Operational impedance	Diagrammatic representation
R	Resistor	R	
C	Capacitor	$1/sC$	
Q	Constant phase element	$1/Q(j\omega)^n$	
L	Inductor	sL	
W	Warburg impedance	$\sigma (1-j)/\omega^{1/2}$	

From **Table 4.14**, s represents Laplace transformation of frequency response (ω), j represents complex number $(-1)^{1/2}$ and σ represents diffusion constant of species involved in corrosion reaction and is inversely proportional to the area of the working electrode [135].

The arrangement of the elements used in the equivalent circuit model presented in the **Table 4.10** to **Table 4.13** were obtained from a series of existing models available in the Zsimpwin 3.10 software [245]. The circuit elements within the brackets represent circuit elements in parallel combination, while the circuit element outside the bracket shows combination in series. The diagrammatic representations of the equivalent circuit models mentioned in Table 4.10 to Table 4.13 are shown in **Figure 4.61**.

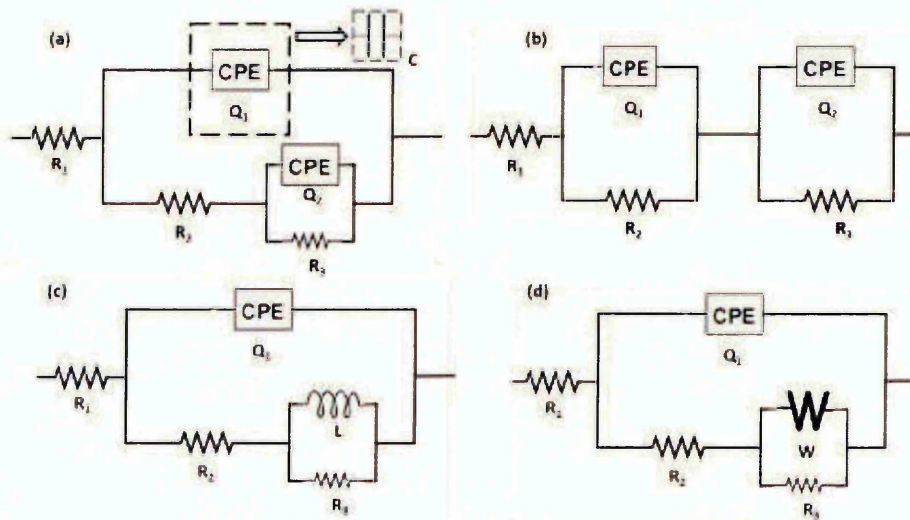


Figure 4.61: Diagrammatic representation of (a) $R(Q(R(QR)))$ or $R(C(R(QR)))$, (b) $R(QR)(QR)$, (c) $R(Q(R(LR)))$, (d) $R(Q(R(RW)))$, the equivalent circuit models used during the interpretation of impedance data shown in **Table 4.10** and **Table 4.13**.

It is important to note that during the fitting of the equivalent circuit model to analyse the experimental impedance data, following assumptions were made [99,135,136,245]:

- As the coating-electrolyte system was examined for a finite frequency range, from 1 kHz to 1 mHz, for different NaCl concentrations (3.5% w/v, 1.0% w/v, 0.1% w/v and 0.01% w/v) and the data obtained was K-K transformable, the deviation of the experimental impedance data from the analysed impedance data was negligible. This was also confirmed from the χ^2 (chi-squared) values, which were reported to be <0.005 , that showed no significant difference between the experimental and analysed impedance values.
- During previous investigations conducted on Al anodes containing In, Sn and Zn, a non-ideal capacitor or constant phase element (CPE), was used to compensate for the inhomogeneities of the working electrode-electrolyte. The impedance of the CPE is given by the relation shown in **Table 4.14**. Due to the inherent surface roughness of the coatings, see **Table 4.9** which could cause inhomogeneities in the coating-electrolyte interface on a microscopic level, CPE was incorporated in the equivalent circuit model as shown in **Figure 4.61**. The behaviour of CPE is determined by the values of the exponential parameter n , which are mentioned in **Table 4.15**.

Table 4.15: Behaviour of CPE according to n values.

n values	CPE behaviour
-1	Inductor
0	Resistor
0.5	Warburg impedance
+1	Capacitor

From the Nyquist plots for Al coating at various chloride concentrations, shown in **Figure 4.57** (a)-(d), two time constants, were deduced with equivalent circuit model shown in **Figure 4.61** (a) from which the impedance parameters were derived, see **Table 4.10**. The equivalent circuit model for Al coating subjected to 3.5% w/v NaCl solution for 1 hour reported an ideal capacitive behaviour, see **Table 4.10**, this was also noticed from the complex Nyquist plot shown in **Figure 4.57** (a), which records formation of a vertical line starting from mid frequency range of 10 kHz and continues to 1 mHz, confirming that the imaginary component was inversely proportional to the frequency. However, this behaviour was not observed with the increase in the exposure period, nor was observed for Al coating exposed to 1.0% w/v, 0.1% w/v and 0.01% w/v NaCl solution for all exposure period used during experiment.

During the earlier work conducted on understanding the activation and passivation mechanism of Al in both chloride and alkaline media, formation of similar Nyquist plots as shown in **Figure 4.57** have been reported, see **Figure 2.41** [135]. However the Nyquist plots shown in **Figure 2.41**, did not show such a high capacitive behaviour which was observed for Al coating after 1 hour in 3.5% w/v NaCl solution.

In an earlier work reported by *MacDonald* [136] on impedance analysis of porous electrodes, complex Nyquist plots with sharp rise in the capacitance, similar to the one shown in **Figure 4.57**, was observed. The authors suggested that the operational impedance function of the semi-infinite cylindrical pore (Z_p) was directly proportional to modulus of Z and phase angle Φ , given by the following relationship [136]:

$$Z_p = (R_p |z|)^{1/2} e^{j\Phi/2}$$

Where, R_p represents the resistance per unit depth of the pore. Using the above relation, the authors suggested that the locus with slope $> \pi/4$ observed in the complex Nyquist plot indicated formation of pore on the electrode, which was found to be further dependent on the shape of the pore.

According to the authors [136], the shape of the Nyquist plot shown in **Figure 4.57 (a)** could have shown formation of a pore either with a right circular cylindrical geometry or semi-spherical geometry. The present work seemed to be very similar to the deductions made by *MacDonald* [136] on EIS of porous electrodes, but this capacitive behaviour was not observed further during the EIS investigation of either Al, Al-Zn, Al-Zn-In or Al-Ti-C coating at any exposure time and NaCl concentration.

The equivalent circuit model shown in **Figure 4.61** (a) which aided in obtaining impedance parameters for Al coating exposed to various NaCl concentrations recorded in **Table 4.10** showed formation of two time dependent constants. The first CPE (Q_1) at higher frequency range between 100 kHz to 10 kHz, could be associated with the initial formation of Al oxide layer on the surface of the working electrode.

Similarly at higher frequency range, R_1 is associated with the resistance offered by the electrolyte solution. Increase in the value of R_1 with reduction in NaCl concentration was reported in **Table 4.10**, indicating increase in the electrolyte resistance with decrease in Cl^- ion concentration.

At lower frequencies (<10 kHz), the presence of R_2 , Q_2 and R_3 indicated complex interactions at Al coating surface-Al oxide-electrolyte interface. The fitting results showed that the n values for Q_1 were recorded to be mostly in the range of 0.7 to 1, except for Al coating exposed to 1.0% w/v NaCl for 1 hour, 0.1% w/v NaCl for 168 hours and 0.01% w/v NaCl for 48 hours, which reported n values of 0.5, see **Table 4.10**.

The Nyquist plots for Al obtained in the present study were similar to the results reported by other researchers [133-137,232,238] who

investigated the corrosion mechanism of Al and Al alloys using similar equivalent circuit model.

The dominant mechanism explaining the formation of higher frequency time constant (Q_1) was attributed to the dielectric properties of Al oxide layer [135,139]. It was shown that the capacitance of the Al oxide layer holds an inverse relation with the thickness of the film [139] (C or $Q \approx \epsilon_0 \epsilon / d$, where ϵ_0 and ϵ represents relative permittivity of vacuum and Al oxide film and d is the thickness)

Thus, the reduction in the Q_1 values as seen from **Table 4.10**, with increase in the exposure period suggested increase in the thickness of the passive Al oxide layer formed on the Al coating exposed to different NaCl concentrations (notice the OCP values recorded prior to impedance data collection were in a more electronegative region with increase in the period of exposure in NaCl solution, see **Table 4.10.**)

Further to the formation of Al oxide layer, a complex mechanism involving diffusion of Al^{3+} ions across the $Al(OH)_3$ film was used to explain the behaviour at Al coating-oxide-electrolyte interface [135,136], which was represented by the time constant, observed at lower frequencies, see **Figure 4.61** (a). This complex mechanism of diffusion of metal cation through the oxide film was referred to as a point defect model [136,137], and was used in understanding the

passive oxide layer formed on metals like Ni, Al, Ti, Cr, Zn and Zr. This model was also used in understanding the activation mechanism of Al by Zn and In in the chloride media [138-140]. During the present study of Al coatings at various chloride concentrations and exposure time period, the following observations made were in accordance with the point defect model theory of passive oxide film [136,137]:

- The formation of Al oxide layer, which increased in thickness with longer exposure periods, was evident from the values of Q_1 recorded in **Table 4.10**.
- It was envisaged that the passive oxide film contained a large density of vacancies of Al^{3+} ions ($V_{Al^{3+}}$) which diffused from from the surface of Al beneath the passive layer and vacancies of oxygen atoms (V_{O_2}) resulting in a p-n type junction causing development of electric field across the oxide film which is independent of the thickness of the oxide film. As seen from **Table 4.10**, that lower Q_2 values at 3.5% w/v NaCl solution were recorded than 1.0% w/v, 0.1% w/v and 0.01% w/v NaCl solution, this indicated the formation of a stable Al oxide layer with maximum thickness at 3.5% NaCl concentration. Thus suggesting that, even though diffusion of Al^{3+} ions from the underlying surface took place, shown in **Figure 4.61 (a)** by the equivalent circuit model with R_2 , Q_2 and

R_3 , the process could not produce uniform dissolution of the oxide layer for activation of Al (see section 2.8.6.3 (b), chapter 2).

The equivalent circuit model shown in **Figure 4.61** (a) was also used in analysing the impedance data obtained for Al-Ti-C coating exposed to various NaCl concentrations and exposure periods, see **Figure 4.60** (a)-(d). **Table 4.13** also indicated the formation of passive oxide layer on the surface of Al-Ti-C coating during first hour of exposure, however in comparison to Al coating, the Q_1 values were recorded minimum for 0.01% w/v NaCl exposure followed by 3.5% w/v NaCl exposure.

However, for Al-Ti-C coating exposed to various NaCl concentration and exposure period, the decrease in the thickness of oxide film was evident from the Q_2 values, see **Table 4.13**, which were recorded at lower frequencies. These results indicated that unlike Al, the passive oxide layer formed on Al-Ti-C coating is unstable possibly due to the presence of Ti and C as alloying elements which tends to increase the cation vacancy in the Al oxide layer which in turn promotes further diffusion of Al^{3+} ions from the surface of Al-Ti-C coating. However the OCP measurements of Al-Ti-C coatings were also similar to the ones recorded for Al coating, see **Table 4.13**.

For Al-Zn and Al-Zn-In coating, the equivalent circuit models shown in Figure 4.61 (b)-(d) were used to obtain the impedance parameters mentioned in **Table 4.11** and **Table 4.12**. Similar to Al and Al-Ti-C coating analysis, two time constants which also included an Inductor and Warburg diffusion impedance were observed at lower frequencies, see **Figure 4.58** and **Figure 4.54**.

The complex Nyquist plot for Al-Zn coating, **Figure 4.58** (a) revealed formation of an inductive loop during the first hour of immersion in 3.5% w/v NaCl solution, whereas the Nyquist plot for Al-Zn-In coating exhibited what appears to be single time constant over the frequency range of 100 kHz to 1 mHz. However with increase in the time period of exposure in 3.5% w/v NaCl solution, the Al-Zn coating showed formation of two semi-circles at 24 and 48 hours, which were not seen for Al-Zn-In coating, see **Figure 4.58** and **Figure 4.59**.

It is important to note that at lower NaCl concentrations of 1.0% w/v, 0.1% w/v and 0.01% w/v, only Al-Zn-In coating exhibited inductive loops (at 1.0% w/v and 0.01% w/v NaCl concentration), see **Figure 4.59**, while Al-Zn coating exhibited capacitive loops (CPE's) along with diffusion constants at lower frequencies, see **Figure 4. 58**.

The Nyquist plots along with the impedance parameters obtained for Al-Zn and Al-Zn-In coating at various chloride concentrations suggested the mechanism of activation of Al as suggested by previous investigators using EIS technique [137-140].

After careful examination of the impedance parameters obtained for Al-Zn and Al-Zn-In, see **Table 4.11** and **Table 4.12** coating using the circuit models shown in **Figure 4.61** (b)-(d), it was shown that Al-Zn-In coating showed an enhanced inductive behaviour than Al-Zn coating and both coatings showed formation of Warburg impedance at lower frequencies, even for lower chloride concentrations, this behaviour has been reported during the previous investigation conducted by *Venugopal and Raja* [138], who investigated addition of Zn and In ions to Al exposed in 3.5% w/v NaCl solution.

As indicated in the earlier discussion that the formation of the first constant phase element is attributed to the dielectric properties of Al oxide film and depends upon the thickness of the oxide film [135,137]. In order to explain the interaction of Zn and In with the initially formed oxide layer, the time

constant observed at lower frequencies were explained using point defect model [135,135] in the present study.

As seen from **Table 4.12**, the n values of the second time constant, CPE were mostly in the range of 0.7 to 0.9, at lower frequencies. This can be attributed to the formation of spinel $ZnAl_2O_4$ phase in the Al-oxide layer, which has been reported in previous investigations [91,92,96].

However Warburg diffusion impedance was also observed at lower frequencies, see **Table 4.12**. This can be attributed due to diffusion of Zn^{2+} ions from the surface to the oxide layer to form the spinel structure. As shown previously that dissolution of Zn from the surface of Al is higher than its diffusion into the Al matrix [126], which favours formation of $ZnAl_2O_4$ spinel causing the oxide layer to behave like an n- type junction which in turn increases the diffusion of Zn^{2+} ion in Al oxide layer [126,138].

This phenomenon supports the formation of low frequency CPE along with Warbug diffusion observed for Al-Zn coating, see **Table 4.11** and suggested that presence of Zn in Al causes the formation of electron rich regions on the initial Al oxide layer due to formation of Zn spinel, hence producing active sites on Al-Zn coatings.

For Al-Zn-In coating, the values of n closer to 0.5, See **Table 4.12**, suggested the inductive nature of the time constant which was observed at lower frequencies. This has been attributed due to formation of intermediate In-chloro complex, see section 2.8.6.3 (a) of chapter 2, at the active sites produced by Zn [126,138,139].

As it has been shown from the previous investigations that thermodynamically In exhibits three oxidation states, out of which In^{3+} has been shown to be the most stable state [118-121]. In presence of Cl^- ions, the formation of InCl_2^+ due to adsorption of Cl^- ion produces an inductive behaviour [138], which is also seen in the present study. However during formation of InCl_2^+ , formation of an intermediate In^+ has also been reported [118-121].

This thermodynamically unstable In^+ formed within the Al oxide layer lowers the electron excess regions in Al oxide layer which were produced by Zn causing vacancies in the oxide film to be filled up by anions. These anionic vacancies are filled up by Cl^- ions leading to rupturing of oxide layer.

This phenomena also validates the impedance results obtained for Al-Zn-In coating, see **Table 4.12** suggesting that presence of In in Al-Zn coating increases the inductive behaviour due to adsorption of Cl^- ion, even at lower chloride concentrations, see **Figure 4.59**.

Chapter 4: Results and Discussion-Part 2

This part of the current study includes:

- Included to understand the influence of the sprayed coating's microstructure and hardness on the wear resistance of the Al-Ti-C alloy coating.
- The Al-Ti-C coating's wear performance has been compared with that of a pure Al sprayed coating, a widely used wear resistant 13%Cr Steel sprayed coating and the mild steel substrate. A comparison of wear rates has also been made between the pre-sprayed aluminium alloys which were used to form the wires for arc spraying, and the sprayed coatings.
- The second objective was to understand the effect of identified phases in the microstructure of Al-Ti-C coating on the wear performance of the coatings, when exposed to elevated temperature. The wear resistance and the hardness of Al-Ti-C coating exposed to two heat treatment regimens was evaluated in conjunction with microstructural analysis in order to comprehend the effect of change in microstructure on the wear resistance performance of Al-Ti-C coating.

4.5 Evaluation of coefficient of wear for Al-Ti-C coatings.

4.5.1 Microstructure of Al-Ti-C and pure Al feedstock

Figure 4.62 (a) and (b) shows the backscattered electron micrographs of the transverse section of pure Al and Al-Ti-C alloy feedstock alloy rod.

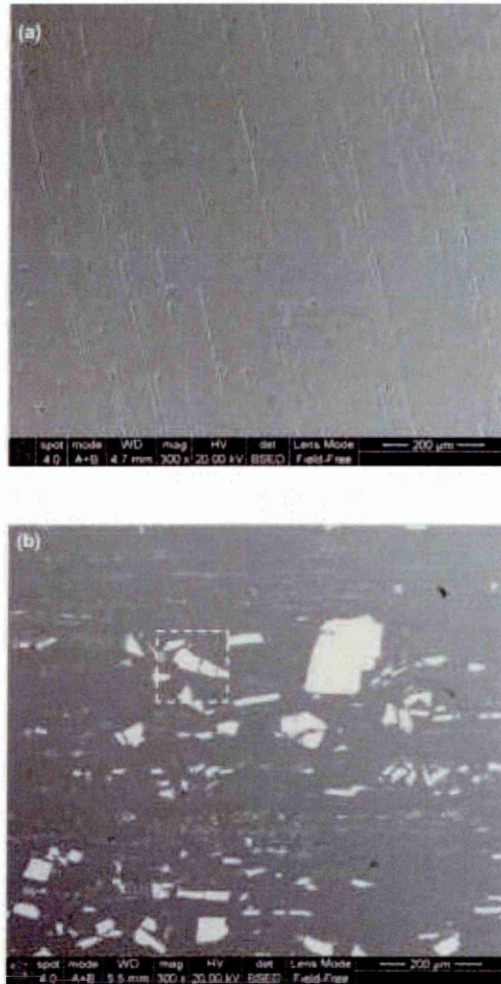


Figure 4.62: Backscattered electron micrograph of transverse section of (a) Al and (b) Al-Ti-C feedstock material.

For pure Al feedstock no microstructural features were observed (the linear features observed in **Figure 4.62** (a) are artefacts of polishing and the extrusion direction of the rod). It was apparent from the micrographs of the Al-Ti-C material that two distinct phases existed in the structure

- A large blocky phase with a large aspect ratio and
- A smaller equiaxed phase, both of which were evenly distributed in the aluminium matrix as shown in **Figure 4. 62** (b).

Figure 4.63 (a) and (b) shows a higher magnification image of the enclosed area shown in figure 1(b) where the two phases are clearly discernible. The Energy dispersive X-ray analysis on each phase highlighted in **Figure 4.63** (a) and (b) was used to quantify the average composition of each phase as shown in **Table 4.16**. The analysis suggests that the larger blocky phase has an Al to Ti ratio $\approx 2.8:1$ while the small equiaxed phase has a metal (Ti+Al) to C ratio of $\approx 1:1$. Note that carbon is often found to be present on the surface of samples being analysed using EDX and as such any figure for C may not be entirely due to the material itself and some of the Al signal may have been from the surround Al matrix due to the EDX interaction volume.

Table 4.16: Average composition analysis of different phases observed in Al-Ti-C feedstock alloy.

Phase	Average Composition		
	Al (at%)	Ti (at%)	C (at%)
A. Blocky phase with high aspect ratio	67 ± 1	24 ± 1	8 ± 1
B. Smaller equiaxed phase	28 ± 4	21 ± 4	51 ± 4

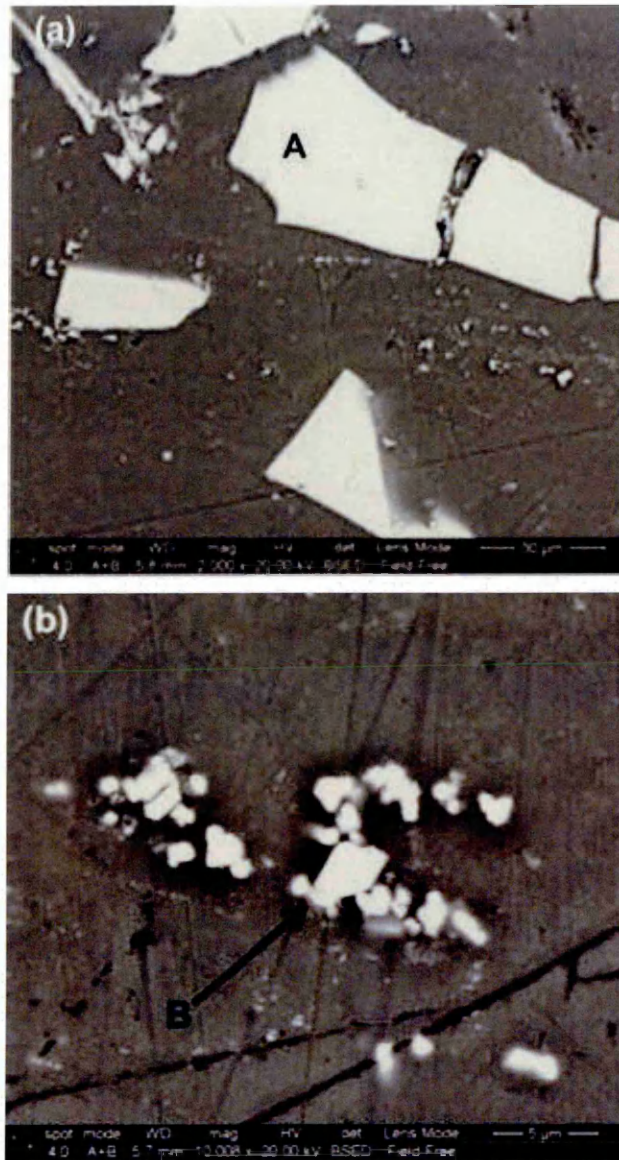


Figure 4.63: EDX analysis of the enclosed area shown in figure 1(b) showing different phases observed in the Al-Ti-C feedstock alloy (a) large blocky phase (A) with large aspect ratio and (b) smaller equiaxed particle (B).

As the production of the alloys involves the slow cooling of the alloy from the melt the phase expected to be present is the equilibrium structure tetragonal Al_3Ti [155]. The smaller equiaxed phase appeared to contain both Ti and Al along with equal atomic amounts of C and was thus probably a phase with the structure of the ceramic titanium carbide (TiC) but with possible Al substitution for some of the Ti. The XRD of the polished transverse section of the alloy confirmed the presence of tetragonal Al_3Ti phase, see **Figure 4.64**, along with presence of a cubic TiC phase in the feedstock alloy concurring the observation of the EDX analysis.

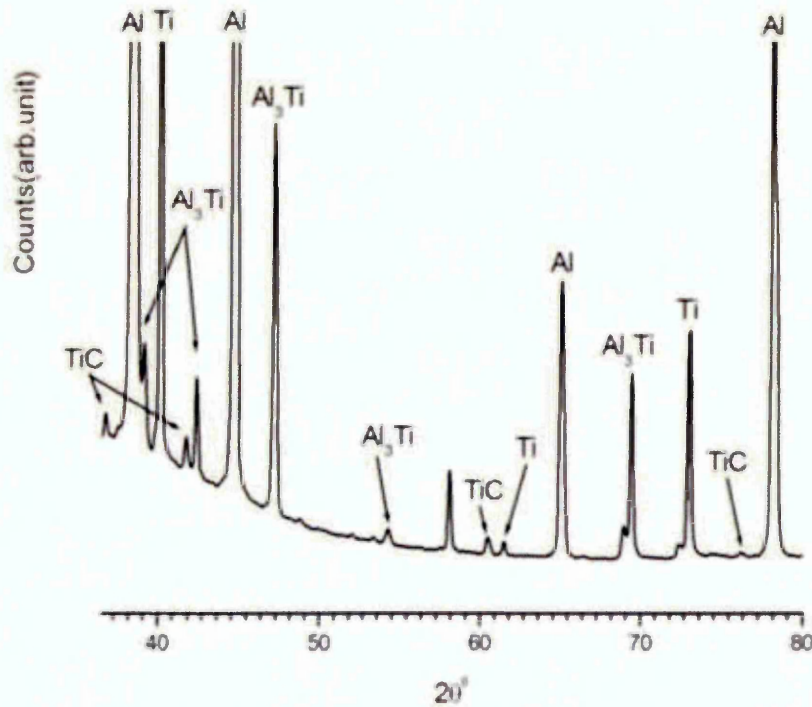


Figure 4.64: XRD trace of Al-Ti-C feedstock alloy confirming the presence of Al_3Ti and TiC phase. The unmarked peak at $2\theta^\circ \approx 58^\circ$ is the $\text{Cu K}\beta$.

4.5.2 Microstructure of Al-Ti-C alloy and pure Al coatings.

Figure 4.65 shows the backscattered electron micrographs of the cross-sections of (a) the arc sprayed pure Al coating and (b) the arc sprayed Al-Ti-C alloy coating.

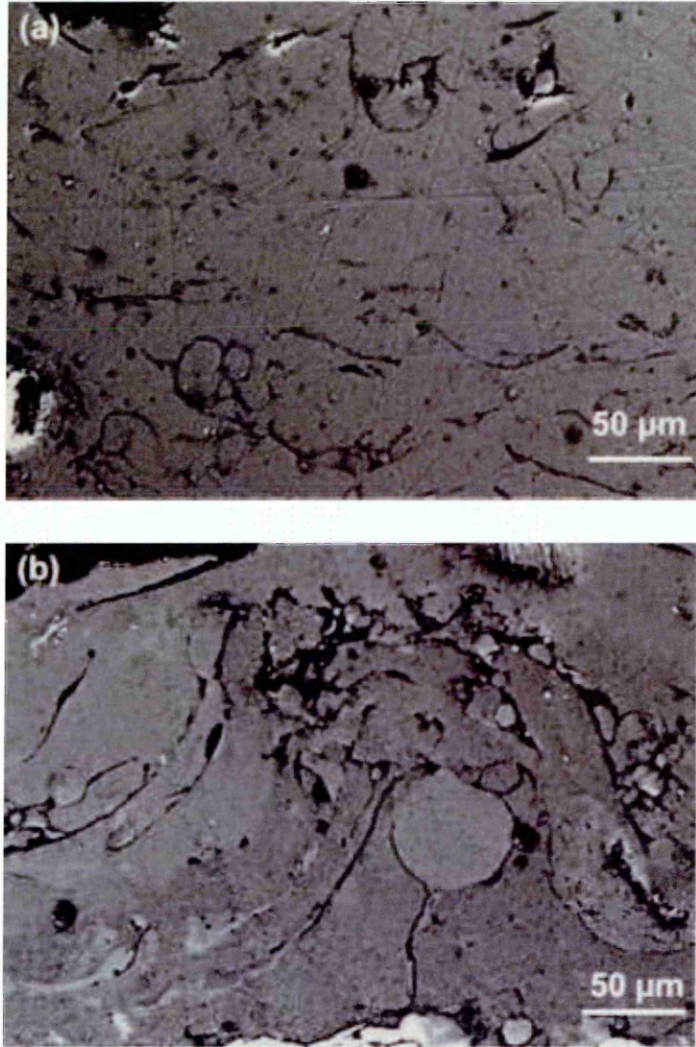


Figure 4.65: Backscattered electron micrograph showing the cross-section of (a) pure Al and (b) Al-Ti-C coating.

In contrast to the bulk feedstock (**Figure 4.63**) an inhomogeneous layered structure was observed with dark regions which were inter-splat porosity or oxides. The Al-Ti-C sprayed coating showed regions of varying contrast in the backscattered electron images indicating the inhomogeneous distribution of the Ti in the Al matrix.

However, the microstructure was significantly different from that observed in the feedstock of Al-Ti-C as shown in **Figure 4.63**. Higher magnification images of the Al-Ti-C coating, see **Figure 4.66** (a) and (b) revealed “speckled” regions, dark grey and light grey regions. EDX analysis of each of these regions was conducted and the average composition of a number of measurements is shown in **Table 4.17**. High titanium or high carbon content phases, as observed in the Al-Ti-C alloy feedstock alloy (**Table 4.16**), were not observed in the sprayed coating. The overall Ti level was slightly below the expected level suggesting that the distribution of Ti was heterogeneous with some small regions having a much higher Ti content than others. A general increase in the detected oxygen levels was noted although this was not high enough to indicate the presence oxygen content.

Table 4.17: Average composition analysis of different phases observed in Al-Ti-C coating.

Phase	Average Composition		
	Al (at%)	Ti (at%)	O (at%)
Speckled region	91 ± 0.5	1 ± 0	7 ± 0.5
Dark grey region	91 ± 0.4	1 ± 0.2	8 ± 0.2
Light grey region	92 ± 0.2	2 ± 1	6 ± 0.3

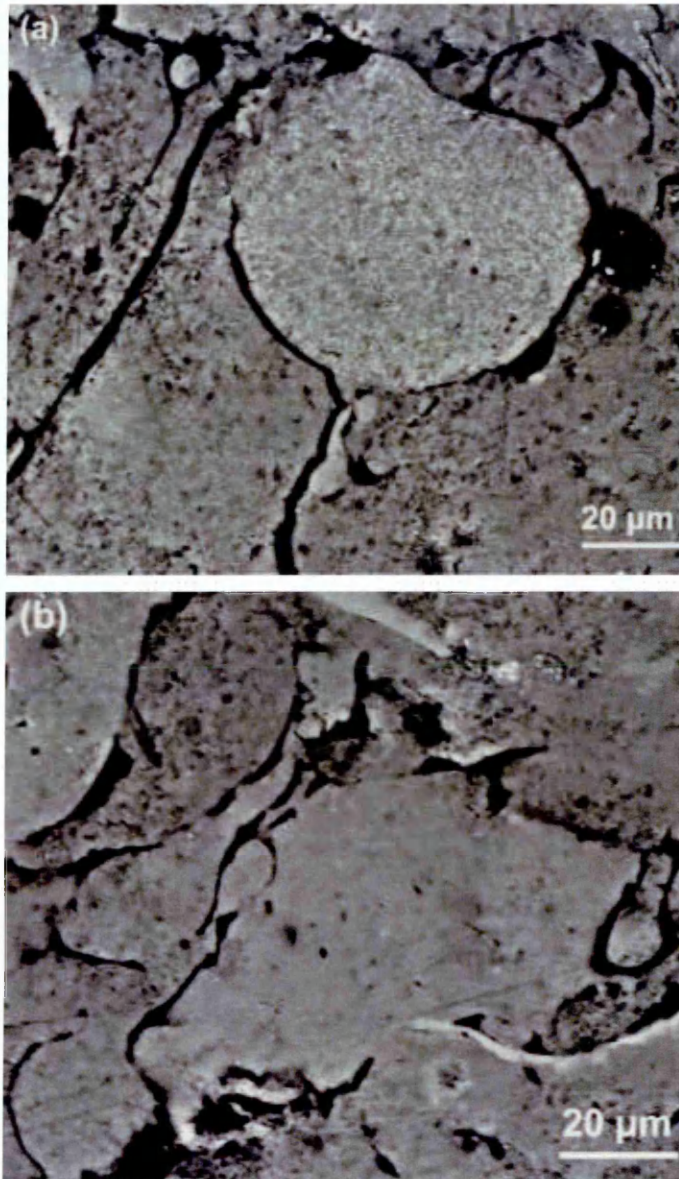


Figure 4.66: Backscattered electron micrograph of Al-Ti-C coating showing (a) speckled region and (b) dark and light grey regions.

The XRD analysis of the as sprayed Al-Ti-C alloy, see **Figure 4.64**, revealed the formation of tri-aluminide Al_3Ti intermetallic phase, however unlike the feedstock Al-Ti-C alloy, which showed formation of Al_3Ti which exhibited tetragonal structure of DO_{22} or DO_{23} type, see **Figure 4.67**, the sprayed form of the alloy showed formation of cubic Al_3Ti (L1_2), which due to symmetry of the crystal structure is significantly less brittle than its equilibrium tetragonal structure [156-159]. Similarly an intermediate ceramic titanium carbide phase of the form Ti_8C_5 with rhombohedral crystal structure was detected by the XRD analysis.

It is probable that the melting and rapid cooling which is characteristic of the arc spraying process has taken the Ti in the alloy in to solution during melting and subsequently the rapid cooling which occurs during splat formation, has produced the metastable cubic phase of Al_3Ti [156]. Possible evidence for this is seen in the presence of the speckled regions in the structure where precipitates of sub-micron scale (the magnification of the image not high enough to accurately predict the size of these precipitates) with an atomic number $> \text{Al}$ are observed in **Figure 4.66 (a)**.

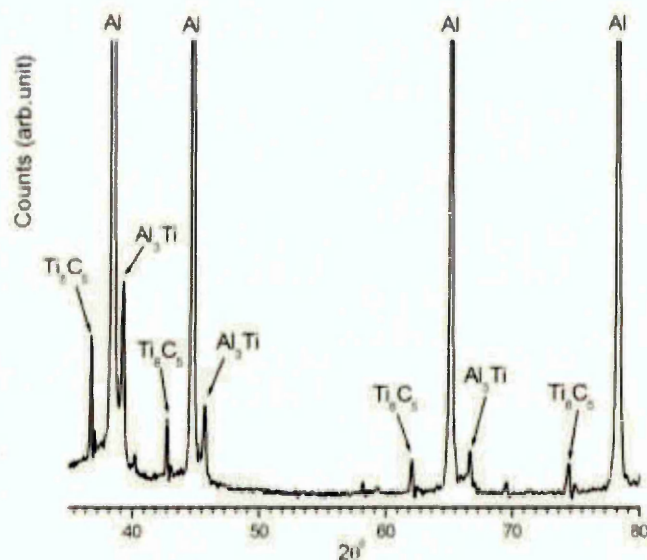


Figure 4.67: XRD trace of as sprayed Al-Ti-C coating showing formation of different phases (see appendix for more details). The unmarked peaks at $2\theta^{\circ} \approx 40^{\circ}, 58^{\circ}, 69^{\circ}$ are $\text{CuK}\beta$.

4.5.3 Micro-hardness of Al-Ti-C alloy and pure Al feedstock and coatings.

Table 4.18 shows the micro-hardness values measured on the feedstock alloys of the pure Al and the Al-Ti-C materials. A larger range of micro-hardness values were recorded for Al-Ti-C alloy than for pure Al as is indicated by the coefficient of variation and as demonstrated in **Figure 4.68**. There were a small number of regions in the Al-Ti-C alloy which exhibited hardness as high as $\text{HV}_{0.98} = 0.78 \text{ GPa}$ (80 kgf/mm^2).

Table 4.18: Vickers micro-hardness of the pure Al and Al-Ti-C feedstock.

	$\text{HV}_{0.98} \text{ GPa (kgf/mm}^2\text{)}$	Coefficient of variation (%)
Pure Al feedstock	0.32 (33 ± 1)	3
Al-Ti-C feedstock	0.43 (44 ± 8)	18

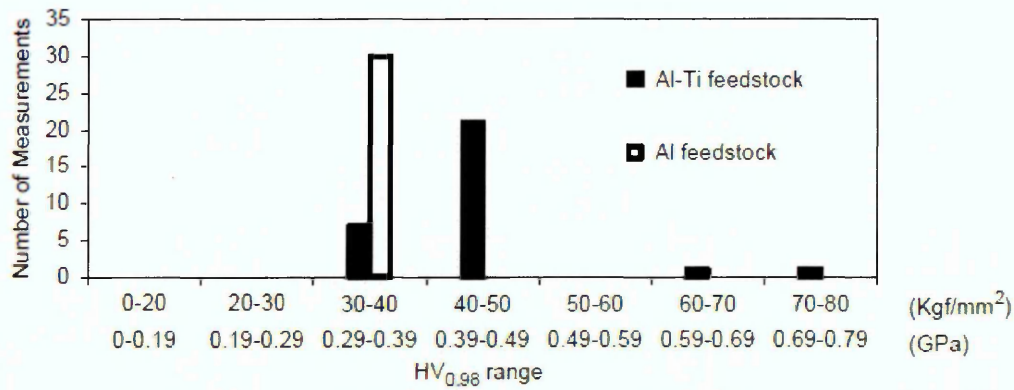


Figure 4.68: Frequency distribution histogram of micro-hardness (HV_{0.98}) for pure Al and Al-Ti-C feedstock alloy material.

The hardness results from the cross-section of the coating are shown in **Table 4.18**. A significant increase of $\approx 70\%$ in the micro-hardness of the Al-Ti-C coating when compared to its feedstock was observed. The pure Al coating showed similar hardness to its feedstock material. The Al-Ti-C coating was significantly harder (117%) than the pure Al coating. The 13 % Cr coating which was used as a reference in the wear testing was also measured for reference. In terms of the spread in the hardness values, the Al-Ti-C exhibited the largest coefficient of variation (35%) with some regions exhibiting a hardness of upto HV_{0.98} = 1.37 GPa (140 kgf/mm²), as shown in **Figure 4.69**.

Table 4.19: Vickers micro-hardness of the pure Al, Al-Ti-C and 13 % Cr steel coatings.

	HV _{0.98} GPa (kgf/mm ²)	Coefficient of variation (%)
Pure Al coating	0.34 (35 ± 8)	22
Al-Ti-C coating	0.74 (75 ± 26)	35
13 % Cr steel coating	3.97 (405 ± 82)	20

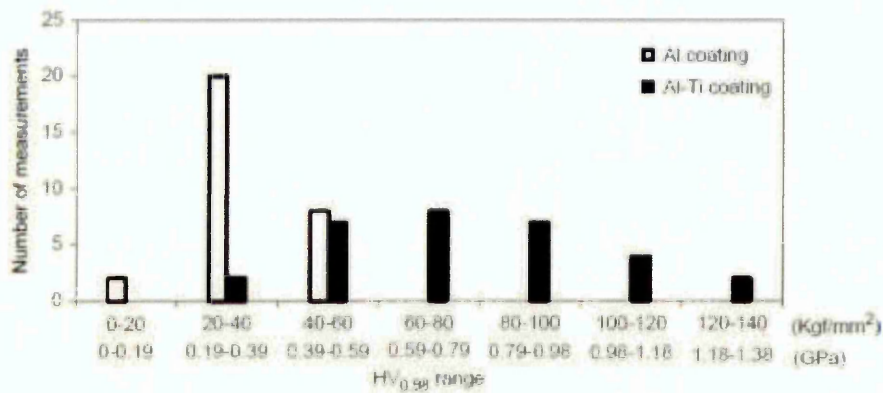


Figure 4.69: Frequency distribution histogram of variation in micro-hardness of pure Al and Al-Ti-C coating.

The influence of the intermetallic tri aluminide Al_3Ti and ceramic titanium carbide (with probable Al substitution in the ceramic phase) phases was observed in the micro-hardness of the Al-Ti-C feedstock alloy which was 33% higher than that of the pure Al feedstock alloy. Pure TiC is known to have a micro-hardness of $HV_{0.98} = 28-33$ GPa(2850–3390 kgf/mm²) [158,159] while the micro-hardness of Al_3Ti has been measured by others to be $HV_{2.0} \approx 5.0$ GPa (510 kgf/mm²) [158]. Despite the absence of the two hard phases, the micro-hardness of the sprayed Al-Ti-C coating was more than twice (114%) that of the sprayed aluminium alloy and 71% higher than its own feedstock alloy, with some regions exhibiting upto $HV_{0.98} = 1.18$ GPa(120 kgf/mm²). This could have been possible due to formation of $L1_2$ type cubic Al_3Ti and Ti_8C_5 intermediate ceramic carbide due to spraying process, as shown by XRD analysis, see **Figure 4.67** and are evident from **Figure 4.66** (a) in form of sub-micron structure.

4.5.4 Coefficient of wear for Al-Ti-C and pure Al feedstock material and coatings.

The coefficient of wear for pure Al and Al-Ti-C feedstock and coatings were calculated from the gradient of the graphs shown in **Figure 4.70** and **Figure 4.71**, where the volume of the wear crater (in mm³) formed during the micro-scale abrasive wear test is plotted against sliding distance (in m) multiplied by the applied load (in N). Excellent linear regression fits were observed with $R^2 > 0.97$.

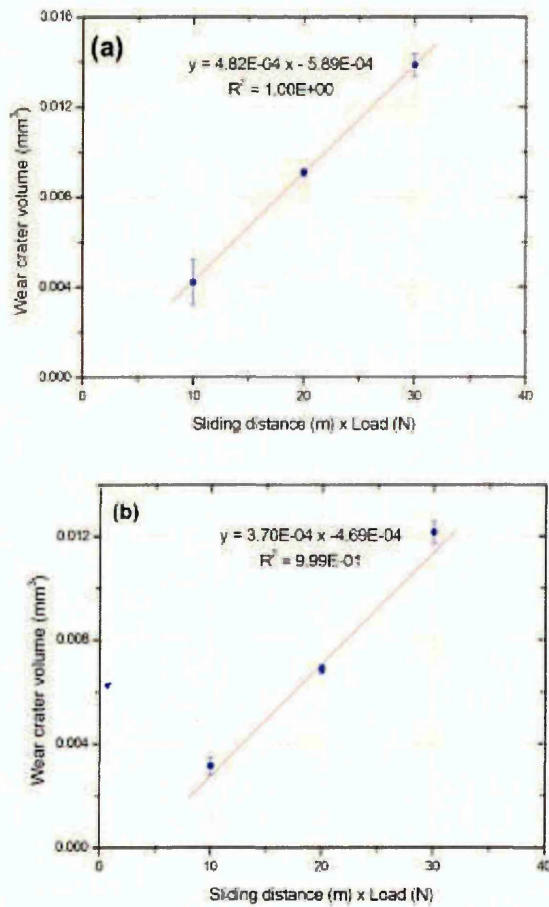


Figure 4.70: Graphs showing wear crater volume vs. Sliding distance x load for (a) pure Al and (b) Al-Ti-C feedstock material.

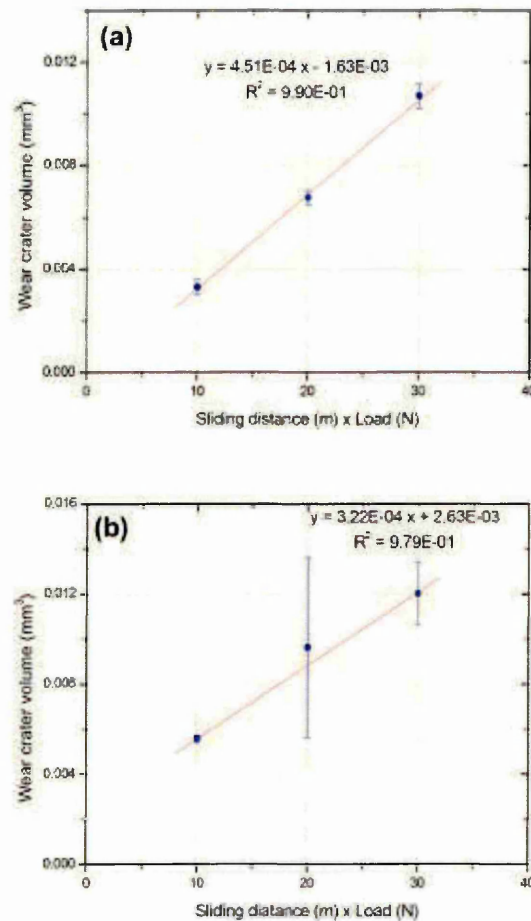


Figure 4.71: Graphs showing wear crater volume vs. sliding distance x Load for (a) Pure Al and (b) Al-Ti-C coatings.

It was observed, as shown in **Table 4.20**, that the coefficient of wear for Al-Ti-C feedstock was 18% less than that of the pure Al feedstock. The coefficient of wear for Al-Ti-C coatings was 33% lower than for pure Al coating as reported in **Table 4.21**. The difference between the feedstock alloy and the sprayed coating was not significant for the pure Al alloy but there was a difference between the feedstock alloy and sprayed coating of Al-Ti-C with the sprayed coating exhibiting marginally better wear resistance.

Similar wear resistance was exhibited by the Al-Ti-C feedstock and the sprayed coating despite the significantly different microstructure, hardness and porosity in the coating. The wear tracks shown in **Figure 4.72** and **Figure 4.73** show two body grooving wear mechanism in both feedstock's and coatings, caused by the ploughing of the surface by the 2.5 mm SiO₂ particles in the abrasive slurry, a mechanism that has been reported by other researchers [271].

Table 4.20: Coefficient of wear for Al and Al-Ti-C feedstock alloys.

	Coefficient of wear (mm ³ N ⁻¹ m ⁻¹)
Al feedstock alloy	4.5E-04 ± 0.5E-04
Al-Ti-C feedstock alloy	3.7E-04 ± 0.1E-04

Table 4.21: Coefficient of wear for Al and Al-Ti-C coatings.

	Coefficient of wear (mm ³ N ⁻¹ m ⁻¹)
Al coating	4.8E-04 ± 0.03E-04
Al-Ti-C coating	3.2E-04 ± 0.5E-04

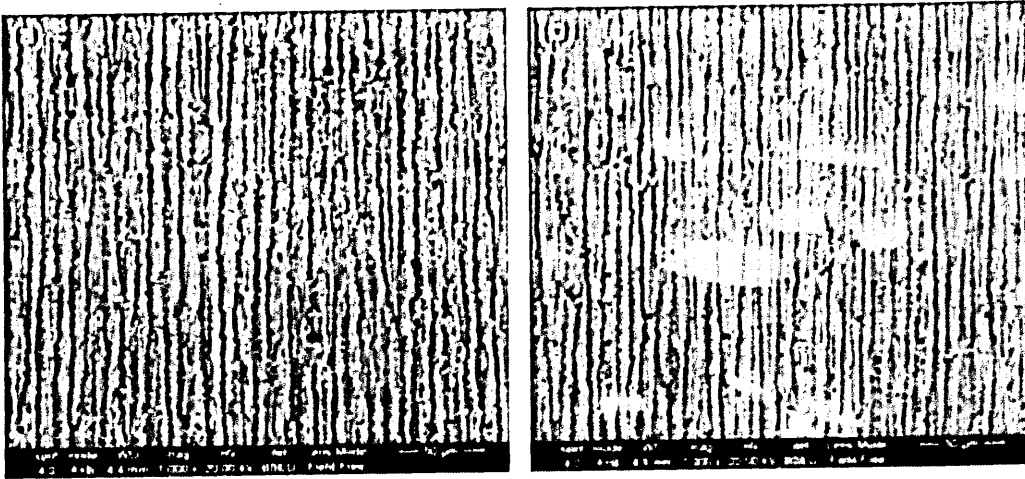


Figure 4.72: Backscattered micrographs showing the directionality of the wear tracks for (a) Al and (b) Al-Ti-C feedstock.

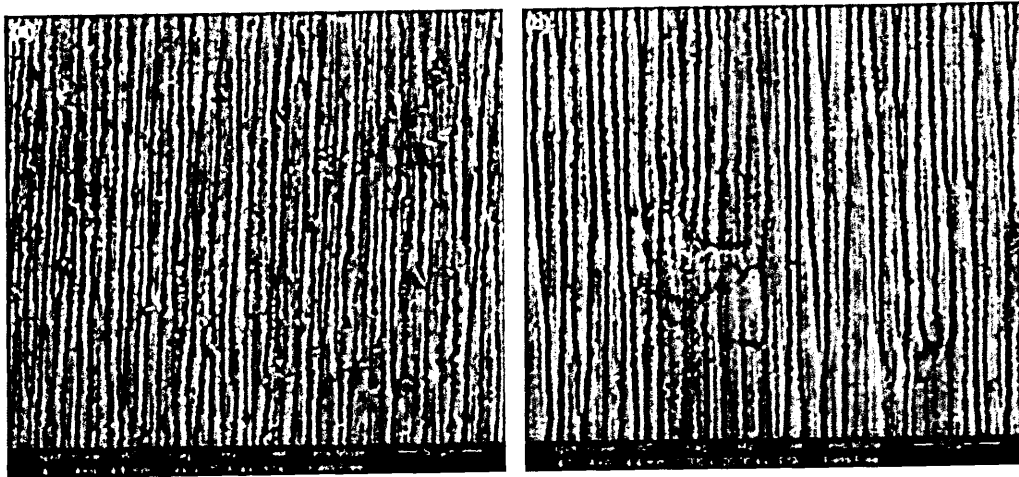


Figure 4.73: Backscattered micrographs showing directionality of the wear tracks for (a) Al and (b) Al-Ti-C coating.

The wear coefficient of Al-Ti-C feedstock alloy was 18% lower (thus better) than that of the pure Al feedstock alloy, which can be attributed primarily to the harder intermetallic Al_3Ti tri-aluminide phases in the alloy as these appear to be resisting indentation by the abrasive particles more than the surrounding Al matrix, see **Figure 4.72** (b). The hard ceramic (Ti,Al)C phase (which was detected using EDX analysis and XRD confirmed it to be cubic titanium carbide with possible Al substitution) which is known to be present, was too small to be observed on the wear scar and as such its contribution to the wear resistance cannot be verified.

The arc sprayed Al-Ti-C coating exhibited a 33% lower wear coefficient than the arc sprayed pure Al coating, with the lower wear coefficient being attributed to the overall higher micro-hardness (114% harder) and the presence of regions with hardness upto $\text{HV}_{0.98} = 1.37 \text{ GPa}$ (120 kgf/mm^2). While Al_3Ti and (Ti,Al)C phases were not observed in the coating structure the high hardness regions may have contained the nano-scale precipitates of cubic Al_3Ti , observed by the XRD analysis of the as sprayed Al-Ti-C coating, which may have influenced the hardness and wear resistance through precipitation strengthening [157].

It was noted that even though the arc sprayed 13 wt % Cr steel coating had a significantly higher hardness the difference in the coefficient of wear between 13 wt% Cr steel coating and Al-Ti-C was negligible ($\approx 2\%$). The mild steel substrate material had the lowest wear coefficient which most probably can be attributed to the fact that it has a fully dense steel structure rather than a porous sprayed coating.

A graph illustrating the comparison of the wear coefficients and hardness (HV9.8 and HV0.98) of all the materials tested is shown in **Figure 4.74**.

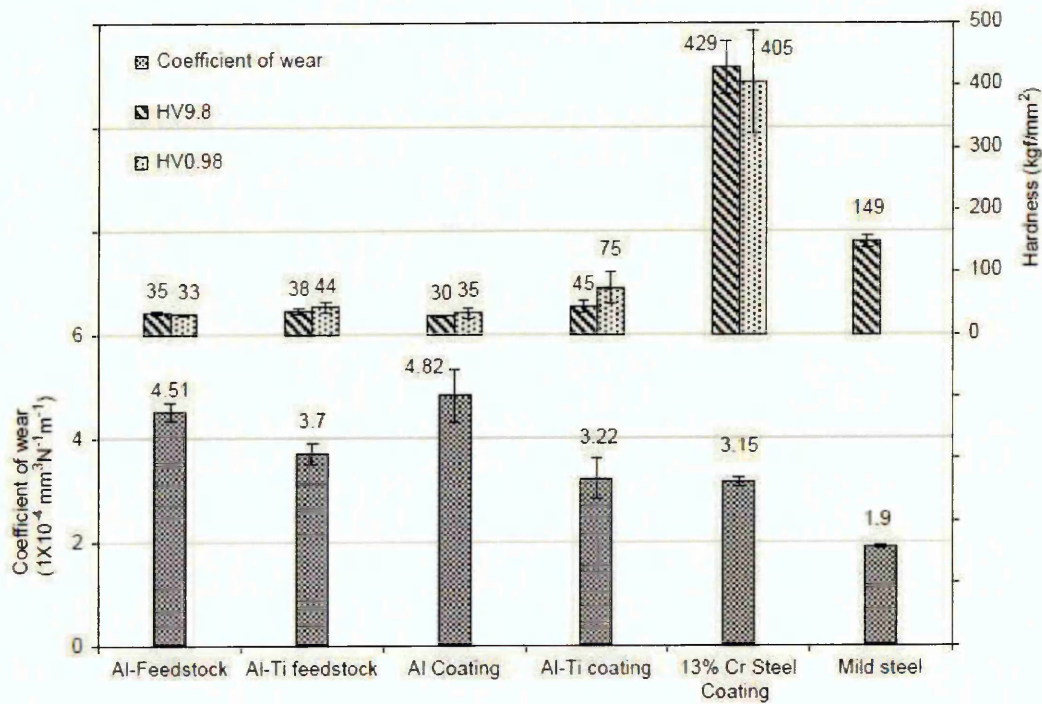


Figure 4.74: Comparison of coefficient of wear and hardness of pure Al and Al-Ti-C alloy feedstock material and coatings with 13 % Cr steel coating and mild steel substrate.

4.6 The effect of exposure temperature on the microstructure and wear resistance performance of Al-Ti-C coating.

The backscattered electron micrographs of Al-Ti-C coating revealed presence of sub-micron precipitates of cubic Al_3Ti , the speckled regions, along with dark and light grey regions which were identified using atomic number contrast. Unlike the feedstock Al-Ti-C alloy, which contained tetragonal Al_3Ti intermetallic tri-aluminide and cubic titanium carbide phase with some Al substitution, the difference in the phases of the corresponding coating was attributed to the precipitation strengthening caused by rapid melting and solidification during arc spraying of the alloy, which resulted in an increased hardness ($\approx 114\%$) and lower coefficient of wear ($\approx 10\%$) of coating, see **Figure 4.74**.

In an attempt to understand the role of identified constituent phases on the wear resistance performance of Al-Ti-C coating, the Al-Ti-C coatings were subjected to two different heat treatment cycles which were as follows:

- The coatings were exposed to pre-heated furnace at 150°C , 350°C and 550°C for one and three hours followed by rapid quenching (RQ) using deionised water at 25°C .
- The second cycle involved heating the coatings with the same temperature and exposure period but followed by normal room temperature cooling (AC) by keeping the coatings out of furnace at normal room temperature for 5 hours.

This heat treatment cycle was followed by conducting the micro-scale abrasive wear test, hardness measurements and microstructural evaluation of coating with exactly same parameters used earlier in the work. A series of backscattered electron micrographs of Al-Ti-C coatings exposed to two heat treatment cycles have been presented in the further sections to identify the precipitated phases. As the backscattered coefficient of light elements such as O and C is significantly lower than Al and Ti, the compositional contrast was not evident for oxygen or carbon rich phases (limitations as discussed in section 3.4.2).

4.6.1 Microstructure of Al-Ti-C coating subjected to 150°C for 1 hour and 3 hours followed by rapid quenching.

Figure 4.75 (a) and (b) shows the backscattered electron micrograph of Al-Ti-C coating exposed to 150°C for 1 hour and 3 hours at 150°C followed by rapid quenching.

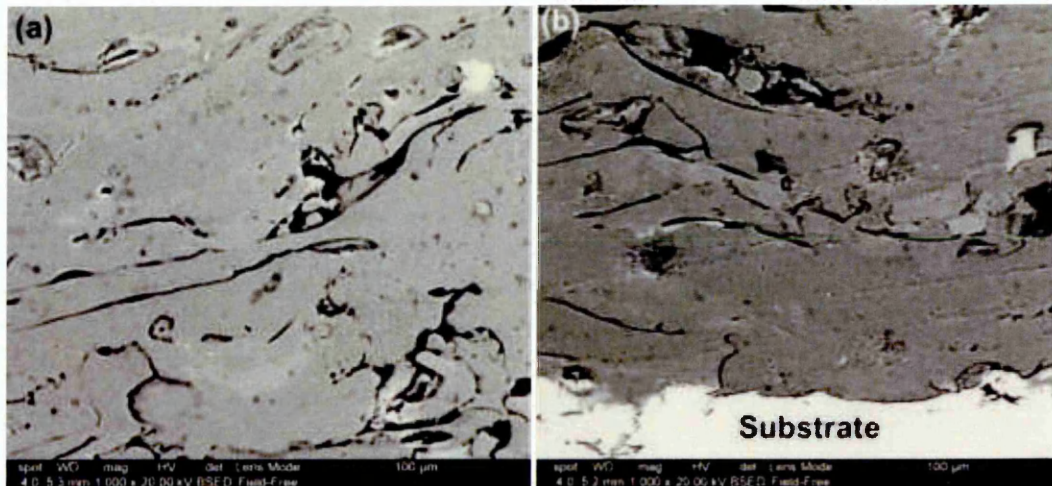


Figure 4.75: Backscattered electron micrograph of Al-Ti-C coating exposed to 150°C for (a) 1 hour and (b) 3 hours, followed by rapid quenching.

The backscattered atomic number contrast reveals formation of similar phases in the Al-Ti-C coating exposed to 150°C for 1 hour and 3 hours followed by rapid quenching as seen in the as sprayed coatings, see Figure 4.66 (a) and (b). However a closer examination of the microstructure of Al-Ti-C coating exposed to 150°C for 1 hour and 3 hours, revealed formation of regions containing larger speckled spots, see Figure 4.76 (a) and Figure 4.77 (a).

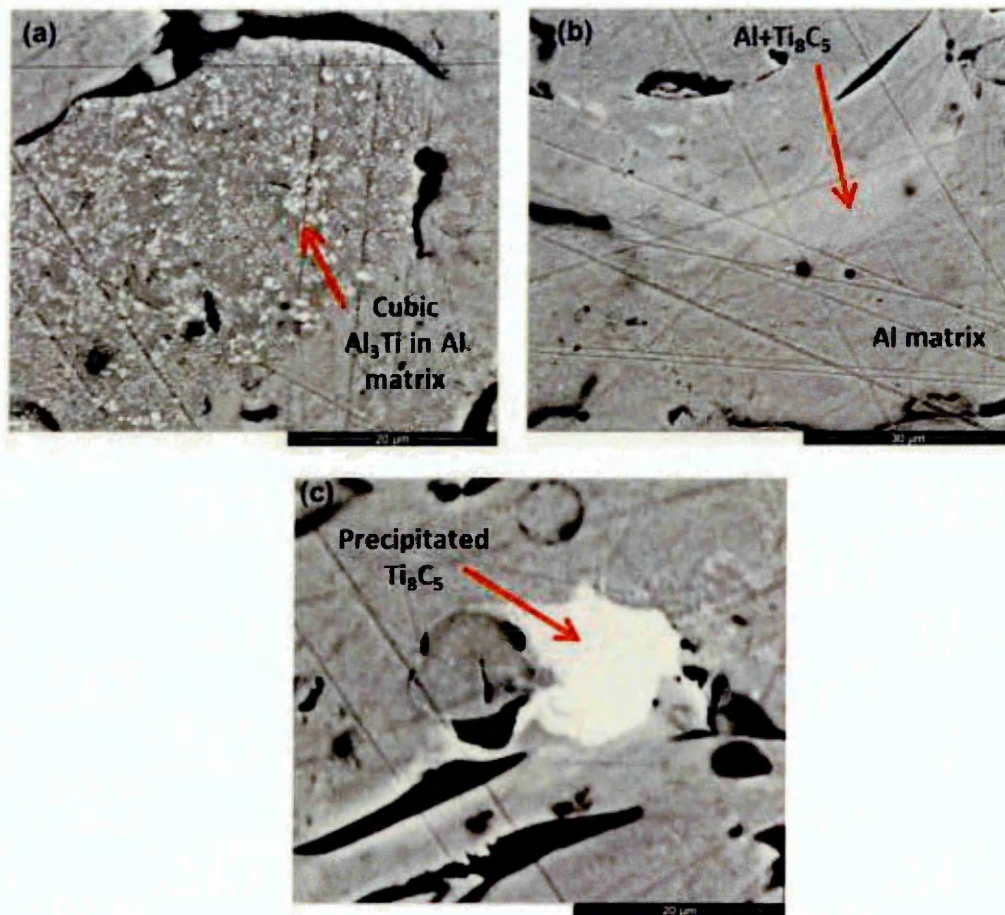


Figure 4.76: A higher magnification, @ x 5000, Backscattered electron micrographs of Al-Ti-C coating exposed to 150°C for 1 hour showing (a) small and large speckled spots (b) light and dark grey regions and (c) higher atomic number contrast light grey region. The coating was rapidly quenched post exposure.

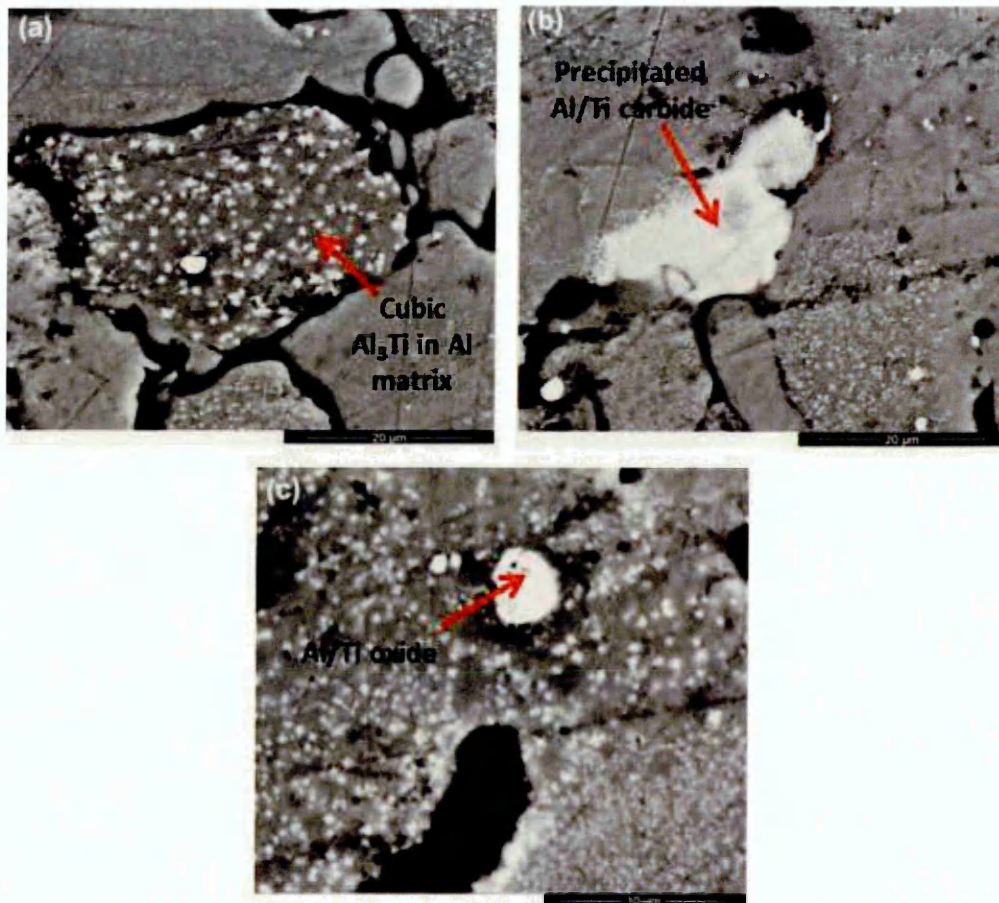


Figure 4.77: A higher magnification (a) and (b) @ x 5000 and (c) @ x 10,000, backscattered electron micrograph of Al-Ti-C coating exposed to 150⁰C for 3 hours showing (a) distinctive growth of large speckled spots, (b) high atomic number contrast region and (c) spherical equiaxed phase. The coatings were rapidly quenched post exposure.

After 1 hour of exposure @ 150⁰C followed by rapid quenching, a distinctive increase in the size of speckled spots was observed, see **Figure 4.76** (a) along with existing speckled spots of similar size as observed in the as sprayed coating, see **Figure 4.66** (a).

With increase in the exposure time to 3 hours, two discernable regions of different speckled spot size, see **Figure 4.77** (a) and (c) were observed, which were not seen in the cross-section of Al-Ti-C coating @150⁰C after 1 hour of exposure.

A bright region with higher atomic number contrast, see **Figure 4.76** (c) and **Figure 4.77** (b), was also seen in Al-Ti-C coating @ 150⁰C after 1 hour and 3 hour of exposure. An additional spherical equiaxed phase, similar to the one observed in Al-Ti-C feedstock alloy, was also seen in the microstructure of Al-Ti-C coating @ 150⁰C for 3 hours, see **Figure 4.77** (c), which was not observable in the Al-Ti-C coating @ 150⁰C for 1 hour. The EDX analysis, see **Table 4.22** and **Table 4.23**, of each phase shown in **Figure 4.76** (a), (b), (c) and **Figure 4.77** (a), (b), (c) was used to quantify the average composition of each phase present in Al-Ti-C coating @ 150⁰C for 1 hour and 3 hours followed by rapid quenching.

Table 4.22: Average composition analysis of different phases observed in Al-Ti-C coating @ 150⁰C for 1 hour followed by rapid quenching.

Phase	Average composition			
	Al (at%)	Ti (at%)	C (at%)	O (at%)
Speckled region	80 ± 2	2 ± 0.2	14 ± 2	5 ± 0.6
Dark grey region	80 ± 0.1	2 ± 0.2	14 ± 0	5 ± 0
Light grey region	79 ± 2	2 ± 0.7	15 ± 2	5 ± 1
High atomic number Contrast region	75 ± 2	8 ± 0.1	11 ± 2	6 ± 0.2

Table 4.23: Average composition analysis of different phases observed in Al-Ti-C coating @ 150⁰C for 3 hours followed by rapid quenching.

Phase	Average composition			
	Al (at%)	Ti (at%)	C (at%)	O (at%)
Speckled region	81 ± 1.3	2 ± 0.2	12 ± 1.2	5 ± 0.5
Dark grey region	82 ± 2.5	2 ± 0.1	12 ± 2	5 ± 0.5
Light grey region	72 ± 6	2 ± 0.3	21 ± 7	6 ± 1
High atomic number Contrast region	75 ± 2	8 ± 0.4	11 ± 2	7 ± 1
Spherical equiaxed phase	41 ± 12	13 ± 4	11 ± 3	35 ± 10

A similar average composition of the speckled and the dark grey region for both Al-Ti-C coating @ 150⁰C for 1 hour and 3 hours followed by rapid quenching was seen from EDX selected area analysis. However comparing the composition of light grey region, a higher C content in Al-Ti-C coating @ 150⁰C for 3 hours was recorded in comparison to 1 hour exposure @ 150⁰C,. A higher C content detected from EDX analysis could be attributed to the polishing of the cross-section of the coating during metallographic sample preparation prior to analysis.

A heterogeneous distribution of Ti as seen in the as sprayed Al-Ti-C coating, see **Table 4.17**, was evident even after 150⁰C exposure for 1 hour and 3 hours by varying Ti concentration in the Al-Ti-C coating's identified phases, see **Table 4.22** and **Table 4.23**.

The bright high contrast region observed in Al-Ti-C coating @ 150⁰C for 1 hour and 3 hours exhibited a higher Ti concentration with respect to the other identified phases. Comparing the Ti to C ratio for this bright high contrast phase obtained from EDX analysis of Al-Ti-C coating @ 150⁰ C for 1 hour

and 3 hours and the XRD trace shown in **Figure 4.78** (a), (b), formation of an intermediate form of titanium carbide phase, Ti_8C_5 with rhombohedral crystal structure was clearly evident. A higher Al content during the selected area analysis of a phase could be a result of EDX volume interaction detecting the background Al matrix.

The precipitation of intermetallic tri-aluminide Al_3Ti in the Al-Ti alloy containing $Ti \leq 5$ wt%, upon rapid solidification has been reported previously by researchers [176-180]. For Al alloys containing ≈ 3.5 wt% Ti and ≈ 0.15 wt % C, Zang *et al.*[177,180] showed that upon rapid solidification, formation of cubic titanium carbide phase along with Al_3Ti phase was not evident. The XRD trace of the Al-Ti-C coating subjected to exposure of $150^{\circ}C$ for 1 hour and 3 hours followed by rapid quenching also showed formation of cubic Al_3Ti phase, which was observed by Zang *et al.*[177,180], but also showed formation of intermediate titanium carbide phase. Bearing in mind that this could be attributed to the fact that the observation made by Zang *et al.* [177,180] was on rapidly solidified Al-Ti-C alloys, which constitute a different formation process in comparison with arc sprayed Al-Ti-C coating, however stability of such intermediate titanium carbide phases up to temperatures as high as 1450 K has also been observed [181-184].

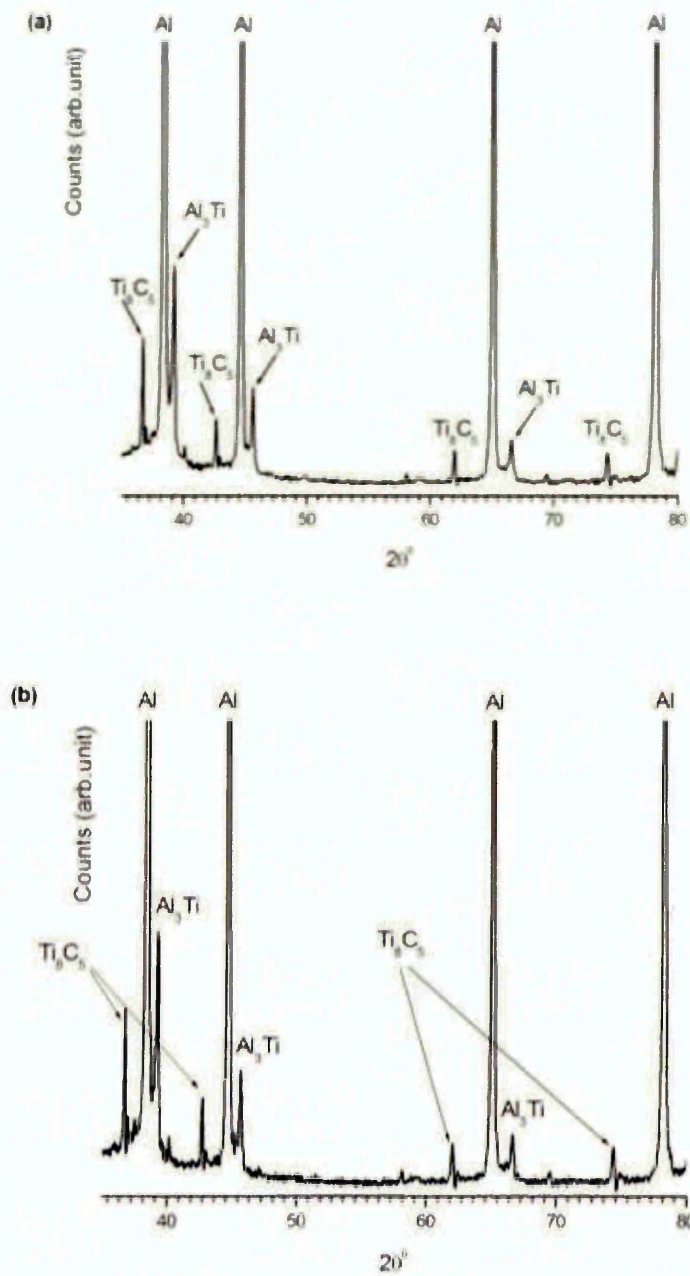


Figure 4.78: XRD trace of Al-Ti-C coating post 150°C exposure for (a) 1 hour and (b) 3 hours followed by rapid quenching. The unmarked peaks at $2\theta \approx 40^\circ$, 58° and 69° are $\text{CuK}\beta$.

4.6.2 Microstructure of Al-Ti-C coating subjected to 350°C for 1 hour and 3 hours followed by rapid quenching.

Figure 4.79 (a) and (b), shows the backscattered electron micrographs of Al-Ti-C coating subjected to 350°C for 1 hour and 3 hours followed by rapid quenching.

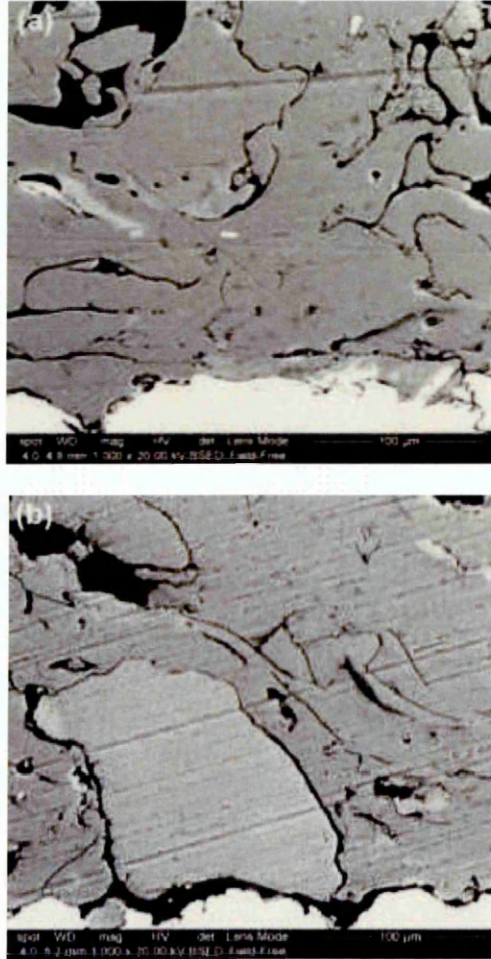


Figure 4.79: Backscattered electron micrograph of Al-Ti-C coating exposed to 350°C for (a) 1 hour and (b) 3 hours, followed by rapid quenching. (The linear features are caused due to polishing).

Figure 4.80(a), (b), (c) and **Figure 4.81 (a), (b), (c)** shows a higher magnification backscattered electron micrographs of Al-Ti-C coating @ 350°C for 1 hour and 3 hours followed by rapid quenching along with the average composition of each of the identified phases in **Table 4.24** and **Table 4.25** respectively.

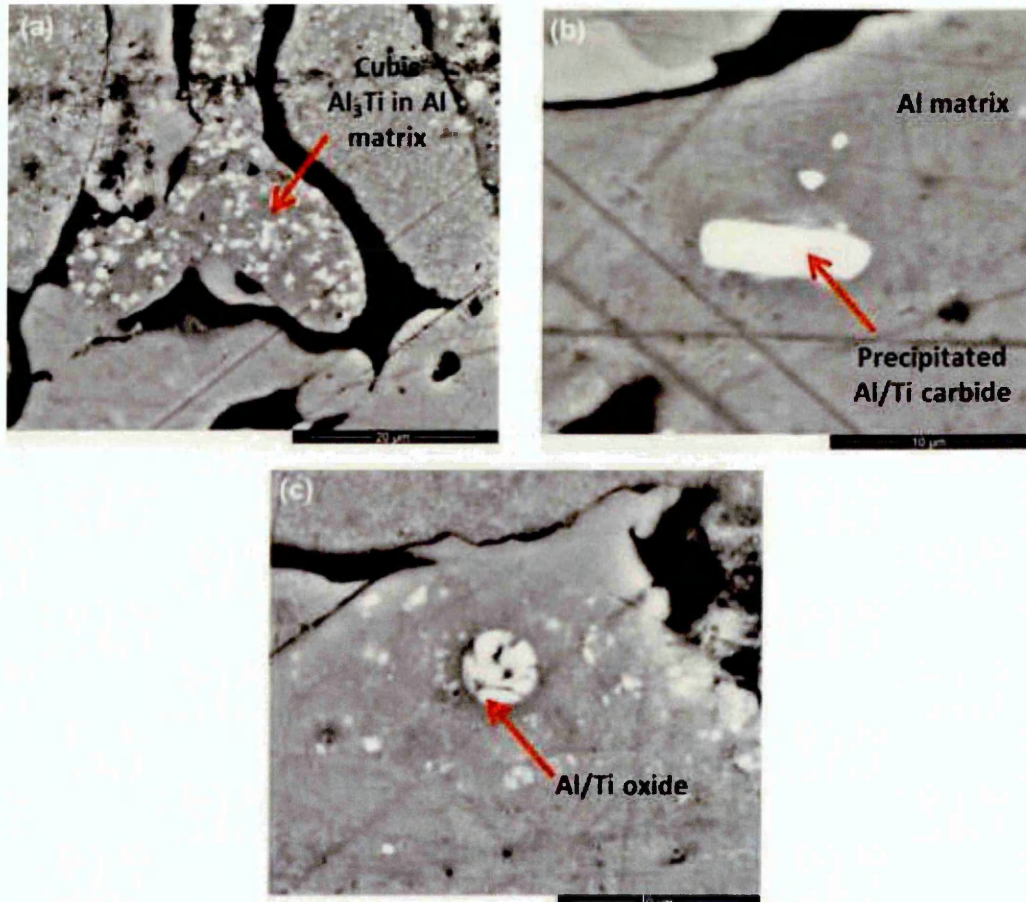


Figure 4.80: A higher magnification, (a) @ x 5000, (b) and (c) @ x 10,000, backscattered electron micrograph of Al-Ti-C coating exposed to 350°C for 1 hour showing (a) small and large speckled spots (b) a higher aspect ratio phase and (c) spherical equiaxed phase. The coating was rapidly quenched post exposure.

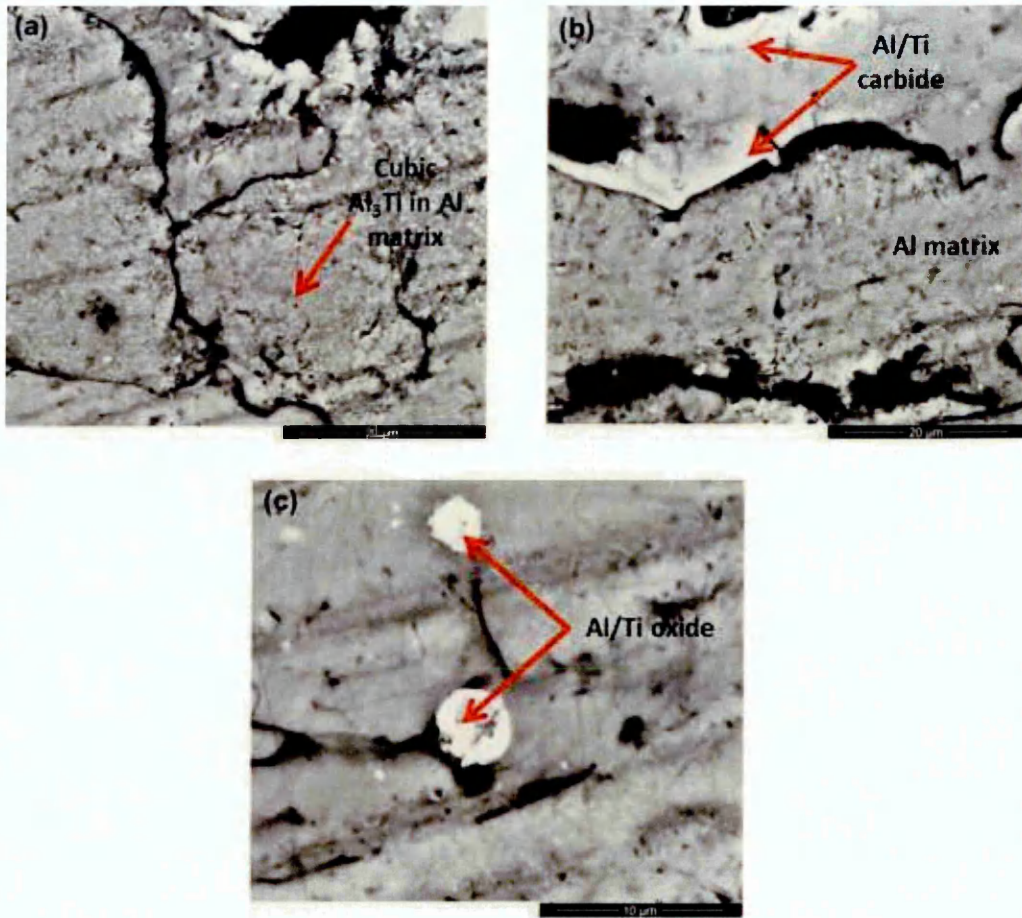


Figure 4.81: A higher magnification, (a), (b) @ x 5000 and (c) @ x 10,000, backscattered electron micrograph of Al-Ti-C coating exposed to 350⁰C for 3 hours showing (a) small and large speckled spots, (b) dark and light grey regions and (c) spherical equiaxed phase. The coating was rapidly quenched post exposure.

Table 4.24: Average composition analysis of different phases observed in Al-Ti-C coating @ 350⁰C for 1 hour followed by rapid quenching.

Phase	Average composition			
	Al (at%)	Ti (at%)	C (at%)	O (at%)
Speckled region	80 ± 4	2 ± 0.1	13 ± 4	6 ± 0.6
Dark grey region	84 ± 0.8	2 ± 0.3	10 ± 0	4 ± 0.5
Light grey region	82 ± 1.8	2 ± 0.3	10 ± 0.3	5 ± 1
High contrast high aspect ratio phase	74 ± 0.6	14 ± 3	9 ± 1	3 ± 1
Spherical equiaxed phase	40 ± 2.4	10 ± 1.7	7 ± 2.3	43 ± 7

Table 4.25: Average composition analysis of different phases observed in Al-Ti-C coating @ 350⁰C for 3 hours followed by rapid quenching.

Phase	Average composition			
	Al (at%)	Ti (at%)	C (at%)	O (at%)
Speckled region	77 ± 1	2 ± 0.4	14 ± 1	7 ± 0.3
Dark grey region	80 ± 3	2 ± 0	12 ± 1	6 ± 2
Light grey region	82 ± 1	2 ± 0.7	11 ± 0.4	5 ± 1.1
Spherical equiaxed phase	26 ± 14	15 ± 4	7 ± 2	53 ± 13

A growth in the speckled region for Al-Ti-C coating exposed to 350⁰C for 1 hour and 3 hours was observed, which was similar to Al-Ti-C coating subjected to 150⁰C for 1 hour and 3 hours. Note that @ 150⁰C for 1 hour, mixed speckled region containing both small and relatively large speckled regions was observed, but with increase in temperature and exposure period two separate regions containing small and relatively large speckled spots was discernable. The average composition of the speckled region observed in Al-Ti-C coating after 1 hour and 3 hours of exposure @ 350⁰C rapidly quenched Al-Ti-C coating, see **Table 4.24** and **Table 4.25** was also similar to that for Al-Ti-C coating @150⁰C followed by rapid quenching, see **Table 4.22** and **Table 4.23**.

With an increased exposure temperature, @ 350⁰C, appearance of the atomic number contrast regions, see **Figure 4.80(b)** and **Figure 4.81(b)**, the dark and the light grey regions with average composition, see **Table 4.24** and **Table 4.25**, similar to Al-Ti-C coating @ 150⁰C was seen, however, the dark and light grey regions were seen more pronounced in the Al-Ti-C coating @ 350⁰C for 1 hour.

Precipitation of a high contrast and high aspect ratio phase was also seen in Al-Ti-C coating @ 350⁰C for 1 hour. The EDX compositional analysis revealed that this phase showed a higher Ti (at%) concentration than the high atomic number contrast phase which was observed in Al-Ti-C coating @ 150⁰C for 1 hour and 3 hours. The stoichiometric C at% for this phase as shown in **Table 4.24** reveals formation of intermediate titanium carbide phase (Ti₈C₅, possibly with Al substitution from matrix) which was also confirmed by XRD, see **Figure 4.82 (a)** Note that this high contrast high aspect ratio phase was not seen in Al-Ti-C coating @ 350⁰C for 3 hours.

This could have been an indication of precipitation of an intermediate Al-Ti intermetallic compound which dissolved with increase in the exposure temperature. As mentioned earlier, precipitation of approximately twelve forms of Al-Ti intermetallic compounds during alloy formation has been reported by researchers [149].

Appearance of a spherical equiaxed phase, which was seen in Al-Ti-C coating @ 150⁰C for 3 hours, was also evident in Al-Ti-C coating @ 350⁰C for 1 hours and 3 hours, see

Figure 4.80 (c) and **Figure 4.81(c)**. The increased amount of O (at %) in the spherical equiaxed phase detected by EDX analysis, see **Table 4.23** to **Table 4.25**, indicated formation of oxides of Al with possible Ti oxidation.

As the coatings were exposed to elevated temperature in a pre-heated furnace, the formation of oxides which appear to be brittle in nature, was possible due to lack of moisture.

The XRD analysis confirmed the presence of cubic Al_3Ti tri-aluminide intermetallic phase in Al-Ti-C coating @ 350°C for both 1 hour and 3 hours of exposure period, see **Figure 4.81 (a)** and (b). Intermediate titanium carbide, Ti_8C_5 , of rhombohedral crystal structure was detected for Al-Ti-C coating @ 350°C for 1 hour, which was also seen in Al-Ti-C coating @ 150°C for 1 hour and 3 hours.

With an increase in the exposure period to 3 hours, formation of cubic TiC phase was reported by XRD analysis, however the stoichiometric ratio of Al:(Ti+C) from EDX results suggested the formation of aluminium substituted titanium carbide phase, see **Figure 4.81(b)**. A higher aluminium concentration could be attributed due to the fact that initial precipitation of intermediate titanium carbide phase could have resulted in Al substitution to the carbide phase from the matrix.

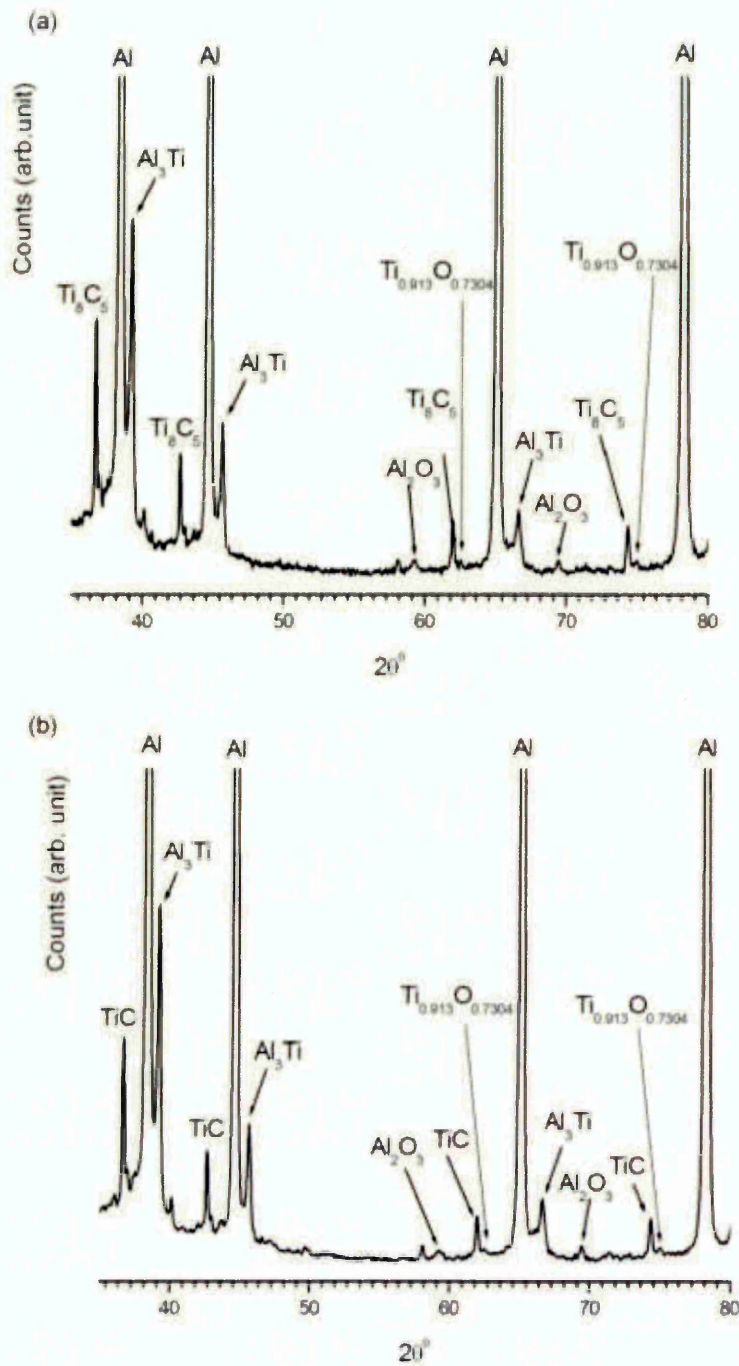


Figure 4.82: XRD trace of Al-Ti-C coating post 350°C exposure for (a) 1 hour and (b) 3 hours followed by rapid quenching. The unmarked peaks at $2\theta \approx 40^\circ$, 58° are $\text{CuK}\beta$.

The XRD analysis of the Al-Ti-C coating @ 350⁰C for 1 hour and 3 hours also showed formation of Al₂O₃. This was also indicated by higher concentration of O (at %) by the EDX analysis of the equiaxed spherical phase, see **Table 4.25**. It is important to note that higher Ti concentration in spherical equiaxed phase, see **Figure 4.81(c)** and the stoichiometric ratio of (Al+Ti):O obtained from EDX analysis could be attributed to Ti substitution in the Al oxide (Al₂O₃) phase.

4.6.3 Microstructure of Al-Ti-C coating subjected to 550°C for 1 hour and 3 hours followed by rapid quenching.

Figure 4.83 (a) and (b) shows the backscattered electron micrograph of Al-Ti-C coating exposed to 550°C for 1 hour and 3 hours respectively followed by rapid quenching.

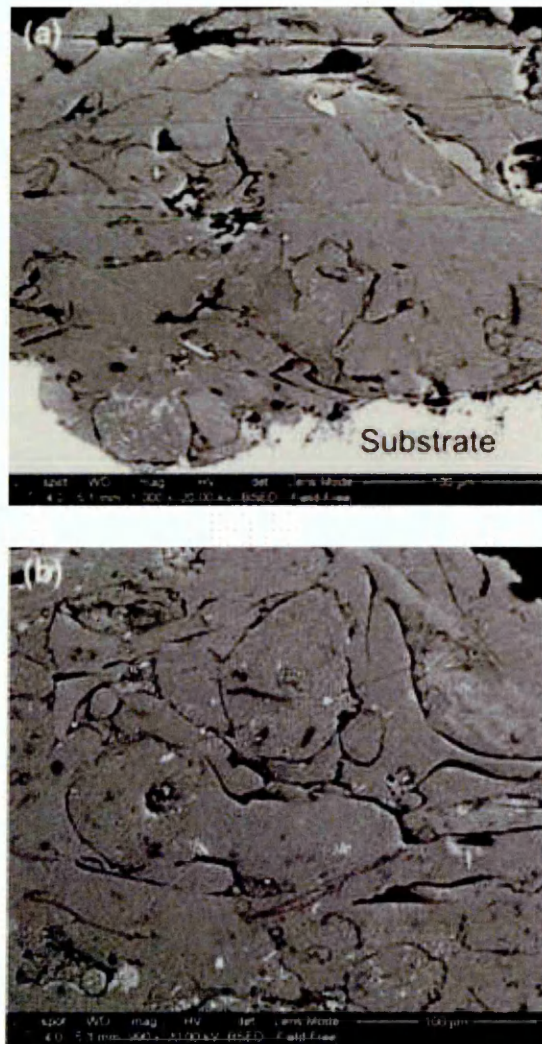


Figure 4.83: Backscattered electron micrograph of Al-Ti-C coating exposed to 550°C for (a) 1 hour and (b) 3 hours, followed by rapid quenching.

A higher magnification backscattered electron micrographs of Al-Ti-C coating @ 550⁰C for 1 hour and 3 hours along with average composition of each of the identified phases is shown in **Figure 4.84** (a), (b), (c) , **Figure 4.85** (a), (b), (c), **Table 4.26** and **Table 4.27** respectively.

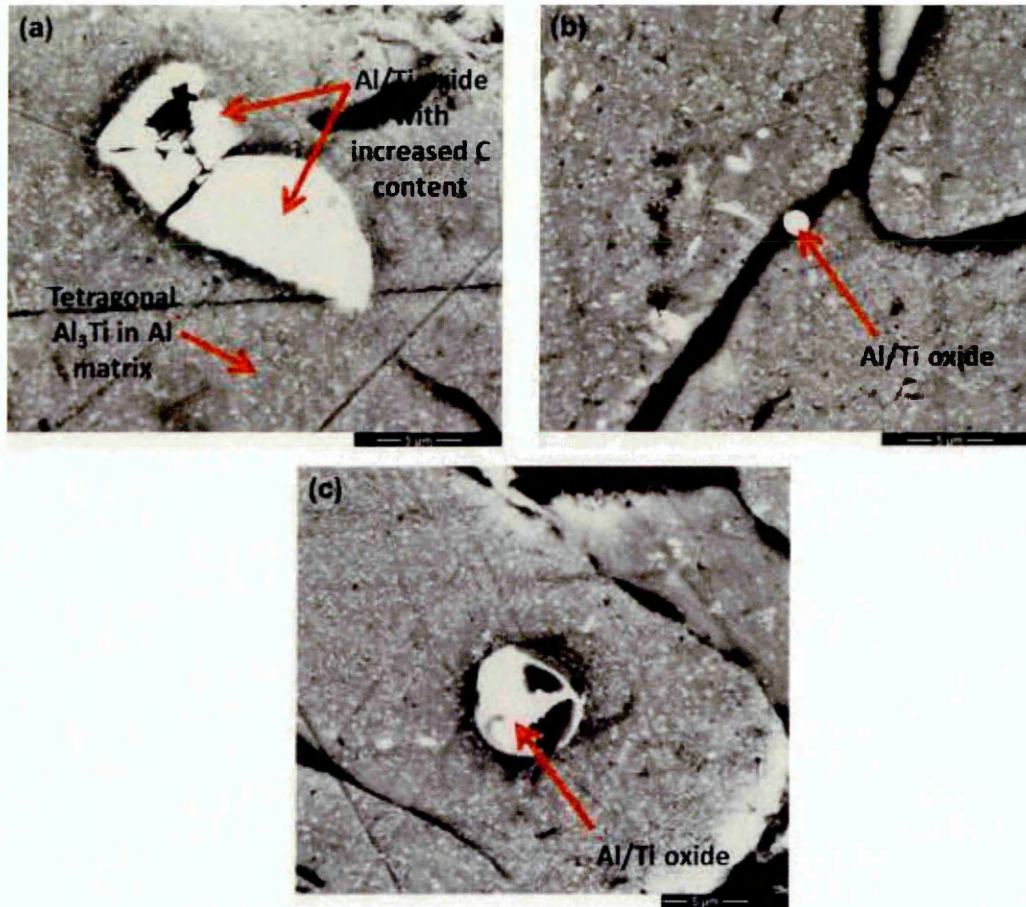


Figure 4.84: A higher magnification @ x 10,000, Backscattered electron micrograph of Al-Ti-C coating exposed to 550⁰C for 1 hour showing (a) formation of brittle phase, with high atomic number contrast, (b) phase with rectangular geometry within the speckled region and (c) spherical equiaxed phase. The coating was rapidly quenched post exposure.

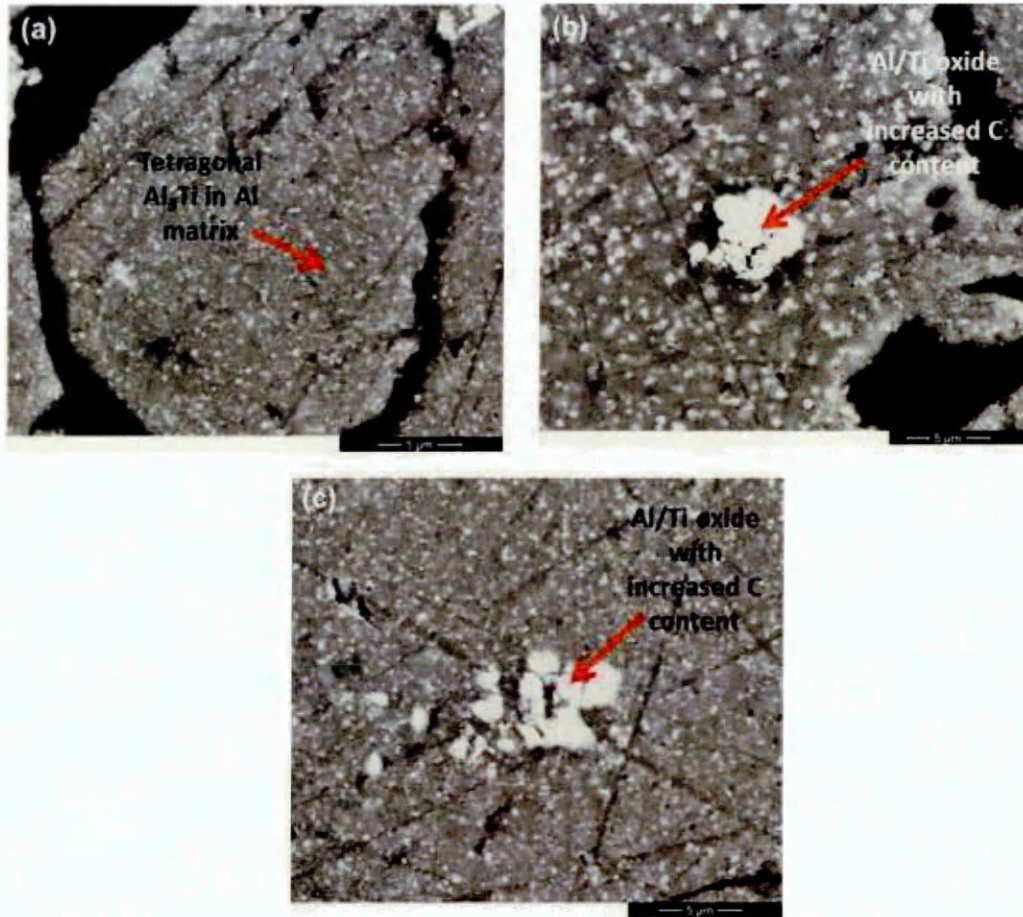


Figure 4.85: A higher magnification @ x 10,000, Backscattered electron micrograph of Al-Ti-C coating exposed to 550⁰C for 3 hour showing (a) formation of speckled region,(b) and (c) formation of brittle phase with high atomic number contrast with uniform distribution of speckled region.

Table 4.26: Average composition analysis of different phases observed in Al-Ti-C coating @ 550⁰C for 1 hour followed by rapid quenching.

Phase	Average composition			
	Al (at%)	Ti (at%)	C (at%)	O (at%)
Speckled region	81 ± 0.7	2 ± 0.3	13 ± 0.5	4 ± 0.3
Phase with rectangular geometry	55 ± 10	1 ± 0.1	25 ± 4.0	12 ± 5
Spherical equiaxed phase	30 ± 6.0	15 ± 3.0	7 ± 2.3	48 ± 8
Brittle phase	20 ± 9	33 ± 10	7 ± 3	40 ± 13

Table 4.27: Average composition analysis of different phases observed in Al-Ti-C coating @ 550⁰C for 3 hours followed by rapid quenching.

Phase	Average composition			
	Al (at%)	Ti (at%)	C (at%)	O (at%)
Speckled region	83 ± 1	2 ± 0.1	11 ± 2	4 ± 0.3
Brittle phase	53 ± 10	20 ± 7	24 ± 8	3 ± 0

Precipitation of a Ti rich brittle oxide phase, see **Figure 4.84** (a), was observed in the Al-Ti-C coating @ 550⁰C for 1 hour followed by rapid quenching. The presence of the speckled region was also seen in the Al-Ti-C coating after 1 hour of exposure at 550⁰C followed by rapid quenching, however the distribution of the speckled region was found to be significantly increased, see **Figure 4.84** (a), (b) and (c), in comparison to the speckled region observed in the previous exposure temperatures.

From **Figure 4.84** (b), precipitation of a phase with rectangular geometry within the speckled regions was observed. The formation of this phase could have been due to the increase in the exposure temperature allowing the sub-micron size speckled phases to grow.

However the EDX analysis of this phase compared with the speckled region, see showed an increased C (at %) and reduced Al (at %) than the speckled

region. The appearance of this phase (with rectangular geometry) was not very evident @ 550⁰C for 3 hours. This could also be attributed to the formation of intermediate Al/Ti carbide phase.

The Al to C ratio of the rectangular phase which precipitated within the speckled region, see **Figure 4.84** (b), obtained by EDX analysis, see **Table 4.26**, was $\approx 2.2 : 1$, which could have been an indication of formation of Al₄C₃ (Al:C ratio $\approx 1.3:1$). Note the higher Al concentration could have been due to the interaction volume of EDX detecting Al from the background Al matrix of the coating. The formation of Al₄C₃ in Al matrix containing Al-3wt%Ti-0.15wt%C grain refiner as inoculant has been reported earlier by researchers [189].

The mechanism of formation of Al₄C₃ was proposed either by slow dissolution of TiC particles when the Al melt was kept at $\approx 700^0$ C or by formation of Al₄C₃ separately [189]. The authors emphasised that either way the formation of Al₄C₃ was too slow to be controlled by diffusion of C in the Al melt therefore the impairment of the grain refinement properties was expected to be time dependent [189].

The XRD analysis of the Al-Ti-C coating @ 550⁰C for 1 hour, see **Figure 4.86** (a), did not show the formation of Al₄C₃, however confirmed the formation of Al and Ti oxides, which can be seen in the form of spherical equiaxed phase, see **Figure 4.84** (c) and confirmed by the EDX compositional analysis of the phase.

A uniform distribution of the speckled region throughout the cross-section of the Al-Ti-C coating @ 550⁰C for 3 hours was seen from **Figure 4.85** (a), (b)

and (c), with similar average composition of the phase as observed after 1 hour of exposure @ 550⁰C. Spherical equiaxed oxide phase formation in the cross-section of Al-Ti-C coating @ 550⁰C for 3 hours was not seen. Instead, appearance of a high contrast brittle oxide phase was more dominant throughout the cross-section of the Al-Ti-C coating subjected to 550⁰C for 3 hours, see **Figure 4.85** (b) and (c).

The brittle phase observed in Al-Ti-C coating @ 550⁰C for both 1 hour and 3 hours of exposure showed an increased Ti (at%) concentration but the variation in levels of C (at %) was also noticeable, see **Table 4.26** and **Table 4.27**. Such an increase in the Ti concentration upon holding the Al melt containing Al-3wt %Ti-0.15wt%C at ≈ 700⁰C was also reported previously [189]. The authors also reported that due to similar diffusivity of Ti and C in the Al melt, the formation of TiC and Al₄C₃ in the alloy was possible, as mentioned earlier, the mechanism of formation of Al₄C₃ was proposed to be nucleation of Al₄C₃ particles in separate sites rather than conversion of TiC to Al₄C₃ [2.48]. However the XRD analysis of the Al-Ti-C coating @ 550⁰C for 3 hours did not show the formation of either Ti or Al carbide, see **Figure 4.86** (b), but similar to what was seen in Al-Ti-C coating @ 550⁰C for 1 hour did show formation of Al and Ti oxide.

The intermetallic Al₃Ti phase with tetragonal crystal structure, similar to the one in Al-Ti-C feedstock alloy, was also revealed from the XRD analysis of Al-Ti-C coating @ 550⁰C for both 1 hour and 3 hours of exposure followed by rapid quenching, see **Figure 4.86** (a) and (b).

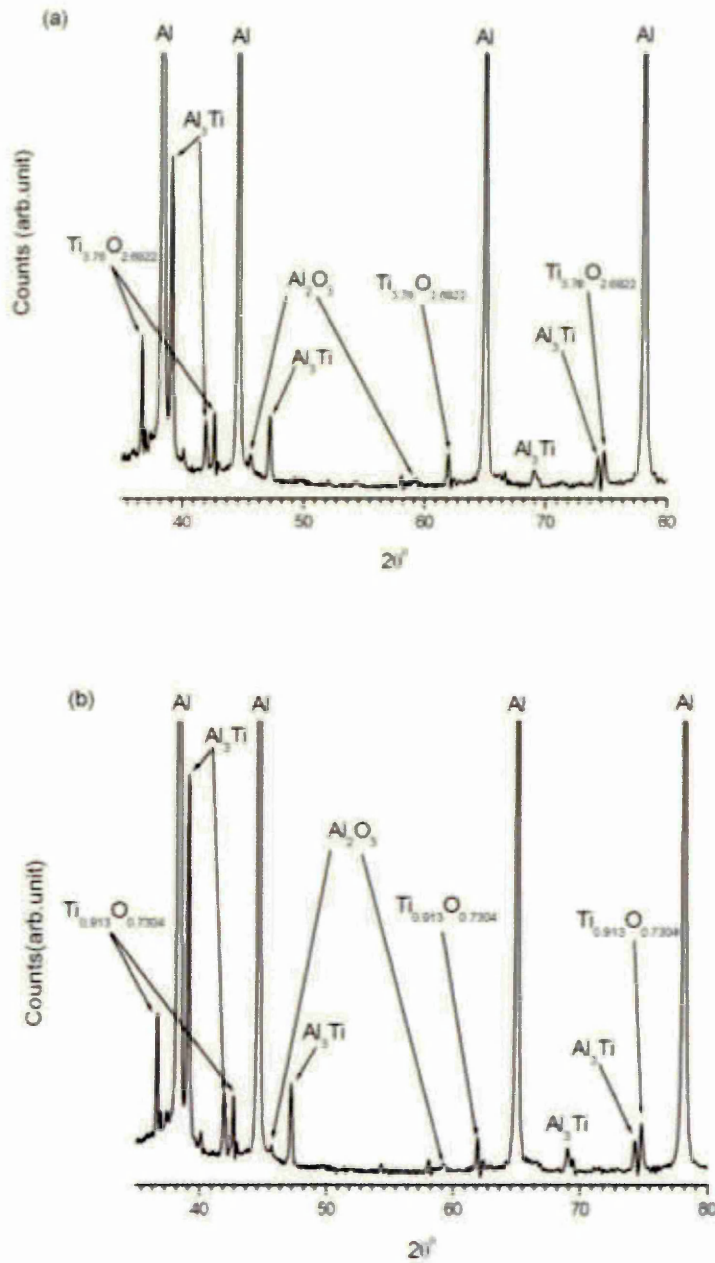


Figure 4.86: XRD trace of Al-Ti-C coating post 550°C exposure for (a) 1 hour and (b) 3 hours followed by rapid quenching. The unmarked peaks at $2\theta^\circ \approx 40^\circ, 58^\circ$ are $\text{CuK}\beta$.

4.6.4 Micro-hardness of Al-Ti-C coating subjected to 150°C, 350°C, 550°C for 1 hour and 3 hours followed by rapid quenching.

Table 4.28 shows the average Vickers micro-hardness values measured for Al-Ti-C coating subjected to 150°C, 350°C and 550°C for 1 hour and 3 hours respectively followed by rapid quenching.

Table 4.28: Vickers micro-hardness of Al-Ti-C coating subjected to 150°C, 350°C and 550°C for 1 hour and 3 hours followed by rapid quenching.

Temperature (°C)	Time of exposure (hours)	HV _{0.98} GPa(kgf/mm ²)	Coefficient of variation (%)
@ 150	1	0.72 (74 ± 24)	31
	3	0.83 (85 ± 29)	35
@ 350	1	0.76 (78 ± 25)	32
	3	0.73 (74 ± 18)	24
@ 550	1	0.56 (57 ± 13)	23
	3	0.51 (52 ± 13)	25

A large range of micro-hardness values were recorded for Al-Ti-C coating exposed to 150°C for 1 hour and 3 hours respectively, as indicated by the coefficient of variation as shown in **Table 4.28**. A reduction in the values of coefficient of variation was observed with the increase in temperature of exposure with lowest value obtained for Al-Ti-C coating @ 550°C for 1 hour. The range of micro-hardness values for Al-Ti-C coating subjected to 150°C, 350°C and 550°C was also shown by the frequency distribution histograms shown in **Figure 4.87** to **Figure 4.89**.

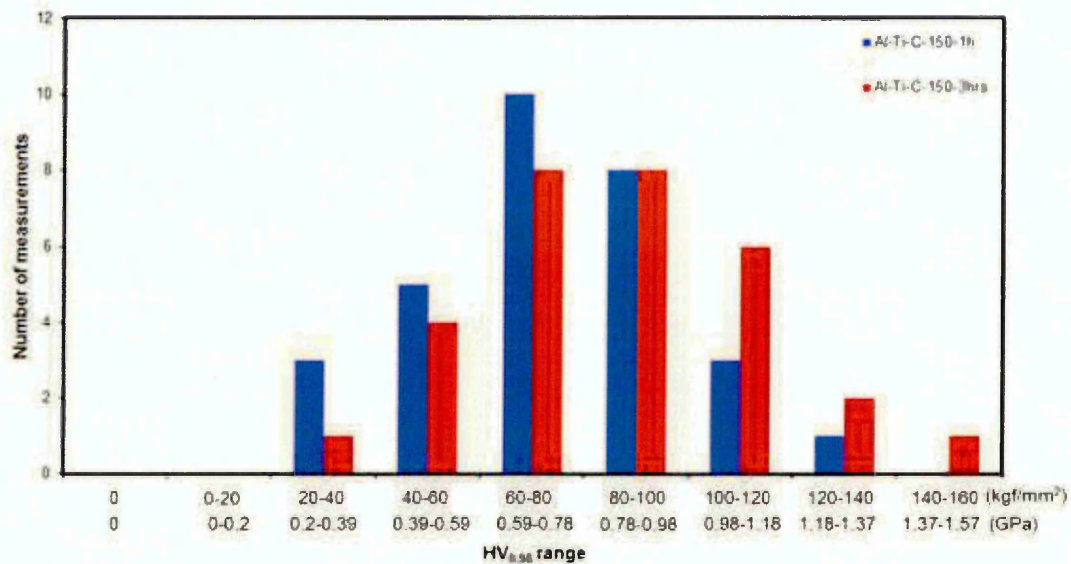


Figure 4.87: Frequency distribution histogram of micro-hardness (HV_{0.98}) for Al-Ti-C coating exposed to 150⁰C for 1 hour (violet shade) and 3 hours (Dark red shade).

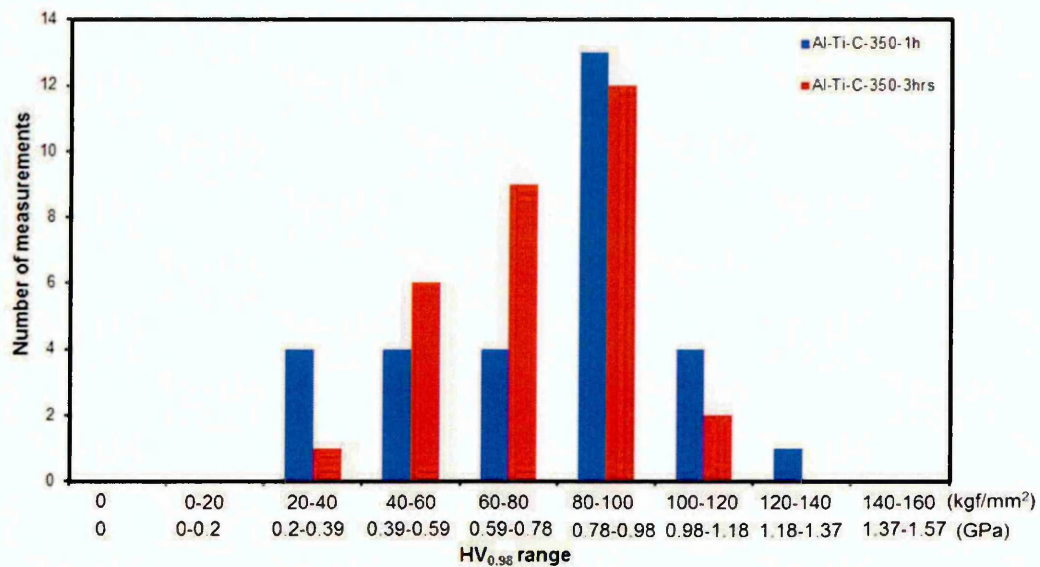


Figure 4.88: Frequency distribution histogram of micro-hardness (HV_{0.98}) for Al-Ti-C coating exposed to 350⁰C for 1 hour (violet shade) and 3 hours (Dark red shade).

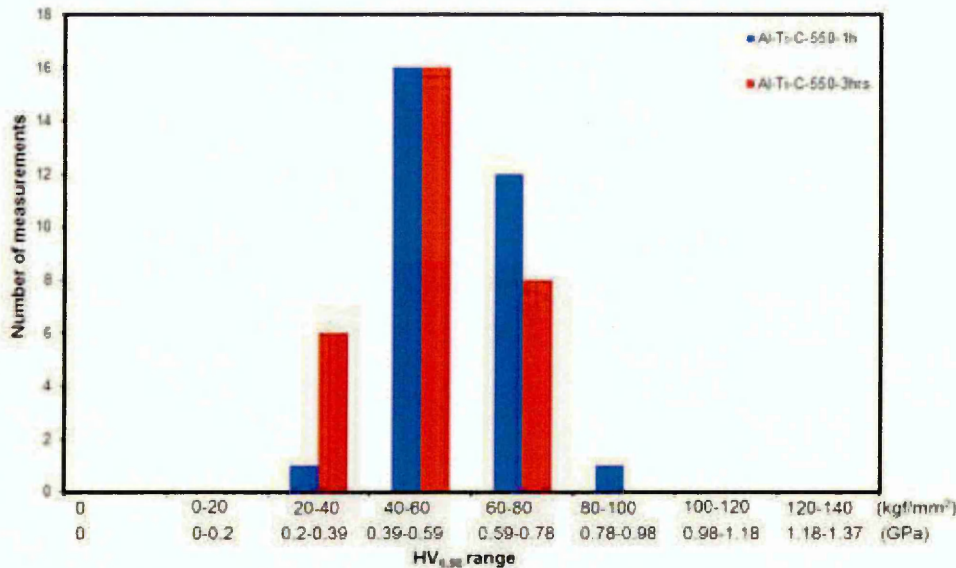


Figure 4.89: Frequency distribution histogram of micro-hardness ($HV_{0.98}$) for Al-Ti-C coating exposed to 550°C for 1 hour (violet shade) and 3 hours (Dark red shade).

The influence of the precipitation of various phases after 150°C , 350°C and 550°C of exposure for 1 hour and 3 hours on the micro-hardness of the Al-Ti-C coating was clearly evident, see and **Figure 4.87** to **Figure 4.89**. The Al-Ti-C coatings @ 150°C for 1 hour showed similar distribution of hardness values as as-sprayed Al-Ti-C coating, with highest hardness value $HV_{0.98} \approx 1.18\text{-}1.37$ GPa. An overall increase of 13 % in the $HV_{0.98}$ value was seen with increase in the exposure period from 1 to 3 hours @ 150°C with some values of $HV_{0.98}$ as high as 1.47 GPa. This could have been due to precipitation of a higher Ti concentration (at %) phase which was seen after 150°C for 1 hour and 3 hours followed by rapid quenching. The formation of large speckled region, which were observed after 3 hours of exposure @ 150°C along with brittle oxide phase could have also resulted in formation of high hardness regions ($HV_{0.98} \approx 1.47$ GPa), in Al-Ti-C coating, see **Figure 4.87**.

A reduction in the spread of micro-hardness values with the increase in the exposure temperature to 350⁰C was seen from the frequency distribution histogram , **Figure 4.88**, and coefficient of variation shown in **Table 4.28**. Regions of HV_{0.98} value in the range of 0.79 GPa to 0.98 GPa were mostly observed in the Al-Ti-C coating @ 350⁰C for 1 hour and 3 hours followed by rapid quenching, see **Figure 4.88**. Only small regions of HV_{0.98} value between 1.18 GPa to 1.37 GPa was seen in Al-Ti-C coating @ 350⁰C for 1 hour with overall 4 % decrease in the micro-hardness value with increase in the exposure period to 3 hours. This could have been due to the formation of Ti rich high aspect ratio phase which was seen in Al-Ti-C coating after 1 hour of exposure at 350⁰C, which was not observed after 3 hours of exposure period at same temperature of exposure.

The frequency distribution histogram obtained for the micro-hardness of Al-Ti-C coating after 550⁰C for 1 hour and 3 hours showed overall reduction in the hardness value regions with HV_{0.98} value between 0.39 GPa to 0.59 GPa, see **Figure 4.89**, in comparison to previous exposure temperatures. An overall reduction in the coefficient of variation of micro-hardness values (lowest of 23 % obtained for Al-Ti-C coating @ 550⁰C for 1 hour and 25 % @ 550⁰C for 3 hours) was also seen after 550⁰C for 1 hour and 3 hours. This could have been due to the Precipitation of the Ti rich (at %, from EDX analysis) brittle phase resulting from slow dissolution of intermediate Ti₈C₅ (as reported in the previous research [189]), which was detected using XRD analysis of Al-Ti-C coating at 150⁰C and 350⁰C for 1 hour and 3 hours, causing reduction in the overall Ti distribution throughout the Al-Ti-C coating, which in turn resulted in increase in the lower hardness value regions.

The XRD analysis of the Al-Ti-C coating after 550⁰C of exposure (both after 1 hour and 3 hours), confirmed no presence of carbides which could have led to higher hardness regions.

The XRD analysis of the Al-Ti-C coating post 550⁰C exposure (both 1 hour and 3 hours of exposure period) also showed that the formation of tetragonal Al₃Ti, which has been reported to be inherently brittle by researchers [162]. The tetragonal Al₃Ti intermetallic has also been reported to show reduction in the micro-hardness value with increase in temperature of exposure [162].

Table 4.28, showed that with increase in the period of exposure to 3 hours @ 550⁰C, ≈ 9 % reduction in the HV_{0.98} value was recorded. The effect of precipitation of different phases at various exposure temperatures on the micro-hardness of Al-Ti-C coating is shown in **Figure 4.90**.

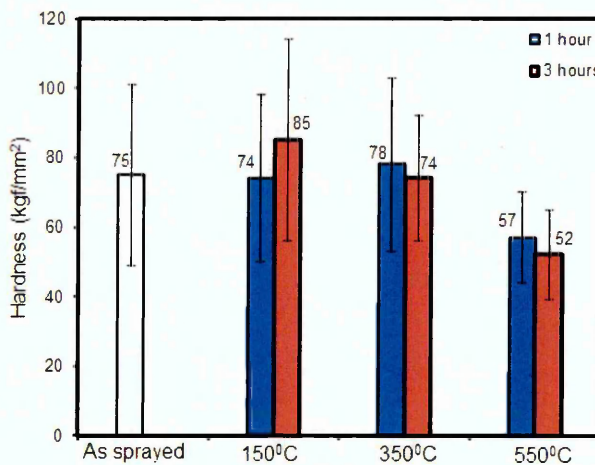


Figure 4.90: Comparison of micro-hardness values obtained for as sprayed Al-Ti-C coating and Al-Ti-C coating exposed to 150⁰C, 350⁰C and 550⁰C for 1 hour and 3 hours followed by rapid quenching.

4.6.5 Coefficient of wear for Al-Ti-C coating subjected to 150°C, 350°C, 550°C for 1 hour and 3 hours followed by rapid quenching.

Table 4.29 shows the values of coefficient of wear for Al-Ti-C coating exposed to 150°C, 350°C and 550°C followed by rapid quenching.

Table 4.29: Coefficient of wear for Al-Ti-C coating exposed to 150°C, 350°C and 550°C for 1 hour and 3 hours followed by rapid quenching.

Temperature (°C)	Time of exposure (hours)	Coefficient of wear (mm ³ N ⁻¹ m ⁻¹)
@ 150	1	5.77E-04 ± 1.66E-04
	3	5.34E-04 ± 0.80E-04
@ 350	1	4.28E-04 ± 0.01E-04
	3	4.88E-04 ± 2.02E-04
@ 550	1	3.62E-04 ± 0.48E-04
	3	4.62E-04 ± 0.20E-04

The values of coefficient of wear for Al-Ti-C coating at a given exposure temperature and period of exposure were obtained from the gradient of the graphs shown in **Figure 4.91** to **Figure 4.93**, where wear crater volume (in mm³) obtained during micro-scale abrasion test was plotted against the sliding distance (in m) multiplied with the applied load (in N).

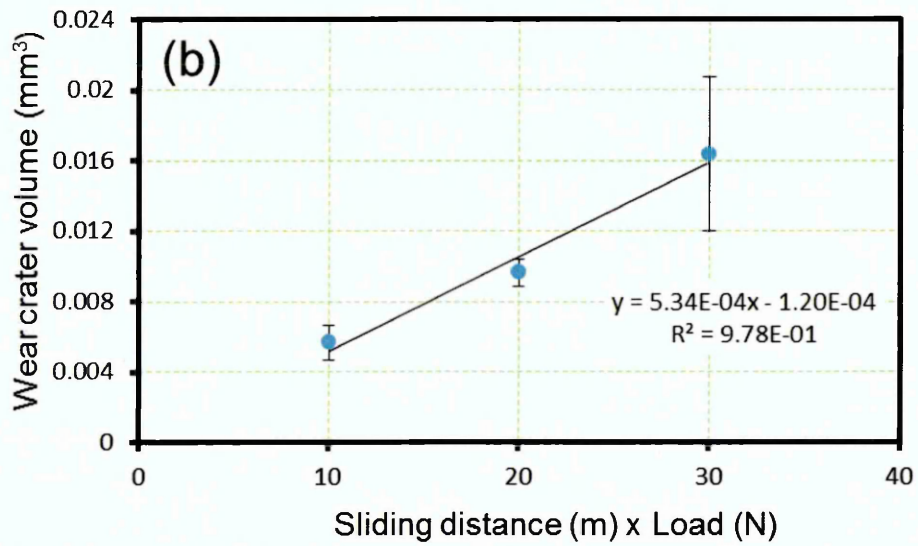
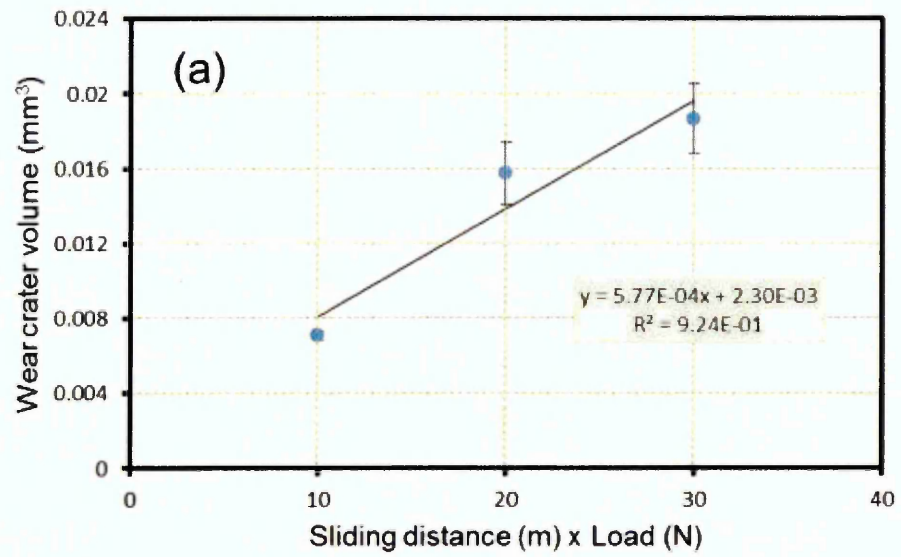


Figure 4.91: Graphs showing wear crater volume vs. sliding distance x load for Al-Ti-C coating subjected to 150⁰C for (a) 1 hour and (b) 3 hours followed by rapid quenching.

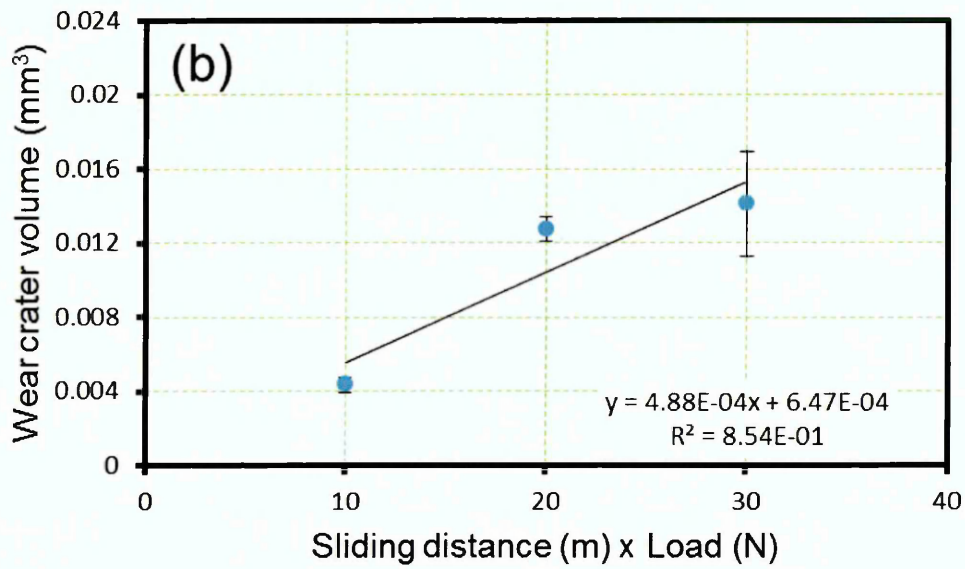
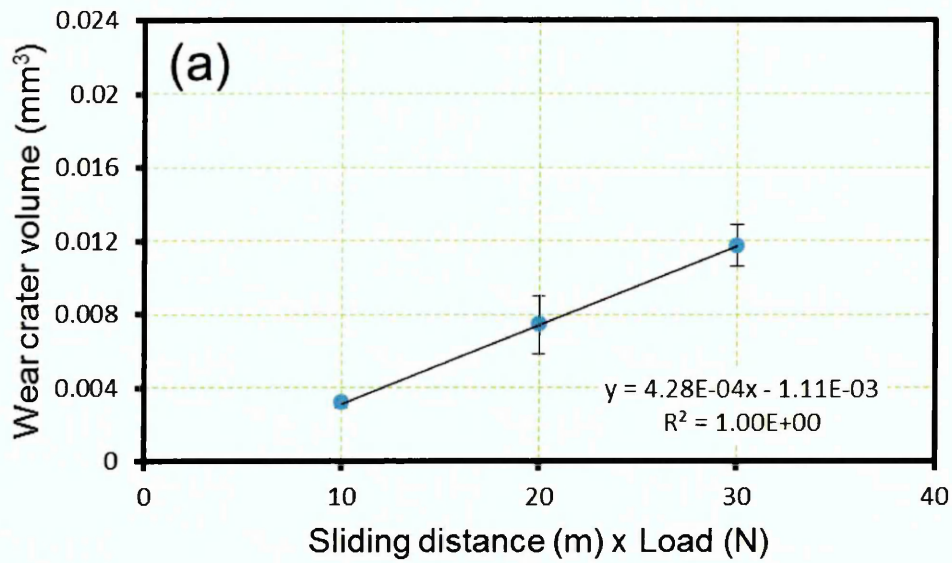


Figure 4.92: Graphs showing wear crater volume vs. sliding distance x load for Al-Ti-C coating exposed to 350⁰C for (a) 1 hour and (b) 3 hours followed by rapid quenching.

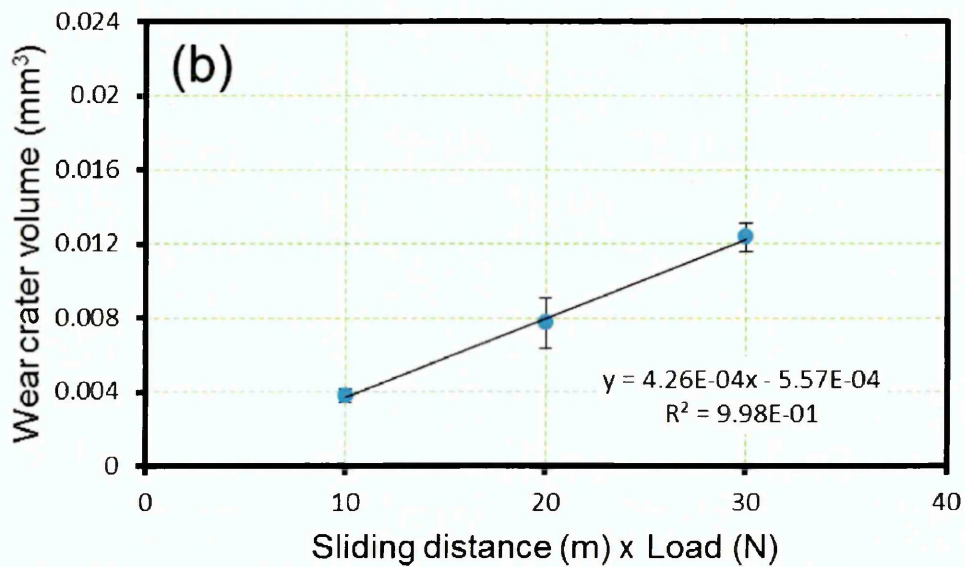
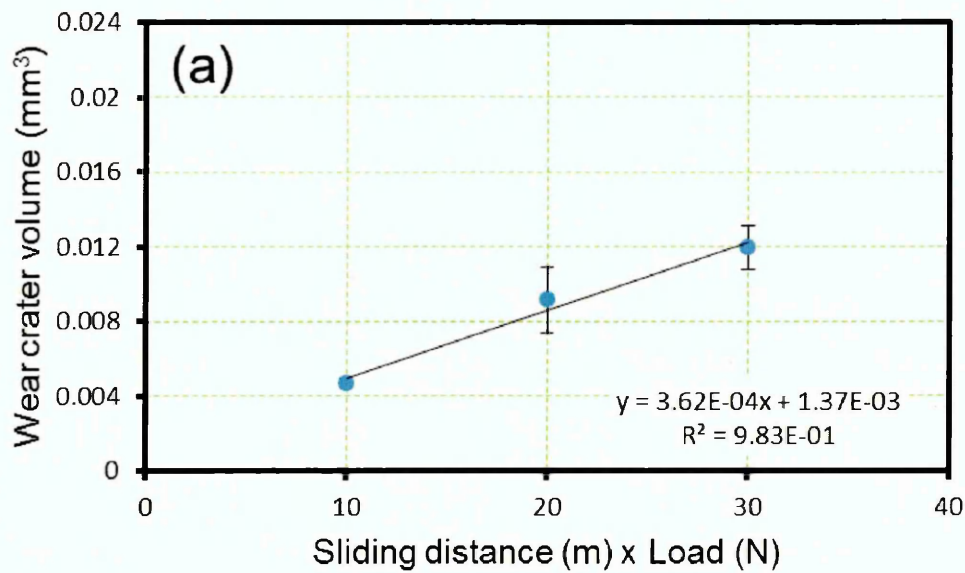


Figure 4.93: Graphs showing wear crater volume vs. sliding distance x load for Al-Ti-C coating exposed to 550⁰C for (a) 1 hour and (b) 3 hours followed by rapid quenching.

Comparing the wear coefficient values obtained for Al-Ti-C @ 150⁰C for 1 hour and 3 hours to the as sprayed Al-Ti-C coating, ≈ 44 % and 40 % increase in the wear coefficient values were reported, implying lowering of wear resistance of the Al-Ti-C coating. A difference of ≈ 7 % in the wear coefficient of Al-Ti-C coating @ 150⁰C for 1 hour and 3 hours was also

reported. **Figure 4.94** and **Figure 4.95** shows the wear track, notice the directionality of the wear tracks.

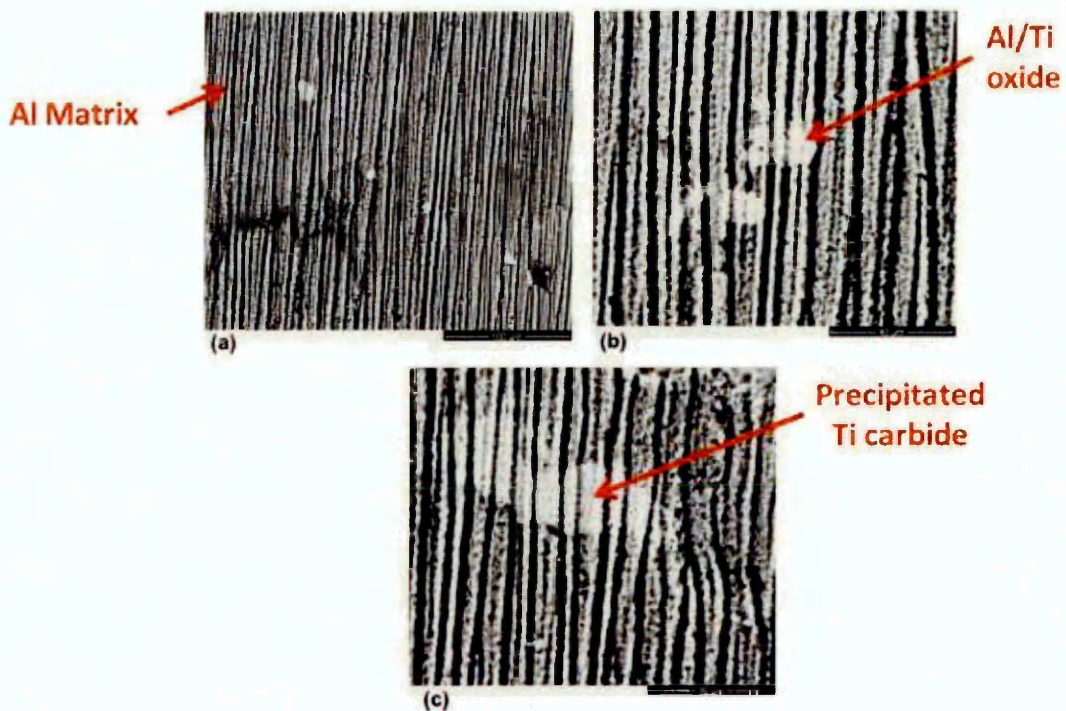


Figure 4.94: Backscattered electron micrograph showing directionality of the wear tracks and precipitation of Al and Ti containing oxide and carbide phases in Al-Ti-C coating @150°C for 1 hour. (a), (b) and (c) are backscattered electron micrographs at different magnifications.

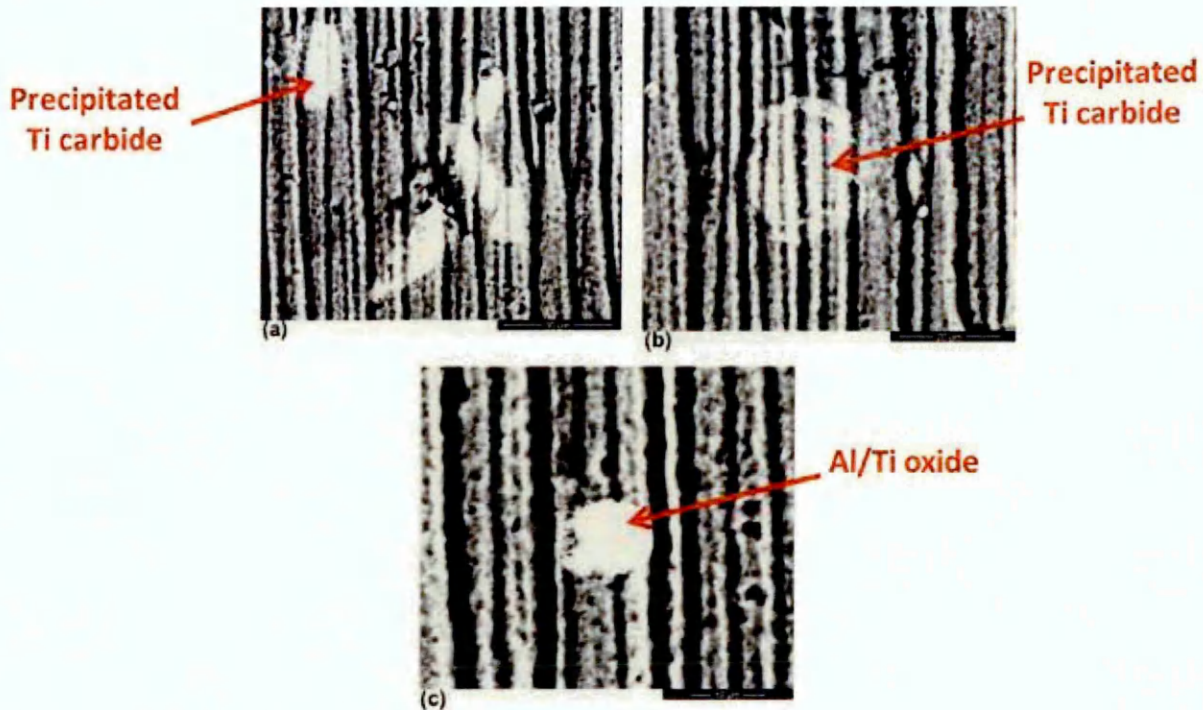


Figure 4.95: Backscattered electron micrograph showing directionality of the wear tracks and precipitation of Al and Ti containing oxide and carbide phases in Al-Ti-C coating @ 150⁰C for 3 hour. (a), (b) and (c) are backscattered electron micrographs at different magnifications.

Even though @ 150⁰C for 1 hour and 3 hours, presence of Ti rich (detected from EDX) regions were observed in Al-Ti-C coating, the overall micro-hardness value obtained for Al-Ti-C coating @ 150⁰C for 1 hour followed by rapid quenching was similar to that of as sprayed Al-Ti-C coating,

At same exposure temperature but with increased time of exposure to 3 hours, higher hardness regions (HV_{0.98} between 1.37 GPa to 1.57 GPa) were observed in the Al-Ti-C coating. These Ti rich precipitates in Al-Ti-C coating @ 150⁰C for 3 hours could have contributed in providing greater resistance against abrasive action of the SiO₂ particles during micro-scale abrasive

wear test. **Figure 4.95** (a) and (b) showed that the Ti rich carbide regions were providing resistance against abrasive particles, which in turn resulted in obtaining lower volume loss at each sliding distance at 0.2 N load, in comparison to Al-Ti-C coating @ 150⁰C for 1 hour. A similar observation for Ti rich regions resisting wear was also seen in Al-Ti-C coating @ 150⁰C for 1 hour, see **Figure 4.94** (b) and (c), but an additional spherical equiaxed phase (which also showed higher Ti concentration), which was seen in Al-Ti-C coating @ 150⁰C for 3 hours also provided additional resistance against abrasive particles, aiding towards obtaining lower wear loss.

With an increase in the exposure temperature to 350⁰C for 1 hour and 3 hours, ≈ 25 % and 34 % increase in the wear coefficient value in comparison with as sprayed Al-Ti-C coating was observed. The wear coefficient of Al-Ti-C coating @ 350⁰C for 1 hour was found to be ≈ 12 % lower than Al-Ti-C coating @ 350⁰C for 3 hours. This could be attributed to formation of higher hardness regions, which were recorded for Al-Ti-C coating @ 350⁰C for 1 hour (with HV_{0.98} value between 1.18 GPa to 1.37 GPa), resulting in overall higher micro-hardness value in comparison with Al-Ti-C coating @ 350⁰C for 3 hours. **Figure 4.96** (a), (b), (c) and **Figure 4.97** (a), (b), (c) shows the effect of different phases on the wear track morphology of Al-Ti-C coating @ 350⁰C for 1 hour and 3 hours respectively.

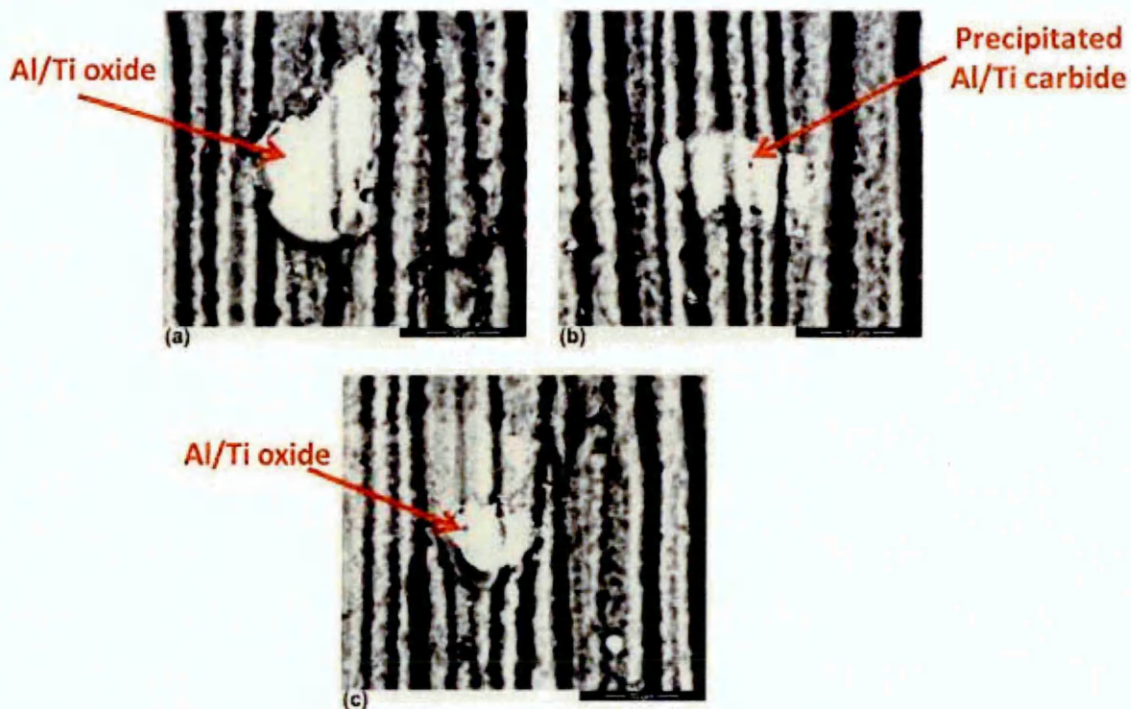


Figure 4.96: Backscattered electron micrograph showing directionality of the wear tracks and precipitation of Al and Ti containing oxide and carbide phases in Al-Ti-C coating @ 350⁰C for 1 hour. (a), (b) and (c) are backscattered electron micrographs at different magnifications.

The wear track morphology for Al-Ti-C coating @ 350⁰C for 1 hour and 3 hours from backscattered electron micrographs shown in **Figure 4.96** and **Figure 4.97** (a), (b) and (c) clearly showed that the precipitated high Ti concentration oxide and carbide phases resisted the abrasion caused by SiO₂ particles (hindrance in the wear track around high Ti concentration phases).

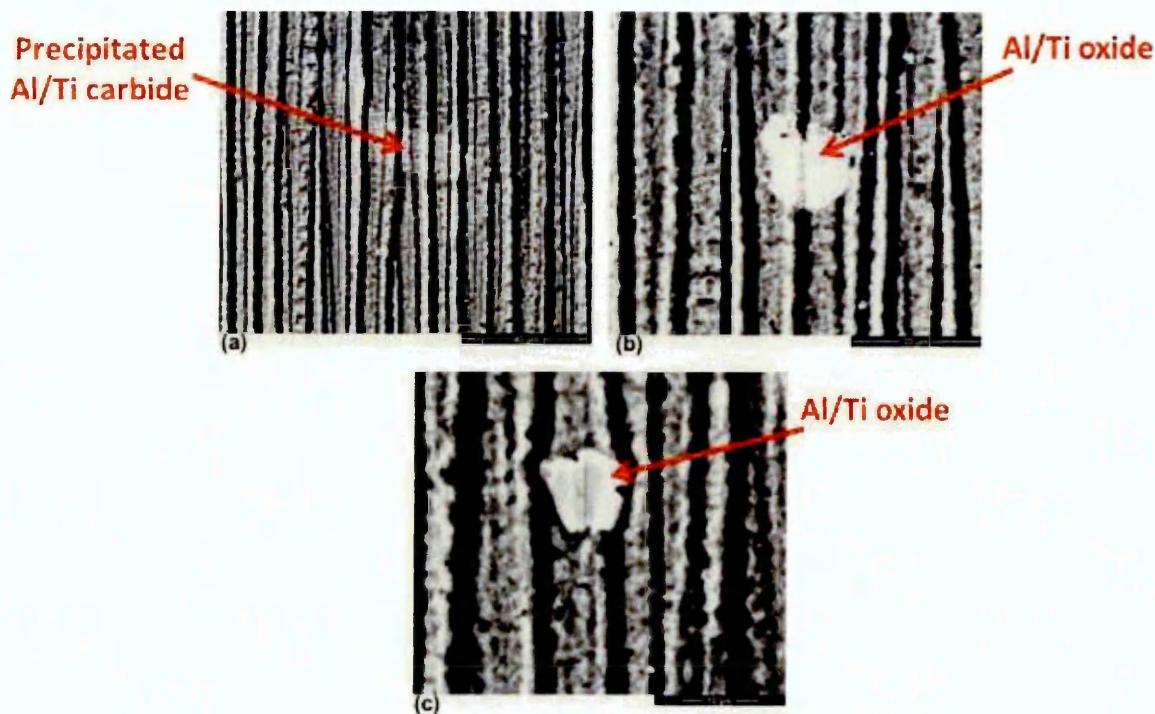


Figure 4.97: Backscattered electron micrograph showing directionality of the wear tracks and precipitation of Al and Ti containing oxide and carbide phases in Al-Ti-C coating @ 350⁰C for 3 hour. (a), (b) and (c) are backscattered electron micrographs at different magnifications.

Due to presence of a higher hardness regions observed in Al-Ti-C coating @ 350⁰C for 1 hour, the volume of the wear crater formed at each sliding distance was found lower than Al-Ti-C coating @ 350⁰C for 3 hours, thus lowering the wear coefficient value.

A difference in the wear coefficient of $\approx 11\%$ was observed between Al-Ti-C coatings @ 550⁰C for 1 hour (higher) compared with as sprayed Al-Ti-C coating. With increase in the holding time @ 550⁰C to 3 hours, $\approx 24\%$ higher value of wear coefficient for Al-Ti-C coating was observed in comparison with as sprayed coating.

It is important to note that a significant reduction in the micro-hardness values of Al-Ti-C @ 550⁰C for 1 hour and 3 hours in comparison with previous exposure temperatures (@ 150⁰C and 350⁰C for 1 hour and 3 hours) was also reported, suggesting that even with lower micro-hardness values, the least value of wear coefficient (or value of wear coefficient closer to as sprayed value) was recorded for Al-Ti-C coating @ 550⁰C for 1 hour followed by 3 hours of exposure at same temperature. The wear track morphologies for Al-Ti-C coating @ 550⁰C for 1 hour and 3 hours are shown in **Figure 4.98** (a), (b), (c) and **Figure 4.99** (a), (b), (c).

The Ti rich brittle phase seen in Al-Ti-C coating @ 550⁰C for 1 hour (which was considered to be a result of dissolution of Ti₈C₅ intermediate carbide causing increase in the Ti concentration in some regions of the coating), can also be seen in **Figure 4.98** (a), (b) and (c) resisting the wearing action caused by SiO₂ abrasive particles. Same can be seen from **Figure 4.99** (a), (b) and (c), however it is important to note that some regions with higher HV_{0.98} value (0.78 GPa to 0.98 GPa) for Al-Ti-C coating @ 550⁰C for 1 hour was seen which may have resulted in lower wear crater volume in Al-Ti-C coating @ 550⁰C for 1 hour than what was seen after 3 hours of exposure.

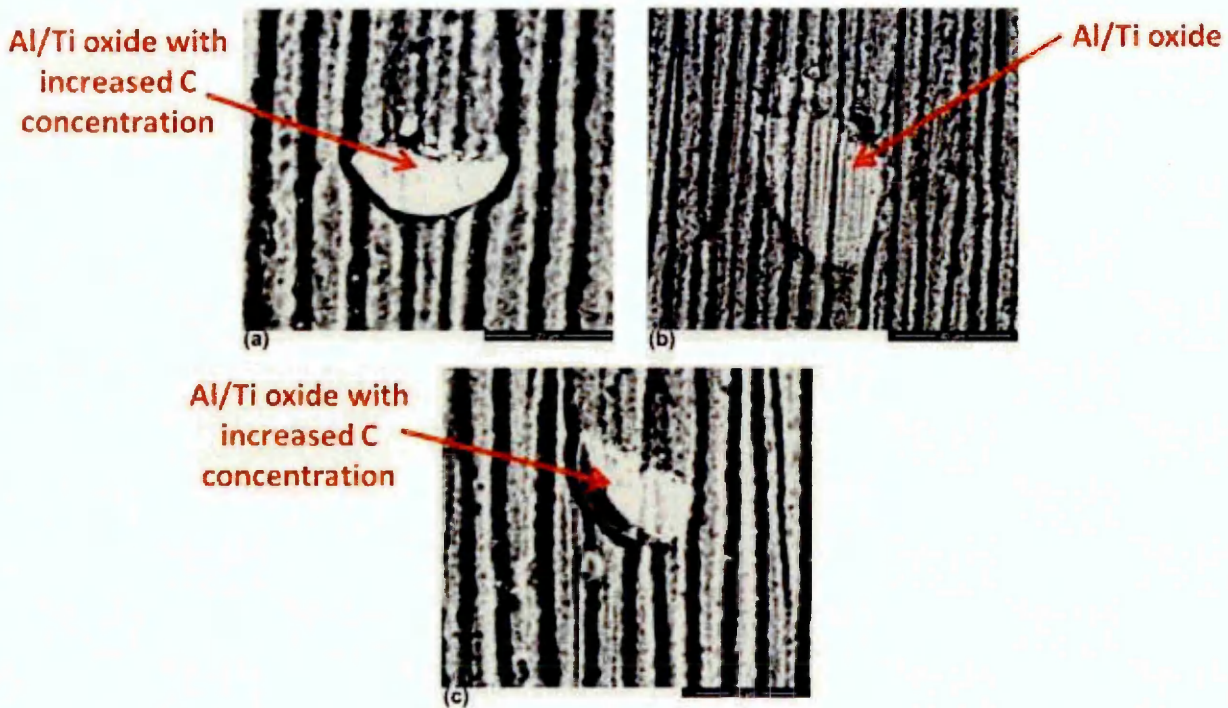


Figure 4.98: Backscattered electron micrograph showing directionality of the wear tracks and precipitation of Al and Ti containing oxide and carbide phases in Al-Ti-C coating @ 550⁰C for 1 hour. (a), (b) and (c) are backscattered electron micrographs at different magnifications.

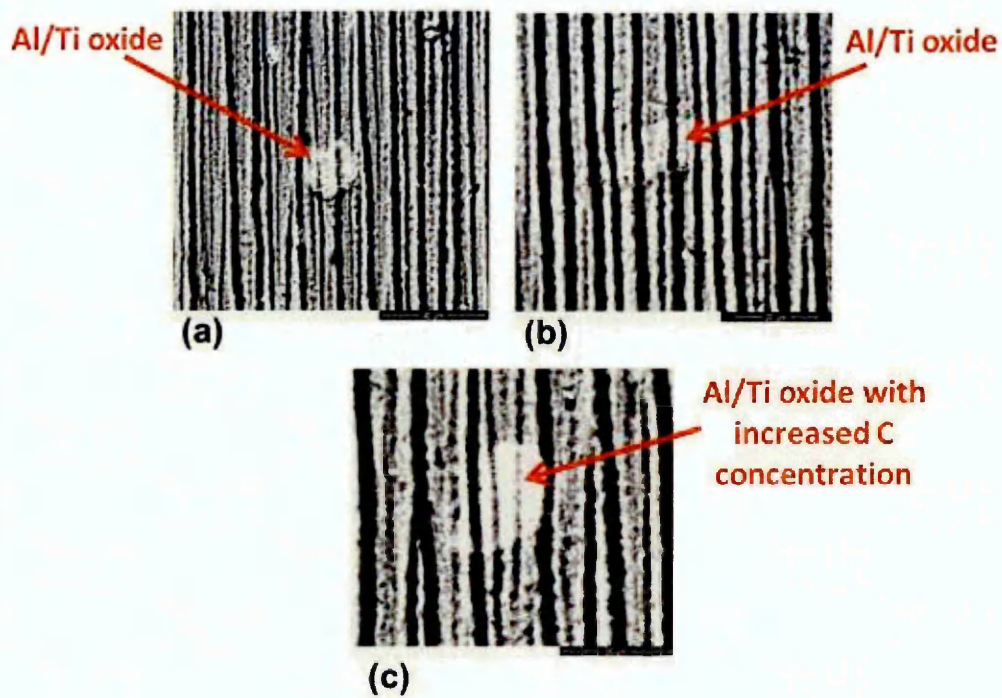


Figure 4.99: Backscattered electron micrograph showing directionality of the wear tracks and precipitation of Al and Ti containing oxide and carbide phases in Al-Ti-C coating @ 550⁰C for 3 hour. (a), (b) and (c) are backscattered electron micrographs at different magnifications.

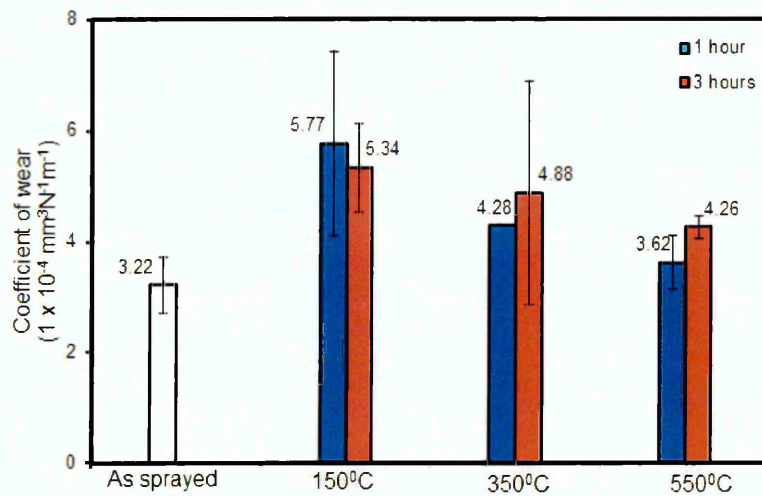


Figure 4.100: Comparison of wear coefficient values obtained for as sprayed Al-Ti-C coating and Al-Ti-C coating exposed to 150⁰C, 350⁰C and 550⁰C for 1 hour and 3 hours followed by rapid quenching.

A graph comparing the wear coefficient value of as sprayed Al-Ti-C coating with coating exposed to 150⁰C, 350⁰C and 550⁰C for 1 hour and 3 hours followed by rapid quenching is shown in **Figure 4.100**.

4.6.6 Microstructure of Al-Ti-C coating subjected to 150°C for 1 hour and 3 hours followed by exposure to normal room temperature (25°C) for 5 hours.

Figure 4.101 (a) and (b) shows the backscattered electron micrograph of Al-Ti-C coating exposed to 150°C for 1 hour and 3 hours followed by normal room temperature exposure for 5 hours period.

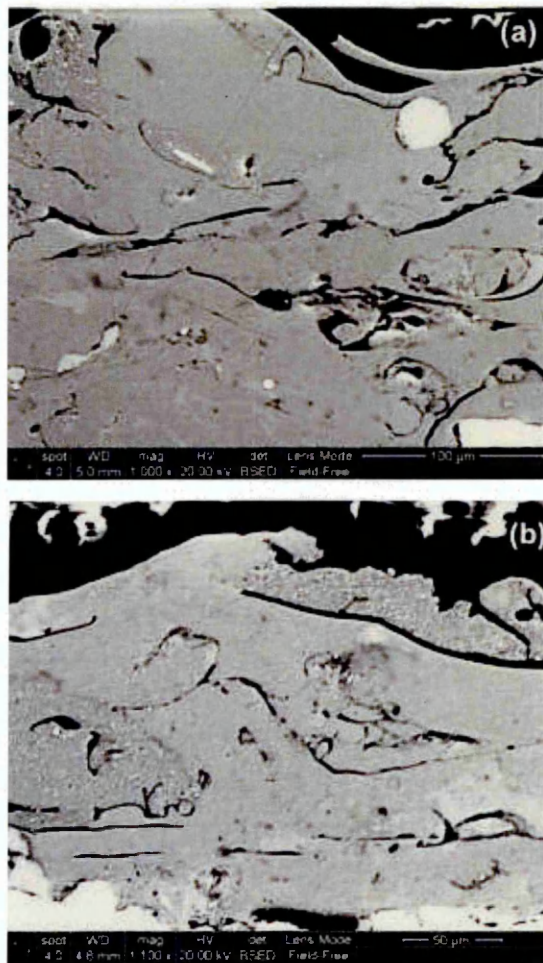


Figure 4.101: Backscattered electron micrograph of Al-Ti-C coating exposed to 150°C for (a) 1 hour and (b) 3 hours, followed by normal room temperature exposure (25°C) for 5 hours.

Figure 4.102 (a-d) and **Figure 4.103** (a-d) shows a higher magnification electron micrographs of Al-Ti-C coating @ 150⁰C for 1 hour and 3 hours followed by exposure to normal room temperature for 5 hours along with the average composition of each of the identified phases in **Table 4.30** and **Table 4.31**.

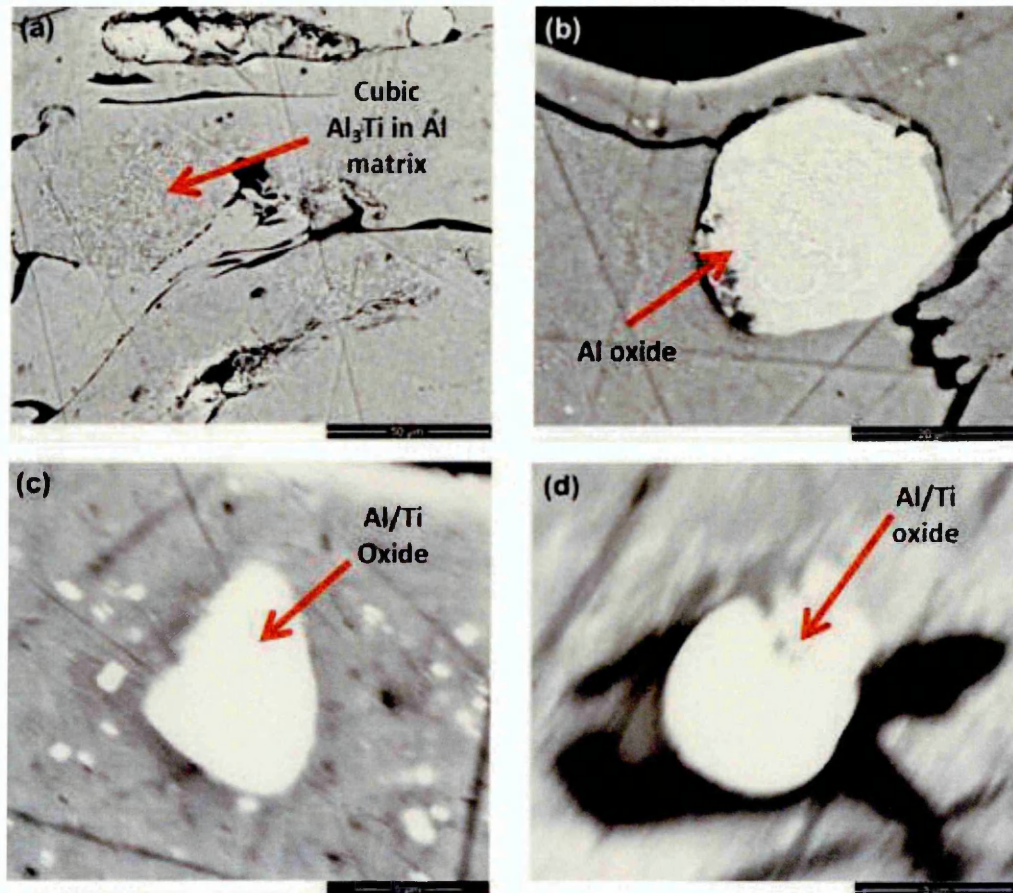


Figure 4.102: A higher magnification, @ (a) x 2000, (b) x 5000 and (c) x 10,000, (d) x 30,000 backscattered electron micrograph of Al-Ti-C coating exposed to 150⁰C for 1 hour showing (a) speckled region, (b) high contrast region, (c) triangular shaped brittle phase and (d) a brittle spherical equiaxed phase. The coatings were exposed to room temperature for 5 hours after 150⁰C exposure.

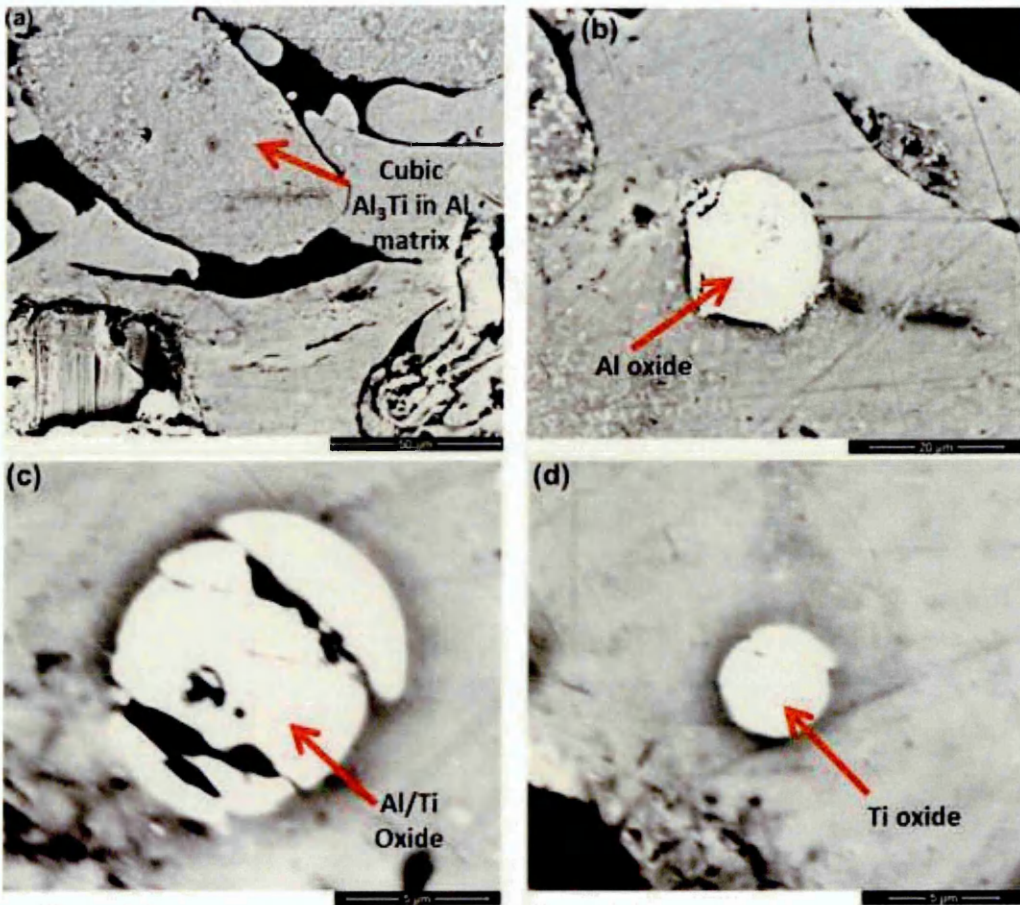


Figure 4.103: A higher magnification, @ (a) x 2000, (b) x 5000, (c) and (d) x 20,000, backscattered electron micrograph of Al-Ti-C coating exposed to 150°C for 3 hours showing (a) speckled region with observable growth in size (formation of a crater observed in (a), could be a result of coating removal during mechanical polishing), (b) high contrast region, (c) and (d) brittle spherical equiaxed phase. Notice the difference in the size of phases shown in (c) and (d). The coatings were exposed to room temperature for 5 hours after 150°C exposure.

Table 4.30: Average composition analysis of different phases observed in Al-Ti-C coating @ 150°C for 1 hour followed by normal room temperature exposure for 5 hours.

Phase	Average composition			
	Al (at%)	Ti (at%)	C (at%)	O (at%)
Speckled region	35 ± 1	1 ± 0.1	3 ± 0.7	61 ± 0.1
High atomic number contrast region	33 ± 1.2	3 ± 0.7	3 ± 0.4	61 ± 0.2
Dark and light grey regions	35 ± 0.1	1 ± 0.1	3 ± 0	61 ± 0
Triangular brittle phase	26 ± 0.5	7 ± 0.1	4 ± 0.5	62 ± 0.1
Spherical equiaxed brittle phase	17 ± 7	14 ± 5	5 ± 0.5	64 ± 1.1

Table 4.31: Average composition analysis of different phases observed in Al-Ti-C coating @ 150°C for 3 hours followed by normal room temperature exposure for 5 hours.

Phase	Average composition			
	Al (at%)	Ti (at%)	C (at%)	O (at%)
Speckled region	36 ± 1	1 ± 0.1	3 ± 1	61 ± 0.2
High atomic number contrast region	27 ± 2	8 ± 2	3 ± 0.5	62 ± 0.2
Dark and light grey regions	37 ± 0.1	1 ± 0.1	3 ± 0	61 ± 0.1
Spherical equiaxed brittle phase	7 ± 1	24 ± 1.2	4 ± 0.5	65 ± 0.2

Formation of speckled region in Al-Ti-C coating, shown in **Figure 4.102 (a)** and **Figure 4.103 (a)** after 150°C for 1 hour and 3 hours followed by room temperature exposure for 5 hours was seen. Similar to Al-Ti-C coating subjected to same exposure temperature followed by rapid quenching, growth in the size of the speckled spots was observable after 3 hours of exposure @ 150°C followed by normal room temperature exposure, see **Figure 4.103 (a)**. A similar average composition of the speckled region was seen after 1 hour and 3 hours of exposure detected from EDX analysis, see **Table 4.30** and **Table 4.31**.

Figure 4.102 (b) and **Figure 4.103 (b)** also revealed formation of a high atomic number contrast regions similar to the regions which were observed in Al-Ti-C coating @ 150⁰C followed by rapid quenching (for both 1 hour and 3 hours). As seen from **Table 4.30** and **Table 4.31**, an increase in the Ti concentration (at %) \approx 167% after 3 hours of exposure was seen in comparison to 1 hour of exposure @ 150⁰C followed by normal room temperature exposure for 5 hours. The dark and light grey regions after 1 hour and 3 hours of exposure, were also observed with similar average composition (detected using EDX analysis) after both 1 hour and 3 hours of exposure.

Precipitation of two brittle phases, see in **Figure 4.102 (c)** and (d), was also observed in Al-Ti-C coating after 1 hour of exposure at 150⁰C followed by normal room temperature exposure for 5 hours. However, the brittle spherical equiaxed phase shown in **Figure 4.103 (d)** was reported to contain twice the amount of Ti concentration (detected using EDX) than the triangular brittle phase (**Figure 4.103 (c)**), see **Table 4.30**.

The triangular shaped brittle phase was not observed in Al-Ti-C coating after 3 hours of exposure under similar exposure, however formation of brittle spherical equiaxed phase was reported. A \approx 71 % increase in the Ti concentration (at%) was detected in the brittle spherical equiaxed phase after 3 hours, in comparison to the brittle spherical equiaxed phase observed after 1 hour of exposure of Al-Ti-C coating at 150⁰C followed by normal room temperature exposure for 5 hours.

The XRD analysis of Al-Ti-C coating after 150⁰C exposure for 1 hour and 3 hours followed by room temperature exposure for 5 hours clearly showed formation of both Al and Ti oxides, see **Figure 4.104** (a) and (b), which can also be seen from the higher O concentration (at%) detected from EDX analysis of identified phases. Formation of cubic Al₃Ti intermetallic which was also detected in as-sprayed Al-Ti-C coating, Al-Ti-C coating exposed to 150⁰C and 350⁰C for 1 hour and 3 hours followed by rapid quenching, was also seen in Al-Ti-C coating cooled under normal room temperature condition.

The phases such as high contrast regions, dark or light grey regions and speckled regions which were identified using backscattered electron micrographs for Al-Ti-C coating exposed to 150⁰C for both 1 hour and 3 hours (cooled under normal room temperature conditions), the Al (at%) to O (at%) ratio \approx 0.4-0.5 :1 indicated the formation of Al₂O₃ which was confirmed by the XRD analysis, see **Figure 4.104** (a), (b).

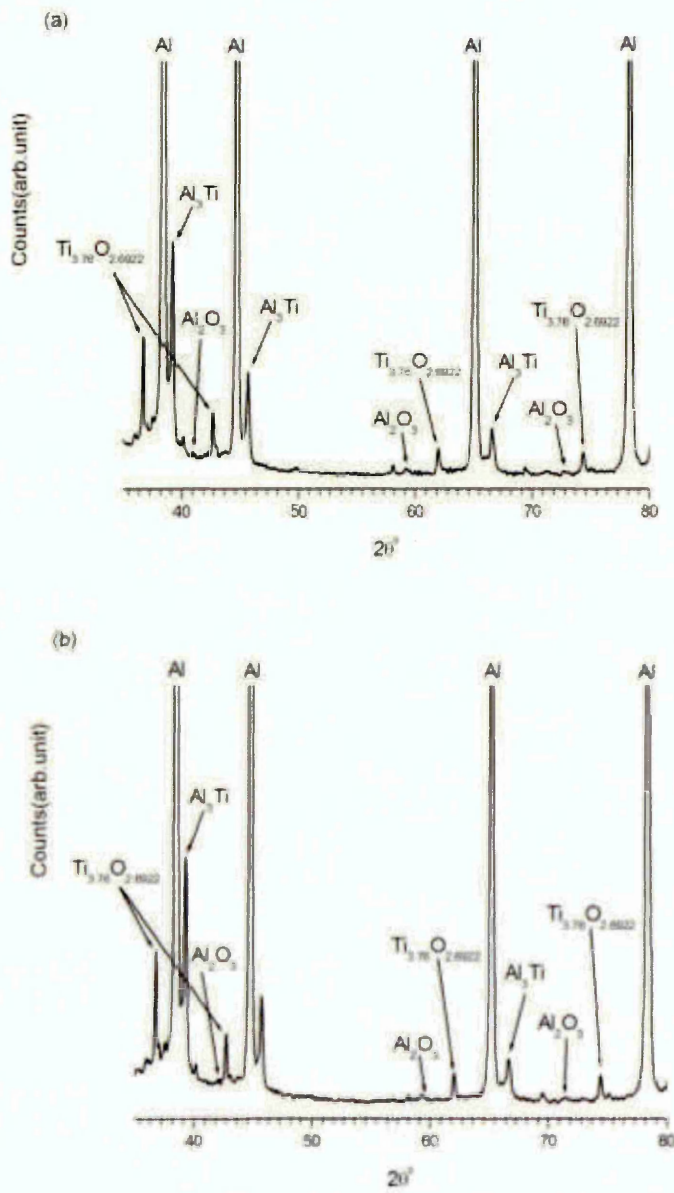


Figure 4.104: XRD trace of Al-Ti-C coating post 150°C exposure for (a) 1 hour and (b) 3 hours followed by normal room temperature exposure for 5 hours.

The (Al+Ti) : O ratio for all the brittle phases observed in Al-Ti-C coating @150⁰C (for both 1 hour and 3 hours followed by room temperature cooling), detected using average EDX compositional analysis showed a similar ratio of 0.5 :1. However this stoichiometric ratio of 0.5:1 was close to Al: O ratio for Al₂O₃ (0.67:1) detected using XRD analysis, this could have been possible due to Ti substitution during formation of Al oxide.

The XRD analysis also indicated formation of titanium oxide (Ti_{3.76}O_{2.6922}), however the stoichiometric ratio of Ti: O for this oxide was ≈ 1.4:1, which was not detected using EDX compositional analysis of each of the identified phase.

4.6.7 Microstructure of Al-Ti-C coating subjected to 350°C for 1 hour and 3 hours followed by exposure to normal room temperature (25°C) for 5 hours.

Figure 4.105 (a) and (b) shows the backscattered electron micrograph of Al-Ti-C coating exposed to 150°C for 1 hour and 3 hours followed by normal room temperature exposure for 5 hours period.

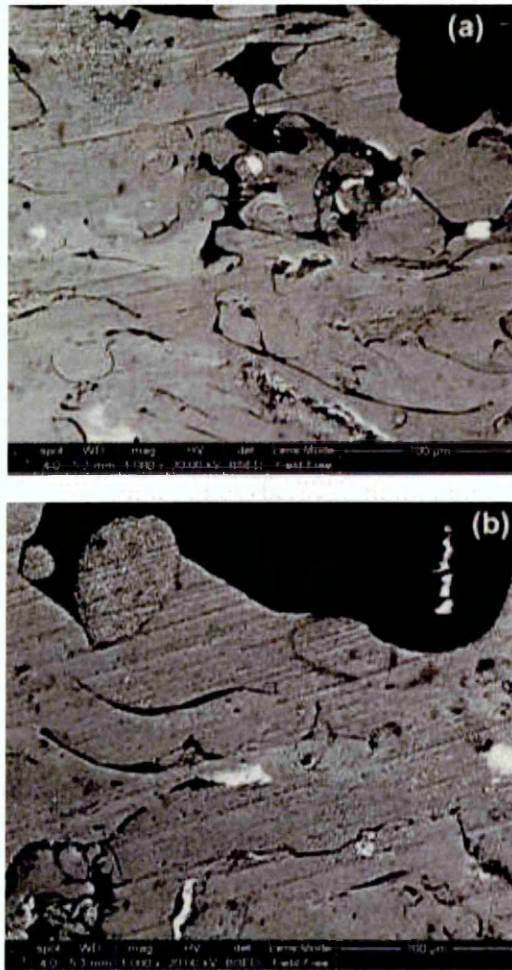


Figure 4.105: Backscattered electron micrograph of Al-Ti-C coating exposed to 350°C for (a) 1 hour and (b) 3 hours, followed by normal room temperature exposure (25°C) for 5 hours.

Figure 4.106 (a-d) and **Figure 4.107** (a-d) shows a higher magnification electron micrographs of Al-Ti-C coating @ 350°C for 1 hour and 3 hours followed by exposure to normal room temperature for 5 hours along with the average composition of each of the identified phases in **Table 4.32** and **Table 4.33**.

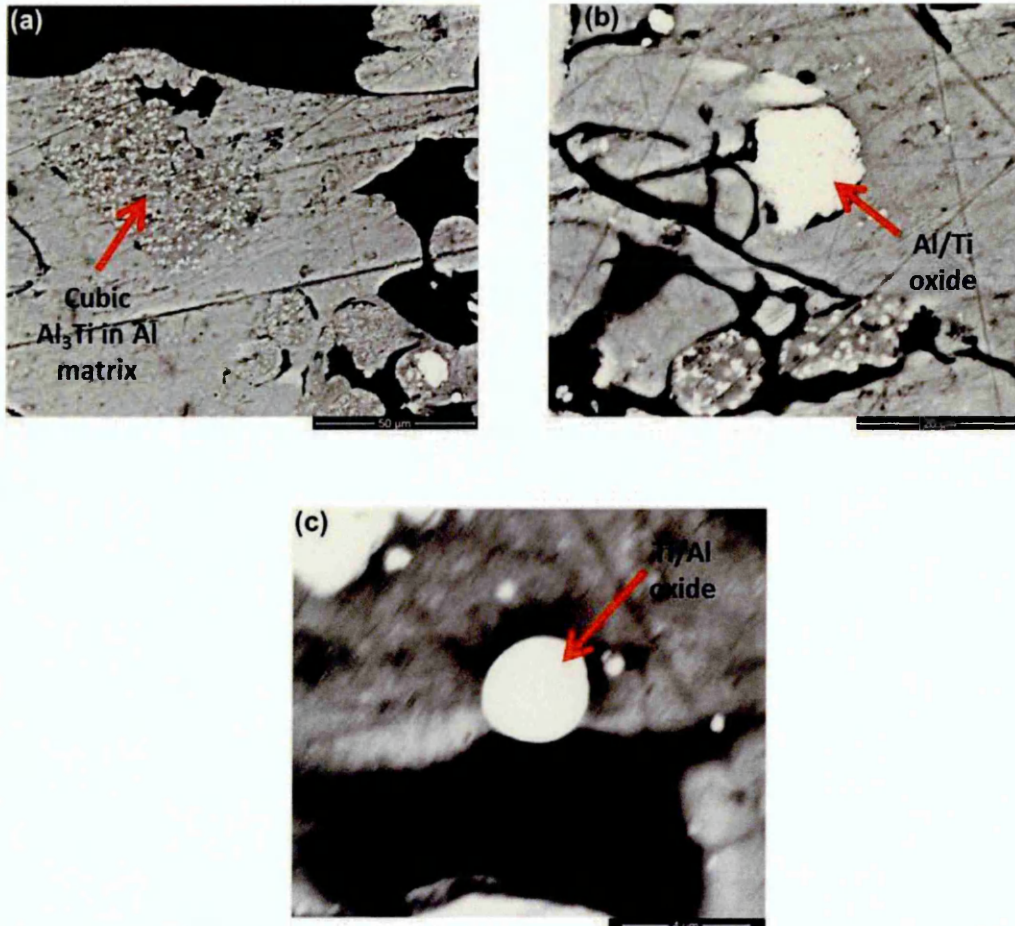


Figure 4.106: A higher magnification, @ (a) x 2000, (b) x 5000 and (c) 20,000, backscattered electron micrograph of Al-Ti-C coating exposed to 350°C for 1 hour showing (a) speckled region with observable growth in size, (b) high contrast region and (c) brittle spherical equiaxed phase. The coatings were then exposed to normal room temperature for 5 hours.

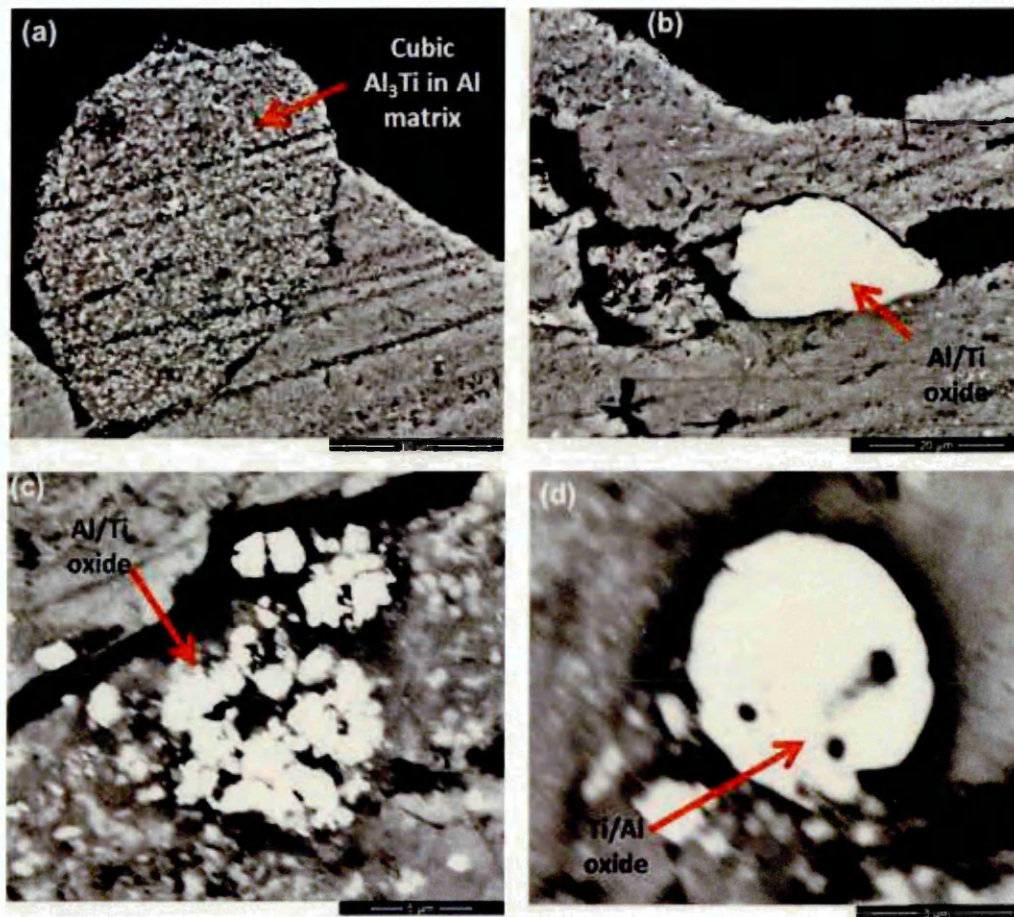


Figure 4.107: A higher magnification, @ (a) x 2000, (b) x 4000 and (c) 12,000 and (d) 30,000 backscattered electron micrograph of Al-Ti-C coating exposed to 350⁰C for 3 hours showing (a) speckled region with observable growth in size, (b) high contrast region and (c) brittle spherical equiaxed phase. The coatings were then exposed to normal room temperature for 5 hours.

Table 4.32: Average composition analysis of different phases observed in Al-Ti-C coating @ 350⁰C for 1 hour followed by normal room temperature exposure for 5 hours.

Phase	Average composition			
	Al (at%)	Ti (at%)	C (at%)	O (at%)
Speckled region	34 ± 3	1 ± 0.1	5 ± 0.7	61 ± 0.1
High atomic number contrast region	29 ± 1.5	7 ± 1.5	3 ± 0.2	61 ± 0.2
Dark and light grey regions	36 ± 0.2	1 ± 0.1	3 ± 0	60 ± 0
Spherical equiaxed brittle phase	10 ± 2	13 ± 7	12 ± 4	65 ± 1.1

Table 4.33: Average composition analysis of different phases observed in Al-Ti-C coating @ 350⁰C for 3 hours followed by normal room temperature exposure for 5 hours.

Phase	Average composition			
	Al (at%)	Ti (at%)	C (at%)	O (at%)
Speckled region	35 ± 3	1 ± 0.1	3 ± 0.5	61 ± 0.1
High atomic number contrast region	32 ± 0.1	4 ± 1.5	3 ± 0.1	61 ± 0.2
Dark and light grey regions	34 ± 1.4	1 ± 0.1	4 ± 1.3	60 ± 0
Brittle phase	25 ± 3	8 ± 1	5 ± 2	63 ± 0.4
Spherical equiaxed brittle phase	15 ± 3	12 ± 0.5	9 ± 2	64 ± 0.4

Speckled region similar to the one seen in Al-Ti-C coating @ 150⁰C for 1 hour and 3 hours followed by normal room temperature exposure for 5 hours with similar average composition, detected using EDX analysis, was also seen after 350⁰C for similar exposure periods, see **Figure 4.106** (a) and **Figure 4.107** (a). The dark and the light grey contrast regions were also seen in Al-Ti-C coating after 350⁰C exposure for 1 hour and 3 hours followed by normal room temperature exposure, however they were more pronounced in Al-Ti-C coating @ 350⁰C for 1 hour in comparison to 3 hours of exposure at same temperature (with similar average composition).

The high contrast regions (which were also seen @ 150⁰C of exposure, see **Figure 4.104 (b)** and **Figure 4.105 (b)**) were also seen in Al-Ti-C coating @ 350⁰C for 1 hour and 3 hours followed by normal room temperature cooling for 5 hours, see **Figure 4.106 (b)** and **Figure 4.107 (b)**, with (Al+Ti):O ratio \approx 0.6:1 for both 1 hour and 3 hours (from EDX compositional analysis) of exposure at same temperature.

The backscattered electron micrographs of Al-Ti-C coating @ 350⁰C followed by room temperature cooling for 5 hours also revealed formation of brittle spherical equiaxed phase for both 1 hour and 3 hours of exposure with similar average Ti concentration (at%). However formation of another distinct brittle phase was also seen after 3 hours of exposure with \approx 33 % less Ti concentration than spherical phase observed in Al-Ti-C coating after 3 hours at 350⁰C followed by room temperature cooling, see **Figure 4.107 (c)**.

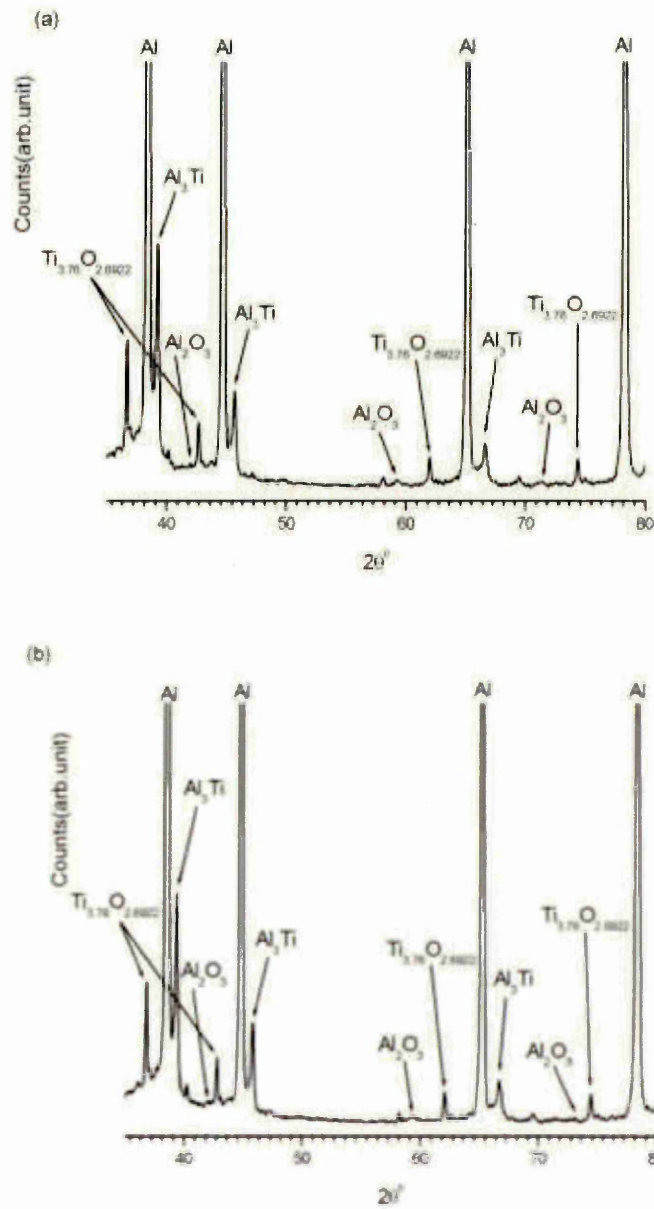


Figure 4.108: XRD trace of Al-Ti-C coating post 350°C exposure for (a) 1 hour and (b) 3 hours followed by normal room temperature exposure for 5 hours.

The XRD analysis of the Al-Ti-C coating @ 350⁰C for both 1 hour and 3 hours followed by normal room temperature cooling, see **Figure 4.108** (a) and (b), also showed formation of cubic Al₃Ti intermetallic which was also seen in Al-Ti-C @ 150⁰C for 1 hour and 3 hours followed by normal room temperature cooling. The formation of both Al and Ti oxide in form of cubic Al₂O₃ and Ti_{3.76}O_{2.9622} were also seen in Al-Ti-C coating @ 350⁰C for both 1 hour and 3 hours followed by normal room temperature cooling. The stoichiometric Al to O ratio obtained from EDX analysis of speckled region, high contrast region, dark and light grey region seen in Al-Ti-C coating after 1 hour and 3 hours of exposure @ 350⁰C clearly indicated the formation of Al oxide, which was detected using XRD analysis.

The XRD analysis did not reveal the formation of TiC phase. The Al to Ti ratio for brittle phase seen in Al-Ti-C coating after 3 hours, was \approx 3.1:1 (using EDX analysis), suggesting precipitation of intermetallic tri-aluminide Al₃Ti, which was also seen from XRD analysis, **Figure 4.108** (b). The possibility of formation of intermediate titanium carbide (for the same brittle phase), with Ti to C ratio of 8:5 (see **Table 4.33**), which has also been reported earlier in as sprayed coating, Al-Ti-C coating @ 150⁰C, 350⁰C followed by rapid quenching, was not detected in the XRD analysis of Al-Ti-C coating @ 350⁰C for 3 hours followed by room temperature cooling for 5 hours, see **Figure 4.108** (b).

4.6.8 Microstructure of Al-Ti-C coating subjected to 550°C for 1 hour and 3 hours followed by exposure to normal room temperature (25°C) for 5 hours.

Figure 4.109 (a) and (b) shows the backscattered electron micrograph of Al-Ti-C coating exposed to 550°C for 1 hour and 3 hours followed by normal room temperature exposure for 5 hours period.

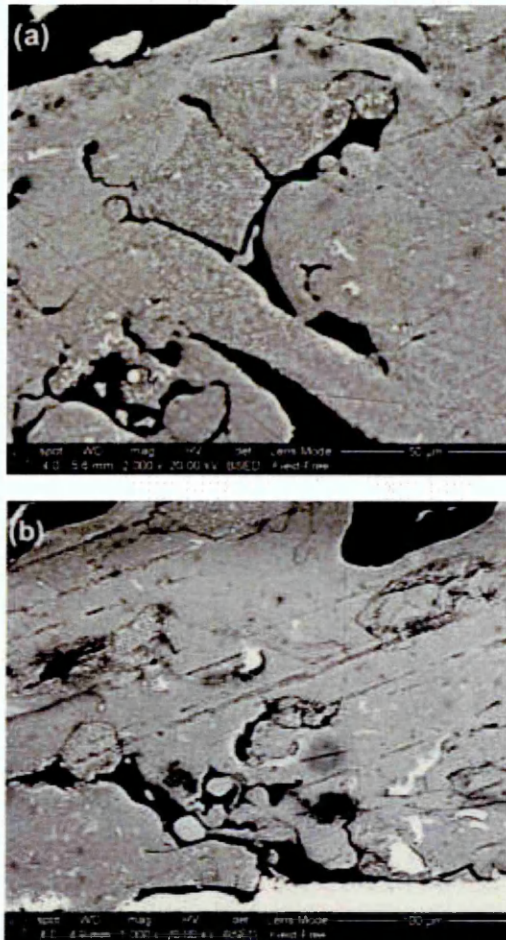


Figure 4.109: Backscattered electron micrograph of Al-Ti-C coating exposed to 550°C for (a) 1 hour and (b) 3 hours, followed by normal room temperature exposure (25°C) for 5 hours.

Figure 4.110 (a-b) and **Figure 4.111** (a-c) shows a higher magnification electron micrographs of Al-Ti-C coating @ 350⁰C for 1 hour and 3 hours followed by exposure to normal room temperature for 5 hours along with the average composition of each of the identified phases in **Table 4.34** and **Table 4.35**.

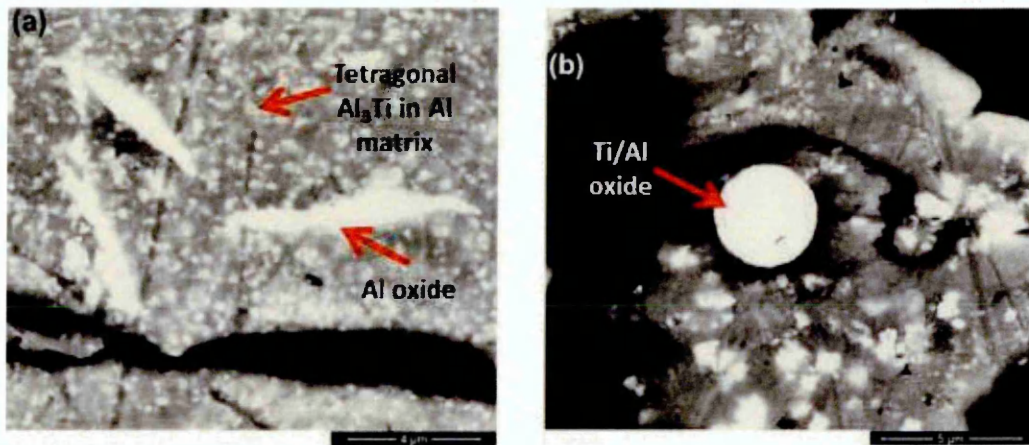


Figure 4.110: A higher magnification, @ (a) and (b) x 20,000 backscattered electron micrograph of Al-Ti-C coating exposed to 550⁰C for 1 hour showing (a) speckled region with feather shaped regions and (b) showing brittle spherical equiaxed phase along with large speckled spots. The coatings were then exposed to normal room temperature for 5 hours.

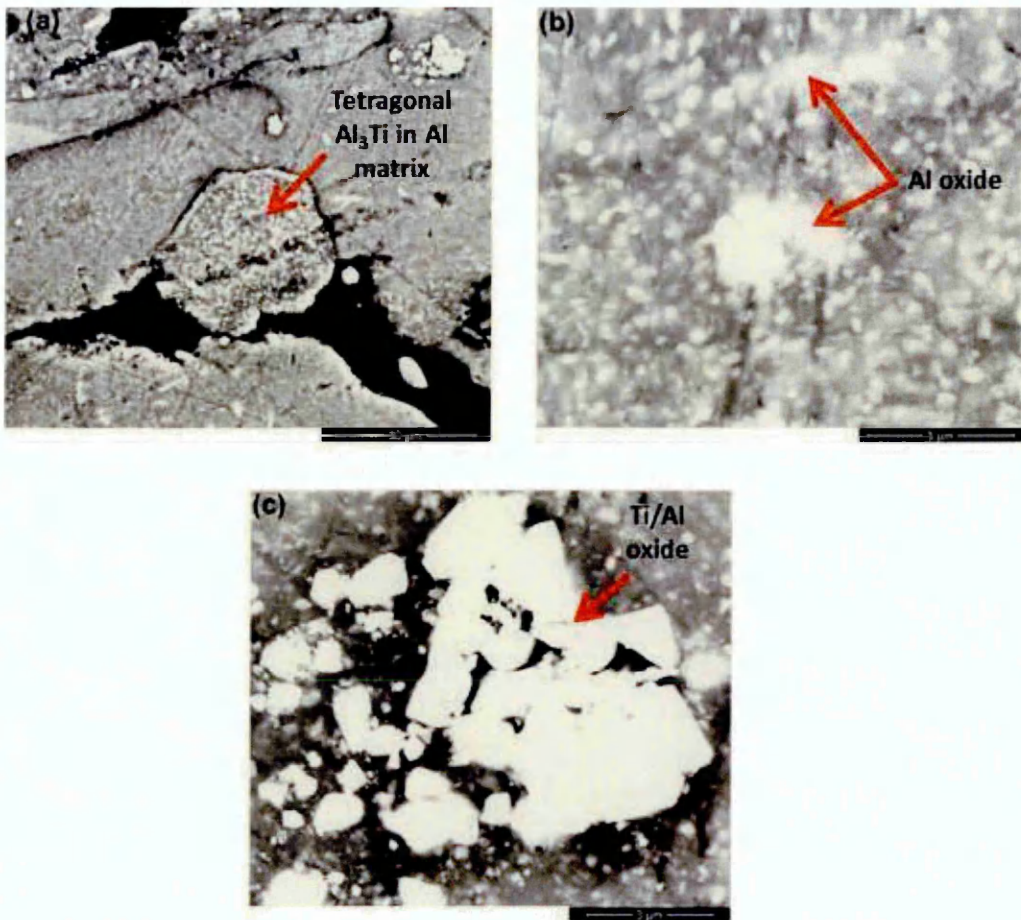


Figure 4.111: A higher magnification, @ (a) x 3000, (b) and (c) x 30,000 backscattered electron micrograph of Al-Ti-C coating exposed to 550⁰C for 1 hour showing (a) speckled region (b) Speckled region with observable growth and feather shaped region and (c) brittle phase along with speckled spots. The coatings were then exposed to normal room temperature for 5 hours.

Table 4.34: Average composition analysis of different phases observed in Al-Ti-C coating @ 550⁰C for 1 hour followed by normal room temperature exposure for 5 hours.

Phase	Average composition			
	Al (at%)	Ti (at%)	C (at%)	O (at%)
Speckled region	36 ± 0.4	1 ± 0	2 ± 0.3	61 ± 0.1
Region showing growth in the size of speckled spots	31 ± 3	1 ± 0.2	7 ± 2	61 ± 0.5
Feather shaped regions	34 ± 0.6	1 ± 0.1	5 ± 4	60 ± 0
Spherical equiaxed brittle phase	18 ± 2	14 ± 0.2	6 ± 1.1	62 ± 0.3

Table 4.35: Average composition analysis of different phases observed in Al-Ti-C coating @ 550⁰C for 3 hours followed by normal room temperature exposure for 5 hours.

Phase	Average composition			
	Al (at%)	Ti (at%)	C (at%)	O (at%)
Speckled region	32 ± 3	1 ± 0.2	6 ± 3	61 ± 0.5
Feather shaped region	24 ± 1.1	1 ± 0	12 ± 1	63 ± 0.2
High contrast regions	30 ± 1	6 ± 0	4 ± 1	60 ± 0.3
Brittle phase	8 ± 4	11 ± 0.2	16 ± 1	65 ± 0.6

Apart from the speckled region, the Al-Ti-C coating @ 550⁰C for both 1 hour and 3 hours showed formation of distinct feather shaped regions after 1 hour @ 550⁰C, see **Figure 4.110** (a). These feather shaped oxide regions were also seen after 3 hours of exposure @ 550⁰C, see **Figure 4.111** (b), but were more profound after 1 hour of exposure at same temperature. The average EDX compositional analysis revealed that speckled region and feather shaped regions had similar concentrations of Al (at%), Ti (at%) and O (at%), however the C levels varied (also due to metallographic sample preparation), see **Table 4.34** and **Table 4.35**. A growth in the size of the speckled region was also observed in Al-Ti-C coating @ 550⁰C for 1 hour, with similar average composition as speckled phase.

Note that for Al-Ti-C coating @ 550⁰C for 3 hours, a similar growth was also seen, see **Figure 4.110** (b) but the EDX analysis showed that the average composition of these large speckled phases was similar to the ones seen after 1 hour of exposure at same temperature. Some high contrast phases in Al-Ti-C coating @ 550⁰C for 3 hours were found to be similar in composition to the ones seen after 150⁰C and 350⁰C for same exposure period.

A spherical equiaxed oxide phase, with similar Ti concentration (at%) to the spherical phase observed in Al-Ti-C coating after 350⁰C for 1 hour and 3 hours, was also seen in Al-Ti-C coating @ 550⁰C for 1 hour followed by room temperature cooling for 5 hours. However this spherical equiaxed phase was not seen after 3 hours of exposure at same temperature.

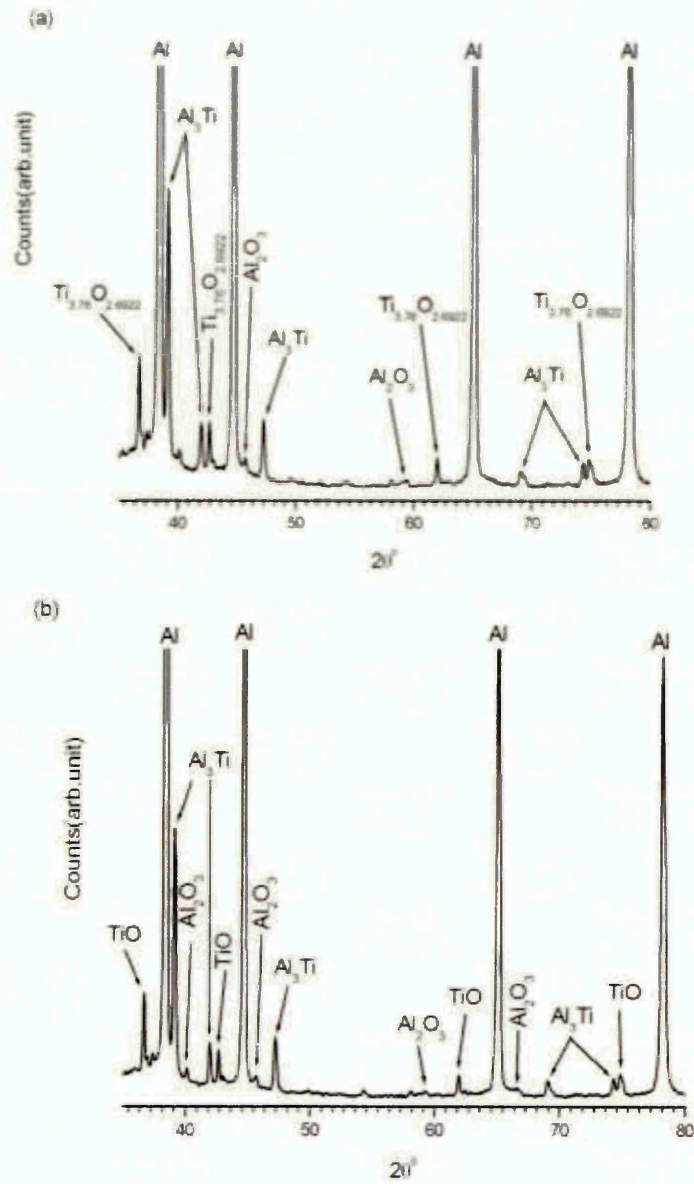


Figure 4.112: XRD trace of Al-Ti-C coating post 550⁰C exposure for (a) 1 hour and (b) 3 hours followed by normal room temperature exposure for 5 hours.

Precipitation of a brittle oxide phase was observed in Al-Ti-C coating after 3 hours of exposure @ 550⁰C followed by room temperature cooling for 5 hours, see **Figure 4.111** (c). A similar brittle oxide phase formation was also seen in Al-Ti-C coating exposed to 150⁰C for 1 hour and 350⁰C for 3 hours (room temperature cooled for 5 hours), however after 550⁰C of exposure for 3 hours, the Ti concentration (at%) was found to be ≈ 27 % more than the value obtained in the previous exposure temperatures.

The XRD trace in **Figure 4.112** (a) and (b) showed formation of tetragonal Al₃Ti intermetallic which was also seen in the rapid quenched Al-Ti-C coating exposed at same temperature and period. Formation of cubic Al₂O₃ was also detected using XRD analysis of Al-Ti-C coating @ 550⁰C for both 1 hour and 3 hours followed by room temperature cooling for 5 hours. This was also in accordance with the stoichiometric ratio of Al:O obtained using average EDX compositional analysis (≈ 0.6:1) of identified phases in Al-Ti-C coating @ 550⁰C for both 1 hour and 3 hours, except for spherical equiaxed phase after 1 hour and brittle phase after 3 hours of exposure at 550⁰C followed by room temperature cooling for 5 hours.

Formation of cubic Ti oxide was also confirmed using XRD analysis, however a difference in the stoichiometric Ti:O ratio of oxide phases was observed after 1 hour (Ti_{3.76}O_{2.6922}) and 3 hours (TiO) of exposure @ 550⁰C followed by room temperature cooling for 5 hours. It is important to note that these stoichiometric Ti:O ratios were not deduced from average compositional EDX analysis of identified phases.

4.6.9 Micro-hardness of Al-Ti-C coating subjected to 150°C, 350°C, 550°C for 1 hour and 3 hours followed by normal room temperature cooling for 5 hours.

Table 4.36 shows the average Vickers micro-hardness values measured for Al-Ti-C coating subjected to 150°C, 350°C and 550°C for 1 hour and 3 hours respectively followed by room temperature cooling for 5 hours.

Table 4.36: Vickers micro-hardness of Al-Ti-C coating subjected to 150°C, 350°C and 550°C for 1 hour and 3 hours followed by room temperature cooling for 5 hours.

Temperature (°C)	Time of exposure (hours)	HV _{0.98} GPa(kgf/mm ²)	Coefficient of variation (%)
@ 150	1	0.67 (68 ± 23)	33
	3	0.83 (85 ± 28)	33
@ 350	1	0.70 (71 ± 21)	30
	3	0.77 (78 ± 19)	25
@ 550	1	0.60 (61 ± 17)	28
	3	0.52 (53 ± 14)	25

The range of micro-hardness values for Al-Ti-C coating subjected to 150°C, 350°C and 550°C followed by room temperature cooling was also shown by the frequency distribution histograms in **Figure 4.113** to **Figure 4.115**. The effect of precipitation of different phases at various exposure temperatures followed by normal room temperature cooling for 5 hours on the micro-hardness of Al-Ti-C coating is shown in **Figure 4.116**.

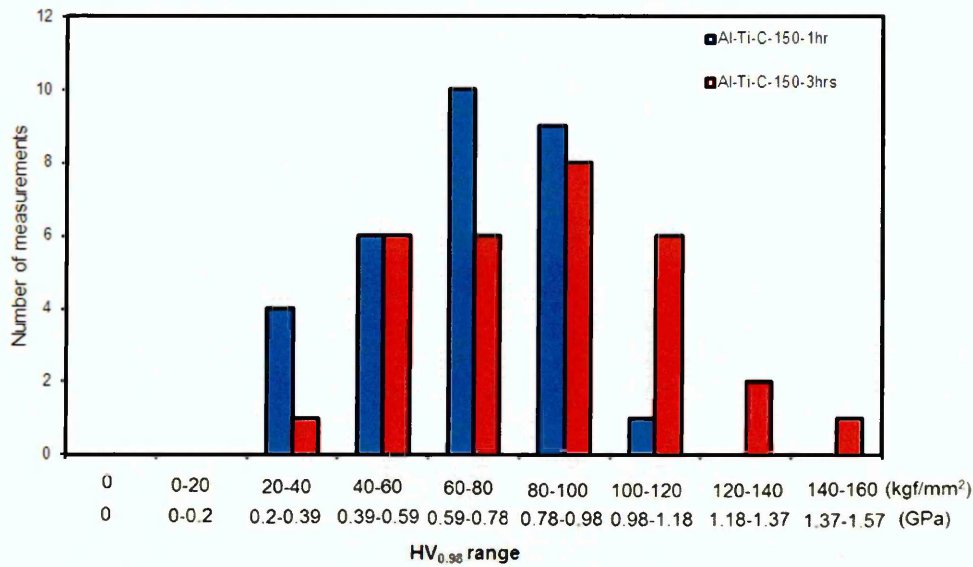


Figure 4.113: Frequency distribution histogram of micro-hardness (HV_{0.98}) for Al-Ti-C coating exposed to 150°C for 1 hour (violet shade) and 3 hours (Dark red shade). The coatings were room temperature cooled (5 hours) after exposure.

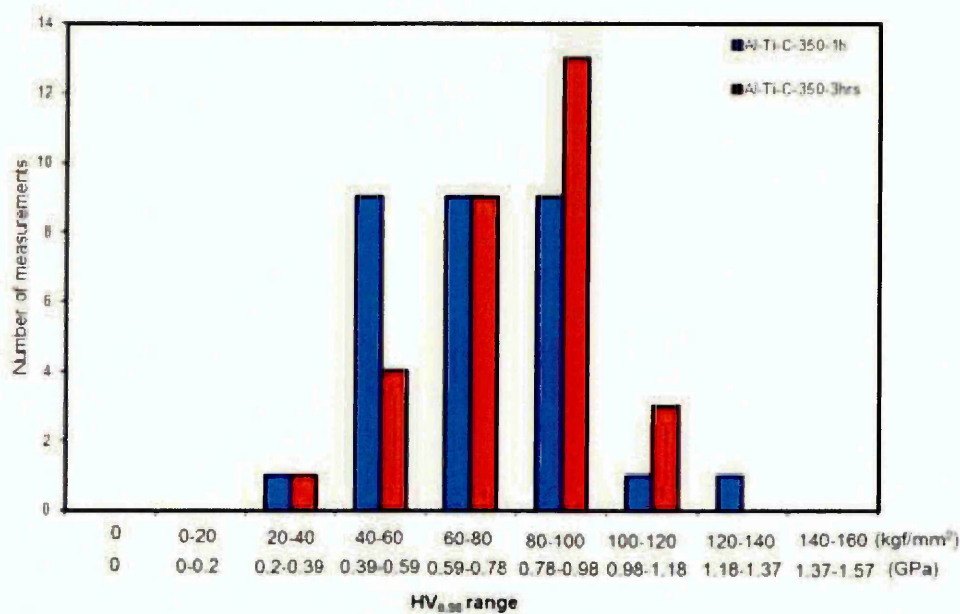


Figure 4.114: Frequency distribution histogram of micro-hardness (HV_{0.98}) for Al-Ti-C coating exposed to 350°C for 1 hour (violet shade) and 3 hours (Dark red shade). The coatings were room temperature cooled (5 hours) after exposure.

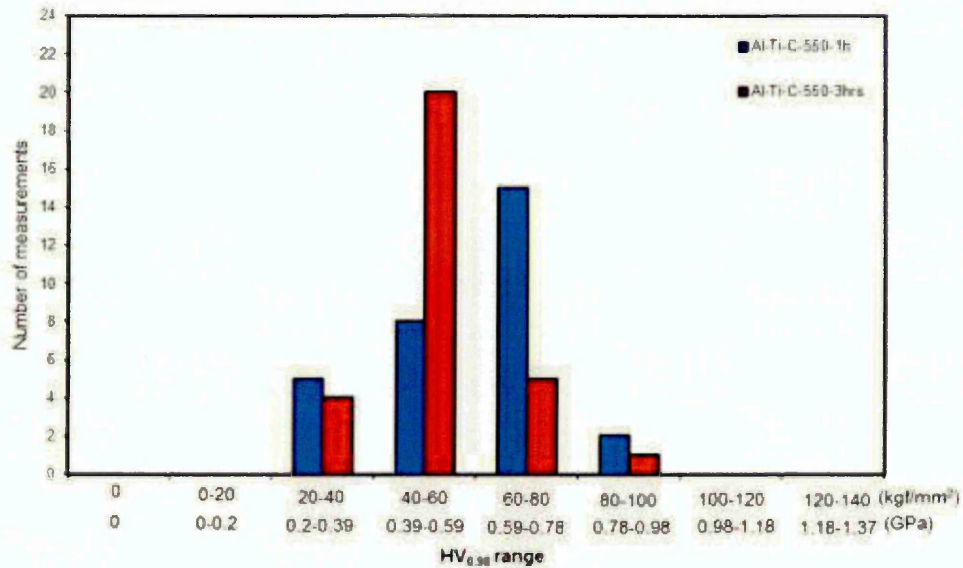


Figure 4.115: Frequency distribution histogram of micro-hardness ($HV_{0.98}$) for Al-Ti-C coating exposed to 550°C for 1 hour (violet shade) and 3 hours (Dark red shade). The coatings were room temperature cooled (5 hours) after exposure.

For the Al-Ti-C coating @ 150°C for 1 hour, followed by room temperature cooling, regions with micro-hardness value in the as high as 0.98 GPa to 1.18 GPa were observed, however with an increase in the exposure period to 3 hours for same exposure temperature, regions of much higher micro-hardness values (1.37GPa-1.57 GPa) were also recorded, see **Figure 4.113**. This could have been due to the formation of Ti rich brittle oxide phase which was seen in Al-Ti-C coating after 3 hours of exposure @ 150°C (followed by room temperature cooling for 5 hours), resulting in an overall 13% increase in the micro-hardness value of Al-Ti-C coating subjected to 150°C of exposure for 3 hours (followed by room temperature cooling) in comparison to as sprayed coating, see **Figure 4.116**.

Even though Al-Ti-C coating exposed to 150⁰C for 3 hours showed regions with higher micro-hardness values than what was observed after 1 hour same coefficient of variation value of 33% was observed for both exposure period (1 hour and 3 hours at 150⁰C). This could be attributed to the detection of large number of regions with micro-hardness values in the range of 0.59 GPa to 0.98 GPa which were seen in Al-Ti-C coating @ 150⁰C for 1 hour than after 3 hours of exposure (even though higher micro-hardness regions were observed).

With an increase in the exposure temperature to 350⁰C, a reduction in the spread of micro-hardness value and coefficient of variation values were observed, see **Figure 4.114**. The regions of micro-hardness value in the range 0.59 GPa to 0.78 GPa were significantly higher after 3 hours of exposure than 1 hour of exposure @ 350⁰C, see **Figure 4.115**. With regions having micro-hardness value in the range of 1.18 GPa to 1.37 GPa observed in Al-Ti-C coating @ 350⁰C for 1 hour (these micro-hardness range were not seen after 3 hours of exposure @ 350⁰C) an overall 5 % decrease in the micro-hardness value in comparison with as sprayed coating was recorded. Precipitation of brittle Ti rich oxide phases which were seen Al-Ti-C coating @ 350⁰C for 1 hour and 3 hours, could have resulted in formation of regions with similar hardness (0.59 GPa to 0.78 GPa), however formation of additional Ti rich brittle phase in Al-Ti-C coating @ 350⁰C for 3 hours, could have resulted in overall increase in the micro-hardness value in comparison with as sprayed Al-Ti-C coating.

The Al-Ti-C coating @ 550⁰C for both 1 hour and 3 hours of exposure showed ≈ 19 % and 21 % reduction in the micro-hardness values respectively in comparison with as sprayed Al-Ti-C coating, see **Figure 4.116**. This reduction in the overall micro-hardness can be explained by the fact that maximum regions of micro-hardness in the range of 0.39 GPa to 0.78 GPa were seen during this exposure temperature and exposure. However regions with micro-hardness value in the range of 0.78 GPa to 0.98 GPa were also seen in the Al-Ti-C coating @ 550⁰C for both 1 hour and 3 hours followed by room temperature cooling, see **Figure 4.115**. Precipitation of Ti rich brittle oxide phases observed in Al-Ti-C coating @ 550⁰C for 1 hour and 3 hours which would have led to the decrease in the overall Ti distribution in the coating could have resulted in the overall decrease in the micro-hardness of the Al-Ti-C coating see **Figure 4.116**.

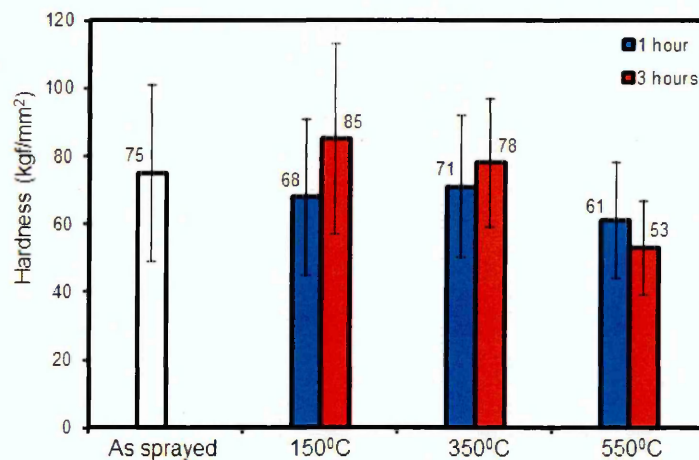


Figure 4.116: Comparison of micro-hardness values obtained for as sprayed Al-Ti-C coating and Al-Ti-C coating exposed to 150⁰C, 350⁰C and 550⁰C for 1 hour and 3 hours followed by room temperature cooling for 5 hours.

4.6.10 Coefficient of wear for Al-Ti-C coating subjected to 150°C, 350°C, 550°C for 1 hour and 3 hours followed by room temperature cooling for 5 hours.

Table 4.37 shows the values of coefficient of wear for Al-Ti-C coating exposed to 150°C, 350°C and 550°C followed by room temperature cooling for 5 hours.

Table 4.37: Coefficient of wear for Al-Ti-C coating exposed to 150°C, 350°C and 550°C for 1 hour and 3 hours followed by room temperature cooling for 5 hours.

Temperature (°C)	Time of exposure (hours)	Coefficient of wear (mm ³ N ⁻¹ m ⁻¹)
@ 150	1	5.79E-04 ± 1.44E-04
	3	4.64E-04 ± 0.04E-04
@ 350	1	6.03E-04 ± 0.4E-04
	3	4.00E-04 ± 0.2E-04
@ 550	1	3.90E-04 ± 0.08E-04
	3	2.75E-04 ± 1.40E-04

The values of coefficient of wear for Al-Ti-C coating at a given exposure temperature and period of exposure were obtained from the gradient of the graphs shown in where wear crater volume (in mm³) obtained during micro-scale abrasion test was plotted against the sliding distance (in m) multiplied with the applied load (in N). A graph comparing the wear coefficient values of as sprayed Al-Ti-C coating with coating exposed to 150°C, 350°C and 550°C for 1 hour and 3 hours followed by room temperature cooling is shown in **Figure 4.125**.

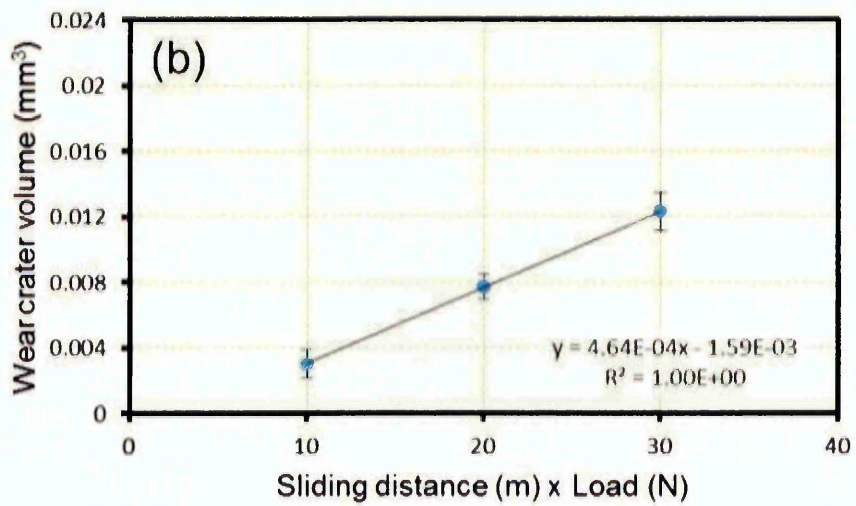
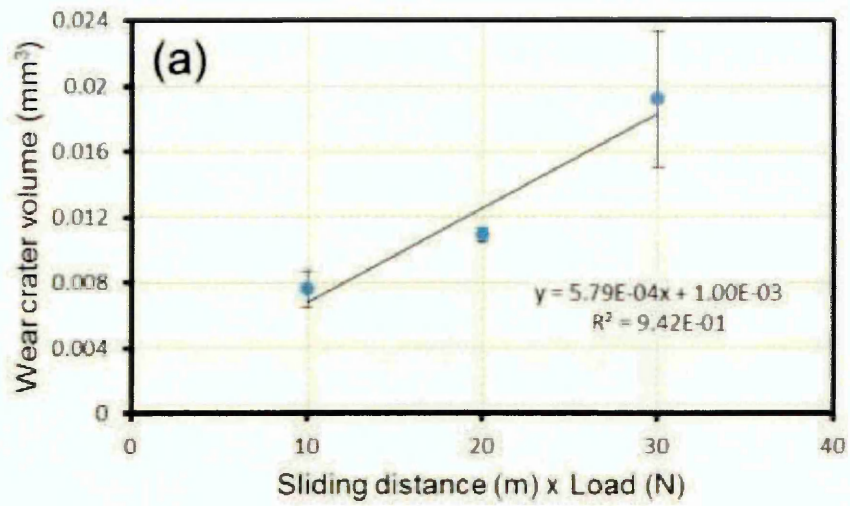


Figure 4.117: Graphs showing wear crater volume vs. sliding distance x load for Al-Ti-C coating subjected to 150°C for (a) 1 hour and (b) 3 hours followed by room temperature cooling for 5 hours.

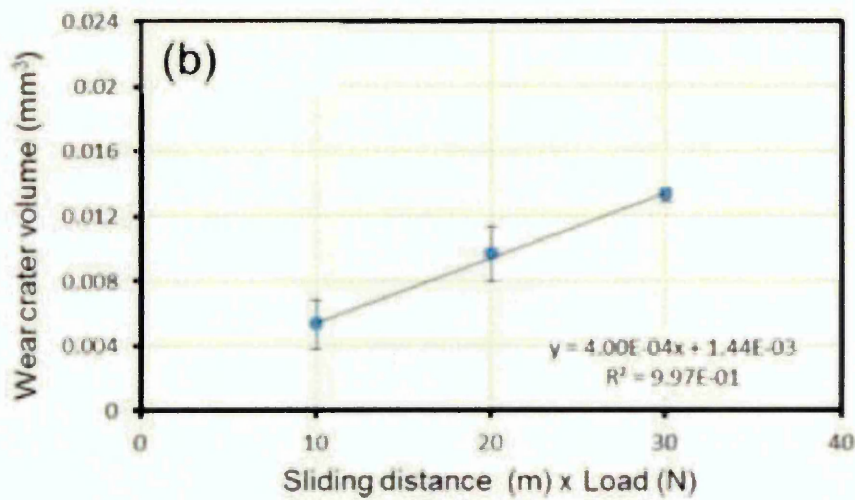
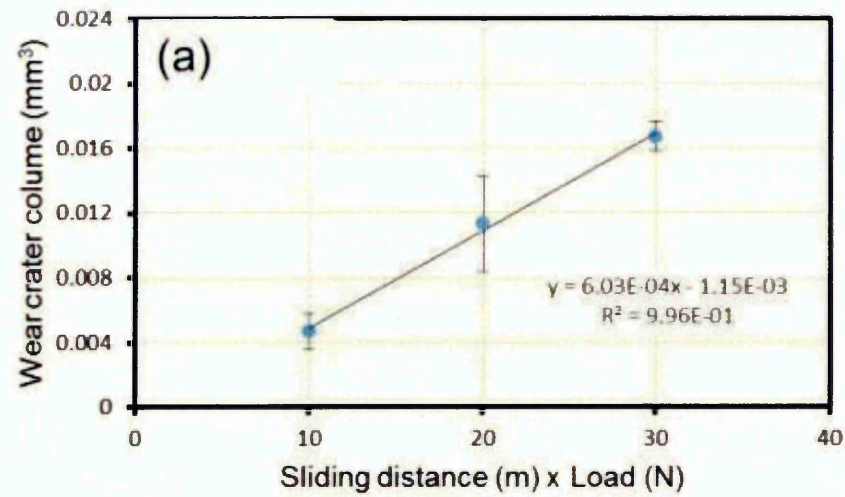


Figure 4.118: Graphs showing wear crater volume vs. sliding distance x load for Al-Ti-C coating subjected to 350⁰C for (a) 1 hour and (b) 3 hours followed by room temperature cooling for 5 hours.

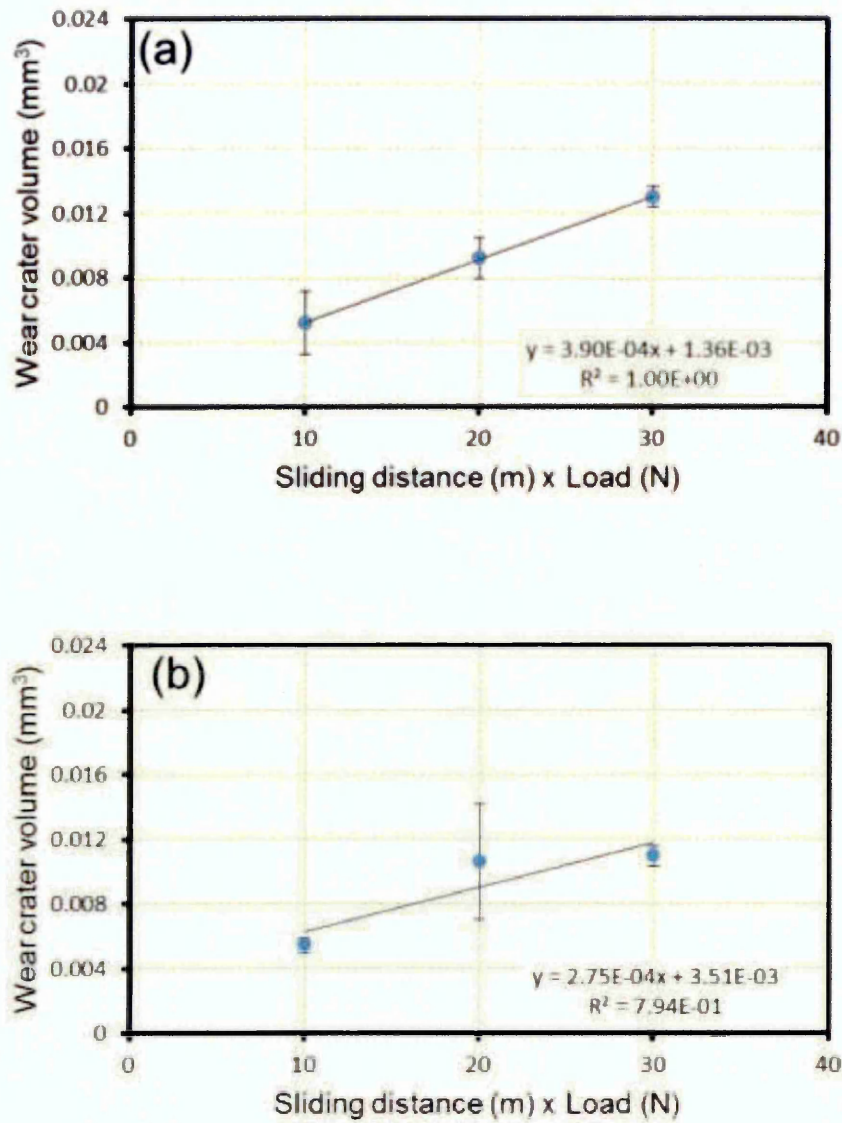


Figure 4.119: Graphs showing wear crater volume vs. sliding distance x load for Al-Ti-C coating subjected to 550⁰C for (a) 1 hour and (b) 3 hours followed by room temperature cooling for 5 hours.

A significant increment of $\approx 80\%$ and 44% in the values of the wear coefficient for Al-Ti-C coating subjected to 150⁰C for 1 hour and 3 hours followed by room temperature cooling (for 5 hours) in comparison with as sprayed Al-Ti-C coating was recorded, implying lowering of wear resistance

performance of Al-Ti-C coating @ 150⁰C followed by room temperature cooling (for both 1 hour and 3 hours). **Figure 4.120** (a), (b), (c) and **Figure 4.121** (a), (b), (c) shows the wear track morphology (notice the directionality of the wear track) of Al-Ti-C coating @ 150⁰C for 1 hour and 3 hours followed by room temperature cooling for 5 hours.

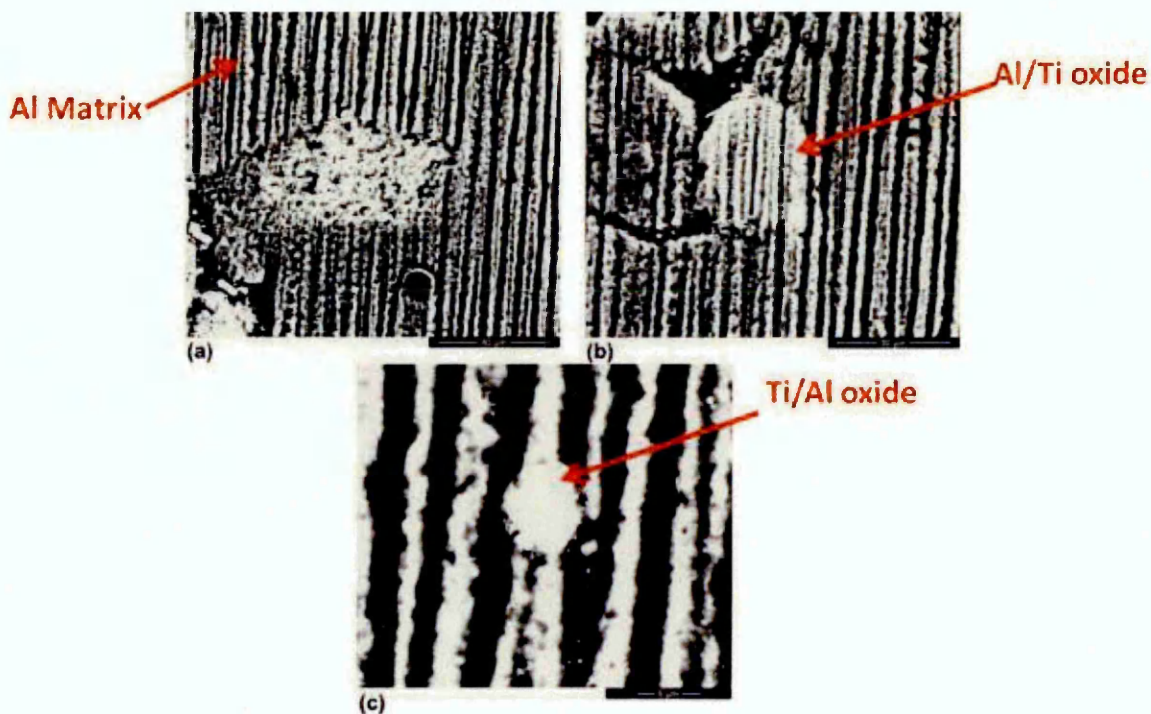


Figure 4.120: Backscattered electron micrograph showing directionality of the wear tracks and precipitation of Al and Ti containing oxide phases in Al-Ti-C coating @150⁰C for 1 hour followed by room temperature cooling for 5 hours (a), (b) and (c) are backscattered electron micrographs at different magnifications.

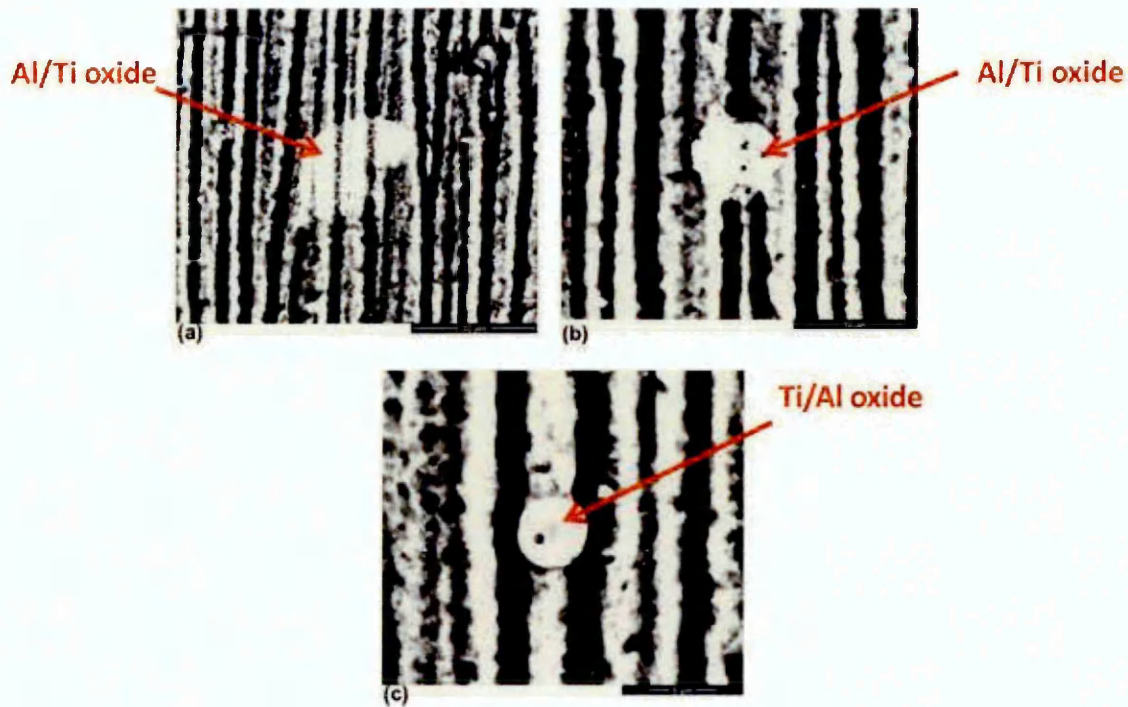


Figure 4.121: Backscattered electron micrograph showing directionality of the wear tracks and precipitation of Al and Ti containing phases in Al-Ti-C coating @150⁰C for 3 hour followed by room temperature cooling for 5 hours (a), (b) and (c) are backscattered electron micrographs at different magnifications.

A \approx 20% reduction in the value of wear coefficient was recorded for Al-Ti-C coating @ 150⁰C for 3 hours than the value obtained after 1 hour at same exposure temperature followed by room temperature cooling, see **Figure 4.126**. Even though Ti rich oxide phases which were identified in Al-Ti-C coating @ 150⁰C for both 1 hour and 3 hours, could have resisted the abrasion caused by SiO₂ particles during the micro-scale abrasive wear test,

the graph in **Figure 4.117 (a)** showed that the volume of the wear crater formed at each sliding distance after 1 hour @ 150⁰C was higher than the volume of the wear crater obtained after 3 hours of exposure at same sliding distances, see **Figure 4.117 (b)** under constant load of 0.2 N.

This can be attributed to the 25 % increase in the micro-hardness value which was reported for Al-Ti-C coating @ 150⁰ for 3 hours in comparison with the value obtained after 1 hour of exposure. It is important to note that a higher volume loss in Al-Ti-C coating @ 150⁰ C for 1 hour during abrasive wear test could have also been due to loss of coating itself during abrasion testing, which can be seen from **Figure 4.120 (a)**.

An increase of ≈ 87 % and 24% in the value of wear coefficient for Al-Ti-C coating @ 350⁰C for 1 hour and 3 hours respectively (followed by room temperature cooling) in comparison with as sprayed Al-Ti-C coating was observed. **Figure 4.122 (a), (b), (c)** and **Figure 4.123 (a), (b), (c)** shows the morphology and effect of identified phases on the wear tracks obtained for Al-Ti-C coating @ 350⁰C for both 1 hour and 3 hours during micro-scale abrasive test. A reduction of ≈ 34 % in the value of the wear coefficient of Al-Ti-C coating @ 350⁰C for 3 hours in comparison to 1 hour of exposure was also observed, see **Figure 4.126**.

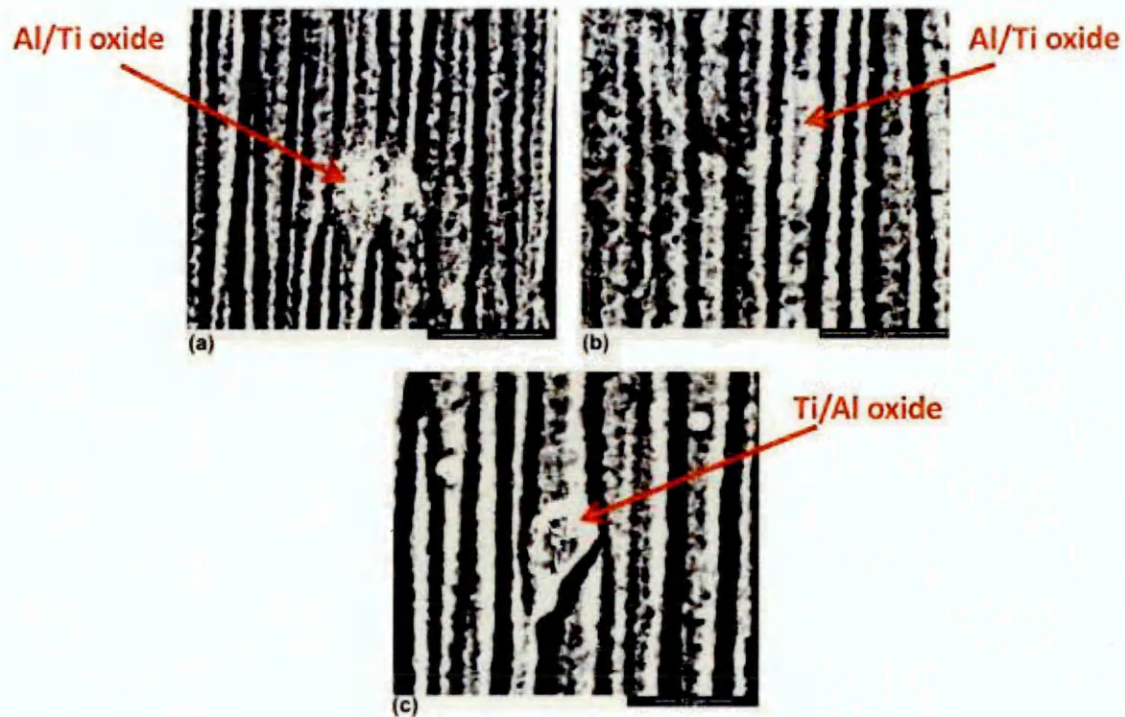


Figure 4.122: Backscattered electron micrograph showing directionality of the wear tracks and precipitation of various phases in Al-Ti-C coating @350⁰C for 1 hour followed by room temperature cooling for 5 hours (a), (b) and (c) are backscattered electron micrographs at different magnifications.

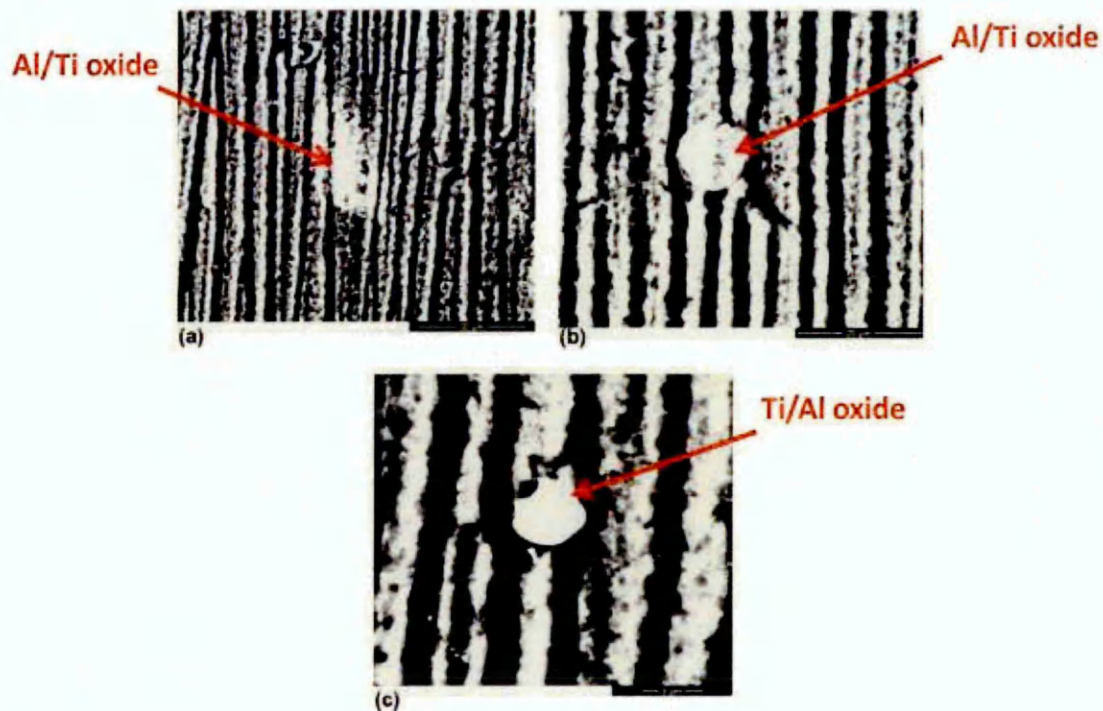


Figure 4.123: Backscattered electron micrograph showing directionality of the wear tracks and precipitation of various phases in Al-Ti-C coating @350⁰C for 3 hours followed by room temperature cooling for 5 hours (a), (b) and (c) are backscattered electron micrographs at different magnifications.

As seen from **Figure 4.122** (a) and (b), no evidence of resistance against abrading SiO₂ particles was observed except for the Ti rich brittle spherical oxide phase which was observed in Al-Ti-C coating @ 350⁰C for 1 hour, appeared to be resisting the ploughing action by the abrasive SiO₂ particles.

Precipitation of another Ti rich brittle oxide phase (apart from spherical equiaxed phase) which was seen in Al-Ti-C coating after 350⁰C for 3 hours, could have been responsible for providing lower volume of the wear craters formed at each sliding distance in Al-Ti-C coating @ 350⁰C for 3 hours in

comparison with 1 hour of exposure, see **Figure 4.118** (a), (b), at constant load of 0.2 N (note that the wear crater formed after 50 m sliding distance for Al-Ti-C coating after 3 hours @ 350⁰C showed a higher volume value than wear crater volume after 1 hour at 50 m sliding distance). The evidence of Ti rich brittle phase aiding wear can also be seen from **Figure 4.123** (b), (c).

With an increase in the exposure temperature to 550⁰C, ≈ 21% increase in the wear coefficient value in Al-Ti-C coating after 1 hour of exposure (followed by room temperature cooling) was observed in comparison to as sprayed coating, see **Figure 4.126**. However after 3 hours of exposure at 550⁰C, the value of wear coefficient was found to be ≈ 15 % less than that of as sprayed coating. **Figure 4.124** (a), (b), (c) and **Figure 4.125** (a), (b), (c) shows the morphology and effect of identified phases on the wear tracks obtained for Al-Ti-C coating @ 350⁰C for both 1 hour and 3 hours during micro-scale abrasive test. A reduction of ≈ 30 % in the value of the wear coefficient after 3 hours of exposure in comparison to 1 hour of exposure of Al-Ti-C coating @ 550⁰C was also deduced. It is important to note that the wear coefficient obtained for Al-Ti-C coating subjected to 550⁰C for both 1 hour and 3 hours (followed by room temperature cooling) showed minimum difference in comparison with as sprayed Al-Ti-C coating (15% reduction in wear coefficient value for Al-Ti-C coating @ 550⁰C for 3 hours), that the previous exposure temperatures, see **Figure 4.126**.

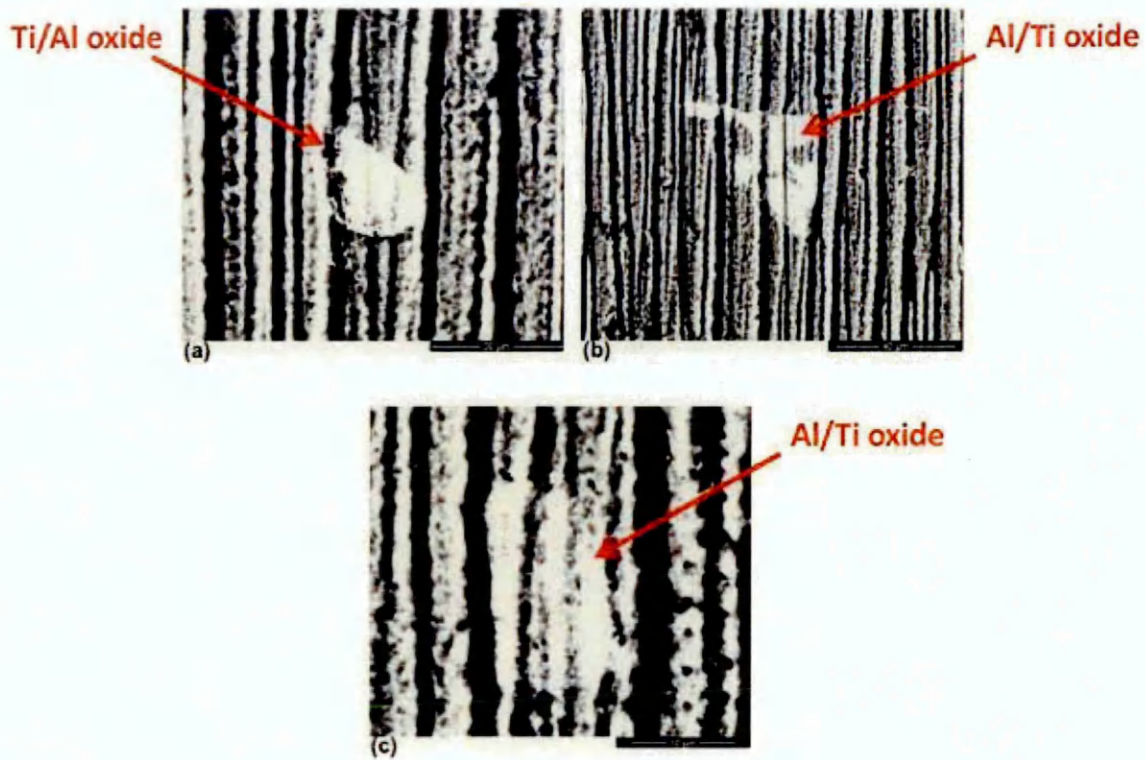


Figure 4.124: Backscattered electron micrograph showing directionality of the wear tracks and precipitation of various phases in Al-Ti-C coating @550⁰C for 1 hour followed by room temperature cooling for 5 hours (a), (b) and (c) are backscattered electron micrographs at different magnifications.

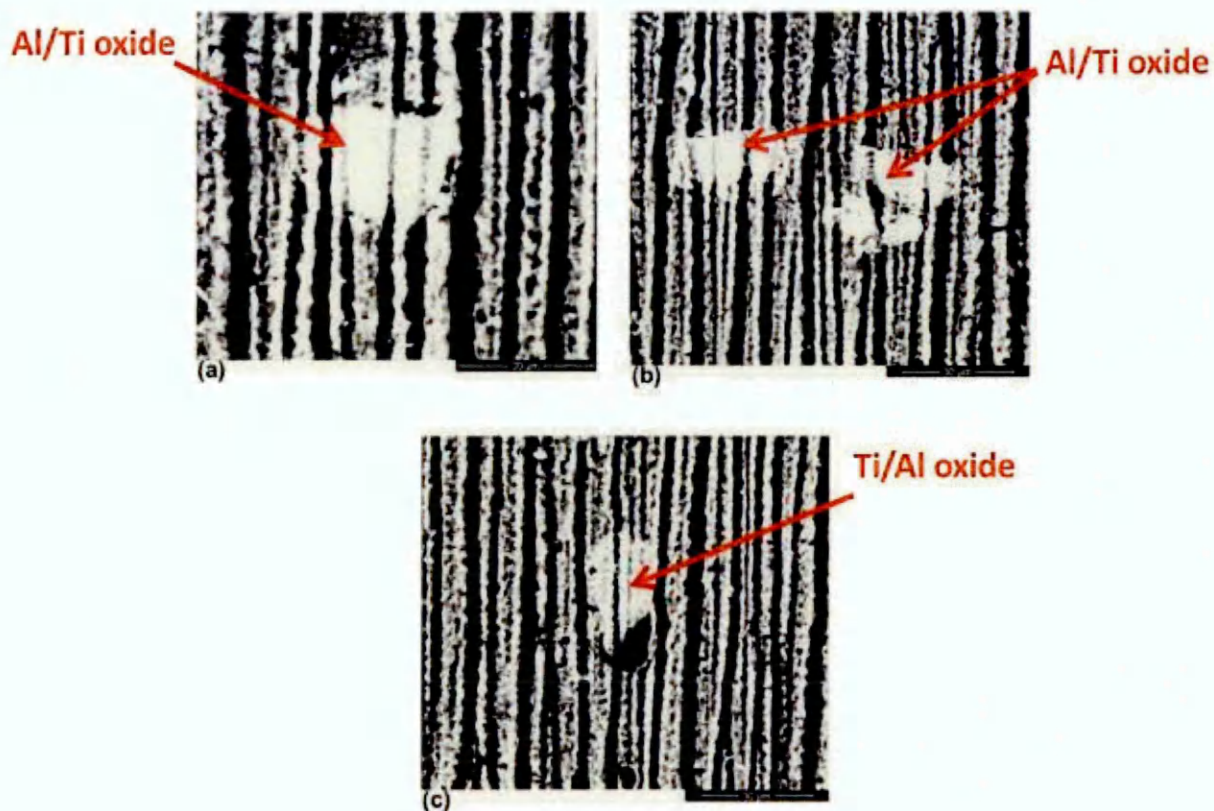


Figure 4.125: Backscattered electron micrograph showing directionality of the wear tracks and precipitation of various phases in Al-Ti-C coating @550⁰C for 3 hours followed by room temperature cooling for 5 hours (a), (b) and (c) are backscattered electron micrographs at different magnifications.

Despite the fact that Ti rich brittle oxide phases, which were identified in Al-Ti-C coating @ 550⁰C for both 1 hour and 3 hours of exposure, the least values of the micro-hardness, 0.60 GPa and 0.52 GPa were obtained after 1 hour and 3 hours of exposure respectively.

The wear track micrographs shown in **Figure 4.124** and **Figure 4.125** (a, b and c) illustrates that presence of Ti rich brittle oxide phase appear to hinder the indentation caused by SiO_2 particles during micro-scale abrasive wear test in Al-Ti-C coating @ 550°C equally for both 1 hour and 3 hours of exposure. However the graphs shown in **Figure 4.119** (a) and (b) indicated that the volume of the wear crater formed in Al-Ti-C coating @ 550°C after 50 m and 150 m of sliding distance (during micro-scale abrasive wear test) had similar values for both 1 hour and 3 hours.

With the increase in the sliding distance to 200 m during wear test, the volume of the wear crater formed in Al-Ti-C coating @ 550° for 1 hour was found to be $\approx 23\%$ higher than the value observed in Al-Ti-C coating after 3 hours of exposure (note that after 150 m and 200 m the wear crater volume in Al-Ti-C coating @ 550°C for 3 hours had almost similar values, see **Figure 4.119** (b) resulting in lowering of the coefficient of wear value of Al-Ti-C coating after 3 hours of exposure @ 550°C in comparison to 1 hour of exposure.

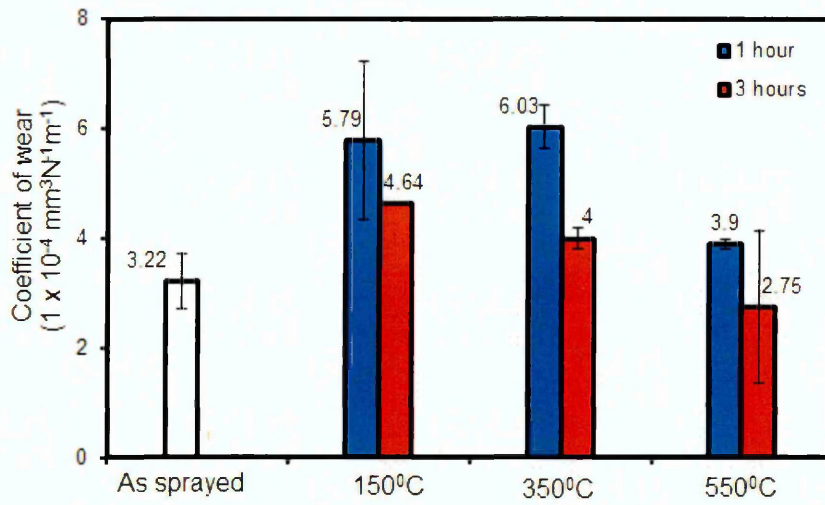


Figure 4.126: Comparison of wear coefficient values obtained for as sprayed Al-Ti-C coating and Al-Ti-C coating exposed to 150⁰C, 350⁰C and 550⁰C for 1 hour and 3 hours followed by room temperature cooling for 5 hours.

Chapter 5: Conclusion

The two main objectives of this research were:

- To investigate the sacrificial corrosion protection ability of newly developed arc sprayed Al-Zn-In coating deposited on mild steel substrates. Using accelerated and electrochemical corrosion tests, establish an understanding of the key properties of Zn and In that plays the major role in activation of arc sprayed Al-Zn-In coating.
- To investigate the wear resistance performance of arc sprayed Al-Ti-C coating deposited on mild steel substrate by three body micro-scale abrasive wear test and establish the role of identified tri aluminide Al_3Ti and carbide $(Al,Ti)C$ particles in increasing the wear resistance performance of the coating.

The critical assessment of the arc sprayed Al-Zn-In and Al-Ti-C was achieved by these objectives

Arc Sprayed Al-Zn-In coating

The salt spray corrosion test conducted on Al, Zn-Al and Al-Zn-In coating indicated that when the coatings were exposed to 5%w/v NaCl, the Al-Zn-In coating showed evidence of superior sacrificial corrosion protection than Al coating. The Zn-Al coating was less effective in sacrificially protecting mild steel substrate and showed greater overall corrosion in comparison to Al and Al-Zn-In coating.

The Backscattered SEM micrograph of Al coating after 1000 hours showed evidence of delamination, whereas Al-Zn-In showed less evidence of oxide formation than Al coating. The cross section analysis of Zn-Al coating after 1000 hours showed formation of cracks which indicated cohesive failure of the coating.

The X-ray diffraction analysis of the corrosion products after 500 and 1000 hours indicated the formation of Bayerite ($\text{Al}(\text{OH})_3$) and Dawsonite ($\text{NaAl}(\text{CO}_3)(\text{OH})_2$) as dominant phases present in the corrosion product obtained from the Al and Al-Zn-In coatings. Although the composition of the Al and Al-Zn-In coatings was different, similar corrosion phases were identified in the corrosion product. Zinc aluminium carbonate hydroxide hydrate ($\text{Zn}_{0.61}\text{Al}_{0.39}(\text{OH})_2(\text{CO}_3)_{0.195}\cdot x\text{H}_2\text{O}$) was identified as a dominant phase present in corrosion product of Zn-Al coating after 500 and 1000 hours of corrosion testing.

In an attempt to understand the effects of long term exposure tests on Al, Al-Zn, Al-Zn-In and Al-Ti-C feedstock alloys and coatings, the weight change for both feedstock materials and coatings after specified exposure period in the neutral salt spray test was recorded.

Over a period of 840 hours in the neutral salt spray test, the pure Al and Al-Zn feedstock material showed almost linear increase in the weight change per unit area, except for Al-Zn-In and Al-Ti-C. This behaviour of weight change per unit area for Al-Zn-In feedstock material was attributed to either large variation of weight change within the triplicate samples or by removal of loose corrosion product. However for the Al, Al-Zn, Al-Zn-In and Al-Ti-C coatings, non-linear (polynomial function with degree>3) increase in the weight change per unit area with time was observed.

The weight change per unit area revealed that Al-Zn and Al-Zn-In in form of feedstock material were uniformly corroding in comparison to pure Al feedstock material. These results supported the fact that Al-Zn alloy and Al-Zn-In alloy, containing Zn from 3.5wt% to 5wt% and In up to maximum of 0.05wt% were effective in making the surface of the Al alloy corrode uniformly when exposed to ASTM D1141 artificial sea water, which was established in the earlier researches [227].

However, Bessone *et al.* [227] stated that the anode performance of Al alloyed with either Zn or In remains unaltered with adherence of corrosion product, is in contradiction with the present weight change per unit area obtained for Al-Zn-In feedstock material.

Similar observations were made for Al-Zn and Al-Zn-In coatings in comparison with Al coatings, which showed that even after 840 hours of exposure in the neutral salt spray test, the Al-Zn and Al-Zn-In coatings were actively showing increase in weigh per unit area, while Al coating showed formation of a plateau, indicating that Al-Zn and Al-Zn-In coating were actively corroding in the 5%w/v NaCl fog environment. These finding were also in accordance with previous researches conducted on arc and flame sprayed Al-Zn and Al-Zn-In coatings in marine environment [220,227], which showed

- That even after 2 to 15 years of exposure, Al-Zn and Al-Zn-In coatings showed superior corrosion protection than Al coatings, which were sprayed on to steel reinforced concrete structures and exposed to both dry and wet marine environment at La Guardia airport, north New York, USA.

Complementing the findings of salt spray corrosion test, were the results obtained from electrochemical tests conducted on arc sprayed Al-Zn-In and Al-Ti-C coatings at various NaCl concentrations.

The fluctuations in the OCP of Al-Zn-In coating at various chloride concentrations was attributed to the synergetic interaction of Zn and In in cyclic formation and rupturing of passive Al oxide layer. It was shown in the earlier researches that the effectiveness of activation of Al by Zn and In increases in the presence of halide ions in the order $F > Cl > Br > I$ and higher concentrations of Cl^- ions favours the activation. The OCP measurements showed that even at lower concentration of NaCl (0.01%w/v) the synergetic interaction of Zn and In was effectively able to maintain the OCP of Al-Zn-In coating electronegative.

The OCP results were also complemented by the CCP measurements, which showed that for coupling of coatings with mild steel substrate at 3.5%, 1.0%, 0.1% and 0.01%w/v NaCl solution, the active CCP values were found to follow the order Al-Zn-In > Al-Zn > Al > Al-Ti-C. An empirical relationship between corrosion current per unit area values and area of cathode to anode was also established, which was found to vary with varying NaCl concentration.

The EIS results indicated formation of capacitive time constants for Al-Zn coating, while Al-Zn-In coating showed formation of inductive time constants at lower frequencies (<10kHz). This was reported for all NaCl concentrations used during experiment. The capacitive time constant observed for Al-Zn coating was attributed to the formation of $ZnAl_2O_4$ spinel causing the Al oxide layer to create vacancies of cations, while the inductive loop observed for Al-Zn-In coating suggested adsorption of Cl^- ions due to formation of a In chloro complex due to anionic vacancy. This Cl^- ions adsorption was suggested to be the cause of rupturing of passive Al oxide layer.

Arc Sprayed Al-Ti-C coating

The work conducted on Al-Ti-C coating showed that:

- The Al-Ti-C feedstock alloy produced using slow cooling showed the presence of evenly distributed intermetallic tetragonal Al_3Ti and carbide (Ti,Al)C phases which, because of their inherent higher hardness results in a 33% higher micro-hardness of Al-Ti-C feedstock alloy in comparison with pure Al feedstock.
- The 18% lower coefficient of wear of the Al-Ti-C feedstock compared to that of the pure Al feedstock can also be explained by the presence of the hard intermetallic tetragonal Al_3Ti tri-aluminide and (Ti,Al)C phases present in the structure.

- The microstructure of the arc sprayed Al-Ti-C coating did not contain Al_3Ti and $(\text{Ti,Al})\text{C}$ particles but did show regions of varying atomic number contrast suggesting the formation of the metastable cubic phase of Al_3Ti (confirmed by XRD analysis) formed from the rapid cooling that takes place in arc spraying . The resulting precipitation strengthening may explain the 114% increase in the hardness of the sprayed Al-Ti-C coating compared to its feedstock alloy and also the regions with a high hardness up to $\text{HV}_{0.98} = 1.18 \text{ GPa}$ (120kgf/mm^2).
- The arc sprayed Al-Ti-C coating showed a 33% lower coefficient of wear than the pure Al coating which was attributed to precipitation strengthening resulting in an overall higher micro-hardness and the presence of regions of high micro-hardness ($\text{HV}_{0.98} > 1.18 \text{ GPa}$) in the Al-Ti-C coating.
- In the micro-scale abrasive wear test using 2.5 mm SiO_2 abrasive in deionised water, the wear coefficient of an arc sprayed Al-Ti-C coating was found to be very close to that of an arc sprayed 13wt%Cr steel coating with a much higher hardness.
- The study of the microstructure of Al-Ti-C coating, subjected to both heat treatment cycles, by SEM revealed precipitation of sub-micron sized speckled region which showed a relative growth (still sub-micron) with increase in exposure temperature from 150°C to 350°C and 550°C (followed by rapid cooling and room temperature cooling).

- The other varying atomic number contrast regions were also identified along with speckled regions. The average compositional analysis using EDX showed a high Ti concentration (at%) in the high atomic number contrast phases which suggested precipitation of cubic Al_3Ti phase. This was confirmed by the XRD analysis of the heat treated coating, however @ 550°C the Al_3Ti phase was found to be tetragonal as observed in the Al-Ti-C feedstock alloy.
- Precipitation of brittle phases having near spherical and rectangular morphology were also seen in Al-Ti-C coating subjected to both heat treatment regimens. The EDX analysis of brittle phases in both heat treatment regimens showed higher Ti (at%) concentration than other high atomic number contrast regions.
- The XRD of the rapidly quenched heat treated Al-Ti-C coating at 150°C and 350°C showed presence of intermediate Ti_8C_5 carbide, while the presence of this carbide was not detected at 550°C . The formation of carbide phase was not detected by XRD in the room temperature cooled Al-Ti-C coating instead presence of Al and Ti oxides were observed.

- The variation in micro-hardness values of Al-Ti-C coating which was subjected to rapidly quenched heat treatment cycle was attributed to the precipitation of Ti to form Ti rich phases in the coatings lowering the heterogeneous distribution of Ti in the coating causing lowering of wear resistance performance of the coating.
- A similar effect of Ti precipitation on the micro-hardness variation was also seen in the room temperature cooled Al-Ti-C coating heat treatment. However higher values of coefficient of wear were recorded for Al-Ti-C coating subjected to 150⁰C, 350⁰C followed by room temperature cooling, but a 15% reduction in the coefficient of wear value (in comparison with as sprayed coating) after 3 hours of exposure at 550⁰C (room temperature cooled) suggested evidence of higher degree of resistance against abrasive particles provided by Ti rich phases.

Recommendation for future Work

The results presented in the thesis have shown the effectiveness of the use of arc sprayed Al-Zn-In and Al-Ti-C coating on the basis of corrosion and wear resistance performance. However, the investigations can be furthered in the following ways:

- The enhanced sacrificial properties of arc sprayed Al-Zn-In coating was shown to be governed by the presence of In in the alloy. The results obtained from both accelerated and electrochemical tests were complemented by the literature [108-131]. However, the surface enrichment theory which was discussed in chapter 2 was not validated for arc sprayed Al-Zn-In coating. By incorporating Secondary Ion Mass Spectroscopy (SIMS) analysis for as sprayed Al-Zn-In coating before and after exposure in the chloride media could provide satisfactory results for the validation of the theory.
- The use of localised electrochemical technique such as Scanning Vibrating Electrode Technique (SVET) could also be involved in better understanding of the sacrificial performance of the Al-Zn-In coating at the coating substrate interface.
- Transmission Electron Microscopy (TEM) could also be used to support the evidence that Al_3Ti and $(\text{Al},\text{Ti})\text{C}$ phases imparted superior wear resistance characteristic of arc sprayed Al-Ti-C coating

There is clearly much work to be done on arc sprayed Al-Zn-In and Al-Ti-C coatings, the most direct of which has been mentioned above, will provide sufficient knowledge to cover some obscurities in understanding the behaviour of the coatings.

References

- [1] L. Pawlowski, The science and engineering of thermal spray coatings, John Wiley and Sons, England, 1995.
- [2] A. Goldschmidt, J.H. Streitberger, Basics of coating technology, Primedia, Germany, 2003.
- [3] D.R. Gabe, Principles of metal surface treatment and protection, 1st edition, A. Wheaton and Co., England, 1972.
- [4] V. Carter, Metallic coatings for corrosion control, Newnes - Butterworths, England, 1977.
- [5] J.F. Stanner, Control of corrosion in common environment, Elsevier Publishing, United States of America, 1965.
- [6] D.S. Rickerby, A. Matthews, Advanced surface coatings: A handbook of surface engineering, 1st edition, Blackie and sons., United States of America, 1991.
- [7] J.C. Scully, The fundamentals of corrosion, 3rd edition, Pergamon press, England, 1990.
- [8] W.E. Ballard, Metal spraying and the flame deposition of ceramics and plastics, 4th edition, Charles Griffin and company Ltd., England, 1963.
- [9] United States Patent, Apparatus for spraying molten metal and other fusible substances, 1,133,507, Patented: Mar. 30, 1915.
- [10] C.C. Berndt, G. Montanov, Thermal spray: Preserving 100 years of technology, Journal of thermal spray technology, 2006, 15(1), 5-8.
- [11] The birth place of Metallisation, Available at <<http://www.metallisation.com/news/the-birth-of-metallisation.html>>, accessed: Feb 2014.
- [12] Cathodic protection of steel in concrete, Available at <<http://www.metallisation.com/applications/cathodic-protection-of-steel-in-concrete.html>>, accessed: Feb 2014.
- [13] Thermal Spray wear coatings finds growing market and greater competition, SPRATIME, Published by The International Thermal Spray Association, 2013, 20(1).

- [14] Annual energy outlook, U.S. Energy Information Association (EIA), Office of Integrated and International Energy Analysis, U.S Department of Energy, DOE/EIA, 2012.
- [15] The outlook for energy: A view to 2040, Exxon Mobil Corporation publication, 2012.
- [16] Overview of the global thermal spray market and trends in Europe, Linde AG, GTS Association of Thermal Sprayers, 2013.
- [17] M. Fukomoto, The current status of thermal spraying in Asia, Journal of thermal spray technology, 2008, 17(1), 5-13.
- [18] S. Sampath, Thermal spray applications in electronics and sensors: Past present and future, Journal of thermal spray technology, 2010, 921-949.
- [19] P. Fauchais, A. Vardelle and B. Dussoubs. *Quo vadis thermal spraying?*. Journal of Thermal spray technology 1999;10(1):44-66.
- [20] Y. Z. Jian, , W. S. Bao, F. Wei, T. X. Hai, T. S. Yan, D. C. Xian. Evolution and Prospect of Thermal Spraying Technique. 2011;26(3):225-232.
- [21] S. Grainger, J. Blunt, Engineering Coatings - Design and application, Woodhead Publishing Ltd; England, 1989.
- [22] T. Watanabe, X. Wang, E. Pfender, J. Heberlein, Correlations between electrode phenomena and coating properties in wire arc spraying, Thin Solid Films 316 (1–2) (1998) 169–173 3/21.
- [23] I. Gedzevicius, A.V. Valiulis, Analysis of wire arc spraying process variables on coatings properties, Journal of Materials Processing Technology 175 (1–3) (2006) 206–211.
- [24] A.P. Newbery, P.S. Grant, R.A. Neiser, The velocity and temperature of steel droplets during electric arc spraying, Surface and Coatings Technology 195 (1) (2005) 91–101 5/23.
- [25] X. Wang, J. Heberlein, E. Pfender, W. Gerberich, Effect of nozzle configuration, gas pressure, and gas type on coating properties in wire arc spray, Journal of Thermal Spray Technology 8 (4) (1999) 565–575.
- [26] E.R. Sampson, M.P. Zwetsloot, Arc spray process for the aircraft and stationary gas turbine industry, Journal of Thermal Spray Technology, 1997, 6(2), 150-152.

- [27]. M. Kelkar, N. Hussary, J. Schein, and J.V. Heberlein: in Thermal Spray: Meeting the Challenges of the 21st Century C. Coddet, ed., ASM International, Materials Park, OH, 1998, 329-334.
- [28]. T. Watanabe, X. Wang, J.V. Heberlein, E. Pfender, and W. Herwig: in Thermal Spray: Industrial Applications, C.C. Berndt and S. Sampath, eds., ASM International, Materials Park, OH, 1996, 577-583.
- [29]. R.H. Hunger, V.E. Belashchenko, W.R. Kratochvil, J.P. Dunkerley, V. Sedov, and E.A. Smith: in Thermal Spray: Meeting the Challenges of the 21st Century, C. Coddet, ed., ASM International, Materials Park, OH, 1998, 1489-1493.
- [30]. J. Sheard, J.V. Heberlein, K. Stelson, and E. Pfender: in Thermal Spray: A United Forum for Scientific and Technological Advances, C.C. Berndt, ed., ASM International, Materials Park, OH, 1997, 613-618.
- [31]. V.F. Hock, R. Benary, R. Ganertz, and H. Herman: in Thermal Spray: A United Forum for Scientific and Technological Advances, C.C. Berndt, ed., ASM International, Materials Park, OH, 1997, 435-444.
- [32]. T. Lester, D.J. Kinglerley, S.J. Harris, and S P. Matthews: in Thermal Spray: Meeting the Challenges of the 21st Century, C. Coddet, ed., ASM International, Materials Park, OH, 1998, 49-55.
- [33]. B. Xu, X. Liu, S. Ma, and Z. Chen: in Thermal Spray: Meeting the Challenges of the 21st Century, C. Coddet, ed., ASM International, Materials Park, OH, 1998, 1039-1042.
- [34]. H. Llewellyn, P.S. Grant, A P. Newbery, and RM. Jordan: in Thermal Spray: Meeting the Challenges of the 21st Century, C. Coddet, ed., ASM International, Materials Park, OH, 1998, 263-268.
- [35]. H.D. Steffens, J. Wilden, and T. Duda: High Temp. Chem. Processes, 1994, 3, 653-664.
- [36]. E.R. Sampson: in Thermal Spray: Meeting the Challenges of the 21st Century C. Coddet, ed., ASM International, Materials Park, OH, 1998, 133-137.
- [37] S.Seth, A.H. Jones, O.D. Lewis, Wear resistance performance of thermally sprayed Al - Ti alloy measured by three body micro-scale abrasive wear test, Wear, 2013, 302, 972-980.
- [38] R.S.C. Paredes, S.C. Amico, A.S.C.M D'Oliveira, The effect of roughness and pre-heating of the substrate on the morphology of aluminium coatings deposited by thermal spraying. Surface and Coatings Technology 2006, 200(9), 3049-3055.

- [39] V.V. Sobolev , J.M. Guilemany, Oxidation of coatings in thermal spraying. *Mater Lett* 1998 11;37, 231-235.
- [40] C. J. Li, A. Ohmori, Relationships between the microstructure and properties of thermally sprayed deposits, *Journal of Thermal Spray Technology*, 2002, 11(3), 365–374.
- [41] S. Deshpande, S. Sampath, H. Zhang, Mechanisms of oxidation and its role in microstructural evolution of metallic thermal spray coatings—Case study for Ni–Al, *Surface and Coatings Technology*, 2006, 200, 5395-5406.
- [42] R. Dhiman , A.G. McDonald , S. Chandra, Predicting splat morphology in a thermal spray process. *Surface and Coatings Technology* 2007;201(18), 7789-7801.
- [43] G. Antou, G. Montavon, F. Hlawka, A. Cornet, C. Coddet, Characterisations of pore-crack network architecture of thermal-sprayed coatings, *Materials Characterisation*, 2004, 53, 361-372.
- [44] R. Wang, D. Song, W. Liu, X. He, Effect of arc spraying power on the microstructure and mechanical properties of Zn-Al coating deposited onto carbon fiber reinforced epoxy composites, *Applied surface science*, 2010, 257, 203-209.
- [45] S. Deshpande, A. Kulkarni, S. Sampath, H. Herman, Application of image analysis for characterisation of porosity in thermal spray coatings and correlation with small angle neutron scattering, *Surface and Coatings Technology*, 2004, 187, 6-16.
- [46] D.A. Jones, *Principles and Prevention of corrosion*, Prentice-Hall Publication; USA, 1996.
- [47] N.M. Farmilo, *The corrosion resistance of sprayed aluminium coatings*, 1990.
- [48] S. Kuroda, J. Kawakita, M. Takemoto, Marine exposure tests of thermal sprayed coatings in Japan, *Thermal spray 2003: Advancing the science and applying the technology*, ASM International, Materials Park, USA, 2003, 343-352.
- [49] A. Gulec, O. Cevher, F. Ustel, A. Turk, A. Akinci, F. Yilmaz, Performance comparison of thermal-sprayed coatings for ductile iron pipe, *Materials Performance*, NACE International, 2011, 50(2), 30-36.

- [50] D.J. Varacalle Jr., D.P. Zeek, V. Zanchuck, E. Sampson, K.W. Couch, D. Benson, G.S. Cox, Experimental studies of twin wire arc sprayed zinc/aluminium alloy coatings, *Journal of Thermal Spray Technology*, 1998, 7(4), 513-520.
- [51] K.R. Tretheway, J. Chamberlain, *Corrosion for students of science and engineering*, Longman Scientific & Technical, 1988, 303.
- [52] P.R. Roberge, *Corrosion engineering principles and practice*, McGraw Hill, 2008, 175-176.
- [53] M.G. Fontana, *Corrosion engineering*, Third edition, B & JO enterprise Pte Ltd, Singapore, 1986, 46.
- [54] U.R. Evans, *An Introduction to Metallic Corrosion*, third edition, Edward Arnold Publishers, 57.
- [55] J.R. Davis, *Corrosion: Understanding the basics*, ASM International, 2000, 106, 408-412.
- [56] J.A. Von Fraunhofer and A.T. Lubinski, Polarity Reversal in the Zinc-Mild steel Couple, *Corrosion Science*, 1974, 14, 225-232.
- [57] E.G. Haney, The Zinc-Steel Potential Reversal in Cathodic Protection, *Materials Performance*, 1982, Vol. 21(4), 42-51.
- [58] V. Ashworth and D. Fairhurst, The effect of Temperature on the Behaviour of a Zinc-Mild Steel Couple in a Solution Containing Chloride Ions, *Corrosion Science*, 1975, 15, 669-686.
- [59] A. Groysman, *Corrosion for everybody*, Springer publication, 2010, 231-264.
- [60] L.L. Sheir, *Corrosion Volume 2*, Butterworth-Heinemann Ltd, 1994, Third Edition, 10:29-10:55.
- [61] W.V. Baeckmann, W. Schwenk, *Handbook of Cathodic Protection: The theory and practice of electrochemical corrosion protection techniques*, Portcullis press Ltd., 1975, 11.

- [62] C.Gabelle, F. Baraud, L. Biree, S. Gouali, H. Hamdoun, C. Rousseau, E. Van Veen, L.Leleyter, The Impact of Aluminium Sacrificial Anodes on Marine Environment: A Case Study, Applied Geochemistry, 2012, 27, 2088-2095.
- [63] D.A. Shifler, Understanding Material Interactions in Marine Environments to Promote Extended Structural Life, Corrosion Science, 2005, 27, 2335-2352.
- [64] P. A. Schweitzer, Corrosion of linings and coatings, CRC press, second edition, 2007, 44.
- [65] H.Z. Wang, D.Y.C. Leung, M.K.H. Leung, M.Ni, A Review on hydrogen Production Using Aluminium and Aluminium Alloys, Renewable and Sustainable Energy Reviews, 2009,13, 845-853.
- [66] E.A. Brandes and G.B. Brook, Smithells Light Metals Handbook, Butterworth-Heinmann Ltd, 1998,5.
- [67] M.Schumacher, Seawater Corrosion Handbook, Noyes Data Corporation, 1979, 58.
- [68] N. Idusuyi, O.O Oluwole, Aluminium Anode Activation Research- A Review, International Journal of Science and Technology, 2012, 2 (8), 561-566.
- [69] E. Ghali, Corrosion Resistance of Aluminium and Magnesium Alloys Understanding, Performance and Testing, John Wiley & Sons Inc., 2010, 105.
- [70] L.F. Mondolfo, Aluminium Alloys: Structure and Properties, Butterworth & Co Ltd, 1976, 122.
- [71] I. Gurrappa, Cathodic Protection of Cooling Water Systems and Selection of Appropriate Materials, Journal of Materials Processing Technology, 2005, 166, 256-267.
- [72] http://www.npl.co.uk/upload/pdf/cathodic_protection_in_practise.pdf, P.E. Fransis, last accessed on 8th Feb 2013.
- [73] HE Jun-Guang, Wen Jiu-ba, LI Xu-dong, Wang Guo-wei, Xu Chun-hua, Influence of Ga and Bi on eletrochemical performance of Al-Zn-Sn

sacrificial anodes, Transactions of non-ferrous metals society of china, 2011, 21, 1580-1586.

- [74] M.R. Saeri, A. Keyvani, Optimisation of manganese and magnesium contents in as cast Aluminium-Zinc-Indium alloy as sacrificial anode, Journal of material science and technology, 2011,27(9), 785-792.
- [75] L.E. Umoro, O.O. Ige, Effect of Tin on Al-Zn-Mg alloys as sacrificial anode in sea water, J.Miner.Mater.Char.Eng., 2007,7(2), 105-113.
- [76] K. Fagbayi, D. Scantlebury, Adverse effect of temperature on operating potential behaviour of Al-Zn-In anodes, Journal of corrosion science and engineering,2003,4,1-12.
- [77] B. Crundwell, The future for sacrificial anodes, Cathodic Protection conference at University of Manchester Institute of Science and Technology (UMIST), Feb 2013.
- [78] S.M.A Shibli, V.S. Gireesh, Activation of aluminium alloy sacrificial anodes by selenium, Corrosion Science, 2005, 47, 2091-2097.
- [79] E.Lemieux, W.H. Hartt, K.E. Lucas, A critical review of aluminium anode activation, dissolution mechanisms and performance, Corrosion, 2001, NACE international (Paper No 01509).
- [80] G. Gibson, Behaviour of Al-Zn-In anodes at elevated temperature, Corrosion, 2010, NACE International (Paper no. 10396).
- [81] J. Genescá, J. Juárez, Development and testing of galvanic anodes for cathodic protection, Contributions to Science, 2000, 1(3), 331-343.
- [82] J.T. Reding and J.J. Newport, The influence of alloying elements on aluminium anodes in sea water,Materials protection, 1966,5,15-18.
- [83] E.Aragon, L. Cazenave-vergez, E. Lanza, A.Giroud, A.Sebaoun, Influence of alloying elements on electrochemical behaviour of ternary Al-Zn-Ga alloys for sacrificial anodes, British corrosion journal 1997,32(4),263-268.
- [84] M.C Reboul, P.H. Gimenez, J.J. Rameau, A proposed activation mechanism for Al anodes, Corrosion-NACE,1984,40(7),366-370.
- [85] D.S. Kier, M.J. Pryor and P.R. Sperry, Galvanic corrosion characteristic of Al alloyed with group IV metals, J. Electrochem. Soc., 1967, 114(8), 777-782.

- [86] ASM handbook online, www.asmhandbookonline.com, accessed on 3/7/2013.
- [87] Q. Song, R.C. Newmann, R.A. Cottis and K. Sieradzki, Computer simulation of alloy passivation and activation, *Corrosion Science*, 1990, 31,621-626.
- [88] A. Sharma, C. Zhang, Y. Austin Chang, R. Knoeppel, D. Morgan, Ab-initio and thermodynamic modelling of alloying effects on activity of sacrificial anodes, *Corrosion Science*, 2011, 1724-1731.
- [89] D.S. Keir, M.J. Pryor, P.R. Sperry, The influence of ternary alloying addition on galvanic behaviour of Al-Sn alloys, *J. Electrochem.Soc.*, 1969, 116, 319-322.
- [90] Yu.Ya. Andreev, A.V. Goncharov, Thermodynamic calculation and experimental investigation of the surface enrichment of electrochemically activated Al-Me (Sn,In,Zn) alloys, *Electrochimica Acta*, 50, 2005, 2629-2637.
- [91] E.D. Hondros, Rule for surface enrichment in solutions, *Scripta Metallurgica*, 1980, 14, 345-348.
- [92] L.Vitos, A.V. Ruban, H.L. Skriver, J.Kollar, The surface energy of metals, *Surface Science*, 1998, 186-202.
- [93] Yu.Ya. Andreev, Model thermodynamic calculation of the dependence of concentration of vacancies and adatoms in surface layer of Ag on electrode potential, *Electrochimica Acta*, 1998, 43(18), 2627-2631.
- [94] Yu. Ya. Andreev, I.A. Safonov, The negative adsorption of Cr atoms on alloy-oxide film boundaries during oxidation in air and anodic passivation of Fe-Cr and Ni-Cr alloys, *Rus.J Phy. Chem.*, 2009, 83(10), 1763-1774.
- [95] Yu.Ya. Andreev, Adsorption equilibrium at the metal oxide film interface in oxidation reactions of Ni, Cr and their alloys, *Rus. J. Phys. Chem.*, 2007, 81(6), 967-973.
- [96] R.A. Swalin, *Thermodynamic of solids*, 2nd edition, 1962, Wiley-Interscience publication, 143-147.

- [97] Yu. Ya. Andreev, Thermodynamic causes of the high diffusion rates of atoms in the superficial layer of a metallic electrode, *Protection of Metals*, 2007, 43(1), 16-21.
- [98] A. Venugopal, P. Veluchamy, P. Selvam, H. Minoura, V.S. Raja, X-Ray Photoelectron Spectroscopic study of oxide film on Aluminium-Tin alloy in 3.5% sodium chloride solution, *Corrosion Science*, 1997, 39(10), 808-812.
- [99] S. Gudić, J. Radošević, M. Kliškić, study of passivation of Al and Al-Sn alloy in borate buffer solution using electrochemical impedance spectroscopy, *Electrochimica Acta*, 2002, 47, 3009-3016.
- [100] M. Kliškić, J. Radošević, S. Gudić, Yield of hydrogen during cathodic polarisation of Al-Sn alloys, *Electrochimica Acta*, 2003, 48, 4167-4174.
- [101] H.W. Pickering, C. Wagner, Electrolytic dissolution of binary alloys containing a noble metal, *J. Electrochem. Soc.*, 1967, 114(7), 698-705.
- [102] K.E. Heusler, Fundamental aspects of the corrosion of alloys, *Corrosion Science*, 1997, 39(7), 1177-1191.
- [103] J.T.B. Gundersen, A Aytaç, J.H. Nordlien, K. Nişancioğlu, Effect of heat treatment on electrochemical behaviour of binary aluminium model alloys, *Corrosion Science*, 2004, 46, 697-714
- [104] J.T.B. Gundersen, A Aytaç, S. Ono, J.H. Nordlien, K. Nişancioğlu, Effects of heat treatment on electrochemical properties and corrosion of aluminium alloy AA3102, *Corrosion Science*, 2004, 46, 265-283.
- [105] S. Aloni, M. Polak, Lead segregation at clean and oxygen covered surface of Al-0.01%Pb solid solution, *Surface Science Letters*, 1996, 349, 123-127.
- [106] D.R. Salinas, S.G. Garcia and J.B. Bessone, Influence of alloying elements and microstructure on aluminium sacrificial anode performance: case of Al-Zn, *Journal of applied electrochemistry*, 29, 1063-1071.
- [107] N. Birbilis and R.G. Buchheit, Electrochemical characteristics of intermetallic phases in aluminium alloys: An experimental survey and discussion, *Journal of the electrochemical society*, 2005, 152(4), 140-157.

- [108] T.Sakano, K. Toda, M. Handa, Tests on effects of In for high performance aluminium anodes, *Materials Protection*, 1966, 45-50.
- [109] T.Sakano and K. Toda, Aluminium alloy for galvanic anodes, United States Patent, No. 3,312,545, Patent Approved: April 1967.
- [110] Sun Hejian and Huo Shizhong, Zn's role in dissolution of Al sacrificial anodes, *chinese journal of oceanology and limnology*, 1990, 8(4), 354-362.
- [111] M.C. Reboul and M.C. Delatte, Activation mechanism for sacrificial Al-Zn-Hg anodes, *Materials Performance*, 1974, 19(5), 35-40.
- [112] J.B. Bessone, Activation of aluminium by mercury ions in non-aggressive media, *Corrosion Science*, 2006, 48, 4243-4256.
- [113] A.H.Al-Saffer, V. Ashworth, W.A. Grant and P.M. Procter, The role of mercury in dissolution of aluminium sacrificial anodes: A study using ion-implantation, *Corrosion Science*, 18, 687-700.
- [114] W.M. Carroll, C.B. Breslin, Activation of aluminium in halide solutions containing activator ions, *Corrosion Science*, 1992, 33(7), 1161-1177.
- [115] C.B. Breslin, L.P. Friery and W.M. Carroll, The electrochemical behaviour of Al-Zn-In and Al-Zn-Hg alloys in aqueous halide solutions, *Corrosion science*, 1994, 36(1), 85-97.
- [116]. M. Karaminezhad, A.H. Jafari, A. Sasrafi, Gh. Safi, Influence of bismuth on electrochemical properties of sacrificial aluminium anodes, *Anti-corrosion Methods and Materials*, 2006, 53(2), 102-109.
- [117] D.O. Flamini, S.B. Saidman, Electrochemical behaviour of Al-Zn-Ga and Al-In-Ga alloys in chloride media, *Materials Chemistry and Physics*, 2012, 136, 103-111.
- [118] R. Piercy, N.A. Hampson, The electrochemistry of indium: The metal in relation to other solid metal electrodes, *Surface Technology*, 1978,6, 437-446.
- [119] A.G. Muñoz, J.B. Bessone, Effect of different anions on electrochemical behaviour of indium, *Electrochimica Acta*, 1998, 43(9), 1067-1075.

- [120] A.G. Muñoz, J.B. Bessone, Cathodic behaviour of In in aqueous sodium chloride solution, *Electrochimica Acta*, 1998, 43 (14-15), 2033-2040.
- [121] C.B. Breslin, W.M. Carroll, The activation of aluminium by indium ions in chloride, bromide and iodide solutions, *Corrosion Science*, 1993, 34(2), 327-341.
- [122] S.B. Saidman, J.B. Bessone, Activation of aluminium by indium ions in chloride solution, *Electrochimica Acta*, 1997, 42(3), 413-420.
- [123] A. Venugopal, V.S. Raja, The self-regulating nature of In on the potential of Al in 3.5%NaCl solution, *Corrosion Science*, 1997, 39(7), 1285-1289.
- [124] A.R. Despić, D.M. Dražić, M.M. Purenović, N. Giković, Electrochemical properties of aluminium alloys containing indium, gallium and thallium, *Journal of Applied Electrochemistry*, 1976, 6, 527-542.
- [125] A.G. Muñoz, S.B. Saidman, J.B. Bessone, Influence of In on the corrosion of Zn-In alloys, *Corrosion Science*, 2001, 43, 1245-1265.
- [126] C.B. Breslin, L.P. Friery, The synergetic interaction between indium and zinc in activation of aluminium in aqueous electrolytes, *Corrosion Science*, 1994, 36(2), 231-240.
- [127] G. Burri, W. Leudi, O. Haas, Electrochemical properties of aluminium in weakly acidic sodium chloride solution; Part I: Influence of the electrolyte additives In^{3+} and Zn^{2+} , *Journal of Electrochemical Society*, 1989, 136(8), 2167-2171.
- [128] J.F. Equey, S. Müller, J. Desilvestro, O. Haas, Electrochemical properties of aluminium in weakly acidic sodium chloride solution; Part II: Influence of electrolyte additives Hg^{2+} , In^{3+} , Ga^{3+} and Sn^{2+} , *Journal of Electrochemical Society*, 1992, 136(9), 1499-1502.
- [129] J.B. Bessone, D.O. Flamini, S.B. Saidman, Comprehensive model for activation of Al-Zn alloys produced by indium, *Corrosion Science*, 2007, 47, 95-105.
- [130] A.G. Muñoz, S.B. Saidman, J.B. Bessone, Corrosion of an Al-Zn-In alloy in chloride media, *Corrosion Science*, 2002, 2171-2182.

- [131] C.B. Breslin, W.M. Carroll, The effect of indium precipitates on the electrochemical dissolution of Al-In alloys, *Corrosion Science*, 1993, 34(7), 1099-1109.
- [132] J.R. Macdonald, Impedance spectroscopy, *Annuals of Biomedical Engineering*, 1992, 20, 289-305.
- [133] D.A. Harrington, P. Vanden Driessche, Mechanism and equivalent circuit in electrochemical impedance spectroscopy, *Electrochimica Acta*, 2011, 56, 8005-8013.
- [134] E. Barsoukov, J.R. Macdonald, *Impedance spectroscopy: Theory, Experiment and application*, Wiley-Interscience, 2nd Edition, 2005, 343-408.
- [135] D.D. Macdonald, Review of mechanistic analysis by electrochemical impedance spectroscopy, *Electrochimica Acta*, 1990, 35(10), 1509-1525.
- [136] D.D. Macdonald, Reflections on the history of electrochemical impedance spectroscopy, *Electrochimica Acta*, 2006, 51, 1376-1388.
- [137] J.H.W. De Wit, H.J.W. Lenderink, Electrochemical impedance spectroscopy as a tool to obtain mechanistic information on passive behaviour of aluminium, *Electrochimica Acta*, 1996, 41(7/8), 1111-1119.
- [138] A. Venugopal, V.S. Raja, A.C impedance study on the activation mechanism of aluminium by indium and zinc in 3.5% NaCl medium, *Corrosion Science*, 1997, 39(12), 2053-2065.
- [139] S. Gudić, I. Smoljko, M. Kliškić, The effect of small addition of indium and tin on the corrosion behaviour of aluminium in chloride solution, *Journal of Alloys and Compounds*, 2010, 505, 54-63.
- [140] C.B. Breslin, A.L. Rudd, Activation of pure Al in an indium containing electrolyte- An electrochemical noise and impedance study, *Corrosion Science*, 2000, 42, 1023-1039.
- [141] S.J. Shaffer, *Tribology 101-Introduction to the basics of Tribology*, Available at http://www.bruker.com/fileadmin/user_upload/8-PDF-Docs/SurfaceAnalysis/TMT/Webinars/Tribology_101_Webinar-1_Intro_and_Basics_29-Jan-2013.pdf, Accessed January 2014.

- [142] J.F. Archard, Contact and rubbing of flat surfaces, *J.Appl.Phys.*, 1953,24, 981-987.
- [143] R.J.K. Wood, Tribo-corrosion of coatings: a review, *J. App. Phys.*, 2007, 40, 5502-5521.
- [144] J.T. Burwell Jr., Survey of possible wear mechanisms, *Wear*, 1957, 1(2), 119-141.
- [145] B.Bhushan, B.K. Gupta, *Handbook of tribology: Materials, coatings and surface treatments*, Mcgraw-Hill Inc., 1991.
- [146] M. H. Pombo Rodriguez R, Paredes RSC, Wido SH, Calixto A. Comparison of aluminum coatings deposited by flame spray and by electric arc spray. *Surface and Coatings Technology* 2007;202 (1):172-179.
- [147] 28E Arctec Brochure, available at < <http://www.metallisation.com/products/wires/28e-arctec/> > , Accessed January 2014.
- [148] D.Batalu, G.CoşmeleaŢă, A.Aloman, Critical analysis of the Ti-Al phase diagrams, *U.P.B. Sci.Bull.*, 2006, 68(4),77-90.
- [149] K.E. Knipling, D.C. Dunand and D.N. Seidman, Nucleation and precipitaion strengthening in dilute Al-Ti and Al-Zr alloys, *Metallurgical and materials transactions* , 2007, 38A, 2552-2563.
- [150] M. Easton and D. StJohn, Grain refinement of aluminium alloys: Part 1. The nucleant and solute paradigms- A review of the literature, *Metallurgical and materials transactions*, 1999, 30A, 1613-1623.
- [151] D. Hu, X. Wu, M.H. Loretto, Advances in optimisation of mechanical properties in cast TiAl alloys, *Intermetallics*, 2005, 13, 914-919.
- [152] D. Hu, Effect of composition on grain refinement in TiAl-based alloys, *Intermetallics*, 2001, 1037-1043.
- [153] D.H.StJohn, L.M. Hogan, Metallography and growth crystallography of Al₃Ti in Al-Ti alloys upto 5wt%Ti, *Journal of crystal growth*, 1979, 46, 387-398.
- [154] G. Ghosh, A. Van De Walle, M. Asta, First - Principles phase stability calculations of pseudobinary alloys of (Al,Zn)₃Ti with L₁₂, DO₂₂ and DO₂₃ structures, *Journal of phase equilibria and diffusion*, 2007, 28(1), 9-22.

- [155] Y. Nakayama, H. Mabuchi, Formation of ternary L_{12} compounds in Al_3Ti -base alloys, *Intermetallics*, 1993, 1, 41-48.
- [156] Y. Fu, R. Shi, J. Zhang, J. Sun, G. Hu, Microstructure and mechanical behaviour of multiphase Al_3Ti - based intermetallic alloy, *Intermetallics*, 2000, 8, 1251-1256.
- [157] A. Majumdar, B.C. Muddle, Microstructure in rapidly solidified Al-Ti alloys, *Materials science and engineering*, 1993, 169A, 135-147.
- [158] Y.V. Milman, D.B. Miracle, S.I. Chugunova, I.V. Voskoboinik, N.P. Korzhova, T.N. Legkaya, Y.N. Podrezov, Mechanical behaviour of Al_3Ti intermetallic and L_{12} phases on its basis, *Intermetallics*, 2001, 9, 839-845.
- [159] F.J. Shackelford, *CRC Materials Science and Engineering handbook*, 2nd edition, CRC press, 1994, 471.
- [160] Z. Wang, Mechanical properties of L_{12} structure intermetallics produced from elemental powder mixtures, *Journal of material science letters*, 2001, 20, 171-173.
- [161] R.A. Varin, M.B. Winnicka, Plasticity of structural intermetallic compounds, *Materials science and engineering*, 1991, A137, 93-103.
- [162] Z.L. Wu, D.P. Pope, L_{12} Al_3Ti based alloys with Al_2Ti precipitates-I. structure and stability of the precipitates, *Acta metall. Mater.*, 1994, 42(2), 509-517.
- [163] J.E. Benci, J.C. Ma, T.P. Feist, Evaluation of the intermetallic compound Al_2Ti for elevated temperature applications, *Materials science and engineering*, 1995, A192/193, 38-44.
- [164] J.E. Benci, J.C. Ma, The mechanical behaviour of and deformation mechanisms in Al_2Ti , *Materials science and engineering*, 1997, A239-240, 195-201.
- [165] N.S. Stoloff, C.T. Liu, S.C. Deevi, Engineering applications of intermetallics, *Intermetallics*, 2000, 8, 1313-1320.
- [166] A. Lasalmonie, *Intermetallics: Why is it so difficult to introduce them in the gas turbine engines?*, *Intermetallics*, 2006, 14, 1123-1129.
- [167] R. Kainuma, M. Palm, G. Inden, Solid-phase equilibrium in the Ti-rich part of the Ti-Al system, *Intermetallics*, 1994, 2, 321-332.
- [168] J.L. Smialek, D.L. Humphrey, Oxidation kinetics of cast Al_3Ti , *Scripta Metallurgica et Materialia*, 1992, 26, 1763-1768.

- [169] I. Ohnuma, Y. Fujita, H. Mitsui, K. Ishikawa, R. Kainuma, K. Ishida, Phase equilibrium in the Ti-Al binary system, *Acta Mater.*, 2000, 3113-3123.
- [170] L. Kaufman, H. Nesor, Coupled phase diagrams and thermochemical data for transition metal binary systems, *Calphad*, 1978, 2(4), 325-348.
- [171] T.T. Cheng, The mechanism of grain refinement in TiAl alloys by boron addition-an alternative hypothesis, *Intermetallics*, 2000, 8, 29-37.
- [172] P. Cooper, A. Barber, Review of the latest development and the best use of grain refiners, 2nd international melt quality workshop, Parague, 2003.
- [173] P. Cooper, P. Fisher, Grain refining of strip cast aluminium, 123rd TMS annual meeting and exhibition, California, 1994.
- [174] I. Naglič, A. Smolej, M. Doberšek, P. Mrvar, The influence of TiB₂ particles on the effectiveness of Al-3Ti-0.15C grain refiner, *Materials characterisation*, 2008, 59, 1458-1465.
- [175] M. Łopaciński, J. Puszynski, J. Lis, Synthesis of Ternary Titanium Aluminum Carbides Using Self-Propagating High-Temperature Synthesis Technique, *J. Am. Ceram. Soc.*, 2001, 84(12), 3051-3053.
- [176] V. Raghvan, Al-C-Ti (Aluminium-Carbon-Titanium), *Journal of phase equilibria and diffusion*, 2006, 27(2), 148-149.
- [177] Z. Zang, X. Bian, Z. Wang, X. Liu, Y. Wang, Microstructure and grain refinement performance of rapidly solidified Al-Ti-C master alloys, *Journal of alloys and compounds*, 2002, 339, 180-188.
- [178] Y. Birol, Grain refining efficiency of Al-Ti-C alloys, *Journal of alloys and compounds*, 2006, 422, 128-131.
- [179] C.D. Mayes, D.G. McCartney, G.J. Tatlock, Observation on the microstructure and performance of an Al-Ti-C grain refining master alloys, *Materials science and engineering*, 1994, A188, 283-290.
- [180] Z. Zang, X. Bian, Y. Wang, X. Liu, Z. Wang, TEM observation of a rapidly solidified Al-Ti-C alloy, *Journal of alloys and compounds*, 2003, 349, 121-128.
- [181] L. Xiangfa, W. Zhenqing, Z. Zuogui, B. Xiufang, the relationship between microstructures and refining performances of Al-Ti-C master alloys, *Materials science and engineering*, 2002, A332, 70-74.

- [182] Y. Birol, The performance of Al-Ti-C grain refiners in twin-roll casting of aluminium foilstock, *Journal of alloys and compounds*, 2007, 430, 179-187.
- [183] G.S.V. Kumar, B.S. Murty, M. Chakraborty, Development of Al-Ti-C grain refiners and study of their grain refining efficiency on Al and Al-7Si alloy, *Journal of alloys and compounds*, 2005, 396, 143-150.
- [184] A.R. Kennedy, D.P. Weston, M.I. Jones, Reaction in Al-TiC metal matrix composites, *Materials science and engineering*, 2001, A316, 32-38.
- [185] L. Xiangfa, Y. Liana, L. Jianwen, W. Zhenqing, B. Xiufang, A new technique to refine pure aluminium by Al-Ti-C mold, *Materials science and engineering*, 2005, 399A, 267-270.
- [186] J. Nie, X. Ma, H. Ding, X. Liu, Microstructure and grain refining performance of a new Al-Ti-B master alloy, *Journal of alloys and compounds*, 2009, 486, 185-190.
- [187] B.S. Murty, S.A. Kori, M. Chakraborty, Grain refinement of aluminium and its alloys by heterogeneous nucleation and alloying, *International materials review*, 2002, 47(1), 4-29.
- [188] K.T. Kashyap, T. Chandrashekar, Effects and mechanisms of grain refinement in aluminium alloys, *Bull. Mater. Sci.*, 2001, 24(4), 345-353.
- [189] A. Tronche, M. Vandyoussefi, A.L. Greer, Instability of TiC particles in aluminium melts inoculated with an Al-Ti-C grain refiner, *Materials Science and Technology*, 2002, 18, 1072-1078.
- [190] A. Jafors, H. Fredriksson, L. Froyen, On the thermodynamics and kinetics of carbides in the aluminium rich corner of the Al-Ti-C phase diagram, *Materials science and engineering*, 1991, A135, 119-123.
- [191] L. Svendsen, A. Jarfors, Al-Ti-C phase diagram, *Materials Science and Technology*, 1993, 9, 948-957.
- [192] H. Ding, X. Liu, L. Yu, G. Zhao, the influence of forming processes on the distribution and morphologies of TiC in Al-Ti-C master alloys, *Scripta Materialia*, 2007, 57, 575-578.
- [193] C. Limmaneevichitr, W. Eidhed, Fading mechanism of grain refinement of aluminium-silicon alloy with Al-Ti-B grain refiners, *Materials science and engineering*, 2003, A3494, 197-206.

- [194] P.S. Mohanty, J.E. Gruzleski, Grain- refinement mechanism of hypoeutectic Al-Si alloys, *Acta mater.*, 1996, 44(9), 3749-3760.
- [195] Materials Data sheet for 01E Aluminium, Available at <<http://www.metallisation.com/products/wires/01ealuminium/>>, Accessed Feb. 014.
- [196] Materials Data sheet for 27E Aluminium Zinc 95/5, Available at <<http://www.metallisation.com/products/wires/27ealuminiumzinc955/>>, Accessed Feb 2014.
- [197] Materials Data sheet for 21E Zinc/Aluminium 85/15, Available at <<http://www.metallisation.com/products/wires/21ezincaluminium8515/>> , Accessed Feb 2014.
- [198] Material Data sheet for 60E 13%Cr Steel, Available at <<http://www.metallisation.com/products/wires/60e13chromesteel/>>, Accessed Feb 2014.
- [199] New 28E ARCTEC Durable Non-slip Coating brochure, Available at <<http://www.metallisation.com/products/wires/28e-arctec/>>, Accessed Feb 2014.
- [200] Al-Zn-In metal spraying, Available at <http://www.bacgroup.com/Global/BAC/Brochures/Al-Zn-In_Metal_Spraying_Brochure.pdf>, Accessed Feb 2014.
- [201] Q-Panel standard substarte application guide, available at <<http://www.q-lab.com/documents/public/1d3db539-4267-4092-9e4e-098b6a991e23.pdf>>, Accessed Feb 2014.
- [202] ISO 8501-1 Pictorial Standards of Cleanliness, Available at <http://tesi.si/media/uploads/public/document/128-svedska_skala_sl.pdf>, Accessed Feb 2014.
- [203] Metallisation Arcspray 140/S250-CL, Available at <<http://www.metallisation.com/products/arc spray/arc140s250cl.html>> , Accessed Feb 2014.
- [204] Private Communication with Alan Jones, Technical Service manager at Metallisation Ltd, March 2011.
- [205] Metallography and image analysis, Available at <<http://products.asminternational.org/hbk/index.jsp>> , Accessed Feb 2014.

- [206] M.L. Brendt, C.C. Brendt, Thermal spray coatings, ASM Handbook, Corrosion: Fundamentals, Testing and protection, 2003, 13A, 803-813.
- [207] Testing of coatings,
Available at <<http://products.asminternational.org/hbk/index.jsp>>,
Accessed Feb 2014.
- [208] Preparation of thermally sprayed coatings.
Available at: <http://www.buehler-asia.com/brochure/apps_support-tech-notes_vol1_issue2.pdf>. Accessed, August, 2012.
- [209] Y. Leng, Material Characterisation Introduction to Microscopic and spectroscopic Methods. Singapore: John Wiley & Sons (Asia); 2008.
- [210] G. Friedbacher, H. Bubert, Surface and Thin film analysis, Wiley VCH, Germany, 2011.
- [211] G. Lawes, A.M. James, Scanning electron microscopy and X-ray microanalysis, John Wiley and Sons publications, England, 1987.
- [212] S. Amelinckx, D. Van Dyck, J. Van Landuyt, G. Van Tendeloo, Electron Microscopy: Principles and fundamentals, VCH publication, Germany, 1997.
- [213] G.E. Lloyd, Atomic number and crystallographic contrast images with SEM: A review of back scattered electron techniques, Mineralogical Magazine, 1987, 51, 3-19.
- [214] X'Pert PRO users guide, Philips Analytical.
- [215] D. Brandon, W.D. Kaplan, Microstructural characterisation of materials, 2nd edition, John Wiley and sons, England, 2008.
- [216] E. Calla, C. Modi, Long life corrosion protection of steel by Zinc-Aluminium coatings formed by thermal spray process, Corrosion its mitigation and Preventive Maintenance, Presented at CORCON, 2000, India.
- [217] S.J. Kim, J.Y. Ko, Electrochemical properties of Al and Al alloys relevant to corrosion protection in sea water environments, Korean J. Chem. Eng, 2006, 23(5), 847-853.
- [218] S. Shrestha, A. Sturgeon, Characteristics and electrochemical corrosion behaviour of thermally sprayed aluminium (TSA) coatings prepared by various wire thermal spray processes, Presented at EUROCORR, Portugal, 2005.

- [219] ASTM B117, Standard practice for operating salt spray (fog) apparatus, 1997.
- [220] N.Y. Tang, Y. Liu, Corrosion performance of Aluminium-containing Zinc coating, *ISIJ International*, 2010, 50(3), 455-462.
- [221] S. Shürz, G.H. Luckeneder, M. Fleischanderl, P. Mack, H. Gsaller, A.C. Kneissl, G. Mori, Chemistry of corrosion products on Zn-Al-Mg alloy coated steel, *Corrosion Science*, 2010, 3271-3279.
- [222] C. Jun, S.Y. Wei, S.D. Young, H.E. Hou, Properties of dawsonite conversion film on AZ31 magnesium alloy, *Trans. Nonferrous Met. Soc. China*, 2011, 936-942.
- [223] ASTM G1, Standard practice for preparing, cleaning and evaluating corrosion test specimens, 1990.
- [224] ASTM G16, Standard guide for applying statistics to analysis of corrosion data, 1995.
- [225] ASTM G69, Standard test method for measurement of corrosion potentials of aluminium alloys, 1997.
- [226] ASTM G71, Standard guide for conducting and evaluating galvanic corrosion tests in electrolytes, 1992.
- [227] J.B. Bessone, R.A.S Baldo, S.M.D. De Micheli, Sea water testing of Al-Zn, Al-Zn-Sn and Al-Zn-In sacrificial anodes, *Corrosion-NACE*, 1981, 37(9), 533-540.
- [228] B. Tsujino, S. Miyase, On area ratio of anode to cathode for iron in neutral solution, *Corrosion-NACE*, 1981, 37(9), 540-545.
- [229] W. J. Lorenz, F. Mansfeld, Determination of corrosion rates by electrochemical DC and AC methods, *Corrosion Science*, 1981, 21(9), 647-672.
- [230] C. Andrade, C. Alonso, Corrosion rate monitoring in the laboratory and on site, *Construction and building materials*, 1996, 10(5), 315-328.
- [231] I. Thompson, D. Campbell, Interpreting Nyquist response from defective coatings on steel substrates, *Corrosion Science*, 1994, 36(1), 187-198.
- [232] F. Mansfeld, S.L. Jeanjaquet, M.W. Kendig, An electrochemical impedance spectroscopy study of reactions at the metal/coating interface, *Corrosion Science*, 1986, 26(9), 735-742.

- [233] P.L. Bondora, F. Deflorian, L. Fedrizzi, Electrochemical impedance spectroscopy as a tool for investigating underpaint corrosion, *Electrochimica Acta*, 1996, 41(7/8), 1073-1082.
- [234] G.W. Walter, A review of impedance plot methods used for corrosion performance analysis of painted metals, *Corrosion Science*, 1986, 26(9), 681-703.
- [235] Y. Hamlaoui, F. Pedraza, L. Tifouti, Corrosion monitoring of galvanised coatings through electrochemical impedance spectroscopy, *Corrosion Science*, 2008, 50, 1558-1566.
- [236] E. Cano, D. Lafuente, D.M. Bastidas, Use of EIS for the evaluation of the protective properties of coatings for metallic culture heritage: a review, *Journal of Solid State Electrochemistry*, 2010, 14, 381-391.
- [237] F.L. Floyd, S. Avudaiappan, J. Gibson, B. Mehta, P. Smith, T. Provder, J. Escarsega, Using electrochemical impedance spectroscopy to predict the corrosion resistance of unexposed coated metal panels, *Progress in Organic Coatings*, 2009, 66, 8-34.
- [238] M.A. Talavera, S. Valdez, J.A. J. Islas, B. Mena, J. Genesca, EIS Testing of new sacrificial anodes, *Journal of Applied Electrochemistry*, 2002, 32, 897-903.
- [239] K. Hladky, L.M. Callow, J.L. Dawson, Corrosion rates from impedance measurements: An introduction, *Br. Corros. J.*, 1980, 15(1), 20-25.
- [240] ASTM G3, Standard practice for conventions applicable to electrochemical measurements in corrosion testing, 1989 (reapproved 2010).
- [241] ASTM G106, Standard practice for verification of algorithm and equipment for electrochemical impedance measurements, 1989 (reapproved 2010).
- [242] D. Vladikova, abc'c of impedance, IEES-BAS, Bulgaria, available at <www.bas.bg/cleps/poemes/eschool/abcImpedanceSchool.php>, Accessed on Feb 2014.
- [243] V. Shtrauss, FIR Kramers-Kronig transformers for relaxation data conversion, *Signal Processing*, 2006, 86, 2887-2900.
- [244] A. Lasia, *Electrochemical Impedance Spectroscopy and its Applications: Modern Aspect of Electrochemistry*, Kluwer Academic/Plenum Publishers, USA, 1999, 32, 143-284.

- [245] Technical Note 1: ZSimpWin Version 3.0, Electrochemical Impedance Spectroscopy Data Analysis Software, Extrapolation using Kramers-Kronig relations, 2002.
- [246] Technical Note 12: Studies of reaction mechanisms, 2003.
- [247] J. Nohava, B. Bonferroni, G. Bolelli, L. Lusvarghi, Interesting aspects of indentation and scratch methods for characterisation of thermally sprayed coatings, *Surface and Coatings Technology*, 2010, 205, 1127-1131.
- [248] A.J. Perry, Scratch adhesion testing of hard coatings, *Metallurgical and Protective Coatings, Thin Solid Films*, 1983, 107, 167-180.
- [249] BS EN ISO 4516:2002 Metallic and other inorganic coatings- Vickers and Knoop micro-hardness tests, Available at <https://bsol-bsigroup-com.lcproxy.shu.ac.uk>, Accessed August 2012.
- [250] T. Valente, Statistical evaluation of Vicker's indentation test results for thermally sprayed materials, *Surface and Coatings Technology*, 90 (1-2) (1997), pp. 14-20.
- [251] C.C. Brendt, Tensile testing adhesion methodology for thermally sprayed coatings, *Journal of Materials Engineering*, 1990, 12, 151-158.
- [252] ASTM C633, standard test Method for Adhesion or Cohesion Strength of thermal spray coatings, 2001.
- [253] BS EN 13144, Metallic and other inorganic coatings method for quantitative measurement of adhesion by tensile test, 2003, Available at <https://bsol-bsigroup-com.lcproxy.shu.ac.uk>, Accessed August 2012.
- [254] ASTM G190, Standard guide for developing and selecting wear test, 2006.
- [255] S.D. Siegmann, O.C. Brandt, N.M. Margadant, Tribological requirements of thermally sprayed coatings for wear resistance applications, 1st International Thermal Spray Conference, Canada, 2000, 1135-1140.
- [256] S. Hogmark, S. Jacobson, M. Larsons, Design and evaluation of tribological coatings, *Wear*, 2000, 246, 20-33.
- [257] K. Holmberg, A. Matthews, H. Ronkainen, Coatings tribology-contact mechanisms and surface design, *Tribology International*, 1998, 31(1-3), 107-120.

- [258] E. Rabinowicz, L.A. Dunn, P.G. Russell, A study of abrasive wear under three-body conditions, *Wear*, 1961, 4, 345-355.
- [259] A.J. Gant, M.G. Gee, A review of micro-scale abrasion testing, *Journal of Applied Physics*, 2011, 44, 1-15.
- [260] K.L. Rutherford, I.M. Hutchings, Theory and application of micro-scale abrasive wear test, *Journal of Testing and Evaluation*, 1997, 25(2), 250-260.
- [261] M.G. Gee, A. Gant, I. Hutchings, R. Bethke, K. Schiffman, K. Van Acker, S. Poulat, Y. Gachon, J. Von Stebut, Ball Cratering or Micro-Abrasion Wear Testing of coatings. NPL (National Physical Laboratory) November 2002.
- [262] M.G. Gee, Wear testing methods and their relevance to industrial wear problem. NPL (National Physical Laboratory) December 1997; NPL Report CMMT (A) 92.
- [263] R.I. Trezona, D.N. Allsopp, I.M. Hutchings, Transitions between two-body and three-body abrasive wear: Influence of test conditions in the micro-scale abrasive wear test, *Wear*, 1999, 225-229, 205-214.
- [264] D.N. Allsopp, R.I. Trezona, I.M. Hutchings, The effects of ball surface condition in the micro-scale abrasive wear test, *Tribology Letters*, 1998, 5, 259-264.
- [265] Y. Kusano, K. Van Acker, I.M. Hutchings, Methods of data analysis for the micro-scale abrasion test on coated substrates, *Surface and Coatings Technology*, 183 ,2-3 ,2004, 312-327.
- [266] P.H. Shipway, A mechanical model for particle motion in the micro-scale abrasion wear test, *Wear*, 2004, 257, 984-991.
- [267] A. Adachi, I.M. Hutchings, Sensitivity of wear rates in the micro-scale abrasion test to test conditions and materials hardness, *Wear*, 2005, 258, 318-321.
- [268] A. Adachi, I.M. Hutchings, Wear-mode mapping for the micro-scale abrasion test, *Wear*, 2003, 23-29.
- [269] F.J.G. Silva, R.B. Casais, R.P. Martinho, A.P.M. Baptista, Role of abrasive material on micro-abrasion wear tests, *Wear*, 2011, 271, 2632-2639.
- [270] M.G. Gee, A. Gant, I. Hutchings, R. Bethke, K. Schiffman, K. Van Acker, S. Poulat, Y. Gachon, J.V. Stebut, Progress towards standardisation of ball cratering *Wear*, 255 ,1-6, 2003, 1-13.

- [271] R.I. Trezona, I.M. Hutchings, Three-body abrasive wear testing of soft materials, *Wear*, 233–235, 1999, 209–221.
- [272] P.H. Shipway, N.K. Ngao, Microscale abrasive wear of polymeric materials, *Wear*, 2003, 255, 742-750.
- [273] K.L. Rutherford, I.M. Hutchings, A micro-abrasive wear test, with particular application to coated systems, *Surface and Coatings Technology*, 1996, 79, 231–239.
- [274] C. Leroy, K.I. Schiffmann, K. Van Acker, J. Von Stebut, Ball cratering an efficient tool for 3 body microabrasion of coated systems, *Surface and Coatings Technology*, 2005, 200, 153–156.
- [275] R. Gåhlin, M. Larsson, P. Hedenqvist, S. Jacobson, S. Hogmark, The crater grinder method as a means for coating wear evaluation—an update, *Surface and Coatings Technology*, 1997, 90, 107–114.
- [276] M.A. Heine, D.S. Keir, M.J. Pryor, The specific effects of chloride and sulphate ions on oxide covered aluminium, *Journal of Electrochemical Society*, 1965, 112(1), 24-32.
- [277] H. Sina, M. Ememy, M. Saremi, A. Keyvani, M. Mahta, J. Campbell, The influence of Ti and Zr on electrochemical properties of aluminium sacrificial anodes, *Material Science and Engineering*, 2006, 431A, 263-276.
- [278] J.C. Lin, H.C. Shih, Improvement of the current efficiency of Al-Zn-In anode by heat treatment, *Journal of Electrochemical Society*, 1987, 134(4), 817-823.
- [279] M. Pourbaix, Application of electrochemistry in corrosion science and practice, *Corrosion Science*, 1974, 14, 25-82.
- [280] A. Ali El-Feki, P. Broadbridge, G.W. Walter, Potential transients for an electrochemical corrosion reaction under constant current condition, *Mathematical and Computer Modelling*, 1999, 30, 111-131.
- [281] F. Mansfeld, J.V. Kenkel, Galvanic corrosion of Al alloys-III: The effect of Area ratio, *Corrosion Science*, 1975, 15, 239-250.

Appendix

The formation of Dawsonite ($\text{NaAl}(\text{CO}_3)(\text{OH})_2$) was also reported by *Bozec et al.*¹ who investigated the mechanism of filiform corrosion on commercially available Ti-Zr coated aluminium alloy (AA6016).

The coated aluminium alloys with 0.5 mm wide artificially induced defects (to act as a site of corrosion, which was similar to the approach followed in the present study) were exposed to various corrosive environments such as 16wt% HCl, saturated AlCl_3 solution, ASTM B117 salt fog and various concentrations of NaCl solution (not specified by authors). After the exposure, the samples were further subjected to 85% relative humidity at 25°C for 1008 hours to propagate filiform corrosion and then followed by drying cycle (drying period not specified by authors).

The potential distribution on the artificially induced defect area was investigated using Scanning Kelvin Probe (SKP) technique and corrosion products on the surface of the defect was analysed using FTIR micro-spectroscopy.

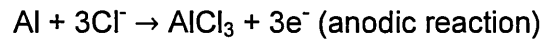
Different composition of the Al corrosion products such as hydrolysed aluminium chlorides ($\text{AlCl}_3 \cdot 6\text{H}_2\text{O}$), aluminium hydroxide gel containing carbonates ($\text{Al}(\text{OH})_{3-2x}(\text{CO}_3)_x$) and Dawsonite ($\text{NaAl}(\text{CO}_3)(\text{OH})_2$), along the length of the defect was reported by the authors.

¹ N.Le Bozec, D. Persson, A. Nazarov and D. Thierry, Investigation of filiform corrosion on coated aluminium alloys by FTIR Microspectroscopy and Scanning Kelvin Probe, *Journal of the electrochemical society*, 2002, 149(9), B403-B408.

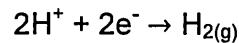
This work has not been cited in the present study as the materials and techniques used by the authors were beyond the scope of the present study.

The formation of Dawsonite in the corrosion product on the surface of the defect was explained as follows:

1. In presence of aqueous media containing Cl^- ions, the artificially induced defect site acts as localised corrosion cell, where OH^- ions are formed on cathodic sites and dissolution of aluminium occurs at anodic sites. Both anodic and cathodic reactions can be represented as:

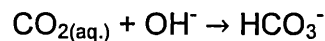
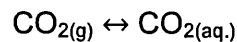


However in case of aluminium, a secondary cathodic reaction of hydrogen emission is also possible, which can be represented as:

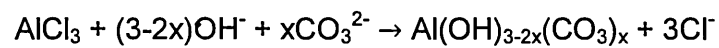


2. The CO_2 present in a high relative humidity environment further interacts with OH^- ions formed at the cathodic sites to form CO_3^{2-} ions.

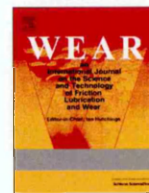
This can be represented as:



3. The aluminium chloride (AlCl_3) formed as a result of aluminium dissolution reaction at local anode, in presence of OH^- containing environment is fully hydrolysed to form $\text{Al}(\text{OH})_3$ gel and intermediate AlOH^{2+} , $\text{Al}(\text{OH})^+$ and $\text{Al}_{13}\text{O}_4(\text{OH})_{24}(\text{H}_2\text{O})_{12}^{7+}$ colloidal species. These intermediate colloidal species further react with CO_3^{2-} ions to form crystallites of carbonate containing aluminium hydroxide compounds and release Cl^- ions. This can be represented as follows:



4. This release of Cl^- ions again initiates further dissolution of Al at anodic sites and process mentioned in steps 1 to 3 are repeated to form a catalytic reaction under high relative humidity conditions. The presence of Na^+ ions from NaCl solution also interacts with $\text{Al}(\text{OH})_{3-2x}(\text{CO}_3)_x$ crystallites to form mineral Dawsonite ($\text{NaAl}(\text{CO}_3)(\text{OH})_2$).



Wear resistance performance of thermally sprayed Al–Ti alloy measured by three body micro-scale abrasive wear test



S. Seth*, A.H. Jones, O.D. Lewis

Materials and Engineering Research Institute (MERI), Norfolk Building, City Campus, Sheffield Hallam University, Howard Street, S1 1WB, Sheffield, UK

ARTICLE INFO

Article history:

Received 14 September 2012

Received in revised form

19 January 2013

Accepted 26 January 2013

Available online 8 February 2013

Keywords:

Thermal spraying

Arc-spraying

Micro-scale abrasive wear test

Wear rate

ABSTRACT

Thermally sprayed aluminium alloys are often used as coatings to protect steel structures from corrosion. However, in many applications the alloys also need to be sufficiently wear resistant to prevent premature removal of the coatings. The addition of titanium to sprayed aluminium coatings is one approach to enhance the wear resistance. In this study the wear performance of a newly developed and commercially available aluminium coating with 3 wt% Ti was studied in terms of its micro-structure, hardness and wear resistance. Micro-scale abrasive wear tests were conducted on the pre-sprayed alloys, and the arc sprayed coatings produced from these alloys in order to determine the influence the spraying process has on the structure and wear properties of the coatings. The wear performance of the coatings with Ti was compared with a 99.5 wt% Al coating, a thermally sprayed 13% Cr steel coating and with the mild steel substrate.

Significant changes were observed in the microstructure of the sprayed coatings when compared with pre-sprayed alloys. The aluminium with 3 wt% Ti coating exhibited a large increase in its hardness value compared with the pre-sprayed alloy and it was significantly harder than the 99.5 wt% Al coating. It was observed that under micro-scale abrasive wear test conditions, the coefficient of wear of the coating with 3 wt% Ti was 33% lower than that of the 99.5 wt% Al coating and it was approximately the same as that of the 13 wt% Cr steel coatings.

© 2013 Elsevier B.V. All rights reserved.

1. Introduction

Surface degradation of steel structures by mechanisms such as abrasion, corrosion and fatigue is common in industrial sectors [1]. Many of the structures in industry are exposed to both corrosive and abrasive environment which can cause surface deterioration [1,2]. Coatings are widely used to protect the steel and in particular thermal spraying has been used to effectively mitigate the effects of wear and corrosion by depositing various alloys and ceramics on to engineering structures [3–5].

Aluminium (Al) in pure and alloyed form has been an attractive material for thermal spraying on to steel structures for protection against corrosion and wear [6]. The effect of Al deposited by various thermal spraying techniques such as electric arc spraying, flame spraying and High Velocity Oxy-Fuel (HVOF) has been studied previously [6–8]. Electric wire arc spraying has been widely used as an economical process to deposit Al and Al alloys due to its high deposition rates [6,9].

The operating principle of wire arc spraying involves the melting of the feedstock material by the formation of an arc

between two continuously fed wires acting as consumable electrodes and projecting the molten particles towards a roughened substrate by an atomising gas [10–12], as shown in Fig. 1.

The molten particles impact the surface of the substrate forming layers of “splats”. The rapid solidification and overlaying of the splats results in the formation of some oxides and inter-splat porosity [13,14]. This microstructure of the coating, often referred as a lamellar structure, is often significantly different from that of the bulk material of the same composition and this can have an effect on coating properties such as wear resistance [2,15].

In order to understand the behaviour and performance of thermally sprayed coatings, evaluation of the coating’s microstructure needs to be characterised and considered in conjunction with wear tests to evaluate its performance. There are a large range of wear tests that can be applied but guidance as to the most appropriate test can be found, for example, in ASTM G190 which lists tests which to some extent replicate the actual conditions of exposure during the service life of the coating [16,17].

The micro-scale abrasive wear test (sometimes referred to as the ball-crater wear test) has been used by many researchers to evaluate the wear resistance of coatings in abrasive condition [18–22]. This test has been used to study the wear behaviour of an aluminium alloy containing 3 weight% titanium (Al–3 wt% Ti) produced as an arc sprayed coating on to a mild steel substrate.

* Corresponding author. Tel.: +44 771451 5907; fax: +44 114 225 3501.
E-mail addresses: s.seth@shu.ac.uk, sampanseth@gmail.com (S. Seth).

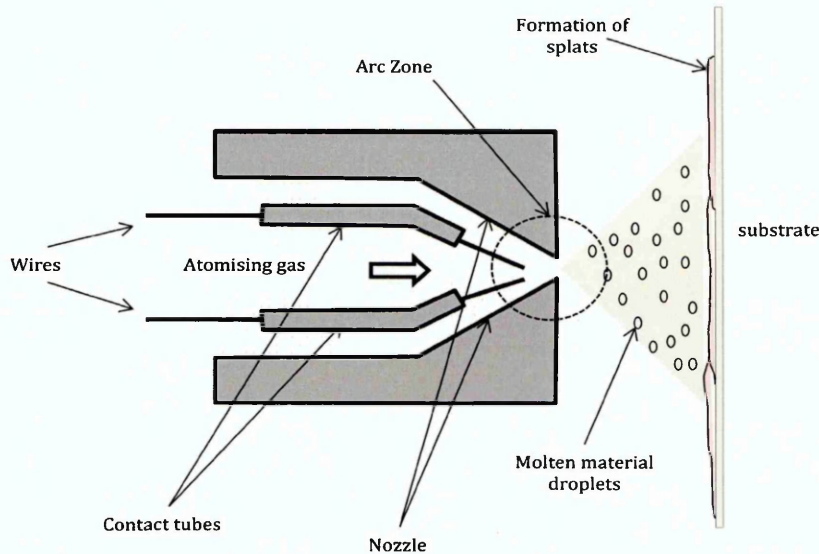


Fig. 1. Schematic diagram of wire arc spraying.

Table 1
Feedstock alloy wire composition.

Coating	Composition	Wire diameter (mm)
Al–Ti	97 wt% Al, 3 wt% Ti	2.0
Al	99.5 wt% Al	1.6
13% Cr steel	Fe 13 wt% Cr	1.6

The primary objective of the study was to understand the influence of the sprayed coating's microstructure and hardness on the wear resistance of the Al–3 wt% Ti alloy coating. The Al–3wt% Ti containing coating's wear performance has been compared with that of a 99.5% Al sprayed coating, a 13%Cr Steel sprayed coating and the mild steel substrate. A comparison of wear rates has also been made between the pre-sprayed aluminium alloys which were used to form the wires for arc spraying, and the sprayed coatings.

2. Experimental procedure

2.1. Coating preparation

The alloys identified as “Al–3 wt%Ti”, “99.5 wt%Al” and “13% Cr steel” were deposited by arc spraying on to mild steel coupons. The composition of the alloy wires used and the wire diameter of the alloys are shown in Table 1.

The coatings were prepared at Celcoat Ltd using an Energiser S250 arc spray gun from Metallisation Ltd. The mild steel coupons were solvent degreased to remove surface contamination, and then grit blasted using chilled iron grit to increase surface roughness and remove surface oxides. The mild steel coupons were vertically attached on magnetic disc and the spray gun was mounted on a vertical traversing unit, so as to keep the spray gun perpendicular to the coupon and maintain a constant traversing speed. Each vertical pass of the spray gun deposited $\sim 50 \mu\text{m}$ of coating. A nominal coating thickness of $300 \mu\text{m}$ was produced during spraying using six passes. The coating thickness was measured after every pass using a commercially available micrometre.

Table 2
Arc spraying parameters.

Coating parameters	Al–3 wt% Ti	99.5 wt%Al	13% Cr steel
Spray current (A)	30	30	30
Spray voltage (V)	200	200	200
Spray distance (mm)	150	150	150
Air pressure (MPa)	0.5	0.5	0.5
Number of passes ($\sim 50 \mu\text{m}/\text{pass}$)	6	6	6

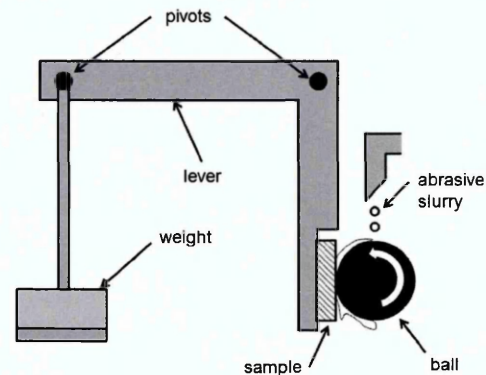


Fig. 2. Schematic diagram of a three body micro-scale abrasive wear tester [20].

Table 2 shows the spraying parameters, which were used during spraying and which were chosen following discussion with staff from Celcoat Ltd during coating preparation.

2.2. Coating characterisation

The metallographic preparation of the coatings for microstructure evaluation was done in accordance with the technical notes for preparing thermal spray coatings published by Buehler [23]. The cross-section of the coating was done using ISOMET 4000 precision saw using a diamond 15 HC blade. The samples cut were then mounted using epoxy resin followed by grinding using SiC abrasive paper, starting with grade 120 and finishing with 1200. The samples were then polished, using a $6 \mu\text{m}$ and then $1 \mu\text{m}$ diamond suspension.

An FEI Nova Nano 200 Scanning Electron Microscope (SEM) equipped with Energy Dispersive X-Ray Spectroscopy (EDS) was used to analyse the microstructure and composition of the feedstock alloy and the coatings. An accelerating voltage of 20 kV and working distance between 5.0 mm and 5.5 mm was chosen for acquisition of images in backscattered electron mode (atomic number contrast).

Vickers micro-hardness measurements using a Mitutoyo MVK-H1 hardness testing machine in accordance with BS EN ISO 4516 were done on the polished cross-section of the coatings [24]. A load of 0.98 N (100 g) was applied for 10 s to obtain a single measurement of the hardness. Thirty indentations on the polished cross-sections of both Al-3 wt%Ti and 99.5 wt% Al coatings were carried out in order to determine the range of hardness values

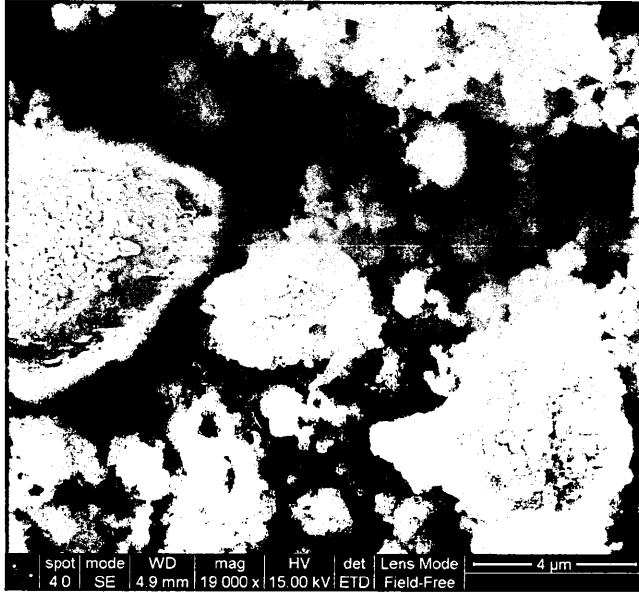


Fig. 3. Secondary electron micrograph showing SiO₂ powder morphology.

Table 3
Micro-scale abrasive wear test parameters.

Test parameters	
Diameter of the steel ball	25.4 mm
Ball material	Tool steel HV~800
Ball sliding speed	0.13 ms ⁻¹
Sliding distance	50 m, 100 m, 150 m

caused by the complex microstructure of the coatings. The micro-hardness of Al-3 wt%Ti and 99.5 wt%Al feedstock alloys was also carried out in order to determine the influence of the spraying process on the alloy's hardness.

Macro-hardness measurements using a 9.8 N (1 kg) load were also carried out on the polished surface of the coatings. The depths of the indentations were always 25% less than the thickness of the coating.

In making micro-hardness measurements care was taken to avoid obvious porosity within the coating. As such the micro-hardness measurements will be higher than a higher load macroscopic measurement that will be influenced by the porosity of the coatings.

2.3. Micro-scale abrasive wear test

A three body micro-scale abrasive wear test [25,26] was conducted to evaluate the abrasive wear resistance. Commercially available Phoenix Tribology Ltd. model PLINT TE-66 micro-scale abrasive wear tester was used [18] and is shown schematically in Fig. 2. The sample to be tested was vertically mounted on a lever that rotates about the pivot and is pressed against rotating ball under the application of the applied load. A constant feed of abrasive slurry of specific concentration is maintained between rotating ball and the sample.

A constant load of 0.2 N was applied and the abrasive slurry had a concentration of 20 vol% (0.66 g/cm³) of crystalline silicon dioxide in deionised water (nominal particle size D₅₀=2.5 µm Silicon (IV) oxide, crystalline quartz, Alfa Aesar). During the experiment slurry was constantly stirred using a magnetic stirrer to avoid settling of the silicon dioxide. In a steel ball on a flat aluminium sample configuration the Hertzian contact pressure at 0.2 N is in theory 0.04 GPa. However, in the wear test the two materials are separated by a layer of liquid containing the abrasive slurry and thus it is unlikely that this contact pressure is ever experienced. Fig. 3 shows the morphology of the silica particles. A particle shape with rounded edges was observed with the average particle of the silicon dioxide in the range of 2.0 µm–3.0 µm but with some larger agglomerates. Table 3 shows the test parameters used in the experiment.

All test samples were ground and polished to a final stage of 1 µm diamond suspension. The wear test was repeated three times at each sliding distance to ensure the reproducibility of the results. The diameter of the circular wear craters was measured using an optical microscope and the volume loss was calculated assuming the spherical cap geometry of the wear crater [27], given by

$$V = \pi b^4 / 64R \quad (1)$$

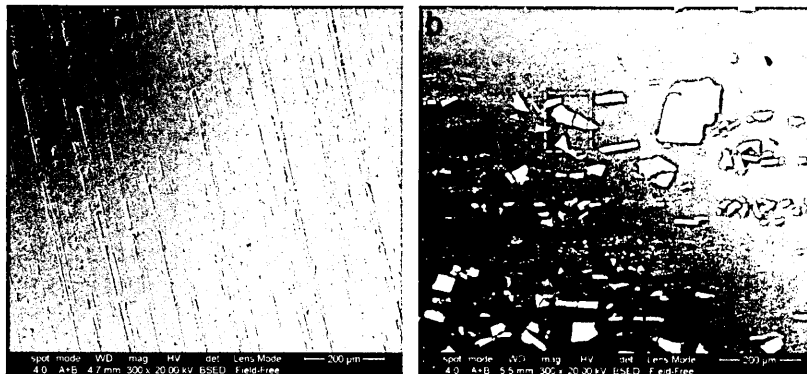


Fig. 4. Backscattered electron micrograph of transverse section of (a) 99 wt% Al and (b) Al-3 wt% Ti feedstock materials.

where b is the diameter of the wear crater and R is the radius of the rotating ball, Eq. (1) is used when $b \ll R$. The graph of the volume of the wear crater vs. sliding distance multiplied by the load was plotted to calculate the coefficient of wear ($\text{mm}^3 \text{N}^{-1} \text{m}^{-1}$) from the gradient of the graph [21,28]. During

the micro-scale abrasion test the wear crater did not penetrate to the substrate.

3. Results

3.1. Microstructure and micro-hardness of Al–3 wt% Ti and 99.5 wt% Al feedstock

Fig. 4(a) and (b) shows the backscattered electron micrographs of the transverse section of 99 wt% Al and Al–3 wt%Ti alloy feedstock alloy rod. For 99% aluminium no microstructural features were observed (the linear features observed in Fig. 4(a) are artefacts of polishing and the extrusion direction of the rod). It was apparent from the micrographs of the Al–3 wt% Ti material that two distinct phases existed in the structure (i) a large blocky phase with a large aspect ratio and (ii) a smaller equiaxed phase, both of which were evenly distributed in the aluminium matrix as shown in Fig. 4(b). Fig. 5 shows a higher magnification image where the two phases are clearly discernible. The larger particle is cracked, probably as a result of sample preparation, indicating it is inherently brittle.

The Energy dispersive X-ray analysis on each phase highlighted in Fig. 5 was used to quantify the average composition of each phase as shown in Table 4. The analysis suggests that the larger blocky phase has an Al to Ti ratio $\sim 2.8:1$ while the small equiaxed phase has a metal (Ti+Al) to C ratio of $\sim 1:1$. Note that carbon is often found to be present on the surface of samples being analysed using EDX and as such any figure for C may not be entirely due to the material itself and some of the Al signal may have been from the surround Al matrix due to the EDX interaction volume.

Table 5 shows the micro-hardness values measured on the feedstock alloys of the 99.5 wt% Al and the Al–3 wt% Ti materials. A larger range of micro-hardness values were recorded for Al–3 wt% Ti alloy than for 99.5 wt% Al as is indicated by the coefficient of variation and as demonstrated in Fig. 6. There were a small number of regions in the Al–3 wt%Ti alloy which exhibited hardness as high as $\text{HV}_{0.98} = 0.78 \text{ GPa}$ (80 kgf/mm^2).

3.2. Microstructure and micro-hardness of Al–3 wt% Ti and 99.5 wt% Al coatings

Fig. 7 shows the backscattered electron micrographs of the cross-sections of (a) the arc sprayed 99.5 wt% Al coating and (b) the arc sprayed Al–3 wt% Ti alloy coating. In contrast to the bulk feedstock (Fig. 4) an inhomogeneous layered structure was observed with dark regions which were inter-splat porosity or oxides. The Al–3 wt% Ti sprayed coating showed regions of varying contrast in the backscattered electron images indicating the inhomogeneous distribution of the Ti in the Al matrix.



Fig. 5. EDX analysis of (region indicated in Fig. 4b) showing the different phases observed in the Al–3 wt% Ti feedstock alloy; large blocky phases (A) with large aspect ratios and smaller equiaxed particles (B).

Table 4
Average composition analysis of different phases observed in Al–3 wt% Ti feedstock alloy.

Phase	Average composition		
	Al (at%)	Ti (at%)	C(at%)
A. Blocky phase with high aspect ratio	67 ± 1	24 ± 1	8 ± 1
B. Smaller equiaxed phase	28 ± 4	21 ± 4	51 ± 4

Table 5
Vickers micro-hardness of the 99.5 wt% Al and Al–3 wt% Ti feedstock.

	$\text{HV}_{0.98}$ GPa (kgf/mm ²)	Coefficient of variation (%)
99.5 wt% Al feedstock	0.32 (33 ± 1)	3
Al–3 wt%Ti feedstock	0.43 (44 ± 8)	18

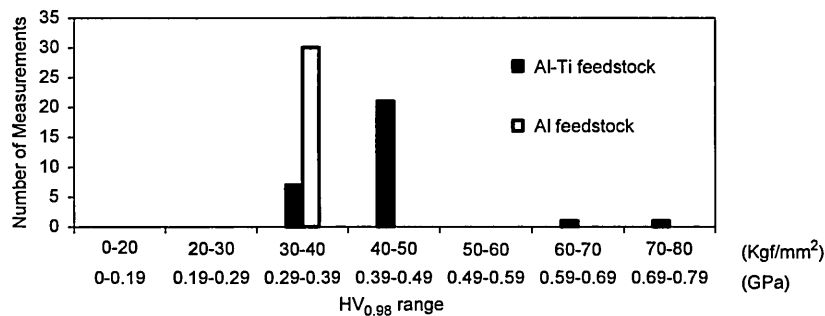


Fig. 6. Frequency distribution histogram of micro-hardness ($\text{HV}_{0.98}$) for 99.5 wt% Al and Al–3 wt% Ti feedstock material.

However, the microstructure was significantly different from that observed in the feedstock of Al–3 wt% Ti as shown in Fig. 4. Higher magnification images of the Al–3 wt% Ti coating (Fig. 8) revealed “speckled” regions, dark grey and light grey regions. EDX analysis of each of these regions was conducted and the average composition of a number of measurements is shown in Table 6. High titanium or high carbon content phases, as observed in the Al–3 wt% Ti alloy feedstock alloy (Table 4), were not observed in the sprayed coating. The overall Ti level was slightly below the expected level suggesting that the distribution of Ti was heterogeneous with some small regions having a much higher Ti content than others. A general increase in the detected oxygen levels was noted although this was not high enough to indicate the presence of oxides.

The hardness results from the cross-section of the coating are shown in Table 7. A significant increase of ~70% in the micro-hardness of the Al–3 wt% Ti coating when compared to its feedstock was observed. The 99.5 wt% Al coating showed similar hardness to its feedstock material. The Al–3 wt% Ti coating was significantly harder (117%) than the 99.5 wt% Al coating. The Fe–13 wt% Cr coating which was used as a reference in the wear testing was also measured for reference. In terms of the spread in the hardness values, the Al–3 wt% Ti exhibited the largest coefficient of variation (35%) with some regions exhibiting a hardness of upto $HV_{0.98} = 1.37$ GPa (140 kgf/mm²), as shown in Fig. 9.

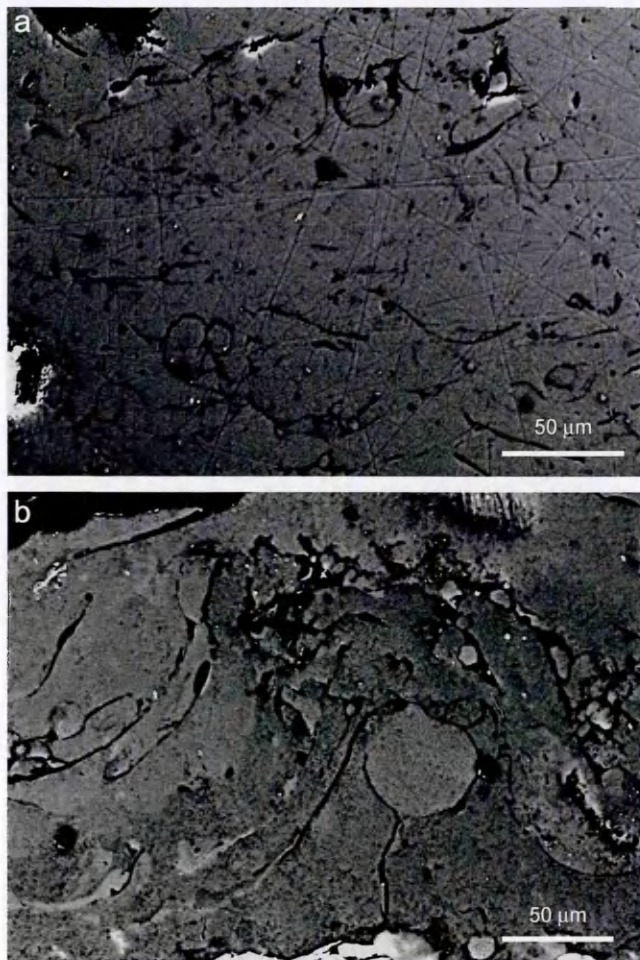


Fig. 7. Backscattered electron micrograph showing the cross-section of (a) 99.5 wt% Al and (b) Al–3 wt% Ti coatings.

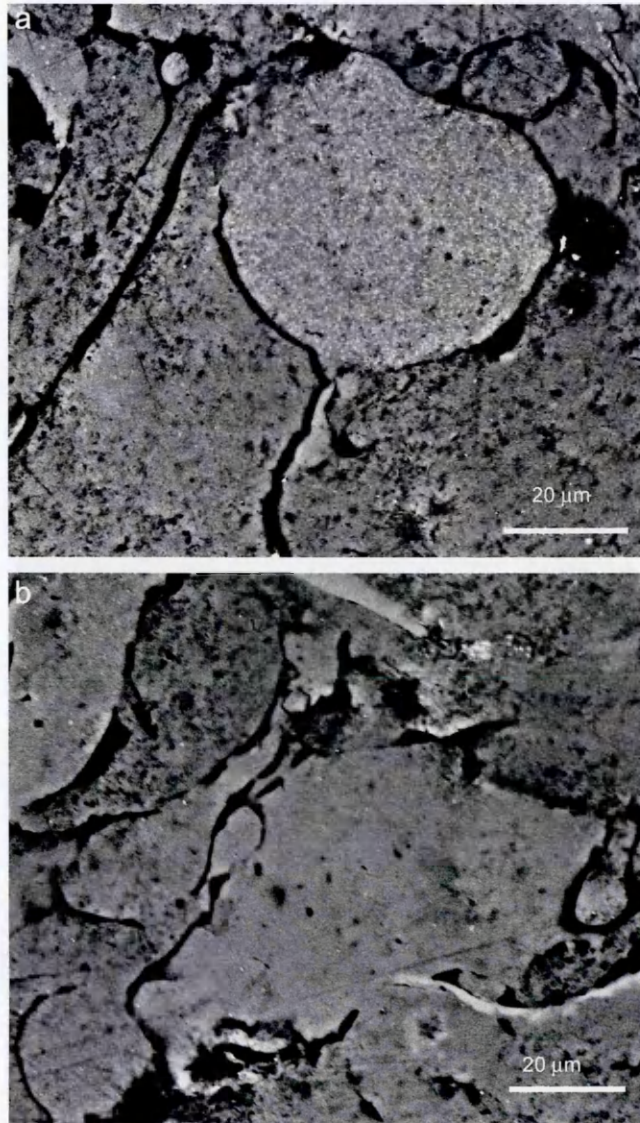


Fig. 8. Backscattered electron micrograph of Al–3 wt% Ti showing (a) speckled region and (b) dark and light grey regions.

Table 6

Average composition analysis of different phases observed in Al–3 wt% Ti coating.

Phase	Average composition		
	Al (at%)	Ti (at%)	O (at%)
Speckled region	91 ± 0.5	1 ± 0	7 ± 0.5
Dark grey region	91 ± 0.4	1 ± 0.2	8 ± 0.2
Light grey region	92 ± 0.2	2 ± 1	6 ± 0.3

Table 7

Vickers micro-hardness of the Al–3 wt% Ti, 99.5 wt% Al and Fe–13 wt% Cr coatings.

	$HV_{0.98}$ GPa (kgf/mm ²)	Coefficient of variation (%)
99.5 wt% Al coating	0.34(35 ± 8)	22
Al–3 wt% Ti coating	0.74(75 ± 26)	35
Fe–13 wt% Cr coating	3.97(405 ± 82)	20

3.3. Coefficient of wear for Al–3 wt% Ti and 99.5 wt% Al feedstock material and coatings

The coefficient of wear for 99.5 wt% Al and Al–3 wt% Ti feedstock and coatings were calculated from the gradient of the graphs shown in Figs. 10 and 11, where the volume of the wear crater (in mm^3) formed during the micro-scale abrasive wear test is plotted against sliding distance (in m) multiplied by the applied load (in N). Excellent linear regression fits were observed with $R^2 > 0.97$.

It was observed, as shown in Table 8, that the coefficient of wear for Al–3 wt% Ti feedstock was 18% less than that of the 99.5 wt% Al feedstock. The coefficient of wear for Al–3 wt% Ti coatings was 33% lower than for 99.5 wt% Al coating as reported in Table 9. The difference between the feedstock alloy and the sprayed coating was not significant for the 99.5% Al alloy but there was a difference between the feedstock alloy and sprayed coating of Al–3wt%Ti with the sprayed coating exhibiting marginally better wear resistance. A point worthy of note is that the broadly similar wear resistance was exhibited by the Al–3wt%Ti feedstock and the sprayed coating despite the significantly different microstructure, hardness and porosity in the coating. The wear tracks shown in Figs. 12 and 13 show two body grooving wear mechanism in both feedstock's and coatings, caused by the ploughing of the surface by the $2.5 \mu\text{m}$ SiO_2 particles in the abrasive slurry, a mechanism that has been reported by other researchers [29].

A graph comparing the wear coefficients and hardness ($\text{HV}_{9,8}$ and $\text{HV}_{0,98}$) of all the materials tested is shown in Fig. 14. When comparing the Al–3 wt% Ti coating with the Fe–13 wt% Cr coating a small difference of only 2% in the wear coefficient was observed despite a significant difference in the hardness value. Compared to the Al–3 wt% Ti coating the mild steel had 41% lower (and thus better) wear coefficient.

4. Discussion

The microstructure of the Al–3 wt% Ti feedstock alloy (Fig. 4(b)) showed the presence of two distinct phases. The larger blocky phase with a high aspect ratio in which the Al:Ti ratio was close to 3:1, suggested it was the intermetallic phase Al_3Ti . As the production of the alloys involves the slow cooling of the alloy from the melt the phase expected to be present is the equilibrium structure tetragonal Al_3Ti [32]. The smaller equiaxed phase appeared to contain both Ti and Al along with equal atomic amounts of C and was thus probably a phase with the structure of the ceramic titanium carbide (TiC) but with possible Al substitution for some of the Ti. The influence of the intermetallic Al_3Ti and ceramic (Ti,Al)C phases was observed in the micro-hardness of

the Al–3 wt% Ti feedstock alloy which was 33% higher than that of the 99.5 wt% Al feedstock alloy. Pure TiC is known to have a micro-hardness of $\text{HV}_{0,98} = 28\text{--}33 \text{ GPa}$ ($2850\text{--}3390 \text{ kgf/mm}^2$) [30] while the micro-hardness of Al_3Ti has been measured by others to be $\text{HV}_{2,0} \sim 5.0 \text{ GPa}$ (510 kgf/mm^2) [31].

In contrast to the feedstock alloys the Al–3 wt% Ti and 99.5 wt% Al arc sprayed coatings exhibited a layered microstructure with some inter-splat porosity and oxides. It is evident from Fig. 7(b) that Al–3 wt% Ti coating has a microstructure which is completely different from that observed in the feedstock material. The large blocky tetragonal Al_3Ti or the small (Ti,Al)C phases were not detected in the cross-section of the coating. There was some back scattered electron contrast difference noted in the material at a sub-micron scale which was suggestive of a sub-micron

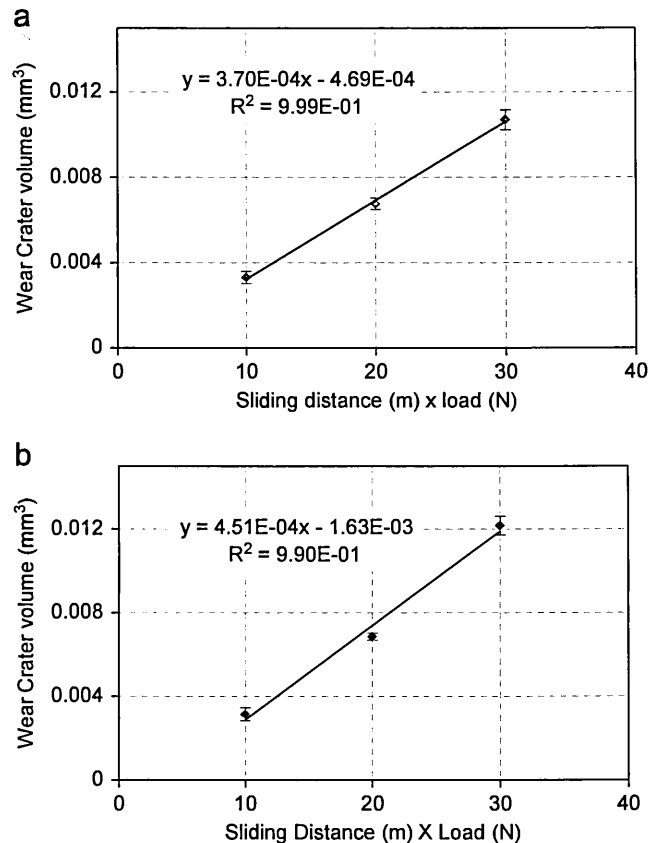


Fig. 10. Graphs showing Wear crater volume vs. Sliding distance \times load for (a) 99.5 wt% Al and (b) Al–3 wt% Ti feedstock.

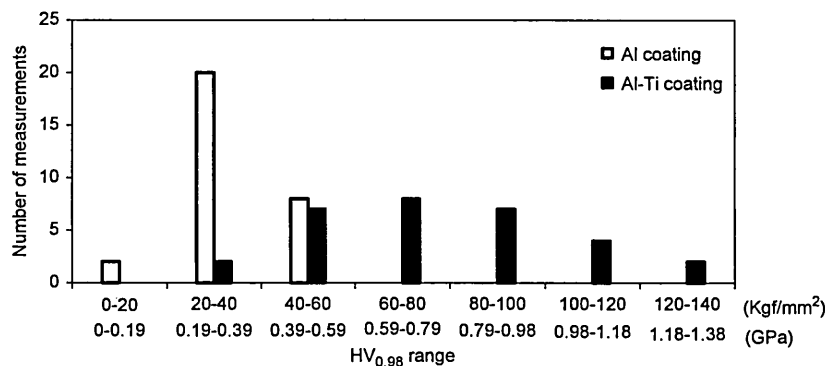


Fig. 9. Frequency distribution histogram of variation in micro-hardness of 99.5 wt% Al and Al–3 wt% Ti coating.

structure in some regions. Despite the absence of the two hard phases the micro-hardness of the sprayed Al–3wt%Ti coating was more than twice (114%) that of the sprayed aluminium alloy and 71% higher than its own feedstock alloy, with some regions exhibiting upto $HV_{0.98}=1.18$ GPa (120 kgf/mm²). It is probable that the melting and rapid cooling which is characteristic of the arc spraying process has taken the Ti in the alloy into solution during melting and subsequently the rapid cooling which occurs during splat formation, has produced the metastable cubic phase of Al₃Ti [32]. Possible evidence for this is seen in the presence of the speckled regions in the structure where nano-scale precipitates with an atomic number > Al are observed in Fig. 8(a).

The wear coefficient of Al–3 wt% Ti feedstock alloy was 18% lower (thus better) than that of the 99.5 wt% Al feedstock alloy, which can be attributed primarily to the harder intermetallic Al₃Ti phases in the alloy as these appear to be resisting indentation by the abrasive particles more than the surrounding Al matrix (Fig. 11b). The hard ceramic (Ti,Al)C phase, which is known to be present, was too small to be observed on the wear scar and as such its contribution to the wear resistance cannot be verified.

The arc sprayed Al–3 wt% Ti coating exhibited a 33% lower wear coefficient than the arc sprayed 99.5% Al coating, with the lower wear coefficient being attributed to the overall higher micro-hardness (114% harder) and the presence of regions with hardness up to $HV_{0.98}=1.37$ GPa (120 kgf/mm²). While Al₃Ti and (Ti,Al)C phases were not directly observed in the coating structure the high hardness regions may have contained the nano-scale precipitates of cubic Al₃Ti, which may have influenced the hardness and wear resistance through precipitation strengthening [32].

It was noted that even though the arc sprayed 13 wt% Cr steel coating had a significantly higher hardness the difference in the coefficient of wear between it and Al–3 wt% Ti was negligible (~2%). The mild steel substrate material had the lowest wear coefficient which most probably can be attributed to the fact that it has a fully dense steel structure rather than a porous sprayed coating.

5. Conclusions

- (1) The Al–3wt% Ti feedstock alloy produced using slow cooling showed the presence of evenly distributed intermetallic tetragonal Al₃Ti and ceramic (Ti,Al)C phases which, because

Table 8

Coefficient of wear for 99.5 wt% Al and Al–3 wt% Ti feedstock alloys.

	Coefficient of wear (mm ³ N ⁻¹ m ⁻¹)
99.5 wt% Al feedstock	$4.5 \times 10^{-04} \pm 0.5 \times 10^{-04}$
Al–3 wt% Ti feedstock	$3.7 \times 10^{-04} \pm 0.1 \times 10^{-04}$

Table 9

Coefficient of wear for 99.5 wt% Al and Al–3 wt% Ti coating.

	Coefficient of wear (mm ³ N ⁻¹ m ⁻¹)
99.5 wt% Al coating	$4.8 \times 10^{-04} \pm 0.03 \times 10^{-04}$
Al–3 wt% Ti coating	$3.2 \times 10^{-04} \pm 0.5 \times 10^{-04}$

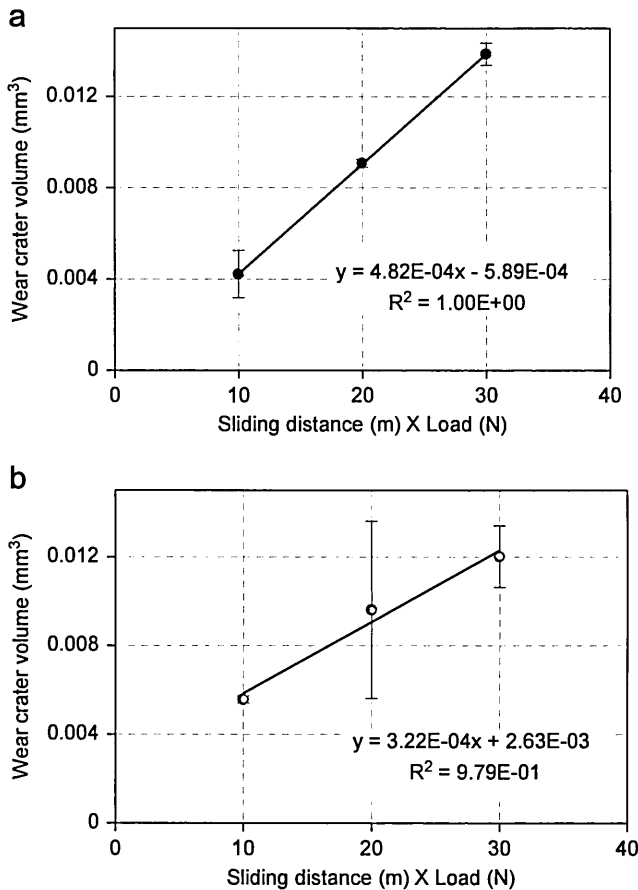


Fig. 11. Graphs showing wear crater volume vs. Sliding distance × Load for (a) 99.5 wt% Al and (b) Al–3 wt% Ti coatings.

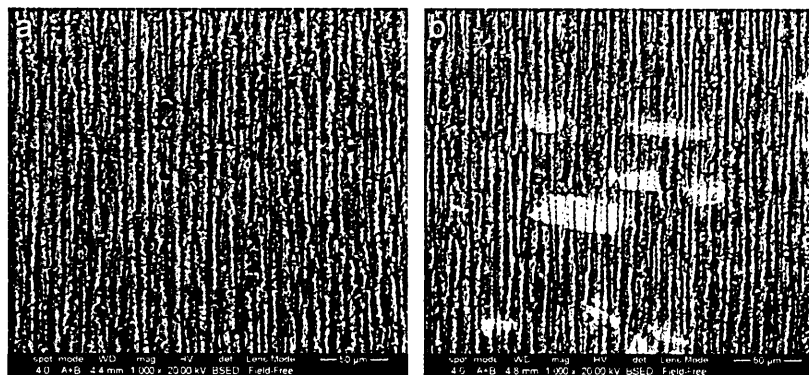


Fig. 12. Backscattered micrographs showing the directionality of the wear tracks for (a) 99.5 wt% Al and (b) Al–3 wt% Ti feedstock.

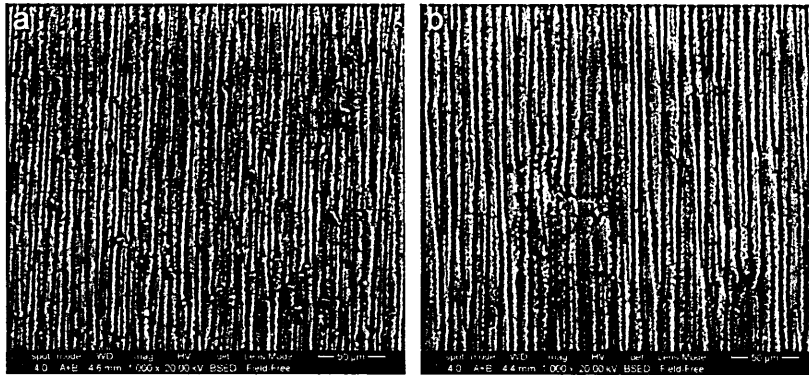


Fig. 13. Backscattered micrographs showing the directionality of the wear tracks for (a) 99.5 wt% Al and (b) Al-3 wt% Ti coatings.

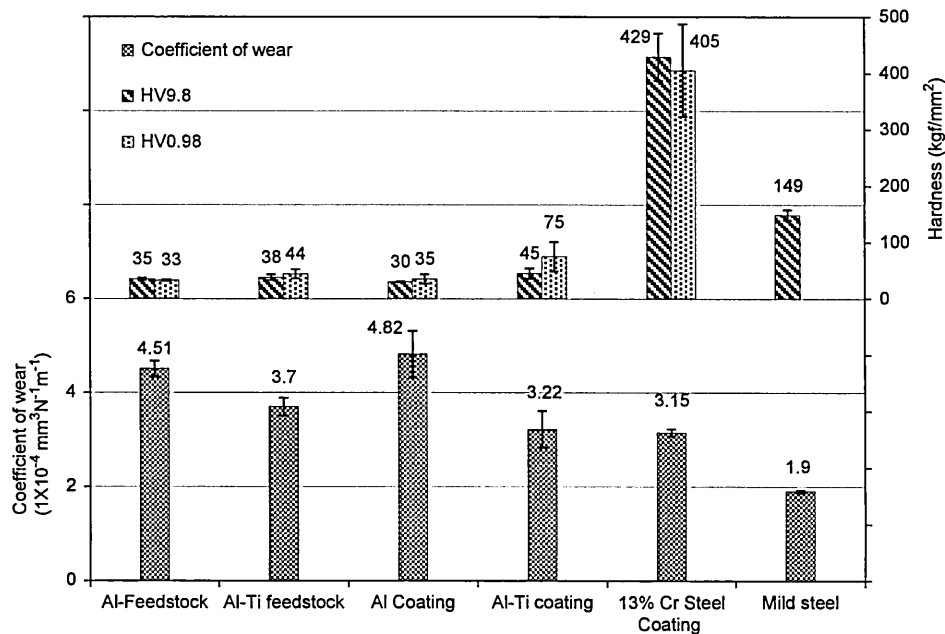


Fig. 14. Comparison of coefficient of wear and hardness of 99.5 wt% Al, Al-3 wt% Ti alloy feedstock and coatings with 13% Cr Steel coating and Mild steel substrate.

of their inherent higher hardness results in a 33% higher micro-hardness of Al-3 wt% Ti feedstock alloy in comparison with 99.5 wt% Al feedstock.

- (2) The 18% lower coefficient of wear of the Al-3 wt% Ti feedstock compared to that of the 99.5 wt% Al feedstock can also be explained by the presence of the hard intermetallic tetragonal Al_3Ti and $(\text{Ti},\text{Al})\text{C}$ phases present in the structure.
- (3) The microstructure of the arc sprayed Al-3 wt% Ti coating did not contain Al_3Ti and $(\text{Ti},\text{Al})\text{C}$ particles but did show regions of varying atomic number contrast suggesting the formation of the metastable cubic phase of Al_3Ti formed from the rapid cooling that takes place in arc spraying. The resulting precipitation strengthening may explain the 114% increase in the hardness of the sprayed Al-3 wt% Ti coating compared to its feedstock alloy and also the regions with a high hardness up to $\text{HV}_{0.98} = 1.18 \text{ GPa}$ (120 kgf/mm^2).
- (4) The arc sprayed Al-3 wt% Ti coating showed a 33% lower coefficient of wear than the 99.5 wt% Al coating which was attributed to precipitation strengthening resulting in an overall higher micro-hardness and the presence of regions of high micro-hardness ($\text{HV}_{0.98} > 1.18 \text{ GPa}$) in the Al-3 wt% Ti coating.

- (5) In the micro-scale abrasive wear test using $2.5 \mu\text{m SiO}_2$ abrasive in deionised water, the wear coefficient of an arc sprayed aluminium containing 3 wt% Ti was found to be very close to that of an arc sprayed 13%Cr steel coating with a much higher hardness.

Acknowledgements

The authors would like to acknowledge the Celcoat Ltd for providing the arc spray equipment and professional guidance during sample preparation.

References

- [1] J.T. Burwell Jr., Survey of possible wear mechanisms, *Wear* 1 (2) (1957) 109–141.
- [2] L. Prchlik, S. Sampath, Effect of the microstructure of thermally sprayed coatings on friction and wear response under lubricated and dry sliding conditions, *Wear* 262 (1–2) (2007) 11–23 1/4.
- [3] L. Pawlowski, *The Science and Engineering of Thermal Spray Coatings*, John Wiley & sons, England, 1995.
- [4] W.E. Ballard, *Metal Spraying and the Flame Deposition of Ceramics and Plastics*, 4th edition, Griffin-London, London, 1963.

- [5] P. Fauchais, A. Vardelle, B. Dussoubs, Quo vadis thermal spraying? *Journal of Thermal Spray Technology* 10 (1) (1999) 44–66.
- [6] M.H. Pombro Rodríguez, R. Paredes, R.S.C. Wido, S.H. Calixto, A. Comparison of aluminum coatings deposited by flame spray and by electric arc spray, *Surface and Coatings Technology* 202 (1) (2007) 172–179.
- [7] R.S.C. Paredes, S.C. Amico, A.S.C.M. d'Oliveira, The effect of roughness and pre-heating of the substrate on the morphology of aluminium coatings deposited by thermal spraying, *Surface and Coatings Technology* 200 (9) (2006) 3049–3055.
- [8] M. Abu-Aesh, Dependence of sliding wear resistance and microhardness of al-spray coating layers on substrate conditions using high-velocity oxygen fuel (HVOF), *Materials and Manufacturing Processes* 23 (7) (2008) 726–733.
- [9] I. Gedzevicius, A.V. Valiulis, Analysis of wire arc spraying process variables on coatings properties, *Journal of Materials Processing Technology* 175 (1–3) (2006) 206–211.
- [10] T. Watanabe, X. Wang, E. Pfender, J. Heberlein, Correlations between electrode phenomena and coating properties in wire arc spraying, *Thin Solid Films* 316 (1–2) (1998) 169–173 3/21.
- [11] X. Wang, J. Heberlein, E. Pfender, W. Gerberich, Effect of nozzle configuration, gas pressure, and gas type on coating properties in wire arc spray, *Journal of Thermal Spray Technology* 8 (4) (1999) 565–575.
- [12] A.P. Newbery, P.S. Grant, R.A. Neiser, The velocity and temperature of steel droplets during electric arc spraying, *Surface and Coatings Technology* 195 (1) (2005) 91–101 5/23.
- [13] S. Deshpande, S. Sampath, H. Zhang, Mechanisms of oxidation and its role in microstructural evolution of metallic thermal spray coatings—Case study for Ni–Al, *Surface and Coatings Technology* 200 (18–19) (2006) 5395–5406 5/8.
- [14] C-Li, A. Ohmori, Relationships between the microstructure and properties of thermally sprayed deposits, *Journal of Thermal Spray Technology* 11 (3) (2002) 365–374.
- [15] T. Valente, Statistical evaluation of Vicker's indentation test results for thermally sprayed materials, *Surface and Coatings Technology* 90 (1–2) (1997) 14–20.
- [16] ASTM 190-06, Standard guide for developing and selecting wear test, ASTM international, 03.02, 792–796.
- [17] B. Wielage, S. Steinhäuser, T. Schnick, D. Nicklmann, Characterization of the wear behavior of thermal sprayed coatings, *Journal of Thermal Spray Technology* 8 (4) (1999) 553–558.
- [18] H. Chen, C. Xu, Q. Zhou, I.M. Hutchings, P.H. Shipway, J. Liu, Micro-scale abrasive wear behaviour of HVOF sprayed and laser-remelted conventional and nanostructured WC–Co coatings, *Wear* 258 (1–4) (2005) 333–338 1.
- [19] R. Gählin, M. Larsson, P. Hedenqvist, S. Jacobson, S. Hogmark, The crater grinder method as a means for coating wear evaluation—an update, *Surface and Coatings Technology* 90 (1–2) (1997) 107–114 3/15.
- [20] C. Leroy, K.I. Schiffmann, K. Van Acker, J. Von Stebut, Ball cratering an efficient tool for 3 body microabrasion of coated systems, *Surface and Coatings Technology* 200 (1–4) (2005) 153–156 10/1.
- [21] K.L. Rutherford, I.M. Hutchings, A micro-abrasive wear test, with particular application to coated systems, *Surface and Coatings Technology* 79 (1–3) (1996) 231–239 2.
- [22] G. Nothnagel, Wear resistance determination of coatings from cross-section measurements of ball-ground craters, *Surface and Coatings Technology* 57 (2–3) (1993) 151–154 5/28.
- [23] Preparation of thermally sprayed coatings. Available at: <http://www.buehler-asia.com/brochure/apps_support-tech-notes_vol1_issue2.pdf>. Accessed, August, 2012.
- [24] BS EN ISO 4516:2002 Metallic and other inorganic coatings- Vickers and Knoop microhardness tests, Available at <<https://bsol-bsigroup-com.lcproxy.shu.ac.uk>>, Accessed August 2012.
- [25] M.G. Gee, Wear testing methods and their relevance to industrial wear problem. NPL (National Physical Laboratory) December 1997; NPL Report CMMT (A)92.
- [26] M.G. Gee, A. Gant, I. Hutchings, R. Bethke, K. Schiffman, K. Van Acker, S. Poulat, Y. Gachon, J. Von Stebut, Ball Cratering or Micro-Abrasion Wear Testing of coatings. NPL (National Physical Laboratory) November 2002.
- [27] M.G. Gee, A. Gant, I. Hutchings, R. Bethke, K. Schiffman, K. Van Acker, Progress towards standardisation of ball cratering, *Wear* 255 (1–6) (2003) 1–13 0.
- [28] Y. Kusano, K. Van Acker, I.M. Hutchings, Methods of data analysis for the micro-scale abrasion test on coated substrates, *Surface and Coatings Technology* 183 (2–3) (2004) 312–327.
- [29] R.I. Trezona, I.M. Hutchings, Three-body abrasive wear testing of soft materials, *Wear* 233–235 (1999) 209–221.
- [30] F. James Shackelford, *CRC Materials Science and Engineering Handbook*, 2nd edition, CRC press, 1994, p. 471.
- [31] Y.W. Milman, D.B. Miracle, S.I. Chugunova, I.V. Voskoboinik, N.P. Korzhova, T.N. Legkaya, Mechanical behaviour of Al₃Ti intermetallic and L12 phases on its basis, *Intermetallics* 9 (9) (2001) 839–845 9.
- [32] K.E. Knippling, D.C. Dunad, D.N. Seidman, Nucleation and Precipitation Strengthening in Dilute Al–Ti and Al–Zr Alloys, *Metallurgical and Materials Transactions A* 38A (2007) 2553–2563.